From recovered metal waste to effective catalysts for C–C bond formation

Sean McCarthy

Submitted as a requirement for the degree of
Doctor of Philosophy (PhD)

May 2024

Supervised by Professor James D. E. T. Wilton-Ely and Professor D. Christopher Braddock

Department of Chemistry

Faculty of Natural Sciences

Imperial College London

Abstract

Catalysts containing palladium or gold are ubiquitous in modern synthetic chemistry. However, unrelenting demand for the finite natural reserves of palladium has resulted in supply deficits and record prices. Palladium production is also plagued with the environmental impact of mining and refining processes. The production of gold bears similar economic and environmental challenges. As a result, palladium and gold consumption in their current forms is unsustainable and improvements to the lifecycle of the metals are needed. For both palladium and gold, there exists significant quantities of metal-enriched waste that is typically destined for landfill. These waste streams – waste electronic and electrical equipment, and automotive three-way catalytic converters – offer an valuable 'urban mine' of metals for catalytic applications. This has led to the research of this thesis, which demonstrated the application of molecular palladium and gold compounds which are recoverable from waste as homogeneous catalysts. The molecular gold compounds were explored in chapter two as catalysts for a variety of transformations which broadly covered the mechanistic modes of gold catalysis. Molecular palladium compounds were explored in chapters three and four as catalysts for one of the largest industrial scale Suzuki-Miyaura cross-coupling reactions. The catalytic studies in chapter three were underpinned by a 'Design of Experiments' optimisation, which revealed a non-linear influence of the catalyst loading on the performance of the catalyst. Strategies to isolate and recover palladium for reuse as catalysts have also been presented in chapter three. Kinetic and mechanistic analysis of the recovered palladium compounds presented in chapter four revealed a novel chloride anion mediated catalyst inhibition mechanism alongside aggregation of the active catalyst. The chemical understanding reported in this thesis aims to incentivise increased recycling of metal waste and thus support the transition to a 'closed-loop' consumption of palladium and gold in the chemical industry.

Statement of Originality

I hereby declare that the contents of this thesis are my own work. Work from others, where included, is clearly acknowledged and referenced in the text and acknowledgement sections.

Copyright Declaration

The copyright of this thesis rests with the author. Unless otherwise indicated, its contents are licensed under a Creative Commons Attribution-Non Commercial 4.0 International Licence (CC BY-NC). Under this licence, you may copy and redistribute the material in any medium or format. You may also create and distribute modified versions of the work. This is on the condition that: you credit the author and do not use it, or any derivative works, for a commercial purpose. When reusing or sharing this work, ensure you make the licence terms clear to others by naming the licence and linking to the licence text. Where a work has been adapted, you should indicate that the work has been changed and describe those changes. Please seek permission from the copyright holder for uses of this work that are not included in this licence or permitted under UK Copyright Law.

Acknowledgments

Firstly, a massive thank you to my supervisors, James and Chris. Not only for the thoroughly enjoyable scientific discussions and advice, but also for supporting me in all the additional activities that I was fortunate enough to undertake during my PhD. You have supported both my PhD research and my personal career development, and I am very grateful for that. It has been a pleasure to work with you both, and I hope that we keep in contact. Thank you also to Angela Serpe, whose fundamental work in metal recycling and collaborations with the Wilton-Ely group made this thesis possible.

Thank you also to all of the Wilton-Ely group members, but especially to Tamzin, Rian, Faysal, Khairil and Yu for their assistance and discussions in the lab – it has been a pleasure to work with such a fantastic group of people.

Thank you also to the rEaCt CDT directors – for giving me the opportunity to conduct my PhD at Imperial College and for constructing a programme that has enabled me to learn so many modern chemical techniques. Having started a new job, I've already begun to see how the skills I've learnt through the CDT are going to be vital during my career in chemical research. I feel very fortunate to have gotten the leg-up that the CDT has provided me.

Thank you also to Benjamin Deadman, who provided his time to train me to use the ReactIR which provided some fascinating results. Similarly, thank you to Lisa Haigh who ran all of the mass spectrometry presented in this thesis, and to Andrew White for performing single-crystal X-ray diffraction and solving the structures. Thank you also to Peter Haycock for the useful discussions in the NMR lab and for collecting some of the NMR spectra. Finally, thank you also to Adila Islam and Andrew Rogers for collecting the TEM images presented in this thesis, and to Patricia Carry for running the ICP-MS samples.

The past four years as part of the rEaCt CDT have been so much fun, so thank you to everyone on the CDT, but especially to my cohort. Being a part of a CDT has been fantastic – we've had great scientific discussions, struggled through taught content, and most importantly we laughed together at the pub! I have been lucky enough to form lifelong friendships, and I'm very excited to see how everyone's careers progresses and where we all end up.

Finally, I can't forget to thank Dr Isabella. We have shared so many incredible moments together and you have very quickly become my best friend. I will always cherish the memories that we have, without which my PhD would not have been as enjoyable (or at times bearable!). I am so proud of us both for finishing our PhDs and I can't wait to see what the future holds!

Table of Contents

Chapter One

1.1. Sustainability of palladium in catalysis ... 17

1.1.1. Palladium supply concerns ... 17

1.1.2. Palladium recycling ... 19

1.1.3. Palladium catalysts derived from recycled waste ... 21

1.1.4. Low-loading palladium catalysts ... 37

1.1.5. Reusable homogeneous palladium catalysts ... 47

1.2. Sustainability of gold in catalysis ... 54

1.2.1. Gold supply concerns ... 54

1.2.2. Gold recycling ... 57

1.2.3. Gold catalysts derived from recycled waste ... 60

1.3. Conclusions ... 63

1.4. References ... 64

Chapter Two

2.1. Introduction ... 73

2.1.1. Gold recycling ... 73

2.1.2. Research aims and objectives ... 74

2.1.3. Mechanistic modes of gold catalysis ... 75

2.2. Results and Discussion ... 81

2.2.1. Synthesis of gold complexes 3 and 4 ... 81

2.2.2. Trihalide anion metathesis of 3 and 4 ... 83

2.2.3. Alternative synthesis of Me_2dazdt ... 91

2.2.4. Gold catalysis – Alkyne bond activation ... 94

2.2.5. Gold catalysis – Carbonyl bond activation ... 101

2.2.6. Gold catalysis – Oxidative C–C coupling of arenes and aryl silanes ... 104

2.2.7. Gold catalysis – Catalyst recovery and reuse ... 110

2.2.8. Gold catalysis – Mechanistic analysis ... 113

2.3. Conclusions ... 125

2.4. Future work ... 127

2.5. References ... 129

Chapter Three

3.1. Introduction ... 133

3.1.1. Palladium recycling ... 133

3.1.2. Research aims and objectives 135
3.1.3. $[Cation]_2[Pd_2I_6]$ as a palladium precatalyst 136
3.1.4. Model Suzuki-Miyaura cross-coupling 137
3.2. Results and Discussion 140
3.2.1. Synthesis of $[Cation]_2[Pd_2I_6]$ salts 140
3.2.2. Optimisation of the model cross-coupling reaction 143
3.2.3. Model reaction catalyst performance comparison 153
3.2.4. Model reaction process design 155
3.2.4.1. Catalyst recycling 155
3.2.4.2. Recovery and reuse of tetrabutylammonium bromide 157
3.2.4.3. Unified work-up and recycling procedures 160
3.2.4.4. Expanding the catalyst recycling procedure 165
3.3. Conclusions 169
3.4. Future work 170
3.4. References 171

Chapter Four
4.1. Introduction 175
4.1.1. Research aims and objectives 175
4.1.2. Speciation of active palladium from palladium precatalysts 176
4.1.3. Elucidation of reaction orders and constants 178
4.2. Results and Discussion 180
4.2.1. Visual time normalisation analysis of the model reaction catalysed by $[N^nBu_4]_2[Pd_2I_6]$ 180
4.2.1.1. VTNA Methodology 180
4.2.1.2. Reaction orders in aryl chloride and catalyst deactivation 181
4.2.1.3. Reaction orders in $[N^nBu_4]_2[Pd_2I_6]$ 191
4.2.1.4. Deconvolution of [Active Site] using VTNA 197
4.2.1.5. Quantifying [Active Site] using Transmission Electron Microscopy 199
4.2.1.6. Deconvolution of palladium black formation kinetics using VTNA 207
4.2.2. Mechanism of the reduction of $[N^nBu_4]_2[Pd_2I_6]$ 210
4.2.3. Role of the cation in $[Cation]_2[Pd_2I_6]$ 212
4.3. Conclusions 219
4.4. Future work 222
4.5. References 224

Chapter Five
5.1. Final conclusions and future work 229
5.2. References 234

Chapter Six
6.1. General experimental 237
6.2. Chapter Two Experimental 237
6.2.1. Synthesis of gold complexes 3-6 and 10-12 237
6.2.2. Synthesis of organic substrates for catalytic testing 244
6.2.3. Catalytic testing of gold recovery products 3-6 245
6.2.3.1. Cyclisation of N-propargylic amides 15 and 17 245
6.2.3.2. Cyclisation of 2-phenylethynyline (22) to indole 23 247
6.2.3.3. Condensation of *o*-iodoaniline (24) and acetylacetone (25) 248
6.2.3.4. Addition of nucleophilic arenes to α,β-unsaturated carbonyl compounds 248
6.2.3.5. Oxidative coupling of aryl silanes and arenes 251
6.2.4. Mechanistic studies 255
6.3. Chapter Three Experimental 257
6.3.1. Synthesis of organic iodides for palladium recovery 258
6.3.2. Synthesis of palladium recovery complexes $[Cation]_2[Pd_2I_6]$ 258
6.3.3. HPLC reaction monitoring of the model cross-coupling reaction 260
6.3.4. Initial optimisation of the model cross-coupling reaction 261
6.3.5. Design of Experiments modelling 262
6.3.6. Definitive screening design experimental methodology 263
6.3.7. Final optimised conditions 264
6.3.8. ReactIR reaction monitoring 265
6.3.9. Notes on the commercial source of K_2CO_3 268
6.3.10. Model cross-coupling reaction process design 268
6.3.11. Green metrics 270
6.3.12. ICP-MS analysis 271
6.3.13. Catalyst recycling scope 274
6.4. Chapter Four Experimental 276
6.4.1. VTNA of the model cross-coupling reaction catalysed by $[N^nBu_4]_2[Pd_2I_6]$ 276
6.4.2. Detecting the formation of 1-bromo-2-nitrobenzene (4) 276
6.4.3. Transmission electron microscopy of the model cross-coupling reaction 277
6.4.4. Mechanism of the reduction of $[N^nBu_4]_2[Pd_2I_6]$ 279
6.4.5. Role of the cation in $[Cation]_2[Pd_2I_6]$ 280

6.4.6. Suzuki-Miyaura coupling of 2,4-dihalogenated pyridines 280
6.4.7. More detailed overview of VTNA Background and Methodology 282
6.5. References 289

Chapter Seven
7. Appendix 292
7.1. UV-Vis Spectroscopy 292
7.2. ^{1}H NMR Spectra 295
7.3. ^{13}C NMR Spectra 311
7.4. ^{31}P NMR Spectra 318
7.5. ^{19}F NMR Spectra 320
7.6. 2D NMR 320
7.7. X-Ray crystallographic information 321
7.8. ReactIR Profiles and tabulated data 330
7.9. Transmission electron microscopy 340
7.10. Kinetic elucidation of reaction orders and constants 346
7.11. Journal figure permissions 347

Table of Schemes

Scheme 1. Pd^{2+} adsorption by UiO-66-Pyta, and possible Pd^{2+} binding modes and binding energies… 21
Scheme 2. Products formed from Suzuki-Miyaura coupling catalysed by Pd^0-UiO-66 MOF.[50] 23
Scheme 3. Pd^{2+} recovery by 1 and 2 into an aqueous micellar solution of 3.[51] 24
Scheme 4. Zhao et al. palladium catalysed gelation and palladium capture.[58] 25
Scheme 5. Recovered Pd^0-aerogel as a Suzuki-Miyaura catalyst.[58] 26
Scheme 6. Selected substrate examples in the Pd^0-gel bead catalysed Suzuki-Miyaura reaction… 27
Scheme 7. Selected substrate examples from Søbjerg et al's Bio-Pd^0 as catalysts for Suzuki-Miyaura… 30
Scheme 8. a) Reactivity of the triiodide salt 11 with both Pt^0 and Pd^0. b) Mechanistic rational for the… 32
Scheme 9. Catalytic activity of recovered palladium complex n in the C-H bond functionalisation of… 33
Scheme 10. Wilton-Ely and Serpe oxidation of Pd^0 by the more atom economical 1:1 mixture of… 34
Scheme 11. Mechanochemical oxidation of Pd^0 metal and subsequent transformation into some… 35
Scheme 12. Selected substrate examples from Zengin's report on the use of scrap TWC powder… 36
Scheme 13. Luque et al. application of scrap TWC powder as an in-flow hydrogenation catalyst… 36
Scheme 14. Selected substrate examples from Kwong et al $Pd(OAc)_2$/21 catalysed Suzuki-Miyaura… 38
Scheme 15. Selected substrate Suzuki-Miyaura coupling examples catalysed by 25.[85] 40
Scheme 16. Palladacycle 26-catalysed Suzuki-Miyaura coupling at low palladium loadings.[86] 41
Scheme 17. Carrow et al. cyclometallation stability of PAd_3 complex 27, compared to Hartwig's… 42
Scheme 18. Suzuki-Miyaura coupling catalysed by carbene complex 29 selected substrate examples.[89] 42
Scheme 19. Selected Buchwald-Hartwig coupling substrate examples, catalysed by low-loading 30.[89] 43
Scheme 20. Selected substrate examples from Xu et al. Suzuki-Miyaura reaction catalysed by… 45
Scheme 21. Lorenz et al. rare application of a palladium catalyst at a low loading as part of a multi-kg… 46
Scheme 22. Akhavan and Karimi water-soluble NHC-Pd polymer 32 as a reusable Suzuki-Miyaura… 48
Scheme 23. Domínguez et al. reusable homogeneous palladium pincer complex 33 as a catalyst for… 48
Scheme 24. Riisager et al. ethylene methoxycarbonylation catalysed by homogeneous… 49
Scheme 25. Bergbreiter et al. Buchwald-Hartwig amination catalysed by $Pd(dba)_2$ and phosphine 36… 51
Scheme 26. Stille coupling catalysed by a reusable polymer-supported NHC palladium complex (37).[142] 52
Scheme 27. Spiropyran precatalyst 38, and pH dependent structure and solubility which permitted… 53
Scheme 28. Cyclisation of 4-pentyn-1-ol catalysed by Au^{3+}-loaded MOF. 62
Scheme 29. McAuliffe's pioneering research on the use of dihalogen-pnictogen adducts, $Me_3E{\cdot}I_2$,… 73
Scheme 30. Deplano et al. oxidation of Au^0 by bis(dihalogen) adducts Me_2dazdt·2IX 1 and 2.[2,3] 74
Scheme 31. Selected substrate examples from Hashmi et al. cyclisation of terminal… 76
Scheme 32. Hashmi et al. proposed cyclisation of N-propargylamides mechanism… 76
Scheme 33. Arcadi et al. cyclisation of 2-alkynylanilines and one-pot halogenation catalysed by… 77
Scheme 34. Arcadi et al. activation of 1,3-dicarbonyl compounds toward nucleophilic attack catalysed… 78
Scheme 35. Dyker and Hashmi et al. activation of α,β-unsaturated carbonyl compounds toward the… 78
Scheme 36. a) Strain energy barrier associated with distortion of linear Au^{1+} to approximately square… 79
Scheme 37. Selected examples from Russell and Lloyd-Jones oxidative cross-coupling catalysed by… 80
Scheme 38. Synthesis of Me_2dazdt·IX adducts 1 and 2. 81
Scheme 39. Oxidation of Au^0 metal powder by Me_2dazdt·IX. 81
Scheme 40. Recovery of complex 3a from scrap SIM cards using Serpe's patented process.[4] 83
Scheme 41. Failed anion metathesis using Zn^0 metal and AgOTf, which instead yielded bimetallic… 85
Scheme 42. Trimethyloxonium tetrafluoroborate as a reagent for anion metathesis. a) Irreversible… 87
Scheme 43. Unsuccessful anion metathesis of complexes 3 and 4 by the immediate addition of… 88
Scheme 44. a) Solution behaviour of complexes 3 and 4 in acetone with pictures illustrating colour… 90
Scheme 45. a) Viehe et al. synthesis of dithiooxamides from glyoxal and S_8.[42] b) This study –… 91
Scheme 46. Direct thioamidation of aldehydes in water.[43] 92
Scheme 47. Direct amidation of benzoic acid and propargylamine by TMOS. 94
Scheme 48. Synthesis of non-terminal alkyne 17 via Sonogashira coupling. 96
Scheme 49. Confirmation of 5-exo structure in 20 by lithiation and subsequent protonolysis to yield 18. 98
Scheme 50. Three possible mechanisms of the formation of vinyl iodide 20. 99
Scheme 51. $[Ph_3PAu]$OTs precatalyst activation reported by Russell and Lloyd-Jones.[29] 110

Scheme 52. Some typical mechanistic pathways seen for literature gold(I) and gold(III) catalysts. 113
Scheme 53. Possible mechanistic pathways to enable substrate binding by generating a vacant… 114
Scheme 54. Unsuccessful attempt at employing a base to trap a vinyl gold intermediate from… 115
Scheme 55. Synthesis of gold(I) complex 30 during an unsuccessful attempt at trapping a vinyl gold… 115
Scheme 56. Formation of a vinyl gold intermediate from the reaction of complexes 3 and 5… 116
Scheme 57. Chemical distinction between either possible vinyl gold (32) and vinyl iodide (33) … 118
Scheme 58. Unsuccessful attempt at employing a proton sponge to trap a vinyl gold intermediate… 118
Scheme 59. The Gutmann-Beckett method for quantifying Lewis acid oxophilicity ([LA] = Lewis Acid). 119
Scheme 60. Hydrolysis of tetrafluoroborate in acetone-d_6 and resulting hydrolysis products… 122
Scheme 61. a) Identical colour change observed upon the dissolution of complexes 3-6/11-12 in… 123
Scheme 62. Synthesis of gold complexes 3 and 4 from gold powder. 125
Scheme 63. Recovery of 3 from scrap SIM cards using Me_2dazdt•$2I_2$ 125
Scheme 64. Two anion metathesis strategies employed for the synthesis of a range of gold(III) … 126
Scheme 65. Overview of substrates and modes of catalytic activity explored for gold complexes 3-6 127
Scheme 66. Future work which could: a) Improve on previously unsuccessful attempt at isolating… 128
Scheme 67. a) Oxidation and dissolution of metallic Au^0 by potassium iodide/triiodide… 133
Scheme 68. Transformation of $[N^nBu_4]_2[Pd_2I_6]$ into three phosphine complexes that are often… 136
Scheme 69. Model Suzuki-Miyaura coupling utilised throughout the kinetic and mechanistic… 137
Scheme 70. Literature example of the Suzuki-Miyaura reaction yielding 3. 140
Scheme 71. Mechanistic rationalisation for the non-linear and influence of catalyst loading… 150
Scheme 72. Modified and simplified mechanism for the aggregation of $[Pd^0]$ in the presence… 152
Scheme 73. Mechanistic rationale for the 'reactivation' of palladium black by catalytic aryl iodide (5). 156
Scheme 74. Full process design for the model cross-coupling reaction, including catalyst recycling,… 160
Scheme 75. Full process design for the model cross-coupling reaction, including catalyst recycling,… 163
Scheme 76. Model cross-coupling reaction yielding 3 catalysed by $[N^nBu_4]_2[Pd_2I_6]$ at a low catalyst… 169
Scheme 77. Aggregation of active Pd^0 was implicated for the model cross-coupling reaction… 175
Scheme 78. Atypical C4 selectivity in the coupling of 2,4-dichloropyridine via multinuclear active $[Pd^0]$.[37] 178
Scheme 79. Complete model cross-coupling reaction scheme, including all of the possible side… 180
Scheme 80. Postulated mechanistic cycle for the protodehalogenation of 1 based on the formation… 189
Scheme 81. Arresting β-hydride elimination by performing the reaction in ^{t}BuOH. Under these… 190
Scheme 82. Cross-coupling reaction yielding 3 run at a catalyst loading below the concentration… 195
Scheme 83. Reduction in the fraction of active sites at loadings >0.033 mol% which dominates… 196
Scheme 84. Increase in intrinsic activity as a result of aggregation at increased loadings that… 196
Scheme 85. a) Dissolution of $[N^nBu_4]_2[Pd_2I_6]$ in 1-butanol and in the absence of aryl chloride (1)… 210
Scheme 86. Suzuki-Miyaura coupling of 7 and 8 catalysed by $[N^nBu_4]_2[Pd_2I_6]$. 216
Scheme 87. Mechanistic rationalisation for the influence of $[PPh_4]^+$ on the C2/C4 selectivity of the… 218
Scheme 88. Possible role of tetraphenylphosphonium as a cross-coupling reagent and subsequent… 219
Scheme 89. Summary of the transformations which were successfully catalysed by gold recovery… 230
Scheme 90. New catalytic activity obtained for an "oxophilic" gold Lewis-acid, compared to the… 231

Table of Figures

Figure 1. Palladium, gold and platinum price (GBP/gram) since 06/04/2015. Data mined from… 17
Figure 2. Five examples of large-scale industrial cross-coupling reactions catalysed by palladium… 18
Figure 3. Johnson Matthey TWC recycling process. Heating step performed at ~1600 °C in an… 20
Figure 4. Overview of techniques employed in the hydrometallurgical separation of palladium… 20
Figure 5. Capture and reduction of Pd^{2+} from a mixed metal ethylene glycol/water solution… 22
Figure 6. Palladium on carbon black nanoparticles synthesised by impact electrochemical… 26
Figure 7. Smith et al. hybrid gel components used to synthesise Pd-loaded gel beads.[60] 27
Figure 8. Bedford et al. comparison of palladacycle activity in the Suzuki-Miyaura cross-coupling… 39
Figure 9. De Vries low-loading $Pd(OAc)_2$ catalysed Heck reaction with a comparison of catalyst… 44
Figure 10. Riisager et al. ethylene methoxy carbonylation reaction mixture, with the palladium… 50
Figure 11. Environmental impact of gold production. a) Cradle-to-gate global warming… 55
Figure 12. Selected modern examples of homogeneous gold catalysis. 56
Figure 13. Umicore WEEE refinery plant overview. Reproduced directly from reference 183 (Open Access). 59
Figure 14. PA12 Adsorbent used to recover Au^{3+} ions from an acidic mixed metal WEEE… 60
Figure 15. Liu et al Au^{3+} capture and subsequent supported Au^0 nanoparticle formation… 61
Figure 16. Single crystal X-ray diffraction structures of Ca^{2+}/Cu_6^{2+} MOF decorated with… 62
Figure 17. Tetrafluoroborate anion metathesis products 5 and 6. 75
Figure 18. The X-ray crystal structure of $[Me_2dazdt(AuBr)_2]$ (10) illustrating the chain of molecules… 86
Figure 19. Single-crystal X-ray diffraction structures for complexes 5 and 6 (thermal ellipsoids… 88
Figure 20. Single-crystal X-ray structure of anion metathesis product 11 (thermal ellipsoids… 91
Figure 21.Two possibly vinyl iodide products 5-exo 20 and 6-endo 21 from the cyclisation… 97
Figure 22. Definitive screening design predictive model for the oxidative cross-coupling… 106
Figure 23. Definitive screening design predictive model for the oxidative cross-coupling yielding 28… 107
Figure 24. Recovery and reuse of gold complexes 3-6 in the addition of 2-iodoaniline to acetylacetone. 111
Figure 25. Recovery and reuse of gold complex 3 in the addition of 2-methlyfuran to methyl vinyl ketone. 112
Figure 26. Recovery and reuse of gold complexes 3-6 in the cyclisation of N-propargylbenzamide. 112
Figure 27. Single-crystal X-ray structure of gold(I) complex 30 (thermal ellipsoids drawn at 50%… 115
Figure 28. 2,6-di-^{t}Bu-pyridinium ^1H (blue, bottom) and $^1H\{^{14}N\}$ (red, top) decoupled NMR spectra. 116
Figure 29. Possible products and associated ^1H NMR data from the stoichiometric reaction of… 117
Figure 30. Comparison of the ^{31}P Δδ values obtained for complexes 3-6 (a) with literature… 120
Figure 31. Alternative gold complexes which may exhibit improved solubility in protic and… 128
Figure 32. Definitive screening design predictive model for the cross-coupling yielding 3 catalysed… 147
Figure 33. Definitive screening design predictive model for the cross-coupling yielding 3 catalysed… 148
Figure 34. Definitive screening design predictive model for the cross-coupling yielding 3 catalysed… 149
Figure 35. Definitive screening design predictive model for the cross-coupling yielding 3 catalysed… 152
Figure 36. Temporal concentration profile for the model cross-coupling to yield 3, catalysed by… 154
Figure 37. Attempt at 'reactivating' palladium black from a model reaction run by the addition… 157
Figure 38. Kinetic profiles for four repeats of the model cross-coupling under the standard reaction… 161
Figure 39. ICP-MS data illustrating a large buildup of residual palladium in the reaction mixture… 162
Figure 40. a) Kinetic profiles for five repeats of the model cross-coupling under the standard… 164
Figure 41. a) Observation of a power law in the relationship between TOF and Pd loading… 177
Figure 42. Temporal concentration profiles for the consumption of 1 and formation of 3… 181
Figure 43. a) Two original ReactIR profiles at [1] = 0.70 M (blue) and 0.56 M (red). b) Two… 182
Figure 44. A comparison of the visual overlap of the two 'different excess' profiles at an: a)… 183
Figure 45. a) Non-overlapping 'same excess' and standard conditions indicated catalyst… 184
Figure 46. a) Overlapping ‘same excess’ and standard conditions when $[N^nBu_4]Cl$ was also… 185
Figure 47. Both ‘different excess’ reactions were run in the presence of 2 equiv. of KBr. 186
Figure 48. Rationalisation for observed reaction order in [1] of 0.9 at the beginning of the… 187
Figure 49. Rationalisation for observed reaction order in [1] of 0.5 toward the end of the… 187
Figure 50. Formation of aryl bromide 4 as a mechanistic ‘handle’ to confirm the postulated… 188
Figure 51. Application of VTNA to determine the reaction order in $[N^nBu_4]_2[Pd_2I_6]$ at 0.011/0.022… 192

Figure 52. Application of VTNA to determine the model reaction orders in $[N^nBu_4]_2[Pd_2I_6]$, at… 193
Figure 53. a) Temporal [1] profile was linearised using the top equation. Profiles do not overlap… 197
Figure 54. a) A plot of deconvoluted [Active Site] against $[N^nBu_4]_2[Pd_2I_6]$ loading. b) A plot… 198
Figure 55. Four literature examples of class-II surface sensitivity nanoparticles. a) Influence… 199
Figure 56. Two TEM images of an aliquot of the model reaction mixture. The sample was filter… 200
Figure 57. Final procedure for stabilising and preparing the reaction samples for imaging by TEM… 201
Figure 58. a) TEM image of an aliquot of the model reaction mixture which was diluted into… 202
Figure 59. Comparison of the DLS data of a fresh aliquot of the model reaction mixture (red) … 203
Figure 60. A cuboctahedral palladium nanoparticle of 2.1 nm. a) LCN surface sites labelled… 204
Figure 61. Values of [Active Site] determined by TEM (blue) and by deconvolution of the reaction… 205
Figure 62. a) Non-overlapping VTNA profiles using $[N^nBu_4]_2[Pd_2I_6]$ at an order of 1.1. b)… 206
Figure 63. Application of VTNA to determine the model reaction orders in $[N^nBu_4]_2[Pd_2I_6]$,… 207
Figure 64. a) Linearisation of temporal [1] profile at 0.066 mol% $[N^nBu_4]_2[Pd_2I_6]$ loading… 208
Figure 65. a) Deconvoluted temporal [Pd] from linearised temporal [1] profiles (Figure 65). b)… 209
Figure 66. Cross-coupling yielding 3 catalysed by $[N^nBu_4]_2[Pd_2I_6]$ (red) and $[PPh_4]_2[Pd_2I_6]$… 212
Figure 67. Cross-coupling reaction to yield 3 from 1 and 2 catalysed by a series of… 213
Figure 68. Cross-coupling yielding 3 catalysed by $[N^nBu_4]_2[Pd_2I_6]$ in the presence of 0.088 mol%… 214
Figure 69. Cross-coupling reaction to yield 3 catalysed by 0.044 mol $[N^nBu_4]_2[Pd_2I_6]$ with… 215
Figure 70. Cross-coupling reaction yielding 3 catalysed by 0.044 mol% $[N^nBu_4]_2[Pd_2I_6]$… 216
Figure 71. Surmounting chloride mediated catalyst deactivation and subsequent mechanistic… 220
Figure 72. Evidence for the role of nanoparticles formed from $[N^nBu_4]_2[Pd_2I_6]$ in the cross-coupling… 220
Figure 73. Influence of $[PPh_4]^+$ cations on the catalytic activity of the nanoparticles formed from… 222
Figure 74. The synthesis of Boscalid and the possibility of applying $[N^nBu_4]_2[Pd_2I_6]$ as a catalyst… 223
Figure 75. Left: Two literature palladium complexes with ligands designed to improve the steric… 229
Figure 76. Top: Comparison of literature models for the stabilisation of palladium nanoparticles… 233
Figure 77. Monitoring ReactIR peak at 1111 cm^{-1} over time (Left: original spectrum, right:… 266
Figure 78. Monitoring ReactIR peak at 750 cm^{-1}. Peak assigned to cross-coupling product (3) … 266
Figure 79. Left: Comparison between peak intensities at 1111 cm^{-1} in a 1-chloro-2-nitrobenzene… 267
Figure 80. Example of how initial rates are determined and its pitfalls demonstrated on an… 283
Figure 81. RPKA applied to the ‘different excess’ reaction curves for entries 1-3 in Table 58… 285
Figure 82. Non-overlapping 'Same excess' indicated catalyst deactivation/product inhibition… 287
Figure 83. Normalisation of temporal [P] profiles from reactions 1 and 2 (Table 55) for a… 288

Table of Tables

Table 1. Comparison of rate constants for the catalytic reduction of 4-nitrophenol to 4-aminophenol.[50] 23
Table 2. Suzuki-Miyaura coupling catalysed by aqueous micellar palladium recovered from MLCCs.[51] 24
Table 3. Catalytic activity of two bio-supported Pd^0 nanoparticles in the hydrogenation of itaconic acid.[63] 28
Table 4. 2-pentyne hydrogenation catalysed by E. Coli bio-Pd^0, with comparisons made to… 29
Table 5. Oxidation of Pd^0 in model scrap TWCs by dithiooxamide·I_2 8 as reported by Deplano,… 31
Table 6. Suzuki-Miyaura reaction catalysed by 38, which was reused eight times, with details… 53
Table 7. Concentration of copper, silver and gold present in gold-enriched ores and mobile phones.[175,176] 57
Table 8. Global emissions from WEEE disposal and recycling, assuming 20 Mt/year of global… 58
Table 9. Reaction conditions explored for the anion metathesis of 3 to yield BF_4^- salt 5. 84
Table 10. Synthesis of Me_2dazdt using S_8 in water. 93
Table 11. Cyclisation of N-propargylbenzamide (15) catalysed by 3-6. 95
Table 12. Cyclisation of non-terminal alkyne 17 catalysed by 3-6. 96
Table 13. Cyclisation of 2-phenylethynyline (22) to indole 23 catalysed by 3-6. 100
Table 14. Condensation of 1,3-dicarbonyl 24 and aniline 25 to β-enaminone 26 catalysed by 3-6. 101
Table 15. Addition of nucleophilic arenes to electrophilic α,β-unsaturated carbonyl compounds… 103
Table 16. Optimisation of the oxidative coupling of 26 and 27 using gold complex 3. 104
Table 17. Reaction variables included in the DoE optimisation of the oxidative coupling of 26 and 27. 105
Table 18. Definitive screening design predictive model for the oxidative cross-coupling yielding… 106
Table 19. Definitive screening design predictive model validation – Comparison of the… 108
Table 20. Oxidative cross-coupling of aryl silanes and arenes catalysed by recovered complexes 3 and 4.[a] 109
Table 21. Gutmann-Beckett analysis of gold complexes 3-6 with triphenylphosphine oxide in MeCN-d_3. 120
Table 22. Gutmann-Beckett analysis of gold complexes 3-6 with triphenylphosphine oxide in acetone-d_6. 121
Table 23. Attempted 5-catalysed fluorination of either phenylacetylene or 1,2-diphenylethyne. 124
Table 24. Recovery of palladium from model scrap TWCs by triiodides in methyl ethyl ketone.[7] 134
Table 25. Comparison of the performance of a series of recovered palladium complexes and… 136
Table 26. Palladium complexes which have been utilised for the cross-coupling reaction… 139
Table 27. Synthesis of $[Cation]_2[Pd_2I_6]$ salts from palladium, organic [cation] iodides and iodine.[a, 7] 142
Table 28. Initial optimisation results for the cross-coupling reaction yielding 3 catalysed by… 144
Table 29.Reaction variables included in the DoE optimisation of the model cross-coupling reaction.[a] 145
Table 30. Definitive screening design predictive model for the cross-coupling yielding 3… 146
Table 31. Definitive screening design predictive model for the cross-coupling yielding 3… 147
Table 32. Definitive screening design predictive model validation – Comparison of the… 151
Table 33. Comparison of the performance of three different palladium precatalysts in the… 153
Table 34. Application of palladium recovered from a model reaction as a catalyst in a second run.[a] 155
Table 35. Partitioning of $[N^nBu_4]Br$ into various organic solvents upon extraction with water.[a] 158
Table 36. Recovery of the tetrabutylammonium salts from the model reaction mixture and… 159
Table 37. Recovery yields of $[N^nBu_4]_2[Pd_2I_6]$ for each reaction run. 161
Table 38. Five model reaction repeats on a 0.5 mol scale, with $[N^nBu_4]_2[Pd_2I_6]$ and $[N^nBu_4]Br$… 164
Table 39. Recovery of $[N^nBu_4]_2[Pd_2I_6]$ from palladium waste isolated from the model cross-coupling… 166
Table 40. C-H activation reaction of benzo[h]quinoline catalysed by $[N^nBu_4]_2[Pd_2I_6]$ and subsequent… 167
Table 41. Synthesis of 13 by a Mizoroki-Heck reaction catalysed by $[N^nBu_4]_2[Pd_2I_6]$ and subsequent… 168
Table 42. Comparison of the performance of $[N^nBu_4]_2[Pd_2I_6]$ with a state-of-the-art catalyst for… 170
Table 43. Reaction conditions and starting concentrations for the reaction profiles presented in… 182
Table 44. Reaction conditions and starting concentrations for the reaction profiles presented in… 183
Table 45. Reaction conditions and starting concentrations for the reaction profiles presented in… 184
Table 46. Reaction conditions and starting concentrations for the reaction profiles presented in… 185
Table 47. Comparison of protodehalogenation products in deuterated and non-deuterated solvents.[a] 189
Table 48. Reaction conditions and starting concentrations for the reaction profiles presented in… 192
Table 49. Reaction conditions and starting concentrations for the reaction profiles presented in… 193
Table 50. Conditions explored for stabilising Pd^0 to enable TEM imaging. 200
Table 51. Average particle diameters obtained from TEM imaging of PVP-stabilised aliquots of the… 203

Table 52. [Active Site] values determined from average particle diameters and the corresponding… 205
Table 53. The reduction of $[N^nBu_4]_2[Pd_2I_6]$ in the presence of K_2CO_3 and $[N^nBu_4]Br$ in different solvents. 211
Table 54. Suzuki-Miyaura coupling of 9 and 8 catalysed by different palladium complexes in the… 217
Table 50. Design of experiments (DoE) definitive screening design – Variables and variable limits. 251
Table 51. DoE design and results table. 252
Table 57. Definitive screening design predictive model for the cross-coupling yielding 3 –… 263
Table 58. Aldol addition of 5 to 6 and 'different excess' kinetic experiments. Data taken from the… 284
Table 59. Hydrolytic ring opening of epoxide 9 and 'same excess' kinetic experiments. Data taken… 286
Table 60. Simulated dataset to demonstrate VTNA. Data is openly available from reference 60. 288

List of Abbreviations

TWC – Three-way catalytic converter
WEEE – Waste electrical and electronic equipment
MOF – Metal organic framework
ICP-AES – Inductively coupled plasma-atomic emission spectroscopy
ICP-MS – Inductively coupled plasma-mass spectrometry
SEM – Scanning electron microscopy
NP – Nanoparticles
TEM – Transmission electron microscopy
MLCC – Multi-layer ceramic capacitors
TON – Turnover number
TOF – Turnover frequency
CB – Carbon black
DFT – Density functional theory
Me_2dazdt – *N,N'*-dimethyl-perhydrodiazepine-2,3-dithione
TGA – Thermogravimetric analysis
NHC – *N*-heterocyclic carbene
TFA – Trifluoroacetate
PEG – Polyethylene glycol
SBMI – 1-methyl-3-(4-sulfobutyl)-1H-imidazolium
p-TSO – *p*-tolyl sulfonate
PA12 – Polyamide-12/Nylon-12
TEMPO – (2,2,6,6-Tetramethylpiperidin-1-yl)oxyl
Piv – Pivaloyl ($COCMe_3$)
NPhth – *N*-phthalimido
TMOS – Tetramethylorthosilicate
DoE – Design of Experiments
DSD – Definitive screening design
$(PhNH)_2$DTL – bis(phenylamino)-1,2-dithiolylium
VTNA – Visual Time Normalisation Analysis
RPKA – Rate Progress Kinetic Analysis
CTAB – Cetyltrimethylammonium bromide
PVP – Polyvinylpyrrolidone
DLS – Dynamic light scattering

Chapter 1 – Introduction: The Sustainability of Gold and Palladium in Catalysis

1.1. Sustainability of palladium in catalysis

1.1.1. Palladium supply concerns

Palladium is a critical element – numerous modern technologies rely on the supply of palladium. Yet, palladium is a finite natural resource present in a very low natural abundance. Unrelenting demand for palladium has consequently compromised the supply of the metal.[1,2] This demand has outweighed supply since 2016 and has culminated in record prices (Figure 1).[3–5] These price increases were exacerbated by the 2015 Volkswagen diesel emission scandal, which led to an increased demand for palladium-based three-way catalytic converters (TWC) which are used in petrol engines in place of platinum-based technology.[6] Moreover, recent geopolitical events in Russia, supplier of 28% of global palladium, resulted in a record breaking price for the metal in February 2022 (£81/gram).[3,7] Both the record palladium price and overall price increases outweigh those seen for gold and platinum (Figure 1). These extreme price increases have prompted a transition toward platinum-based TWC technology,[3] which has recently resulted in a reduction in the cost of palladium.

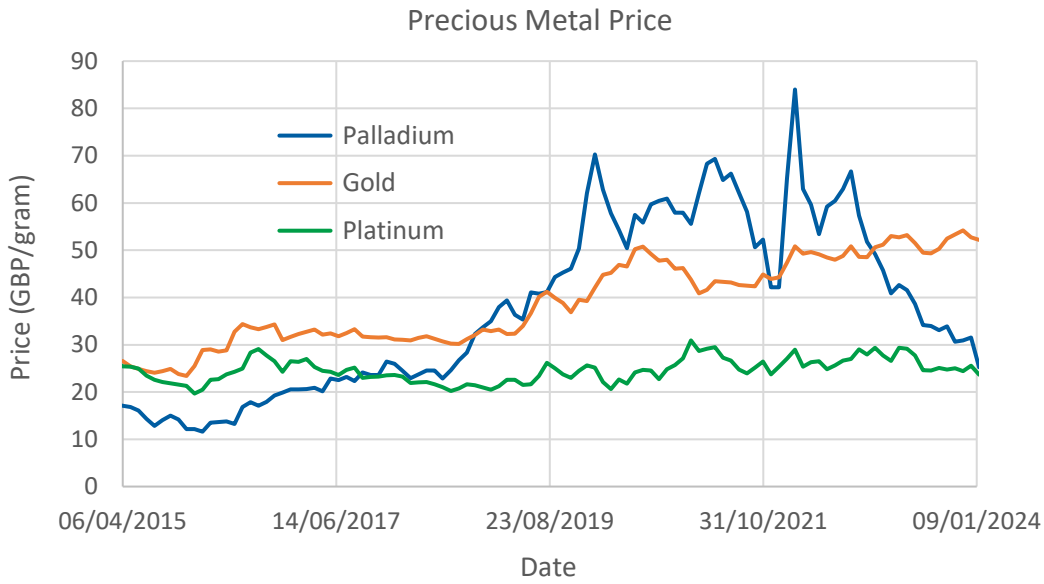

Figure 1. Palladium, gold and platinum price (GBP/gram) since 06/04/2015. Data mined from Bullion Vault and replotted in excel.[7]

The supply of palladium is also plagued with significant environmental concerns. The presence of other transition metals alongside the low concentration of palladium in ore (<10 g/tonne) means that the production of palladium is highly resource intensive.[8] Pyrometallurgical refining involves heating at 800–1450 °C,[9] whilst subsequent hydrometallurgical steps typically utilise Cl_2 and NO_x releasing reagents like *aqua regia*.[10] Consequently, the production of one kilogram of palladium is reported to emit 3880 kg of CO_2 equivalents (CO_2e), a value which is higher than that reported for aluminium (8 kg CO_2e/kg) , iron (2 kg CO_2e/kg), copper (3 kg CO_2e/kg) and zinc (3 kg CO_2e/kg).[11] The

high environmental and economic costs associated with palladium refining has also resulted in limited global secondary palladium supplies of ~25-30%,[3–5,12,13] in spite of the high recycling rates (~100%) reported by Johnson Matthey.[14] Thus, the supply of palladium is unsustainable in its current form.

The synthesis of fine chemicals is an area of industry that is dependent on the supply of palladium. Palladium catalysed C–C and C–N bond forming reactions are amongst the most common in medicinal and agricultural chemistry.[15–20] The impact of palladium mediated cross-coupling reactions prompted the award of the 2010 Nobel prize in chemistry to Heck, Negishi and Suzuki.[21] These catalytic transformations have become crucial in applications that range from bench scale research to industrial production. Figure 2 summarises a handful of hundreds of known examples wherein a palladium catalysed step has been applied in the industrial synthesis of fine chemicals.[15–20]

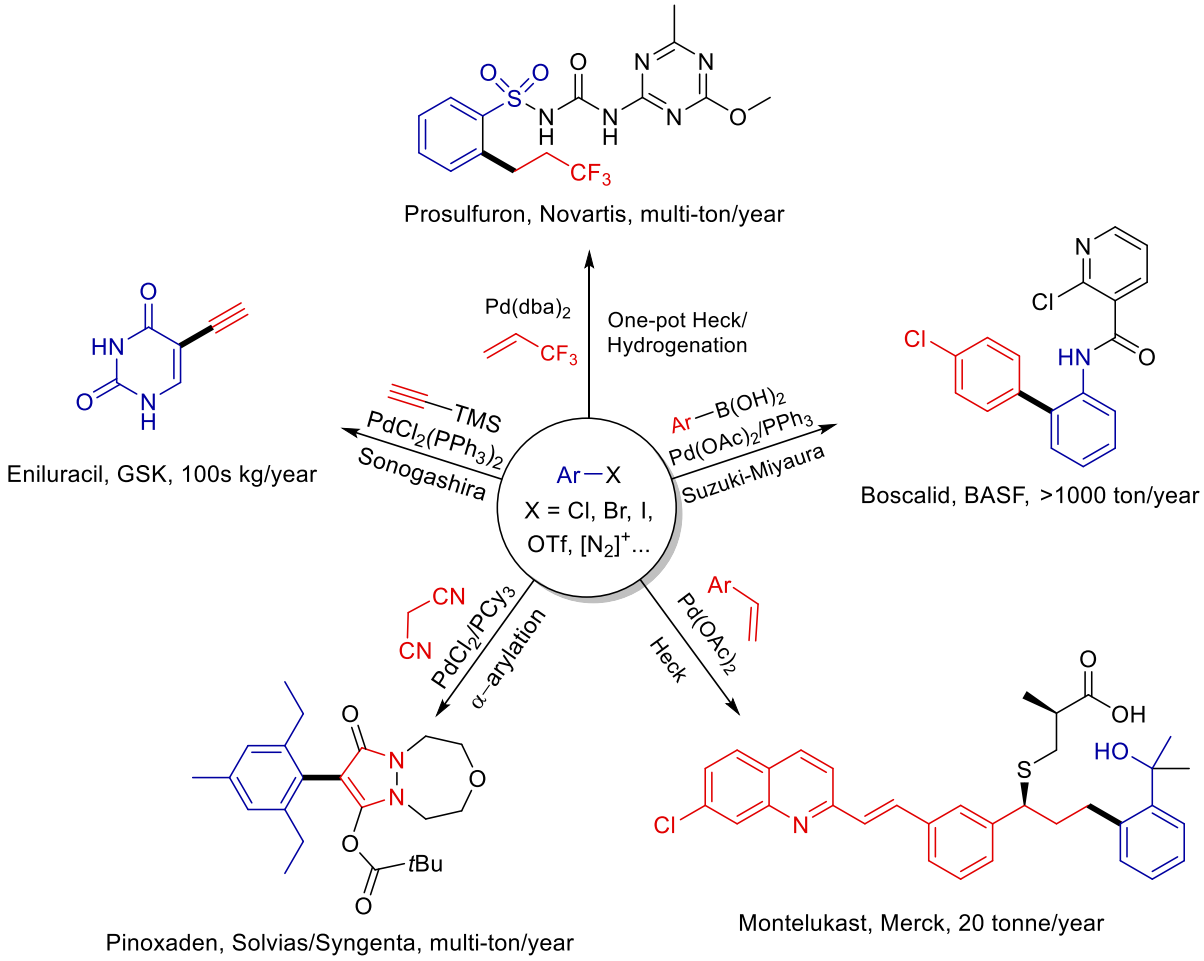

Figure 2. Five examples of large-scale industrial cross-coupling reactions catalysed by palladium complexes.[15–20]

The efficiency and scope of palladium-facilitated sp^2–sp^2 bond formation has even biased molecular drug discovery toward sp^2 dominated structures.[22,23] It is thus clear that palladium catalysis is entrenched within the pharmaceutical and agrochemical industries. Given the growing concerns over

the supply of palladium metal, both the supply and consumption of palladium catalysts must be rendered more sustainable if society is to continue benefiting from the many useful properties of this metal.

Various strategies have emerged to address palladium supply concerns. These broadly aim to: a) source palladium in a more sustainable way e.g. from waste materials; or b) consume palladium in a more sustainable way e.g. by employing highly-active and highly-stable catalysts that function at low catalyst loadings, or by employing palladium catalysts that can be recovered and reused.[24] The following discussion will cover selected examples of these approaches.

It is worth noting that a great deal of effort has also been focused on replacing palladium catalysts entirely. Metals that are more abundant than palladium (e.g. Fe, Co, Ni, Cu) have exhibited promising catalytic activities toward a range of palladium catalysed transformations.[25–28] Whilst significant advancements have been made, the precatalysts of these third-row transition metals are often unstable and require inert handling, or require strong reducing agents to access active [M^0] species from their [$M^{n>0}$] precatalyst, which consequently limits substrate scope. Moreover, many third-row transition metal catalysts do not react with the *soft* organometallic reagents (e.g. boronated aryl species) that are typically encountered in palladium catalysis. These limitations have led to significant inertia in attempts to replace palladium catalysts. Thus, improved palladium sustainability in the chemical industry remains a key goal.

1.1.2. Palladium recycling

Unrelenting demand for palladium metal is driven by its application in automotive three-way catalytic converters (TWCs). Palladium is present in TWCs as metallic Pd^0, where it is utilised as a catalyst for the oxidation of exhaust carbon monoxide and hydrocarbon emissions. In addition, the high thermal stability and conductivity of palladium metal make it a key component in electronic equipment. These two applications account for 90% (84% automotive catalytic converters, 6% electronic equipment) of global palladium demand.[3] The concentration of palladium in catalytic converters (2 kg/tonne), and waste electrical and electronic equipment (WEEE) (300 g/tonne) is orders of magnitude higher than that found in palladium ore (<10 g/tonne).[8] As a result, the finite lifetime of TWCs render them an excellent 'urban-mine' for palladium. However, the stability of metallic Pd^0 and presence of a range of other elements in TWCs and WEEE (Pt, Rh, Al, Ce, Ca, Mg, Al, Pb, Fe, Ce, Cu, Zn, Mn, Cr, Cd, Au, Ag, etc.)[29–32] makes the separation of palladium challenging. For example, the Johnson Matthey process for recycling TWCs involves smelting the waste material in electric arc furnaces at ~1600 °C, followed by extensive hydrometallurgical refining (Figure 3).[33,34]

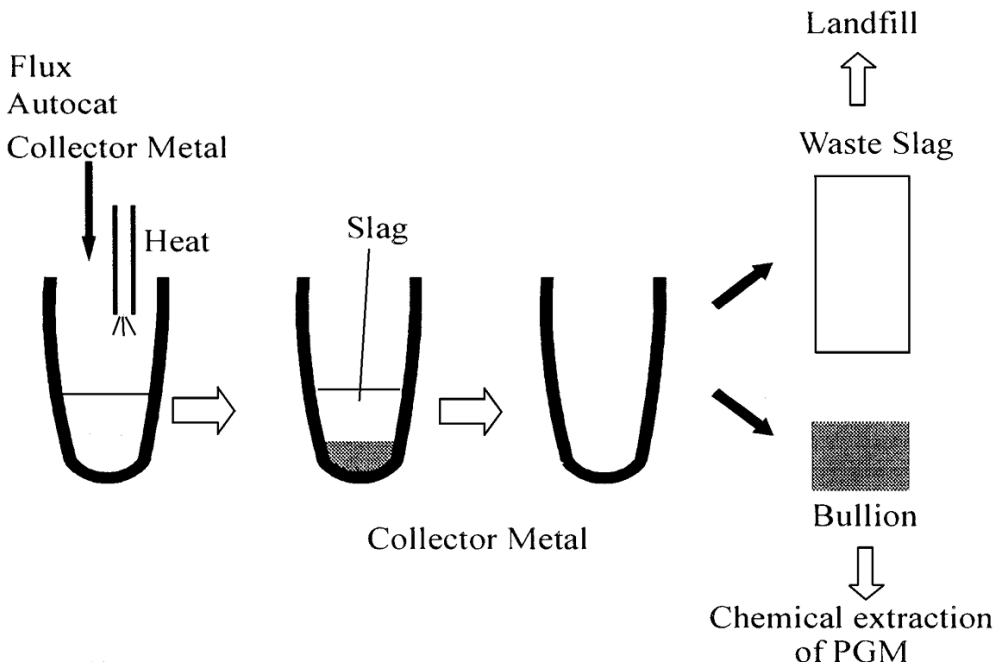

Figure 3. Johnson Matthey TWC recycling process. Heating step performed at ~1600 °C in an electric arc furnace. Reproduced with permission from reference 34.

Palladium recycling consequently comes at a significant resource and environmental cost. A lifecycle assessment conducted by Ramnäs and Amatayakul reported that TWC recycling resulted in increased emissions and energy consumption when compared to primary production from palladium ore.[35] The authors attributed this to the increase in natural gas and oil consumption during recycling outweighing any decrease in coal consumption used in generating energy for mining. As a result, a number of methods which aim to achieve a more sustainable recovery of palladium from scrap TWCs and WEEE have emerged (Figure 4).

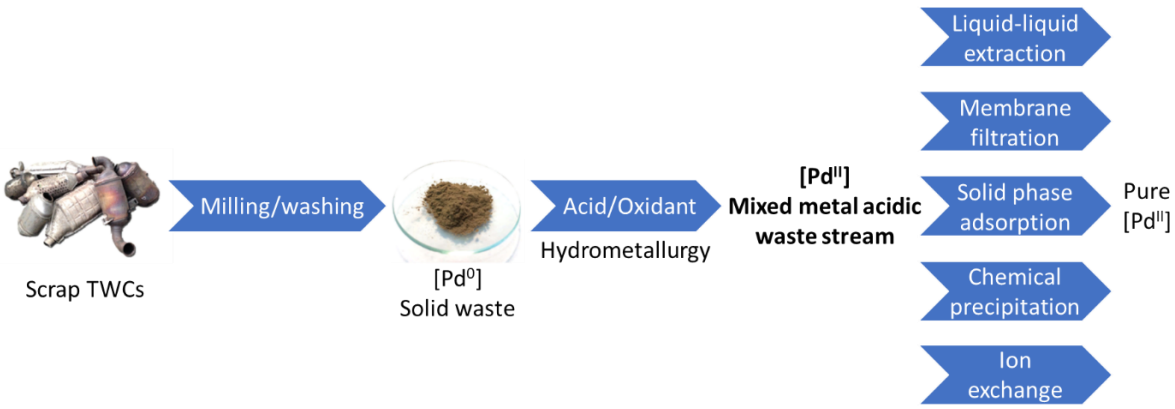

Figure 4. Overview of techniques employed in the hydrometallurgical separation of palladium from scrap TWCs.

Research efforts have primarily focused on hydrometallurgy, as it is considered to be less resource intensive than pyrometallurgy. Typically, the TWC waste material is milled and washed, and the resulting mixed metal powder oxidised under acidic conditions (Figure 4). The resulting mixed metal acidic solution is subsequently manipulated to selectively remove palladium. Liquid-liquid extraction,[36,37] solid-phase adsorption,[38,39] chemical precipitation,[40,41] membrane filtration and ion-exchange have all been employed to recover palladium from the mixed metal solution (Figure 4).[42,43] All of these strategies have been reviewed extensively and will be not be covered here.[30,44–48] Instead, this section will detail examples of palladium catalysts which have been sourced from end-of-life waste streams.

1.1.3. Palladium catalysts derived from recycled waste

The prominence of hydrometallurgy has prompted a number of research teams to utilise acidic metal waste streams as a direct source of palladium for catalysis. For example, García *et al*. recently utilised a zirconium-based metal organic framework (MOF), UiO-66-Pyta, to adsorb and recover Pd^{2+} from an acidic solution.[49] Pyridyl-triazole functionality was introduced into UiO-66-Pyta in order to improve the rate and capacity of palladium adsorption (Scheme 1).

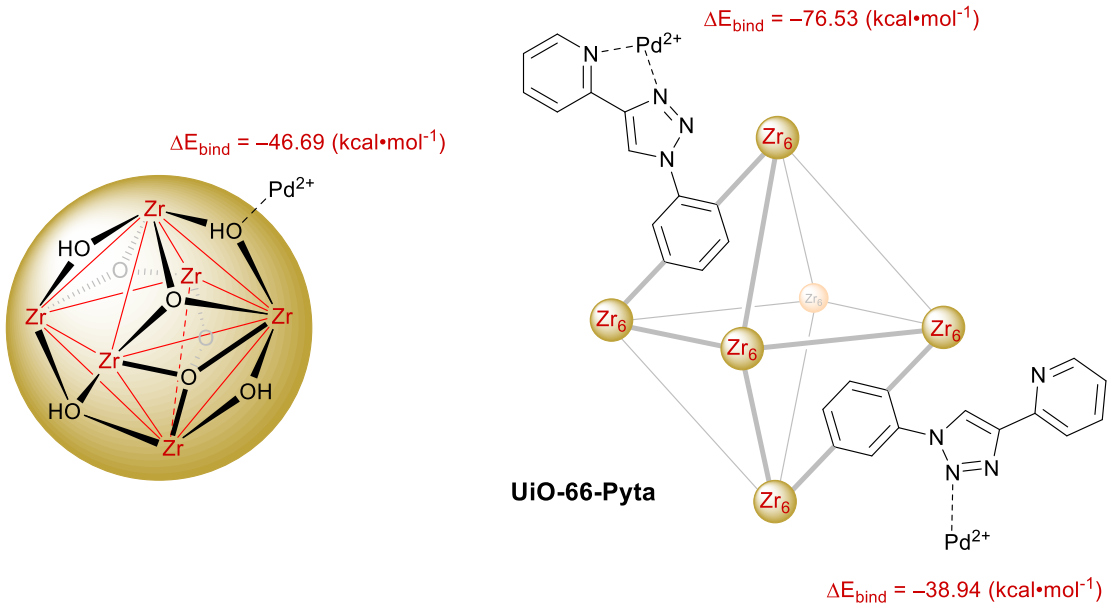

Scheme 1. Pd^{2+} adsorption by UiO-66-Pyta, and possible Pd^{2+} binding modes and binding energies (determined by DFT). Adapted from reference 49.

Palladium was recovered in a 97% yield from a model waste stream containing a mixture of Al^{3+}, Mn^{3+}, Fe^{3+}, Co^{3+}, Ni^{2+}, Cu^{2+}, Zn^{2+}, Ag^{+} and Pb^{2+} ions. Unfortunately, specific details of the selectivity for Pd^{2+} over the other metal ions were not provided. The Pd^{2+}-loaded MOF was then utilised as a catalyst for

the Suzuki-Miyaura coupling of bromobenzene and phenyl boronic acid. Biphenyl was produced in an 80% yield for three catalyst reuse cycles. Trace metal analysis (ICP-AES) of the reaction mixture contained 'negligible' palladium leaching, whilst scanning electron microscopy (SEM) images of the recovered catalyst appeared to be identical to images of the unused palladium-loaded MOF.

Huang *et al*. similarly explored MOFs to recover and reduce aqueous Pd^{2+} ions to yield catalytically active Pd^0 NPs.[50] The authors explored the capture of Pd^{2+} from a mixed metal ethylene glycol/water solution containing Fe^{2+}, Co^{2+}, Ni^{2+}, Cu^{2+}, Zn^{2+} and Pb^{2+}. Palladium capture was performed under sonication for 30 min at room temperature, resulting in the reduction of captured Pd^{2+} to Pd^0 nanoparticles (NPs) without the need for an external reducing agent. The efficiency and selectivity of Pd^{2+} capture and reduction were compared for three different MOFs - UiO-66, MOF-808 and ZIF-8 (Figure 5).

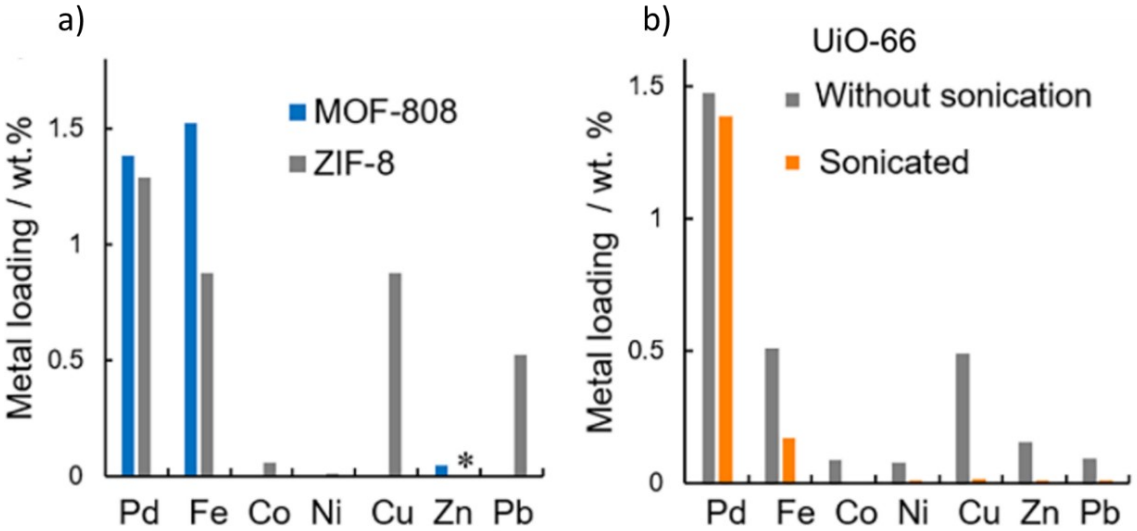

Figure 5. Capture and reduction of Pd^{2+} from a mixed metal ethylene glycol/water solution by sonication with three different MOFS (metal content determined by ICP-OES). a) Metal adsorption (wt.%) comparison between MOF-808 and ZIF-8. b) Metal adsorption (wt.%) by UiO-66, before and after sonication to reduce Pd^{2+} to Pd^0 NPs. Reproduced with permission directly from reference 50.

No Pd^0 NPs were formed for ZIF-8, which was attributed to the significant co-adsorption of Fe^{2+}, Cu^{2+} and Pb^{2+} ions (Figure 5a). Pd^0 NPs were formed for MOF-808, however Fe^{2+} ions were co-adsorbed in large amounts (1.5 wt.%) (Figure 5a). The best performance was provided by UiO-66, which was able to selectively capture and reduce Pd^{2+} (1.5 wt.% loading) alongside the co-adsorption of iron (~0.2 wt.% loading) (Figure 5b). UiO-66 was also able to selectively recover and reduce Pd^{2+} from a model acidic (pH <1) waste stream containing Fe^{2+}, Co^{2+}, Ni^{2+}, Cu^{2+}, Zn^{2+} and Pb^{2+}, resulting in the formation of Pd^0 NPs that were 4.6 nm in diameter. The resulting Pd^0-loaded UiO-66 MOF was used as a catalyst

for the $NaBH_4$ reduction of 4-nitrophenol. Quantitative conversion to 4-aminophenol was observed after 8 min. Rate constant comparisons were made with commercial Pd-based catalysts (Table 1).

Table 1. Comparison of rate constants for the catalytic reduction of 4-nitrophenol to 4-aminophenol.[50]

Catalyst	rate constant k (min^{-1})[a]
Pd^0-UiO-66 MOF	0.450
Commercial Pd/C	0.025
Commercial Pd/SiO_2	0.036
Commercial Pd/Al_2O_3	0.042

[a] Rate constants determined by gradient of $ln(C_t/C_0)$ vs t (min) plots, assuming a pseudo-first order reaction.

Pd^0-UiO-66 MOF was recovered at the end of the 4-nitrophenol reduction reaction and transmission electron microscopy (TEM) illustrated that the morphology of the MOF had not changed during its use as a catalyst. Pd^0-loaded UiO-66 was reused eight times, maintaining >90% conversion to 4-aminophenol for the first 5 runs, with a drop to 80% conversion by the 8th run. The authors did not explore the source, e.g. metal leaching, aggregation etc., of this drop in catalytic efficiency. Pd^0-UiO-66 MOF was also shown to be an effective Suzuki-Miyaura catalyst for several electronically deactivated aryl iodides and phenyl boronic acids (Scheme 2).

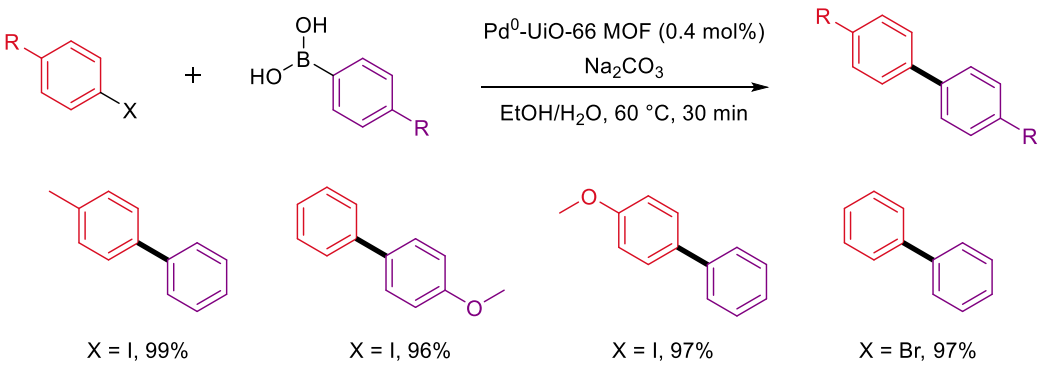

Scheme 2. Products formed from Suzuki-Miyaura coupling catalysed by Pd^0-UiO-66 MOF.[50]

Bourgeois *et al* recently reported the recovery of palladium from waste multi-layer ceramic capacitors (MLCC) and subsequent application of the recovery product as a Suzuki-Miyaura catalyst.[51] The presence of palladium in this waste material as a Pd/Ag alloy enabled the dissolution of palladium in hot nitric acid (3 M). Palladium was selectively extracted from the resulting Pd^{2+}, Zn^{2+}, Fe^{3+}, Cu^{2+} and

Ni^{2+} mixed metal solution using either sulfoxide or amide extractants, such as bis(2-ethylhexyl)sulfoxide (**1**) or *N,N'*-dimethyl-*N,N'*-dibutyltetradecylmalonamide (**2**). Palladium was then stripped from either **1** or **2** into an aqueous micellar solution containing the surfactant tris-(hydroxymethyl)acrylamide (**3**) (Scheme 3).

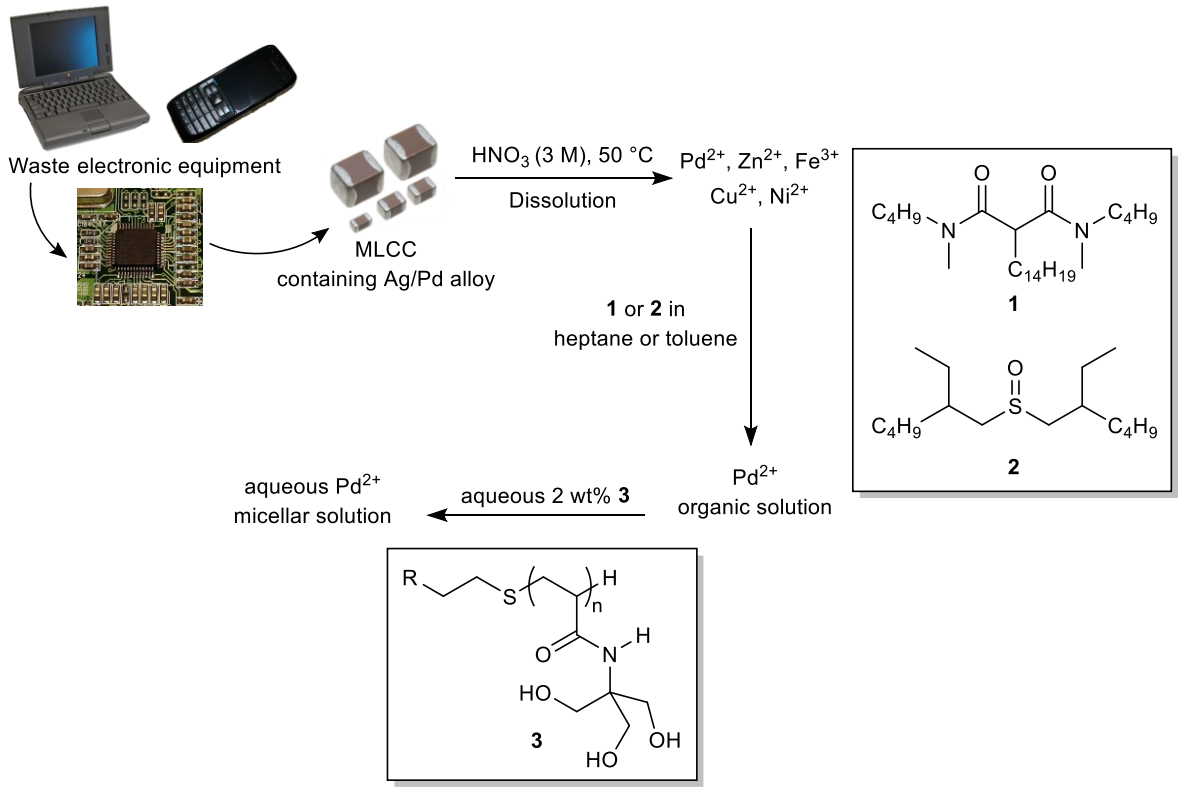

*Scheme 3. Pd^{2+} recovery by **1** and **2** into an aqueous micellar solution of **3**.*[51]

Depending on the lixiviant and solvent used, 86-97% recovery of palladium was obtained and the resulting aqueous micellar palladium solution was employed as a Suzuki-Miyaura catalyst (Table 2).

Table 2. Suzuki-Miyaura coupling catalysed by aqueous micellar palladium recovered from MLCCs.[51]

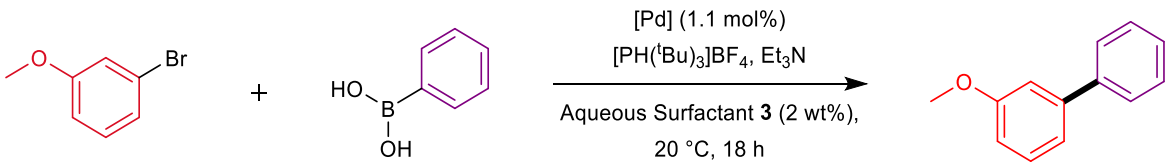

Entry	Palladium source	Yield (%)
1	Recycled Pd	77
2	$Pd(OAc)_2$	85

The recycled palladium catalyst performed comparably to $Pd(OAc)_2$. The ability to extract organic products from aqueous micellar catalyst solutions has been utilised extensively by the Lipshutz group as a tool to enable catalyst recovery and reuse.[52–57] Despite also employing organic solvent extraction in their Suzuki-Miyaura work-up, Bourgeois *et al*. did not explore the possibility of reusing their micellar palladium solution. Possibly this was a result of catalyst leaching from the micellar solution into the organic phase during extraction, although data on palladium leaching was also not reported.

Differences in metal coordination, size and electronic properties are typically utilised to selectively recover palladium from mixed metal waste streams. Zhao *et al*. recently employed a novel approach, by exploiting differences in catalytic activity to selectively recover palladium from a mixed metal solution.[58] A palladium catalysed Glaser coupling was utilised as a final cross-linking step in the formation of a diyne gel (Scheme 4), resulting in the capture of palladium within the pores of the gel. The gel was then separated from the source solution and washed.

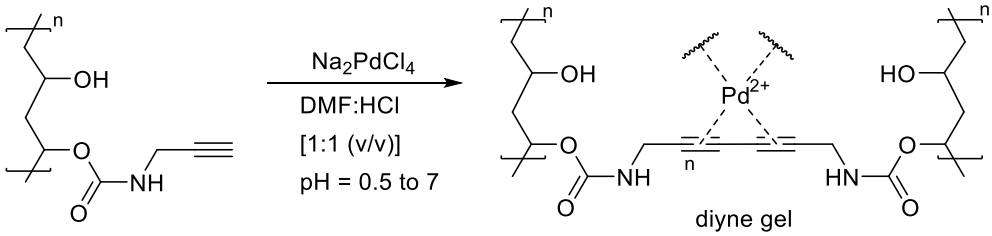

Scheme 4. Zhao et al. palladium catalysed gelation and palladium capture.[58]

The selectivity of the palladium catalysed gelation step was illustrated by comparing the catalytic activity of a variety of metal ions. Out of Al^{3+}, Mn^{2+}, $Fe^{2+/3+}$, Co^{2+}, Ni^{2+}, Cu^{2+}, Zn^{2+}, Ru^{3+}, Rh^{3+}, Pd^{2+}, Pt^{4+} and Au^{3+}, only palladium and platinum ions were catalytically active for the Glaser coupling. Moreover, when applied to a mixed metal solution containing Al^{3+}, Fe^{3+}, Co^{2+}, Ni^{2+}, and Zn^{2+}, palladium was recovered selectively. The resulting Pd^{2+}-loaded gel was treated with $NaBH_4$, which facilitated the reduction of Pd^{2+} to Pd^0 nanoparticles that were ~1.9 nm in diameter. The gel was subsequently freeze-dried and the resulting Pd^0-aerogel (**4**) applied as a Suzuki-Miyaura catalyst (Scheme 5).

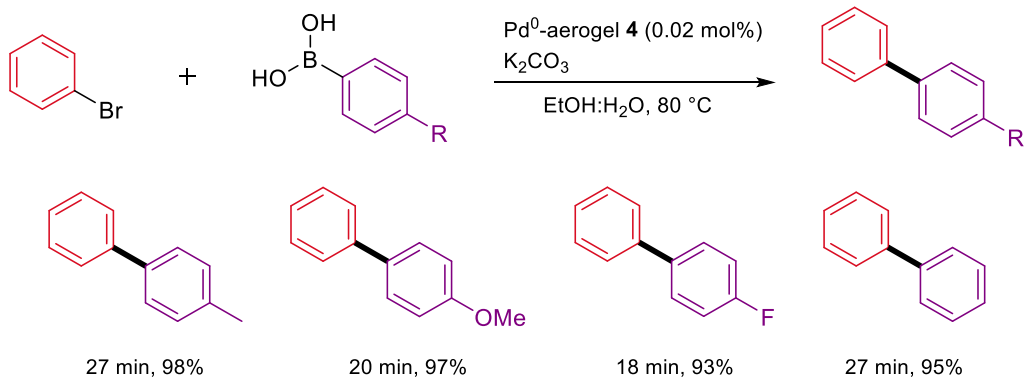

Scheme 5. Recovered Pd^0-aerogel as a Suzuki-Miyaura catalyst.[58]

Although not directly applying their technique to a real or model waste stream, other authors have proposed the suitability of their catalyst synthesis for recovering palladium from aqueous waste streams. To this end, Rees *et al.* recently reported the synthesis of palladium on carbon black nanoparticles (CB NPs) using impact electrochemistry.[59] The group utilised a dilute aqueous solution (0.5 mM) of $PdCl_2$ as a palladium source and described this solution as a proxy for industrial waste streams. Palladium was deposited on CB NPs over 168 h by impact electrochemical reduction, with >85% of palladium being recovered from the dilute $PdCl_2$ solution (Figure 6).

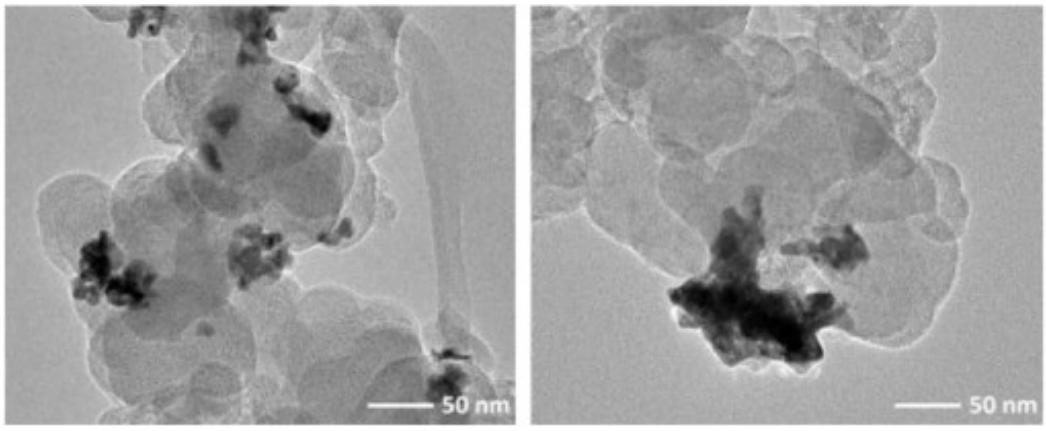

Figure 6. Palladium on carbon black nanoparticles synthesised by impact electrochemical reduction from a dilute (0.5 mM) aqueous $PdCl_2$ solution. Reproduced directly from reference 59 (Open Access publication).

The resulting 14% Pd (wt%) on CB NPs were employed as a catalyst (3.8 mol%) for the Suzuki-Miyaura coupling of iodobenzene and phenylboronic acid in water. Quantitative conversion to biphenyl was obtained after 6 h at 80 °C. It should be noted that the catalytic activity of the Pd on CB NPs was not compared to that of the dilute (0.5 mM) $PdCl_2$ solution employed in their synthesis, which would also have been a competent catalyst for this transformation.

Smith *et al*. similarly employed an aqueous (pH = ~4-5) dilute solution of $PdCl_2$ as a proxy for industrial aqueous palladium waste.[60] In their report, the group utilised hybrid gel beads to capture and reduce Pd^{2+} to Pd^0 nanoparticles. The gel beads were produced from a mixture of agarose (**5**) and a functionalised low-molecular-weight-gelator (LMWG, **6**) (Figure 7).

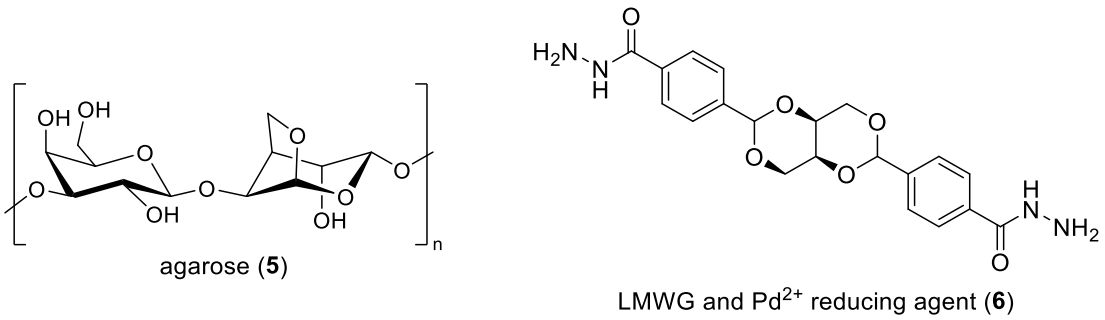

Figure 7. Smith et al. hybrid gel components used to synthesise Pd-loaded gel beads.[60]

The functionality in **6** facilitated the reduction of captured Pd^{2+} to Pd^0 nanoparticles that were ≤3 nm in diameter. These gel-loaded palladium nanoparticles were shown to be a competent Suzuki-Miyaura catalyst. A range of aryl halides and aryl boronic acids were explored and selected examples are summarised in Scheme 6.

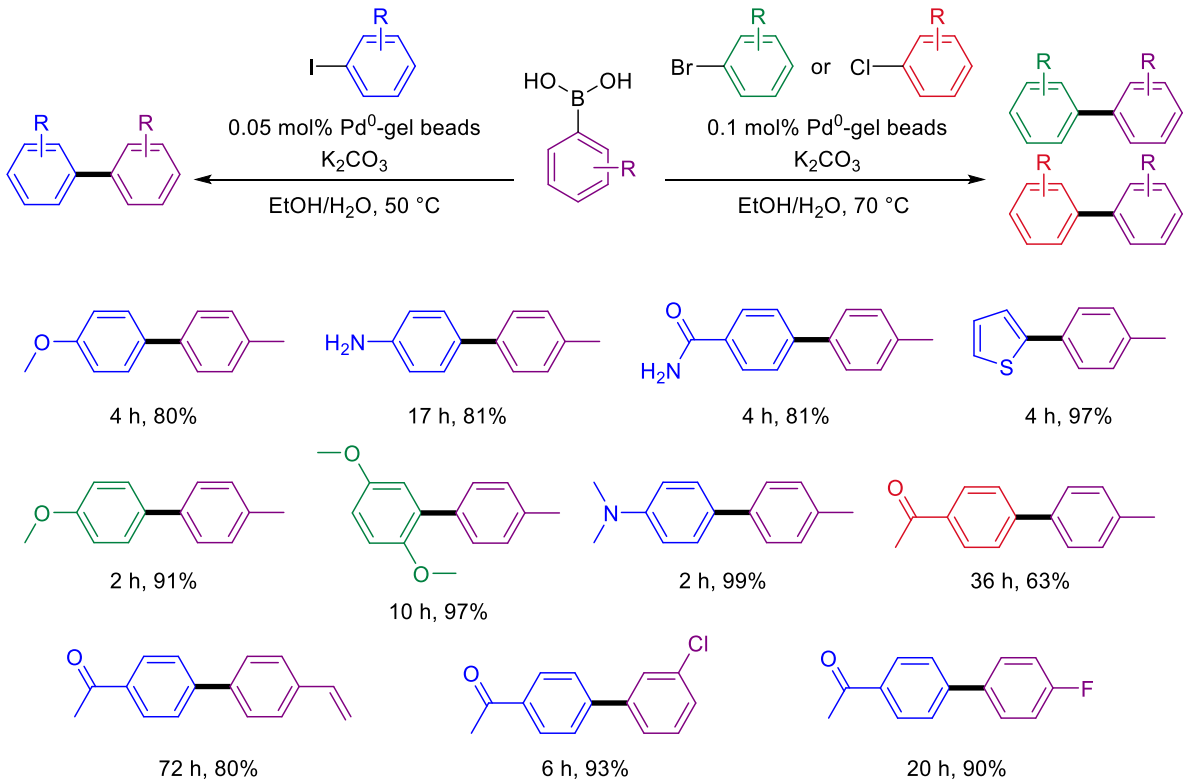

Scheme 6. Selected substrate examples in the Pd^0-gel bead catalysed Suzuki-Miyaura reaction, reported by Smith et al.[60]

Notable examples include electron-rich aryl iodides and bromides, and a mildly activated aryl chloride. The development of the novel hybrid gel formulation, consisting of both agarose (**5**) and the LMWG (**6**), also enabled the recovery and reuse of the gel beads. Previous gels produced by the Smith group were mechanochemically unstable, resulting in significant catalyst leaching and difficulties isolating and reusing the catalyst.[61] The hybrid gels composed of **5** and **6** however were reused three times for the Suzuki-Miyaura coupling of 4'-iodoacetophenone and 4-tolylboronic acid. A cumulative TON of 5000 was obtained for the new gel design, compared with a cumulative TON of 1375 for the group's previous design.

A popular strategy that has been explored for recovering palladium from aqueous waste streams is the use of microorganisms.[62] In these examples the microbe is employed to adsorb Pd^{2+} ions from an aqueous solution and the microbe subsequently used as a biocatalyst for the reduction of adsorbed Pd^{2+} to supported Pd^0 nanoparticles. The resulting bio-Pd^0 nanoparticles have been employed as catalysts for several different transformations. The first example of this approach was described by Creamer *et al*,[63] who utilised two bacteria types, gram-positive (*B. sphaericus*) and gram-negative (*D. desulfuricans*), to adsorb Pd^{2+} ions from an aqueous solution of sodium tetrachloropalladate. The solution was then exposed to hydrogen gas, resulting in the formation of supported bio-Pd^0 nanoparticles that were ~4.6 nm in diameter. These nanoparticles were used as a catalyst for the hydrogenation of itaconic acid (Table 3).

Table 3. Catalytic activity of two bio-supported Pd^0 nanoparticles in the hydrogenation of itaconic acid.[63]

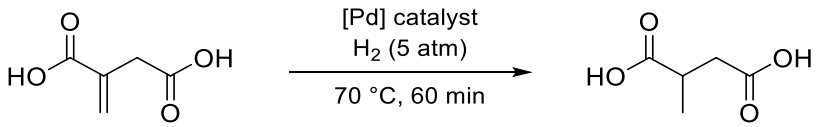

Pd catalyst	initial rate (x 10^{-3} mol·gPd^{-1}·s^{-1})	conversion (%)
5 wt% *D. desulfuricans* bio-Pd^0	11	85
2 wt% *B. sphaericus* bio-Pd^0	12	92
commercial 5 wt% Pd/C	13	92

Initial reaction rates and conversions provided by the two bio-Pd^0 nanocatalysts were comparable to that of a commercial palladium on carbon catalyst (Table 3). Creamer *et al* later expanded on this work by applying their 5 wt% *D. desulfuricans* bio-Pd^0 nanoparticles as a catalyst for the hydrogenation of 2-pentyne.[64] In this example, the group utilised an acidic (pH = 2-3) solution of sodium tetrachloropalladate as a Pd^{2+} source, which more closely mimics acidic palladium waste streams. The

Pd^{2+} bio-adsorbed material was treated with hydrogen gas, resulting in the formation of bio-Pd^0 nanoparticles that were ~1.7 nm in diameter. These particles were found to be an effective catalyst for the hydrogenation of 2-pentyne, although reaction rates were ~30% slower than were provided by a commercial palladium on alumina catalyst (Pd/Al_2O_3). The same group later illustrated that bio-Pd^0 nanoparticles derived instead from *E. Coli* were a more effective catalyst.[65] When compared to commercial palladium on alumina (Pd/Al_2O_3), the *E. Coli* derived catalyst provided a ~1.4x faster rate of 2-pentyne hydrogenation, and a 1.5x improved selectivity for cis-2-pentene. Finally, research from the same group conducted by Murray *et al.* later employed a real acidic leachate as a palladium source.[66] The group treated ground spent TWC material with *aqua regia* in a microwave at 105 °C for 15 min, and the resulting acidic leachate was diluted with sodium hydroxide until a pH of 2.2 was obtained. To improve the bio-adsorption of metals from this acidic leachate, *E. Coli* cells were initially 'seeded' with Pd^0 nanoparticles by treatment with sodium tetrachloropalladate, followed by reduction with hydrogen gas. These preloaded bio-Pd^0 cells were then used to recover Pd^{2+} from the acidic TWC leachate, resulting in complete adsorption of palladium after 60 h. The leaching time of 60 h necessary to remove palladium from the real waste leachate was considerably longer than the ~5 min needed to remove palladium from a model palladium-only solution. Control palladium recovery studies on model solutions illustrated that the presence of aluminium and silicon ions in the real TWC leachate significantly slows the rate of recovery. Selectivity of the technique for palladium over the other metals present was not explored. The resulting bio-Pd^0 nanoparticles were employed as catalysts for the hydrogenation of 2-pentyne (Table 4).

Table 4. 2-pentyne hydrogenation catalysed by E. Coli bio-Pd^0, with comparisons made to commercial Pd/Al_2O_3 catalyst. Reproduced from 66.

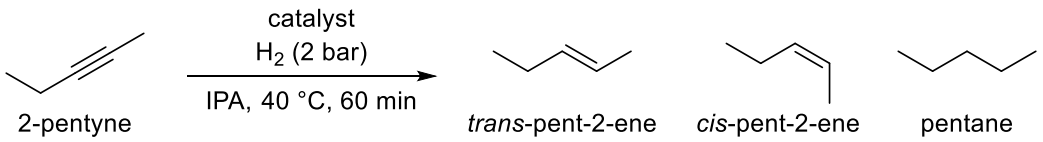

Catalyst[a,b]	Commercial Pd/Al_2O_3		*E. Coli* bio-Pd^0 Preloaded bio-Pd^0		*E. Coli* bio-Pd^0 Bio-Pd^0 after metal recovery	
Loading (wt.%)	2	5	2	5	16	20
trans selectivity (mol%)	38	35	20	20	21	16

[a] All values are reported after 100% 2-pentyne conversion. [b] *trans*- selectivity given as mol% of total product moles

The bio-Pd^0 catalyst containing the highest loading (20 wt.%) sourced from the acidic leachate provided the best selectivity for *cis*-pent-2-ene (Table 4).

Bio-Pd^0 nanoparticles have also been utilised as catalysts for cross-coupling reactions. Søbjerg *et al* were the first to investigate the activity of bio-Pd^0 as a catalyst in the Suzuki-Miyaura and Mizoroki-Heck reactions.[67] *Cupriavidus necator* and *Pseudomonas putida* bacteria were used to adsorb Pd^{2+} ions from an aqueous solution of sodium tetrachloropalladate, followed by reduction by formate to bio-Pd^0 nanoparticles. The group explored a broad range of aryl iodide and several aryl bromide starting materials (Scheme 7).

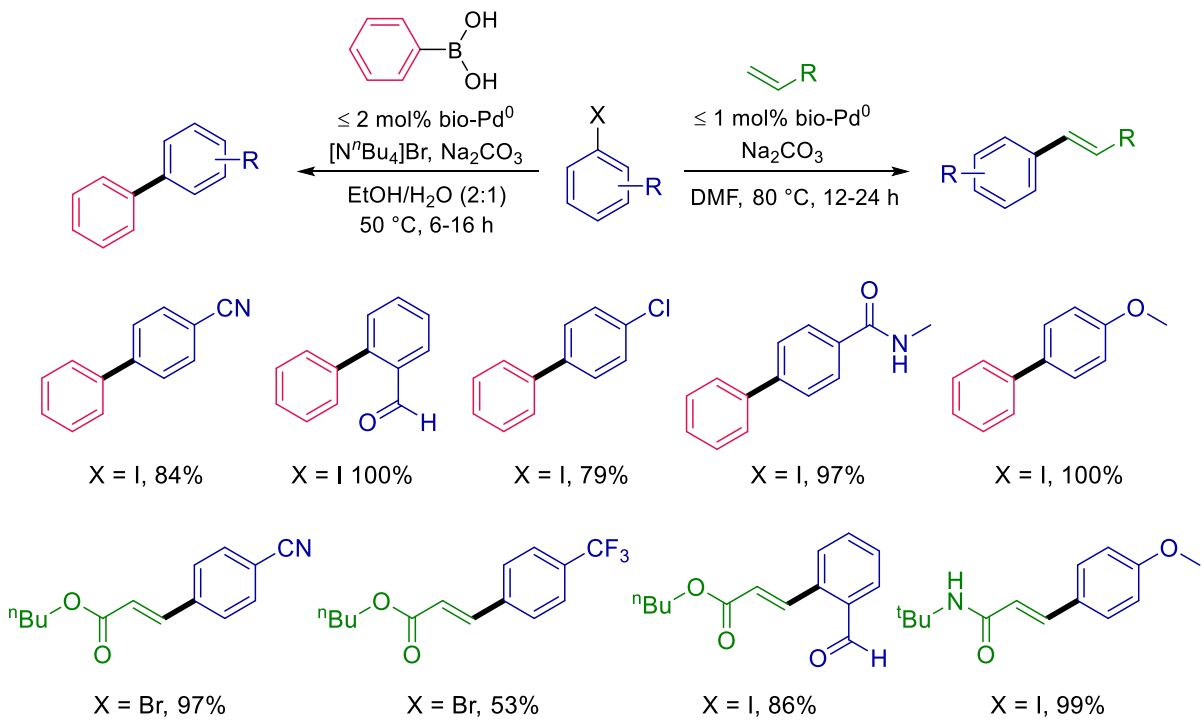

Scheme 7. Selected substrate examples from Søbjerg et al's Bio-Pd^0 as catalysts for Suzuki-Miyaura and Mizoroki-Heck cross-coupling.[67]

C. necator derived bio-Pd^0 nanoparticles were also recovered at the end of the reaction and reused four times without any observed loss in catalytic activity in the coupling of phenyl boronic acid and *p*-iodotoluene. In later work,[68] Søbjerg *et al* applied *C. necator* bacteria to recover palladium from a model acidic (pH = 1.4) waste leachate containing palladium alongside a mixture of copper, rhodium, silver, iridium, platinum, gold and lead. Palladium was recovered in a 96-100% yield, although the technique was not selective, as rhodium (55%) and platinum (70%) were also both recovered. Nevertheless, the ability to recover palladium from a model leachate containing copper is impressive, since copper is typically reported to inhibit the bacterial hydrogenase enzymes involved in metal

reduction.[69] Unfortunately, only a 50% yield was obtained in the Mizoroki-Heck coupling of *p*-iodoanisole and *n*-butyl acrylate when the bio-Pd^0 nanoparticles sourced from the model acidic leachate were employed as a catalyst. This is a considerably reduced yield when compared to the 96% provided by the bio-Pd^0 derived from a pure solution of sodium tetrachloropalladate.

Whilst avoiding the need for pyrometallurgical separations, these hydrometallurgical techniques all still utilise an initial oxidation step that relies on reagents like *aqua regia*. The highly-corrosive nature of these reagents, alongside the release of Cl_2/NO_x gases, imparts a significant limitation to the techniques described above which utilise acidic palladium waste streams. This has prompted a few groups to utilise softer/milder oxidants which are able to selectively oxidise and recover Pd^{2+} directly from the scrap material. One of the first examples of this approach was described in 2005 by Deplano and Serpe *et al*, who reported the selective oxidation and dissolution of palladium directly from scrap TWCs.[70] The diiodine adduct of a dithiooxamide lixiviant, $Me_2dazdt{\cdot}2I_2$ (**8**) (Me_2dazdt = *N,N'*-dimethyl-perhydrodiazepine-2,3-dithione, **7**) was used to oxidise Pd^0 present in scrap TWCs, yielding $[Pd(Me_2dazdt)_2](I_3)_2$ (**9**). Excellent palladium recovery yields (90-99%) were achieved irrespective of the scrap palladium content (Table 5, Entries 1 and 2) or the support material (Table 5, Entries 2 and 3).

*Table 5. Oxidation of Pd^0 in model scrap TWCs by dithiooxamide·I_2 **8** as reported by Deplano, Serpe and co-workers.*[70]

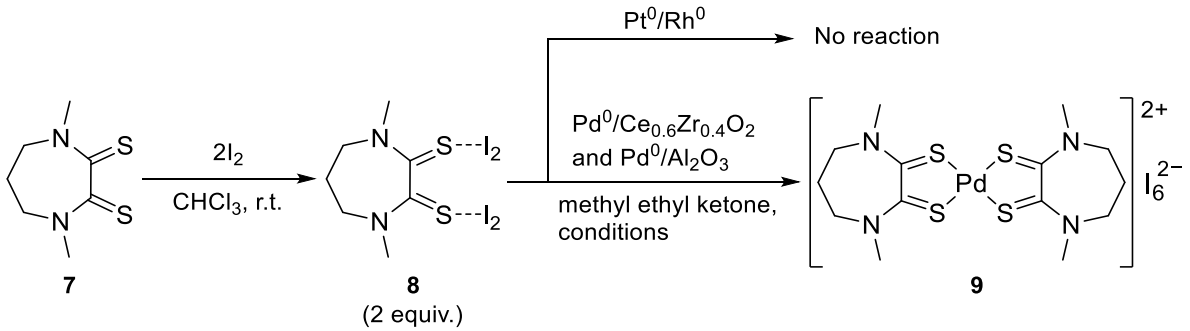

entry	Pd-content (wt%)	support	temperature	yield[a] (%)
1[a]	2.8	$Ce_{0.6}Zr_{0.4}O_2$	80 °C	99
2[a]	0.7	$Ce_{0.6}Zr_{0.4}O_2$	80 °C	92
3[a]	0.7	Al_2O_3	80 °C	90
4[b]	Pd metal		r.t.	77

[a] *Conditions*: 2:1 ratio of dithioxamide and Pd content in methyl ethyl ketone for 168 h.
[b] Oxidation of Pd^0 metal powder complete after ~1 h.

Interestingly, the Deplano and Serpe groups illustrated that treating the six-membered ring analogue of **7**, *N,N'*-dimethyl-piperazine-2,3-dithione **10**, with iodine instead yielded the triiodide salt of the protonated ligand, **11** (Scheme 8a), and not the diiodine adduct.[71] Unlike the diiodine adduct **8**, triiodide salt **11** oxidises both Pt^0 and Pd^0 (Scheme 8a). Mechanistic insight into the differences in reactivity of the six- and seven-membered dithiooxamides with iodine was recently uncovered by Serpe *et al* in 2023.[72] DFT analysis illustrated that the smaller S--C--C--S dihedral angle (40° vs 74°) and thus shorter S--S contact (2.78 Å vs 3.46 Å) in the six-membered dithiooxamide **10** results in the stabilisation of a radical cation (**12**) which undergoes homolytic C-H bond cleavage, yielding the protonated triiodide salt **11** (Scheme 8b).

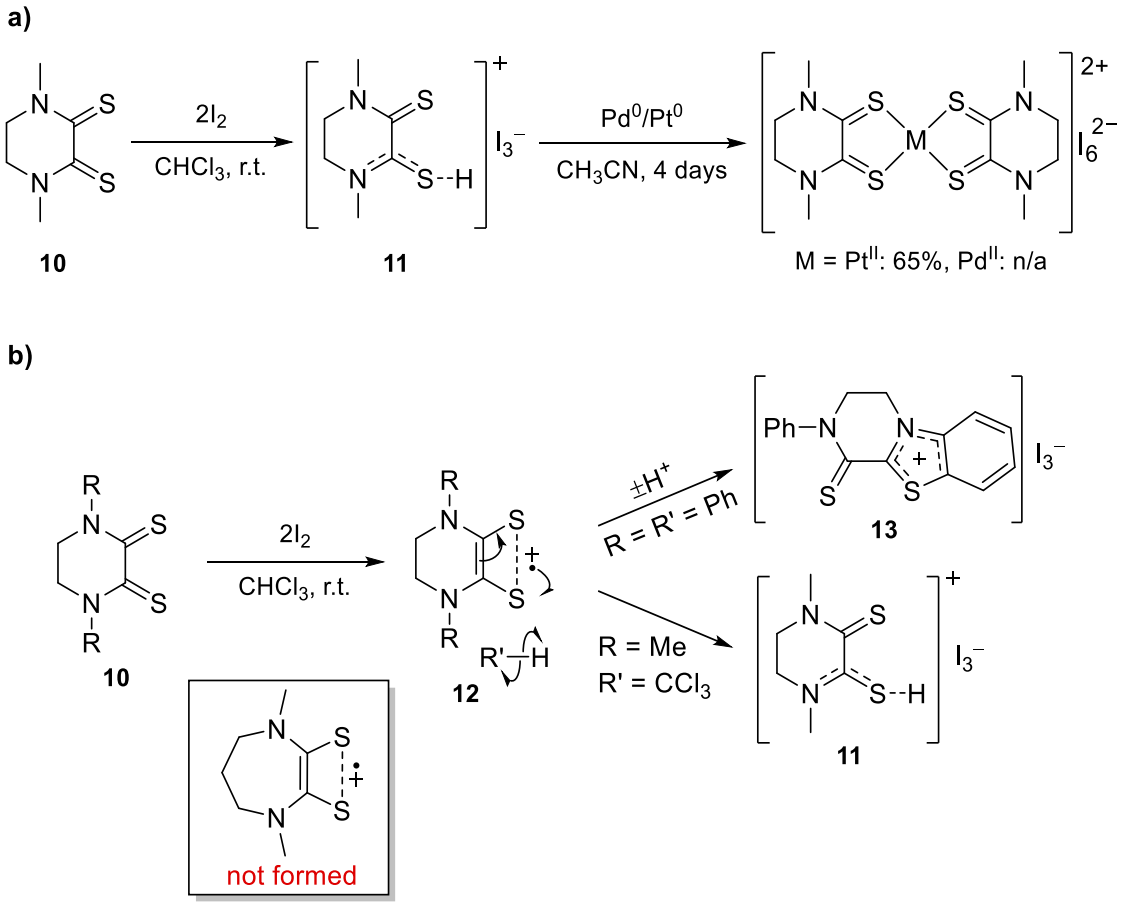

*Scheme 8. a) Reactivity of the triiodide salt **11** with both Pt^0 and Pd^0. b) Mechanistic rational for the formation of the triiodide salt **11**.*[72]

Further indirect experimental evidence of the proposed mechanism was provided through the intramolecular trapping of the ligand-centred radical **12** and formation of the triiodide salt **13** when R = Ph (Scheme 8b).

Since the original report from Deplano, Serpe and co-workers, the Wilton-Ely group has explored the application of the recovered palladium complex **9** as a catalyst for the regioselective C-H bond functionalisation of 8-methylquinoline and benzo[*h*]quinoline (Scheme 9) in collaboration with Serpe and Deplano.[73]

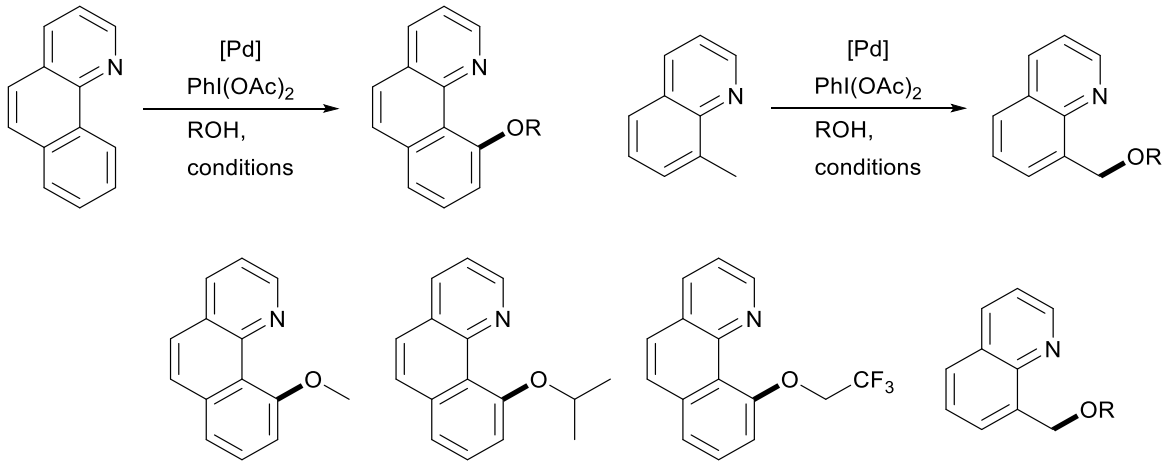

9[a]:	1 mol%, 5 h, 85%	2 mol%, 2 h, 79%	2 mol%, 1 h, 74%	2 mol%, 1 h, 74%
$Pd(OAc)_2$[b]:	1 mol%, 22 h, 95%	3 mol%, 27 h, 72%	1 mol%, 21 h, 71%	1 mol%, 21 h, 71%

*Scheme 9. Catalytic activity of recovered palladium complex **n** in the C-H bond functionalisation of with comparisons made to Sanford's results with $Pd(OAc)_2$. [a] Reactions catalysed by **9** performed at 50 °C.[73] [b] Reactions catalysed by $Pd(OAc)_2$ performed at 100 °C.[74]*

Recovered complex **9** was found to provide improved TOFs and TONs under milder conditions when compared with Sanford's original report utilising $Pd(OAc)_2$.[74] The Serpe and Wilton-Ely groups later showed that the recovery product **14** could be formed from the oxidation of palladium metal powder by the more atom economical 1:1 mixture of Me_2dazdt:I_2 in refluxing acetone (Scheme 10).[75] This recovery product (**14**) was also shown to be an effective catalyst for the C-H functionalisation of 8-methylquinoline and benzo[*h*]quinoline, providing similar performance to recovery product **9**. Compound **14** was also transformed into some typical phosphine-based catalysts (**15** and **16**), enabling the recovery of **7** (Scheme 10). This approach has not yet been applied to any real or model palladium waste.

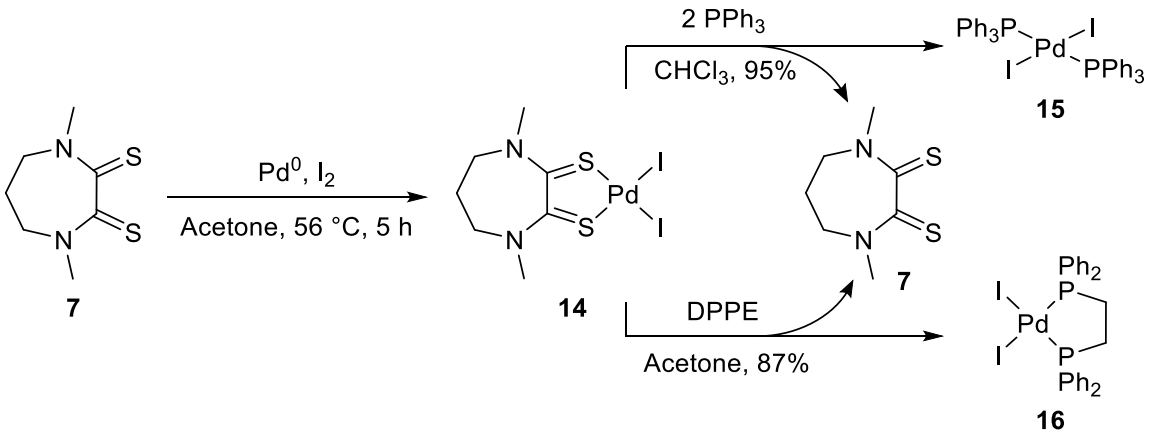

*Scheme 10. Wilton-Ely and Serpe oxidation of Pd^0 by the more atom economical 1:1 mixture of Me_2dazdt (**7**) and I_2, and subsequent transformation into phosphine complexes **15** and **16** (DPPE = [1,2-Bis(diphenylphosphino)ethane]).*[75]

The Friščić group have also utilised direct oxidation of Pd^0 to Pd^{II} for application of the recovery product in catalysis. The group described the first mechanochemical, solvent-free oxidation and recovery of palladium. Palladium metal was converted to $[PdX_4]^-$ using potassium peroxymonosulfate (oxone) and a halide salt (NH_4X).[76] The resulting palladium salts were subsequently converted into some typical palladium precatalysts (**17**-**20**, Scheme 11). A telescoped one-pot process was also performed, wherein Pd^0 metal was converted directly to Pd^{2+} complexes **18** and **20** (Scheme 11). Palladium in the form of pellets, wire, palladium on carbon and waste palladium black from a Suzuki-Miyaura reaction were all successfully utilised as Pd^0 sources. Recovered complex **19** was also found to be an efficient catalyst for the Suzuki-Miyaura coupling of 2,5-dibromo-*p*-xylene and phenyl iodide with phenyl boronic acid. The group also illustrated that the mechanochemical oxidation of a three-component mixture of Au^0, Pt^0 and Pd^0 (1:2:1) resulted in the selective oxidation of palladium and gold over platinum. This result is significant when considering applying the technique to selectively recover palladium from platinum containing scrap TWCs and WEEE. Further work is needed though to establish the efficacy of the technique when applied to real scrap material.

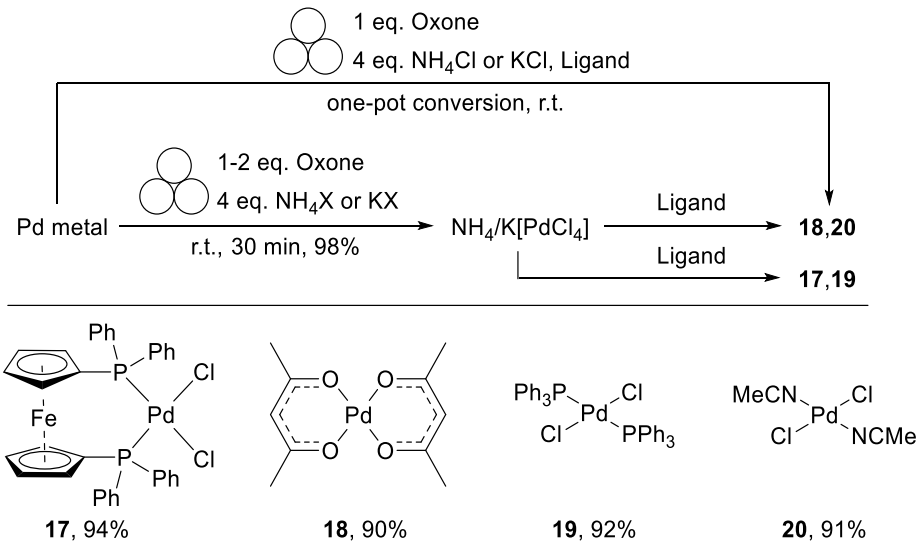

Scheme 11. Mechanochemical oxidation of Pd^0 metal and subsequent transformation into some typical palladium precatalysts.[76]

All of the reports discussed thus far have utilised some initial chemical oxidation step to dissolve palladium as Pd^{2+}. A number of groups have opted to forego any chemical recovery of palladium and instead utilised scrap TWCs directly as a heterogeneous catalyst. The direct application of scrap TWCs as heterogeneous catalysts has the obvious advantage of bypassing pyro- and hydrometallurgical processes involved in metal recovery. However, since TWCs contain a wide range of valuable metals, including precious metals like rhodium and platinum, the economic viability of the approach may be limited when compared to techniques which can fully valorise the content of a scrap TWC. The concomitant presence of palladium, rhodium and platinum in TWCs does appear to render them as particularly effective hydrogenation catalysts. The Zengin group was the first to report this strategy.[77] The group reported on the hydrogenation of 13 different substrates catalysed by scrap TWC powder (Scheme 12). The scrap TWC was reportedly sourced from a Fiat Siena that had run for 1,400,000 km, and the material was initially washed with chromic acid, dried at 120 °C for 12 h and crushed to a powder in an agate mortar. The resulting powder was found to contain a mixture of palladium (0.465%) and rhodium (0.040%) by X-ray fluorescence spectroscopy.

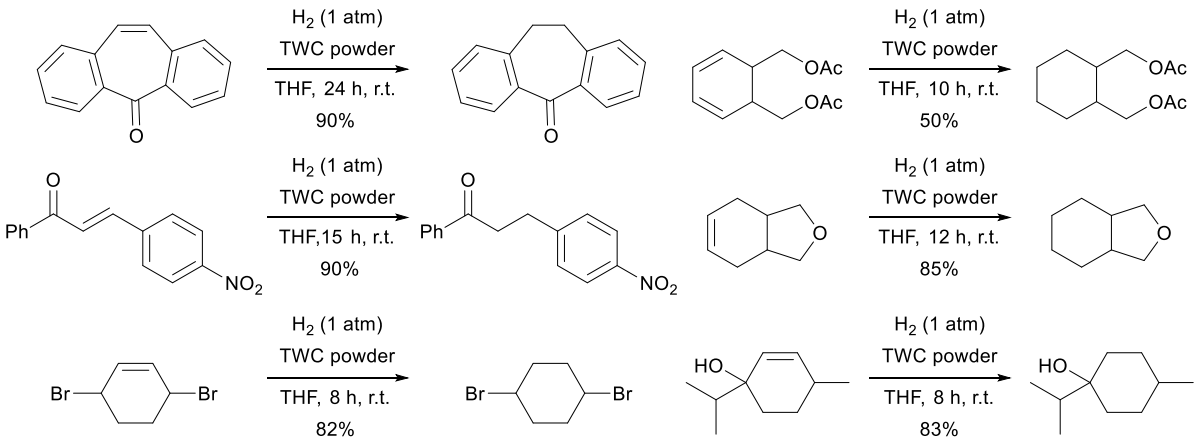

Scheme 12. Selected substrate examples from Zengin's report on the use of scrap TWC powder ([Pd] ~4.4 mol%) as a hydrogenation catalyst.[77]

In each example, 1 g of scrap catalyst powder was employed as a heterogeneous catalyst for the hydrogenation of 1 mmol of substrate (approximately 4.4 mol% palladium loading). The scrap powder could also be isolated at the end of the reaction and reused, with no loss of activity being observed after four reuses.

Luque and co-workers have since published two reports, similarly utilising scrap TWCs as a heterogeneous hydrogenation catalyst.[78,79] Similar to Zengin's report described above, the Luque group also utilised initial washing and drying steps. Thermogravimetric analysis (TGA) of an unwashed scrap sample reported a 20% drop in mass, whilst a washed scrap sample exhibited 4% loss of mass. These results illustrate that the initial washing step is key to removing carbonaceous impurities. The scrap material was subsequently packed into a cartridge for use as an in-flow catalyst for the hydrogenation of 5 different industrially relevant substrates (Scheme 13).

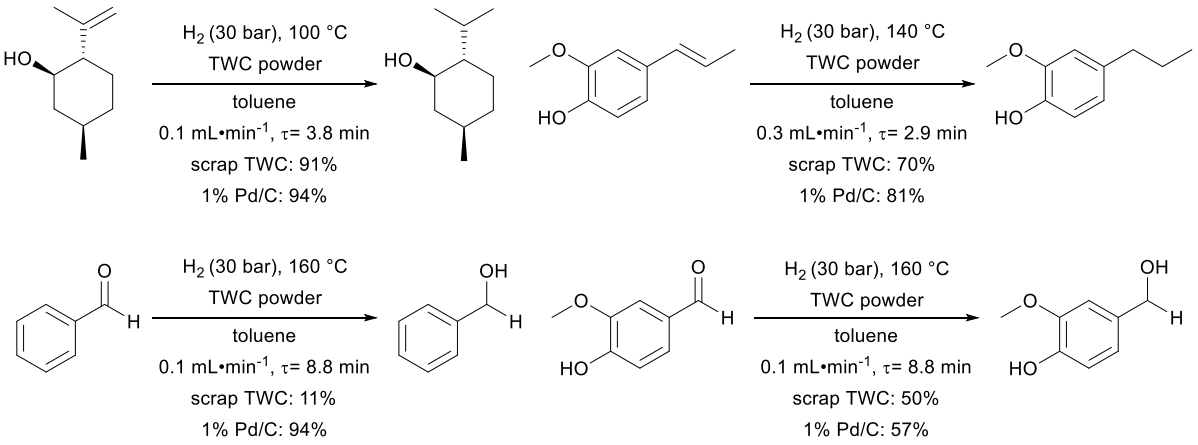

Scheme 13. Luque et al. application of scrap TWC powder as an in-flow hydrogenation catalyst. Yield comparisons made with respect to commercial Pd/C.[78,79]

The scrap TWC powder cartridges were also employed for the continuous in-flow hydrogenation of (−)-isopulegol for 8 h. A small initial decrease in yield from 94% to 85% was observed after 2 h, which was attributed to the adsorption of organic material on the catalyst surface, and the activity of the catalyst could be restored after a toluene wash. Moreover, ICP-MS analysis revealed that no metal had leached into solution, and no particle aggregation was observed by scanning electron microscopy (SEM). These results, alongside those described by Zengin and others,[77,80] illustrate the high stability of scrap TWC powder, even when applied under relatively harsh conditions (e.g. >100 °C, 30 bar H_2 for 8h). This high stability of scrap TWCs as heterogeneous catalysts is consistent when considering their application as automotive exhaust catalysts, where TWCs have been designed to function at incredibly high temperatures (~800 °C) over many years of use.

1.1.4. Low-loading palladium catalysts

Another strategy which can reduce the economic and environmental burden of palladium in the chemical industry is the use of catalysts that function at low loadings (≤0.1 mol%). In many extreme examples, which use palladium loadings of around 0.0001 mol%, the cost of the palladium catalyst has effectively been eliminated.[81] Palladium catalysts which function at low-loadings also benefit from inherently reduced residual metal concentration in the final product. This section details homogeneous palladium-containing catalysts which have been reported in the literature to function at low catalyst loadings. There are hundreds of publications which report a palladium catalyst that functions at ≤0.1 mol% loading, more than could be comprehensively covered here. Instead, key examples have been selected to cover the range of catalyst types which function at ≤0.1 mol% loading. Reports containing more extensive catalytic studies have been favoured when selecting examples for this review of the literature, e.g. extensive substrate scopes or challenging/industrially relevant substrates, kinetic profiles and benchmarking, control studies with comparisons to simple precatalysts, and residual metal analysis.

Phosphine-based palladium complexes have been frequently reported to function at low-loadings. For example, Kwong *et al* reported a monophosphine ligand (**21**, Scheme 14) which was employed with $Pd(OAc)_2$ as a Suzuki-Miyaura catalyst.[82] A range of sterically and electronically deactivated aryl chlorides and heteroaryl chlorides were coupled at low palladium loadings (Scheme 14).

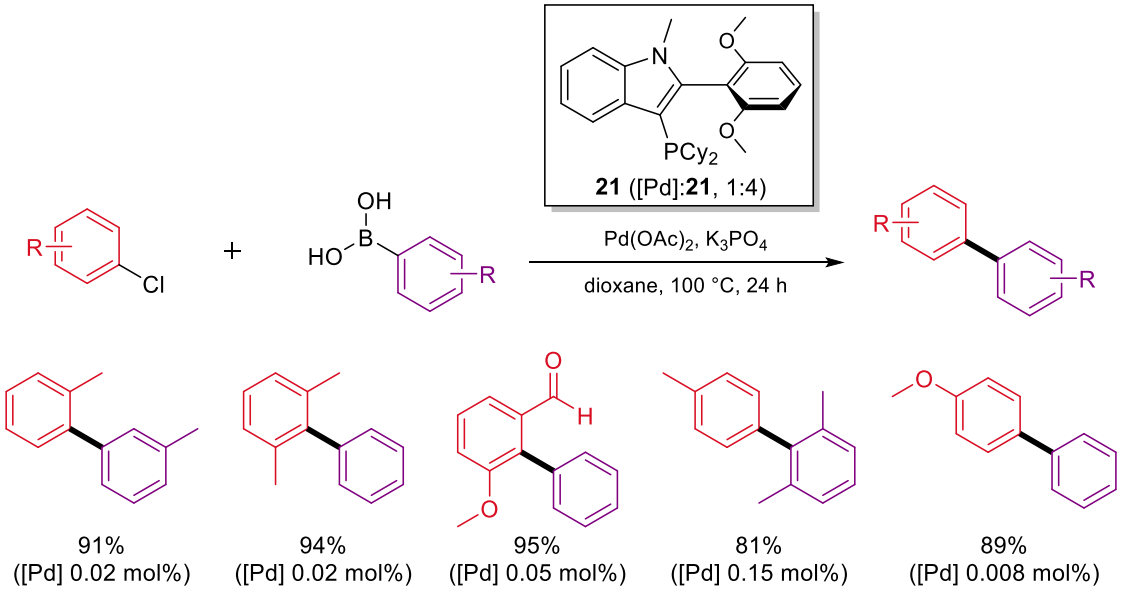

*Scheme 14. Selected substrate examples from Kwong et al Pd(OAc)$_2$/**21** catalysed Suzuki-Miyaura coupling at low palladium loadings.*[82]

Kwong *et al* also utilised **21** to facilitate the late-stage cross-coupling of Griseofulvin, an antifungal agent, with phenyl boronic acid. However the group utilised 1 mol% of Pd(OAc)$_2$, and did not explore this more challenging and industrially relevant transformation with a low catalyst loading.

Palladacycles are one of the most common motifs found in low-loading palladium catalysis. The field of palladacycles has been explored by the research of the Bedford group, who have developed a number of palladacyclic complexes which function at low catalyst loadings.[83,84] In 2002, the Bedford group illustrated that palladacycles can achieve low loading through their high thermal stability, and not through a noticeable increase in rate.[85] Palladacyclic complexes were synthesised with varying phosphite backbones and subsequently employed as catalysts for the Suzuki-Miyaura coupling of 4-chloroanisole and phenyl boronic acid at 0.001 mol% palladium loading. It was found that palladacycles with increasing π-acidity (**25**>**24**>**23**>**22**) in the phosphite backbone remained catalytically active over longer periods of time (Figure 8).

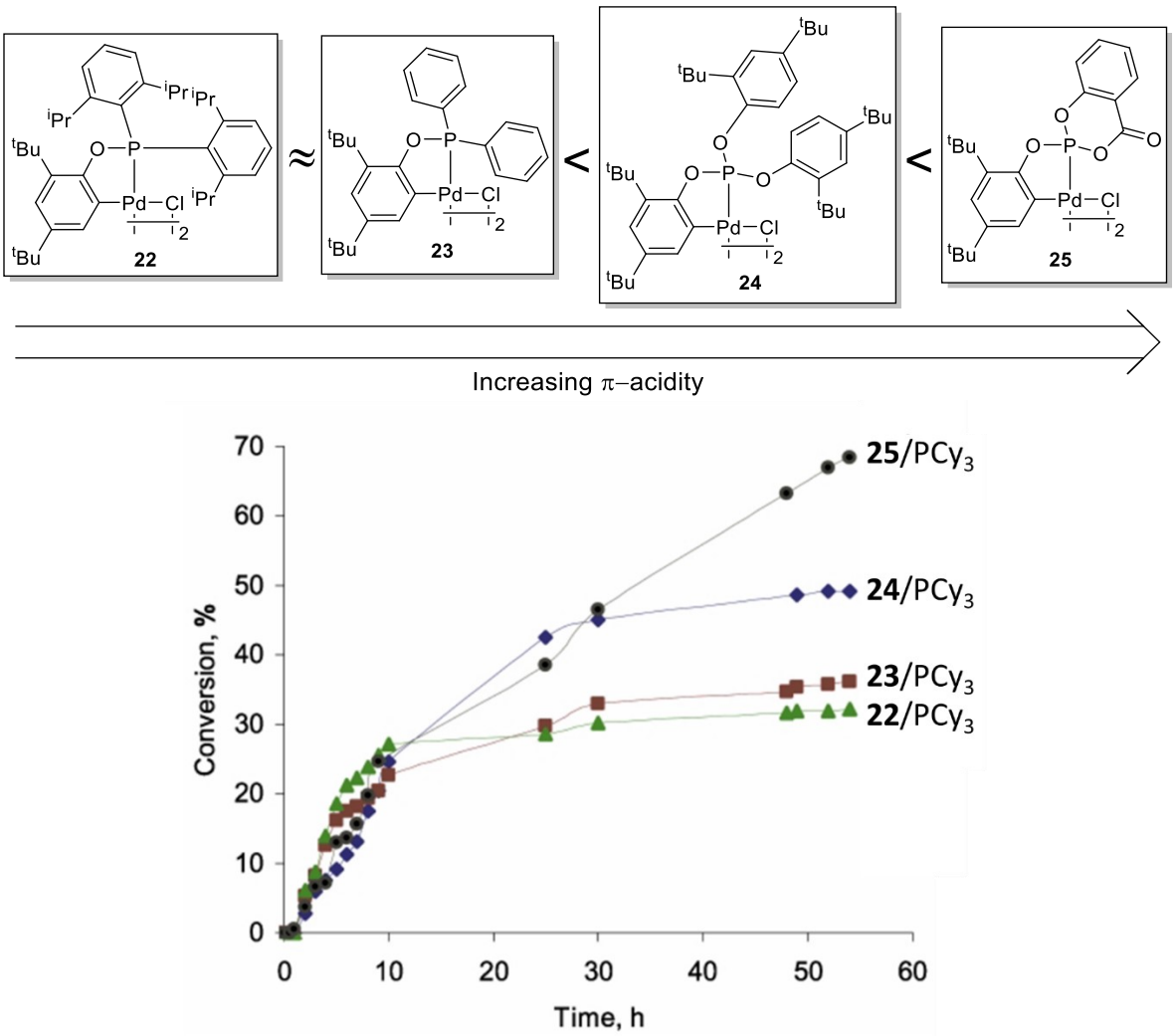

Figure 8. Bedford et al. comparison of palladacycle activity in the Suzuki-Miyaura cross-coupling of 4-chloroanisole and phenyl boronic acid, 0.001 mol% [Pd] loading at 100 °C in 1,4-dioxane. Adapted with permission from reference 85.

It was proposed that, since oxidative addition of 4-chloroanisole to [Pd^0] is the rate-determining step, the catalyst rests as [Pd^0], a species which is prone to decomposition by aggregation and precipitation of Pd^0 metal. Thus, increasing the π-acidity of the phosphite backbone increased the strength of the palladium–phosphite bond, which increased the stability and 'longevity' of the mononuclear [Pd^0] resting state. The same researchers subsequently explored the substrate scope of **25** as a Suzuki-Miyaura catalyst. A range of sterically and electronically deactivated aryl chlorides were coupled with phenyl boronic acid at either 0.0005 or 0.00005 mol% palladium loading, reportedly achieving TONs of up to $2x10^6$ (Scheme 15).

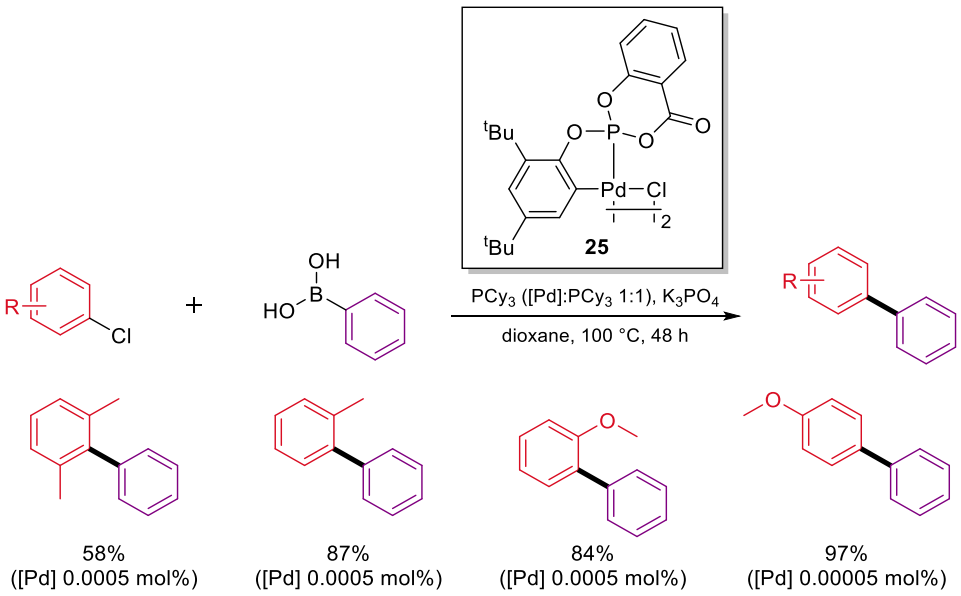

*Scheme 15. Selected substrate Suzuki-Miyaura coupling examples catalysed by **25**.*[85]

In more recent work, Carrow *et al* reported the first synthesis of tri(1-adamantyl)phosphine and subsequently attached the new ligand to a palladacycle.[86] The resulting cationic complex (**26**) was found to be a highly-active Suzuki-Miyaura catalyst, functioning at a low-loading for several industrially relevant and complex substrates (Scheme 16).

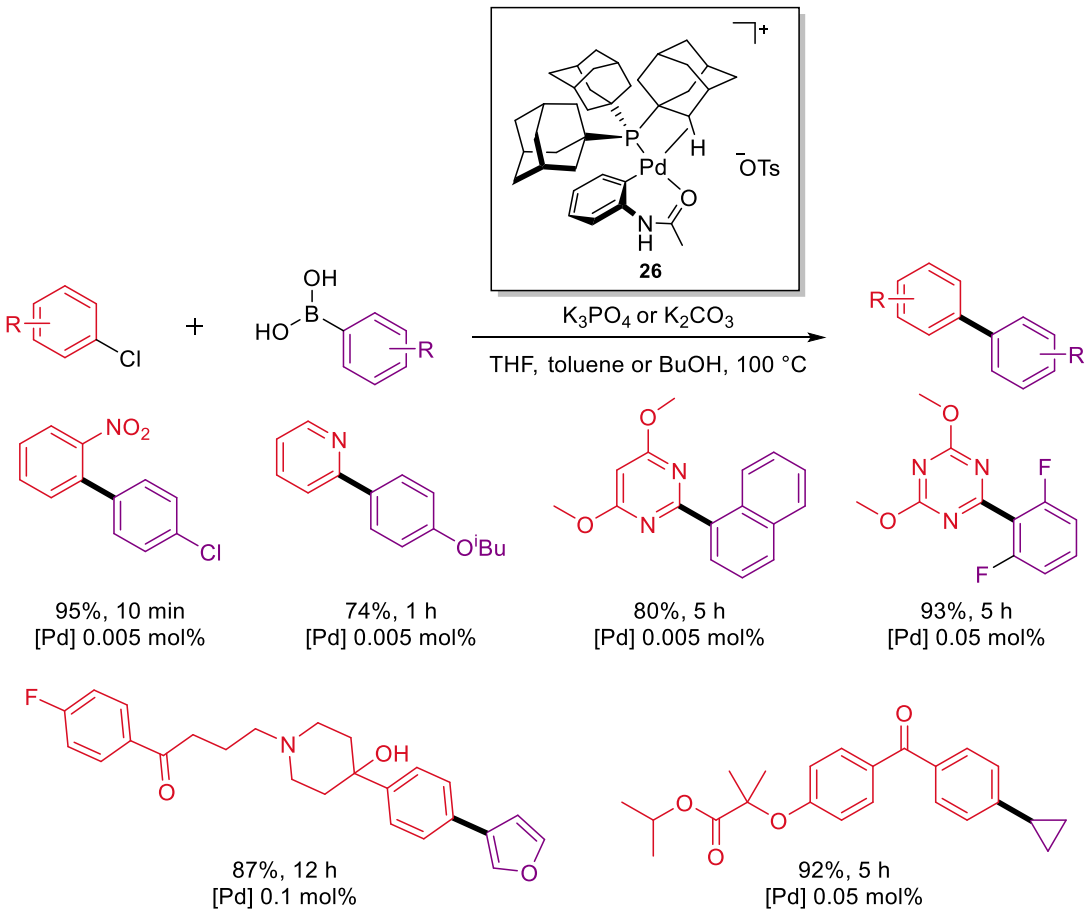

*Scheme 16. Palladacycle **26**-catalysed Suzuki-Miyaura coupling at low palladium loadings.*[86]

Comparison of the cone angles in the solid state structures of [R_3PAuCl] illustrated that PAd_3 (179°) is similar to the value previously reported for $P(^tBu)_3$ (182°).[87] In addition, the buried volumes (%V_{bur}) of PAd_3 and $P(^tBu)_3$ were calculated as 40.5 and 40.0%, respectively. These results illustrated that PAd_3 can be considered isosteric to $P(^tBu)_3$ and it is worth noting though that whilst $P(^tBu)_3$ is pyrophoric, PAd_3 is air stable. Similar studies into the electronic parameters of PAd_3, using Rh and Ni carbonyl complexes, illustrated that PAd_3 is more electron donating than other bulky alkylphosphine ligands, with the strong electron-donating properties of PAd_3 more closely resembling that of N-heterocyclic carbenes than alkylphosphine ligands. The Carrow group also illustrated that palladium-PAd_3 complex **27** did not undergo thermal cyclometallation, a deactivation pathway seen for other alkyl phosphine ligands (Scheme 17).[88]

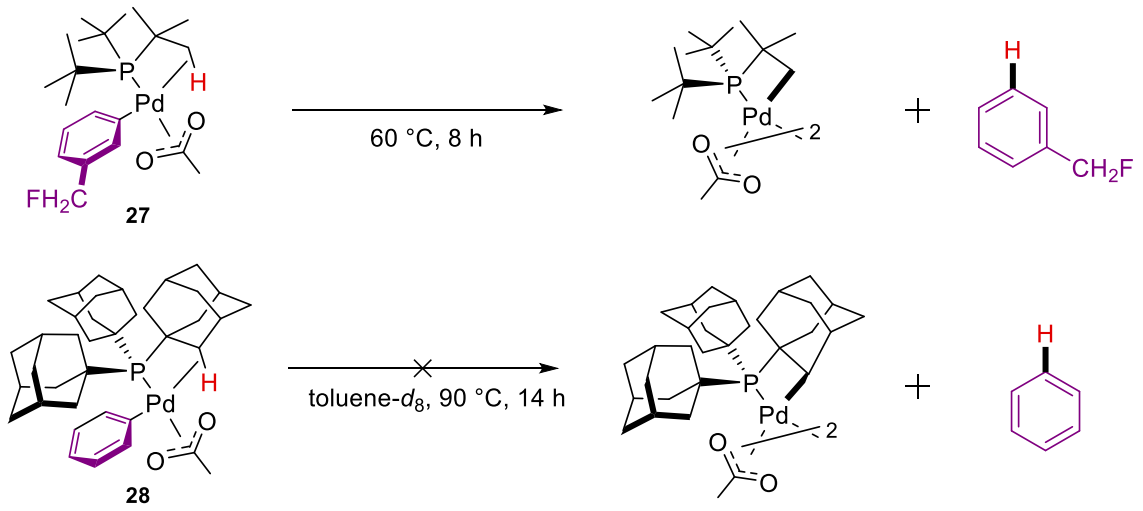

*Scheme 17. Carrow et al. cyclometallation stability of PAd_3 complex **27**, compared to Hartwig's example of $P(^tBu)_3$ complex **28**.*[90]

This thermal stability of PAd_3 likely also contributed to the low-loading activity of **26** at a high temperature (100 °C).

N-heterocyclic carbene (NHC) ligands are ubiquitous in low-loading palladium catalysis. In early work, Nolan *et al* synthesised an η^3-allyl-NHC palladium complex (**29**) which was employed as a Suzuki-Miyaura catalyst under low-loadings.[89] A range of electronically and sterically deactivated aryl chlorides and boronic acids were coupled under impressively mild (room temperature) conditions (Scheme 18).

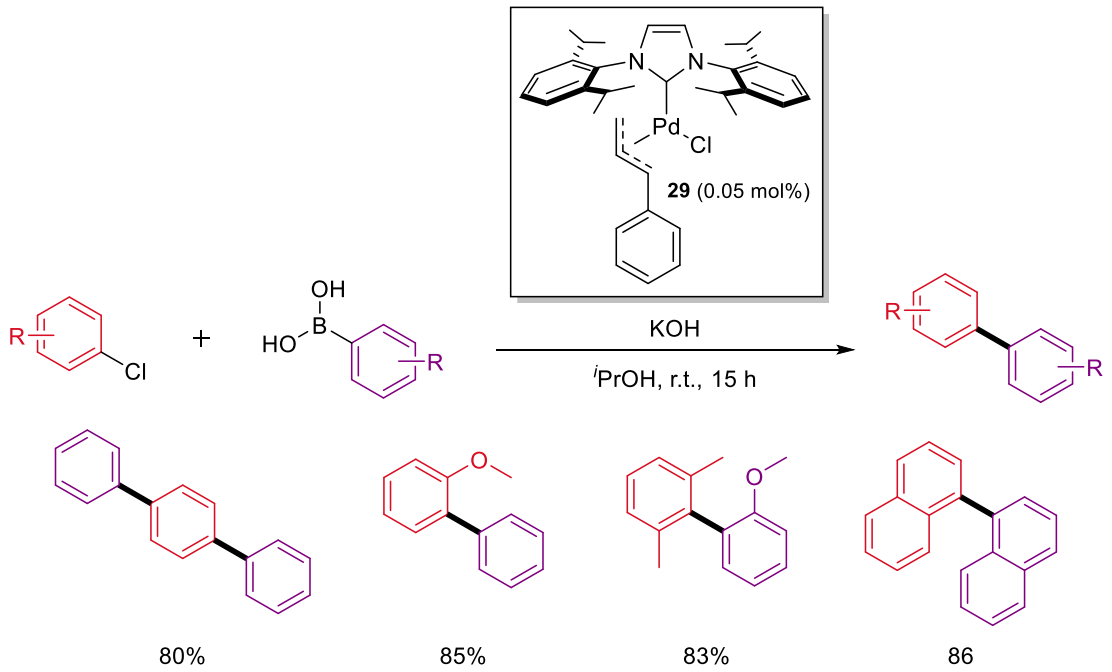

*Scheme 18. Suzuki-Miyaura coupling catalysed by carbene complex **29** selected substrate examples.*[89]

The Nolan group also illustrated that a similar carbene complex (**30**) was an effective Buchwald-Hartwig catalyst. A few challenging electronically and sterically activated aryl chlorides were successfully coupled at low loadings (Scheme 19).

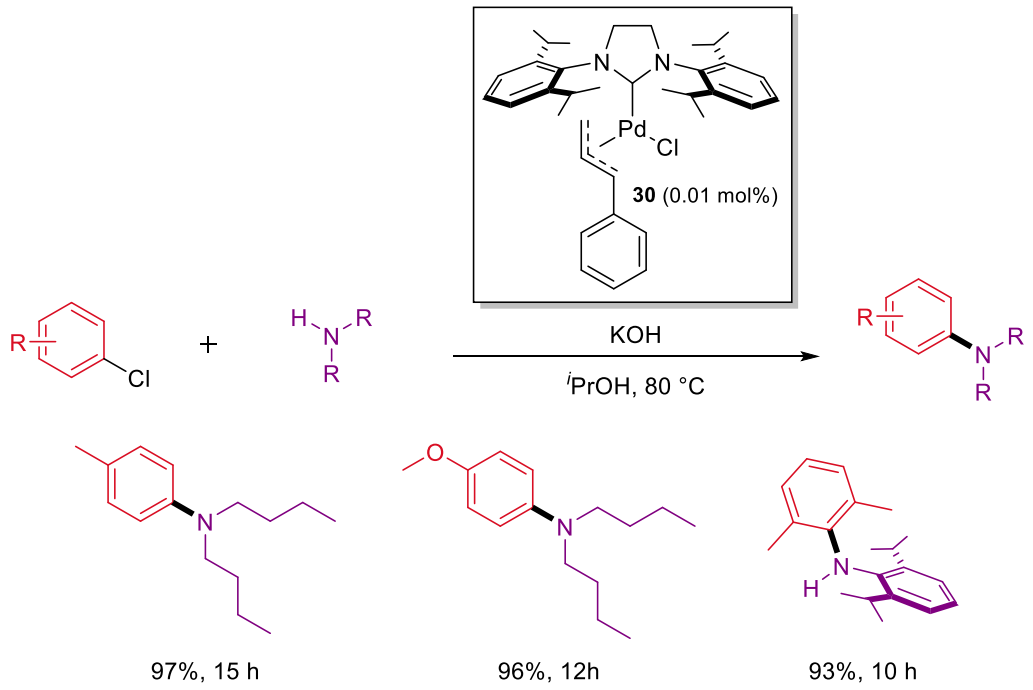

*Scheme 19. Selected Buchwald-Hartwig coupling substrate examples, catalysed by low-loading **30**.*[89]

NHC ligands have been illustrated to be stronger σ donors than phosphine ligands, whilst phosphine ligands are stronger π acceptors.[90] As a result, NHC-palladium complexes typically have greater electron density on the metal centre when compared to phosphine-metal complexes.[91,92] These observations suggest that NHC ligands are better at activating [Pd^0] for oxidative addition of challenging aryl chlorides, and are more tightly-bound to the metal centre in NHC-metal complexes. However, recent work by Ananikov and Chernyshev *et al.* has illustrated that the NHC ligand in palladium-NHC complexes can demonstrate lability under elevated reaction temperatures, resulting in the release of Pd^0 nanoparticles and palladium black.[93–96] A recent review by McCarthy *et al.* highlights that these factors may influence the conditions under which low-loading is achieved.[24] The authors' literature search uncovered almost twice as many low-loading NHC-based catalysts (15 of 23 reports) that function at low temperatures (≤ 80°C) than palladacyclic (8 of 23 reports in the same review) or phosphine based complexes (1 of 8 reports). The application of phosphine- and palladacyclic-based palladium complexes at elevated reaction temperatures also resulted in their use in undesirable polar aprotic solvents which have higher boiling points, e.g. DMF, DMA, dioxane, NMP

etc. This observation may be tied to the mechanism by which these complexes obtain their low-loading activity, *i.e.* thermal stability vs TOF kinetic performance.

Many of the molecular palladium complexes employed at low loadings have been shown, to varying degrees, to proceed via the formation of Pd^0 nanoparticles.[97–101] In the absence of strong-donor ligands to stabilise and prevent palladium aggregation, 'ligand-free' palladium salts will presumably also form nanoparticles *in situ* during cross-coupling reactions. It is unsurprising then that numerous groups have found success in employing simple 'ligand-free' palladium salts as precatalysts at low catalyst loadings. For example, early work by de Vries *et al*. illustrated that the use of $Pd(OAc)_2$ at low loadings was necessary to prevent catalyst deactivation in the Heck reaction.[102] The authors proposed that soluble [Pd^0] clusters, formed from the reduction of $Pd(OAc)_2$, act as a reservoir for monomeric [Pd^0], where increased catalyst loadings favoured aggregation of these clusters to inactive palladium black (Figure 9). It should be noted though that whilst this proposed mechanism is consistent with the trends observed in Figure 9, the authors did not provide any direct evidence for the formation of an aggregated palladium species, *e.g.* through kinetic studies or imaging.

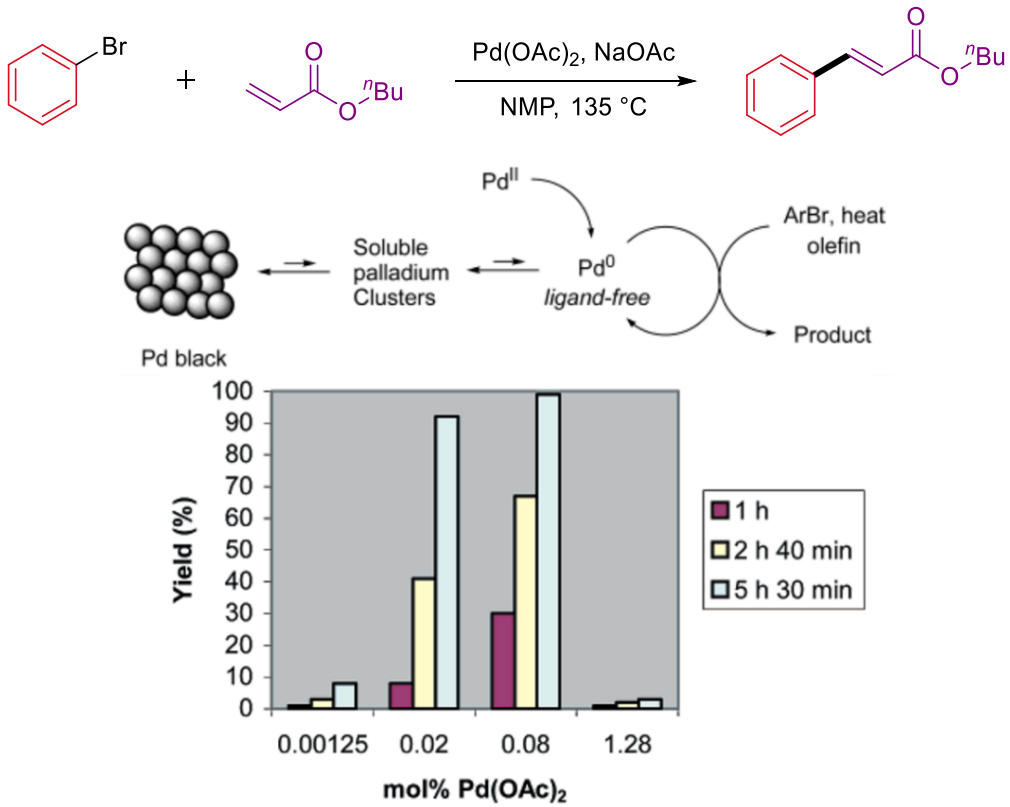

Figure 9. De Vries low-loading $Pd(OAc)_2$ catalysed Heck reaction with a comparison of catalyst loadings and the 'cocktail' of palladium species present. Adapted from reference 102.

Ananikov described this phenomenon as a dynamic 'cocktail' of catalytic species.[103] Recent work exploring this 'cocktail' by Hii *et al*. through kinetic studies supports the hypothesis that low-loadings of $Pd(OAc)_2$ are required to prevent catalyst deactivation.[104] However, contrary to the proposal of De Vries *et al.*, the Hii group proposed that aggregated palladium species are catalytically active, and not simply a reservoir for monomeric palladium (Figure 9). The role of aggregates in palladium catalysis, especially for low-loading ligand-free systems, remains a contested subject.[105–109]

In one example of a low-loading 'ligand-free' palladium catalyst, Xu and co-workers utilised $Pd(TFA)_2$ (TFA = trifluoroacetate) as precatalyst in the Suzuki-Miyaura coupling of allylic halides and boronic acids in water.[110] An impressive range of allylic bromides, chlorides and boronic acids (>50 product examples) were successfully coupled at 0.01 mol% catalyst loading (Scheme 20).

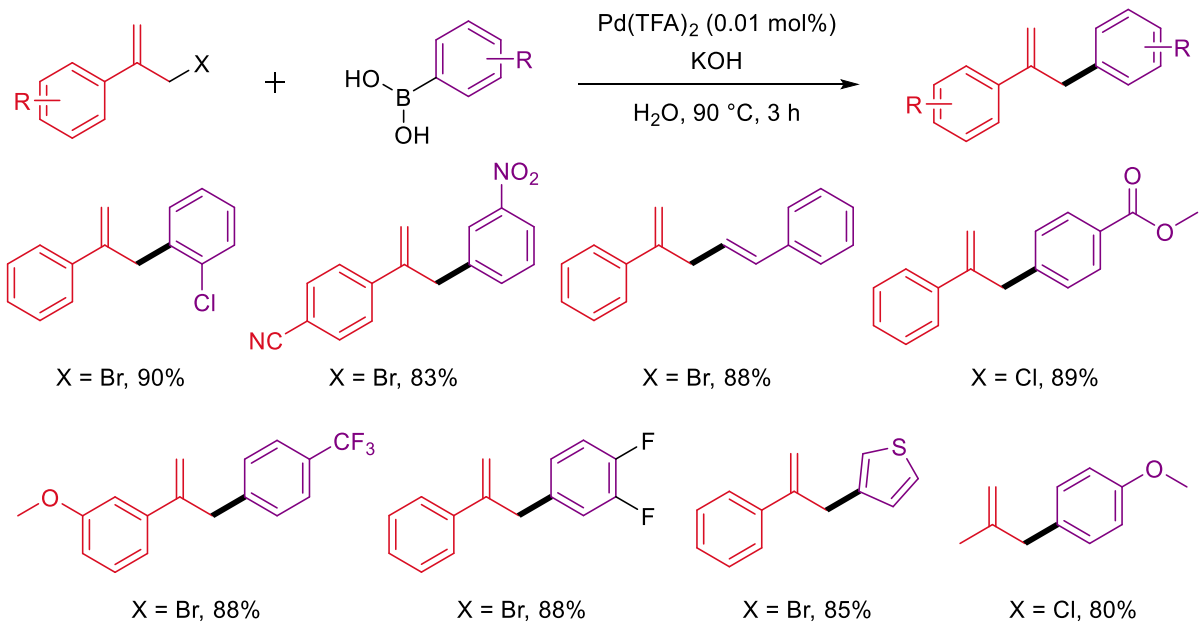

Scheme 20. Selected substrate examples from Xu et al. Suzuki-Miyaura reaction catalysed by low-loading $Pd(TFA)_2$.[110]

Despite the large body of literature which describes palladium catalysts that function at low-loadings,[24,111] there are relatively few reports describing catalysts at a low-loading as part of a process scale-up. For example, despite the hundreds of reports in the journal *Organic Process Research and Development* that utilise a palladium catalyst, only 2 examples utilised a low catalyst loading (≤0.1 mol%).[112,113] Two additional examples have reported using 0.2 mol% (50 kg scale)[114] and 0.25 mol% (183 kg scale)[115] palladium loadings. It is worth noting that three of these four reaction scale-ups were published in the last year (*as of 12/10/23*), possibly indicating that low-loading technology is beginning to have an impact at industrial scale, and an increase in the number of reports might be expected in

the coming years. In one of these examples, Lorenz *et al* reported an asymmetric allylic alkylation catalysed by $[Pd(\eta^3–C_3H_5)Cl]_2$ (0.035 mol%) and chiral phosphine ligand **31** (0.081 mol%) on an 11.8 kg scale (Scheme 21).[112]

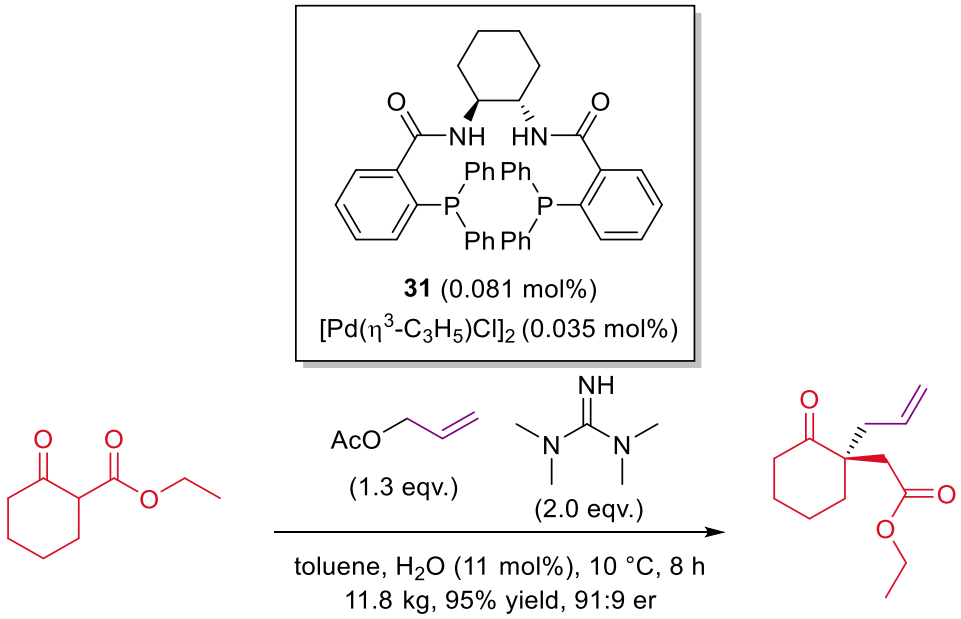

Scheme 21. Lorenz et al. rare application of a palladium catalyst at a low loading as part of a multi-kg process scale-up.[112]

It is not clear why low-loading catalysts are relatively underutilised on an industrial scale when compared to their occurrence in academic research. Some authors have described being concerned with process robustness at low catalyst loadings, possibly due to difficulties ensuring low O_2 concentrations, variability in precatalyst activation, or the presence of catalyst poisoning species in the reagents/solvents which become more significant at larger scales.[113–115] In Li *et al.*'s report on the application of 0.25/0.5mol% of $[Pd(\eta^3–C_3H_5)Cl]_2$/XPhos in a 183 kg cyanation reaction,[115] the authors found that the key to process robustness at lower catalyst loadings was to pre-form the active catalyst species for ~4.5 h prior to the initiation of the reaction. This contradicts Lorenz's report outlined above (Scheme 21), which found that adding the catalyst and ligand last provided superior results. Previous research by Lloyd-Jones *et al.* demonstrated that the active catalyst formed from $[Pd(\eta^3\text{-}C_3H_5Cl_2]_2$/**31** is prone to aggregation, and that the formation of these aggregates results in a drop in reaction rate and enantioselectivity.[116] This may explain Lorenz's observations on the importance of adding the catalyst and ligand to the reaction mixture last. Clearly a better understanding of catalyst speciation and robustness at low-loadings is needed for the technology to transition to process scales, and this will likely be further complicated by the dependence of the speciation on the chemistry and the reaction conditions.

1.1.5. Reusable homogeneous palladium catalysts

The final common strategy employed to improve the sustainability of palladium consumption in the chemical industry is to reuse them. This has traditionally been achieved through their attachment to an insoluble support, rendering them as heterogeneous catalysts, which can be recovered at the end of the reaction. A huge range of heterogeneous supports have been developed,[117–128] and there are a number of comprehensive reviews on the area.[129–137] In more recent years, alternative strategies have emerged which enable homogeneous catalysts to be recovered and reused at the end of the reaction. This section details homogeneous palladium-containing catalysts which can be reused at the end of the reaction. In general, reusable homogeneous catalysts rely on product and catalyst phase separation at the end of the reaction. This is typically achieved by rendering the catalyst more soluble in certain types of solvents, e.g. water or other highly polar solvents, through thermo-responsive phase changes, or through pH/light sensitive chemical handles. As for the previous section on low-loading catalysts, there are more examples of reusable homogeneous catalysts than can be comprehensively covered here. Reports have been selected to cover the range of recycling strategies and examples with more extensive catalytic studies have been favoured.

Since the organic substrates and products encountered in palladium chemistry are typically insoluble in water, adapting palladium catalysts to be water soluble is one approach that has been utilised to separate the catalyst material for reuse. In these examples, the organic products are separated by solvent extraction or filtration, and the aqueous layer containing the catalyst material reused in subsequent reactions. In 2011, Akhavan and Karimi utilised this approach in their report on a water-soluble NHC-Pd polymer (**32**, Scheme 22).[138] The NHC-polymer (**32**) was rendered water-soluble through the attachment of polyethylene glycol (PEG) side chains. The NHC-Pd polymer (**32**) was employed as a Suzuki-Miyaura catalyst for a broad range of aryl bromides and chlorides at 0.005 to 0.1 mol% catalyst loading in water. For the coupling of 4-chlorobenzaldehyde and phenylboronic acid, the organic products were extracted into *n*-hexane at the end of the reaction and the aqueous layer containing 0.05 mol% **32** was reused seventeen times (Scheme 22).

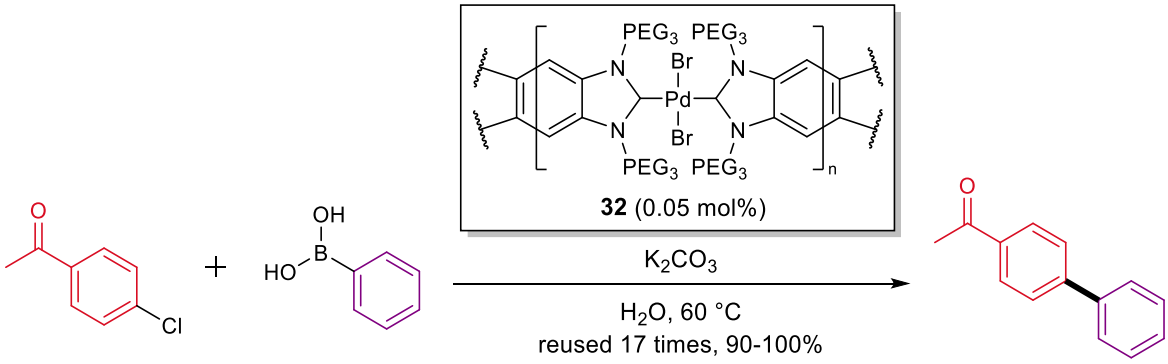

*Scheme 22. Akhavan and Karimi water-soluble NHC-Pd polymer **32** as a reusable Suzuki-Miyaura catalyst (PEG_3 = 3 repeating polyethylene glycol units).*[138]

The authors reported no loss in catalytic activity over the seventeen reuse cycles, although details on the reaction time that was necessary to reach the reaction end-point for each cycle were not provided.

Polar organic solvents have also been used as a medium for recycling homogeneous palladium catalysts. For example, Domínguez *et al.* reported on the synthesis of an NHC-pincer palladium complex (**33**) with a carboxylic acid backbone.[139] The complex (**33**) was used as a catalyst for the oxidation of a broad range of benzylic alcohols and benzyl methylenes in PEG_{400} under 1 atmosphere of O_2. The group found that addition of diethyl ether to the reaction mixture followed by cooling to –78 °C resulted in phase separation of the PEG_{400} and ether layers. The catalyst material was retained in the PEG_{400} layer and was reused six times for the oxidation of 1-phenylethanol. Quantitative conversions were observed for the first 5 cycles, followed by a drop in yield to 87% on the sixth reuse (Scheme 23). The origin of this drop in yield was not explored.

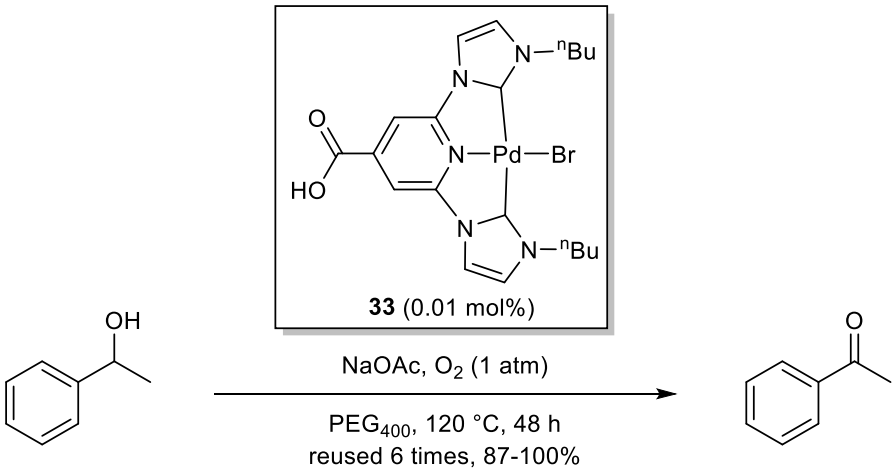

*Scheme 23. Domínguez et al. reusable homogeneous palladium pincer complex **33** as a catalyst for the oxidation of 1-phenylethanol.*[139]

Ionic liquids have also been commonly employed as solvents and supports for reusable homogeneous palladium catalysts. For example, Riisager *et al*. reported using an ionic liquid, [SBMI][*p*-TSO] **34** (SBMI = 1-methyl-3-(4-sulfobutyl)-1H-imidazolium, *p*-TSO = *p*-tolyl sulfonate) as a cosolvent with methanol in the palladium-catalysed methoxycarbonylation of ethylene.[140] Palladium salt $Pd(OAc)_2$ was employed at 0.03 mol% loading alongside a chelating phosphine ligand **35** (Scheme 24).

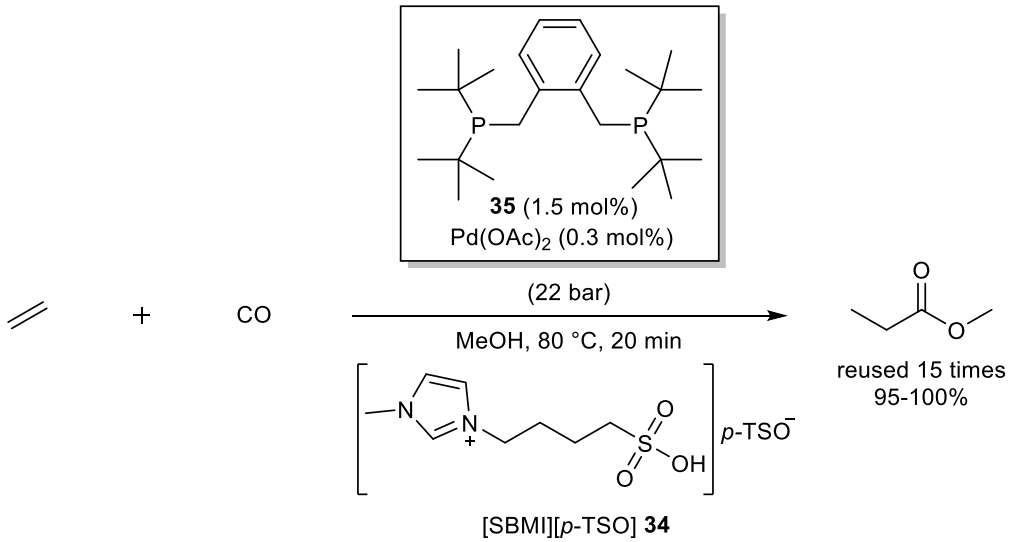

*Scheme 24. Riisager et al. ethylene methoxycarbonylation catalysed by homogeneous $Pd(OAc)_2$/**35** which were reused in an ionic liquid, [SBMI][p-TSO] **34**.*[140]

The resulting methyl propanoate product phase-separated from the ionic liquid phase, enabling isolation and reuse of the catalyst in the ionic liquid. The catalyst was reused fifteen times with no observable drop in catalyst performance. The authors found that pre-forming the catalyst from $Pd(OAc)_2$ and **35** was crucial for catalyst stability, as formation of the catalyst from $Pd(OAc)_2$ and **35** *in situ* resulted in the precipitation of palladium black after the 5th cycle (Figure 10a). Conversely, when the catalyst was pre-formed from $Pd(OAc)_2$ and **35** at 80 °C for 2 h before the addition of carbon monoxide and ethylene, the catalyst remained stable over 15 cycles (Figure 10b).

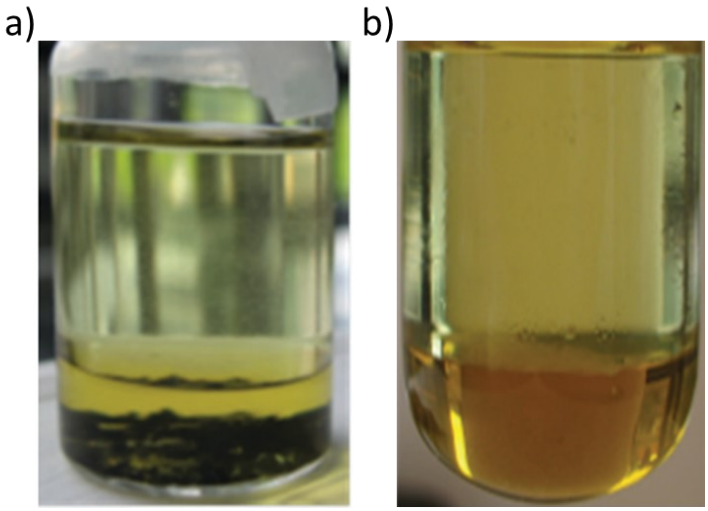

Figure 10. Riisager et al. ethylene methoxy carbonylation reaction mixture, with the palladium catalyst in the lower [SBMI][p-TSO] phase. a) Phase-separated reaction mixture after 5 cycles and in situ catalyst formation, resulting in the precipitation of palladium black. b) Phase-separated reaction mixture after 15 cycles and preformation of the catalyst, resulting in no palladium black formation. Reproduced with permission from reference 140.

In 2015 Bergbreiter *et al.* described an alternative recycling approach.[141] All of the reusable catalysts covered thus far have relied on a highly-polar catalyst design that is phase-separated with a less polar (e.g. hexane, diethyl ether) organic solvent to selectively extract the organic material. The Bergbreiter group, however, utilised the opposite approach, by synthesising a non-polar palladium catalyst that partitions into a non-polar solvent.[141] The group synthesised a polyisobutylene-phosphine ligand (**36**) which was employed alongside $Pd(dba)_2$ as a Buchwald-Hartwig amination catalyst in heptane. At the end of the reaction, the organic amination products were extracted into methanol and the residual catalyst material was reused in heptane. Several different amination substrates were employed in the recycling experiments and the catalyst material was reused up to eight times (Scheme 25). ICP-MS analysis of the amination products revealed that only 0.1%, or ~9 ppm residual palladium content, of the total catalyst palladium material had leached into the product.

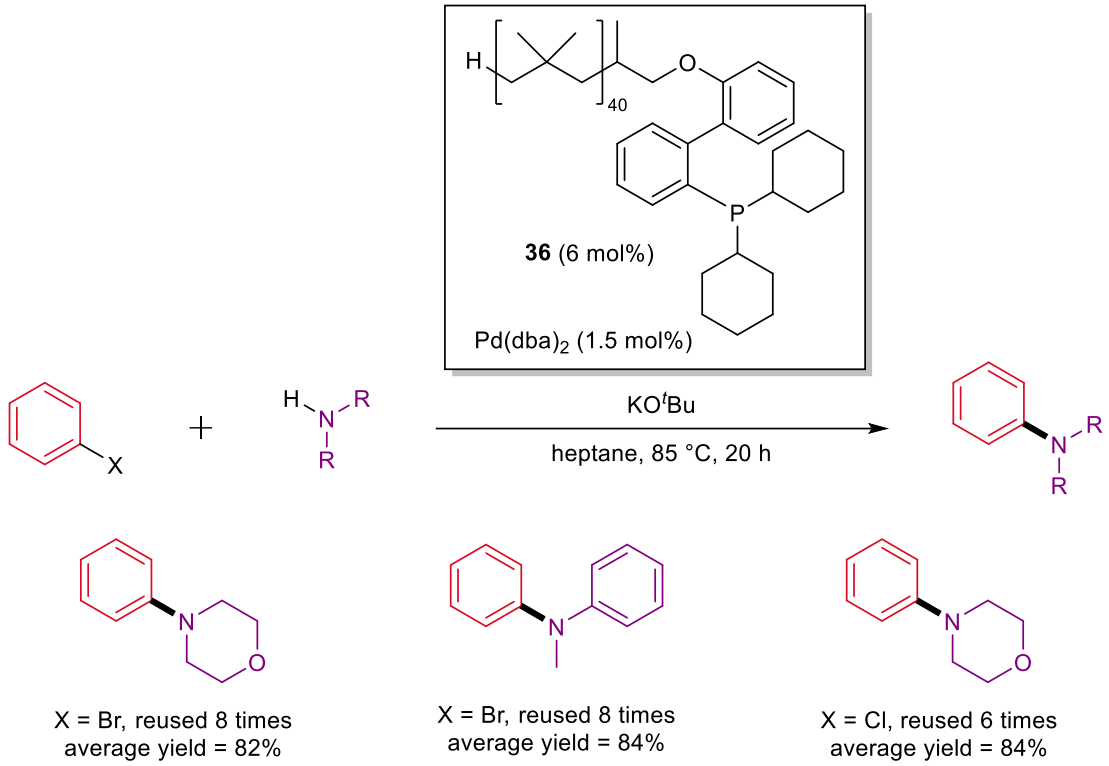

*Scheme 25. Bergbreiter et al. Buchwald-Hartwig amination catalysed by $Pd(dba)_2$ and phosphine **36**. The palladium material was reused in heptane following extraction of the organic materials into methanol.*[141]

Another strategy employed to phase separate the catalyst material from the reagents and products is anti-solvent precipitation. Similar to heterogeneous catalysts, this approach permits homogeneous palladium catalysts to be isolated by filtration for reuse, with the organic substrates retained in the filtrate. In one example of such an approach, Rodionov *et al*. synthesised a star-shaped copolymer containing an NHC palladium complex (**37**, Scheme 26).[142] The imidazolium complex was grafted onto the polymer using an alkyne-azide cycloaddition reaction with the surface azide units, and the imidazolium subsequently deprotonated with K_2CO_3 in the presence of 3-chloropyiridine and $PdCl_2$ to yield **37**. The polymer supported NHC-Pd catalyst was illustrated to be an effective Mizoroki-Heck and Stille cross coupling catalyst for a range of alkenes and organostannanes. At the end of the reaction, the reaction mixture was filtered through a 0.2 μm PTFE membrane and the catalyst material precipitated by the addition of methanol. The precipitate was then isolated and dried for reuse. **37** was reused five times without any observed change in catalytic activity or solubility of the catalyst material (Scheme 26). ICP-MS analysis revealed that the residual palladium content in the product prior to chromatographic purification was 2.8 ppm, and palladium content remained at 0.7 ppm in subsequent runs. It should be noted that the authors intentionally halted the reaction at 30 min – before the reaction had reached quantitative conversion. This way, catalyst deactivation would not be

masked by superfluous reaction times. This aspect of catalytic studies has been highlighted by a number of authors as good practice,[24,143,144] however it is still rarely considered.

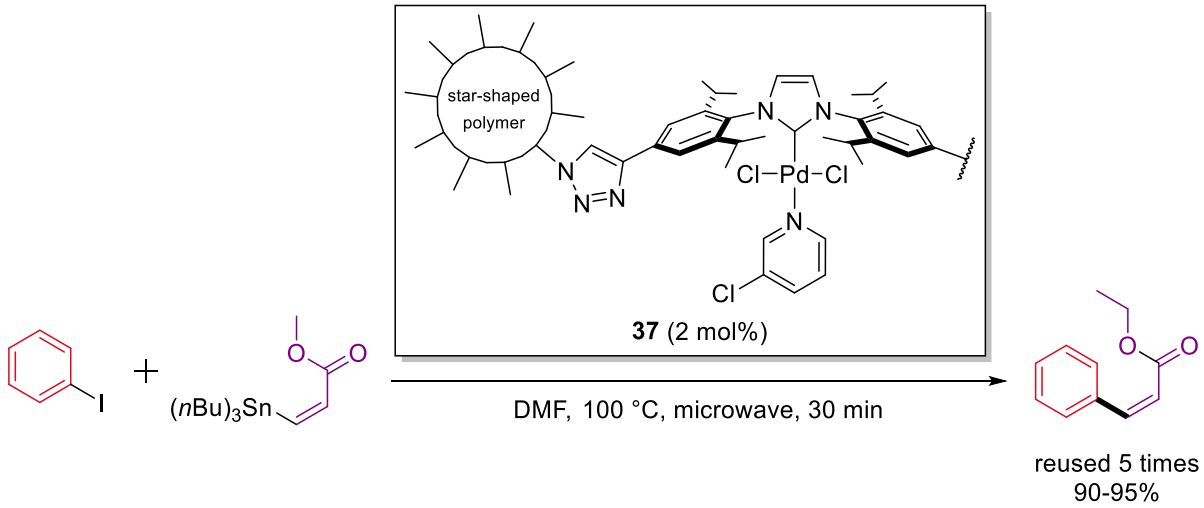

*Scheme 26. Stille coupling catalysed by a reusable polymer-supported NHC palladium complex (**37**).*[142]

The final example of a reusable homogeneous catalyst is the work by Liu *et al* to develop an NHC-Pd complex with a structure and solubility that was pH dependent.[145] The group tethered an NHC-Pd complex to a spiropyran ring (**38**, Scheme 27). Under basic conditions (pH >12), the spiropyran ring in **38** is converted to the open-form phenoxide (**39**, Scheme 27), which is soluble in IPA:H_2O mixtures, permitting its use as a homogeneous Suzuki-Miyaura catalyst. Compound **38** was employed as a Suzuki-Miyaura precatalyst for a range of aryl halides, including aryl chlorides. Upon neutralisation (pH 7), dehydration of phenoxide **39** occurs to form the zwitterion **40** (Scheme 27), which selectively partitions into dichloromethane. Compound **40** was then be converted back to the precatalyst **38** upon irradiation with UV-light, and isolated following removal of dichloromethane.

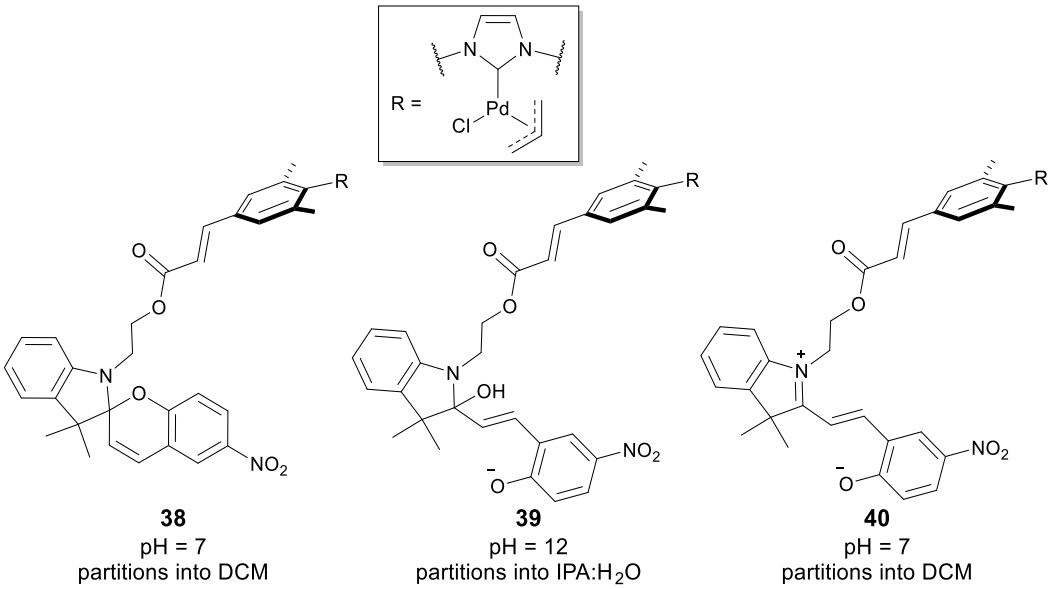

*Scheme 27. Spiropyran precatalyst **38**, and pH dependent structure and solubility which permitted its recovery and reuse.*[145]

Using this process, **38** was recovered and reused eight times as a Suzuki-Miyaura precatalyst for the coupling of *p*-bromotoluene and phenylboronic acid (Table 6).

*Table 6. Suzuki-Miyaura reaction catalysed by **38**, which was reused eight times, with details on catalyst recovery and reaction duration provided for each cycle.*[145]

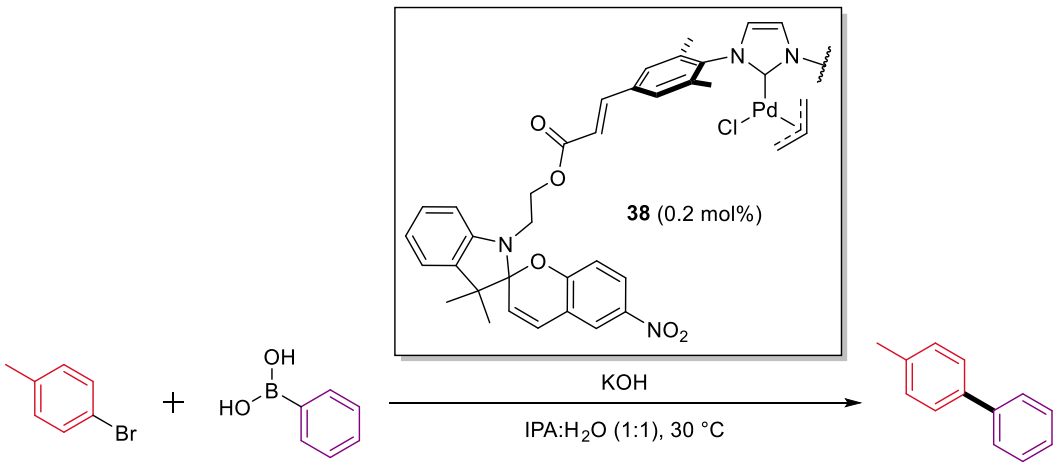

Cycle	1[a]	2[a]	3[a]	4[a]	5[b]	6[c]	7[d]	8[d]
Reaction Yield (%)	98	98	98	98	98	98	97	56
Yield recovered **38** (mol%)	0.194	0.186	0.177	0.164	0.156	0.145	0.130	

[a] Reaction time: 1.5 h. [b] Reaction time: 2.5 h. [c] Reaction time: 3.0 h. [d] Reaction time: 12 h

The researchers provided the recovery yields of the catalyst, which showed that the loading dropped from 0.20 to 0.13 mol% over the eight reuse cycles as a result of the precipitation of palladium black.

1.2. Sustainability of gold in catalysis

1.2.1. Gold supply concerns

Gold is much more widely used in electronics than palladium but is less commonly employed as a catalyst. However, many of the supply and environmental issues associated with palladium are present also for gold, and often to a much greater degree. Aside from the historical significance of gold in jewellery and investment, the metal plays a key role in many modern technologies. The excellent conductivity and stability towards oxidation and corrosion of gold means that the metal is used extensively in electronic equipment. Yet, the mining and refining of gold ore has huge environmental consequences. This has been highlighted by Nuss and Eckelman, and by the United Nations, which reported gold to be one of the biggest polluting elements (Figure 11).[11,146]

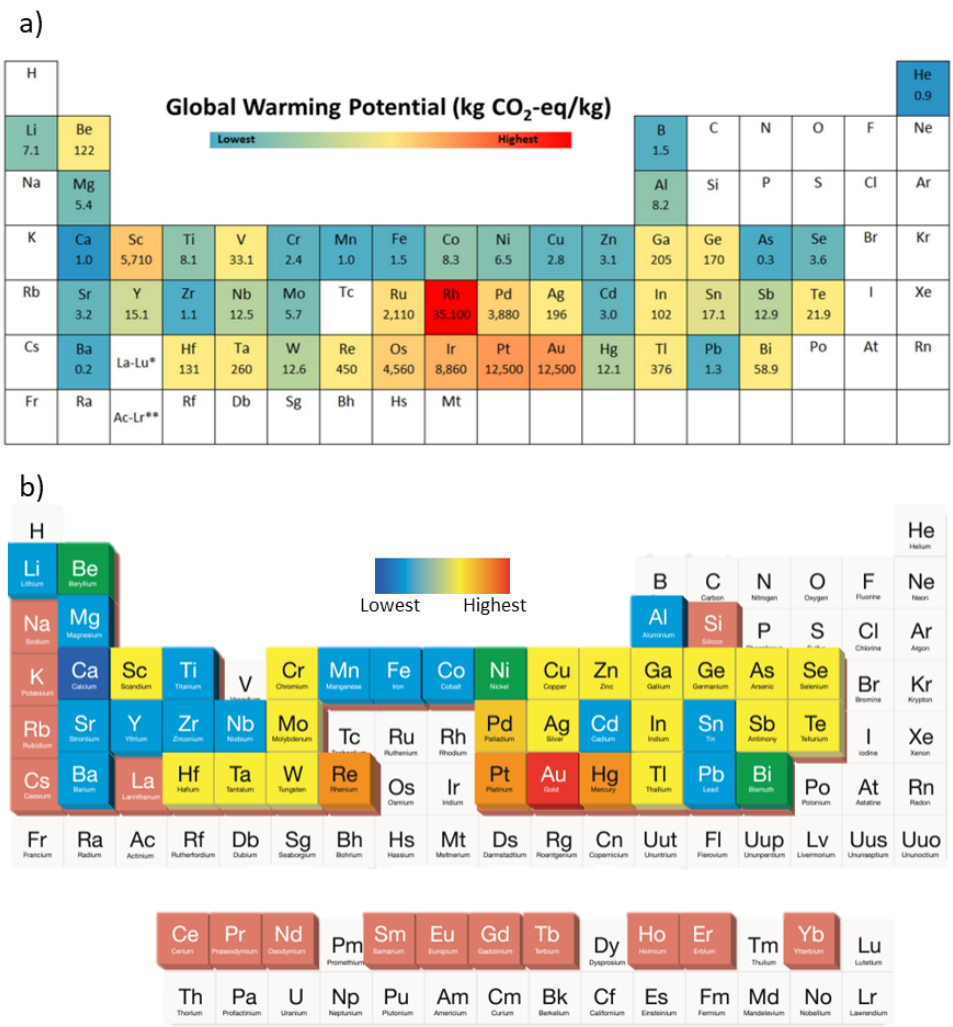

Figure 11. Environmental impact of gold production. a) Cradle-to-gate global warming potential of each element reported by Nuss and Eckelman. b) Environmental impact by mining reported by the United Nations. Reproduced directly from references 11 and 146 (Open Access publications).

This environmental impact comes mainly from the energy and resource intensive processes used to mine and refine gold ore. For example, gold ore was traditionally processed by cyanidation in the presence of oxygen to oxidise Au^0 and extract $[Au(CN)_2]^-$.[147] The mixed metal content of gold ore and limited selectivity of cyanidation means that the recovered $[Au(CN)_2]^-$ must undergo further energy intensive smelting and separation processes.[148,149] Unfortunately, cyanidation generates huge volumes of waste tailings which contain a range of pollutants, including heavy metals and cyanide.[149–151] This has prompted cyanidation bans in the US, Germany, Turkey, Czech Republic and Hungary. Gold recycling is similarly problematic, as it utilises many of the same energy and resource intensive processes.[152] Moreover, whilst mercury amalgamation as a technique for gold refining and recycling has been phased out of large scale mining, it is still widely used in artisanal processes, leading to estimates that mercury/gold amalgamation accounts for ~37% of global mercury emissions.[153]

Alongside these environmental factors, the high demand for gold, its low natural abundance in the earth's crust, and the expensive processes employed in the production of gold from ore lead to the high cost of the metal (£52 per gram in April 2023).[154]

The use of gold complexes in catalysis is one application that is limited by concerns over the supply of this metal. Indeed, homogeneous gold catalysis remained essentially unexplored until the 2000s. However, the scope of transformations which utilise a gold catalyst has grown significantly over the past two decades. Homogeneous gold catalysed cross-coupling,[155–158] borylation,[159] C-H activation,[160] photoredox and oxidation reactions have all now been reported (Figure 12).[161,162] Gold catalysts have also been employed as Lewis acid catalysts,[163,164] especially for the activation of alkyne bonds.[165–169] Some selected examples are summarised in Figure 12.

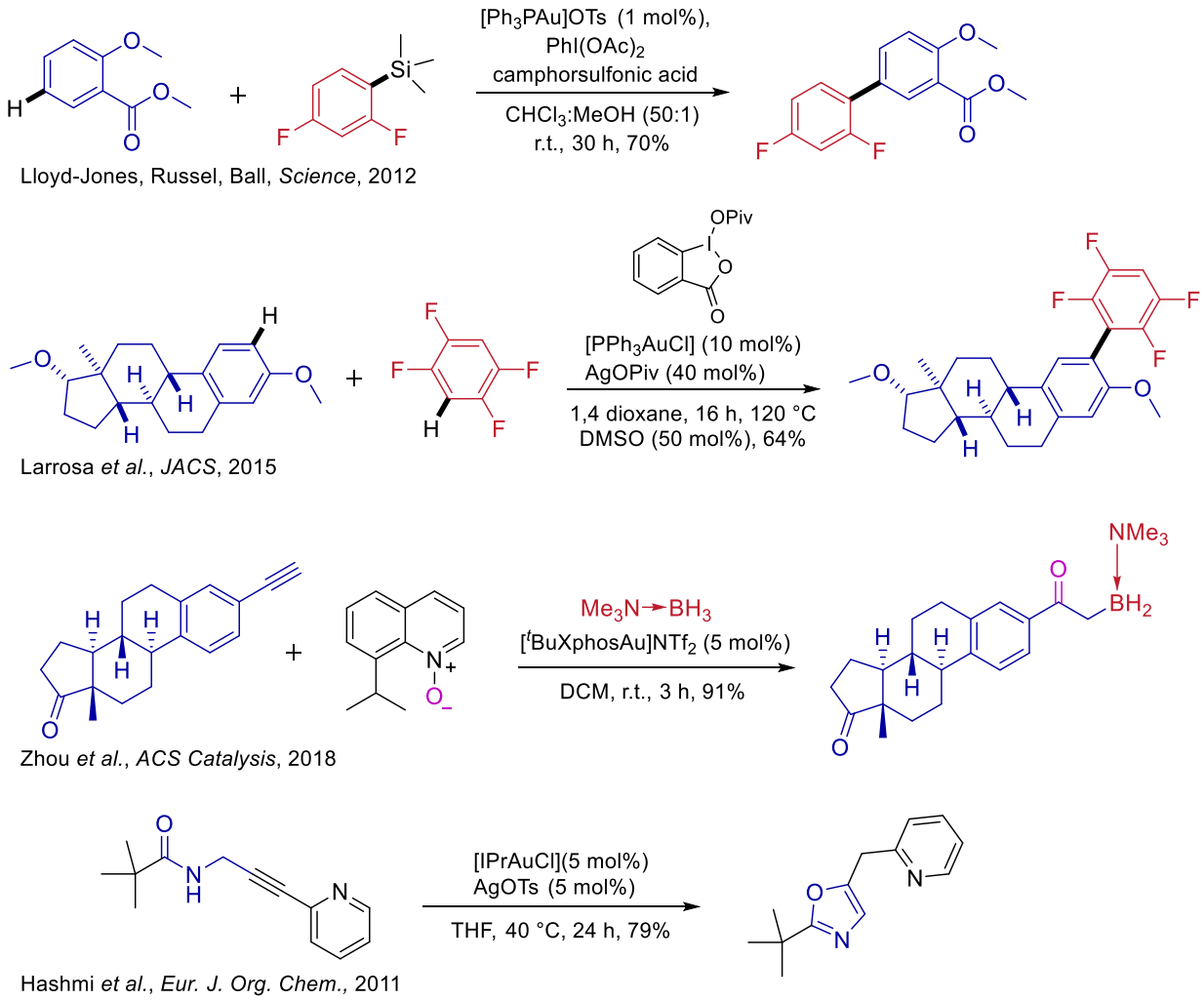

Figure 12. Selected modern examples of homogeneous gold catalysis.

A recent review by Rocchigiani and Bochmann,[170] covering Au^{3+} homogeneous catalysts, contained 565 references, demonstrating the staggering growth in the literature compared to the 13 transformations covered by Dyker's 2008 review.[171] Despite these advancements, there are no fine chemical processes conducted on a large scale which utilise a homogeneous gold catalyst (according to search of the journal *Organic Process Research and Development*). Instead, industrial applications of gold in the chemical industry remains limited to the synthesis of bulk chemicals by supported heterogeneous catalysts.[172] It would clearly be advantageous for the supply of gold to be rendered cheaper and more sustainable, removing this barrier to the adoption of gold catalysts.

1.2.2. Gold recycling

Gold recycling accounts for ~30% of global gold supply,[173] though around 90% of this recycled material comes from high-value sources such as jewellery and coins. This is despite industrial sources like waste electronic equipment (WEEE) being one of the fastest growing sources of waste in the world with over 50 million tonnes of WEEE produced every year.[146,174] This waste contains more gold (e.g. up to 700 g/ton in waste printed circuit boards) than gold ore (1-10 g/ton), as shown in Table 7.[175,176]

Table 7. Concentration of copper, silver and gold present in gold-enriched ores and mobile phones.[175,176]

	Source	
Metal	Gold enriched ores	Mobile phones
Copper	3-7 kg/tonne	50-150 kg/tonne
Silver	4-10 g/tonne	500-700 g/tonne
Gold	1-10 g/tonne	150-400 g/tonne

A recent United Nations report (*Global E-Waste Monitor 2019 report)* estimated that the precious metals present in this WEEE is worth at least £7.9bn.[177] Moreover, life cycle assessments frequently report that urban mining of WEEE has the potential to reduce the environmental cost of primary gold supplies, however the majority of this material is still destined for landfill.[29,178,179] The devastating impact of existing WEEE life-cycles was highlighted in Robinson's highly-cited 2009 review (Table 8).[180] This reported that in Guiyu, the location of the world's largest WEEE processing centre, air toxin concentrations, such as of dioxins released during pyrometallurgy, are 300x higher than in nearby Hong Kong – 50x higher than WHO guidelines. Children in Guiyu were also reported to have higher lead and cadmium blood levels and consequently lower cognitive abilities than children in neighbouring towns. These statistics illustrate the necessity for improvements to the life cycle of

electronic equipment. Governments have consequently begun introducing regulations to incentivise the proper treatment and recycling of WEEE.[181,182]

Table 8. Global emissions from WEEE disposal and recycling, assuming 20 Mt/year of global WEEE production. Adapted from Robinson's 2009 review.[180]

Contaminant	Relationship with WEEE	Annual global emissions in WEEE (tons)
Polybrominated diphenyls and diphenyl ethers, chlorofluorocarbons, polycyclic aromatic hydrocarbons, polyhalogenated aromatics, dioxins and furans	Products of the combustion of halogenated flame retardants and plastics	280
Antimony	Flame retardant, plastics	34,000
Cadmium	Batteries, toners, plastics	3,600
Chromium	Data tapes and floppy disks	198,000
Copper	Wiring	820,000
Lead	Solder, cathode-ray tubes, batteries	58,000
Mercury	Fluorescent lamps, batteries	13.6
Nickel	Batteries	206,000
Tin	Solder	48,000
Zinc	Solder	102,000

As for palladium recycling, current industrial gold recycling relies on a combination of pyrometallurgy and hydrometallurgy. For example, at Umicore's refinery in Belgium (Figure 13),[183] pre-treated WEEE is heated in a blast furnace to generate a lead bullion and a mixed metal matte, followed by smelting of the matte to yield a precious metal containing copper bullion. Electrochemical refining of this bullion produces high purity copper, alongside a sludge residue containing silver, gold, platinum, palladium, rhodium, ruthenium and iridium.[178,184,185] The precious metals are then concentrated and separated by extensive hydrometallurgical refining. Precious metal recovery rates of >95% are reported. Umicore report a CO_2 abatement potential of 1 million tonnes (Mt) when their process is compared with primary metal production, which is estimated to cause 1.3 Mt of CO_2 emissions. Unfortunately, the large capital investment required for such state-of-the-art equipment, and the energy and resource intensive processes involved in pyro- and hydrometallurgy render WEEE recycling economically unfeasible in most countries. Moreover, the application of pyrometallurgy to

plastic containing WEEE produces metallic and carbonaceous particulates, alongside the emission of toxic gaseous dioxin and furans.[183,186] Similarly, existing hydrometallurgy relies on reagents such as *aqua regia* or cyanide, which are expensive to safely handle on a large scale and result in the release of devastating toxic emissions.[151]

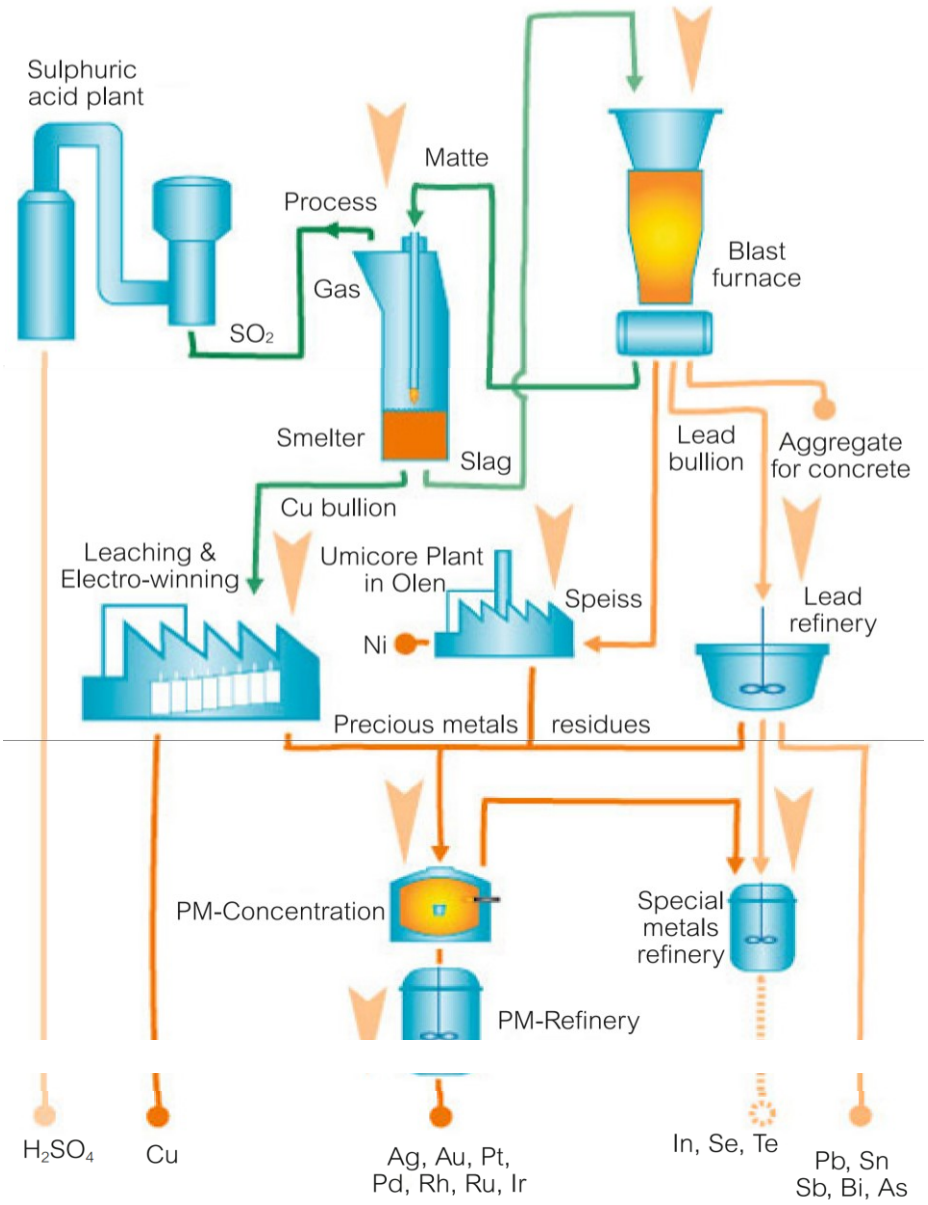

Figure 13. Umicore WEEE refinery plant overview. Reproduced directly from reference 183 (Open Access).

As a result of these concerns, a great deal of effort has been focused on improving the efficiency and sustainability of gold recycling. For example, a number of reports have explored substitutes for *aqua regia* and cyanide, including thiosulfate and oxygen,[187] thiourea or thiocyanate and oxidising iron,[188,189] and milder halide based lixiviants/oxidants such as I^-/I_2.[190–192] Whilst these systems

represent an environmental improvement over *aqua regia*/cyanide, they also typically suffer from high reagent consumption and/or poor efficiency. Several reviews have covered the advantages and disadvantages of these approaches.[186,193] Advances have also been made in methods for extracting gold from the resulting aqueous waste streams. Solvent extraction is the most popular technique, however a number of other modern strategies have emerged, including adsorption onto a solid support, selective oxidation, precipitation and ionic liquid extractants.[36,194–201]

1.2.3. Gold catalysts derived from recycled waste

Increased gold recycling can be incentivised through the direct valorisation of scrap WEEE into high-value catalytic applications. Decoupling the catalytic applications of gold from the metals problematic supply chain would also improve the industrial viability of gold catalysts. This has prompted a number of groups to utilise gold waste streams as sources of gold catalysts.

Researchers have, similar to palladium recycling, utilised acidic gold waste streams as a source for gold catalysts. For example, Haukka *et al* utilised a 3D printed porous polyamide adsorbent, made of polyamide-12/Nylon-12 (PA12), to recover gold.[202] The adsorbent could also be 3D printed into a variety of shapes, such as cylindrical tubes for in-flow recovery of gold.[203] Waste printed circuit boards were digested with *aqua regia* and the groups adsorbent was selective in recovering gold from the resulting acidic solution containing a mixture of gold, platinum, palladium, copper, aluminium, nickel, chromium, lead, zinc, tin and iron. The gold-loaded adsorbent (PA12-Au) was subsequently treated with sodium borohydride to reduce the captured Au^{3+} ions to Au^{0} nanoparticles that were ~16 nm in diameter (diameter determined by PXRD) (Figure 14).

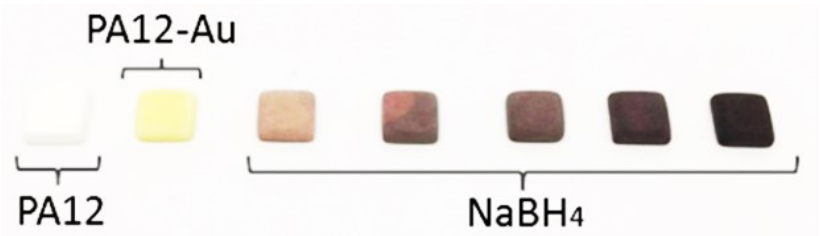

Figure 14. PA12 Adsorbent used to recover Au^{3+} ions from an acidic mixed metal WEEE leachate, and the reduction of the resulting gold-loaded (PA12-Au) adsorbent with $NaBH_4$. $NaBH_4$ from left to right shows samples reduced for 1, 3, 5, 10 and 15 mins. Reproduced directly from reference 202 (Open Access).

The PA12-Au^{0} nanoparticles were shown to be an effective catalyst for the reduction of 4-nitrophenol to 4-aminophenol in water. Complete conversion was observed at room temperature and the PA12-

Au^0 nanoparticles were isolated and reused, with complete conversion being reported in 2 h over ten reuse cycles.

Chitin is a material derived from waste bio-cellulose and is frequently utilised both as an adsorbent for metal recovery,[204–206] and as a heterogeneous catalyst support.[133,207–215] Liu and colleagues recently combined these approaches by using a chitin nanofibrous membrane to recover gold and subsequently employ the supported recovery product in catalysis.[216] An aqueous-organic emulsion containing Au^{3+} ions was employed as an industrial waste stream mimic. It was shown that Au^{3+}, Pt^{4+}, Pd^{2+} and Ag^{+} ions could all be adsorbed onto the chitin membrane, however selectivity for any one metal ion from a mixed metal solution was not reported. Heating the resulting Au^{3+}-loaded chitin membrane at 90 °C for 30 min resulted in the reduction of Au^{3+} to Au^0 nanoparticles of ~5 nm diameter (Figure 15).

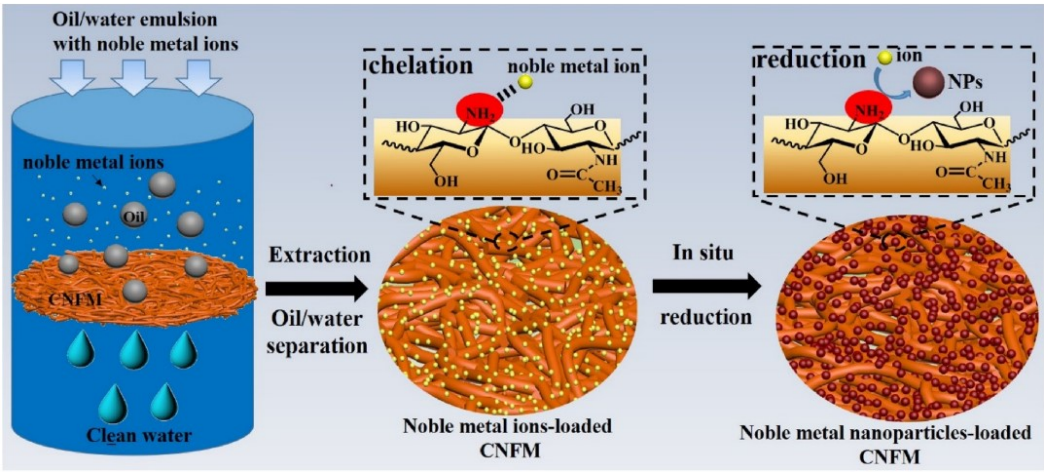

Figure 15. Liu et al Au^{3+} capture and subsequent supported Au^0 nanoparticle formation using a chitin nanofibrous membrane. Reproduced with permission directly from reference 216.

The authors proposed that the amine groups present in the chitin were responsible for Au^{3+} reduction, as a chitin sample oxidised by TEMPO/NaClO did not promote Au^{3+} reduction. The authors did not comment on other factors, such as the possible oxidation of chitin alcohols by TEMPO/NaClO and Au^{3+}. The group subsequently illustrated that the Au^0-loaded chitin was an effective catalyst for the reduction of 4-nitrophenol. The 4-aminophenol product was produced quantitatively at room temperature, although comparing the performance of the recovered catalyst is challenging, since most of the key reaction details were not reported.

Pardo *et al* recently utilised a MOF to recover gold and subsequently employed the gold-loaded MOF in catalysis.[217] The group decorated the channels of a MOF containing Ca^{2+} and Cu_6^{2+} units

with L-methionine to improve gold adsorption. Gold was recovered from water-methanol solutions of both $AuCl_3$ and AuCl. Crucially, trace metal analysis (ICP-OES) revealed that when the MOF was exposed to a mixed metal solution containing $AuCl_3$ alongside $[Pd(NH_3)_4]Cl_2$, $NiCl_2$, $CuCl_2$, $ZnCl_2$, and $AlCl_3$, only Au^{3+} ions were adsorbed. X-ray diffraction of the resulting gold-loaded MOF revealed that the flexible nature of the methionine chains in the MOF pores enabled metal binding to be obtained without disrupting the pore network (Figure 16). This high three-dimensional stability imparted the MOF with unprecedented adsorption capacity for gold ions (15-20 wt. %).

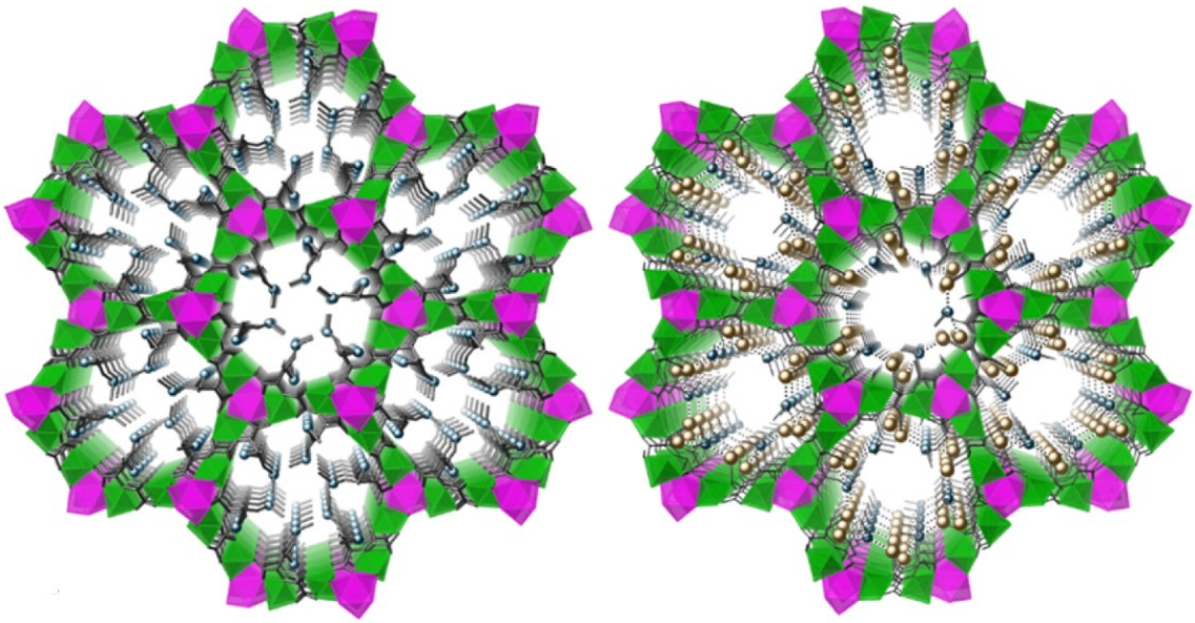

Figure 16. Single crystal X-ray diffraction structures of Ca^{2+}/Cu_6^{2+} MOF decorated with L-methionine and retention of pore structure upon adsorption of Au^{3+} ions (right). Reproduced directly from reference 217.

The resulting Au^{3+}-loaded MOF (**41**) was subsequently illustrated to be an efficient catalyst for the cyclisation of 4-pentyn-1-ol (Scheme 28).

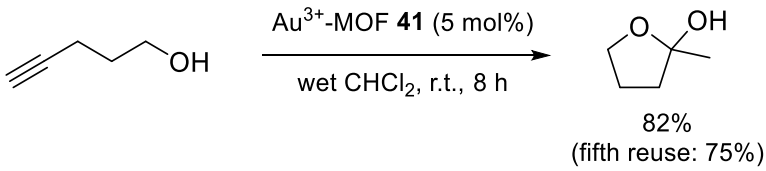

Scheme 28. Cyclisation of 4-pentyn-1-ol catalysed by Au^{3+}-loaded MOF.

It was also reported that whilst the trivalent Au^{3+}-loaded MOF (**41**) was stable and could be reused five times with only a small decrease in catalytic activity (82% to 75%), the equivalent monovalent Au^{+}-

loaded MOF formed catalytically inactive Au^0 nanoparticles when exposed to the 4-pentyn-1-ol cyclisation reaction conditions. These nanoparticles were detected through the presence of a new UV-Vis spectroscopy adsorption band at ~500 nm, which was not observed for the trivalent Au^{3+}-loaded MOF.

All of the examples covered thus far utilised a solid-phase material to adsorb gold, resulting in the application of the recovery product as a heterogeneous gold catalyst. Research in the Wilton-Ely and Serpe groups, however, has utilised molecular gold complexes recovered from WEEE as homogeneous catalysts,[218] which will be covered in the following chapter.

1.3. Conclusions

When evaluating techniques that recycle metals and utilise the recovery product in catalysis, a key point that should be addressed is the selectivity of the recycling process for the desired metal. For example, WEEE contains palladium and gold alongside a broad range of other transition metals, including precious metals such as platinum.[29,219] Similarly, TWCs utilise platinum and rhodium in varying amounts alongside palladium.[32,220] As a result, the selectivity of any recovery process is crucial for obtaining sufficiently pure recovery products for applications in catalysis. Moreover, the potential to valorise the other precious metals present in these waste streams is tied to the selectivity of the recovery process. Yet, many of the reports covered herein, and many not covered,[221] either do not explore selectivity or limit their experiments to some limited combination of alkaline metals, main group elements and first-row transition metals. These selectivity experiments are not representative of any 'real-world' waste stream. Instead, the selectivity of the recovery process must be explored in a way that is relevant to the proposed waste stream, ideally by utilising a real waste material. The lack of selectivity experiments using real waste streams may be due to the exact details of industrial recovery processes and industrial waste streams not being readily available to academic researchers. Moreover, there may be a lack of motivation to fully study the recovery of precious metals for catalytic applications since companies like Johnson Matthey already offer catalyst recycling services. However, these services rely on resource intensive processes and have been operating at capacity whilst global secondary palladium supplies remain at around 25-30%.[3,4,12,13] Therefore, there remains a need for more sustainable and economically accessible processes for recycling precious metals.

A reasonable scope of transformations have been reported with recycled palladium catalysts, although Buchwald-Hartwig amination is notably missing. Reduction reactions are particularly well explored, with the scope of substrates covering industrially relevant commodity and fine chemicals. Often though, the catalytic application of the recovery product is limited to simple substrates with

limited or no in-depth studies on the kinetic performance of the catalyst. If these catalysts are to be adopted by the chemical community, substrates relevant to the target application should be explored, e.g. pharmaceutical or agrochemical compounds in cross-coupling applications. In addition, if incumbent catalysts are to be replaced by recycled alternatives, kinetic studies which provide detailed understanding of intrinsic catalyst performance and stability are needed, instead of just simple yield comparisons.[144] Similarly, if the goal is to obtain closed-loop consumption of palladium, considerations must be made for the end-point of the catalyst at the end of the reaction, even for homogeneous catalysts, and how this end-point permits metal recovery and reuse. Trace metal studies would help to understand the destination of the catalyst material and would thus support studies on recovering palladium at the end of the reaction. Moreover, trace metal analysis will help to encourage the adoption of new recycled catalysts in industries where product residual metal concentrations are heavily regulated.[222] Yet, these studies are seldom conducted for palladium catalysts recycled from waste materials.

All of the examples of gold recovery covered in this review utilised a solid-phase material to adsorb gold, resulting in the application of the recovery product as a heterogeneous gold catalyst. Research in the Wilton-Ely and Serpe groups, however, has utilised molecular gold complexes recovered from WEEE as homogeneous catalysts,[218] which will be covered in the following chapter.

1.4. References

1 ACS Green Chemistry Institute: Endangered Elements, https://www.acs.org/content/acs/en/greenchemistry/research-innovation/endangered-elements.html, (accessed 9 September 2020).

2 EUChemS - Elemental Scarcity, https://www.euchems.eu/euchems-periodic-table/, (accessed 25 July 2023).

3 Johnson Matthey, PGM Market Report, https://matthey.com/products-and-markets/pgms-and-circularity/pgm-markets/pgm-market-reports, (accessed 25 July 2023).

4 J. Matthey, PGM Market Report - February 2021, http://www.platinum.matthey.com/services/market-research/pgm-market-reports, (accessed 28 May 2021).

5 Johnson Matthey, Johnson Matthey PGM Market Report, http://www.platinum.matthey.com/documents/new-item/pgm market reports/pgm market report may 2014.pdf, (accessed 9 September 2020).

6 VW scandal could end platinum's price supremacy over palladium, https://www.reuters.com/article/us-platinum-palladium-parity-vw-idUSKCN0RO0HU20150924, (accessed 27 July 2023).

7 Precious metal price chart, https://www.bullionvault.co.uk/chart-popup.do?, (accessed 27 July 2023).

8 C. Hagelüken, *Platin. Met. Rev.*, 2012, **56**, 29–35.

9 L. A. Cramer, *Jom*, 2001, **53**, 14–18.

10 B. J. Glaister and G. M. Mudd, *Miner. Eng.*, 2010, **23**, 438–450.

11 P. Nuss and M. J. Eckelman, *PLoS One*, 2014, **9**, 1–12.
12 Johnson Matthey, PGM Mark. Rep., http://www.platinum.matthey.com/services/market-research/pgm-market-reports, (accessed 9 September 2020).
13 A. Cowley, PGM Market Report, http://www.platinum.matthey.com/documents/new-item/pgm-market-reports/pgm-market-report-may-2020.pdf, (accessed 26 March 2021).
14 Johnson Matthey PGM Recycling Rates, https://matthey.com/media/2023/johnson-matthey-offers-100-recycled-platinum-group-metal-pgm-content, (accessed 3 August 2024).
15 D. G. Brown and J. Boström, *J. Med. Chem.*, 2016, **59**, 4443–4458.
16 C. Torborg and M. Beller, *Adv. Synth. Catal.*, 2009, **351**, 3027–3043.
17 P. Devendar, R. Y. Qu, W. M. Kang, B. He and G. F. Yang, *J. Agric. Food Chem.*, 2018, **66**, 8914–8934.
18 V. L. Budarin, P. S. Shuttleworth, J. H. Clark and R. Luque, *Curr. Org. Synth.*, 2011, **7**, 614–627.
19 J. Magano and J. R. Dunetz, *Chem. Rev.*, 2011, **111**, 2177–2250.
20 Y. Zhu, W. Dong and W. Tang, *Adv. Agrochem*, 2022, **1**, 125–138.
21 The 2010 Nobel Prize in Chemistry, https://www.nobelprize.org/prizes/chemistry/2010/summary/, (accessed 27 July 2023).
22 F. Lovering, J. Bikker and C. Humblet, *J. Med. Chem.*, 2009, **52**, 6752–6756.
23 F. Lovering, *Med. Chem. Commun*, 2013, **4**, 515–519.
24 S. McCarthy, D. C. Braddock and J. D. E. T. Wilton-Ely, *Coord. Chem. Rev.*, 2021, **442**, 213925.
25 T. Mesganaw and N. K. Garg, *Org. Process Res. Dev.*, 2013, **17**, 29–39.
26 L. J. Cheng and N. P. Mankad, *Chem. Soc. Rev.*, 2020, **49**, 8036–8064.
27 K. Tamao, N. Miyaura, T. Hiyama, E. Shirakawa, K. Fugami, M. Kosugi, A. . Muci, S. L. Buchwald, M. Miura and M. Nomura, *Cross-Coupling Reactions: A Practical Guide*, Springer, Berlin, 2002.
28 N. Hazari, P. R. Melvin and M. M. Beromi, *Nat. Rev. Chem.*, 2017, **1**, 1–17.
29 A. Tuncuk, V. Stazi, A. Akcil, E. Y. Yazici and H. Deveci, *Miner. Eng.*, 2012, **25**, 28–37.
30 H. Li, J. Eksteen and E. Oraby, *Resour. Conserv. Recycl.*, 2018, **139**, 122–139.
31 H. Dong, J. Zhao, J. Chen, Y. Wu and B. Li, *Int. J. Miner. Process.*, 2015, **145**, 108–113.
32 S. Bernal, G. Blanco, J. J. Calvino, J. M. Gatica, J. A. Pérez Omil and J. M. Pintado, *Top. Catal.*, 2004, **28**, 31–45.
33 M. Benson, C. R. Bennett, M. K. Patel, J. E. Harry and M. Cross, *Miner. Process. Extr. M.,* 2000, **109**, 6-10.
34 M. Benson, C. R. Bennett, J. E. Harry, M. K. Patel and M. Cross, *Resour. Conserv. Recycl.*, 2000, **31**, 1–7.
35 W. Amatayakul and O. Ramnäs, *J. Clean. Prod.*, 2001, **9**, 395–403.
36 S. Raiguel, L. Gijsemans, A. Van Den Bossche, B. Onghena and K. Binnemans, *ACS Sustain. Chem. Eng.*, 2020, **8**, 13713–13723.
37 D. Bourgeois, V. Lacanau, R. Mastretta, C. Contino-Pépin and D. Meyer, *Hydrometallurgy*, 2020, **191**, 105241.
38 O. Lanaridi, A. R. Sahoo, A. Limbeck, S. Naghdi, D. Eder, E. Eitenberger, Z. Csendes, M. Schnürch and K. Bica-Schröder, *ACS Sustain. Chem. Eng.*, 2021, **9**, 375–386.
39 O. Buriac, M. Ciopec, N. Duţeanu, A. Negrea, P. Negrea and I. Grozav, *Molecules*, 2020, **25**, 3692.
40 A. Behnamfard, M. M. Salarirad and F. Veglio, *Waste Manag.*, 2013, **33**, 2354–2363.
41 G. Schreier and C. Edtmaier, *Hydrometallurgy*, 2003, **68**, 69–75.
42 D. I. Kim, G. Gwak, P. Dorji, D. He, S. Phuntsho, S. Hong and H. Shon, *ACS Sustain. Chem. Eng.*, 2018, **6**, 1692–1701.
43 B. Godlewska-Zylkiewicz, B. Lesniewska, U. Gasiewska and A. Hulanicki, *Anal. Lett.*, 2000, **33**, 2805–2820.
44 T. Wongsawa, N. Traiwongsa, U. Pancharoen and K. Nootong, *Hydrometallurgy*, 2020, **198**, 105488.

45 H. B. Trinh, J. chun Lee, Y. jae Suh and J. Lee, *Waste Manag.*, 2020, **114**, 148–165.
46 P. Cyganowski, *Solvent Extr. Ion Exch.*, 2020, **38**, 143–165.
47 S. Sharma, A. S. Krishna Kumar and N. Rajesh, *RSC Adv.*, 2017, **7**, 52133–52142.
48 A. P. Paiva, *Metals*, 2017, **7**, 505.
49 S. Daliran, M. Ghazagh-Miri, A. R. Oveisi, M. Khajeh, S. Navalón, M. Âlvaro, M. Ghaffari-Moghaddam, H. Samareh Delarami and H. García, *ACS Appl. Mater. Interfaces*, 2020, **12**, 25221–25232.
50 Y. Li, H. Zhong, Y. Jin, B. Guan, J. Yue, R. Zhao and Y. Huang, *ACS Appl. Mater. Interfaces*, 2022, **14**, 40408-40417.
51 V. Lacanau, F. Bonneté, P. Wagner, M. Schmitt, D. Meyer, F. Bihel, C. Contino-Pépin and D. Bourgeois, *ChemSusChem*, 2020, **13**, 5224–5230.
52 M. Cortes-Clerget, J. Yu, J. R. A. Kincaid, P. Walde, F. Gallou and B. H. Lipshutz, *Chem. Sci.*, 2021, **12**, 4237–4266.
53 S. Handa, M. P. Andersson, F. Gallou, J. Reilly and B. H. Lipshutz, *Angew. Chem. Int. Ed.*, 2016, **55**, 4914–4918.
54 N. R. Lee, A. A. Bikovtseva, M. Cortes-Clerget, F. Gallou and B. H. Lipshutz, *Org. Lett.*, 2017, **19**, 6518–6521.
55 N. R. Lee, R. T. H. Linstadt, D. J. Gloisten, F. Gallou and B. H. Lipshutz, *Org. Lett.*, 2018, **20**, 2902–2905.
56 H. Pang, Y. Hu, J. Yu, F. Gallou and B. H. Lipshutz, *J. Am. Chem. Soc.*, 2021, **143**, 3373–3382.
57 S. Handa, Y. Wang, F. Gallou and B. H. Lipshutz, *Science*, 2015, **349**, 1087–1091.
58 X. Yang, J. Chen, L. Hu, J. Wei, M. Shuai, D. Huang, G. Yue, D. Astruc and P. Zhao, *Chem. Mater.*, 2019, **31**, 7386–7394.
59 A. V. Oladeji, J. M. Courtney, M. Fernandez-Villamarin and N. V. Rees, *J. Am. Chem. Soc.*, 2022, **144**, 18562–18574.
60 M. Albino, T. J. Burden, C. C. Piras, A. C. Whitwood, I. J. S. Fairlamb and D. K. Smith, *ACS Sustain. Chem. Eng.*, 2023, **11**, 1678–1689.
61 C. C. Piras, P. Slavik and D. K. Smith, *Angew. Chem. Int. Ed.*, 2020, **59**, 853–859.
62 S. De Corte, T. Hennebel, B. De Gusseme, W. Verstraete and N. Boon, *Microb. Biotechnol.*, 2012, **5**, 5–17.
63 N. J. Creamer, I. P. Mikheenko, P. Yong, K. Deplanche, D. Sanyahumbi, J. Wood, K. Pollmann, M. Merroun, S. Selenska-Pobell and L. E. Macaskie, *Catal. Today*, 2007, **128**, 80–87.
64 J. A. Bennett, N. J. Creamer, K. Deplanche, L. E. Macaskie, I. J. Shannon and J. Wood, *Chem. Eng. Sci.*, 2010, **65**, 282–290.
65 J. Zhu, J. Wood, K. Deplanche, I. Mikheenko and L. E. Macaskie, *Appl. Catal. B Environ.*, 2016, **199**, 108–122.
66 A. J. Murray, J. Zhu, J. Wood and L. E. Macaskie, *Miner. Eng.*, 2017, **113**, 102–108.
67 L. S. Søbjerg, D. Gauthier, A. T. Lindhardt, M. Bunge, K. Finster, R. L. Meyer and T. Skrydstrup, *Green Chem.*, 2009, **11**, 2041–2046.
68 D. Gauthier, L. S. Sãbjerg, K. M. Jensen, A. T. Lindhardt, M. Bunge, K. Finster, R. L. Meyer and T. Skrydstrup, *ChemSusChem*, 2010, **3**, 1036–1039.
69 J. R. Lloyd, P. Yong and L. E. Macaskie, *Appl. Environ. Microbiol.*, 1998, **64**, 4607–4609.
70 A. Serpe, F. Bigoli, M. C. Cabras, P. Fornasiero, M. Graziani, M. L. Mercuri, T. Montini, L. Pilia, E. F. Trogu and P. Deplano, *Chem. Commun.*, 2005, 1040–1042.
71 F. Bigoli, P. Deplano, M. L. Mercuri, M. A. Pellinghelli, G. Pintus, A. Serpe and E. F. Trogu, *J. Am. Chem. Soc.*, 2001, **123**, 1788–1789.
72 S. Rizzato, G. Manca, M. H. Lemée, L. Marchiò, F. Cesare Marincola, A. Guerri, A. Ienco, A. Serpe and P. Deplano, *Inorg. Chem.*, 2023, **62**, 694–705.
73 K. A. Jantan, C. Y. Kwok, K. W. Chan, L. Marchiò, A. J. P. White, P. Deplano, A. Serpe and J. D. E. T. Wilton-Ely, *Green Chem.*, 2017, **19**, 5846–5853.
74 A. R. Dick, K. L. Hull and M. S. Sanford, *J. Am. Chem. Soc.*, 2004, **126**, 2300–2301.

75 K. A. Jantan, K. Wen Chan, L. Melis, A. J. P. White, L. Marchiò, P. Deplano, A. Serpe and J. D. E. T. Wilton-Ely, *ACS Sustain. Chem. Eng.*, 2019, **7**, 12389–12398.
76 J. L. Do, D. Tan and T. Friščić, *Angew. Chem. Int. Ed.*, 2018, **57**, 2667–2671.
77 M. Zengin, H. Genc, T. Demirci, M. Arslan and M. Kucukislamoglu, *Tetrahedron Lett.*, 2011, **52**, 2333–2335.
78 C. M. Cova, A. Zuliani, R. Manno, V. Sebastian and R. Luque, *Green Chem.*, 2020, **22**, 1414–1423.
79 A. Zuliani, C. M. Cova, R. Manno, V. Sebastian, A. A. Romero and R. Luque, *Green Chem.*, 2020, **22**, 379–387.
80 H. Genc, *Catal. Commun.*, 2015, **67**, 64–67.
81 V. Farina, *Adv. Synth. Catal.*, 2004, **346**, 1553–1582.
82 P. Y. Choy, O. Y. Yuen, M. P. Leung, W. K. Chow and F. Y. Kwong, *Eur. J. Org. Chem.,* 2020, 2846–2853.
83 R. B. Bedford, M. E. Blake, C. P. Butts and D. Holder, *Chem. Commun.*, 2003, **3**, 466–467.
84 D. A. Albisson, R. B. Bedford and P. N. Scully, *Tetrahedron Lett.*, 1998, **39**, 9793–9796.
85 R. B. Bedford, S. L. Hazelwood and M. E. Limmert, *Chem. Commun.*, 2002, **2**, 2610–2611.
86 L. Chen, P. Ren and B. P. Carrow, *J. Am. Chem. Soc.*, 2016, **138**, 6392–6395.
87 C. A. Tolman, *Chem. Rev.*, 1977, **77**, 313–348.
88 Y. Tan, F. Barrios-Landeros and J. F. Hartwig, *J. Am. Chem. Soc.*, 2012, **134**, 3683–3686.
89 N. Marion, O. Navarro, J. Mei, E. D. Stevens, N. M. Scott and S. P. Nolan, *J. Am. Chem. Soc.*, 2006, **128**, 4101–4111.
90 D. J. Nelson and S. P. Nolan, *Chem. Soc. Rev.*, 2013, **42**, 6723–6753.
91 R. Dorta, N. M. Scott, C. Costabile, L. Cavallo, C. D. Hoff and S. P. Nolan, *J. Am. Chem. Soc.*, 2005, **127**, 2485–2495.
92 A. Gómez-Suárez, D. J. Nelson and S. P. Nolan, *Chem. Commun.*, 2017, **53**, 2650–2660.
93 A. V. Astakhov, O. V. Khazipov, A. Y. Chernenko, D. V. Pasyukov, A. S. Kashin, E. G. Gordeev, V. N. Khrustalev, V. M. Chernyshev and V. P. Ananikov, *Organometallics*, 2017, **36**, 1981–1992.
94 O. V Khazipov, M. A. Shevchenko, A. Y. Chernenko, A. V Astakhov, D. V Pasyukov, D. B. Eremin, Y. V Zubavichus, V. N. Khrustalev, V. M. Chernyshev and V. P. Ananikov, *Organometallics*, 2018, **37**, 1483–1492.
95 D. B. Eremin, E. A. Denisova, A. Yu. Kostyukovich, J. Martens, G. Berden, J. Oomens, V. N. Khrustalev, V. M. Chernyshev and V. P. Ananikov, *Chem-Eur. J.,* 2019, **25**, 16564–16572.
96 V. M. Chernyshev, E. A. Denisova, D. B. Eremin and V. P. Ananikov, *Chem. Sci.*, 2020, **11**, 6957–6977.
97 H. Joshi, O. Prakash, A. K. Sharma, K. N. Sharma and A. K. Singh, *Eur. J. Inorg. Chem.*, 2015, **2015**, 1542–1551.
98 I. J. S. Fairlamb, A. R. Kapdi, A. F. Lee, G. Sánchez, G. López, J. L. Serrano, L. García, J. Pérez and E. Pérez, *Dalt. Trans.*, 2004, 3970–3981.
99 A. S. Sigeev, A. S. Peregudov, A. V. Cheprakov and I. P. Beletskaya, *Adv. Synth. Catal.*, 2015, **357**, 417–429.
100 V. M. Chernyshev and V. P. Ananikov, *ACS Catal.*, 2022, **12**, 1180–1200.
101 A. Leyva-Pérez, J. Oliver-Meseguer, P. Rubio-Marqués and A. Corma, *Angew. Chem. Int. Ed.*, 2013, **52**, 11554–11559.
102 A. H. M. de Vries, J. M. C. A. Mulders, J. H. M. Mommers, H. J. W. Henderickx and J. G. de Vries, *Org. Lett.*, 2003, **5**, 3285–3288.
103 D. B. Eremin and V. P. Ananikov, *Coord. Chem. Rev.*, 2017, **346**, 2–19.
104 O. J. Newton, K. Hellgardt, J. Richardson and K. K. M. Hii, *J. Catal.*, 2023, **424**, 29–38.
105 L. Shao, B. Zhang, W. Zhang, S. Y. Hong, R. Schlögl and D. S. Su, *Angew. Chem. Int. Ed.*, 2013, **52**, 2114–2117.
106 P. J. Ellis, I. J. S. Fairlamb, S. F. J. Hackett, K. Wilson and A. F. Lee, *Angew. Chem.*, 2010, **122**, 1864–1868.

107 N. Jeddi, N. W. J. Scott and I. J. S. Fairlamb, *ACS Catal.*, 2022, 12, 11615–11638.
108 J. G. De Vries, *Dalt. Trans.*, 2006, 421–429.
109 A. V. Gaikwad, A. Holuigue, M. B. Thathagar, J. E. Ten Elshof and G. Rothenberg, *Chem-Eur. J.,* 2007, **13**, 6908–6913.
110 C. Dong, L. Zhang, X. Xue, H. Li, Z. Yu, W. Tang and L. Xu, *RSC Adv.*, 2014, **4**, 11152–11158.
111 D. Roy and Y. Uozumi, *Adv. Synth. Catal.*, 2018, **360**, 602–625.
112 Y. Zhang, J. A. H. White, E. Chong, S. Radomkit, Y. Xu, J. Liu and J. C. Lorenz, *Org. Process Res. Dev.*, 2023, **27**, 1406–1410.
113 C. C. Mauger and G. A. Mignani, *Org. Process Res. Dev.*, 2004, **8**, 1065–1071.
114 C. Abercrombie, C. P. Ashcroft, M. Badland, A. Baldwin, L. T. Baldwin, S. Brisley, W. Callar, P. Daddario, E. Hilou, C. James, R. Li, Y. Liu, S. Monfette, J. L. Piper, G. Reyes, H. Risley, F. H. Salingue, K. Saunyama and M. G. Vetelino, *Org. Process Res. Dev.*, 2023, **27**, 866–874.
115 J. Hartung, X. Wang, Z. J. Song, Y. Chen, F. Guo and Z. Li, *Org. Process Res. Dev.*, 2022, **26**, 3161–3165.
116 J. Eastoe, I. J. S. Fairlamb, J. M. Fernández-Hernández, E. Filali, J. C. Jeffery, G. C. Lloyd-Jones, A. Martorell, A. Meadowcroft, P.-O. Norrby, T. Riis-Johannessen, D. A. Sale and P. M. Tomlin, *Faraday Discuss.*, 2010, **145**, 27–47.
117 Z. Wang, Y. Yu, Y. X. Zhang, S. Z. Li, H. Qian and Z. Y. Lin, *Green Chem.*, 2015, **17**, 413–420.
118 L. Duan, R. Fu, Z. Xiao, Q. Zhao, J. Q. Wang, S. Chen and Y. Wan, *ACS Catal.*, 2015, **5**, 575–586.
119 D. Elhamifar, B. Karimi, J. Rastegar and M. H. Banakar, *ChemCatChem*, 2013, **5**, 2418–2424.
120 M. Esmaeilpour and S. Zahmatkesh, *Inorg. Nano-Metal Chem.*, 2019, **49**, 267–276.
121 F. R. Fortea-Pérez, M. Mon, J. Ferrando-Soria, M. Boronat, A. Leyva-Pérez, A. Corma, J. M. Herrera, D. Osadchii, J. Gascon, D. Armentano and E. Pardo, *Nat. Mater.*, 2017, **16**, 760–766.
122 J. Qiu, H. Wang, Y. Zhao, P. Guan, Z. Li, H. Zhang, H. Gao, S. Zhang and J. Wang, *Green Chem.*, 2020, **22**, 2605–2612.
123 J. C. Wang, C. X. Liu, X. Kan, X. W. Wu, J. L. Kan and Y. Bin Dong, *Green Chem.*, 2020, **22**, 1150–1155.
124 C. Boztepe, A. Künkül, S. Yaşar and N. Gürbüz, *J. Organomet. Chem.*, 2018, **872**, 123–134.
125 L. Duan, R. Fu, B. Zhang, W. Shi, S. Chen and Y. Wan, *ACS Catal.*, 2016, **6**, 1062–1074.
126 L. Zhang, A. Wang, J. T. Miller, X. Liu, X. Yang, W. Wang, L. Li, Y. Huang, C. Y. Mou and T. Zhang, *ACS Catal.*, 2014, **4**, 1546–1553.
127 L. Chen, S. Rangan, J. Li, H. Jiang and Y. Li, *Green Chem.*, 2014, **16**, 3978–3985.
128 F. Wang, J. Mielby, F. H. Richter, G. Wang, G. Prieto, T. Kasama, C. Weidenthaler, H. J. Bongard, S. Kegnæs, A. Fürstner and F. Schüth, *Angew. Chem. Int. Ed.*, 2014, **53**, 8645–8648.
129 Á. Molnár, *Chem. Rev.*, 2011, **111**, 2251–2320.
130 J. Liu, *ACS Catal.*, 2017, **7**, 34–59.
131 H. Konnerth, B. M. Matsagar, S. S. Chen, M. H. G. Prechtl, F. K. Shieh and K. C. W. Wu, *Coord. Chem. Rev.*, 2020, **416**, 213319.
132 I. P. Beletskaya, F. Alonso and V. Tyurin, *Coord. Chem. Rev.*, 2019, **385**, 137–173.
133 Á. Molnár, *Coord. Chem. Rev.*, 2019, **388**, 126–171.
134 S. Mitchell, E. Vorobyeva and J. Pérez-Ramírez, *Angew. Chem. Int. Ed.*, 2018, **57**, 15316–15329.
135 H. Huang, K. Shen, F. Chen and Y. Li, *ACS Catal.*, 2020, **10**, 6579–6586.
136 M. Díaz-Sánchez, D. Díaz-García, S. Prashar and S. Gómez-Ruiz, *Environ. Chem. Lett.*, 2019, **17**, 1585–1602.
137 S. Luo, Z. Zeng, G. Zeng, Z. Liu, R. Xiao, M. Chen, L. Tang, W. Tang, C. Lai, M. Cheng, B. Shao, Q. Liang, H. Wang and D. Jiang, *ACS Appl. Mater. Interfaces*, 2019, **11**, 32579–32598.
138 B. Karimi and P. Fadavi Akhavan, *Chem. Commun.*, 2011, **47**, 7686–7688.
139 G. Urgoitia, R. SanMartin, M. T. Herrero and E. Domínguez, *Green Chem.*, 2011, **13**, 2161–2166.
140 E. J. García-Suárez, S. G. Khokarale, O. N. Van Buu, R. Fehrmann and A. Riisager, *Green Chem.*,

2014, **16**, 161–166.
141 T. V. Khamatnurova, D. Zhang, J. Suriboot, H. S. Bazzi and D. E. Bergbreiter, *Catal. Sci. Technol.*, 2015, **5**, 2378–2383.
142 K. V. Bukhryakov, C. Mugemana, K. B. Vu and V. O. Rodionov, *Org. Lett.*, 2015, **17**, 4826–4829.
143 S. L. Scott, *ACS Catal.*, 2018, **8**, 8597–8599.
144 D. P. Debecker, K. Kuok (Mimi) Hii, A. Moores, L. M. Rossi, B. Sels, D. T. Allen and B. Subramaniam, *ACS Sustain. Chem. Eng.*, 2021, **9**, 4936–4940.
145 G. Liu, C. Liu, X. Zhao and J. Wang, *RSC Adv.*, 2016, **6**, 44475–44479.
146 World Economic Forum, A New Circular Vision for Electronics Time for a Global Reboot.
147 J. Cui and L. Zhang, *J. Hazard. Mater.*, 2008, **158**, 228–256.
148 U.S. Environmental Protection Agency, *Extraction and Beneficiation of Ore and Minerals-Gold*, Washington, D.C., 1994.
149 SGS Cyanide Leaching, https://www.sgs.sg/en/mining/metallurgy-and-process-design/cyanidation- technologies/cyanide-leaching (accessed on 22 June 2020).
150 C. A. Johnson, *Appl. Geochemistry*, 2015, **57**, 194–205.
151 Chemistry World Sodium Cyanide, https://www.chemistryworld.com/podcasts/sodium-cyanide/4011120. article (accessed on 4 June 2020).
152 A. Akcil, C. Erust, C. S. ekha. Gahan, M. Ozgun, M. Sahin and A. Tuncuk, *Waste Manag.*, 2015, **45**, 258–271.
153 L. J. Esdaile and J. M. Chalker, *Chem-Eur. J.,* 2018, **24**, 6905–6916.
154 Gold price per gram, https://www.gold.co.uk/gold-price/5-year-gold-price-per-gram-uk/, (accessed 20 October 2023).
155 R. Cai, M. Lu, E. Y. Aguilera, Y. Xi, N. G. Akhmedov, J. L. Petersen, H. Chen and X. Shi, *Angew. Chem. Int. Ed.*, 2015, **54**, 8772–8776.
156 J. Miranda-Pizarro, Z. Luo, J. J. Moreno, D. A. Dickie, J. Campos and T. B. Gunnoe, *J. Am. Chem. Soc.*, 2021, **143**, 2509–2522.
157 L. T. Ball, G. C. Lloyd-Jones and C. A. Russell, *Science*, 2012, **337**, 1644–1648.
158 L. T. Ball, G. C. Lloyd-Jones and C. A. Russell, *J. Am. Chem. Soc.*, 2014, **136**, 254–264.
159 J. M. Yang, Y. T. Zhao, Z. Q. Li, X. S. Gu, S. F. Zhu and Q. L. Zhou, *ACS Catal.*, 2018, **8**, 7351–7355.
160 X. C. Cambeiro, N. Ahlsten and I. Larrosa, *J. Am. Chem. Soc.*, 2015, **137**, 15636–15639.
161 M. N. Hopkinson, A. Tlahuext-Aca and F. Glorius, *Acc. Chem. Res.*, 2016, **49**, 2261–2272.
162 Z. Zheng, X. Ma, X. Cheng, K. Zhao, K. Gutman, T. Li and L. Zhang, *Chem. Rev.*, 2021, **121**, 8979–9038.
163 A. Arcadi, G. Blanchi, S. Di Giuseppe and F. Marinelli, *Green Chem.*, 2003, **5**, 64–67.
164 G. Dyker, E. Muth, A. S. K. Hashmi and L. Ding, *Adv. Synth. Catal.*, 2003, **345**, 1247–1252.
165 A. S. K. Hashmi, J. P. Weyrauch, W. Frey and J. W. Bats, *Org. Lett.*, 2004, **6**, 4391–4394.
166 R. Gauthier, M. Mamone and J. F. Paquin, *Org. Lett.*, 2019, **21**, 9024–9027.
167 A. S. K. Hashmi, A. M. Schuster, M. Schmuck and F. Rominger, *European J. Org. Chem.*, 2011, 4595–4602.
168 J. P. Weyrauch, A. S. K. Hashmi, A. Schuster, T. Hengst, S. Schetter, A. Littmann, M. Rudolph, M. Hamzic, J. Visus, F. Rominger, W. Frey and J. W. Bats, *Chem-Eur. J.*, 2010, **16**, 956–963.
169 D. Mulryan, J. Rodwell, N. A. Phillips and M. R. Crimmin, *ACS Catal.*, 2022, **12**, 3411–3419.
170 L. Rocchigiani and M. Bochmann, *Chem. Rev.*, 2021, **121**, 8364–8451.
171 G. Dyker, *Org. Synth. Set*, 2008, 48–55.
172 R. Ciriminna, E. Falletta, C. Della Pina, J. H. Teles and M. Pagliaro, *Angew. Chem. Int. Ed.*, 2016, **55**, 14210–14217.
173 S. Kramer and F. Gagosz, *Gold Catalysis: An Homogeneous Approach*, Imperial College Press, London, 2014.
174 Mine e-waste, not the earth, say scientists, https://www.bbc.co.uk/news/science-environment-61350996, (accessed 22 September 2023).

175 A. Rigoldi, E. F. Trogu, G. C. Marcheselli, F. Artizzu, N. Picone, M. Colledani, P. Deplano and A. Serpe, *ACS Sustain. Chem. Eng.*, 2019, **7**, 1308–1317.
176 European Commission. Waste Electrical & Electronic Equipment (WEEE), https://ec.europa.eu/environment/ waste/weee/index_en.htm, (accessed on 27 May 2020) 177
177 United Nations Global E-Waste Monitor, 2019 Report, https://globalewaste.org/, (accessed 29 December 2023).
178 C. Hagelüken and C. W. Corti, *Gold Bull.*, 2010, **43**, 209–220.
179 W. Chen, Y. Geng, J. Hong, H. Dong, X. Cui, M. Sun and Q. Zhang, *J. Clean. Prod.*, 2018, **179**, 143–150.
180 B. H. Robinson, *Sci. Total Environ.*, 2009, **408**, 183–191.
181 European Union, *Off. J. Eur. Union*, 2003, **37**, 24–39.
182 European Union, *Off. J. Eur. Union*, 2012, **197**, 38–71.
183 C. Hagelueken, *Acta Metall. Slovaca*, 2006, **12**, 111–120.
184 Y. Ding, S. Zhang, B. Liu, H. Zheng, C. chi Chang and C. Ekberg, *Resour. Conserv. Recycl.*, 2019, **141**, 284–298.
185 Gold Supply, https://www.gold.org/about-gold/gold-supply, (accessed 6 August 2019).
186 M. D. Rao, K. K. Singh, C. A. Morrison and J. B. Love, *RSC Adv.*, 2020, **10**, 4300–4309.
187 V. H. Ha, J. chun Lee, J. Jeong, H. T. Hai and M. K. Jha, *J. Hazard. Mater.*, 2010, **178**, 1115–1119.
188 S. M. Abramov, J. He, D. Wimmer, E. M. Muehe, T. Helle, H. Thorwarth and A. Kappler, *J. Mater. Cycles Waste Manag.*, 2022, **24**, 2243–2254.
189 J. Li, M. S. Safarzadeh, M. S. Moats, J. D. Miller, K. M. Levier, M. Dietrich and R. Y. Wan, *Hydrometallurgy*, 2012, **113–114**, 31–38.
190 Q. Wang, T. Liu, Y. Chen, S. Chen, X. Qin, Y. Nie and F. Zi, *Hydrometallurgy*, 2020, **198**, 105502.
191 B. Lucheva, P. Iliev and D. Kolev, *J. Chem. Technol. Metall.*, 2017, **52**, 326–332.
192 A. Zupanc, E. Heliövaara, K. Moslova, A. Eronen, M. Kemell, Č. Podlipnik, M. Jereb and T. Repo, *Angew. Chem. Int. Ed.,* 2022, **61**, e2021175.
193 G. J. Sparrow & and J. T. Woodcock, *Miner. Process. Extr. Metullargy Rev.*, 1995, **14**, 193–247.
194 A. Nag and T. Pradeep, *ACS Sustain. Chem. Eng.*, 2021, **9**, 2129-2135.
195 Z. Liu, M. Frasconi, J. Lei, Z. J. Brown, Z. Zhu, D. Cao, J. Iehl, G. Liu, A. C. Fahrenbach, Y. Y. Botros, O. K. Farha, J. T. Hupp, C. A. Mirkin and J. Fraser Stoddart, *Nat. Commun.*, 2013, **4**, 1855.
196 A. Cieszynska and D. Wieczorek, *Hydrometallurgy*, 2018, **175**, 359–366.
197 O. Grad, M. Ciopec, A. Negrea, N. Duțeanu, G. Vlase, P. Negrea, C. Dumitrescu, T. Vlase and R. Vodă, *Sci. Rep.*, 2021, **11**, 1–14.
198 W. Liu, L. O. Jones, H. Wu, C. L. Stern, R. A. Sponenburg, G. C. Schatz and J. F. Stoddart, *J. Am. Chem. Soc.*, 2021, **143**, 1984–1992.
199 F. Isaia, M. C. Aragoni, M. Arca, C. Caltagirone, C. Castellano, G. De Filippo, A. Garau, V. Lippolis and T. Pivetta, *Green Chem.*, 2017, **19**, 4591–4599.
200 H. T. Fissaha, R. E. C. Torrejos, H. Kim, W. J. Chung and G. M. Nisola, *Microporous Mesoporous Mater.*, 2020, **305**, 110301.
201 T. Ma, R. Zhao, Z. Li, X. Jing, M. Faheem, J. Song, Y. Tian, X. Lv, Q. Shu and G. Zhu, *ACS Appl. Mater. Interfaces*, 2020, **12**, 30474–30482.
202 E. Lahtinen, E. Kukkonen, V. Kinnunen, M. Lahtinen, K. Kinnunen, S. Suvanto, A. Vaïsänen and M. Haukka, *ACS Omega*, 2019, **4**, 16891–16898.
203 E. Lahtinen, L. Kivijärvi, R. Tatikonda, A. Väisänen, K. Rissanen and M. Haukka, *ACS Omega*, 2017, **2**, 7299–7304.
204 S. Mincke, T. G. Asere, I. Verheye, K. Folens, F. Vanden Bussche, L. Lapeire, K. Verbeken, P. Van Der Voort, D. A. Tessema, F. Fufa, G. Du Laing and C. V. Stevens, *Green Chem.*, 2019, **21**, 2295–2306.

205 S. Nagireddi, A. K. Golder and R. Uppaluri, *Int. J. Biol. Macromol.*, 2019, **127**, 320–329.
206 Z. Zhou, F. Liu, Y. Huang, Z. Wang and G. Li, *Int. J. Biol. Macromol.*, 2015, **77**, 336–343.
207 E. J. Shin, H. S. Kim, S. R. Joo, U. S. Shin and S. H. Kim, *Catal. Letters*, 2019, **149**, 1560–1564.
208 K. Deplanche, J. A. Bennett, I. P. Mikheenko, J. Omajali, A. S. Wells, R. E. Meadows, J. Wood and L. E. Macaskie, *Appl. Catal. B Environ.*, 2014, **147**, 651–665.
209 J. H. Advani, N. H. Khan, H. C. Bajaj and A. V. Biradar, *Appl. Surf. Sci.*, 2019, **487**, 1307–1315.
210 C. Zhang, D. Lu, P. Jiang, J. Li and Y. Leng, *Catal. Letters*, 2017, **147**, 2534–2541.
211 B. C. E. Makhubela, A. Jardine and G. S. Smith, *Appl. Catal. A Gen.*, 2011, **393**, 231–241.
212 L. Liang, L. Nie, M. Jiang, F. Bie, L. Shao, C. Qi, X. M. Zhang and X. Liu, *New J. Chem.*, 2018, **42**, 11023–11030.
213 S.-S. Yi, D.-H. Lee, E. Sin and Y.-S. Lee, *Tetrahedron Lett.*, 2007, **48**, 6771–6775.
214 M. Zeng, X. Zhang, L. Shao, C. Qi and X. M. Zhang, *J. Organomet. Chem.*, 2012, **704**, 29–37.
215 D. Berillo and A. Cundy, *Carbohydr. Polym.*, 2018, **192**, 166–175.
216 Z. Wang, P. Li, Y. Fang, L. Yan, W. Zhou, X. Fan and H. Liu, *Carbohydr. Polym.*, 2019, **223**, 115064.
217 M. Mon, J. Ferrando-Soria, T. Grancha, F. R. Fortea-Pérez, J. Gascon, A. Leyva-Pérez, D. Armentano and E. Pardo, *J. Am. Chem. Soc.*, 2016, **138**, 7864–7867.
218 S. McCarthy, O. Desaunay, A. L. W. Jie, M. Hassatzky, A. J. P. White, P. Deplano, D. C. Braddock, A. Serpe and J. D. E. T. Wilton-Ely, *ACS Sustain. Chem. Eng.*, 2022, **10**, 15726–15734.
219 R. G. Charles, P. Douglas, I. L. Hallin, I. Matthews and G. Liversage, *Waste Manag.*, 2017, **60**, 505–520.
220 M. V. Twigg, *Catal. Today*, 2011, **163**, 33–41.
221 R. Nagarjuna, S. Sharma, N. Rajesh and R. Ganesan, *ACS Omega*, 2017, **2**, 4494–4504.
222 ICH Q3D Elemental Impurities - Scientific Guidelines, https://www.ema.europa.eu/en/ich-q3d-elemental-impurities-scientific-guideline, (accessed 9 October 2023).

Chapter 2 – Homogeneous Gold Catalysis using Complexes Recovered from Waste Electronic Equipment

2.1. Introduction

This chapter details the synthesis and application of a family of related recovered gold compounds, $[(Me_2dazdt)AuX_2]Y$, as homogeneous catalysts. The introduction initially reiterates some key aspects of gold recycling, followed by an introduction to the gold recycling process that was utilised in this thesis. The aims of the chapter are then presented, followed by a brief overview of the catalytic reactions that have been used to achieve the proposed aims. The results and discussion sections then follows the introductory sections, and covers the contents of the results in the same order as the presentation of the introduction: i) the synthesis of the recycled gold complexes, ii) the application of these recycled gold complexes as catalysts, iii) Supplementary mechanistic studies on the chemistry of the recycled gold complexes.

2.1.1. Gold recycling

Dissolution of gold present in waste electrical and electronic equipment (WEEE) is achieved by coordination, to reduce the redox potential of metallic Au^0, and oxidation and subsequent dissolution as molecular $Au^{1+/3+}$. This was traditionally achieved by undesirable reagents like cyanide/oxygen or *aqua regia*. In the 1990s, research by the McAuliffe group pioneered the use of softer dihalogen-pnictogen adducts, $Me_3E{\cdot}I_2$ (E = As, P), as the sole reagents for the oxidation of Au^0 (Scheme 29).[1]

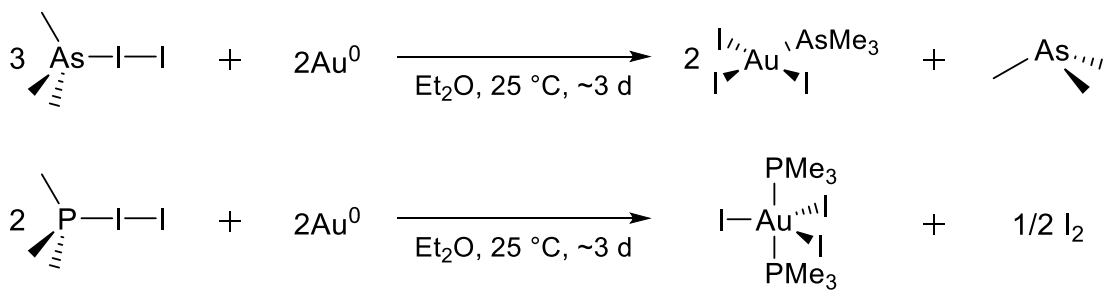

Scheme 29. McAuliffe's pioneering research on the use of dihalogen-pnictogen adducts, $Me_3E{\cdot}I_2$, as reagents for the oxidation of Au^0.[1]

Pnictogen adduct $Me_3As{\cdot}I_2$ yielded the expected square planar Au^{3+} complex $[AuI_3(AsMe_3)]$, whilst $Me_3P{\cdot}I_2$ unusually yielded $[AuI_3(PMe_3)_2]$ as a trigonal bipyramid. Inspired by McAuliffe, Serpe and Deplano *et al*. in 1998 reported on the synthesis of the dithiooxamide bis(diiodine) adduct of *N,N*-dimethylperhydro-1,4-diazepine-2,3-dithione ($Me_2dazdt{\cdot}2I_2$, **1**).[2] This adduct (**1**) was employed to oxidise Au^0, resulting in the formation of ionic Au^{3+} molecular complex $[AuI_2(Me_2dazdt)]I_3$ (**3**). Oxidation of Au^0 and dissolution as Au^{3+} occurred rapidly (5-10 min) at room temperature. The same group later illustrated that an equivalent Au^{3+} leaching product, $[AuBr_2(Me_2dazdt)]IBr_2$ (**2**), could be

synthesised from the oxidation of Au^0 by the bis(iodine monobromide) adduct of *N,N*-dimethylperhydro-1,4-diazepine-2,3-dithione (Me_2dazdt·2IBr, **4**) (Scheme 30).[3]

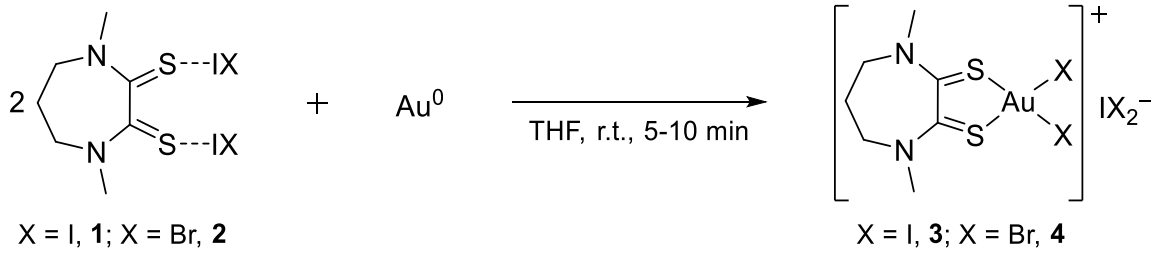

*Scheme 30. Deplano et al. oxidation of Au^0 by bis(dihalogen) adducts Me_2dazdt·2IX **1** and **2**.*[2,3]

The process was patented by Deplano *et al*. in 2008,[4] with the patent detailing the application of adducts **1** and **2** to recover gold from a variety of WEEE sources – namely SIM cards, ink cartridges, and printed PC motherboard and network cards. In each case, gold was recovered as part of a full process which involved dismantling the scrap and step-wise recovery of all the metals present in the waste. Subsequent cementation or electrowinning enabled quantitative recovery of Au^0 and Me_2dazdt, however this final treatment step significantly increases the economic and environmental cost of the recovery process. Moreover, despite the efficacy of gold recovery and the possibility of recovering Me_2dazdt, the cost of synthesising Me_2dazdt also impedes the industrial viability of adducts **1** and **2** in recovering metallic gold from WEEE.

2.1.2. Research aims and objectives

To address these challenges and incentivise WEEE recycling, the aim of the research in this chapter was to explore the direct valorisation of recycling products **3** and **4** as homogeneous gold catalysts. Since the synthesis of Me_2dazdt relies on Lawesson's reagent for sulfur installation, an expensive reagent with very poor atom economy, an improved synthesis of Me_2dazdt which utilises a cheaper and more sustainable sulfur source was also explored. In addition, since complexes **3** and **4** contain potentially non-innocent trihalide anions, and vary in both the metal-bound halides and trihalide counter anions, the synthesis of two related tetrafluoroborate complexes, $[AuI_2(Me_2dazdt)]BF_4$ (**5**) and $[AuBr_2(Me_2dazdt)]BF_4$ (**6**), was explored (Figure 17).

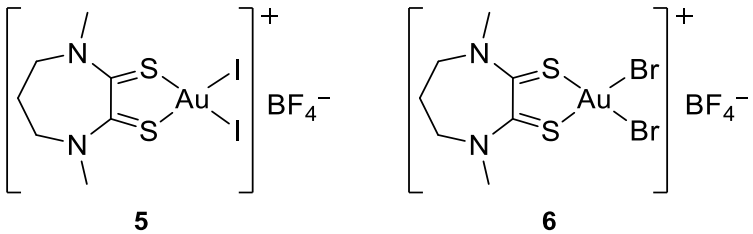

*Figure 17. Tetrafluoroborate anion metathesis products **5** and **6**.*

The aim of synthesising a family of related recovery products, **3**-**6**, was to enable a systematic comparison between the influence of the metal-bound halides and counter anions on catalytic activity. To better understand the chemistry and catalytic activity of these complexes, a range of synthetic transformations which broadly covered the common modes of action of gold catalysts were explored. Mechanistic analysis was also performed to rationalise the results of applying gold complexes **3**-**6** as catalysts.

2.1.3. Mechanistic modes of gold catalysis

Over the past two decades, homogeneous gold catalysis has emerged as a valuable synthetic tool. Many reactions catalysed by gold complexes are transformations for which no other catalysts have yet been identified, or where gold catalysis enables access to considerably milder reaction conditions.[5–12] These gold-complex catalysed reactions have been reported to operate under a variety of mechanistic modes. The reactions employed herein to assess the catalytic activity of complexes **3**-**6** were therefore chosen to reflect these various mechanistic facets of gold catalysis.

The activation of alkynes is one of the most common transformations catalysed by gold complexes and was thus selected as the first class of reaction to evaluate the catalytic activity of recycling products **3**-**6**. The use of gold in place of mercury or palladium alternatives has been illustrated to provide improved performance in the catalytic activation of alkyne bonds.[13] For example, the cyclisation of *N*-propargylamides to oxazoles catalysed by $AuCl_3$ was first reported by Hashmi *et al*. in 2004.[14] A range of substituted oxazoles were synthesised under mild conditions (Scheme 31). Hashmi *et al*. have since expanded the substrate scope to include non-terminal *N*-propargylamides.[15]

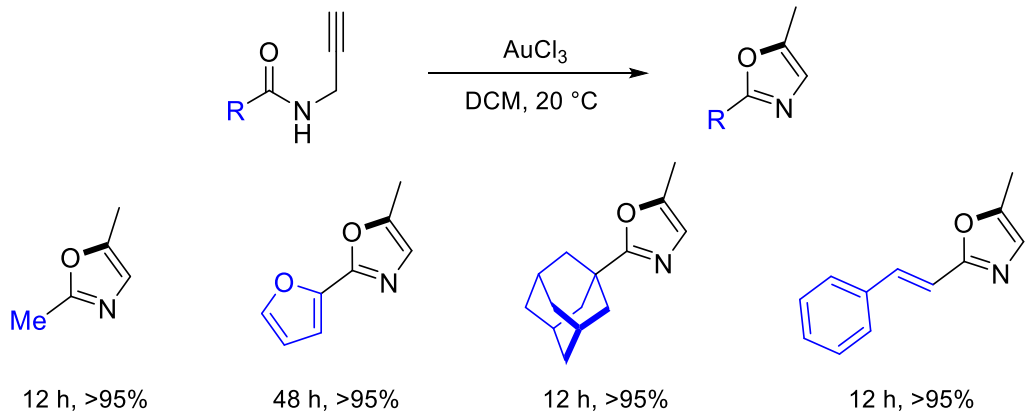

Scheme 31. Selected substrate examples from Hashmi et al. cyclisation of terminal N-propargylcarboxamides catalysed by $AuCl_3$.[14]

The reaction mechanism was studied by *in situ* ^{1}H NMR spectroscopy, which illustrated that the formation of oxazole **8** proceeded via the rearrangement of methylene-dihydrooxazole (**7**) (Scheme 32).[14]

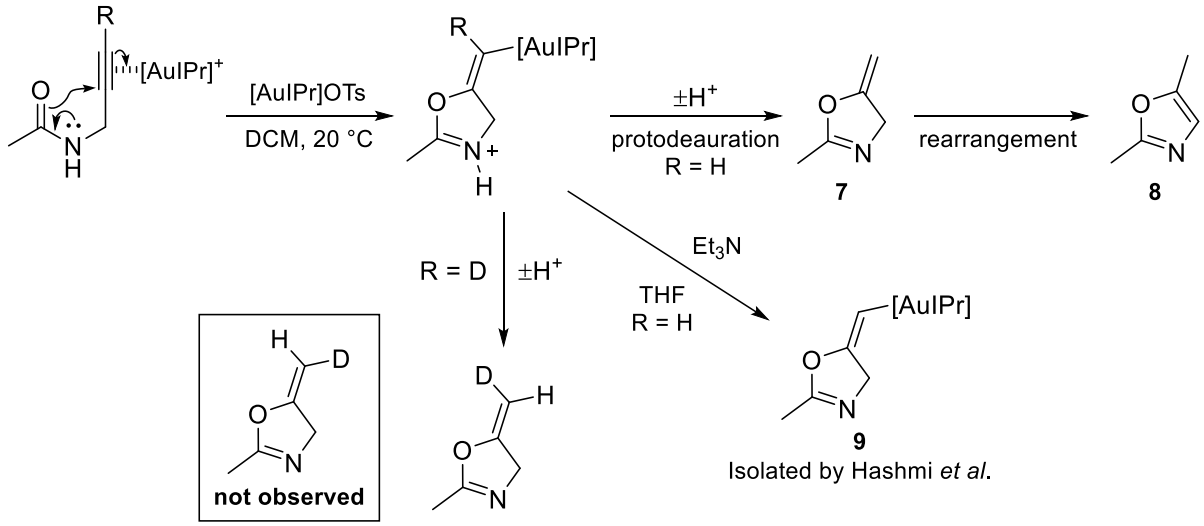

Scheme 32. Hashmi et al. proposed cyclisation of N-propargylamides mechanism (IPr = [1,3-bis(2,6-diisopropylphenyl)imidazol-2-ylidene]).[14,16]

Deuterium labelling of the alkynylic proton and $^3J_{CH}$ values confirmed the anti-addition stereochemistry of the alkyne-carboauration-cyclisation step (Scheme 32, R = D). Mechanistic studies were consistent with the proposed mechanism (Scheme 32), as sequestering protodeauration under basic conditions enabled the isolation of vinyl gold intermediate **9**.[16,17]

Arcadi *et al*. have similarly employed gold as a catalyst for the activation of alkyne bonds. The group reported on the cyclisation of 2-alkynylanilines to yield indoles catalysed by $Na[AuCl_4]$.[18] Prior to Arcadi's report, the cyclisation of 2-alkynylanilines typically required more forcing conditions (strong base, elevated temperature and catalyst loadings) and/or undesirable solvents. The use of $Na[AuCl_4]$ however enabled the synthesis of a range of indoles in ethanol at room temperature (Scheme 33).

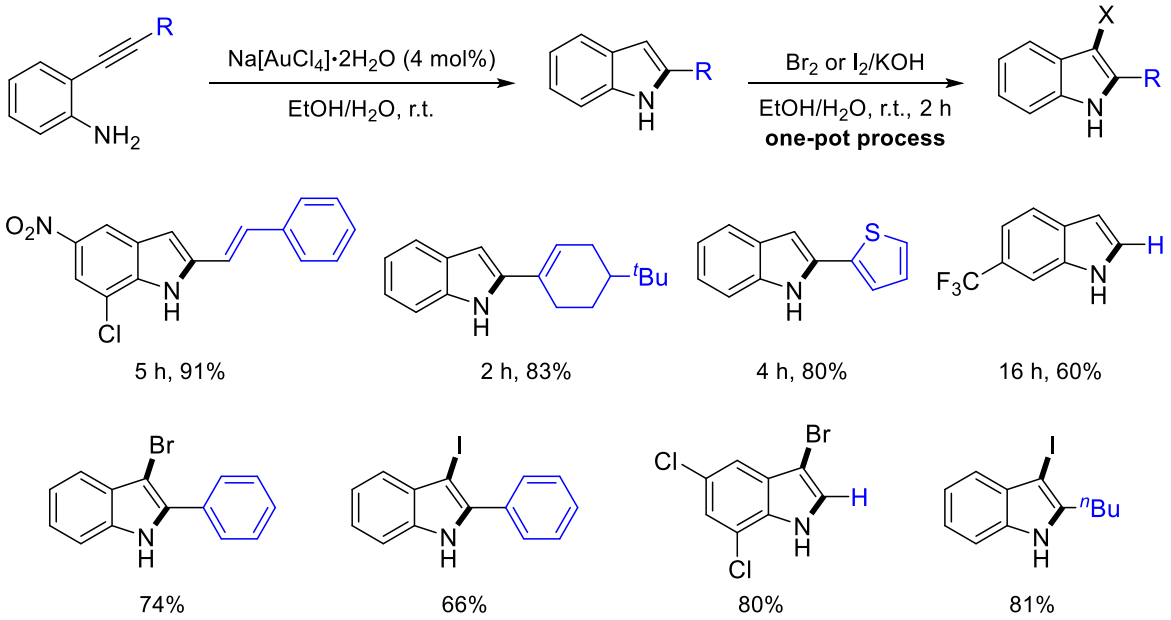

Scheme 33. Arcadi et al. cyclisation of 2-alkynylanilines and one-pot halogenation catalysed by $Na[AuCl_4]$.[18]

Many of the indole products produced using Arcadi *et al.*'s protocol were inaccessible by previous palladium and copper complex, and base promoted cyclisation protocols. Moreover, the resulting indoles were converted in one pot to 3-haloindoles (Scheme 33).

Gold complexes have also been used as oxophilic Lewis acid catalysts, for example in the activation of carbonyl compounds. These reactions are less common than carbophilic examples, but are especially prominent for Au^{3+} catalysts and thus will be explored with recovered complexes **3**-**6**. For example, the Au^{3+} catalysed activation of 1,3-dicarbonyl compounds towards nucleophilic attack for the synthesis of β-enaminones was reported in 2003.[19] Previous β-enaminone syntheses relied on Brønsted acid catalysts in refluxing benzene alongside the use of a Dean-Stark apparatus for azeotropic water removal. However, when gold complex $Na[AuCl_4]$ was employed at 2.5 mol%, a range of nucleophiles were successfully added to a range of 1,3-dicarbonyl compounds under mild conditions (Scheme 34).

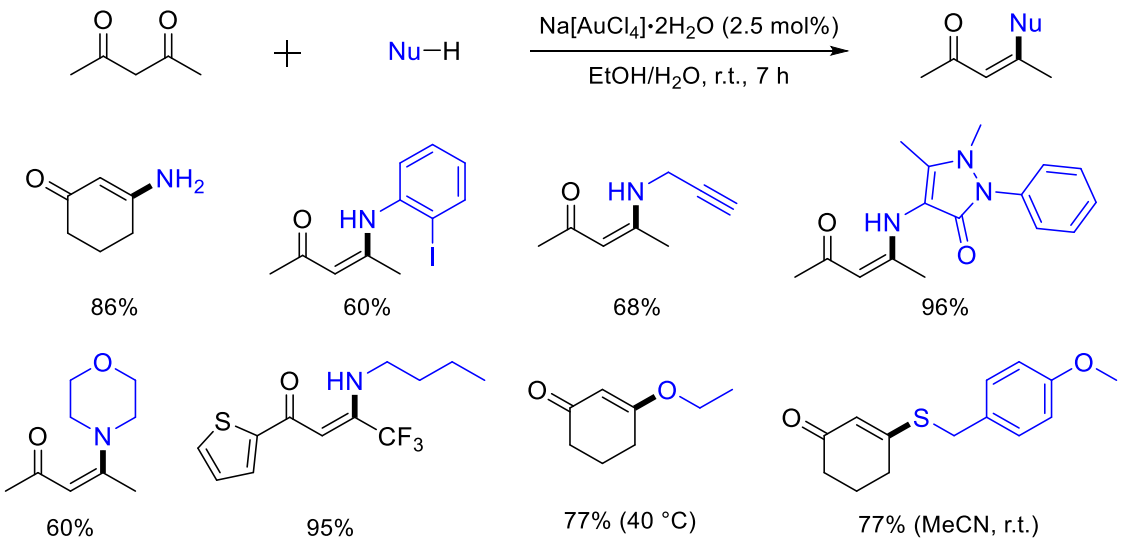

Scheme 34. Arcadi et al. activation of 1,3-dicarbonyl compounds toward nucleophilic attack catalysed by Na[AuCl4].[19]

Gold(III) complexes have similarly been used as Lewis acid catalysts for the activation of α,β-unsaturated carbonyl compounds. This approach was pioneered by Dyker and Hashmi *et al*. in 2003.[20] A range of aromatic nucleophiles were added to both methyl vinyl ketone and cyclopentanone (Scheme 35).

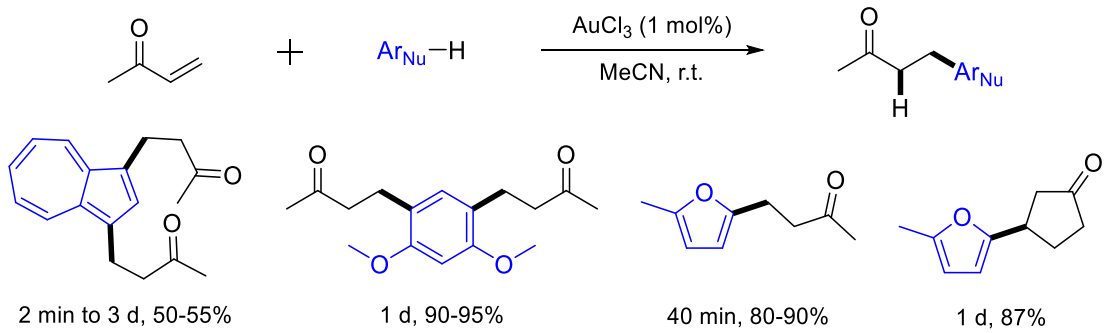

Scheme 35. Dyker and Hashmi et al. activation of α,β-unsaturated carbonyl compounds toward the addition of aromatic nucleophiles catalysed by AuCl3.[20]

More recently, gold complexes have been employed as catalysts for cross-coupling reactions.[21] The typical oxidative addition/reductive elimination cycles seen in cross-coupling reactions which employ d^{10} transition metals (Ni^0, Pd^0, Cu^{1+}) were traditionally not seen for Au^{1+} d^{10} complexes. This is mainly due to the high redox potential of gold (E^0: $Au^{III/I}$ = 1.41 V, $Pd^{II/0}$ = 0.92 V),[22] and the large kinetic barrier associated with the distortion (ΔE_{strain}) of linear Au^{1+} complexes when forming the approximately square planar Au^{3+} transition state (Scheme 36a).[23–25] A number of strategies have emerged to overcome this kinetic barrier. These include radical mediated oxidation

via Au^{2+} (Scheme 36b),[26] and chelating ancillary ligands that force Au^{1+} into a distorted trigonal planar geometry which more readily undergoes oxidative addition by reducing the transition state ΔE_{strain} (Scheme 36c).[22,27]

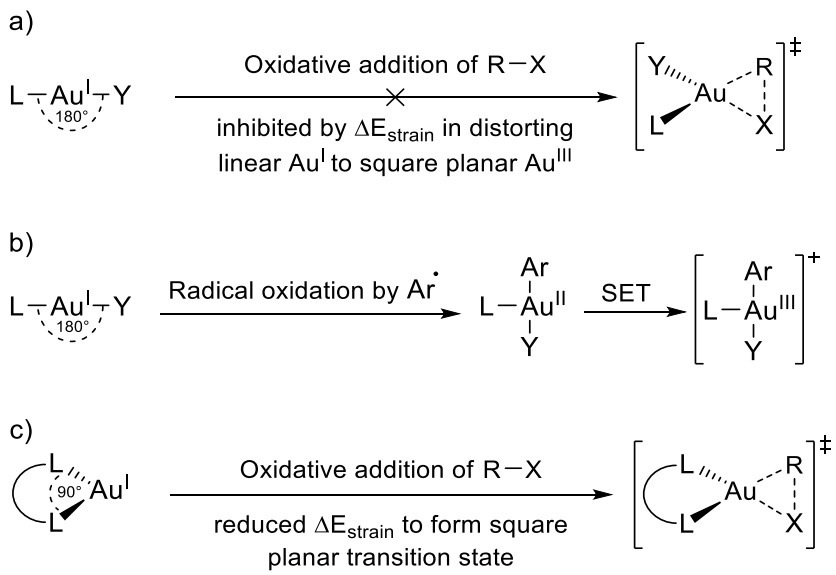

Scheme 36. a) Strain energy barrier associated with distortion of linear Au^{1+} to approximately square planar transition state by oxidative addition of R–X. b) Oxidation of Au^{1+} by $Ar^{\bullet}$ radical and subsequent SET to Au^{3+}. c) Ancillary ligand reduced ΔE_{strain} for formation of Au^{3+} square planar like transition state.

The most common strategy however is the use of sacrificial oxidants which facilitate Au^{1+} to Au^{3+} oxidation (e.g. $PhI(OAc)_2$, Scheme 37), followed by the transmetallation and reductive elimination of two formally nucleophilic coupling partners. A pioneering example of this approach was reported by Russell and Lloyd-Jones in 2012.[28] A range of electron-rich arenes and aryl silanes were successfully coupled in the presence of catalytic $[Ph_3PAu]OTs$ (Scheme 37).

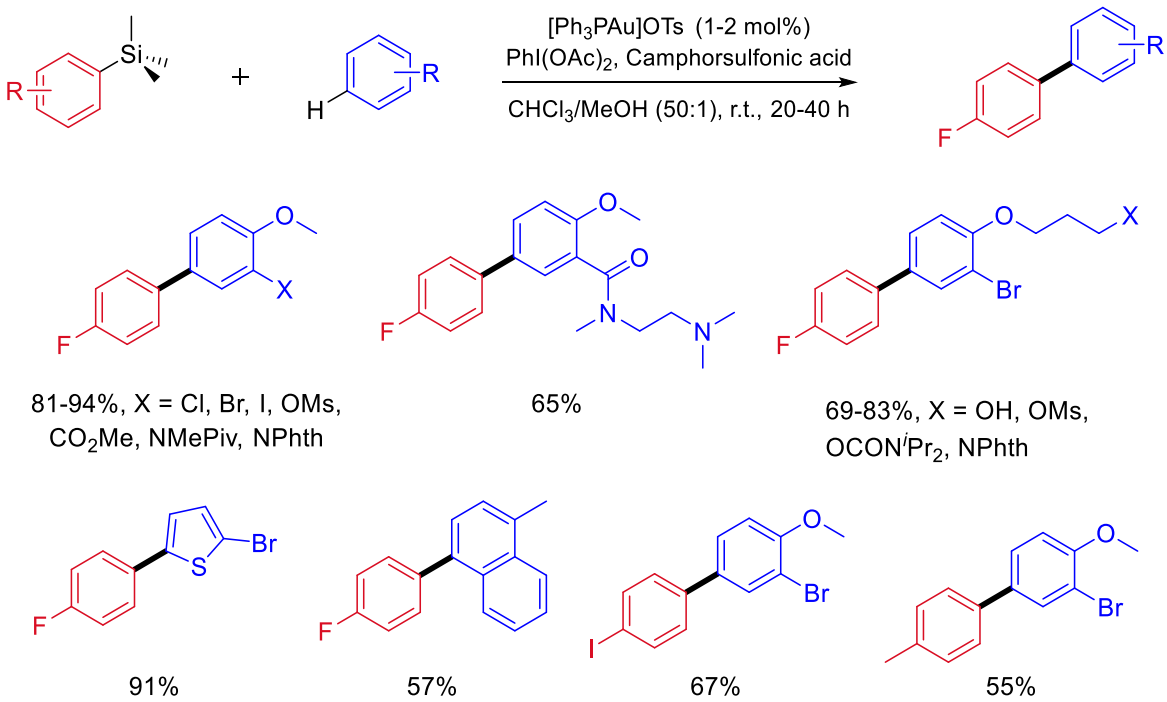

Scheme 37. Selected examples from Russell and Lloyd-Jones oxidative cross-coupling catalysed by [Ph₃PAu]OTs.[28] (Piv = pivaloyl (COCMe₃), NPhth = N-phthalimido).

In later mechanistic work, the Lloyd-Jones and Russel research groups illustrated that Au^{1+} species were not the active catalysts but instead acted as precatalysts, with $[Ph_3PAu]OTs$ speciating into active AuX_3 (X = halogen or MeOH/camphorsulfonic acid and conjugate bases).[29] This active catalyst species formed from oxidation of both Au^{1+} and the ligand (e.g. PPh_3 to $O{=}PPh_3$) by (diacetoxyiodo)benzene during an initial ~45 min induction period. As a result, the structure and reactivity (i.e. selectivity and yield) of the active AuX_3 species was found to be independent of the dissociated and oxidised precatalyst ligand. $[Ph_3PAu]OTs$ was consequently replaced with a simpler Au^{3+} complex containing a labile sacrificial sulfur ligand, $[(tht)AuBr_3]$ (tht = tetrahydrothiophene), the use of which eliminated the precatalyst induction period. Since the success of the cross-coupling protocol (Scheme 37) was mechanistically shown to not rely on a 'designer' (e.g. phosphine, carbene etc.) ligand/catalyst system, recovered complexes **3**-**6** were considered as promising potential catalysts for the oxidative cross-coupling of arenes and aryl silanes, presumably also able to act as precatalysts for active AuX_3. In addition, the 1-2 mol% loading of gold required to catalyse this transformation makes it considerably more expensive than similar transformations catalysed by cheaper metal catalysts. Therefore, the use of gold complexes sourced from recycled waste offer an alternative, potentially cheaper source of gold for the cross-coupling depicted in Scheme 37. The Russell/Lloyd-Jones cross-coupling will thus also be explored using complexes **3**-**6** as catalysts.

2.2. Results and Discussion

2.2.1. Synthesis of gold complexes 3 and 4

The Me_2dazdt ligand employed during the oxidation of Au^0 was synthesised according to the procedure described by Sandstroem *et al*. (Scheme 38)[30] – *N,N'*-dimethylpropane-1,3-diamine and dimethyl oxalate were heated at refluxed in toluene for 4 h (Scheme 38). The crude 1,4-dimethyl-1,4-diazepane-2,3-dione was then recrystallised from hot IPA and subsequently refluxed in toluene in the presence of Lawesson's reagent, yielding Me_2dazdt in a 75% yield following flash column chromatography (Scheme 38). Me_2dazdt could also be isolated by repeated recrystallisations from hot IPA, albeit in a reduced yield (51%).

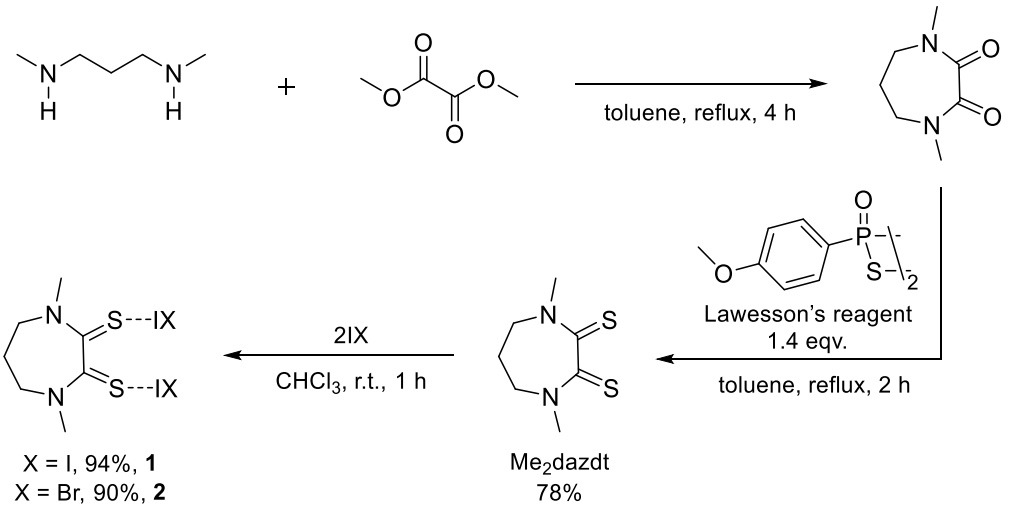

*Scheme 38. Synthesis of Me_2dazdt·IX adducts **1** and **2**.*

Me_2dazdt was then treated with either iodine or iodine monobromide to yield the bis(dihalogen) compounds Me_2dazdt·$2I_2$ (**1**) and Me_2dazdt·2IBr (**2**) compounds respectively. **1** and **2** were subsequently employed to oxidise gold metal powder, producing recovery complexes **3** and **4** in 88% and 85% yield respectively following recrystallisation by vapour-phase diffusion (Scheme 39).

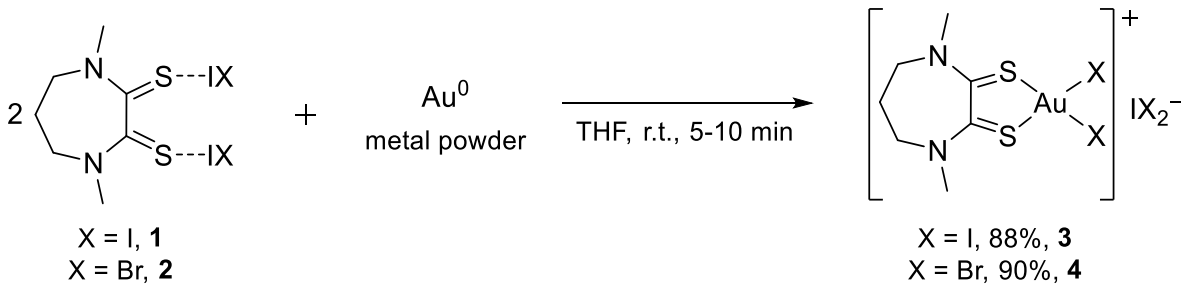

Scheme 39. Oxidation of Au^0 metal powder by Me_2dazdt·IX.

The resulting complexes, **3** and **4**, were characterised by IR and ^{1}H NMR spectroscopy, and the results were found to be consistent with existing data.[2,3] To expedite the investigation, gold metal powder was used to synthesise the majority of **3** and **4** used for catalytic testing. However, as a proof of concept, **3** (labelled from this point as **3a** to distinguish from **3** sourced from Au^0 metal powder) was also recovered from real scrap SIM cards using the patented procedure described by Serpe *et al*.[4] The patent describes the processes for recovering gold from SIM cards, ink cartridges, and printed PC motherboard and network cards. Scrap SIM cards are cheap and readily available in sufficient quantities, and are the easiest scrap material to dismantle and process on a small scale in a research laboratory and were thus used herein. Typically a ball mill would first be used to grind the powder to particles with dimensions between 0.5 and 4 mm, with a Wiley mill SKV SM 2000 being used in Serpe's patent.[4] However, since a ball mill was not available for the present investigation, a secondhand coffee grinder was used instead, which ground the scrap SIM cards to a course scrap powder with particles sizes ranging from ~5 mm to <1 mm in size (Scheme 40a). This scrap powder was then refluxed in THF for 20 h to detach and suspend the plastic support material, which was then separated and discarded by decanting from the scrap metallic powder (Scheme 40b). It is worth noting that some plastic material remains undisturbed by refluxing in THF. However, since THF is also employed in the oxidation of Au^0, this residual THF-inert scrap plastic can be present in the final gold recovery step without interfering with the recovery process. The scrap powder was then treated with aqueous ammonia, ammonium sulfate and hydrogen peroxide to selectively oxidise Cu^0 and dissolve as $[Cu(NH_3)_4](SO_4)$ (Scheme 40c). The blue aqueous solution of Cu^{2+} ions was decanted and the resulting scrap powder treated with aqueous HCl at 50 °C, resulting in the oxidation and dissolution of Ni^{0+} as $NiCl_2$ (Scheme 40d). The green aqueous solution of Ni^{2+} ions was then decanted and the resulting scrap powder treated with bis(diiodine) adduct **1** to oxidise Au^0 in the scrap powder to recovery product **3a** (Scheme 40e), which was isolated by recrystallisation.

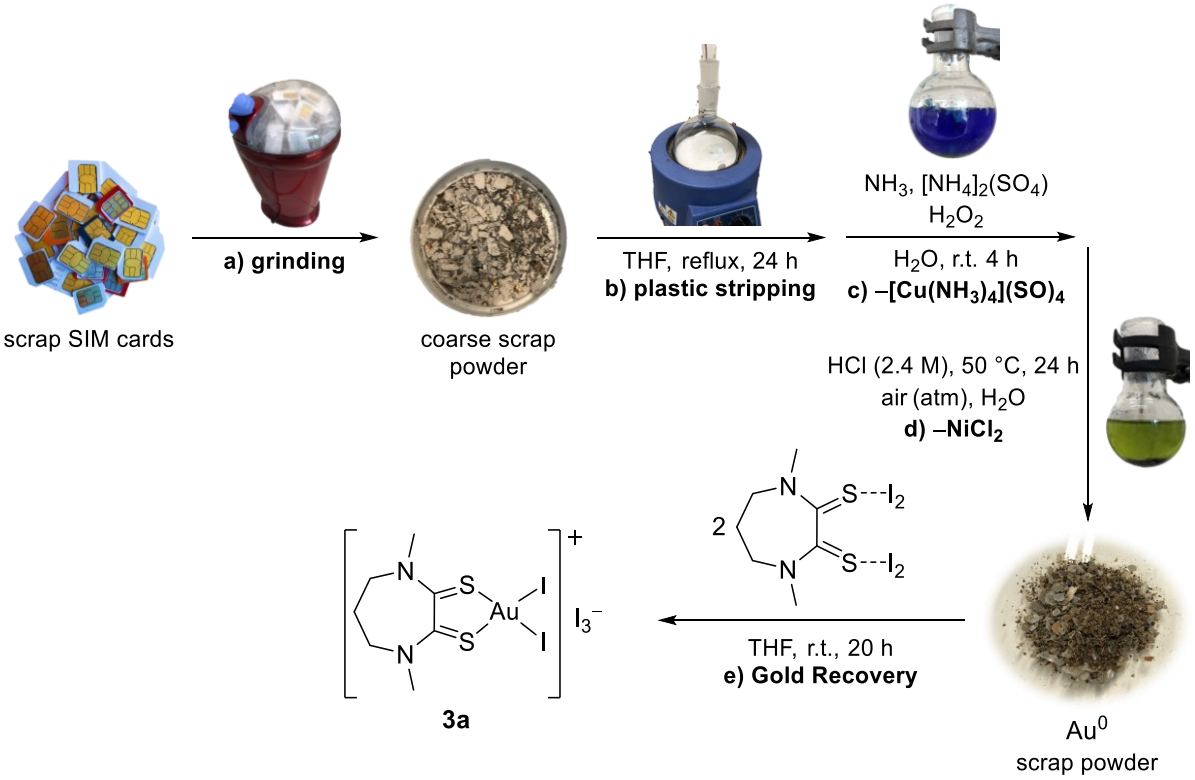

*Scheme 40. Recovery of complex **3a** from scrap SIM cards using Serpe's patented process.*[4]

The analytical data (^{1}H NMR, IR spectroscopy) obtained for complex **3a** recovered from scrap SIM cards were found to be identical to the data obtained when complex **3** was synthesised from gold metal powder. Deplano and Serpe have illustrated that SIM cards contain approximately 0.1 *wt*% Au^0,[4] which equates to 0.4 mg Au^0 per SIM card for a 400 mg SIM card. However, since the mass of a single SIM card from the batch used herein, which contained a mixture of SIM, micro-SIM and nano-SIM cards, ranged from 100-500 mg, this average *wt*% is a rough approximation. Nonetheless, the isolated yield of 130 mg of **3a** is in line with the expected yield for the 17.1 g of SIM cards used, which contain ~17-68 mg of gold and would yield ~89-352 mg of **3a**. Without the use of a ball mill, the scrap material used herein could not be ground to a homogeneous mixture that would be required to determine the average gold *wt*% using ICP-MS. The commercial viability of the process was recently calculated, which found that the cost of the recycling process using Me_2dazdt·$2I_2$ (**1**) (Scheme 40) was cheaper than commercially sourced $AuCl_3$.[31]

2.2.2. Trihalide anion metathesis of 3 and 4

Recovery complexes **3** and **4** vary both in the metal bound halogen atoms and the trihalide anions, which prevents a systematic comparison between the influence that these variables have on

catalytic activity. Moreover, the central halogen atoms in these hypervalent halogen species are electrophilic and can act as an oxidant, and thus the trihalide anions in **3** and **4** may not be spectators to catalytic activity. As a result, the synthesis of two related complexes, **5** and **6**, containing BF_4^- counter anions was explored to enable a systematic investigation of the role of the counter anion and metal bound halogens on catalytic activity.

*Table 9. Reaction conditions explored for the anion metathesis of **3** to yield BF_4^- salt **5**.*

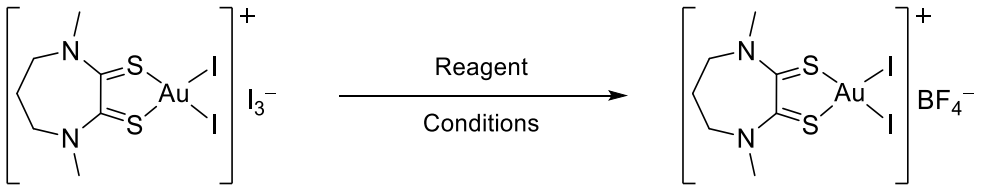

3 **5**

Entry	Reagent	Solvent	Yield **5** (%)
1	$AgBF_4$	MeCN	0[a]
2	AgOTf or AgOTs	MeCN	0[a]
3	$AgBF_4$	MeOH	0[b]
4	$AgBF_4$	EtOH	0[b]
5	$AgBF_4$	acetone	0[b]
6	Zinc then $AgBF_4$	MeCN	0[c]
7	$NaBF_4$ (10 equiv.)	MeCN	0
8	$[Me_3O]BF_4$	MeCN	0[d]
9	$[Me_3O]BF_4$	$MeNO_2$	95
10	$[Me_3O]BF_4$	THF:$MeNO_2$ (*v:v* 30:1)	97
11	$[Me_3O]BF_4$	THF	0[e]

[a] Uncharacterizable black powder formed alongside free Me_2dazdt and colloidal Au^0. [b] Complex **3** is insoluble in alcohols. [c] An Au^{1+} complex was formed (see Scheme 41). [d] Near quantitative recovery of the starting material. [e] $[Me_3O]BF_4$ is insoluble in THF.

An initial metathesis strategy using $AgBF_4$ to precipitate AgI and liberate I_2 was unsuccessful (Table 9, entry 1). Whilst an off-white AgI precipitate was formed instantaneously upon treating **3** with $AgBF_4$, recrystallisation yielded an uncharacterizable black powder that contained only trace quantities of BF_4^- in the ^{19}F NMR spectrum, alongside the presence of I_3^- as the major anion detected by negative phase electrospray ionisation mass spectrometry (ESI-MS). Decomposition of gold to colloidal Au^0 and precipitation of free Me_2dazdt was also observed when **3** was treated with $AgBF_4$ in acetonitrile (Table

9, entry 1). Similar results were seen when other silver salts were used in place of $AgBF_4$ (Table 9, entry 2). Triiodide salts are known to be symmetrical and non-polarised in the presence of aprotic solvents and weakly coordination cations.[32–35] If the reaction of halides with silver salts is charge controlled, and the trihalide anion is unpolarised in acetonitrile, then $AgBF_4$ presumably reacted with the more polarised gold-bound halogen atom. As a result, methanol and ethanol may be more suitable anion metathesis solvents, since a more polarised trihalide anion in these solvents may increase their reactivity toward $AgBF_4$. Unfortunately, this approach was unsuccessful due to the insolubility of **3** and **4** in alcohols (Table 9, entries 3 and 4). Performing the reaction of **3** with $AgBF_4$ in acetone similarly yielded a mixture of uncharacterizable products which contained only minor amounts of BF_4^- by ^{19}F NMR analysis (Table 9, entry 5). The use of Zn^0 to reduce I_3^- in **3** to ZnI_2 and liberate free I^- for anion metathesis with $AgBF_4$ was also unsuccessful (Table 9, entry 6). When this protocol (Table 9, entry 7) was attempted with AgOTf for the bromide recovery complex **4**, a bimetallic Au^{1+} complex, $[Me_2dazdt(AuBr)_2]$ (**10**) was isolated in a 35% yield (Scheme 41).

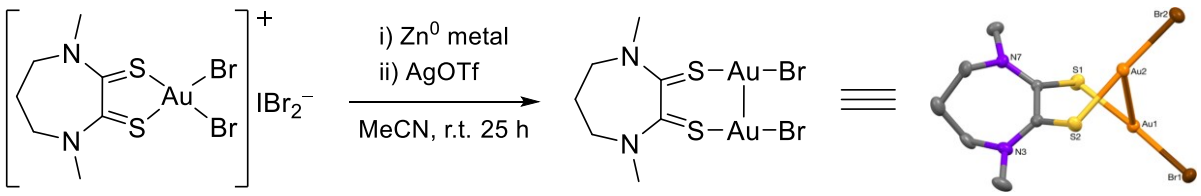

*Scheme 41. Failed anion metathesis using Zn^0 metal and AgOTf, which instead yielded bimetallic complex **10**. Single-crystal X-Ray structure of **10** showing aurophilic interactions between the metal centres(thermal ellipsoids drawn at 50% probability).*

The structure of bimetallic complex **10** was confirmed by single-crystal X-ray diffraction, which illustrated that **10** contained intermolecular Au---Au contacts (3.103 Å) that were slightly shorter than the intramolecular contacts (3.121 Å). Such Au---Au aurophilic interactions are well established,[36] with reported energy values similar to those seen in standard hydrogen bonding,[37] and in the case of **10** these interactions resulted in the formation of a chain of molecules along the direction of the b axis (Figure 18).

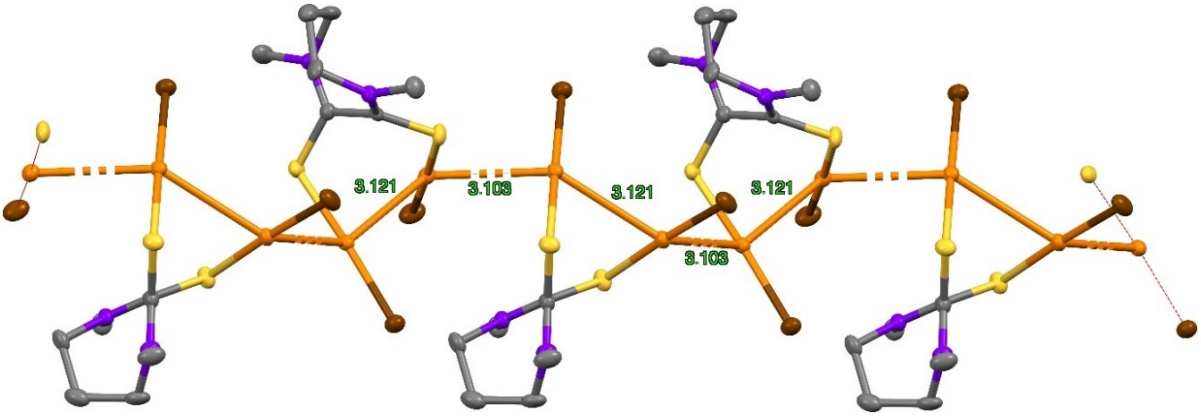

*Figure 18. The X-ray crystal structure of [Me$_2$dazdt(AuBr)$_2$] (**10**) illustrating the chain of molecules along the b axis (thermal ellipsoids drawn at 50% probability). Annotated bond angles are 3.121 (intramolecular) and 3.103 Å (intermolecular).*

Recrystallisation of either **3** or **4** from an acetonitrile solution containing 10 equivalents of $NaBF_4$ was also unsuccessful at producing **5** and **6**. An alternative anion metathesis strategy using trimethyloxonium tetrafluoroborate, an analogue of Meerwein's salt (triethyloxonium tetrafluoroborate), was explored next (Table 9, entries 8-11). Oxonium ions are useful synthetic intermediates and have been employed as electrophiles in the total synthesis of natural products through their reaction at carbon with halide and acetate nucleophiles.[38] This reactivity makes trimethyloxonium tetrafluoroborate a suitable reagent for the anion metathesis of the trihalides in **3** and **4**. Similar to the precipitation of insoluble AgX for anion metathesis with silver salts, the reaction of trimethyloxonium with nucleophiles is rendered irreversible by the evolution of gaseous dimethyl ether (boiling point –24 °C) (Scheme 42a).

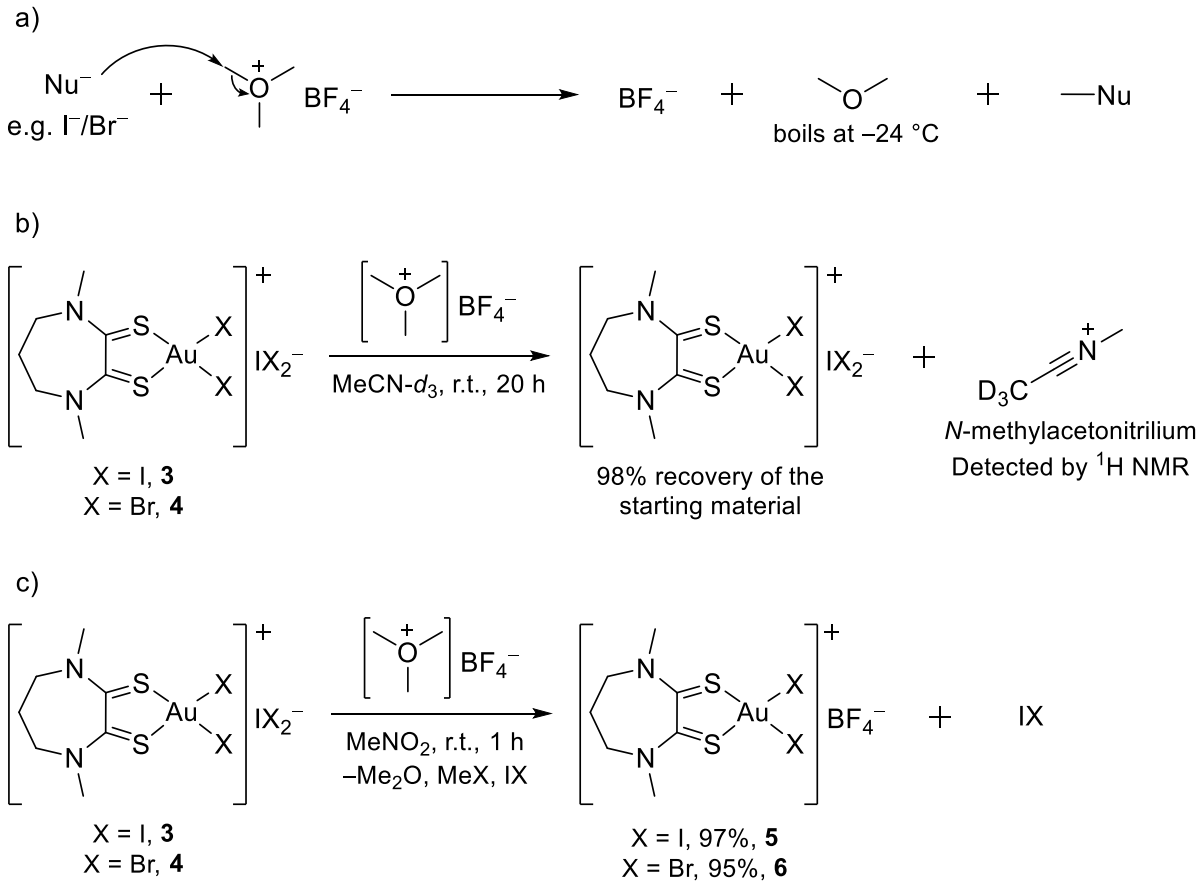

*Scheme 42. Trimethyloxonium tetrafluoroborate as a reagent for anion metathesis. a) Irreversible reaction of trimethyloxonium cations at carbon with halogen nucleophiles to liberate gaseous dimethyl ether. b) Unsuccessful anion metathesis of **3** and **4** with trimethyloxonium in acetonitrile. c) Successful anion metathesis of complexes **3** and **4** with trimethyloxonium in nitromethane.*

An initial attempt at the anion metathesis of either **3** or **4** with trimethyloxonium tetrafluoroborate in acetonitrile resulted in the near quantitative recovery of the gold starting material (Table 9, entry 8 and Scheme 42b). A 1:1:1 triplet with $^{2}J_{NH}$ coupling (3.7 ppm, 2.9 Hz) that is characteristic of the formation of *N*-methylacetonitrilium-d_3 was detected by *in situ* ^{1}H NMR analysis of the reaction between **3**/**4** and trimethyloxonium tetrafluoroborate in acetonitrile-d_3 (Scheme 42b),[39,40] a known transformation originally reported by Meerwein in 1956.[41] With this in mind, anion metathesis product **5** was delivered in excellent yield (97%) when the solvent was switched to nitromethane (Scheme 42c) (Table 9, entry 9). A mixture of tetrahydrofuran and nitromethane (*v:v* 30:1) was also found to be a suitable solvent system (Table 9, entry 10), however neat tetrahydrofuran was unsuitable due to the insolubility of trimethyloxonium tetrafluoroborate in this solvent (Table 9, entry 11). Anion metathesis product **6** was also successfully isolated in an excellent yield from the reaction of **4** with trimethyloxonium tetrafluoroborate (95%) (Scheme 42c). Single-crystal X-ray diffraction was obtained for both anion metathesis products **5** and **6** (Figure 19).

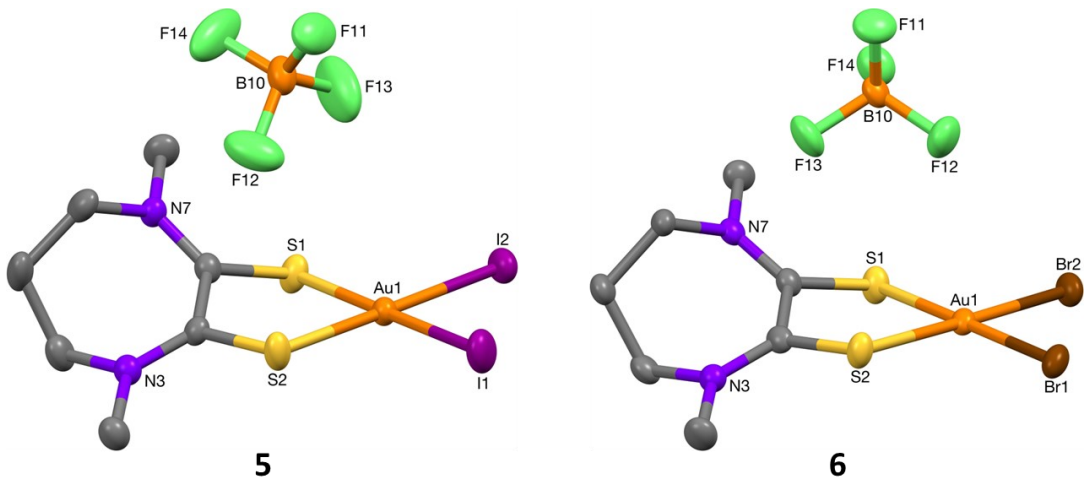

*Figure 19. Single-crystal X-ray diffraction structures for complexes **5** and **6** (thermal ellipsoids drawn at 50% probability).*

The structure and purity of **5** and **6** were confirmed by ^{1}H NMR spectroscopy, ESI-MS, and by CHN elemental analysis, as well as by quantitative comparison of the BF_4^- ^{19}F NMR resonance with an internal standard (fluorobenzene).

Since the solvent is known to influence the polarisation of trihalides anions,[32–35] the solvent choice would likely play a key role in any successful anion metathesis of **3** and **4** with silver salts. As a result, a number of additional solvents for the anion metathesis of **3** and **4** were also explored. Whilst investigating different solvents, an unusual effect was observed when trihalide complexes **3** and **4** were dissolved in acetone. Initial attempts at employing acetone as the reaction solvent was unsuccessful when the silver salt was *immediately transferred* to an acetone solution of **3** and **4** (Scheme 43).

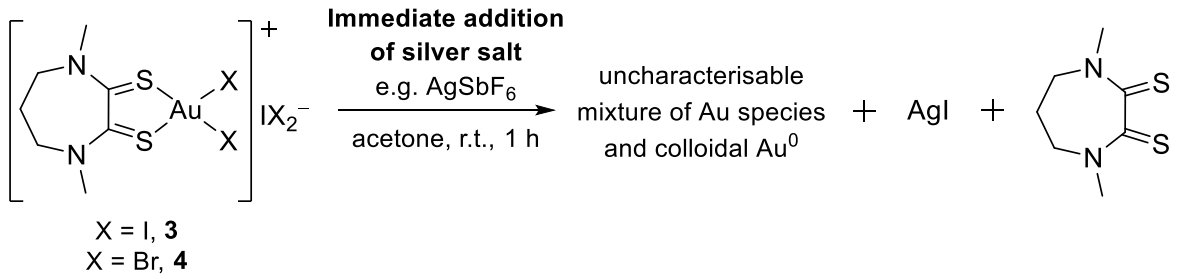

*Scheme 43. Unsuccessful anion metathesis of complexes **3** and **4** by the immediate addition of silver salts to solutions of **3**/**4** in acetone.*

However, when complexes **3** and **4** were stirred in acetone for ~5 min without the addition of a silver salt, the colour of the solution changed dramatically from dark purple/black to pale yellow (Scheme

44a). This process was found to be reversible, as **3** and **4** were reisolated as black solids upon concentration of the acetone solution, and this colour change upon dissolution and concentration from acetone could be repeated multiple times. The black colour of complexes **3** and **4** is presumably due to charge transfer interactions between the Au^{3+} centre and the trihalide anion. Since ^{1}H NMR analysis did not reveal any major change in the ligand environment upon dissolution in acetone-d_6, it was hypothesised that the colour change from black to pale-yellow may be the result of the disruption of the trihalide anion. Indeed, when silver hexafluoroantimonate was added to an acetone solution of complex **4*** *after* the solution had turned pale yellow, anion metathesis product **11** was isolated in a 92% yield (Scheme 44b). The batch of **4** used (**4***) in the synthesis of **11** was isolated by a modified work-up procedure which resulted in the mixed halogen content. This sample of **4**, denoted as **4***, was not employed for catalytic studies. Similarly, treating a yellow solution of **3** in acetone with silver trifluoromethanesulfonate yielded anion metathesis product **12** (Scheme 44c). The possibility of the colour change involving a gold-promoted haloform reaction was ruled out by the absence of any iodoform products and the ability to reform **3** as a black solid and repeat the colour changing process. This colour change was not observed for any of the other solvents explored (DMF, DMA, THF, $MeNO_2$ and MeCN).

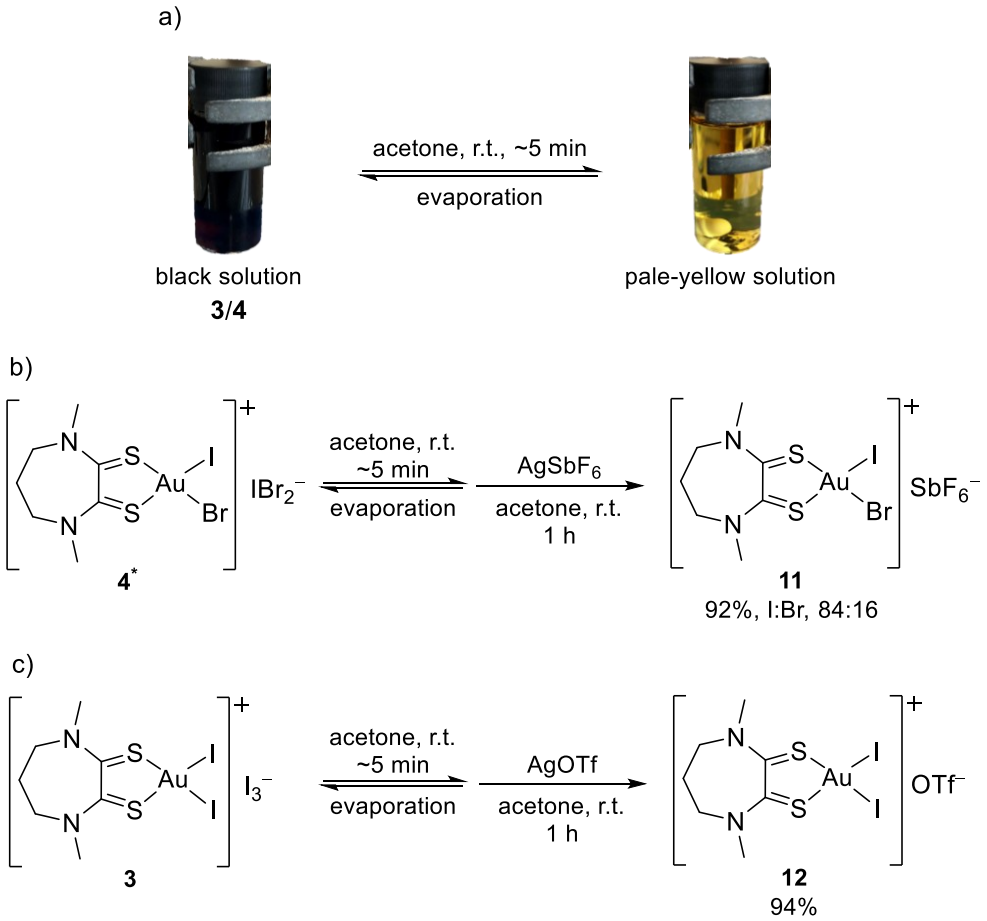

*Scheme 44. a) Solution behaviour of complexes **3** and **4** in acetone with pictures illustrating colour change. b/c) Successful anion metathesis of **4*** and **3** with silver salts after initially allowing the gold complexes to stir in acetone for ~5 min.*

The structure of **11** was confirmed by single-crystal X-ray diffraction (Figure 20), and was found to contain a mixture of gold-bound iodide and bromide ligands (~84:16 I:Br). The structure and purity of **11** and **12** was confirmed by ^{1}H NMR spectroscopy, ESI-MS, by CHN elemental analysis, and by quantitative comparison of the SbF_6^- ^{19}F NMR resonance with an internal standard (fluorobenzene). Additional understanding of the solution behaviour of complexes **3-6** and **11** was uncovered during mechanistic studies, which will be covered in Section 2.2.8.

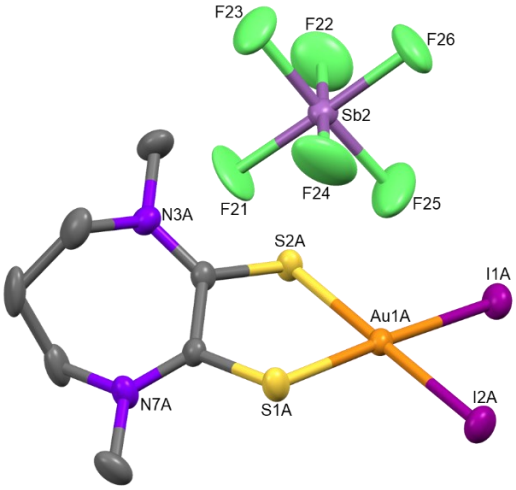

*Figure 20. Single-crystal X-ray structure of anion metathesis product **11** (thermal ellipsoids drawn at 50% probability)*

2.2.3. Alternative synthesis of Me_2dazdt

A few synthetic strategies were explored to develop an improved synthesis of Me_2dazdt which does not rely on Lawesson's reagent. An ideal 'green' sulfur source to replace Lawesson's reagent is elemental sulfur, since it is readily available as a byproduct of tar sand oil production. In 1986, Viehe and colleagues described the synthesis of dithiooxamides **13** and **14** from glyoxal and elemental sulfur (S_8) in DMF via a Willgerodt-Kindler reaction (Scheme 45a).[42] Unfortunately, this procedure was unsuccessful at producing Me_2dazdt, irrespective of the equivalents of amine, S_8, water, or the C_2 source (e.g. glyoxal, dimethyl oxalate, oxalic acid) employed (Scheme 45b).

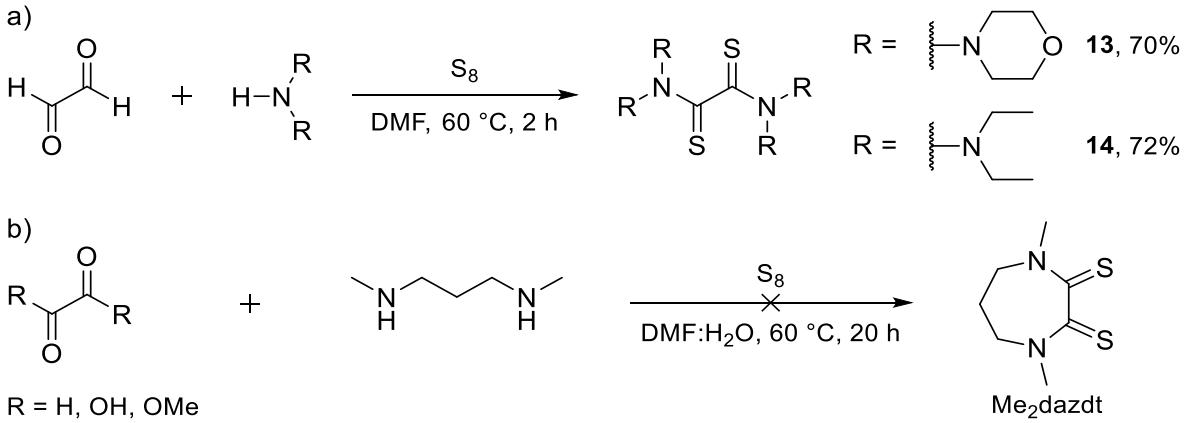

Scheme 45. a) Viehe et al. synthesis of dithiooxamides from glyoxal and S_8.[42] b) This study – unsuccessful synthesis of Me_2dazdt by procedure described by Viehe et al.

In 2022, a report outlining the thioamidation of aldehydes by aqueous solutions (40 *wt*%) of amines was published (Scheme 46).[43]

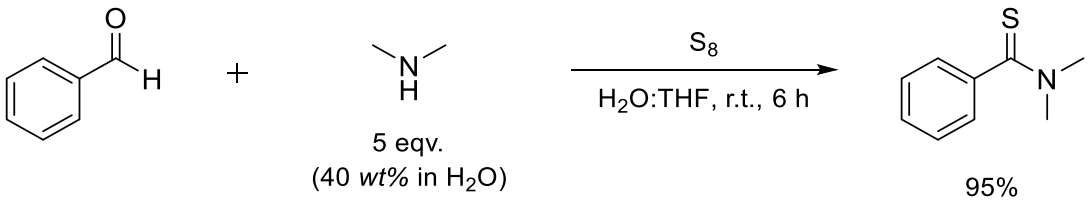

Scheme 46. Direct thioamidation of aldehydes in water.[43]

Since glyoxal is supplied as a 40 *wt*% solution in water, it was hypothesised that this direct thioamidation protocol (Scheme 46) may be suitable for synthesising Me_2dazdt. An initial attempt at replicating the procedure with *N,N'*-dimethylpropane-1,3-diamine and glyoxal produced Me_2dazdt in a 3% isolated yield following flash column chromatography (Table 10, Entry 1). Replacing glyoxal with dimethyl oxalate resulted in 0% conversion to either dioxamide or the dithiooxamide Me_2dazdt (Table 10, Entry 2). Increasing the number of diamine equivalents provided an improved, albeit still poor yield of 8% (Table 10, Entry 3). Since it has been postulated that bases are involved in activation of S_8 to form an open chain nucleophilic '[Base$^+$–S_n–S^-]' species,[43–46] a number of tertiary amine additives were explored to promote the formation of '[Base$^+$–S_n–S^-]' (Table 10, Entries 4-11). At room temperature, the use of various amine additives did not provide any more than trace (<1%) Me_2dazdt by HPLC analysis (Table 10, Entries 4-7). An improved yield of 10% was obtained when 50 mol% pyridine was employed at 70 °C (Table 10, Entry 8). The use of three equivalents of K_2CO_3, a strategy previously employed for thioamide synthesis from S_8 by Yuan *et al*,[45] was unsuccessful at producing Me_2dazdt (Table 10, Entry 11).

Table 10. Synthesis of Me_2dazdt using S_8 in water.

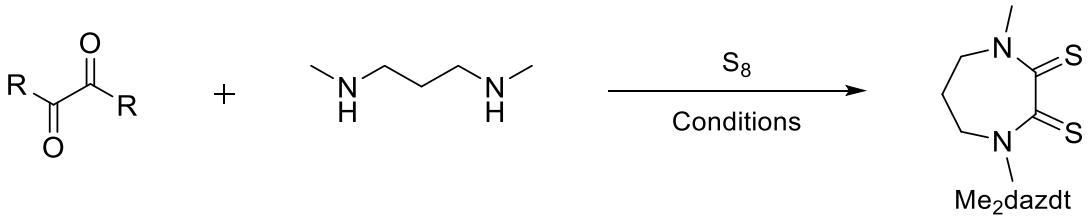

Entry	R	Amine equiv.	S_8 equiv.	Solvent (*v:v*)	Additive (mol%)	Time (min)	Temperature (°C)	Yield[b] (%)
1	H[a]	2	2	THF:H_2O (0.5:1)	-	18 h	21	3[c]
2	OMe	2	4	THF:H_2O (0.5:1)	-	20 h	21	0[d]
3	H[a]	5	4	THF:H_2O (0.5:1)	-	90 h	21	8
4	H[a]	1	4	THF:H_2O (1:2.4)	Pyridine (25)	20 h	21	<1
5	H[a]	1	4	THF:H_2O (1:2.4)	Pyridine (50)	20 h	21	<1
6	H[a]	1	4	THF:H_2O (1:2.4)	DMAP (25)	20 h	21	<1
7	H[a]	1	4	THF:H_2O (1:2.4)	DBU (25)	20 h	21	1
8	H[a]	1	4	THF:H_2O (1:2.4)	Pyridine (50)	20 h	70	10
9	H[a]	1	4	THF:H_2O (1:2.4)	DBU (50)	20 h	70	4
10	H[a]	1	4	THF:H_2O (1:2.4)	Et_3N (50)	20 h	70	7
11	H[a]	1	4	THF:H_2O (1:2.4)	K_2CO_3 (300)	20 h	70	<1
12	H[a]	1	4	THF:H_2O (1:2.4)	*β*-cyclodextrin (20)	20 h	70	8
13	H[a]	1	4	THF:H_2O (1:2.4)	Pyridine (100) *β*-cyclodextrin (20)	20 h	80	6
14	SO_3Na	2	3	H_2O	-	20 h	40	0
15	SO_3Na	2	3	SPGS-750[e]	-	20 h	40	0
16	SO_3Na	2	3	SPGS-750[e]	DMAP (100)	20 h	40	7
17	H[a]	1	4	$CHCl_3$	Pyridine (50)	20 h	50	0
18	SO_3Na	1	4	$CHCl_3$	Pyridine (50)	20 h	50	0
19	OMe	1	4	$CHCl_3$	Pyridine (50)	20 h	50	0

[a)] Glyoxal used as an aqueous (40 *wt*%) solution. [b)] Unless otherwise stated, yields determined by HPLC with reference to naphthalene as an internal standard. [c)] Isolated yield following flash column chromatography. [d)] No conversion of dimethyl oxalate to dioxamide according to HPLC analysis. [e)] SPGS-750 used as a 2 *wt*% solution in H_2O.

An alternative strategy employing *β*-cyclodextrin as an additive for thioamidation from S_8 has also been described in the literature.[46] Unfortunately, when 20 mol% *β*-cyclodextrin was explored herein for the synthesis of Me_2dazdt, only an 8% yield was obtained (Table 10, Entry 12). Since pyridine and *β*-cyclodextrin additives provided the two most promising results, the two were employed in combination at 70 °C. Unfortunately, this approach only yielded Me_2dazdt in a 6% yield (Table 10, Entry 13). The bis-sodium bisulfite adduct of glyoxal was employed as an alternative C_2 source via *in situ* generation of glyoxal (Table 10, Entries 14-16),[47] however no marked improvement in yield was obtained. Finally, since S_8 is considerably more soluble in less polar/chlorinated solvents, chloroform was explored as a solvent for the synthesis Me_2dazdt. This strategy was also unsuccessful at producing Me_2dazdt (Table 10, Entry 17). Despite S_8 being more soluble in chloroform, the lack of Me_2dazdt formed may be the result of the absence of water to promote the formation of/stabilise an activated '[$Base^+$–S_n–S^-]' species.[43,44] A white precipitate was also immediately formed upon the addition of glyoxal to chloroform, which may be the result of polymerisation/instability of glyoxal. Replacing glyoxal with either dimethyl oxalate or the bis-sodium bisulfite adduct of glyoxal also provided 0% Me_2dazdt yield (Table 10, Entries 18 and 19). Since suitable conditions which provide >10% yield could not be uncovered, an alternative synthesis of Me_2dazdt using S_8 was not explored further.

2.2.4. Gold catalysis – Alkyne bond activation

The first mode of action explored with complexes **3-6** was the catalytic activation of alkyne bonds, with the cyclisation of *N*-propargylbenzamide examined first.[14] *N*-propargylbenzamide (**15**) employed in this study was synthesised from benzoic acid and propargylamine in the presence of tetramethylorthosilicate (TMOS), according to the procedure described by Braddock *et al.* (Scheme 47).[48]

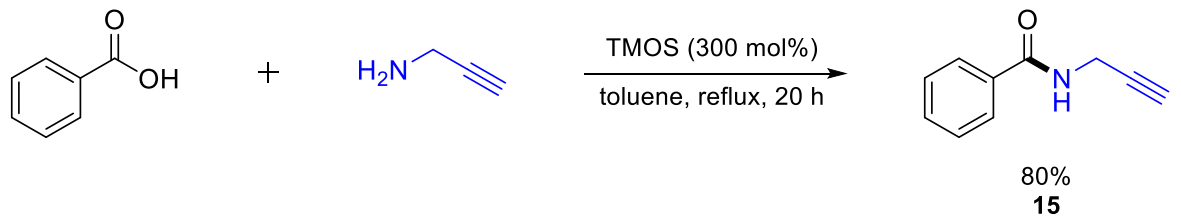

Scheme 47. Direct amidation of benzoic acid and propargylamine by TMOS.

When the resulting *N*-propargylbenzamide (**15**) was treated with the reference catalyst, $HAuCl_4$, in acetonitrile, the desired oxazole (**16**) was isolated in a >95% yield (Table 11, Entry 1).

*Table 11. Cyclisation of N-propargylbenzamide (**15**) catalysed by **3-6**.*

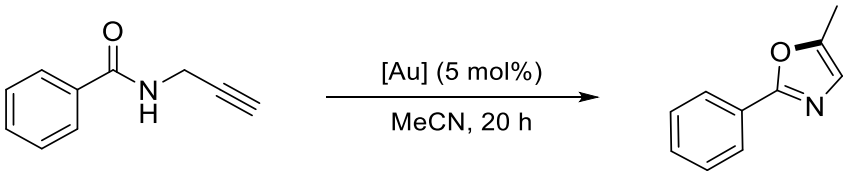

15 **16**

Entry	Temperature (°C)	Additive	Yield (%)[a] Catalyst				
			$HAuCl_4$	**3**	**4**	**5**	**6**
1[b]	25	none	>95	0	0	0	0
2	60	none	-	0	0	0	0
3	25	$AgBF_4$ (10 mol%)	-	0	0	0	0
4[b]	25	*N*-pyridine oxide (15 mol%)	-	46	50	44	51
5[b]	60	*N*-pyridine oxide (15 mol%)	-	82 ± 4	>95	91 ± 2	>95
6[b]	60	*N*-pyridine oxide (15 mol%)	-	79 ± 5[c]	-	-	-

[a)] Yields were determined by ^{1}H NMR spectroscopy. [b] Yields are an average of 3 runs. [c)] Catalysed by gold complex **3a** derived from scrap SIM cards.

When identical conditions were replicated with recovery complexes **3-6**, no conversion of the starting material (**15**) was observed (Table 11, Entry 2). Since silver salts are commonly employed to abstract halides from gold precatalysts to generate an activated species with a vacant coordination site, the addition of 10 mol% $AgBF_4$ was explored. Unfortunately, this approach was unsuccessful (Table 11, Entry 3). Wang *et al*. illustrated in 2014 that for reactions where protodeauration is the rate-limiting step, strong hydrogen bond acceptors are effective at significantly improving the rate of gold catalysis by acting as a 'proton shuffle', whilst bases shut protodeauration down by capturing acidic protons.[49] Thus, *N*-pyridine oxide, a weak base and strong hydrogen bond acceptor, was employed as an additive for the cyclisation of **15**, which resulted in significantly improved conversions of 40-50% (Table 11, Entry 4). Finally, increasing the temperature to 60 °C resulted in excellent yields of oxazole **16** (Table 11, Entry 5). Bromide analogues **4** and **6** provided slightly improved performance when compared to iodides **3** and **5**, whilst there was no significant observed difference in activity between trihalide salts **3** and **4** when compared to tetrafluoroborate salts **5** and **6**. Finally, when gold complex **3a** derived from scrap SIM cards was used as a catalyst, near identical yields were observed compared to when complex **3**, derived from gold powder, was used (Table 11, Entry 6).

The cyclisation of *N*-propargylamides catalysed by **3**-**6** was expanded to non-terminal alkynes. The phenyl-substituted alkyne **17** was synthesised by the Sonogashira reaction of phenyl iodide and *N*-propargylbenzamide (Scheme 48).[50]

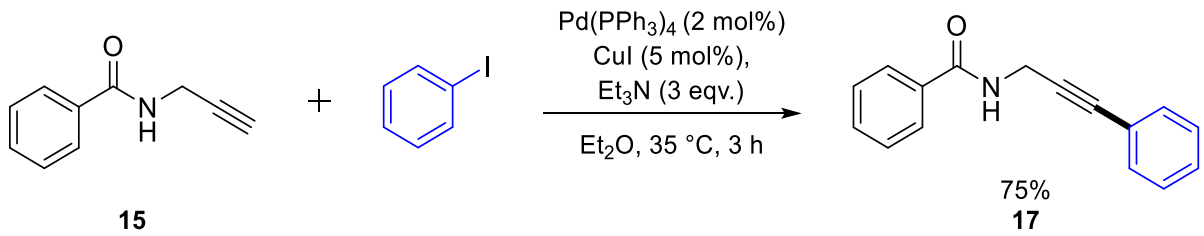

*Scheme 48. Synthesis of non-terminal alkyne **17** via Sonogashira coupling.*

The cyclisation of non-terminal alkyne **17** is more challenging when compared to the cyclisation of terminal alkyne **15**, since a mixture of both the 5-*exo* (**18**) and 6-*endo* (**19**) products are known to form (Table 12).[15,51]

*Table 12. Cyclisation of non-terminal alkyne **17** catalysed by **3**-**6**.*

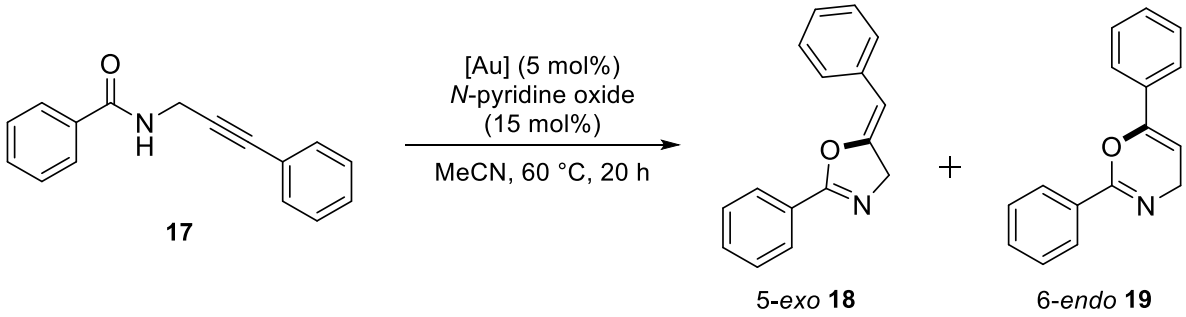

		Yield (%)	
Entry	Catalyst	**18**	**19**
1	$AuCl_3$	65	30
2	**3**	0[a]	0[a]
3	**4**	0[b]	0[b]
4	**5**	72	0
5	**6**	81	0

[a] Vinyl iodide **20** was isolated in an 8% yield, alongside decomposition of the catalyst as colloidal Au^0.

[b] Near quantitative recovery of **17** was obtained.

For tetrafluoroborate complexes **5** and **6**, 5-*exo* **18** was isolated in 72% and 81% yields respectively (Table 12, Entries 4 and 5), which represents a noticeable improvement in reaction selectivity

compared to $AuCl_3$, which yielded a mixture of 65% **18** and 30% **19** (Table 12, Entry 1). Attempts at promoting the cyclisation of **17** with triiodide complex **3** was unsuccessful in yielding either expected products **18** or **19** (Table 12, Entry 2), and conversion of the starting material to an unknown product was observed instead. Only trace conversion of **18** to this unknown product was observed when trihalide complex **4** was employed (Table 12, Entry 3). Characterisation data of the unknown product was consistent with cyclisation, i.e. loss of the amide NH and methylene CH_2 protons present in the ^{1}H NMR of **17**, however the number of protons (12) was one less than expected (13) for either cyclisation products **18** or **19**. Moreover, the CH sp^2 alkene environment (101 ppm) was absent from the ^{13}C NMR spectrum, and was replaced by a quaternary carbon environment at 71 ppm which is consistent with the formation of an sp^2 vinyl iodide. These results pointed toward the formation of either cyclised vinyl iodide **20** or **21** (Figure 21), which was subsequently confirmed by the presence of an $[M+H]^+$ ion in the ESI-HRMS of *m/z* = 362.0047 (calcd. for $C_{16}H_{13}INO$: 362.0042).

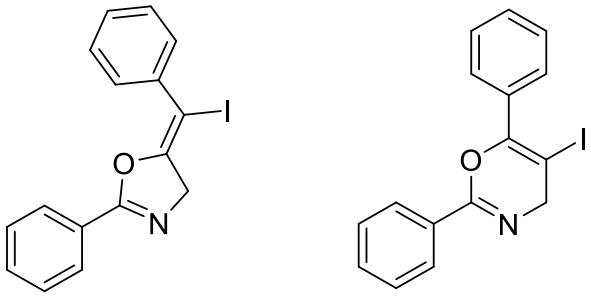

5-*exo* **20** 6-*endo* **21**

ESI-MS confirms vinyl iodide **20** or **21**:
$[C_{16}H_{13}NOI]^+$ Calculated mass = 362.0042
Observed mass = 362.0047

*Figure 21.Two possibly vinyl iodide products 5-exo **20** and 6-endo **21** from the cyclisation of **17** catalysed by **3**.*

Confirmation of the selectivity for either 5-*exo* **20** or 6-endo **21** was challenging, since the diagnostic alkene ^{1}H shifts and allylic/vinylic coupling constants that were used to distinguish between 5-*exo* **18** and 6-*endo* **19** are not present in 5-*exo* **20** and 6-*endo* **21**. Comparison of the NMR data obtained herein with literature data was also unhelpful, since literature data for both structures are conflicting and inconsistent, with **20** and **21** exhibiting near identical NMR spectra. Thus, the structure of the unknown vinyl iodide was confirmed as 5-*exo* product **20** by lithiation with *n*-butyllithium at –78 °C and subsequent protonation to yield 5-*exo* product **18** (Scheme 49).

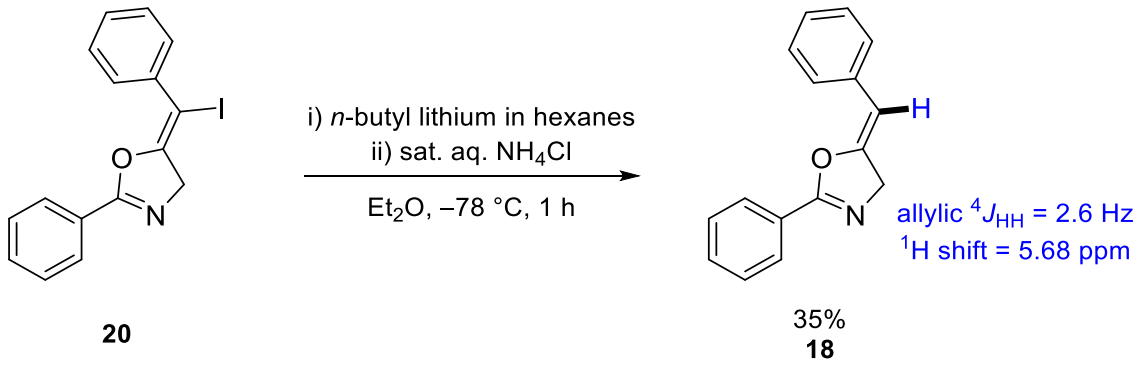

*Scheme 49. Confirmation of 5-exo structure in **20** by lithiation and subsequent protonation to yield **18**.*

The mechanism of the formation of **20** can be rationalised by three possible pathways – either activation of the alkyne π bond by the gold centre in **3** and subsequent iododeauration by electrophilic 'I^+' from triiodide/iodine (Scheme 50, Pathway A), or activation of the alkyne by electrophilic 'I^+' from triiodide/iodine (Scheme 50, Pathway B). A third pathway can also be conceived, in which the vinyl gold intermediate reductively eliminates to give **20** and a gold(I) species (Scheme 50, Pathway C). Evidence for pathway C was uncovered (*vide infra*) during mechanistic studies (Section 2.2.8, Scheme 55), however since the yields of **20** exceed the loading of **3**, formation of **20** via pathway C must also proceed alongside pathway A or B, and/or turnover of the gold(I) species to a gold(III)-iodide.

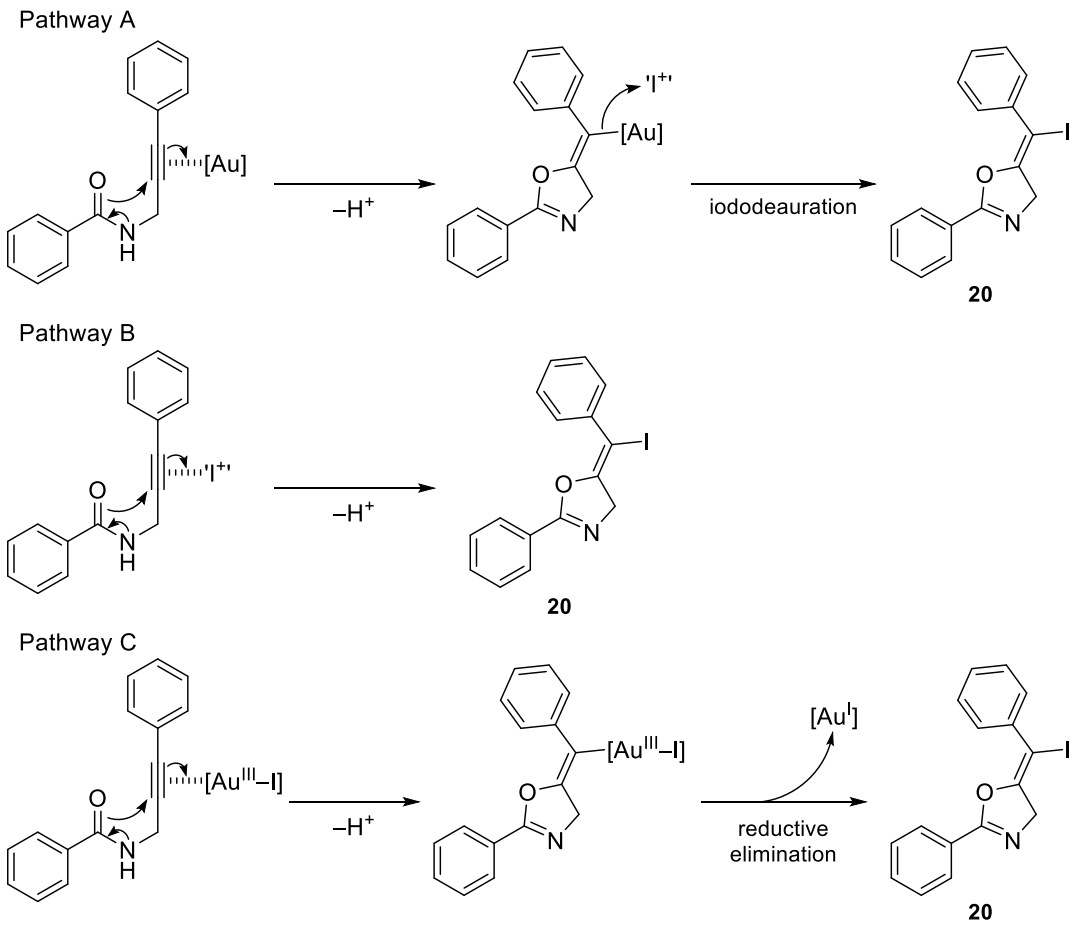

*Scheme 50. Three possible mechanisms of the formation of vinyl iodide **20**.*

Previous work has illustrated that 'I+' sources (e.g. *N*-iodosuccinimide) can be used as electrophiles for promoting the cyclisation of nonterminal propargylic amides.[52–54] Indeed, when **16** was subjected to stoichiometric sodium triiodide (from NaI/I_2) under identical cyclisation conditions (Table 12), a mixture of **20** and **21** were isolated in a 12% total yield. This result confirms that triiodide alone is a sufficient 'I+' source to promote the cyclisation yielding **20**, which initially appears to provide support for mechanistic pathway B. It is worth noting though that the formation of both 5-*exo* (**20**) and 6-*endo* (**21**) regioisomers when **17** was treated with NaI/I_2 also supports pathway A, since the single 5-*exo* regioisomer isolated from gold complex **3** must have proceeded via regioselective gold-alkyne coordination. Attempts were made to optimise the cyclisation of **16** to **19**, since such vinyl iodides represent highly useful synthetic intermediates. Unfortunately, irrespective of the combination of excess iodide and/or iodine that were employed alongside gold complex **3**, the yield of **19** could not be improved beyond ~10%.

The next substrate employed to explore the activation of alkyne bonds is 2-phenylethynyline (**22**) (Table 13). When the conditions reported by Arcadi were employed for gold complexes **3**-**6**,[18] no conversion of **22** to indole **23** was observed (Table 13, Entry 1).

*Table 13. Cyclisation of 2-phenylethynyline (**22**) to indole **23** catalysed by **3**-**6**.*

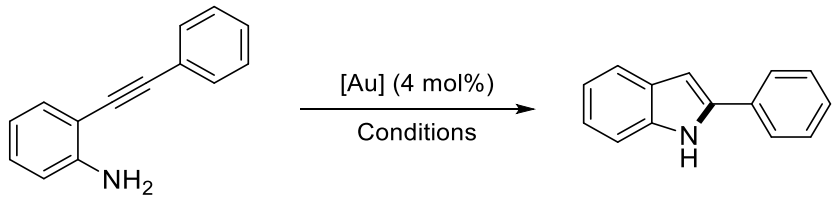

22 **23**

				Yield **23** (%)			
Entry	Solvent	Temperature (°C)	Additive	**3**	**4**	**5**	**6**
1	EtOH	r.t.	-	0	0	0	0
2	EtOH	r.t.	*N*-pyridine oxide (15 mol%)	0	0	0	0
5	MeCN	r.t.	*N*-pyridine oxide (15 mol%)	0	0	0	0

The reaction was monitored by ^{1}H NMR analysis of the crude reaction mixture.

Addition of *N*-pyridine oxide did not promote the cyclisation of **22** (Table 13, Entry 2), suggesting that the lack of product formation was not the result of a sluggish protodeauration step, as was the case for the cyclisation of *N*-propargylamides (Table 11 and Table 12). Whilst complexes **3**-**6** are insoluble in ethanol, **3**-**6** did dissolve in ethanol for the activation of 1,3-dicarbonyl compounds (*vide infra*, Section 2.2.5) once both Lewis acid and Lewis base reaction components had been added to the reaction mixture. This was presumably due to the formation of a soluble gold intermediate. Conversely, no dissolution of **3**-**6** in ethanol was observed in the presence of **22**, which highlights the inability of **3**-**6** to activate the alkyne bond and form a soluble vinyl gold intermediate. Moreover, switching to acetonitrile, in which **3**-**6** are soluble, was also unsuccessful at promoting the cyclisation yielding **23**. No additional attempts were made to catalyse the cyclisation of **22** using complexes **3**-**6**.

2.2.5. Gold catalysis – Carbonyl bond activation

The first carbonyl bond activation reaction explored with complexes **3**-**6** was the condensation of 1,3-dicarbonyl **24** and aniline **25** to give *β*-enaminone **26** (Scheme 34).[19] A control experiment using the conditions from Arcadi's original report performed in the absence of a gold catalyst resulted in only trace conversion of **24** and **25** to *β*-enaminone **26** (Table 14, Entry 1). Benchmark catalyst $HAuCl_4$ yielded **26** in an improved yield (74%) when compared to that provided by $Na[AuCl_4]$ in Arcadi's report (Table 14, Entry 2), likely due to the Brønsted acid content of $HAuCl_4$.

*Table 14. Condensation of 1,3-dicarbonyl **24** and aniline **25** to β-enaminone **26** catalysed by **3**-**6**.*

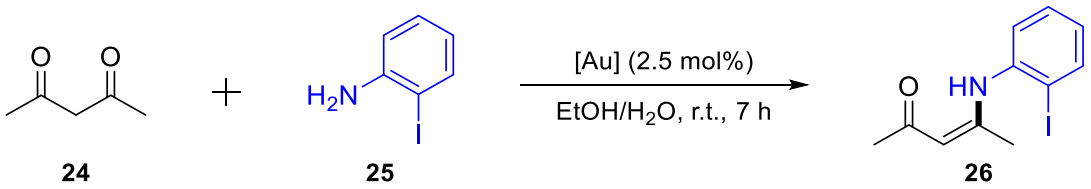

Entry	Catalyst	Yield **26** (%)[a]
1	none	trace
2	$HAuCl_4$	74 ± 0
3	**3**	62 ± 6
4	**4**	64 ± 4
5	**5**	52 ± 4
6	**6**	65 ± 3
7	**3a**[b]	59 ± 5

[a)] Yields were calculated as conversions using ^{1}H NMR spectroscopy and are based on an average of three experiments. [b)] Gold complex **3a** was derived from scrap SIM cards.

Gold complexes **3**-**6** all performed similarly to the benchmark catalyst. This represents a considerable improvement when compared to the activation of alkyne bonds, where complexes **3**-**6** required elevated temperatures and additives to achieve performances similar to the benchmark catalyst. Little difference was observed in performance between complexes **3**-**6**, although a direct comparison of the performance may have been skewed by differences in the solubility of **3**-**6** in ethanol. Compared to the other catalytic reactions studied herein, the yields of **26** exhibited larger standard deviations in the mean. This may be due to the poor solubility of complexes **3**-**6** in ethanol introducing additional variables that were not controlled, e.g. differences in mixing between runs when using 7 mL reaction vials in a multi-well DrySyn® apparatus. Near identical yields were obtained when complex **3**, derived

from gold metal powder, and **3a**, derived from scrap SIM cards, were used as catalysts (Table 14, Entries 3 and 7).

Gold complexes **3**-**6** were next explored as catalysts for the addition of aromatic nucleophiles to electrophilic *α,β*-unsaturated carbonyl compounds. When the conditions employed in Dyker's original report were replicated for complexes **3**-**6**,[20] excellent yields were obtained (Table 15). A range of aromatic nucleophiles were found to successfully react, including 2-methylfuran (Table 15, Entries 1-4), an electron-rich arene (Table 15, Entry 6), azulene (Table 15, Entry 7), and the previously unexplored furanyl-2-boronic acid (Table 15, Entry 5). A few electrophilic *α,β*-unsaturated carbonyl compounds were also coupled, including linear (Table 15, Entry 1) and cyclic ketones (Table 15, Entry 4), and a previously unexplored aldehyde (Table 15, Entry 2). Attempts at using the *α,β*-unsaturated esters methyl acrylate and *tert*-butyl acrylate were unsuccessful (Table 15, Entry 3), even under more forcing (60 °C) conditions. In general, iodide complexes **3** and **5** performed better than the bromide analogues, which is in direct contrast to the results obtained for the activation of alkyne bonds, where bromide complexes **4** and **6** performed better. Little to no difference in catalytic activity was observed between the trihalide (**3** and **4**) and tetrafluoroborate complexes (**5** and **6**) for the majority of the transformations (Table 15, Entries 1-5 and 7). Tetrafluoroborate complexes **5** and **6** did however provide significantly lower yields when compared to trihalide complexes **3** and **4** for the addition of 1,3-dimethoxybenzene to methyl vinyl ketone (Table 15, Entry 6). The mechanistic origin of the differences in performance between **3**/**4** and **5**/**6** could be due to the ability for the central halogen atom in the trihalide anions to act as a carbophilic Lewis acid toward 1,3-dimethoxybenzene. A control experiment to test for the reactivity of triiodide, *e.g* using sodium triiodide, was not explored. This result highlights that the role of the anion can be strongly substrate dependent, and that catalysis may even proceed via different mechanisms for different substrates/precatalysts. Similarly, whilst complexes **3**-**6** performed comparably to $AuCl_3$ (Table 15, Entries 1-6),[20] complexes **3**-**6** provided significantly improved yields for the addition of azulene to methyl vinyl ketone (Table 15, Entry 7), which also illustrates that the optimum catalyst, and possibly the reaction mechanism, is substrate dependent.

*Table 15. Addition of nucleophilic arenes to electrophilic α,β-unsaturated carbonyl compounds catalysed by **3**-**6**.[a]*

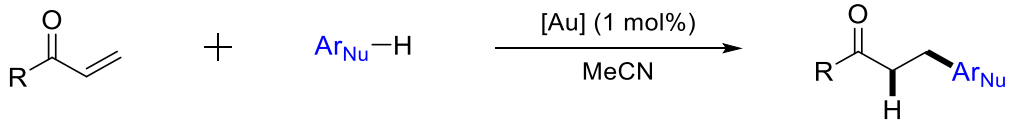

Entry	Product	Time	Yield (%)[b] Catalyst **3**	**4**	**5**	**6**	$AuCl_3$[c]
1	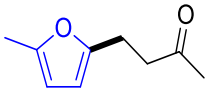	40 min	78 ± 2 73 ± 4[h]	67 ± 4	82 ± 2	70 ± 3	80-90
2	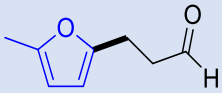	40 min	72 ± 3	65 ± 1	79 ± 3	65 ± 3	n/a
3[d]	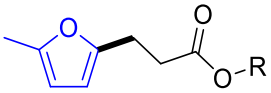 R = ^{t}Bu, Me	24 h	0	0	0	0	n/a
4	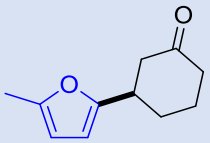	24 h	70 ± 3	63 ± 2	74 ± 4	60 ± 4	74
5[f]	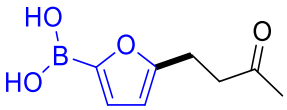	18 h	78 ± 4	65 ± 3	78 ± 2	67 ± 1	n/a
6[d,e,f]	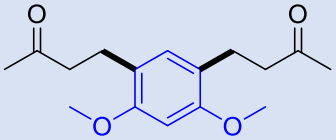	24 h	92 ± 2	78 ± 1	31 ± 3	22 ± 5	90-95
7[d,g]	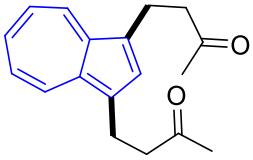	3 h	>99	>99	>99	>99	50-55

[a)] Reactions were carried out using 1 mol % catalyst loading and 1 equivalent of methyl vinyl ketone at room temperature, unless otherwise stated. [b)] Yields are of the isolated pure product unless otherwise stated, and are the average of three runs (this work only). [c)] $AuCl_3$ yields taken from the study of Dyker *et al*. [d)] Reactions were performed at 60 °C. [e)] 4 equivalents of methyl vinyl ketone were used. [f)] Reactions were conducted in MeCN-d_3 and the yields were determined based on ^{1}H NMR analysis of the crude. [g)] Two equivalents of MVK were used. [h] Result obtained with gold complex **3a** derived from scrap SIM cards.

2.2.6. Gold catalysis – Oxidative C–C coupling of arenes and aryl silanes

The final reaction explored to probe the reactivity of gold complexes **3**-**6** is the oxidative coupling of arenes and aryl silanes.[28] An initial attempt at employing the literature conditions for the model coupling of trimethylsilane (**27**) and 1-chloro-2-methoxybenzene (**28**) using gold complex **3** provided poor substrate conversion and low selectivity for the desired cross-coupling product (**29**) (Table 16, Entry 1).

*Table 16. Optimisation of the oxidative coupling of **26** and **27** using gold complex **3**.*

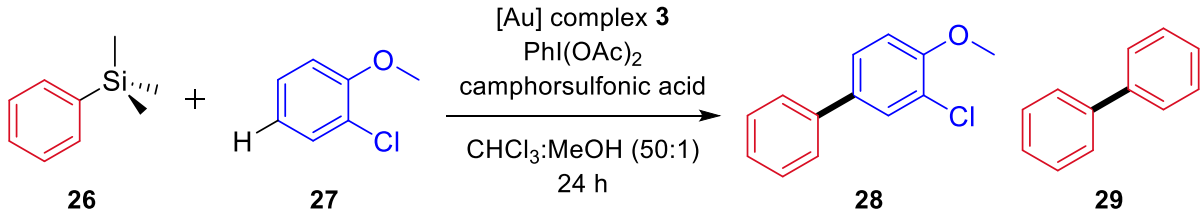

	Conditions			Yield (%)[a]	
Entry	Catalyst loading	Additive	Temperature (°C)	**28**	**29**
1[b]	1 mol%		r.t.	15	18
2	2 mol%		r.t.	20	25
3	1 mol%		60 °C[c]	40	25
4	1 mol%	$AgSbF_6$ (6 mol%)	60 °C[c]	45	28

[a] Yields determined by HPLC with reference to 1,4-dinitrobenzene as an internal standard. [b] Entry 1 are the literature conditions.[28] [c] Increasing the temperature resulted in ~20% drop in arene mass balance, presumably due to arene homocoupling/over-arylation.

Increasing the catalyst loading provided a small increase in yield, but also resulted in reduced selectivity for **28** (Table 16, Entry 2). Increasing the temperature of the reaction provided improved conversion to cross-coupling product **28** (Table 16, Entry 3), however a concomitant 20% drop in arene (**27**) mass balance and formation of a new peak in the HPLC chromatogram was observed – presumably the result of either arene homocoupling or a second arylation of **28**. The presence of an unidentified arene side product under these conditions (Table 16, Entries 3 and 4) was also confirmed by the presence of a new methoxy environment in the crude ^{1}H NMR spectrum. Attempts at isolating and quantifying any arene side product(s) were unsuccessful. The addition of a silver salt resulted in a small increase in the yields of both **28** and **29** (Table 16, Entry 4). As a result of the poor yield and selectivity encountered thus far, a Design of Experiments (DoE) approach was employed to optimise

the reactions conditions. DoE is well-established as a tool for modelling industrial processes,[55,56] and is more recently becoming a feature of academic research.[57–59] DoE-based optimisation provides a few key advantages over traditional 'one factor at a time' optimisation,[60] namely it reveals: a) which variables have an effect on the reaction outcome, b) which variables, if any, interact in their effect on the reaction outcome, c) which variables, if any, have a non-linear effect on the reaction outcome. These advantages make DoE particularly well-suited to systems with selectivity challenges, since the likelihood that the reaction variables will have non-linear or interacting effects on the reaction outcome is increased when each variable is influencing multiple mechanistic pathways. The variables included in the DoE optimisation are summarised in Table 17, and were chosen based on the initial optimisation results (Table 16).

*Table 17. Reaction variables included in the DoE optimisation of the oxidative coupling of **26** and **27**.*

Variable	Minimum	Maximum
Catalyst loading (mol%)	1	3
Silver salt loading (mol%)	0	6
Temperature (°C)	30[a]	60
Concentration (M)	0.1	0.25
Arene equivalents	1	1.5

[a)] A lower temperature limit of 30 °C was set to avoid overnight changes in ambient temperature.

A number of DoE model choices exist which are appropriate for different variable types, e.g. categorical or continuous, and provide increasing details, e.g. interacting/non-linear effects, at a cost of increasing the number of required experiments.[61] A definitive screening design (DSD) was chosen for the optimisation of the oxidative coupling of **26** and **27**, since DSDs will reveal second order and interacting variable effects for five continuous variables (Table 17) using a relatively small number of experiments.

The results of the DoE screen are summarised in Figure 22 and Figure 23, and Table 18 and Table 19. The plot in Figure 22 illustrates that the DoE model provided an accurate prediction of the experimental results. The reaction was found to be reasonably reproducible (±3-5%) during initial optimisation experiments given that stock solutions were not used for the catalyst, sacrificial oxidant and camphorsulfonic acid, and instead these compounds were weighed as powders for each individual reaction. This is reflected in the good predictive power and root-mean-square-error of the model. Additional experiments to validate the predictive power of the model were also performed (*vide infra* Table 19).

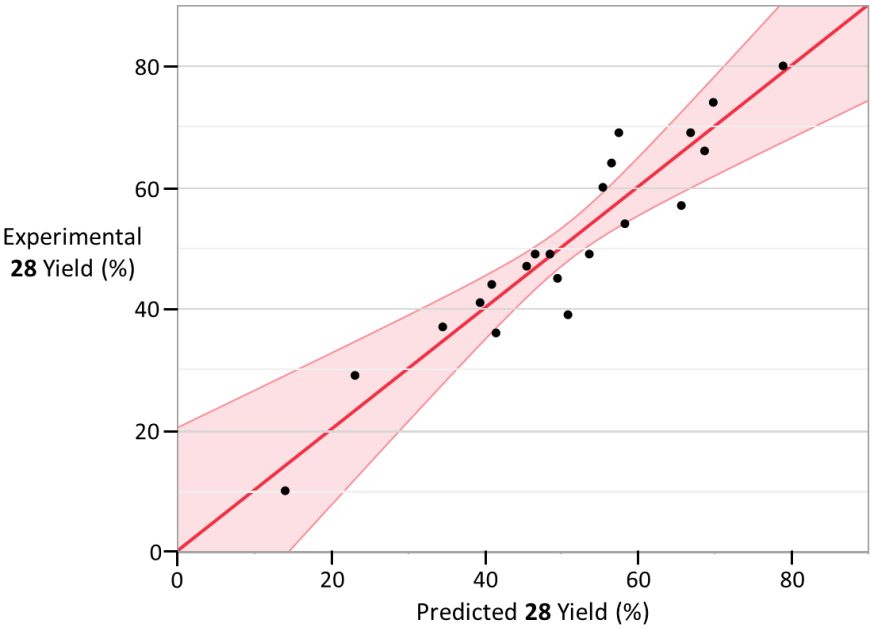

*Figure 22. Definitive screening design predictive model for the oxidative cross-coupling yielding **28** – Actual vs predicted cross-coupling yield. Root-mean-square error = 6.6664; R^2 = 0.89.*

The DoE screen revealed that arene equivalents had the most significant influence on the outcome of the reaction (Table 18, Entry 1), with an excess (1.5 equiv.) providing the best performance (Figure 23b).

*Table 18. Definitive screening design predictive model for the oxidative cross-coupling yielding **28** – The reaction variables included in the model and their relative importance ('LogWorth' depicted numerically and visually).*

Entry	Variable	LogWorth[a]
1	Arene equivalents (1,2)	6.078
2	Concentration*Temperature	2.817
3	Concentration (0.1,0.25)	2.238
4	Arene equivalents*Temperature	1.664
5	Silver salt loading*Temperature	1.652
6	Concentration*Concentration	1.160

[a)] LogWorth = –log(P), represents truncated p values which statistically quantifies the relative significance of a given variable.

The influence of temperature was found to interact with the concentration of the reaction, the arene equivalents and the silver loading (Table 18, Entries 2, 4 and 5) – higher temperatures provided better

performance at lower arene equivalents and lower concentration (Figure 23a), whilst increased arene equivalents and concentration performed better at lower temperatures (Figure 23b). As a result, the lowest temperature (30 °C) was present in both the best and worst sets of conditions (Figure 23a and Figure 23b). This change in temperature influence at different arene equivalents and concentrations likely reflects the complex interplay of influence that these variables have on the reaction pathways yielding **28** and possible side products, e.g. arene/aryl silane homocoupling or double arylation. Indeed, when the set of reaction conditions that were predicted to perform the best (1.5 arene equiv., 0.23 M concentration, 6 mol% $AgSbF_6$, Figure 23b) were conducted at 60 °C, a 35% loss of arene mass balance was observed alongside significant quantities of methoxy-containing side-products in the ^1H NMR. Conversely, at 30 °C only a 5% loss in arene mass balance was observed. Finally, the catalyst loading was not found to have any significant influence on the outcome of the reaction, which may have been the result of a superfluous reaction time (24 h) masking any kinetic differences in catalyst performance at different catalyst loadings.

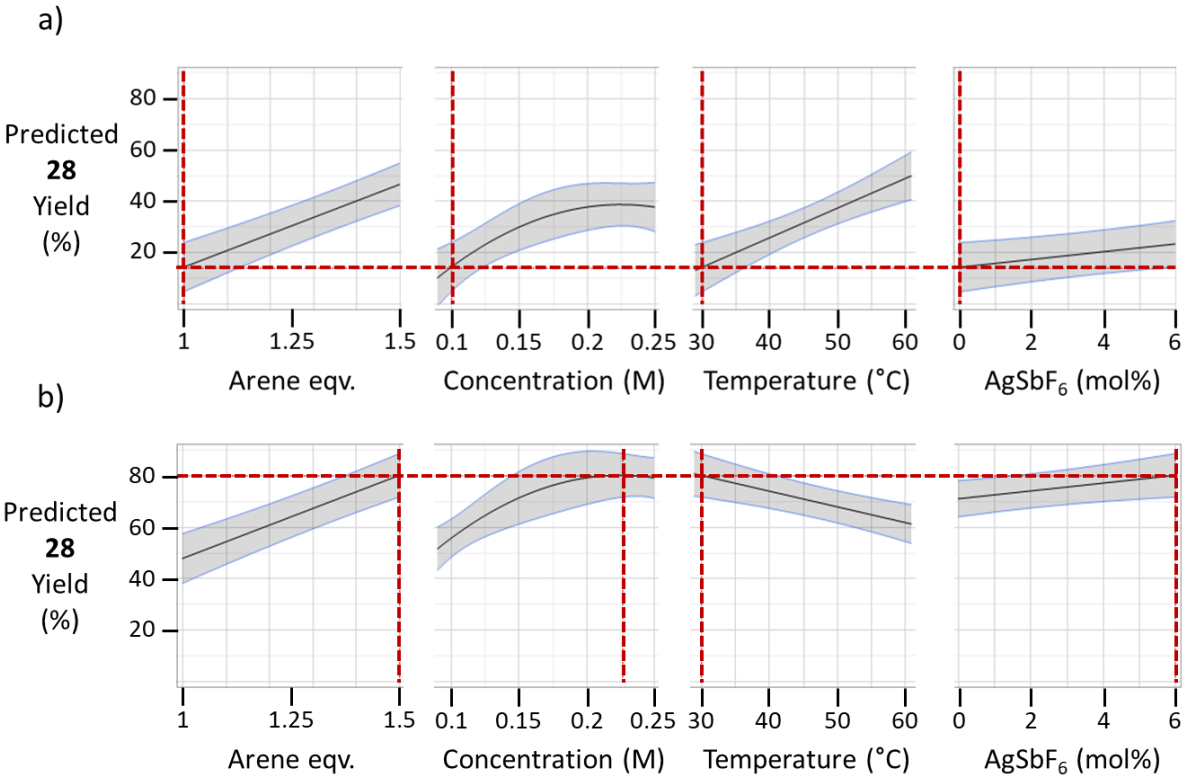

*Figure 23. Definitive screening design predictive model for the oxidative cross-coupling yielding **28** – Variable profiles for the conditions predicted to provide: a) The lowest yield of **28**, b) The highest yield of **28**.*

Additional validation of the predictive power of the model was provided by performing reactions at the conditions predicted to provide both the best (Figure 23b and Table 19, Entry 1) and lowest yields

of **28** (Figure 23a and Table 19, Entry 2). Good agreement between the experimental and predicted yields was obtained (Table 19).

*Table 19. Definitive screening design predictive model validation – Comparison of the experimental and predicted yields for the conditions modelled to provide the best (Entry 1) and lowest (Entry 2) yields of **28**.*

	Conditions[a]				Yield **27** (%)[b]	
Entry	Concentration (M)	Arene equiv.	Additive (mol%)	Temperature (°C)	Experimental	Predicted
1[c]	0.23	1.5	$AgSbF_6$ (6)	30	78	81
2[d]	0.1	1	$AgSbF_6$ (0)	30	19	14

[a)] All reactions were run at 1 mol% catalyst loading. [b)] Yields determined by HPLC with reference to 1,4-dinitrobenzene as an internal standard.

With optimised conditions in hand, the substrate scope of the oxidative cross-coupling of arenes and aryl silanes was explored next. The addition of 6 mol% of $AgSbF_6$ was not included when exploring the substrate scope since the small predicted increase in the yield of **27** provided by $AgSbF_6$ was within the margin of error of the models predictive power. No difference in catalyst performance was observed for the model coupling catalysed by either trihalide complexes **3**-**4** and tetrafluoroborate complexes **5**-**6**. As a result, only complexes **3** and **4** were utilised in the substrate scope. A broad range of substrates were successfully coupled (Table 20).

*Table 20. Oxidative cross-coupling of aryl silanes and arenes catalysed by recovered complexes **3** and **4**.[a]*

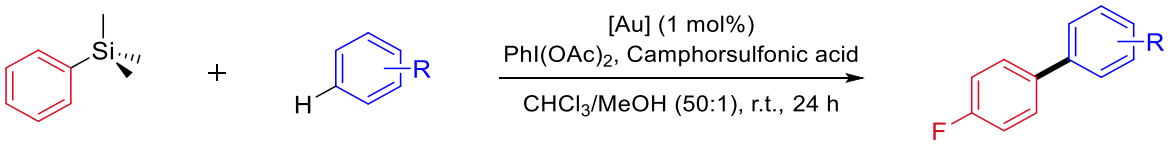

Entry	Product	Yield (%)[b] **3**	**4**	[Ph$_3$PAu]OTs[c] (Literature)[28]
1	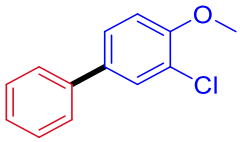	70 ± 4 72[g]	75 ± 3	85
2	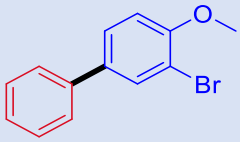	74 ± 5	80 ± 3	92
3	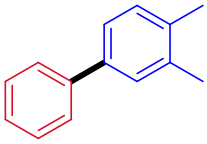	61 ± 5[d]	70 ± 7[d]	82[e]
4	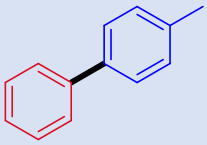	59 ± 4[d]	65 ± 5[d]	93[f]
5	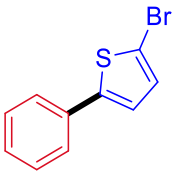	85 ± 3	90 ± 2	67 ± 1
6	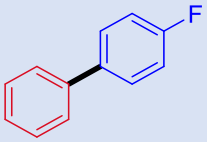	0	0	0

[a)] Reactions were performed under the optimised conditions obtained from the DoE model – [aryl silane] = 0.23 M, [Au] = 1 mol%, 1.5 equivalents arene, r.t. [b)] Yields provided by **3** and **4** are isolated yields following flash column chromatography and are the average of two experiments. [c)] Yields provided by [Ph$_3$PAu]OTs are taken from the literature,[28] with the reactions run for 30 h. [d)] Product was isolated as a single regioisomer. [e)] 6.6:1.0 ratio of *meta*/*ortho* isomers. [f)] 4.1:1 ratio of *para*/*ortho* isomers. [g] Catalysed by gold complex **3a** derived from scrap SIM cards.

Identical reactivity patterns were provided by complexes **3** and **4** as was reported in the literature for [Ph$_3$PAu]OTs,[28] with more electron-rich arenes (Table 20, Entries 1,2 and 5) being more reactive than less electron-rich arenes (Table 20, Entries 3 and 4). An electron-deficient arene was unreactive under

the conditions investigated (Table 20, Entry 6). In general, comparable but slightly lower yields were provided by complexes **3** and **4** when compared to [Ph_3PAu]OTs. Some improvements however were found in the regioselectivity of the products from the less electron-rich arenes (Table 20, Entries 3 and 4). These differences in yield and selectivity between [Ph_3PAu]OTs and **3**/**4** implies that Me_2dazdt in precatalyst **3**/**4** plays a role in the outcome of the reaction.[29] Since Me_2dazdt is not readily oxidised during a precatalyst activation step, as was the case for triphenylphosphine in [Ph_3PAu]OTs (Scheme 51), Me_2dazdt may remain coordinated to the active gold species formed from **3**/**4** and influence the reaction outcome.

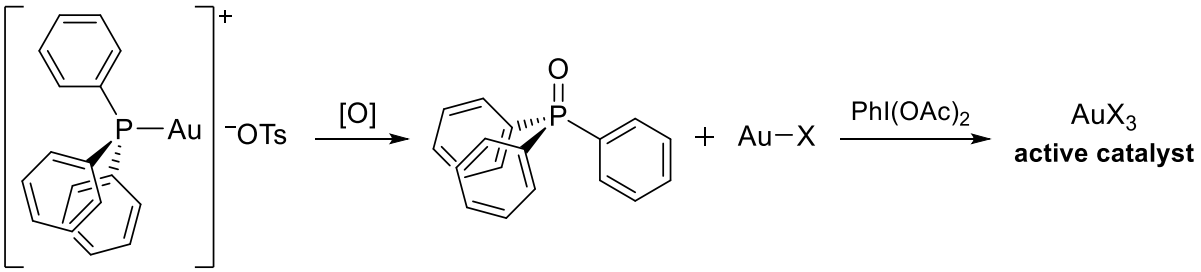

Scheme 51. [Ph_3PAu]OTs precatalyst activation reported by Russell and Lloyd-Jones.[29]

Kinetic and mechanistic work exploring the active catalyst species formed from **3**/**4** and the presence, if any, of an induction period was not within the scope or timeframe of this study.

2.2.7. Gold catalysis – Catalyst recovery and reuse

Gold complexes **3**-**6** are insoluble in non-coordinating and non-polar organic solvents, e.g. ethanol, diethyl ether, chloroform, dichloromethane, hexane, etc. A striking manifestation of this was uncovered during the activation of acetylacetone (**24**, Table 14) – complexes **3**-**6** are insoluble in neat ethanol, but dissolve upon the addition of the two substrates, presumably due to formation of a soluble gold intermediate. At the end of the reaction, a black precipitate formed. Analytical data gathered for this precipitate was consistent with the reformation of gold complexes **3**-**6**. Since gold complexes **3**-**6** were reforming at the end of the reaction, they could be isolated by concentration of the reaction mixture and trituration of the residue with hexane. The organic reaction content was then isolated from hexane, whilst the triturated black solid, effectively free from any reagent contamination (according to ^{1}H NMR analysis), could be reused as a homogeneous catalyst. When this process was performed to recover complexes **3**-**6** following the addition of **25** to **24**, no discernible loss in catalytic activity was observed, even after eight reuse cycles (Figure 24).

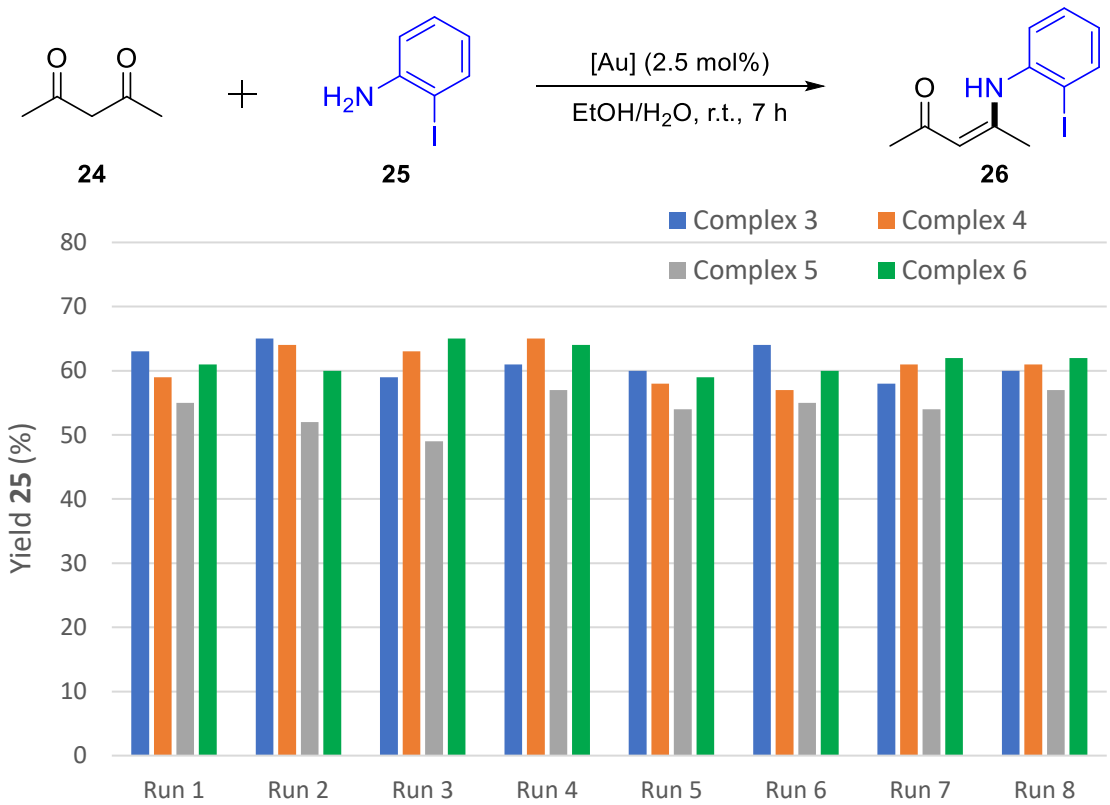

*Figure 24. Recovery and reuse of gold complexes **3**-**6** in the addition of 2-iodoaniline to acetylacetone.*

Since gold complexes **3**-**6** are insoluble in many non-coordinating and non-polar organic solvents, this recycling approach could feasibly be applied to a range of transformations and substrates with differing solubilities in organic solvents. The strategy was consequently expanded to the addition of 2-methylfuran to methyl vinyl ketone (Figure 25). Since there was no observed difference in the reusability of complexes **3**-**6** for the activation of acetylacetone (**24**), only the reusability of complex **3** was explored. Gold complex **3** was recovered and reused eight times with no discernible loss in catalytic activity. After the eighth cycle the catalyst material was recovered and analysed by ^{1}H NMR, which revealed the retention of the ligand environment and C_2 centre of symmetry, indicating that the catalyst material was reformed as **3** at the end of each cycle.

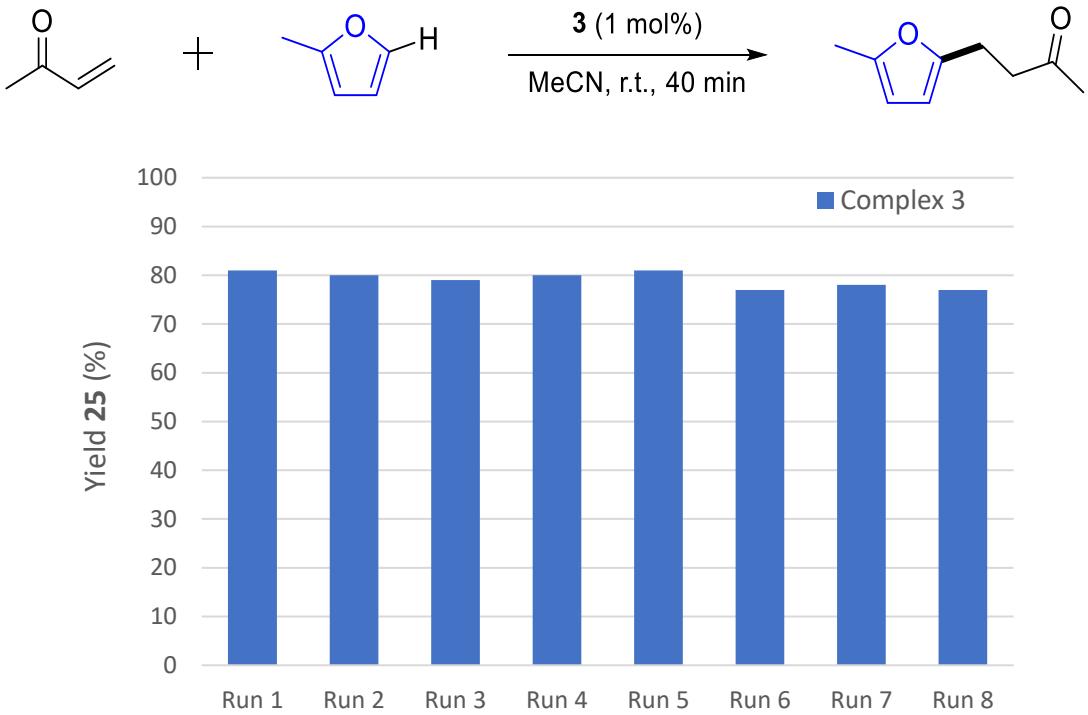

*Figure 25. Recovery and reuse of gold complex **3** in the addition of 2-methlyfuran to methyl vinyl ketone.*

The reusability of complex **3** was also explored for the cyclisation of *N*-propargylbenzamide (**15**) (Figure 26).

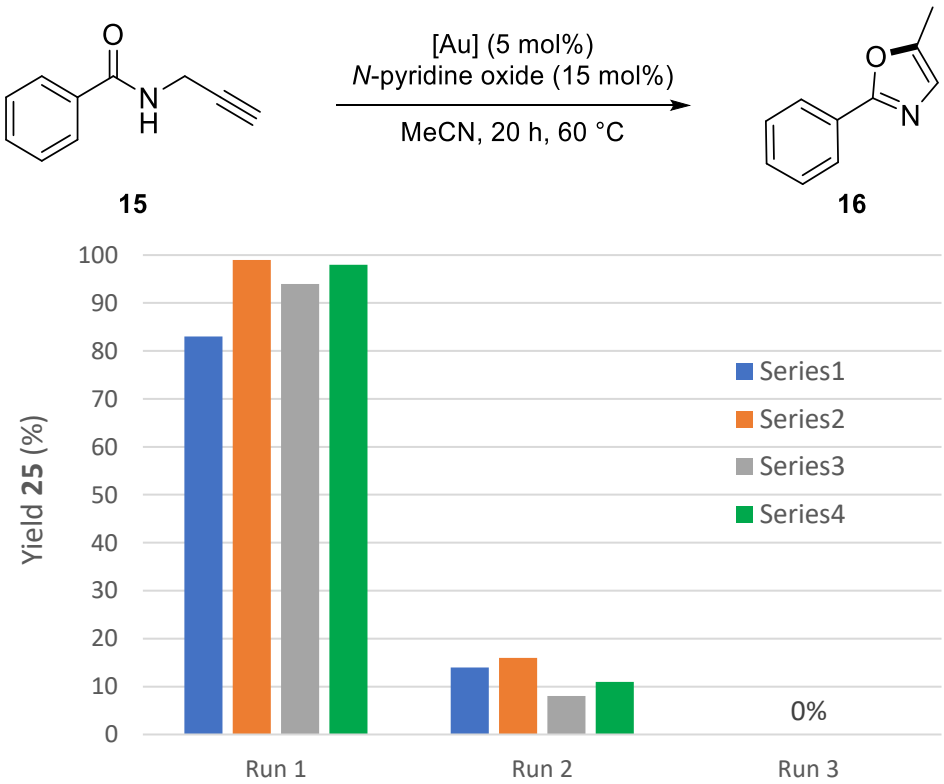

*Figure 26. Recovery and reuse of gold complexes **3**-**6** in the cyclisation of N-propargylbenzamide.*

Unfortunately, complete loss of catalytic activity was observed after the second run. A number of different trituration solvents were explored (diethyl ether, pentane, chloroform), however in each case the recovered gold material was significantly less catalytically active after the first run. Complexes **4**-**6** were also explored, however similarly poor performance was observed after the first run (Figure 26).

2.2.8. Gold catalysis – Mechanistic analysis

Many gold(I) precatalysts are neutral and coordinatively saturated compounds, which are then activated either *ex situ* or *in situ* by generating a vacant coordination site e.g. with a silver salt or a labile ligand (Scheme 52a). Gold(III) catalysts are typically coordinatively unsaturated and contain a vacant coordination site, e.g. $AuCl_3$, either innately or through dissociation of a labile ligand from a precatalyst (Scheme 52a), or can also be activated by the addition of a silver salt as for gold(I) catalysts in order to irreversibly abstract a halide.

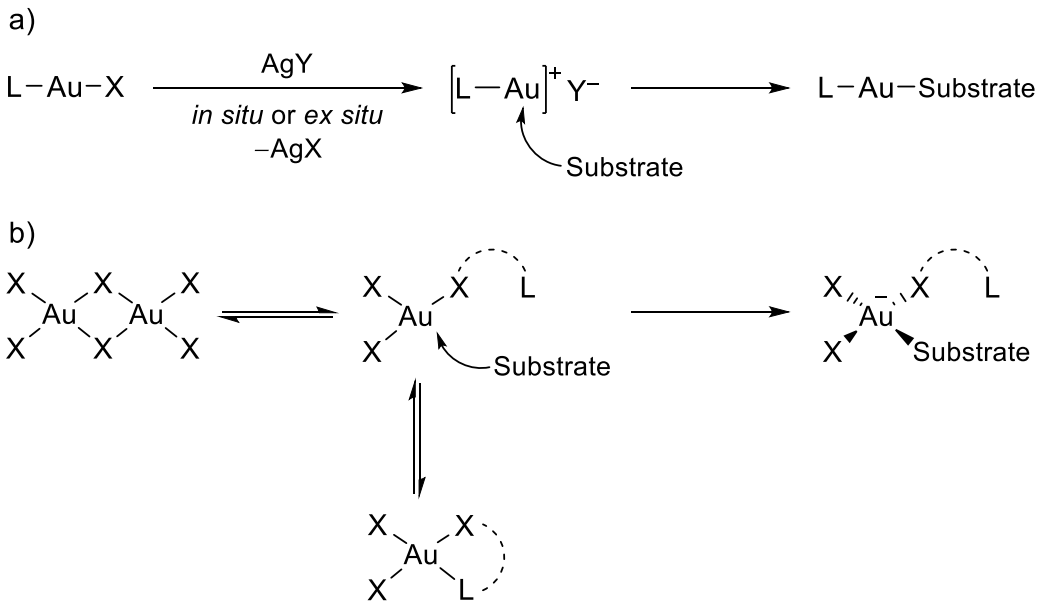

Scheme 52. Some typical mechanistic pathways seen for literature gold(I) and gold(III) catalysts.

Gold complexes **3**-**6** however are cationic, square planar, and coordinatively-saturated by tightly bound halides and a chelating sulfur ligand, and act as effective catalysts without the addition of a silver salt. Thus, a vacant coordination site must be generated either by dissociation of a halide (Scheme 53a), a sulfur atom (Scheme 53c), or a switch to a trigonal bipyramidal geometry (Scheme 53b).

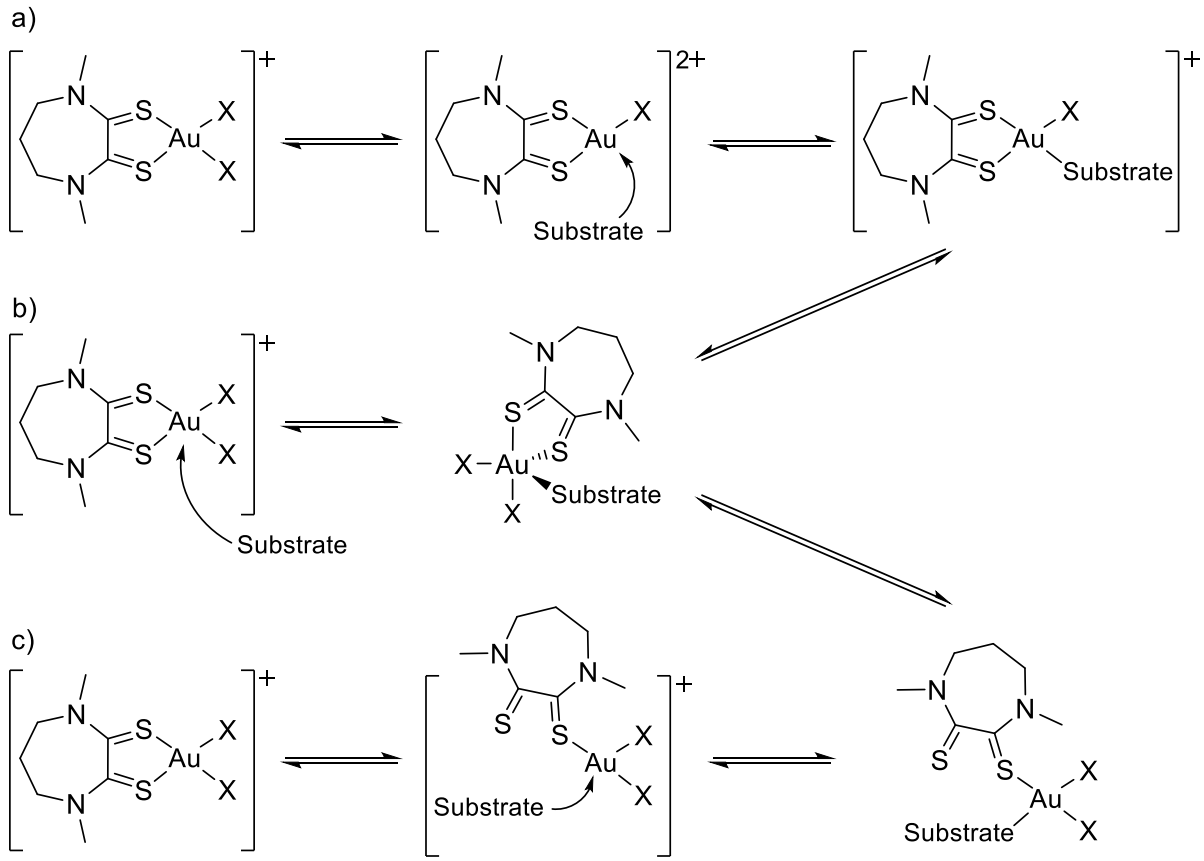

*Scheme 53. Possible mechanistic pathways to enable substrate binding by generating a vacant coordination site in complexes **3**-**6**.*

The trigonal bipyramidal intermediate may also be an intermediate in the formation of either halide (Scheme 53a) or sulfur (Scheme 53c) dissociated gold intermediates. To distinguish between the possible pathways, the stoichiometric reactions of gold complexes **3**-**6** with a few substrates were performed in an attempt to isolate and structurally characterise a gold intermediate. Vinyl gold intermediates from the cyclisation of *N*-propargylbenzamide have already been synthesised by Hashmi *et al*. and their synthesis were thus explored first.[16] Unfortunately, attempts at isolating a vinyl gold intermediate from complexes **3**-**6** by replicating the literature conditions were unsuccessful.[16] When each of complexes **4**-**6** was treated with stoichiometric *N*-propargylbenzamide and triethylamine as a proton scavenger to prevent protodeauration, conversion of **15** to a mixture of organic products was observed by ^{1}H NMR analysis (Scheme 54), and no vinyl gold species was isolated.

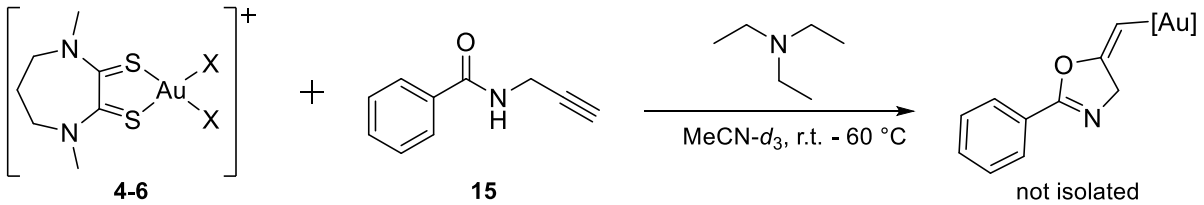

*Scheme 54. Unsuccessful attempt at employing a base to trap a vinyl gold intermediate from complexes **4-6** (trihalide/tetrafluoroborate anions omitted for **4-6**).*

Although no new vinyl gold intermediates were isolated using Hashmi's procedure (Scheme 54), a new gold(I) complex (**30**) was isolated from **3** (Scheme 55).

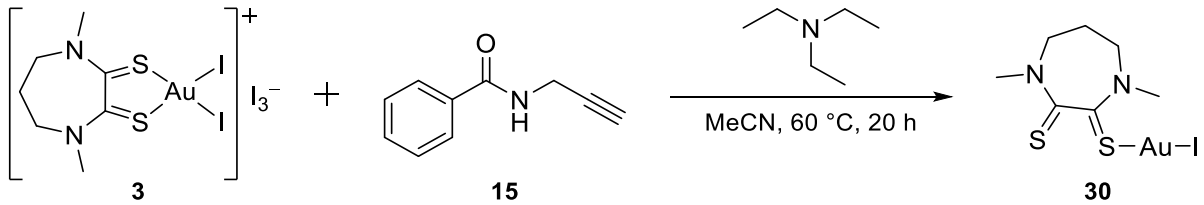

*Scheme 55. Synthesis of gold(I) complex **30** during an unsuccessful attempt at trapping a vinyl gold intermediate from complex **3**.*

Single crystals of **30** were grown and characterised by single crystal X-ray diffraction (Figure 27).

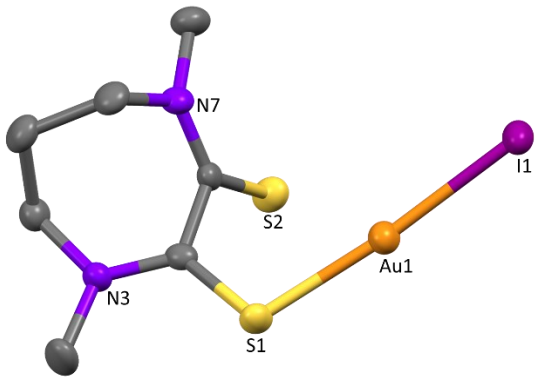

*Figure 27. Single-crystal X-ray structure of gold(I) complex **30** (thermal ellipsoids drawn at 50% probability).*

For each of **3**-**6**, the addition of triethylamine resulted in an immediate colour change from dark purple/black to yellow even in the absence of **15**, possibly due to undesired reactivity of triethylamine with the gold centre in **3**-**6**. The base 2,6-di-^{t}Bu-pyridine was consequently explored as bulkier and thus more selective proton scavenger. A striking colour change from dark-purple/black to either dark green or bright blue was observed for iodide complexes **3** and **5**, respectively, alongside the clean

transformation of **15** to a substituted vinyl oxazoline (Scheme 56). ^{1}H NMR data for the reaction of complexes **3** and **5** with **15** were identical.

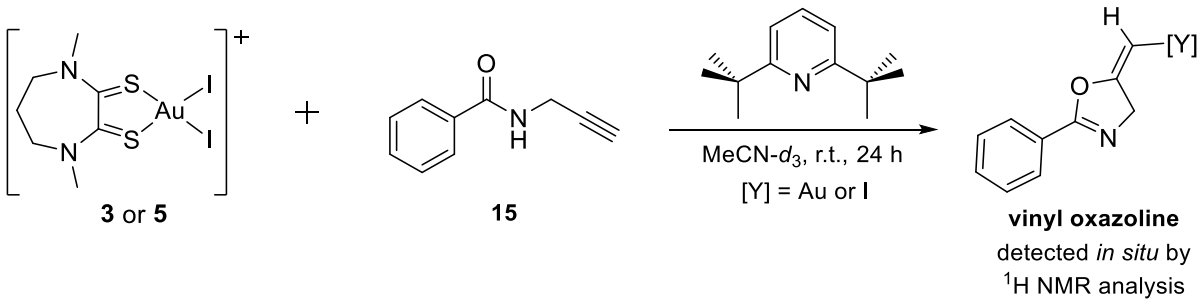

*Scheme 56. Formation of a vinyl gold intermediate from the reaction of complexes **3** and **5** (anions omitted) with **15** in the presence of 2,6-di-^{t}Bu-pyridine.*

The formation of 2,6-di-^{t}Bu-pyridinium was confirmed by the presence of a pyridinium N^{+}–H triplet ($^{1}J_{HN}$ = 59 Hz) at 11.14 ppm in the ^{1}H NMR spectrum which collapsed to a singlet upon ^{14}N decoupling (Figure 28). Heating a solution of 2,6-di-^{t}Bu-pyridine and **15** in acetonitrile-d_3 did not result in any conversion of **15** or the formation of 2,6-di-^{t}Bu-pyridinium, which confirmed the necessity of the gold centre for the transformation of **15** to the vinyl oxazoline and the formation of 2,6-di-^{t}Bu-pyridinium.

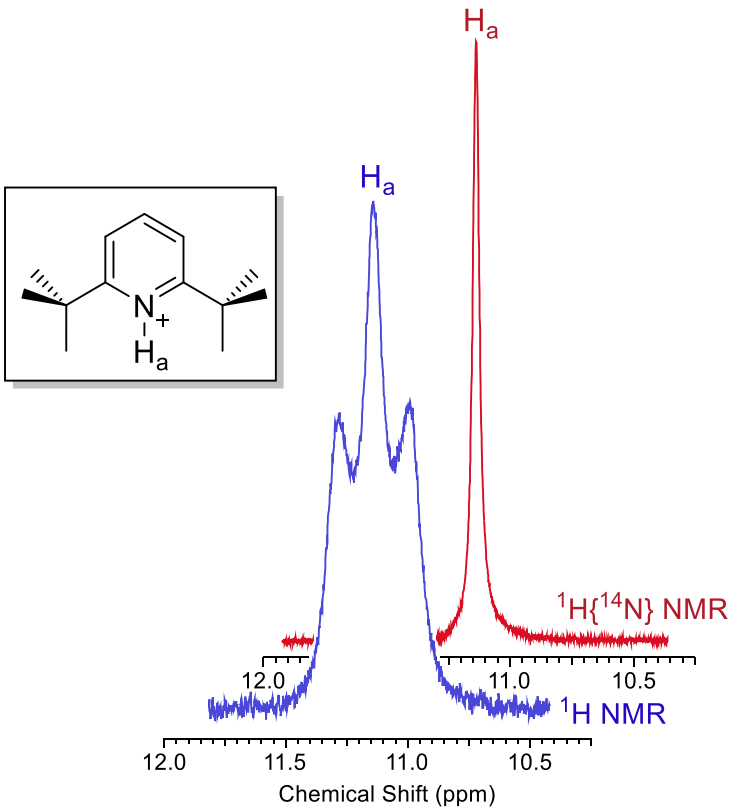

Figure 28. 2,6-di-^{t}Bu-pyridinium ^{1}H (blue, bottom) and ^{1}H{^{14}N} (red, top) decoupled NMR spectra.

^{1}H NMR analysis also confirmed the formation of a substituted vinyl oxazoline by the concomitant presence of a vinylic triplet proton (δ = 5.85 ppm, $^4J_{HH}$ = 3 Hz) and a methylene doublet with an associated allylic coupling constant (δ = 4.61 ppm, $^4J_{HH}$ = 3 Hz). Diagnostic ^{1}H NMR features for either oxazole **16** or oxazoline **31** were absent from the ^{1}H NMR spectrum of the vinyl oxazoline (Figure 29). Whilst these NMR features are consistent with the formation of a substituted vinyl oxazoline, it was not possible to distinguish between either vinyl gold (**32**) or vinyl iodide (**33**) oxazolines by NMR analysis of the crude reaction mixture. The alkene stereochemistry of this vinyl oxazoline was not determined, but was assumed to be the *E*-alkene based on similar cyclisation reports using either 'I$^+$' sources or gold catalysts, which all yielded *E*-oxazolines .[14,15,52–54]

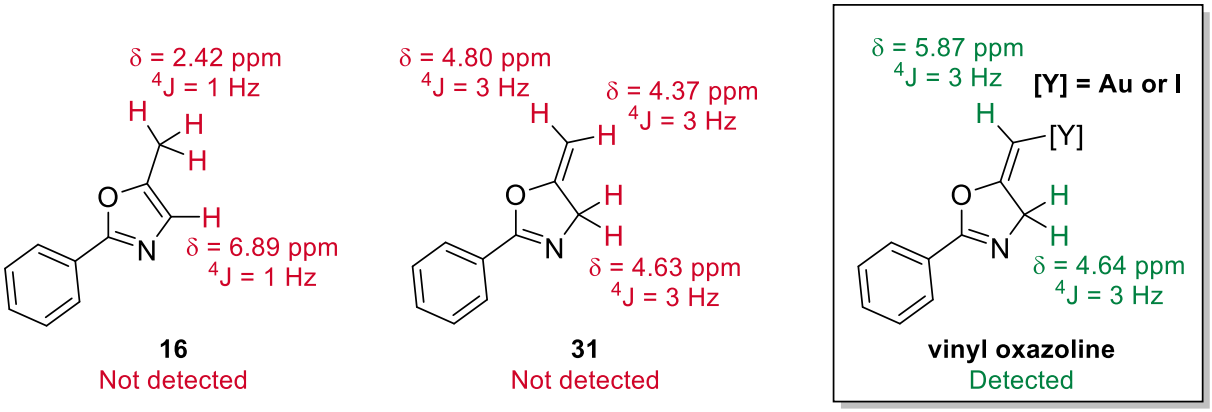

*Figure 29. Possible products and associated ^{1}H NMR data from the stoichiometric reaction of complexes **3**-**6** with **15** in the presence of 2,6-di-^{t}Bu-pyridine.*

A chemical approach was consequently employed to determine the vinyl substituent, since vinyl gold **32** would protodeaurate under acidic conditions to yield oxazole **16** (Scheme 57, [Y] = [Au]), whilst vinyl iodide **33** would remain intact (Scheme 57, [Y] = I). Treating the crude reaction mixture with ten equivalents of acetic acid yielded an identical ^{1}H NMR spectrum (Scheme 57), even after the addition of *N*-pyridine oxide and heating to 60 °C. This confirmed the formation of a vinyl iodide oxazoline and not a desired vinyl gold compound, possibly proceeding mechanistically via the reductive elimination of a vinyl gold species with iodide. Such a reductive elimination is also consistent with the formation of gold(I) complex **30** (Scheme 55).

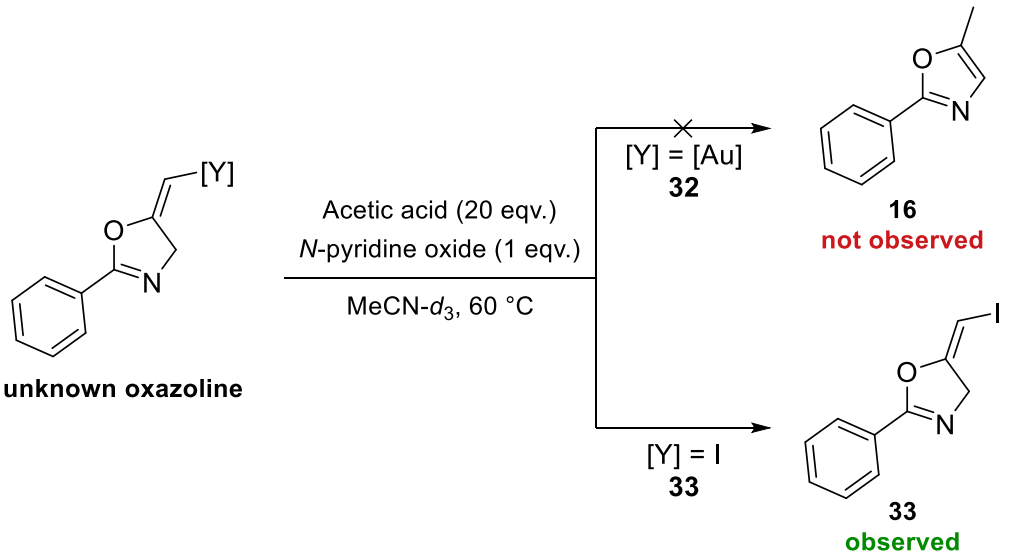

*Scheme 57. Chemical distinction between either possible vinyl gold (**32**) and vinyl iodide (**33**) oxazolines by reaction with acetic acid.*

A similar strategy was applied for the addition of 2-methylfuran to methyl vinyl ketone – the standard reaction conditions were replicated in the presence of either triethylamine or 2,6-di-^{t}butyl pyridine (Scheme 58). Unfortunately, the presence of a proton scavenger did not prevent the formation of the addition product (**34**), and no vinyl gold intermediates were isolated (Scheme 58).

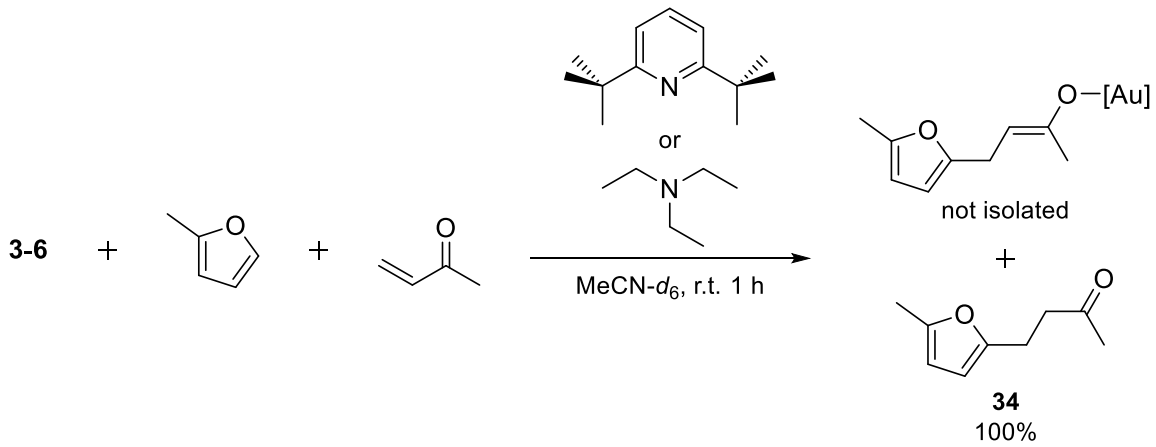

*Scheme 58. Unsuccessful attempt at employing a proton sponge to trap a vinyl gold intermediate from complexes **3**-**6**.*

No additional attempts were made to isolate a vinyl gold intermediate.

For the activation of alkyne π bonds, gold complexes **3**-**6** were either unsuccessful, e.g. in the cyclisation of 2-phenylethynyline (**22**) (Table 13), or required additives and more forcing conditions to achieve activity that is comparable to benchmark and literature gold(I) complexes, e.g. in the

cyclisation of *N*-propargylamides (Table 11 and Table 12). For the activation of carbonyl compounds however, gold complexes **3**-**6** performed as well as, or in some cases better than, benchmark and literature catalysts. This behaviour suggests that complexes **3**-**6** have pronounced oxophilic Lewis acidity, which is in contrast to the softer carbophilic Lewis acidity of gold(I) complexes. One tool that experimentally quantifies the relative oxophilicity of Lewis acids is the Gutmann-Beckett method,[62–64] and the technique has been used to demonstrate the oxophilicity of cationic gold(III) complexes.[7,65–67] The Gutmann-Beckett method measures oxophilicity through the ^{31}P NMR chemical shift of a phosphine oxide upon binding to a Lewis acid (Scheme 59). A more oxophilic Lewis acid will generate a more polarised phosphine oxide bond and thus yield a phosphorous centre with a more deshielded ^{31}P chemical shift.

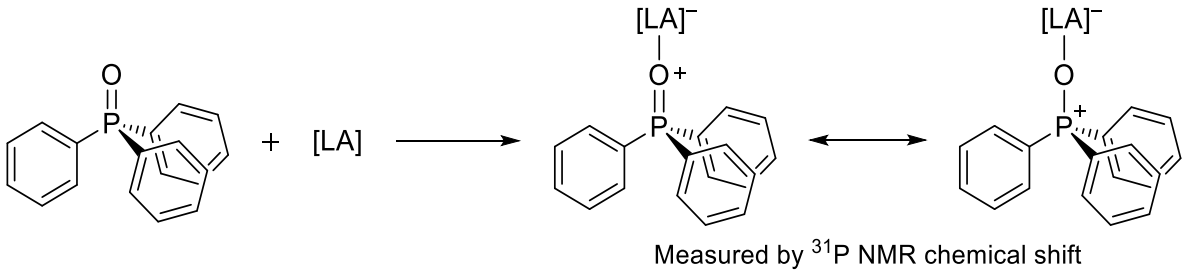

Scheme 59. The Gutmann-Beckett method for quantifying Lewis acid oxophilicity ([LA] = Lewis Acid).

Gutmann-Beckett analysis was consequently performed to probe the oxophilicity of complexes **3**-**6**, and to compare with literature data for other cationic gold(III) complexes. When complexes **3**-**6** were added to a solution of either one or five equivalents of triphenylphosphine oxide in acetonitrile-d_3, no new ^{31}P NMR environments were observed (Table 21, Entry 2), even upon heating to 60 °C. When the procedure was replicated for complexes **5**/**6** in the presence of $AgSbF_6$, a new ^{31}P NMR environment was observed (Table 21, Entry 3). No differences in ^{31}P Δδ between the trihalide complexes and their tetrafluoroborate analogues were observed (i.e. **3** vs **5** and **4** vs **6**). Bromide complex **6** did exhibit slightly increased oxophilicity when compared to iodide complex **5**.

*Table 21. Gutmann-Beckett analysis of gold complexes **3-6** with triphenylphosphine oxide in MeCN-d₃.*

Entry	Conditions[a]	^{31}P NMR Shift (ppm)	Δδ (ppm)
1	Triphenylphosphine oxide	26.1	-
2	Triphenylphosphine oxide[b] + **3-6**	26.2	-
3	Triphenylphosphine oxide + **5** + $AgSbF_6$	36.7	10.6
4	Triphenylphosphine oxide + **6** + $AgSbF_6$	38.5	12.4

[a] Reactions were performed in MeCN-d_3. [b] Identical results were obtained for either 1 or 5 equivalents of triphenylphosphine oxide.

The ^{31}P Δδ values obtained for formally doubly cationic **5-6** (Figure 30a) are consistent with those obtained by Glorius *et al* for their formally doubly cationic gold(III) complexes (Figure 30b),[66] and are larger than those obtained by Toste and co-workers' formally monocationic gold(III) complex (Figure 30c).[67] The values obtained for complexes **5-6** are also considerably larger than have been obtained for a gold(I) complex (Figure 30d).[67]

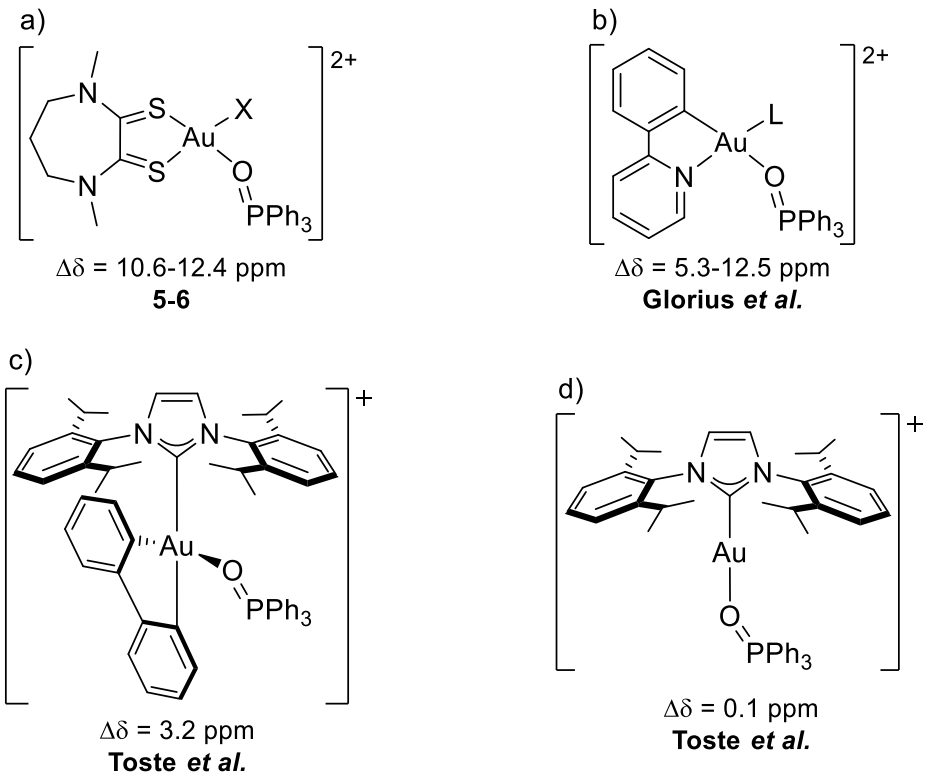

*Figure 30. Comparison of the ^{31}P Δδ values obtained for complexes **3-6** (a) with literature gold(III) (b and c) and gold(I) (d) complexes.[66,67]*

It should be noted that some care should be taken when comparing the literature Δδ values, which were obtained in CD_2Cl_2, with those obtained for **5**-**6** in acetone-d_6, since residual water present in acetone-d_6 can influence the chemical shift of triphenylphosphine oxide. Future work could attempt to replicate the Gutmann-Becket analysis of $[Ph_3P\text{->}AuIPr]^+$ (Figure 30d), whose precursor is commercially available, in acetone-d_6 to better understand the influence of the solvent choice on Δδ.

Gutmann-Beckett analysis of complexes **3**-**5** with triphenylphosphine oxide was also performed in acetone-d_6. As was seen during the anion metathesis of **3** and **4**, dissolution of complexes **3**-**6** in acetone-d_6 resulted in a colour change from dark black to pale yellow (see section 2.2.2, Scheme 44). For trihalide complexes **3** and **4**, no new ^{31}P NMR environments were observed (Table 22, Entry 2). Tetrafluoroborate complex **5** however yielded a new ^{31}P NMR environment at 33.5 ppm (Table 22, Entry 3), with a ^{31}P Δδ of 8.9 ppm when compared to free triphenylphosphine oxide.

*Table 22. Gutmann-Beckett analysis of gold complexes **3**-**6** with triphenylphosphine oxide in acetone-d_6.*

Entry	Conditions[a]	^{31}P NMR Shift (ppm)
1	Triphenylphosphine oxide	24.6
2	Triphenylphosphine oxide[b] + **3**/**4**	24.5, 25.1
3	Triphenylphosphine oxide + **5**	33.5, 43.9

[a)] Reactions were performed in acetone-d_6. [b)] Identical results were obtained for either 1 or 5 equivalents of triphenylphosphine oxide.

In addition to the expected singlets for a $Ph_3P\text{->}[Au]$ complex (33.5 ppm, Table 22, Entry 3), an additional phosphorous containing species was also observed: A ^{31}P quartet was observed at 43.9 ppm, and the observed coupling constant (J = 7.2 Hz) was also present in a doublet in the ^{19}F NMR at –142.9 ppm. This coupling was unambiguously confirmed as $^3J_{PF}$ by both 2D ^{31}P-^{19}F HSQC and $^{31}P\{^{19}F\}$ NMR analysis. This ^{19}F NMR doublet (–142.9 ppm) was also further split into two environments with a characteristic $^{10}B/^{11}B$ isotope ratio. All of this NMR data is consistent with the hydrolysis of tetrafluoroborate in **5**, resulting in the formation of $Ph_3P{=}O{\cdot}BF_3$ (**35**) (Scheme 60). A new ^{19}F singlet with characteristic $^{10}B/^{11}B$ splitting was also observed at –150.0 ppm, which is consistent with the formation of tetrafluoroborate hydrolysis product $HO{\cdot}BF_3$ (**36**) (Scheme 60). A final new ^{19}F NMR singlet was observed at –186.8 ppm, a chemical shift which is consistent with those reported in the literature for numerous gold(III)-fluoride complexes and thus the formation of gold(III)-monofluoride **37** (Scheme 60).[68–70] The NMR data obtained for the two proposed hydrolysis products (**35** and **36**) are consistent with literature data.[71–73]

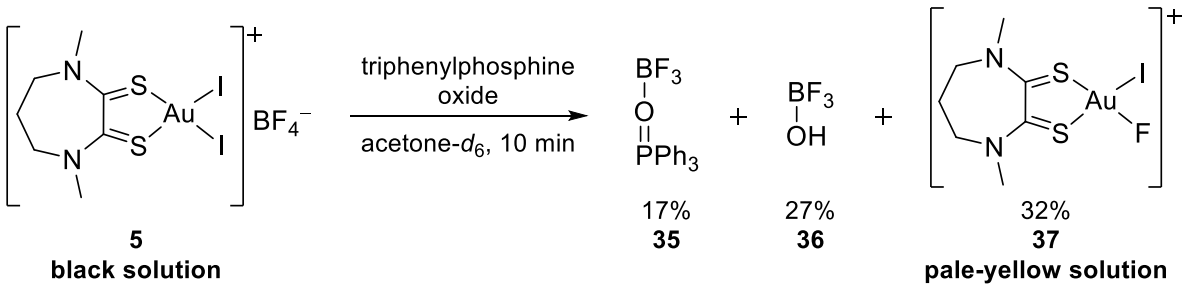

Scheme 60. Hydrolysis of tetrafluoroborate in acetone-d_6 and resulting hydrolysis products. Yields are approximate values determined by relative integration of the ^{19}F NMR environments. The remaining 24% ^{19}F was unconverted tetrafluoroborate

The formation of **36** and **37** and the concomitant colour change was also observed in the absence of triphenylphosphine oxide. No hydrolysis of sodium tetrafluoroborate was observed in acetone-d_6, even upon heating in the presence triphenylphosphine oxide. This gold-promoted hydrolysis of tetrafluoroborate is especially striking considering that the anion is typically considered to be inert, with research in 2023 illustrating that tetrafluoroborate solvolysis in methanol took >12 h even under strongly acidic conditions (pH <1).[74] Furthermore, the SbF_6^- anion in complex **11** was similarly hydrolysed, as monitored by ^{19}F NMR spectroscopy, with an associated black to pale yellow colour change in acetone-d_6. The propensity for gold complexes **5**/**6**/**11** to promote the hydrolysis of typically stable BF_4^-/SbF_6^- anions further highlights their pronounced 'hard' Lewis acidity. Since the colour change upon the dissolution of **5**/**6**/**11** in acetone from black to pale yellow was observed to be the result of anion hydrolysis, the identical colour change observed for trihalide complexes **3**/**4** (Scheme 61a) may also be the result of trihalide anion hydrolysis. This mechanistic rationale explains the successful anion metathesis of the trihalide anions in **3**/**4** with silver salts in acetone *after* the solution of **3**/**4** had been stirred for long enough to change colour, since the proposed hydrolysis liberates a monohalide anion which can then react selectively with silver salts (Scheme 61**b**).

a)

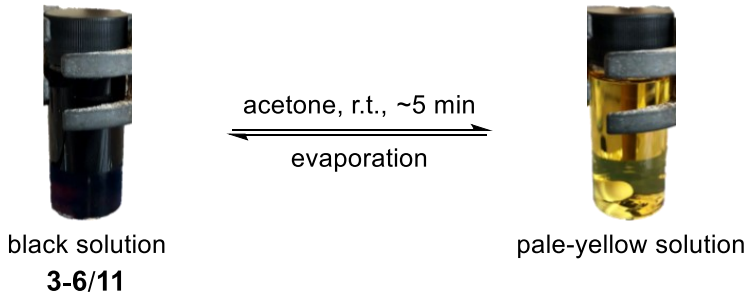

b)

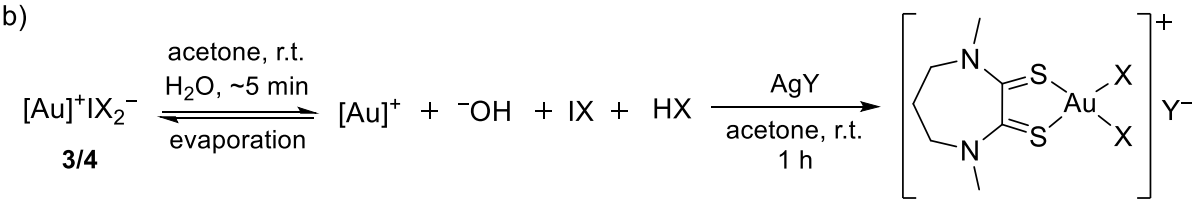

*Scheme 61. a) Identical colour change observed upon the dissolution of complexes **3**-**6**/**11**-**12** in acetone. b) proposed trihalide anion hydrolysis as an explanation for the successful silver salt metathesis of **3**/**4**.*

Recently, tetrafluoroborate compounds have been used as surrogates for HF in fluorination chemistry.[75–77] Moreover, gold complexes have recently been applied as fluorination catalysts and have been reported to proceed via gold-fluoride intermediates.[77,78] Thus, the possibility of developing a fluorination reaction using gold(III)-fluoride **37**, sourced *in situ* from tetrafluoroborate and **5**, is of significant synthetic interest due to the prominence of organofluorides in a range of applications.[79–81] Unfortunately, preliminary stoichiometric experiments employing **5** in acetone-d_6 were unsuccessful at fluorinating two substrates which are commonly used as benchmark substrates in hydrofluorination (Table 23). A number of additives were explored, including various combinations of sodium tetrafluoroborate, triphenylphosphine oxide, *N*-pyridine oxide, and water (Table 23, Entries 1-6).

*Table 23. Attempted **5**-catalysed fluorination of either phenylacetylene or 1,2-diphenylethyne.*

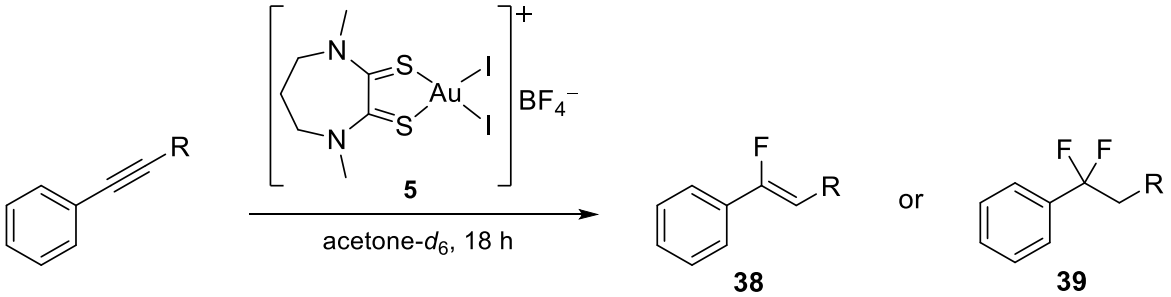

			Conditions		Yield (%)	
Entry	R	**5** loading (mol%)	Reagents	Temperature (°C)	**38**	**39**
1	Ph or H	100	$OPPh_3$ (5 equiv.)	50	0	0
2	Ph or H	5	$NaBF_4$ (1 equiv.)	50	0	0
3	Ph or H	5	$OPPh_3$ (5 equiv.) $NaBF_4$ (1 equiv.)	50	0	0
4	Ph or H	100	$OPPh_3$ (5 equiv.) $NaBF_4$ (1 equiv.)	50	0	0
5	Ph or H	100	$OPPh_3$ (5 equiv.) $NaBF_4$ (1 equiv.) NPO (0.15 equiv.)	50	0	0
6	Ph or H	100	$OPPh_3$ (5 equiv.) $NaBF_4$ (1 equiv.) H_2O (~50 equiv.)	50	0	0

All reactions were conducted in polypropylene falcon tubes. TPPO = triphenylphosphine oxide, NPO = *N*-pyridine oxide. The absence of any conversion to either **38** or **39** was determined by ^{1}H and ^{19}F NMR analysis.

No conversion of the starting material to a new organic compound was observed for each of the explored conditions, despite varying degrees of both tetrafluoroborate hydrolysis and gold(III)-fluoride **37** formation occurring in each case (Table 23, Entries 1-6). Since substrate coordination to gold(III) complex **37** may displace the metal-bound fluoride, the key to a successful fluorination protocol may lie in the formation the difluoride analogue of **37**. This could be achieved using catalytic quantities of AgF, which would irreversibly remove iodide from the reaction mixture. The use of complexes **3**-**6** as fluorination catalysts was not explored further, but remains an interesting avenue for further investigation.

2.3. Conclusions

This study has illustrated the synthesis from metallic gold powder of gold(III) complexes **3** and **4**, which can be obtained directly from WEEE using the process outlined by Deplano and Serpe (Scheme 62).[2]

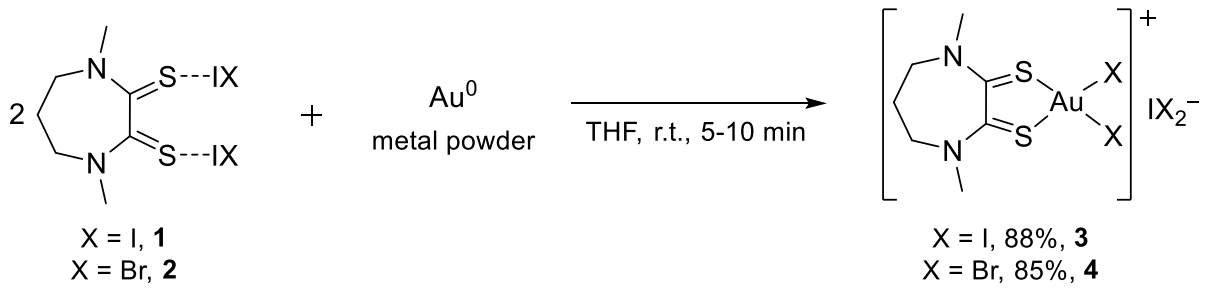

*Scheme 62. Synthesis of gold complexes **3** and **4** from gold powder.*

To illustrate the viability of the process to valorise gold waste and improve the sustainability of gold catalysts, this recovery process was also applied to scrap SIM cards for the synthesis of complex **3a**, which was analytically identical to **3** sourced from gold powder (Scheme 63).

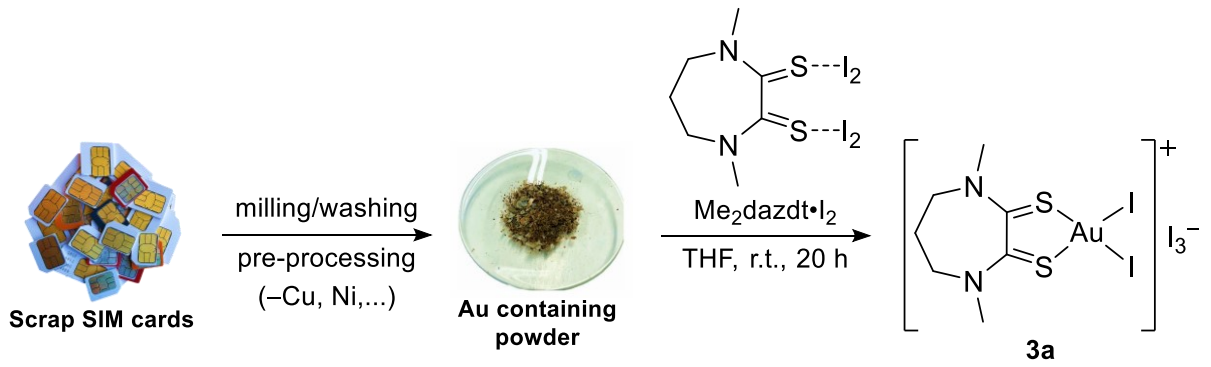

*Scheme 63. Recovery of **3** from scrap SIM cards using $Me_2dazdt{\bullet}2I_2$*

Two strategies were subsequently developed, using either silver or trimethyloxonium salts, which enabled the synthesis of a family of related compounds **5**-**6** and **11**-**12** (Scheme 64). These anion metathesis studies also provided understanding of the solution behaviour of the trihalide anions in **3** and **4**.

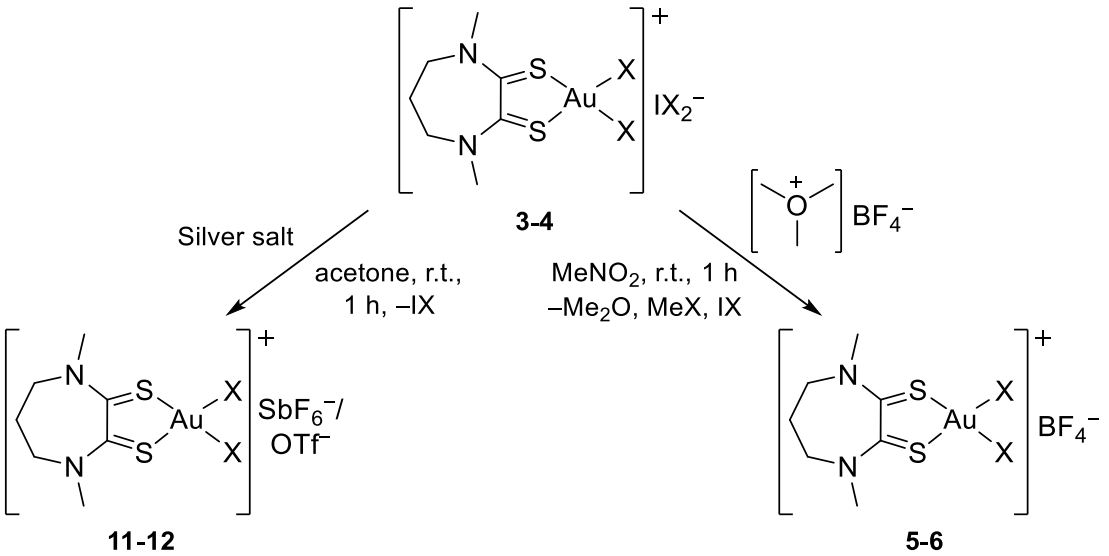

Scheme 64. Two anion metathesis strategies employed for the synthesis of a range of gold(III) complexes.

The resulting gold complexes (**3**-**6**) were illustrated to be effective homogeneous gold catalysts for a range of transformations (Scheme 65). When compared to benchmark and literature catalysts, complexes **3**-**6** exhibited very good activity as oxophilic Lewis acids, namely in the activation of carbonyl compounds for their addition with aromatic and aniline *C*- and *N*-nucleophiles respectively. Complexes **3**-**6** were also employed as carbophilic Lewis acids, namely in the activation of *N*-propargylic amides (**15** and **17**), however elevated temperatures and additives were required to achieve comparable performance to benchmark and literature catalysts. Since complexes **3**-**6** were observed to reform at the end of the carbonyl activation reactions, and their ionic nature renders them insoluble in most non-coordinating organic solvents, it has also been illustrated that they could be easily recovered and reused multiple times without any observed loss in catalyst performance. Good catalytic activity was also observed for complex **3** and **4** in the oxidative cross-coupling of arenes with aryl silanes. For each reaction explored, no differences were observed in the catalytic activity between complexes **3** and **3a** sourced from gold powder and scrap SIM cards respectively.

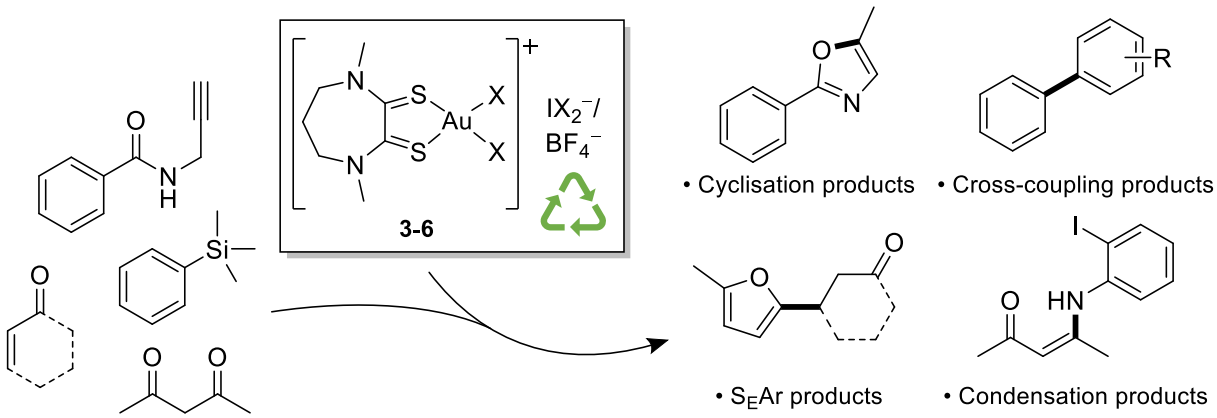

*Scheme 65. Overview of substrates and modes of catalytic activity explored for gold complexes **3-6***

The catalytic results reported herein illustrate the 'hard' oxophilic Lewis acidic nature of complexes **3-6**, and this was supported by Gutmann-Beckett analysis. This analysis revealed that gold(III) complexes **3-6** are considerably more oxophilic than literature gold(I) complexes, and are comparably oxophilic to structurally similar gold(III) complexes reported in the literature. Gutmann-Becket analysis in acetone also revealed a gold-promoted hydrolysis of tetrafluoroborate in **4**/**5** which further illustrated the hard nature of **3-6** as Lewis acids. These catalytic studies are the first examples of the direct application of gold complexes recovered from waste material as homogeneous catalysts. It has been demonstrated that existing gold catalysts derived from environmentally-damaging and expensive primary gold mining can be replaced with **3-6**. This new family of homogeneous gold catalysts, which can be sourced from millions of tonnes of e-waste that would otherwise be sent to landfill, are more sustainable and cheaper alternatives for typical homogeneous gold(III) catalysts.[31]

2.4. Future work

Many of the literature transformations which employ gold(III) complexes utilise non-coordinating and protic solvents in which gold complexes **3-6** are insoluble, *e.g.* alcohols, dichloromethane, diethyl ether. Gold(III) complexes **3-6** were catalytically inactive for many of the transformations which use these solvents, which may have been the result of their poor solubility *e.g.* **3-6** were inactive as catalysts for the cyclisation of **22** (Table 13). One avenue for future work then is the synthesis of a larger family of recovery complexes with different counter anions which may provide improved solubility and thus catalytic activity in protic and non-coordinating solvents (Figure 31).

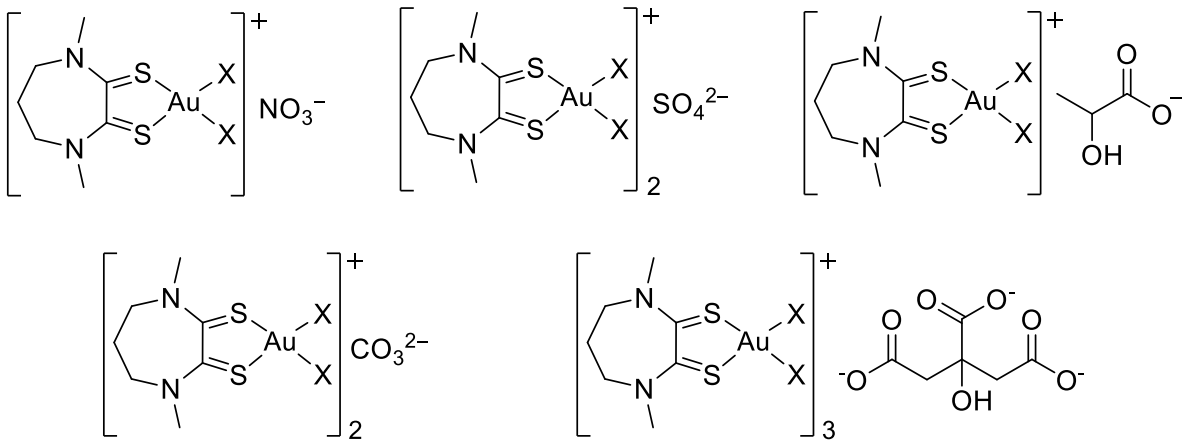

Figure 31. Alternative gold complexes which may exhibit improved solubility in protic and non-coordinating solvents, with anions for which corresponding silver(I) salts are commercially available.

Attempts at isolating a vinyl gold oxazoline (**32**) to better understand the mechanism by which gold complexes **3**-**6** achieve their catalytic activity were unsuccessful. Instead, formation of a linear gold(I) complex (**30**) and a vinyl iodide oxazoline (**33**) revealed that the postulated vinyl gold intermediate was unstable under the conditions explored. Thus, future work could explore alternative conditions which enable the isolation of a vinyl gold compound (Scheme 66a).

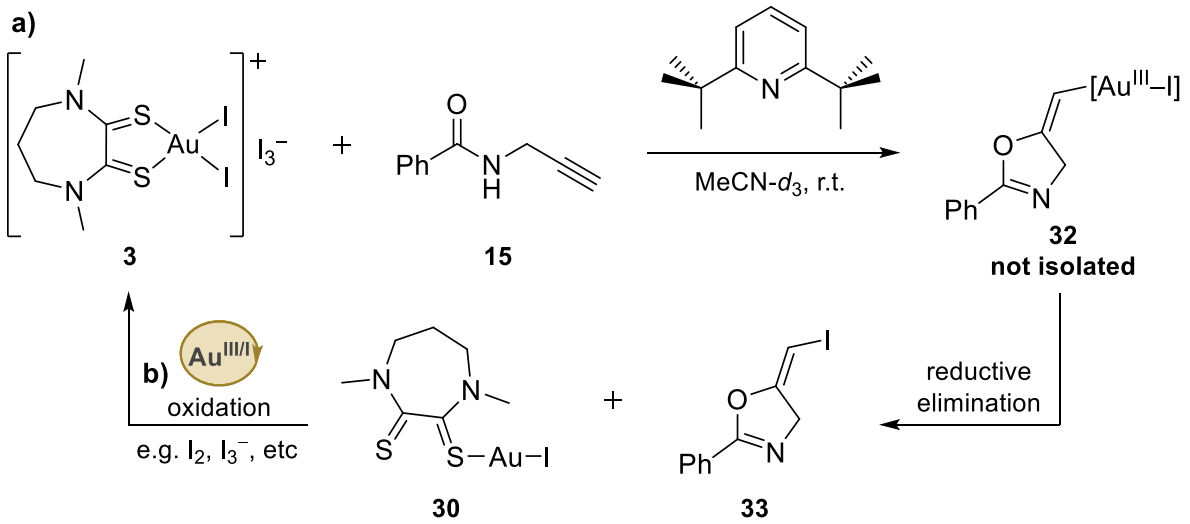

*Scheme 66. Future work which could: a) Improve on previously unsuccessful attempt at isolating a vinyl gold intermediate. b) Possible gold(III/I) redox cycle for the turnover of **29** to **3** and catalytic formation of **32**.*

Moreover, vinyl iodides such as **33** are highly-useful synthetic intermediates. Thus, future work could also explore the possibility of turning over complex **30** back to **3** using an iodine-based oxidant, which would enable the catalytic transformation of **15** to **33** (Scheme 66b). It should be noted though that

the transformation of **15** to **33** is already known to be promoted by iodine-based organic oxidants and therefore a gold mediated transformation may be of little synthetic utility.[52,53]

Finally, attempts at using gold(III)-fluoride **37**, sourced *in situ* from **5** and BF_4^-, as a reagent/catalytic intermediate for fluorination were unsuccessful. However, only two substrates and a narrow range of conditions were explored, and more work is needed to assess the viability of the transformation. Crucially, only gold(III)-monofluoride **37** was detected by *in situ* ^{19}F NMR studies, substrate binding to which may displace fluoride and prevent fluorination. Conditions which result in the formation of a gold(III)-difluoride species may therefore be key to a successful fluorination protocol, and this may require the addition of a silver salt, e.g. AgF, to remove competing iodide/bromide anions. Determining an appropriate substrate will also likely be key, and carbonyl compounds may be more suitable since complexes **3**-**6** were more effective oxophilic Lewis acid catalysts.

2.5. References

1 H. Au, S. M. Godfrey, N. Ho, C. A. Mcauliffe and R. G. Pritchard, *Communications*, 1996, 2343–2346.
2 F. Bigoli, P. Deplano, M. L. Mercuri, M. A. Pellinghelli, G. Pintus, A. Serpe and E. F. Trogu, *Chem. Commun.*, 1998, **484**, 2351–2352.
3 L. Cau, P. Deplano, L. Marchiò, M. L. Mercuri, L. Pilia, A. Serpe and E. F. Trogu, *Dalton Trans.*, 2003, 1969–1974.
4 A. Serpe, P. Deplano, M. L. Mercuri, L. Pilia, M. Vanzi, European Patent, EP1964936B1, 2008.
5 L. Rocchigiani and M. Bochmann, *Chem. Rev.*, 2021, **121**, 8364–8451.
6 S. Kramer and F. Gagosz, *Gold Catalysis: An Homogeneous Approach*, Imperial College Press, London, 2014.
7 H. Yang and F. P. Gabbal, *J. Am. Chem. Soc.*, 2015, **137**, 13425–13432.
8 M. Muuronen, J. E. Perea-Buceta, M. Nieger, M. Patzschke and J. Helaja, *Organometallics*, 2012, **31**, 4320–4330.
9 Z. Cao, D. M. Bassani and B. Bibal, *Chem-Eur. J.,* 2018, **24**, 18779–18787.
10 R. Cai, M. Lu, E. Y. Aguilera, Y. Xi, N. G. Akhmedov, J. L. Petersen, H. Chen and X. Shi, *Angew. Chem. Int. Ed.*, 2015, **54**, 8772–8776.
11 R. Dorel and A. M. Echavarren, *Chem. Rev.*, 2015, **115**, 9028–9072.
12 M. T. Reetz and K. Sommer, *Eur. J. Org. Chem.,* 2003, 3485–3496.
13 A. Stephen and K. Hashmi, *Gold Bull.*, 2003, **36**, 3–9.
14 A. S. K. Hashmi, J. P. Weyrauch, W. Frey and J. W. Bats, *Org. Lett.*, 2004, **6**, 4391–4394.
15 A. S. K. Hashmi, A. M. Schuster, M. Schmuck and F. Rominger, *Eur. J. Org. Chem.*, 2011, 4595–4602.
16 A. S. K. Hashmi, A. M. Schuster and F. Rominger, *Angew. Chem. Int. Ed.*, 2009, **48**, 8247–8249.
17 A. S. K. Hashmi, T. D. Ramamurthi and F. Rominger, *J. Organomet. Chem.*, 2009, **694**, 592–597.
18 A. Arcadi, G. Bianchi and F. Marinelli, *Synthesis*, 2004, **2**, 610–618.
19 A. Arcadi, G. Blanchi, S. Di Giuseppe and F. Marinelli, *Green Chem.*, 2003, **5**, 64–67.
20 G. Dyker, E. Muth, A. S. K. Hashmi and L. Ding, *Adv. Synth. Catal.*, 2003, **345**, 1247–1252.
21 A. Nijamudheen and A. Datta, *Chem-Eur. J.,* 2020, **26**, 1442–1487.
22 M. J. Harper, C. J. Arthur, J. Crosby, E. J. Emmett, R. L. Falconer, A. J. Fensham-Smith, P. J. Gates,

T. Leman, J. E. McGrady, J. F. Bower and C. A. Russell, *J. Am. Chem. Soc.*, 2018, **140**, 4440–4445.
23 I. Fernández, L. P. Wolters and F. M. Bickelhaupt, *J. Comput. Chem.*, 2014, **35**, 2140–2145.
24 M. Livendahl, C. Goehry, F. Maseras and A. M. Echavarren, *Chem. Commun.*, 2014, **50**, 1533–1536.
25 J. H. Teles, *Angew. Chem. Int. Ed.,* 2015, **54**, 5556–5558.
26 M. N. Hopkinson, A. Tlahuext-Aca and F. Glorius, *Acc. Chem. Res.*, 2016, **49**, 2261–2272.
27 M. Joost, A. Zeineddine, L. Estévez, S. Mallet-Ladeira, K. Miqueu, A. Amgoune and D. Bourissou, *J. Am. Chem. Soc.*, 2014, **136**, 14654–14657.
28 L. T. Ball, G. C. Lloyd-Jones and C. A. Russell, *Science,* 2012, **337**, 1644–1648.
29 L. T. Ball, G. C. Lloyd-Jones and C. A. Russell, *J. Am. Chem. Soc.*, 2014, **136**, 254–264.
30 R. Isaksson, T. Liljefors, J. Sandstroem, *J. Chem. Res. 1981,* **43**, 664-672.
31 S. McCarthy, O. Desaunay, A. L. W. Jie, M. Hassatzky, A. J. P. White, P. Deplano, D. C. Braddock, A. Serpe and J. D. E. T. Wilton-Ely, *ACS Sustain. Chem. Eng.*, 2022, **10**, 15726–15734.
32 P. H. Svensson and L. Kioo, *J. Chem. Soc. Dalt. Trans.*, 2000, **951**, 2449–2455.
33 J. Heo, J. G. Kim, E. H. Choi, H. Ki, D. S. Ahn, J. Kim, S. Lee and H. Ihee, *Nat. Commun.*, 2022, **13**, 522.
34 R. M. Lynden-Bell, R. Kosloff, S. Ruhman, D. Danovich and J. Vala, *J. Chem. Phys.*, 1998, **109**, 9928–9937.
35 A. E. Johnson and A. B. Myers, *J. Phys. Chem.*, 1996, **100**, 7778–7788.
36 H. Schmidbaur and A. Schier, *Chem. Soc. Rev.*, 2012, **41**, 370–412.
37 H. Schmidbaur and A. Schier, *Chem. Soc. Rev.*, 2008, **37**, 1931–1951.
38 H. S. Sam Chan, Q. N. N. Nguyen, R. S. Paton and J. W. Burton, *J. Am. Chem. Soc.*, 2019, **141**, 15951–15962.
39 A. Peter, S. M. Fehr, V. Dybbert, D. Himmel, I. Lindner, E. Jacob, M. Ouda, A. Schaadt, R. J. White, H. Scherer and I. Krossing, *Angew. Chem. Int. Ed.*, 2018, **57**, 9461–9464.
40 T. Van Dijk, J. Chris Slootweg and K. Lammertsma, *Org. Biomol. Chem.*, 2017, **15**, 10134–10144.
41 H. Meerwein, P. Laasch, R. Mersch and J. Spille, *Chem. Ber.*, 1956, **89**, 2060–2079.
42 F. Dutron-Woitrin, R. Merényi and H. G. Viehe, *Synth.*, 1985, **1985**, 77–79.
43 A. Gupta, J. K. Vankar, J. P. Jadav and G. N. Gururaja, *J. Org. Chem.*, 2022, **87**, 2410–2420.
44 N. P. Tarasova, E. G. Krivoborodov and Y. O. Mezhuev, *Russ. Chem. Bull.*, 2023, **72**, 415–424.
45 J. Li, X. Ren, G. Li, H. Liang, Y. Zhao, Z. Wang, H. Li and B. Yuan, *J. Sulfur Chem.*, 2020, **41**, 229–237.
46 Y. A. Tayade, A. D. Jangale and D. S. Dalal, *ChemistrySelect*, 2018, **3**, 8895–8900.
47 X. Li, K. S. Iyer, R. R. Thakore, D. K. Leahy, J. D. Bailey and B. H. Lipshutz, *Org. Lett.*, 2021, **23**, 7205–7208.
48 D. C. Braddock, P. D. Lickiss, B. C. Rowley, D. Pugh, T. Purnomo, G. Santhakumar and S. J. Fussell, *Org. Lett.*, 2018, **20**, 950–953.
49 W. Wang, M. Kumar, G. B. Hammond and B. Xu, *Org. Lett.*, 2014, **16**, 636–639.
50 J. Derosa, A. L. Cantu, M. N. Boulous, M. L. O'Duill, J. L. Turnbull, Z. Liu, D. M. De La Torre and K. M. Engle, *J. Am. Chem. Soc.*, 2017, **139**, 5183–5193.
51 A. S. K. Hashmi, C. Lothschütz, K. Graf, T. Häffner, A. Schuster and F. Rominger, *Adv. Synth. Catal.*, 2011, **353**, 1407–1412.
52 J. P. Weyrauch, A. S. K. Hashmi, A. Schuster, T. Hengst, S. Schetter, A. Littmann, M. Rudolph, M. Hamzic, J. Visus, F. Rominger, W. Frey and J. W. Bats, *Chem-Eur. J.*, 2010, **16**, 956–963.
53 A. Urbanaite, M. Jonušis, R. Bukšnaitiene, S. Balkaitis and I. Čikotiene, *Eur. J. Org. Chem.*, 2015, **2015**, 7091–7113.
54 Y. Hu, R. Yi, C. Wang, X. Xin, F. Wu and B. Wan, *J. Org. Chem.*, 2014, **79**, 3052–3059.
55 S. Sjövall, L. Hansen and B. Granquist, *Org. Process Res. Dev.*, 2004, **8**, 802–807.
56 S. A. Weissman and N. G. Anderson, *Org. Process Res. Dev.*, 2015, **19**, 1605–1633.
57 A. F. Williams, A. J. P. White, A. C. Spivey and C. J. Cordier, *Chem. Sci.*, 2020, **11**, 3301–3306.
58 P. M. Murray, F. Bellany, L. Benhamou, D. K. Bučar, A. B. Tabor and T. D. Sheppard, *Org. Biomol.*

Chem., 2016, **14**, 2373–2384.
59 C. L. G. Harman, N. Mac Fhionnlaoich, A. M. King, J. R. H. Manning, W. Lin, P. Scholes, S. Guldin and G.-L. Davies, *Mater. Adv.*, 2022, **3**, 6007–6018.
60 JMP - Design of Experiments, https://www.jmp.com/en_ph/statistics-knowledge-portal/what-is-design-of-experiments.html#:~:text=Why use DOE%3F,factors at the same time., (accessed 21 November 2023).
61 JMP - Design of Experiments Design Types, https://www.jmp.com/en_in/statistics-knowledge-portal/what-is-design-of-experiments/types-of-design-of-experiments.html, (accessed 21 November 2023).
62 U. Mayer, V. Gutmann and W. Gerger, *Monatshefte für Chemie*, 1975, **106**, 1235–1257.
63 M. A. Beckett, G. C. Strickland, J. R. Holland and K. S. Varma, *Polymer*, 1996, **37**, 4629–4631.
64 G. C. Welch, L. Cabrera, P. A. Chase, E. Hollink, J. D. Masuda, P. Wei and D. W. Stephan, *J. Chem. Soc. Dalt. Trans.*, 2006, **9226**, 3407–3414.
65 B. R. Reiner, M. W. Bezpalko, B. M. Foxman and C. R. Wade, *Organometallics*, 2016, **35**, 2830–2835.
66 A. Tlahuext-Aca, M. N. Hopkinson, C. G. Daniliuc and F. Glorius, *Chem-Eur. J.*, 2016, **22**, 11587–11592.
67 C. Y. Wu, T. Horibe, C. B. Jacobsen and F. D. Toste, *Nature*, 2015, **517**, 449–454.
68 N. P. Mankad and F. D. Toste, *J. Am. Chem. Soc.*, 2010, **132**, 12859–12861.
69 M. A. Ellwanger, C. Von Randow, S. Steinhauer, Y. Zhou, A. Wiesner, H. Beckers, T. Braun and S. Riedel, *Chem. Commun.*, 2018, **54**, 9301–9304.
70 N. P. Mankad and F. D. Toste, *Chem. Sci.*, 2012, **3**, 72–76.
71 K. Helmdach, S. Ludwig, A. Villinger, D. Hollmann, J. Kösters and W. W. Seidel, *Chem. Commun.*, 2017, **53**, 5894–5897.
72 N. Burford, B. W. Royan, R. E. V. H. Spence, T. S. Cameron, A. Linden and R. D. Rogers, *J. Chem. Soc. Dalt. Trans.*, 1990, **1**, 1521–1528.
73 A. N. Thadani and R. A. Batey, *Org. Lett.*, 2002, **4**, 3827–3830.
74 J. Lozada, W. Xuan Lin, R. M. Cao-Shen, R. Astoria Tai and D. M. Perrin, *Angew. Chem. Int. Ed.*, 2023, **62**, 1–6.
75 M. C. Leech, D. Nagornîi, J. M. Walsh, C. Kiaku, D. L. Poole, J. Mason, I. C. A. Goodall, P. Devo and K. Lam, *Org. Lett.*, 2023, **25**, 1353–1358.
76 R. Guo, X. Qi, H. Xiang, P. Geaneotes, R. Wang, P. Liu and Y. M. Wang, *Angew. Chem. Int. Ed.*, 2020, **59**, 16651–16660.
77 O. E. Okoromoba, J. Han, G. B. Hammond and B. Xu, *J. Am. Chem. Soc.*, 2014, **136**, 14381–14384.
78 D. Mulryan, J. Rodwell, N. A. Phillips and M. R. Crimmin, *ACS Catal.*, 2022, **12**, 3411–3419.
79 V. P. Reddy, *Organofluorine Chemistry Synthesis and Applications*, Elsevier, 2020.
80 G. Theodoridis, *Fluorine-Containing Agrochemicals: An Overview of Recent Developments*, Elsevier, 2006, pp. 121–175.
81 E. P. Gillis, K. J. Eastman, M. D. Hill, D. J. Donnelly and N. A. Meanwell, *J. Med. Chem.*, 2015, **58**, 8315–8359.

Chapter 3 – A Recovered Palladium Dimer as a Highly Active and Recyclable Catalyst

3.1. Introduction

This chapter details the synthesis and application of a family of related palladium compounds, $[Cation]_2[Pd_2I_6]$, as homogeneous catalysts. The introduction initially reiterates some key aspects of palladium recycling, followed by an introduction to the palladium recycling process that was utilised in this thesis. The research aims and objectives are then presented, followed by an overview of the key results of previous research, and an overview of the model cross-coupling reaction which was chosen to achieve the chapter's aims. The results and discussion sections then covers the contents of the results in the order: i) the synthesis of the recycled palladium complexes, ii) the optimisation of $[N^nBu_4]_2[Pd_2I_6]$ as a catalyst for the model cross-coupling reaction, iii) Design of a complete process for the model cross-coupling reaction, including additive and catalyst recycling, iv) Application of the catalyst recycling strategy to some other important palladium-catalysed transformations.

3.1.1. Palladium recycling

Aqueous solutions of iodide-iodine/triiodide have been successfully employed as lixiviants in gold recycling since the 1980s.[1–6] These iodide-iodine solutions proceed via I^- complexation and I_3^- oxidation to yield $[AuI_2]^-$ (Scheme 67a). Iodide-iodine solutions provide improved recovery yields and rates when compared to *aqua regia* and other halide lixiviants, whilst being considerably greener than cyanide based lixiviants.[1–6] Unfortunately, when applied to palladium recycling, aqueous solutions of iodide/iodine provide low recovery yields and rates due to the passivation of Pd^0 with insoluble PdI_2 (Scheme 67b).

a)

$$2Au^0 + KI + KI_3 \xrightarrow[H_2O]{} \underset{\text{soluble}}{2K[AuI_2]}$$

b)

$$2Pd^0 + 2KI + 2KI_3 \xrightarrow[H_2O]{} \underset{\text{soluble}}{K_2[PdI_4]} + \underset{\text{insoluble}}{PdI_2} + 2KI$$

Scheme 67. a) Oxidation and dissolution of metallic Au^0 by potassium iodide/triiodide. b) Poor recovery yield/rate of metallic Pd^0 oxidation and dissolution due to passivation of PdI_2.

In 2017, Serpe and Marchiò reported the use of weakly-coordinating organic cations as a strategy to overcome the passivation of PdI_2 and enable the application of triiodides to recover palladium from scrap TWCs.[7] Metallic palladium from model scrap TWCs was transformed in high recovery yields (73-98%) into a series of $[Cation]_2[Pd_2I_6]$ salts (Table 24), with the weakly coordination organic cations

enabling the extraction of the resulting $[Pd_2I_6]^{2-}$ salts into an organic solvent (methyl ethyl ketone). The structure of the cation was found to have an influence on the recovery yield, with $[(PhNH)_2DTL]^+$ providing the best performance (Table 24, Entry 4). It was illustrated that the differences in recovery yield between the four cations correlated with increasing second-sphere ion-pair interactions, i.e. $[(PhNH)_2DTL]^+$>$[PPh_4]^+$>$[N^nBu_4]^+$>>K^+ ($(PhNH)_2DTL$ = bis(phenylamino)-1,2-dithiolylium). These ionic couples stabilised $[Pd_2I_6]^{2-}$, providing an alternative and more favourable pathway to the passivation of PdI_2 (Table 24, Entry 1).

Table 24. Recovery of palladium from model scrap TWCs by triiodides in methyl ethyl ketone.[7]

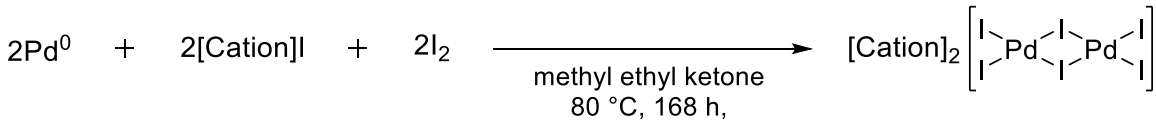

Entry	Cation	Product(s)	Yield (%)[a]
1	Potassium	PdI_2, $K[PdI_4]$	38
2	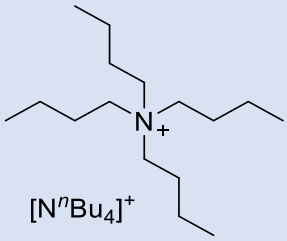 $[N^nBu_4]^+$	$[N^nBu_4]_2[Pd_2I_6]$	73
3	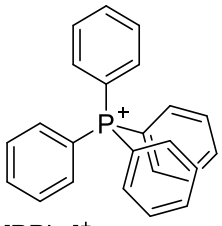 $[PPh_4]^+$	$[PPh_4]_2[Pd_2I_6]$	83
4	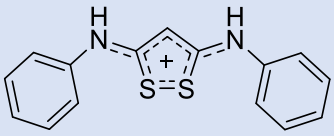 $[(PhNH)_2DTL]^+$	$[(PhNH)_2DTL]_2[Pd_2I_6]$	98%

[a] Palladium recovery yields were determined by ICP-AES.

It was also illustrated that metallic palladium could be recovered from $[(PhNH)_2DTL]_2[Pd_2I_6]$ by chemical cementation with zinc or magnesium, which also permitted the recovery of neutral $[(PhNH)_2DTL]$ by flash-column chromatography. However, the necessity of chemical cementation and

chromatography to achieve a closed-loop recovery of palladium from TWCs limits the economic viability of using organic iodides to recover palladium. Thus, research in the Wilton-Ely and Serpe groups was initiated to explore the application of $[Cation]_2[Pd_2I_6]$ salts as palladium precatalysts to provide an alternative high-value application of recovered palladium waste. Application of $[Cation]_2[Pd_2I_6]$ as precatalysts would provide the chemical industry with an alternative source of palladium which is decoupled from existing unsustainable supply streams.[8–16]

3.1.2. Research aims and objectives

Since $[N^nBu_4]_2[Pd_2I_6]$ has been illustrated to be an especially effective Suzuki-Miyaura precatalyst for a range of simple phenyl iodides and bromides (see **3.1.3.**, *vide infra*),[17–19] the aim of the research in this chapter was to explore the performance of $[N^nBu_4]_2[Pd_2I_6]$ as a precatalyst for a more challenging Suzuki-Miyaura coupling of an industrially relevant aryl chloride (introduced *vide infra*, Section *3.1.4*). This was achieved by optimising the reaction conditions using 'Design of Experiments' (DoE). Previous benchmarking of the performance of $[N^nBu_4]_2[Pd_2I_6]$ as a precatalyst used comparisons of the reaction yields provided by $[N^nBu_4]_2[Pd_2I_6]$ with the yields provided by commercial palladium-phosphine complexes. Such yield comparisons do not provide a full picture of intrinsic catalyst performance and stability.[22] As a result, an additional aim of this chapter was to use kinetic reaction profiles to benchmark the performance of $[N^nBu_4]_2[Pd_2I_6]$ with two typical commercial palladium-phosphine complexes.

With the principles of a circular economy and palladium sustainability in mind, the development of a full process design for the model cross-coupling reaction was also explored to enable the recovery/recycling of the palladium material. The efficacy of the process design and of $[N^nBu_4]_2[Pd_2I_6]$ recovered from the reaction mixture was demonstrated through kinetic reaction profiles. Moreover, to further encourage the adoption of $[N^nBu_4]_2[Pd_2I_6]$ within the pharmaceutical industry, where residual palladium levels in active pharmaceutical ingredients are strictly regulated ([Pd]<5 ppm),[23] trace-metal analysis was conducted on the cross-coupling product obtained from the final process design. The recycling strategy developed to recover and reuse $[N^nBu_4]_2[Pd_2I_6]$ was also explored with some other typical palladium-phosphine complexes, and some other palladium-catalysed transformations. The end goal of these studies was to develop a general palladium recycling procedure which could be used by research laboratories to recycle their catalytic palladium waste locally.

3.1.3. [Cation]$_2$[Pd$_2$I$_6$] as a palladium precatalyst

To further incentivise TWC recycling and provide the chemical industry with a more sustainable source of palladium, the Wilton-Ely and Serpe groups have explored the transformation of [N^{n}Bu$_4$]$_2$[Pd$_2$I$_6$] into three palladium-phosphine complexes (Scheme 68).

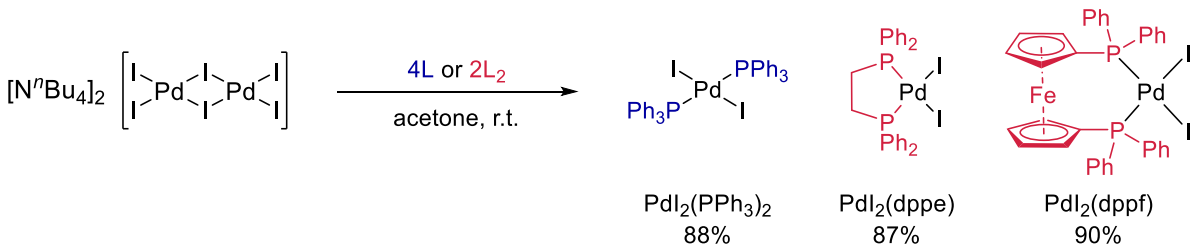

Scheme 68. Transformation of [N^{n}Bu$_4$]$_2$[Pd$_2$I$_6$] into three phosphine complexes that are often employed as their chloride complexes in catalysis (dppf = 1,1'-Bis(diphenylphosphino)ferrocene) (dppe = 1,2-Bis(diphenylphosphino)ethane). Taken from unpublished reports.[16-18]

Previous catalytic studies in the Wilton-Ely group found that [Cation]$_2$[Pd$_2$I$_6$] salts are particularly good precatalysts for the Suzuki-Miyaura coupling reaction, with [N^{n}Bu$_4$]$_2$[Pd$_2$I$_6$] often outperforming many typical phosphine-based palladium complexes (Table 25), including those derived from [N^{n}Bu$_4$]$_2$[Pd$_2$I$_6$].[17–19]

Table 25. Comparison of the performance of a series of recovered palladium complexes and commercial [PdCl$_2$(PPh$_3$)$_2$] (dppf = 1,1'-Bis(diphenylphosphino)ferrocene).[16-18]

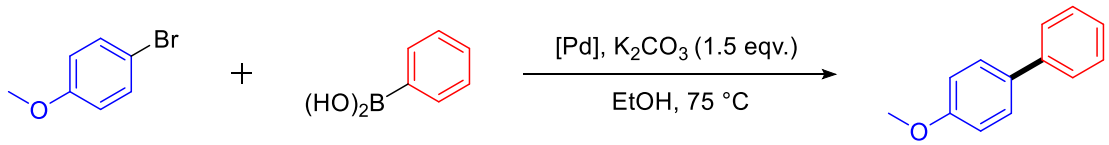

Entry	Catalyst (mol%)	Time (min)	Cross-coupling yield (%)[a]
1	**[N^{n}Bu$_4$]$_2$[Pd$_2$I$_6$] (0.5 mol%)**	**30**	**96**
2	[PdI$_2$(PPh$_3$)$_2$] (1 mol%)	90	78
3	[PdI$_2$(dppf)] (1 mol%)	90	93
4	[PdI$_2$(dppe)] (1 mol%)	150	61
5	[PdCl$_2$(PPh$_3$)$_2$] (1 mol%)	30	97

[a)] Yields were determined by ^{1}H NMR analysis

These results were especially promising since the Suzuki-Miyaura reaction is the second-most common reaction in medicinal chemistry,[20] resulting in the 2010 Nobel Prize in Chemistry being

awarded to Suzuki, Heck and Negishi.[21] The Suzuki-Miyaura reaction is therefore a transformation where recycled metal sources, *e.g.* $[N^nBu_4]_2[Pd_2I_6]$, have the potential to make a large impact.

3.1.4. Model Suzuki-Miyaura cross-coupling

The Suzuki-Miyaura coupling of 2-nitrochlorobenzene (**1**) and 4-chlorophenyl boronic acid (**2**) was chosen as a model reaction for the majority of the work in this Chapter (Scheme 69). This reaction is conducted annually by BASF on ~1000 tonne/year scale and is the largest industrial-scale Suzuki-Miyaura reaction according to a number of published reviews.[24–26] The resulting cross-coupling product, 4'-chloro-2-nitro-1,1'-biphenyl (**3**), serves as an intermediate in the synthesis of Boscalid, a fungicide registered for use on over 100 crop types across 70 different countries world-wide.[24,25,27,28]

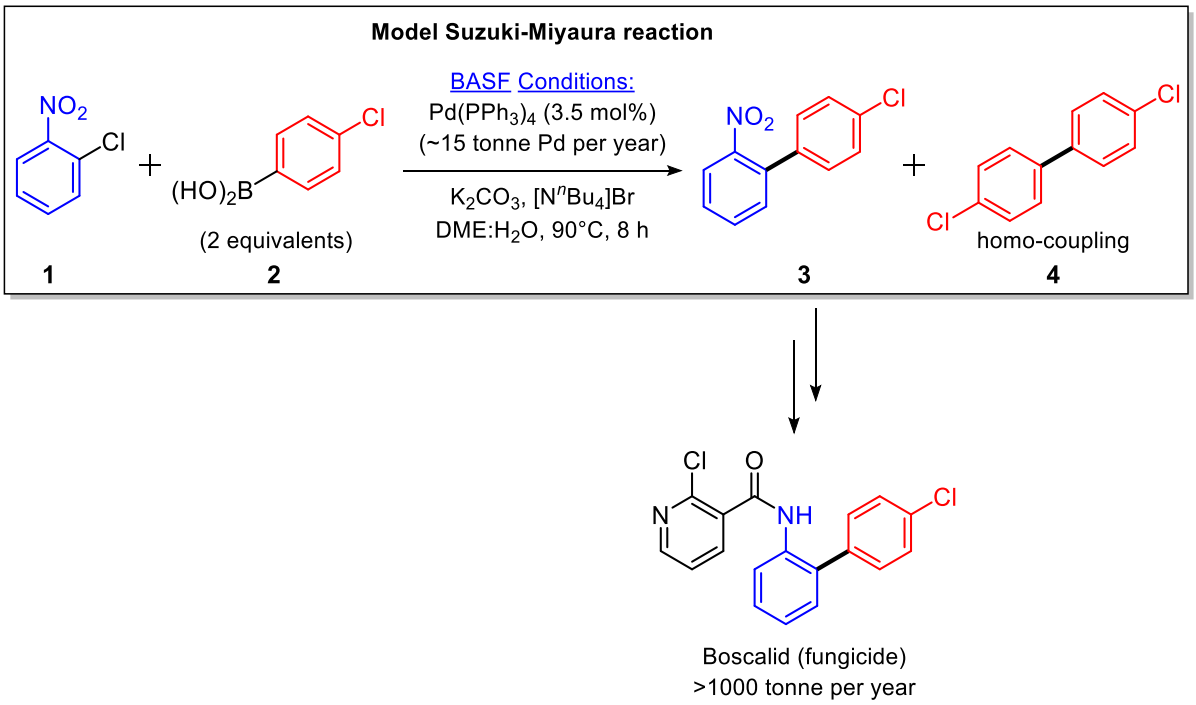

Scheme 69. Model Suzuki-Miyaura coupling utilised throughout the kinetic and mechanistic studies conducted herein with the conditions reported in the original BASF patent.[27–29]

Given the catalyst loading of 3.5 mol% $Pd(PPh_4)_3$ which was reported in BASF patents (Scheme 69),[27–29] the synthesis of 4'-chloro-2-nitro-1,1'-biphenyl (**3**) equates to ~15 tonnes of palladium consumption each year that could, in principle, be replaced with $[N^nBu_4]_2[Pd_2I_6]$. Moreover, the patents utilised a large excess of phenyl boronic acid **2**, presumably due to the poor selectivity for cross-coupling over the boronic acid homo-coupling yielding 4,4'-dichloro-1,1'-biphenyl (**4**) (Scheme 69). The patented conditions also utilised 1,2-dimethoxyethane (Scheme 69) – an environmentally undesirable

solvent.[30,31] Thus, there are a number of improvements that can be made when applying $[N^nBu_4]_2[Pd_2I_6]$ to the Suzuki-Miyaura coupling yielding **3**. It should be noted that presumably some portion of the palladium material used by BASF is recycled, that palladium technology has advanced significantly since the patents were released in 1997-1999, and that the patents provide a general cross-coupling procedure with the coupling of 2-bromo-4-fluoroaniline and 4-fluorophenyl boronic acid used as an example. Therefore, the patent does not necessarily provide specific optimised conditions for the coupling of **1** and **2,** and this should be considered when comparing the conditions. Nevertheless, the reaction yielding **3** is an industrial relevant transformation in which the use of $[N^nBu_4]_2[Pd_2I_6]$ has the potential to make the largest impact.

A number of modern state-of-the-art palladium complexes and systems have been applied to the model cross-coupling reaction (Table 26).[32–36] It should be noted that a number of other state-of-the-art literature palladium catalysts would likely also be competent for the model reaction, however only those examples which report the synthesis of **3** have been covered here. The palladacycle (**5**) containing tri(1-adamantly)phosphine was successfully employed at a very low loading (0.005 mol%) achieving incredibly high TOFs (116,400 h^{-1}) (Table 26, Catalyst **5**). This was however dependent on the use of THF under solvothermal conditions (100 °C), which will greatly contribute to the catalysts increased activity.

*Table 26. Palladium complexes which have been utilised for the cross-coupling reaction yielding **3** and their performance metrics.*

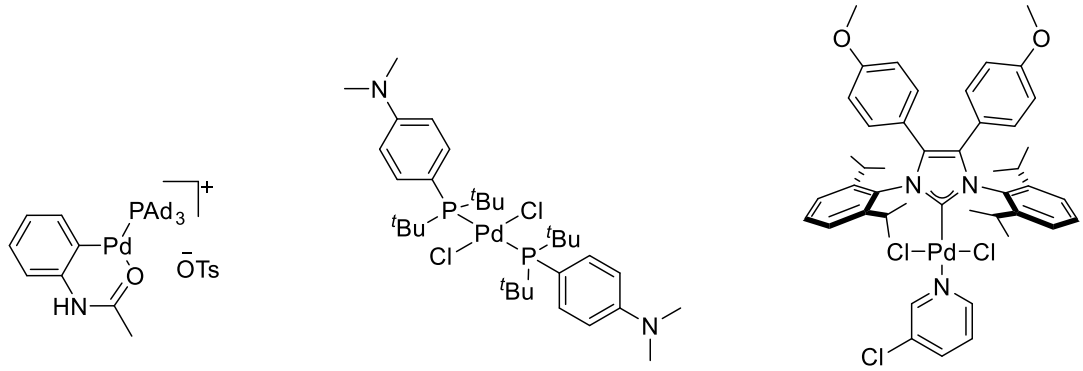

5 **6** **7**

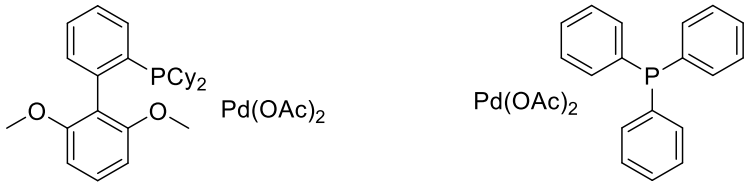

8 (2:1 ligand:Pd) **9** (1:1 ligand:Pd)

Catalyst	Conditions [Pd] loading /solvent/temperature/time	Performance[a] Yield **3** (%)	TON	TOF (h^{-1})	Ref
5	0.005 mol%/THF/100 °C/10 min	97	19400	116400	35
6	0.007 mol%/toluene:H_2O/85 °C/4 h	99	14143	3536	32
7	0.1 mol%/THF:H_2O/60 °C/4 h	98	980	245	33
8	0.07 mol%/THF:H_2O[b]/55 °C/12 h	100	1429	119	36
9	0.42 mol%/THF:H_2O/90 °C/5 h	99	236	47	34

[a)] TON = mol **3**/mol [Pd]. TOF = TON/time (h). [b)] 2 wt% TPGS-750-M.

The application of the palladium phosphine complex **6** in the synthesis of **3** was patented in 2019.[32] The patent reported the use of **6** at a low catalyst loading of 0.007 mol%, resulting in impressive TONs and TOFs (Table 26, Catalyst **6**). The *N*-heterocyclic carbene palladium complex **7** was reported in 2019 and functioned under milder conditions than were employed for **5** and **6**, albeit at an elevated loading (0.1 mol%) (Table 26, Catalyst **7**). Two commercial palladium complexes/ligands have also been employed in the synthesis of **3** (Table 26, Catalyst **8** and **9**). The first example utilised a combination of palladium acetate and triphenylphosphine, which was patented in 2019 (Table 26, Catalyst **9**). A more recent example reported in 2020 utilised a combination of palladium acetate and the commercially available ligand SPhos under very mild conditions at a low catalyst loading (Table 26,

Catalyst **8**). The access to low catalyst loadings (**8**) under mild and aqueous conditions was facilitated by the use of a designer surfactant (TPGS-750-M).

Another recent example of the synthesis of **3** was reported in research led by Schaub at BASF. The synthesis of **3** by a Suzuki-Miyaura reaction catalysed by $Pd(OAc)_2/P(^tBu)Cy_2$ 'on water' was conducted on a 50 g scale using just 0.005 mol% of $Pd(OAc)_2$ (Scheme 70).[37]

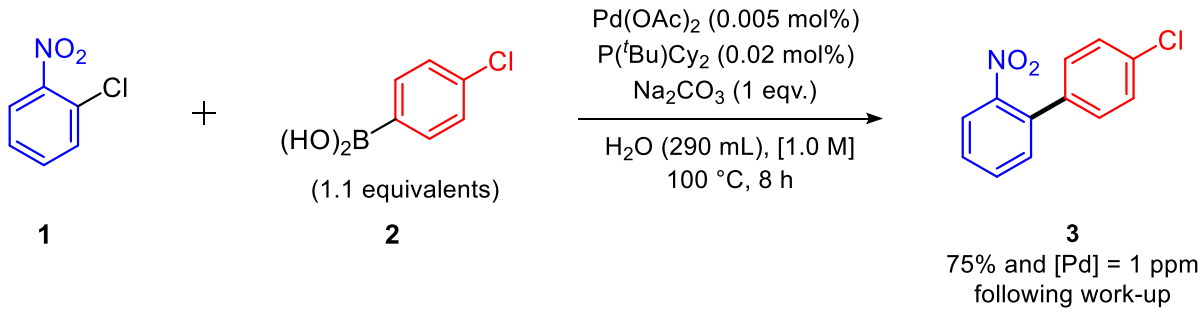

*Scheme 70. Literature example of the Suzuki-Miyaura reaction yielding **3**.*

The product (**3**) was extracted into ethyl acetate, filtered over activated charcoal to remove residual palladium and recrystallised from ethanol. Good isolated yields of the recrystallised product were obtained (75%) on a 50 g scale, and product residual palladium levels were 1 ppm. All of these results render the above conditions as state-of-the-art for the synthesis of **3**, in terms of both catalyst performance and sustainability.

Alongside the kinetic benchmarking of $[N^nBu_4]_2[Pd_2I_6]$ with the two phosphine-palladium complexes conducted herein, comparisons will also be made with each of the state-of-the-art literature examples above (Table 26, Scheme 70).

3.2. Results and Discussion

3.2.1. Synthesis of $[Cation]_2[Pd_2I_6]$ salts

A series of $[Cation]_2[Pd_2I_6]$ salts were synthesised from palladium metal powder according to the procedure reported by Serpe and Marchiò.[7] Since previous work by Serpe and Marchiò had already illustrated that $[Cation]_2[Pd_2I_6]$ salts were the only product recovered from model waste TWCs,[7] palladium powder was used in the synthesis of the $[Cation]_2[Pd_2I_6]$ salts to expedite the current investigation. Characterisation data (UV-VIS absorbances of 340 nm, 450 nm and 540 nm) for the two salts synthesised in the original report,[7] $[N^nBu_4]_2[Pd_2I_6]$ (Table 27, Entry 1) and $[PPh_4]_2[Pd_2I_6]$ (Table 27, Entry 2), were consistent with literature values. The organic cations $[N^nBu_4]^+$ and $[PPh_4]^+$ vary in both

the heteroatom and in the nature of the heteroatomic substituents, *i.e.* aliphatic/aromatic. Thus, the novel aliphatic tetraethylammonium palladium salt (Table 27, Entry 3), a novel aliphatic tetrabutylphosphonium palladium salt (Table 27, Entry 4) and a novel mixed aliphatic-aromatic butyl-triphenylphosphonium palladium salt (Table 27, Entry 5) were also synthesised. These palladium salts were prepared to enable a systematic comparison of the influence of the nature of the organic cation substituents and heteroatom on catalytic activity. Although the iodide salts of tetrabutylphosphonium and butyl-triphenylphosphonium were not readily available, they could be obtained easily by anion metathesis with sodium iodide from the chloride salts in acetone. Unfortunately, tetraphenylammonium salts are not commercially available. Moreover, literature chemical syntheses of tetraphenylammonium salts are laborious and yield the tetrafluoroborate salt $[NPh_4][BF_4]$, which would require further manipulation to obtain the equivalent iodide salt.[38,39] As a result, the synthesis of $[NPh_4]_2[Pd_2I_6]$ was not explored. For each novel salt, characteristic $[Pd_2I_6]^{2-}$ UV-Vis absorptions were observed at λ = 340 nm, 450 nm and 550 nm. The purity of each of the new $[Cation]_2[Pd_2I_6]$ salts was also confirmed by CHN elemental analysis.

Table 27. Synthesis of [Cation]$_2$[Pd$_2$I$_6$] salts from palladium, organic [cation] iodides and iodine.[a, 7]

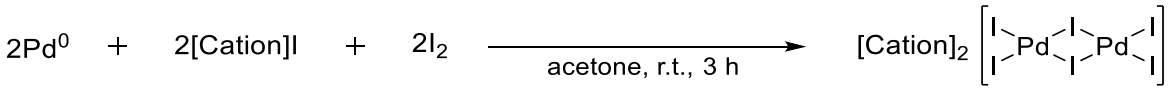

Entry	Cation	Product	Yield (%)
1	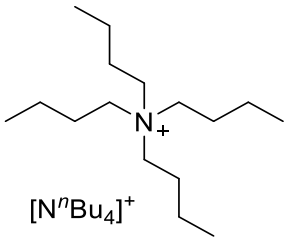 [N^{n}Bu$_4$]$^+$	[N^{n}Bu$_4$]$_2$[Pd$_2$I$_6$]	94
2	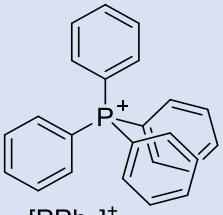 [PPh$_4$]$^+$	[PPh$_4$]$_2$[Pd$_2$I$_6$]	96
3	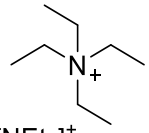 [NEt$_4$]$^+$	[NEt$_4$]$_2$[Pd$_2$I$_6$]	93
4	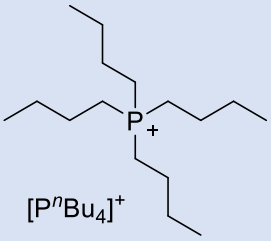 [P^{n}Bu$_4$]$^+$	[P^{n}Bu$_4$]$_2$[Pd$_2$I$_6$]	93
5	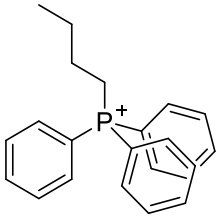 [P(^{n}Bu)Ph$_3$]$^+$	[P(^{n}Bu)PPh$_3$]$_2$[Pd$_2$I$_6$]	95

[a)] When palladium black powder was used in place of palladium metal powder (particle size <1 µm), the reactions were run for 24 h and essentially identical yields were obtained.

3.2.2. Optimisation of the model cross-coupling reaction

Monitoring the progress of the model reaction using ^{1}H NMR analysis was unsuccessful due to a lack of distinct ^{1}H environments for the aryl halide starting material (**1**) and product (**2**). Moreover, concentrating the number of reaction samples required to conduct optimisation and kinetic studies prior to ^{1}H NMR analysis would be significantly time consuming (~30+ min per sample), especially for high boiling point solvents, *e.g.* 1-butanol. Quantitative HPLC is a suitable alternative to NMR spectroscopy, and has many advantages, namely a) all the reaction components (**1**, **2**, **3** and **4**) can be monitored, allowing a mass balance to be determined, b) HPLC, in this case using a HPLC connected to a UV-Vis detector, has a detection limit that is around an order of magnitude higher than ^{1}H NMR spectroscopy, enabling temporal concentration data to be collected from reaction mixtures using considerably smaller aliquot volumes, and c) HPLC sample preparation is rapid as it does not require the sample to be concentrated, which facilities elevated data density for optimisation and kinetic studies. Given these advantages, HPLC methodology was developed and calibration curves constructed for each reaction component (**1**-**4**), using naphthalene as an internal standard (see ESI). This HPLC methodology was used throughout the following body of research to monitor the progress of the cross-coupling reaction to yield **3**. It should be noted that throughout this thesis, the catalyst loading of $[N^{n}Bu_4]_2[Pd_2I_6]$ given in each scheme refers to loading of the palladium dimer and that this value should be doubled to determine the loading of palladium.

When the model cross-coupling reaction was performed under the Suzuki-Miyaura conditions which were previously employed for catalytic $[N^{n}Bu_4]_2[Pd_2I_6]$ (Table 25),[17,18] only 1% **3** was formed, alongside 25% of the boronic acid homo-coupling product **4** (Table 28, Entry 1). Moreover, a palladium black precipitate formed upon heating this reaction mixture (Table 28, Entry 1).

*Table 28. Initial optimisation results for the cross-coupling reaction yielding **3** catalysed by $[N^nBu_4]_2[Pd_2I_6]$.*

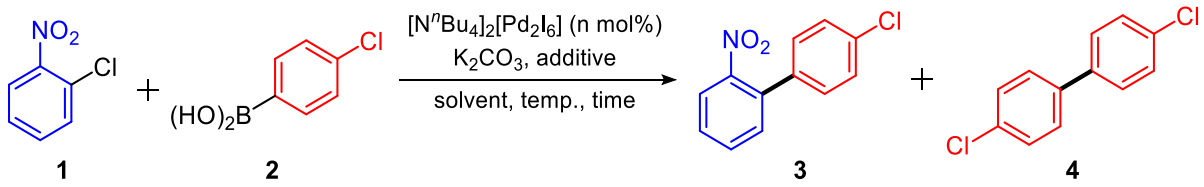

Entry	Conditions[a]					Yield (%)[b]	
	Solvent	Time (h)	Temperature (°C)	$[N^nBu_4]_2[Pd_2I_6]$ loading (mol%)	Additive	**3**	**4**
1[c]	Ethanol	8 h	75	1	none	1	25
2	Ethanol	8 h	75	1	$[N^nBu_4]Br$	10	15
3	Ethylene glycol	8 h	90	1	$[N^nBu_4]Br$	27	23
4	1-butanol	8 h	90	1	$[N^nBu_4]Br$	30	22
5	1-butanol	8 h	90	2	$[N^nBu_4]Br$	19	40
6	1-butanol	8 h	90	0.5	$[N^nBu_4]Br$	48	14
7	1-butanol	8 h	90	0.1	$[N^nBu_4]Br$	64	15

[a] All reactions were run in the presence of K_2CO_3 (1.5 equiv.) and **2** (1.1 equivalents). [b] All yields were determined by HPLC analysis with respect to naphthalene as an internal standard. Yields of **4** are calculated with respect to the theoretical yield from the reaction of two molecules of **2**. [c] A palladium black precipitate was formed immediately upon the heating of the reaction mixture.

Palladium black is generally considered to be a catalytic 'dead end', owing to the formation of catalytically inactive and insoluble Pd^0 aggregates. It is noteworthy though that palladium black remained active as a catalyst for the formation of **4**, which may be due to its propensity to form PdO_2 which can then undergo two transmetallation events with **2** and subsequent reductive elimination to form **4**.[40] The inclusion of one equivalent of tetrabutylammonium bromide ($[N^nBu_4]Br$), an additive known to stabilise $[Pd^0]$ as colloidal nanoparticles,[41–47] provided an improvement in the yield (10%) and selectivity for the formation of **3** (Table 28, Entry 2). The inclusion of tetrabutylammonium bromide also significantly reduced the amount of visible Pd^0 black formed upon the addition of the catalyst. Several other reaction solvents with higher boiling points than ethanol were subsequently

explored at elevated reaction temperatures. Both ethylene glycol (Table 28, Entry 3) and 1-butanol (Table 28, Entry 4) provided a considerable improvement on the outcome of the reaction at 90 °C, and 1-butanol was chosen given its favourable properties as a 'green' solvent.[30,31] As the catalyst loading was increased, a drop in the yield and selectivity for the formation of **3** was observed (Table 28, Entry 5). Thus, improved yields of **3** were obtained by lowering the catalyst loading (Table 28, Entry 6-7). The best yield was obtained during initial optimisation studies under the lowest explored catalyst loading of 0.1 mol% (Table 28, Entry 7). When $[PPh_4]_2[Pd_2I_6]$ was used as a precatalyst under these conditions (Table 28, Entry 7), a significantly reduced yield of **3** of 25% was obtained. This result is especially striking given that $[N^nBu_4]^+$ cations are present from $[N^nBu_4]Br$ in excess when compared to the precatalyst $[PPh_4]^+$ cations. The precatalyst $[PPh_4]_2[Pd_2I_6]$ was not explored further during optimisation studies. The influence of the different precatalyst cations will be reported during kinetic and mechanistic studies (*vide infra*, Chapter Four).

The non-linear influence of $[N^nBu_4]_2[Pd_2I_6]$ loading on the yield and selectivity of the cross-coupling reaction yielding **3** led to the use of a Design of Experiments (DoE) approach to determine the optimum reaction conditions. A definitive screening design (DSD) was chosen to model the cross-coupling yielding **3**, since DSDs are capable of revealing the presence of any second order and interacting variable effects.[48–50] Variables and their limits are outlined in Table 29 and the ranges were chosen based on previous experimental results. The upper limit of the catalyst loading was chosen following previous experiments which found that a loading of 0.1 mol% provided an improved but non-optimum catalytic performance, whilst increasing the loading beyond 0.1% only resulted in a reduction in the yield of **3**. Similarly, the time range of 30-120 min was chosen following previous experiments which revealed that the catalyst precipitated as palladium black at 0.1 mol% around the 1 h mark. Finally, since potassium carbonate is insoluble in 1-butanol, the influence of water as a cosolvent in the DoE was included to probe if the reaction yield could be improved by improving the solubility of the base.

Table 29.Reaction variables included in the DoE optimisation of the model cross-coupling reaction.[a]

Variable	Minimum	Maximum
$[N^nBu_4]_2[Pd_2I_6]$ loading (mol%)	0.01	0.1
Time (min)	30	120
Concentration (M)	0.5	0.7
Solvent water composition (%/*v*)	0	25

[a)] All reactions were run in 1-butanol at 90 °C in the presence of K_2CO_3 (1.5 equiv.), **2** (1.1 equivalents) and $[N^nBu_4]Br$ (1 equiv.).

The complete set of DoE experiments and results are provided in Table 30.

*Table 30. Definitive screening design predictive model for the cross-coupling yielding **3** catalysed by $[N^nBu_4]_2[Pd_2I_6]$ – Experiments performed for the definitive screening design and the corresponding yields of **3**.[a]*

$[N^nBu_4]_2[Pd_2I_6]$ loading (mol%)	Concentration (M)	Water composition (%/*v*)	Time (min)	Yield of **3** (%)[b]
0.055	0.5	0	30	71
0.1	0.7	0	30	65
0.055	0.6	12.5	75	59
0.01	0.6	0	30	30
0.055	0.7	25	120	63
0.1	0.5	12.5	120	58
0.01	0.7	0	120	89
0.1	0.6	25	120	44
0.1	0.7	0	120	62
0.01	0.7	25	75	32
0.01	0.7	12.5	30	20
0.01	0.5	25	120	51
0.1	0.5	0	75	73
0.1	0.5	25	30	44
0.1	0.7	25	30	47
0.01	0.5	0	120	78
0.01	0.5	25	30	12

[a)] All reactions were run in 1-butanol at 90 °C in the presence of K_2CO_3 (1.5 equiv.), **2** (1.1 equivalents) and$[N^nBu_4]Br$ (1 equiv.). [b)] Yields were determined by HPLC with reference to naphthalene as an internal standard.

The plot of experimental yields of **3** vs predicted yields of **3** (Figure 32) illustrates that the DoE model provided an accurate prediction of the experimental results.

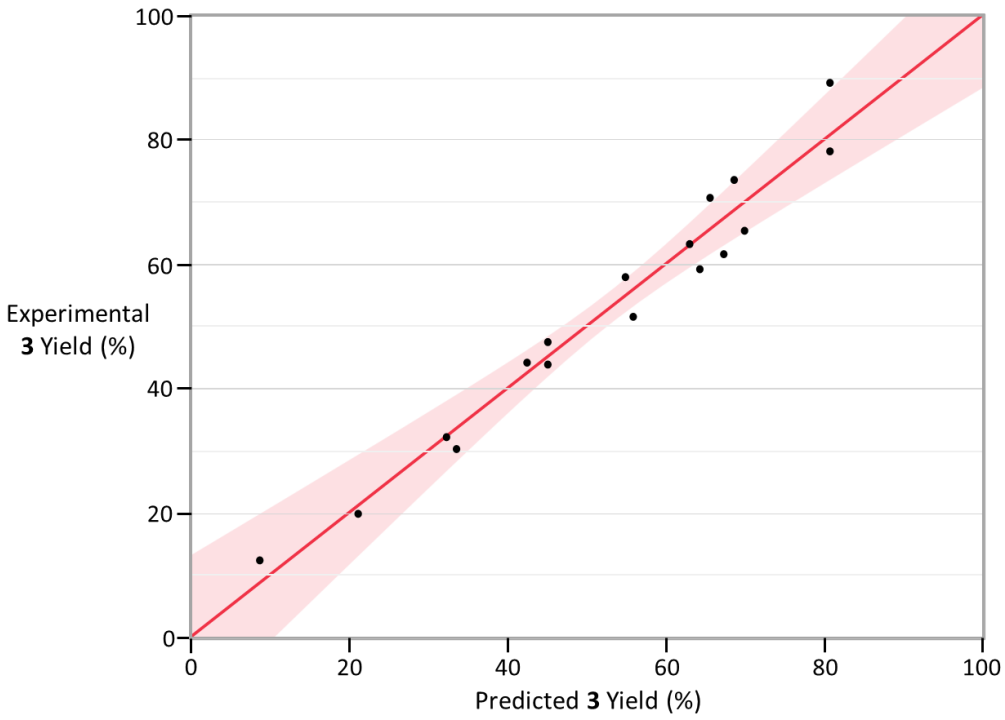

*Figure 32. Definitive screening design predictive model for the cross-coupling yielding **3** catalysed by $[N^nBu_4]_2[Pd_2I_6]$ – Actual vs predicted cross-coupling yield. Root-mean-square error = 4.9646; R^2 = 0.96.*

Table 31 illustrates that the solvent water composition had the largest influence on the outcome of the reaction (Table 31, Entry 1), with the lowest water content (0%/*v*) providing the best catalyst performance. The concentration of the reaction was not found to have a significant influence on the reaction outcome. A concentration of 0.7 M was chosen as the 'optimum' value for the environmental benefits of using a more concentrated reaction mixture.

*Table 31. Definitive screening design predictive model for the cross-coupling yielding **3** catalysed by $[N^nBu_4]_2[Pd_2I_6]$ – The reaction variables included in the model and their relative importance ('LogWorth' depicted numerically and visually).*

Entry	Variable (range)	LogWorth[a]	
1	Solvent Water Composition (0 %/*v*, 25%/*v*)	5.847	
2	Catalyst Loading*Time	5.527	
3	Time (30 min,120 min)	4.524	
4	Catalyst Loading*Catalyst Loading	2.958	
5	Catalyst Loading (0.01 mol%, 0.1 mol%)	2.806	

[a] LogWorth = –log(P), represents truncated p values which are used to statistically define relative variable importance.

The DoE model also contained a significant two-factor interaction between time and catalyst loading (Table 31, Entry 2). This variable interaction is illustrated by the change in the slope of the catalyst loading and time profiles as these variables are changed (Figure 33a and Figure 33b). Upper loadings (e.g. 0.1 mol%) provided essentially identical yields of **3** after both 30 and 120 min (~60% at 0.1 mol%, Figure 33a), which is indicative of catalyst deactivation occurring before 30 min. This catalyst deactivation was not observed at lower catalyst loadings (e.g. 0.01 mol%, Figure 33b), with these lower loadings providing lower initial yields (34% after 30 min at 0.01 mol%, Figure 33b), but also providing a more stable catalyst which was able to achieve improved yields after extended reaction times (81% after 120 min at 0.01 mol%, Figure 33b).

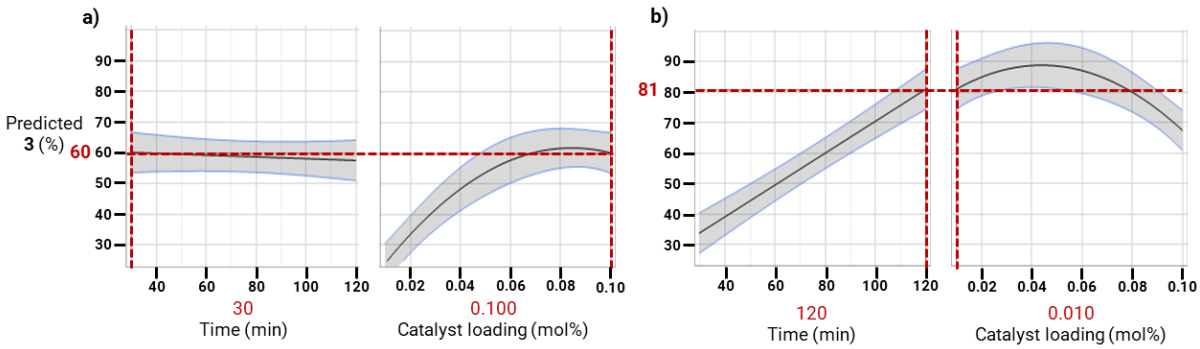

*Figure 33. Definitive screening design predictive model for the cross-coupling yielding **3** catalysed by $[N^nBu_4]_2[Pd_2I_6]$ – Variable profiles for the predicted yield of **3** at: a) 30 min and 0.100 mol% catalyst loading, b) 120 min and 0.010 mol% catalyst loading.*

Ultimately, a balance between improved reaction rates at elevated catalyst loadings and improved catalyst stability at lower catalyst loadings was uncovered at 0.044 mol% (Figure 34c). The surface plot in Figure 34a and Figure 34b provides a 3D representation of the interacting and non-linear time/catalyst loading variables, and the global maximum for the optimum catalyst loading at 0.044 mol%. The profile in Figure 34c illustrates the optimum catalyst loading at 0.044 mol% of $[N^nBu_4]_2[Pd_2I_6]$.

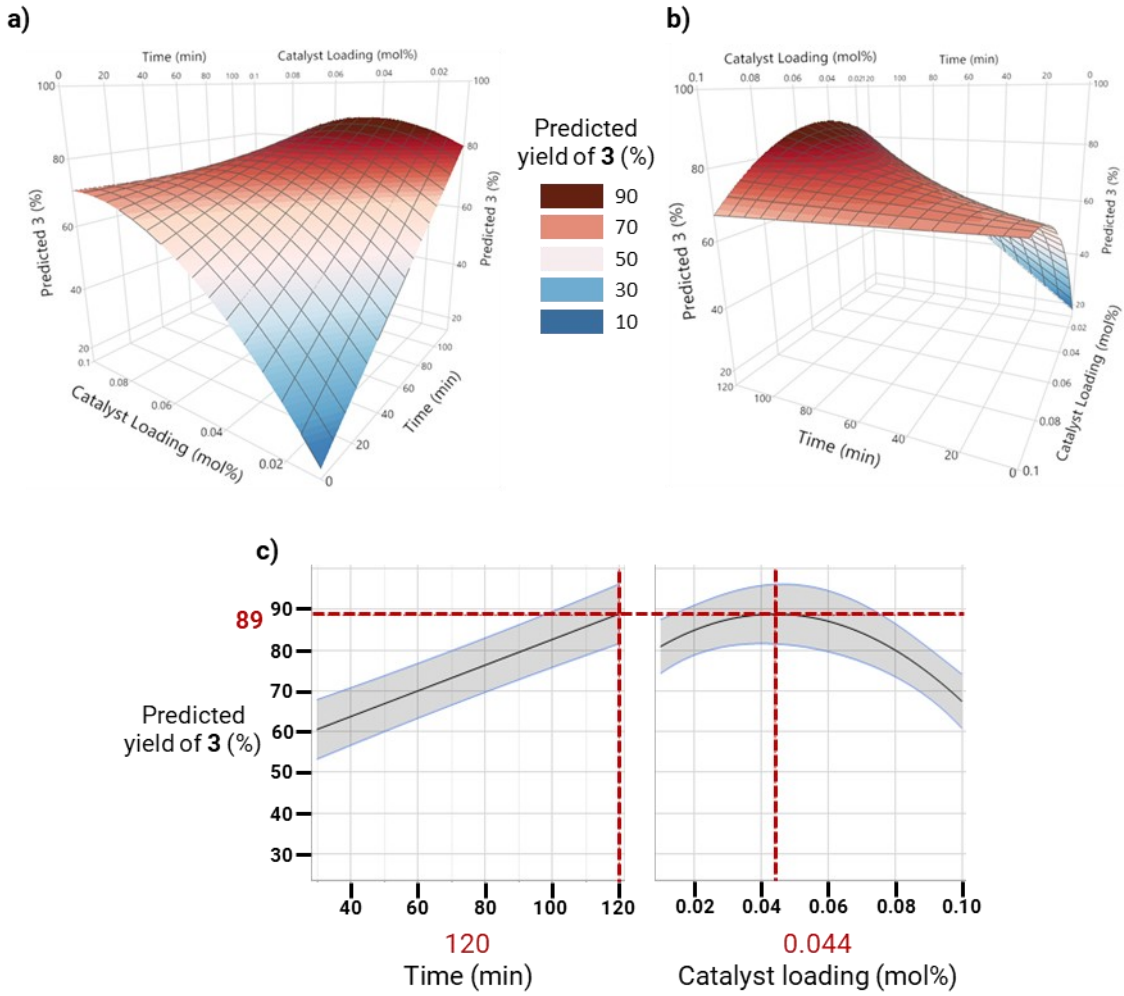

*Figure 34. Definitive screening design predictive model for the cross-coupling yielding **3** catalysed by $[N^nBu_4]_2[Pd_2I_6]$ – a) and b) Surface plot of the influence of time and catalyst loading on the yield of **3**, c) Variable profile illustrating the optimum catalyst loading.*

The observed loading dependent catalyst deactivation can be rationalised by considering the aggregation of $[Pd^0]$ (Scheme 71).

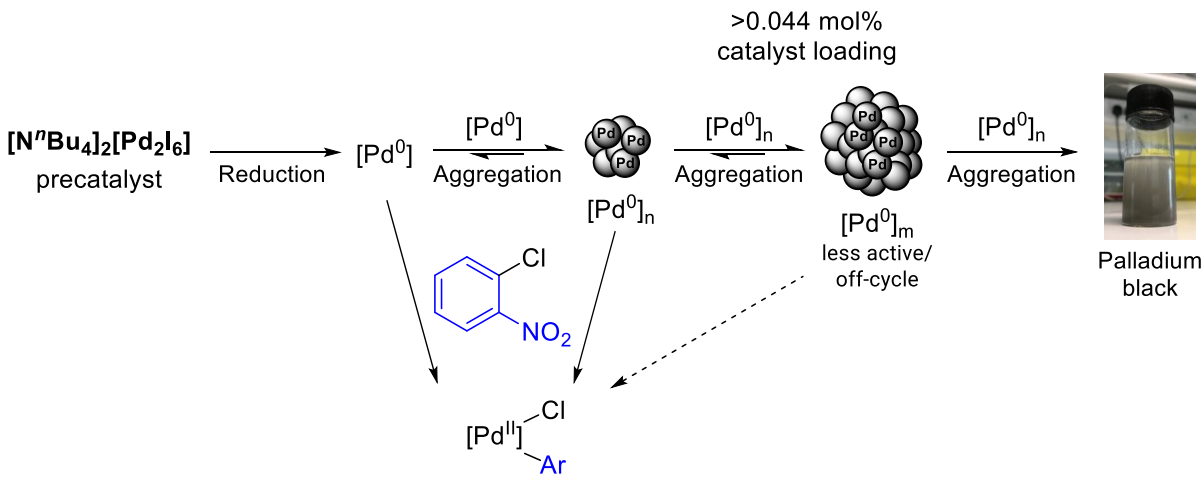

*Scheme 71. Mechanistic rationalisation for the non-linear and influence of catalyst loading on the predicted yields of **3**.*

This mechanism, and its influence on the DoE model, can also be rationalised using simplified rate equations (Equation 1 and Equation 2). The order of the aggregation reaction in [**Pd**], *x* (Equation 2), is inherently greater than the order in [**Pd**] for oxidative addition, *y* (Equation 1), *i.e.* x > y for:

$$rate\ oxidative\ addition = k_1 \cdot [\boldsymbol{ArCl}]^n \cdot [\boldsymbol{Pd}]^y$$

Equation 1

$$rate\ aggregation = k_2 \cdot [\boldsymbol{Pd}]^x$$

Equation 2

Since x > y, increasing the palladium concentration will speed up the rate of aggregation of [**Pd^0**] to a greater extent than it will increase the rate of oxidative addition. Assuming a non-zero order in aryl chloride, the relative oxidative addition/aggregation rate will also depend on the relative aryl chloride and palladium concentrations, as illustrated in Equation 3.

$$\frac{rate\ oxidative\ addition}{rate\ aggregation} = \frac{k_1 \cdot [\boldsymbol{ArCl}]^n}{k_2 \cdot [\boldsymbol{Pd}]^{x-y}}$$

Equation 3

The relative rate depicted in Equation 3 dictates the aryl chloride concentration, and thus the reaction time point, at which aggregation dominates and the catalyst deactivates as palladium black. This consideration contributes to the significant time*catalyst loading term in the DoE model – as the palladium concentration is increased, the concentration in the aryl chloride at which palladium aggregation becomes favourable increases, and thus the catalyst aggregates and deactivates earlier

in the reaction at higher catalyst loadings. The extreme of this effect was observed upon the addition of $[N^nBu_4]_2[Pd_2I_6]$ into the reaction in the absence of **1**, *i.e.* [**ArCl**] = 0, which resulted in the instantaneous precipitation of palladium black. Similarly, palladium black forms at the end of the reaction when the majority (>98%) of the aryl chloride has been consumed. Aggregation-induced catalyst deactivation of palladium has been previously reported,[51–57] although this is the first time it has been modelled using DoE. The speciation of active/inactive $[Pd^0]$ at different catalyst loadings will be explored further during the kinetic and mechanistic studies (*vide infra*, Chapter Four).

It should be noted that whilst the postulated mechanism in Scheme 71 is consistent with the DoE model, there may be other important considerations or explanations for the influence of the catalyst loading on the DoE model, *e.g.* H_2O and O_2 impurities. Further studies investigating the speciation of $[Pd^0]$ are outlined in Chapter Four.

Additional validation of the predictive power of the DoE model was provided by performing reactions under the conditions predicted to provide both the best (Table 32, Entry 1) and lowest yields of **3** (Table 32, Entry 2). Good agreement between the experimental and predicted yields were obtained (Table 32). Some small variability in the yields (>95-98%) obtained under the optimum conditions was observed (Table 32, Entry 1), and the experimental yields obtained under the optimum conditions were consistently larger than those predicted by the model (Table 32, Entry 1).

*Table 32. Definitive screening design predictive model validation – Comparison of the experimental and predicted yields for the conditions modelled to provide the best (Entry 1) and lowest (Entry 2) yields of **3**.*

	Conditions[a]			Yield **3** (%)[b]	
Entry	Solvent H_2O composition (%/*v*)	Catalyst Loading (mol%)	Time (min)	Experimental	Predicted
1	0	0.044	120	95-99+	89
2	25	0.010	30	12	9

[a)] All reactions were run in 1-butanol (0.7 M) at 90 °C in the presence of K_2CO_3 (1.5 equiv.), **2** (1.1 equivalents) and $[N^nBu_4]Br$ (1 equiv.). [b)] Yields determined by HPLC with reference to naphthalene as an internal standard.

To enable a direct comparison of the catalytic performance of $[N^nBu_4]_2[Pd_2I_6]$ with two typical 'off-the-shelf' phosphine-based palladium catalysts, namely $PdCl_2(PPh_3)_2/2PPh_3$ and $Pd(OAc)_2/2PPh_3$, these two phosphine-based catalyst systems were optimised using an identical DoE strategy as was employed above for $[N^nBu_4]_2[Pd_2I_6]$. Unlike $[N^nBu_4]_2[Pd_2I_6]$, the two phosphine-based palladium

complexes exhibited a positive linear influence of their loading on the yield of **3**, with the highest explored catalyst loading (0.2 mol%) providing the best catalyst performance. Variable profiles for $Pd(OAc)_2/2PPh_3$ are provided in Figure 35, and the predicted optimum conditions for both $PdCl_2(PPh_3)_2/2PPh_3$ and $Pd(OAc)_2/2PPh_3$ were identical.

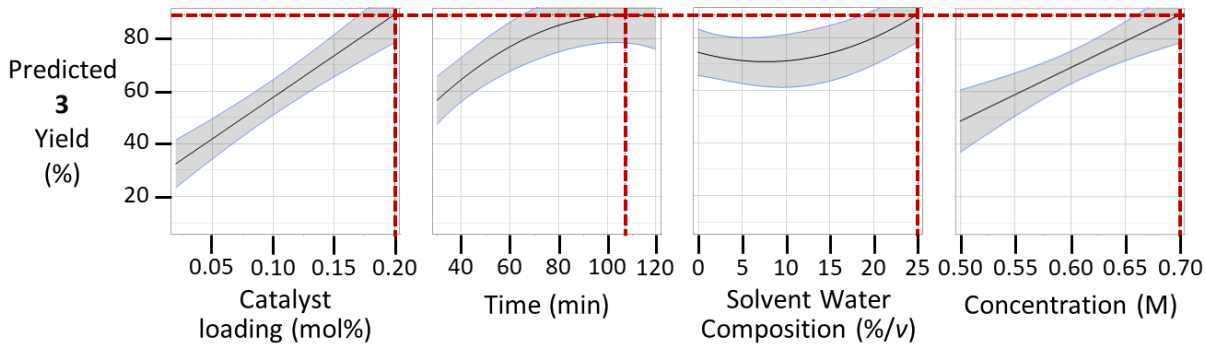

*Figure 35. Definitive screening design predictive model for the cross-coupling yielding **3** catalysed by $Pd(OAc)_2/2PPh_3$ – Variable profiles illustrating the reaction conditions predicted to provide the optimum yield of **3** (PPh_3 loadings in mol% are twice that of the catalyst loading).*

Assuming that the catalyst deactivation that was observed for $[N^nBu_4]_2[Pd_2I_6]$ was the result of aggregation of $[Pd^0]$, then the presence of phosphine ligands in $PdCl_2(PPh_3)_2/2PPh_3$ and $Pd(OAc)_2/2PPh_3$ must stabilise $[Pd^0]$ and enable access to higher loadings without aggregation induced catalyst deactivation (Scheme 72).

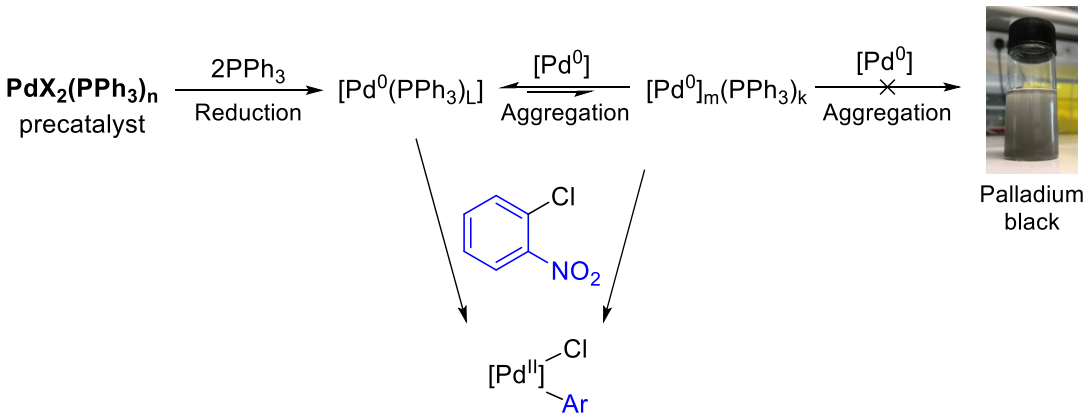

Scheme 72. Modified and simplified mechanism for the aggregation of $[Pd^0]$ in the presence of phosphine ligands. (For $PdCl_2(PPh_3)_2$, X = Cl and n = 2, for $Pd(OAc)_2$, X = OAc and n = 0).

In reality, the speciation of the active catalyst is likely very different for these two different precatalyst systems.[42,58,59] For example, it has been demonstrated that the combination of $Pd(OAc)_2$ and $2PPh_3$

results in the speciation of a dinuclear palladium(I) complex, albeit under different reaction conditions to those explored here.[60] Even if that is the case for the conditions utilised here, differences in the influence of the catalyst loading on the DoE models for $[N^nBu_4]_2[Pd_2I_6]$, $2PPh_3/Pd(OAc)_2$ and $PdCl_2(PPh_3)_2/2PPh_3$ demonstrates that the latter two precatalysts systems speciate into active catalysts with improved stability at elevated catalyst concentrations when compared to the species formed from $[N^nBu_4]_2[Pd_2I_6]$, regardless of the exact nature (*e.g.* dimeric or trimeric) of the species that is formed. No effort was made herein to better understand the speciation of Pd^0 from either $Pd(OAc)_2/2PPh_3$ or $PdCl_2(PPh_3)_2/2PPh_3$.

It should also be noted that whilst the use of phosphine ligands with $Pd(OAc)_2/PdCl_2(PPh_3)_2$ did enable access to higher catalyst loadings, preventing aggregation of Pd^0 may ultimately have a deleterious effect on the performance of the catalyst. More optimised conditions could be envisaged for these phosphine-based catalysts which utilise reduced phosphine loadings, however this was not explored.

3.2.3. Model reaction catalyst performance comparison

The performances of $[N^nBu_4]_2[Pd_2I_6]$ and two 'off-the-shelf' phosphine-based precatalysts, $PdCl_2(PPh_3)_2/2PPh_3$ and $Pd(OAc)_2/2PPh_3$, in the cross-coupling reaction to yield **3** were compared. In each case, *in situ* ReactIR profiles were used to monitor the formation of **3**, and the ReactIR profiles calibrated *ex situ* using HPLC (Figure 36). The conditions employed for each palladium catalyst comes from the DoE models presented previously (Section 3.2.2).

*Table 33. Comparison of the performance of three different palladium precatalysts in the cross-coupling to yield **3**.[a]*

Catalyst	Conditions		Performance			
	Solvent H_2O composition (%/*v*)	Catalyst Loading (mol%)[b]	Yield **3** (%)[d]	Yield **4** (%)[d]	TON[d]	TOF[e] (h^{-1})
$[N^nBu_4]_2[Pd_2I_6]$[c]	0	0.044	99	<1	1125	1227
$Pd(OAc)_2/2PPh_3$	25	0.200	87	7	435	261
$PdCl_2(PPh_3)_2/2PPh_3$	25	0.200	90	6	495	297

[a)] All reactions were run in 1-butanol (0.7 M of **1**) at 90 °C in the presence of K_2CO_3 (1.5 equiv.), **2** (1.1 equivalents). [b)] Catalyst loading refers to the loading of the palladium precatalyst (*i.e.* for $Pd(OAc)_2/2PPh_3$, 0.2 mol%: [Pd] = 0.2 mol% and $[PPh_3]$ = 0.4 mol%). [c)] Run in the presence of $[N^nBu_4]Br$ (1 equiv.) and KBr (2 equiv.) [d)] Yields were determined by HPLC with reference to naphthalene as an internal standard. [d)] TON = mol **3**/mol [Pd]. [e)] TOF (h^{-1}) = TON/t (h).

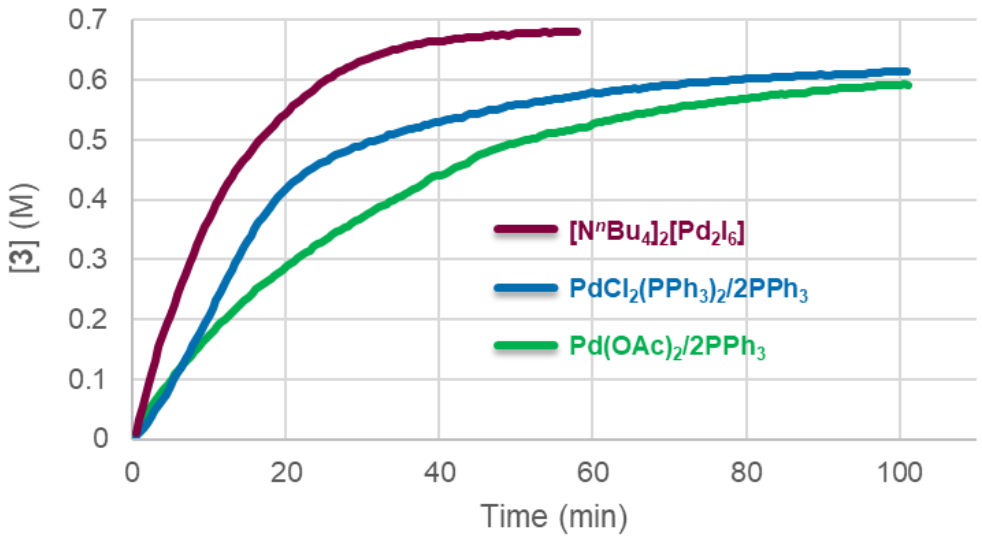

*Figure 36. Temporal concentration profile for the model cross-coupling to yield **3**, catalysed by three different palladium precatalysts. Data obtained by in situ ReactIR and calibrated offline by HPLC*

Comparison of the temporal concentration profiles in Figure 36 and the metrics in Table 33 illustrates the improved performance of [N^{n}Bu$_4$]$_2$[Pd$_2$I$_6$], especially when considering the differences in palladium loading. It should be noted that the TONs and TOFs presented in Table 33 do not account for differences in catalyst speciation or the number of active sites between the three precatalysts, and instead provide a simple comparison of the ratio of product to [Pd] loading. The comparison presented herein is also not meant to establish [N^{n}Bu$_4$]$_2$[Pd$_2$I$_6$] as the best performing palladium catalyst for the model reaction. Instead, the comparison illustrates that the performance is at least comparable or, for the examples explored herein, better than typical phosphine-containing palladium complexes. Indeed, there are numerous literature catalysts which have been utilised which provide improved performance when compared to [N^{n}Bu$_4$]$_2$[Pd$_2$I$_6$] (Table 26). For example, catalyst systems **5** and **6** (Table 26) both provide significantly improved performance when compared to [N^{n}Bu$_4$]$_2$[Pd$_2$I$_6$]. It is notable that the complex *N*-heterocyclic carbene palladium complex **7** provides very similar performance to [N^{n}Bu$_4$]$_2$[Pd$_2$I$_6$], albeit under slightly milder reaction conditions (Table 26, Catalyst **7**). Consideration should be made however for the multi-step synthesis of many of the ligands and palladium compounds illustrated in Table 26, which can diminish the sustainability of these catalysts, especially with respect to palladium consumption.[61] Moreover, most bench-scale research chemists will reach for 'off-the-shelf' combinations of palladium precatalysts and phosphine ligands, *e.g.* **8** and **9**, and will not conduct the multi-step synthetic routes necessary for the synthesis of the ligands and metal centres in complexes **5**-**7**. Finally, the literature complexes summarised in Table 26 are necessarily dependent on unsustainable supplies of palladium from mining.

3.2.4. Model reaction process design

With the principles of a circular economy and elemental sustainability in mind, the development of a full process design for the model reaction catalysed by $[N^nBu_4]_2[Pd_2I_6]$ was explored. Desirable features of an ideal process design include the recycling of the catalyst material, the recycling of the tetrabutylammonium salt additive, and a chromatography-free procedure for isolating **3**.

3.2.4.1. Catalyst recycling

Palladium black formed at the end of the $[N^nBu_4]_2[Pd_2I_6]$-catalysed reaction to yield **3**. This precipitate, which presumably is a mixture of Pd^0 metal and PdO_2, is insoluble in neutral water and organic solvents and can thus be easily purified by washing with water and ethanol following its isolation by filtration. The resulting palladium powder, which was free from any organic contaminants by ^{1}H NMR and HPLC analyses, was utilised as a catalyst for the cross-coupling reaction to provide **3** (Table 34, Entry 1).

Table 34. Application of palladium recovered from a model reaction as a catalyst in a second run.[a]

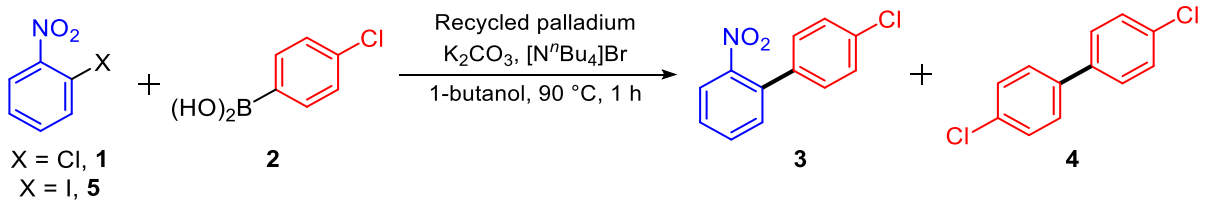

Entry	X	Recycled palladium[b]	Yield (%)[c] **3**	Yield (%)[c] **4**
1[c]	Cl	Palladium black	0	15
2	Cl	$[N^nBu_4]_2[Pd_2I_6]$[d]	99	1
3	I	Palladium black	100	1

[a)] All reactions were run in the presence of $[N^nBu_4]Br$ (1 equiv.), K_2CO_3 (1.5 equiv.) and **2** (1.1 equivalents) in 1-butanol (0.7 M of **1**) at 90 °C. Recycled palladium refers to palladium black which was isolated by filtration and washed from a previous model reaction. [b)] Loadings of palladium black were unknown, but were <0.088 mol% [c)] All yields were determined by HPLC analysis with respect to naphthalene as an internal standard. Yields of **4** are calculated with respect to the theoretical yield from the reaction of two molecules of **2**. [d] Since only 81% $[N^nBu_4]_2[Pd_2I_6]$ was recovered, the reaction was scaled down so that recycled $[N^nBu_4]_2[Pd_2I_6]$ was used in a 0.044 mol% loading.

The recovered palladium black powder was found to be inactive as a catalyst in the model reaction (Table 34, Entry 1). Treating this palladium black powder with tetrabutylammonium iodide and iodide, under identical conditions to those used recycle $[N^nBu_4]_2[Pd_2I_6]$ from TWCs (Table 24, Table 27), resulted in the formation of $[N^nBu_4]_2[Pd_2I_6]$ in an 81% yield. The 19% loss in yield was likely in part to

be the result of loss of palladium to the pores of the filter funnel during filtration. The structure and purity of $[N^nBu_4]_2[Pd_2I_6]$ recycled from palladium black from a model reaction was confirmed by single crystal X-ray diffraction, CHN elemental analysis, UV-Vis spectroscopy and melting point analyses. These analytical results confirm that other cations and anions, especially potassium,[7] were either not present in the washed palladium black precipitate or did not interfere with the reaction of palladium black with $[N^nBu_4]I$ and I_2. Crucially, this recycled sample of $[N^nBu_4]_2[Pd_2I_6]$ provided identical catalytic performance when compared to a sample synthesised from commercial palladium metal powder (Table 34, Entry 2).

When the model reaction was conducted with an equivalent aryl iodide (**5**) in place of **1**, recycled palladium black dissolved and **3** was obtained in a 100% yield (Table 34, Entry 3). This result illustrates that the Ar–I bond in **5** is sufficiently reactive for palladium black to undergo oxidative addition to the Ar–I bond. Attempts were then made to exploit this chemistry to recycle palladium black in subsequent runs. It was suggested that, if palladium black is oxidised by **5** to form a soluble Pd^{2+} oxidative addition product, Ar–$[Pd^{II}]$–I, then a catalytic quantity of **5** could be included alongside **1** in subsequent runs to 'reactivate' and dissolve palladium black (Scheme 73) for reaction with **1**.

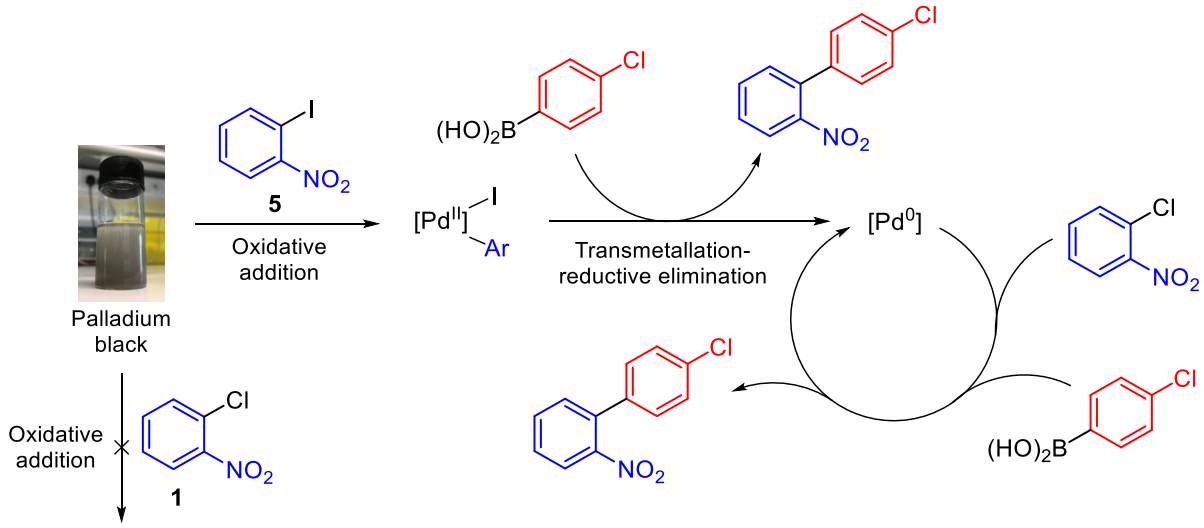

*Scheme 73. Mechanistic rationale for the 'reactivation' of palladium black by catalytic aryl iodide (**5**).*

To test this rationale, the synthesis of **3** was performed (Figure 37, Blue) using fresh aryl chloride **1** (0.9 equiv.), aryl boronic acid **2** (1.1 equiv.) and K_2CO_3 (1.5 equiv.) added directly into the mixture at the end of the first run (Figure 37, Orange). No formation of **3** was observed on addition of fresh **1** and **2**. Aryl iodide (**5**, 0.1 equiv.) was subsequently added to the same reaction mixture, which resulted in the formation of **3** in a 35% yield after 60 min (Figure 37, Green).

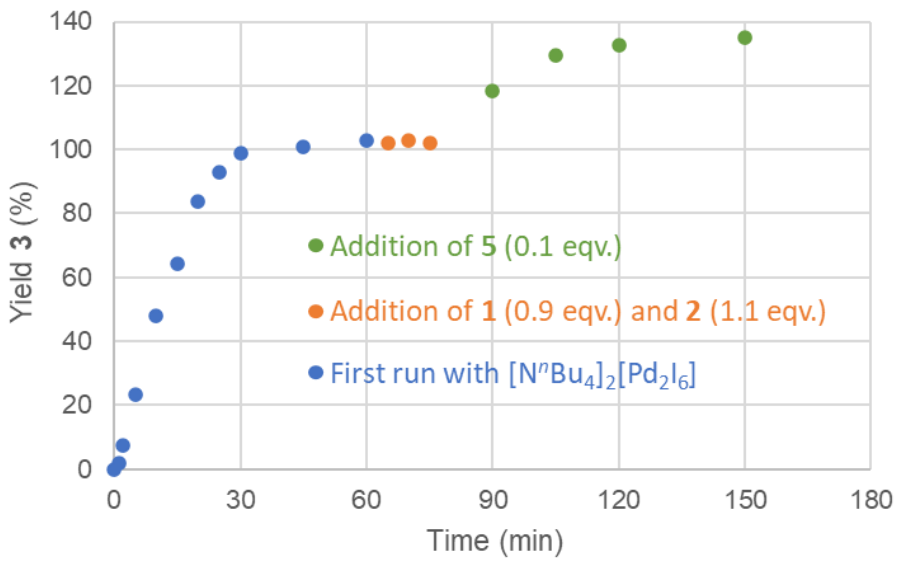

*Figure 37. Attempt at 'reactivating' palladium black from a model reaction run by the addition of catalytic aryl iodide (**5**). Blue: Model reaction catalysed by [N^{n}Bu$_4$]$_2$[Pd$_2$I$_6$] (0.044 mol%). Orange: Addition of fresh **1** (0.9 equiv.), **2** (1.1 equiv.) and K_2CO_3 (1. equiv.) to the completed model reaction mixture (blue). Green: Addition of **5** (0.1 equiv., 10 mol%) to the completed model reaction mixture containing fresh **1** reagents. All reactions were conducted in 1-butanol at 90 °C in the presence of [N^{n}Bu$_4$]Br (1 equiv.).*

The formation of **3** in a 35% yield is greater than the maximum amount of 10% that could be formed from the aryl iodide (**5**) alone. Thus, **5** must have reactivated palladium black toward reaction with **1**.

Although some consumption of **1** did occur, it was limited to 25%. It is likely that not all of the palladium black would be immediately oxidised and dissolved to form Ar–[Pd^{II}]–I, and any mononuclear Pd^0 atoms released from the turnover of palladium black with **5** would be redeposited onto bulk palladium black. Thus, a reaction was performed with pre-stirring of **5** (0.1 equiv.) at 90 °C for 10 min prior to the addition of fresh **1** (0.9 equiv.), **2** (1.1 equiv.) and K_2CO_3 (1.5 equiv.) to ensure that all of the palladium black powder had dissolved. This reaction would in principle be initiated by the reduction of 'precatalytic' Ar–[Pd^{II}]–I to Pd^0. However, **3** was formed in a 45% yield, which is only a marginal improvement to the case when **5** was added last (35%). Unfortunately, 45% was the best yield obtained, regardless of the order of addition of the reagents or when the palladium black powder was isolated prior to its reactivation with **5**. Since palladium black powder could be recycled back to [N^{n}Bu$_4$]$_2$[Pd$_2$I$_6$], the use of **5** to reactivate palladium black was not explored further.

3.2.4.2. Recovery and reuse of tetrabutylammonium bromide

The necessity for a stoichiometric quantity (100 mol%) of tetrabutylammonium bromide as an additive reduces the advantages of [N^{n}Bu$_4$]$_2$[Pd$_2$I$_6$] as a 'designer' ligand-free precatalyst. However,

previous work has illustrated that [N^{n}Bu$_4$]Br can be partitioned into water from a number of organic solvents, and can be partitioned into 1-butanol from water.[62] It should therefore be possible to develop a procedure for recycling [N^{n}Bu$_4$]Br directly into 1-butanol for reuse in subsequent reaction runs.

Attempts at extracting [N^{n}Bu$_4$]Br from the crude reaction mixture into water were unsuccessful (Table 35). In each case, the crude reaction material was concentrated, redissolved in an organic solvent and subsequently extracted with water. Table 35 illustrates the percentage of [N^{n}Bu$_4$]Br which partitioned into the organic solvent, with comparisons made to literature values.[62]

Table 35. Partitioning of [N^{n}Bu$_4$]Br into various organic solvents upon extraction with water.[a]

Entry	Organic solvent	Literature partition (%)[b]	Partition for reaction crude (%)[c]
1	Me-THF	2	15
2	Methyl isobutyl ketone	5	12
3	^{i}Pr-OAc	1	10
4	Toluene	3	14
5	Heptane	0	7

[a)] For each entry, a model reaction run was concentrated, redissolved in the indicated organic solvent and subsequently extracted into water. % indicate the proportion of [N^{n}Bu$_4$]Br which partitioned into the organic solvent. [b)] Literature values were reported for pure [N^{n}Bu$_4$]Br in reference 58. [c)] Partitions were calculated by ^{1}H NMR spectroscopy with respect to trimethoxybenzene as an internal standard.

In each case, [N^{n}Bu$_4$]Br partitioned into the organic layer to a significantly greater degree than was reported in the literature for pure [N^{n}Bu$_4$]Br.[62] At the end of the cross-coupling reaction to provide **3**, a broad mixture of anions will be present, including chloride, butoxide, hydroxide, carbonate, borates and the boronate anion of **2**. Each of the tetrabutylammonium salts of these anions may partition into the organic layer to a greater extent than was expected for pure [N^{n}Bu$_4$]Br.

Whilst anion impurity will influence partitioning into an organic solvent, each of the tetrabutylammonium salts of the above anions will be highly soluble in water. This led to the development of a strategy free from organic solvents. Concentration of the crude reaction mixture and the addition of water to the neat oil resulted in the extraction of 95-100% (range reported for 3 attempts) of the tetrabutylammonium content. Moreover, extracting the tetrabutylammonium content from the neat crude oil into water also resulted in the precipitation of **3** as a crystalline solid in a 79% isolated yield. This solid (**3**) was isolated by filtration and found to be pure (~95-98% by ^{1}H

NMR and HPLC analysis), and the melting point was consistent with literature data.[17] Finally, the aqueous filtrate containing the tetrabutylammonium salts was extracted three times with fresh 1-butanol, which resulted in the recovery of 95% of the tetrabutylammonium salts (determined by ^{1}H NMR analysis with respect to trimethoxybenzene as an external standard). The organic content of the resulting tetrabutylammonium salts was found to be analytically pure by ^{1}H NMR and HPLC analyses (Table 36, Entry 1).

Table 36. Recovery of the tetrabutylammonium salts from the model reaction mixture and subsequent analytical results.

Entry	Sample	^{1}H NMR	HPLC	Melting point (°C)
1	Recovered $[N^{n}Bu_4]X$	>99% pure	>99% pure	83-93
2	Authentic $[N^{n}Bu_4]Br$	-	-	102-103
3	Authentic $[N^{n}Bu_4]Cl$	-	-	82-86

The observed melting point (Table 36, Entry 1) is closer to that of the chloride salt (Table 36, Entry 3), and was well below the expected melting point for authentic tetrabutylammonium bromide (Table 36, Entry 2). Given the ^{1}H NMR and HPLC analytical results, these differences in melting point are presumably the result of impurities in the anion content of the isolated tetrabutylammonium salt. Nevertheless, the 1-butanol solution of recovered $[N^{n}Bu_4]^{+}X$ salts was used directly in subsequent process design studies (Section 3.2.4.3).

3.2.4.3. Unified work-up and recycling procedures

Scheme 74 summarises the steps in the full process design outlined thus far for the model cross-coupling reaction.

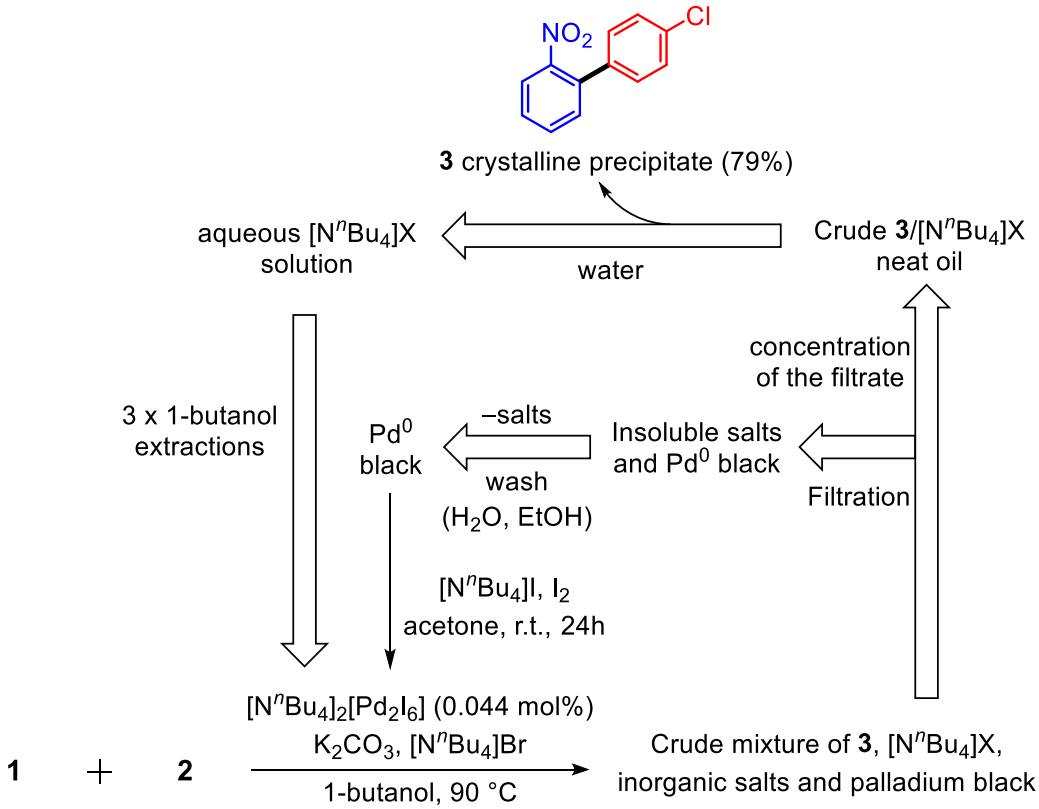

Scheme 74. Full process design for the model cross-coupling reaction, including catalyst recycling, additive recycling and product isolation. Solid arrows indicate chemical reactions and hollow arrows indicate physical manipulations, e.g. filtration, extraction and concentration as indicated.

The work-up, catalyst and tetrabutylammonium recycling procedures were unified and kinetic profiles obtained on a 0.5 mole scale (78.88 g) for four reaction repeats (Figure 38). For each repeat, the palladium material and $[N^nBu_4]X$ salts were recovered and reused using the procedures outlined above (Scheme 74). Since catalyst recovery was not 100%, additional fresh catalyst was included so that 0.044 mol% of $[N^nBu_4]_2[Pd_2I_6]$ was loaded for each run.

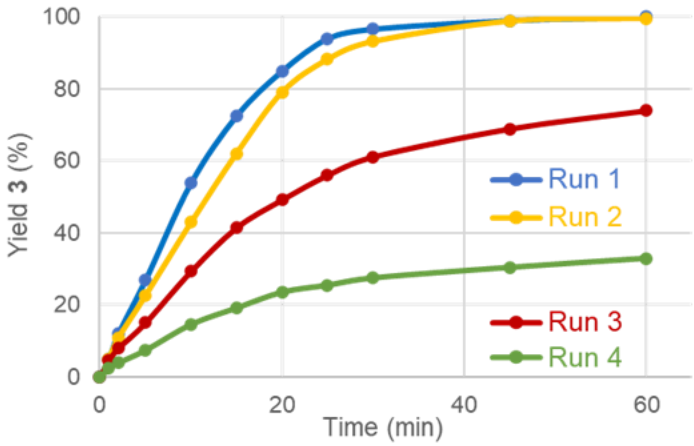

Figure 38. Kinetic profiles for four repeats of the model cross-coupling under the standard reaction conditions, with the reuse of the palladium catalyst and tetrabutylammonium salts. Yields were determined by HPLC analysis with respect to naphthalene as an internal standard.

The kinetic profiles in Figure 38 illustrate that whilst the second reaction run performed well, a significant drop in catalytic activity was observed on the third and fourth runs. This drop in performance was accompanied by a drop in the efficacy of palladium recovery to yield $[N^nBu_4]_2[Pd_2I_6]$ (Table 37) after runs two and three.

Table 37. Recovery yields of $[N^nBu_4]_2[Pd_2I_6]$ for each reaction run.

Entry	Run	$[N^nBu_4]_2[Pd_2I_6]$ recovery yield (%)[a]
1	1	81
2	2	25
3	3	15

[a)] Recovery yields were calculated with respect to the 0.044 mol% $[N^nBu_4]_2[Pd_2I_6]$ loaded into the reaction mixture.

Samples of the reaction mixture were taken *before* the reaction was initiated by the addition of fresh catalyst. These samples should not contain any palladium if the palladium material precipitated at the end of each run and is removed during filtration. However, ICP-MS analysis of these samples illustrated a build-up of palladium contamination (Figure 39).

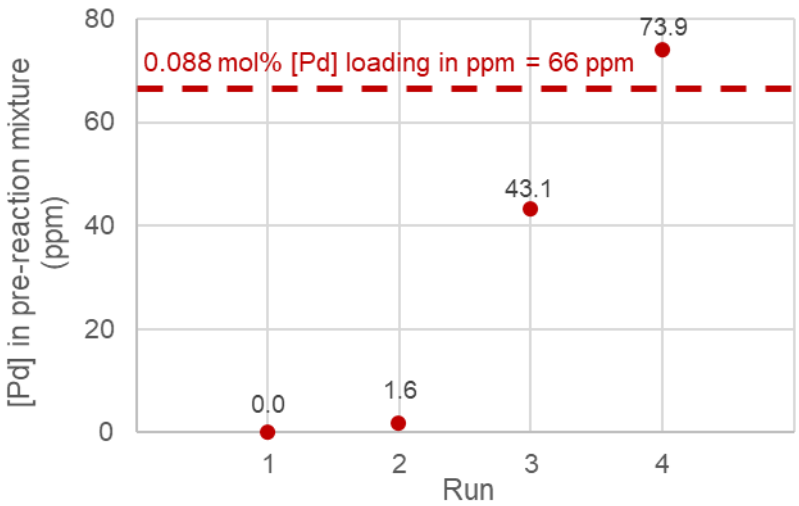

Figure 39. ICP-MS data illustrating a large buildup of residual palladium in the reaction mixture prior to the addition of the catalyst. These samples were taken before the reaction was initiated by the addition of additional 0.044 mol% of $[N^nBu_4]_2[Pd_2I_6]$.

This build up correlates with the drop in the recovery yields of $[N^nBu_4]_2[Pd_2I_6]$ (Table 37). These results illustrate that palladium black did not precipitate at the end of the second run and instead leached into the subsequent reaction mixture via the process for recycling the $[N^nBu_4]X$ salts. By the fourth reaction run, residual palladium levels prior to the addition of $[N^nBu_4]_2[Pd_2I_6]$ were >0.088 mol% of palladium (Figure 39). It was found that palladium that had leached into subsequent reaction mixtures without being recovered back to $[N^nBu_4]_2[Pd_2I_6]$ was catalytically inactive. The presence of increasing quantities of residual palladium in runs three and four (Figure 39) aligns with the drop in catalyst performance during these runs (Figure 38). Presumably, catalytically-inactive residual palladium increased the rate of aggregation and deactivation of the freshly-added $[N^nBu_4]_2[Pd_2I_6]$.

The differences in palladium recovery after the first run illustrates that the recycling process had changed the reaction conditions, though this change did not appear to influence catalyst activity in the second run. The change in conditions did however prevent palladium from precipitating as palladium black at the end of the reaction so that it was not separated from the product and tetrabutylammonium salts by filtration. This resulted in reduced palladium recovery yields (Table 37) and a build-up of residual palladium levels (Figure 39). The visible presence of a water emulsion was observed after the tetrabutylammonium salts had been extracted into 1-butanol for reuse. It was hypothesised that this water contamination was arresting the precipitation of insoluble palladium black at the end of the reaction. To test for this, the five recycling experiments were repeated with the inclusion of an azeotropic drying step prior to the reuse of the 1-butanol solution containing the

tetrabutylammonium salts (Scheme 75). This drying step simply involved placing the recycled 1-butanol solution of tetrabutylammonium salts on the rotary evaporator to remove water as its azeotrope with 1-butanol (boiling point = 93 °C).

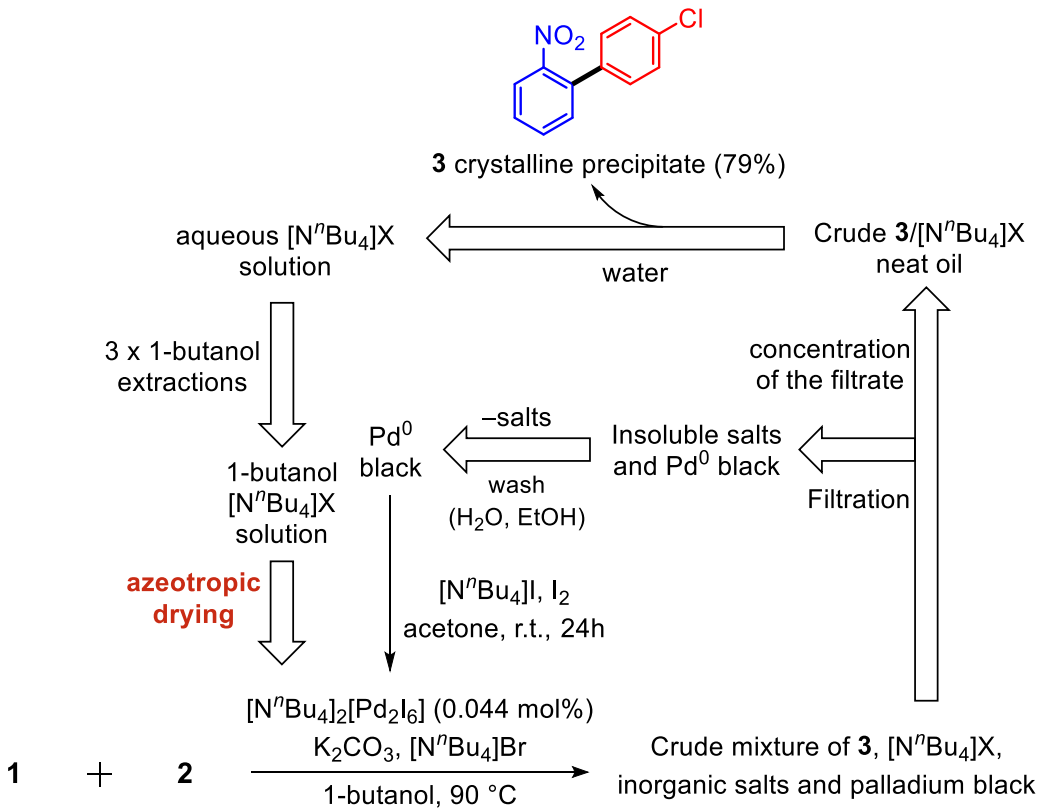

Scheme 75. Full process design for the model cross-coupling reaction, including catalyst recycling, additive recycling and product isolation. 1-butanol containing recycled tetrabutylammonium bromide was azeotropically dried prior to reuse. Solid arrows indicate chemical reactions and hollowed arrows indicate physical manipulations, e.g. filtration, extraction and concentration as indicated.

Kinetic profiles obtained on a 0.5 mol scale illustrate that a good catalyst performance was maintained over five reaction repeats (Figure 40a) when 1-butanol was dried by azeotropic distillation prior to reuse of the tetrabutylammonium salts.

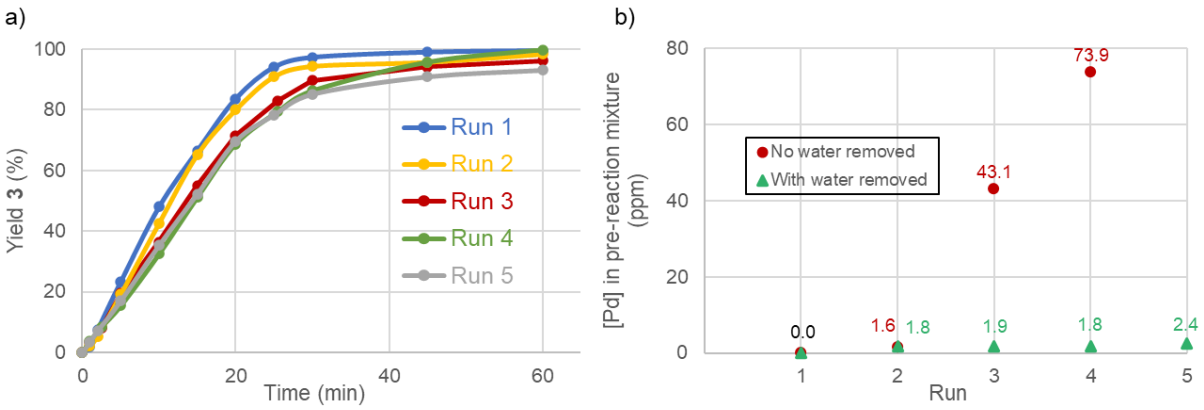

Figure 40. a) Kinetic profiles for five repeats of the model cross-coupling under the standard reaction conditions, with the reuse of the palladium catalyst and azeotropic drying of the 1-butanol which contained the recycled tetrabutylammonium salts. Yields were determined by HPLC analysis with respect to naphthalene as an internal standard. b) ICP-MS data illustrating the influence of water on residual palladium levels.

Removal of water contamination also resulted in a drop in residual palladium levels (Figure 40b) and 79-83% recovery of $[N^nBu_4]_2[Pd_2I_6]$ (Table 38).

Table 38. Five model reaction repeats on a 0.5 mol scale, with $[N^nBu_4]_2[Pd_2I_6]$ and $[N^nBu_4]Br$ recycled and reused.[a]

Run	$[N^nBu_4]_2[Pd_2I_6]$ recovery yield (%)[b]	Yield **3** (%)[c]	**3** Residual [Pd] (ppm)[d]	Cumulative process mass intensity (PMI)
1	81	79	2.8	18.0
2	79	75	2.0	17.5
3	82	84	1.8	16.7
4	82	88	1.8	16.1
5	83	87	2.7	15.9

[a)] All reactions were run in the presence of $[N^nBu_4]Br$ (1 equiv.), K_2CO_3 (1.5 equiv.) and **2** (1.1 equivalents) in 1-butanol (0.7 M of **1**) at 90 °C. [b)] Recovery yields were calculated with respect to the 0.044 mol% $[N^nBu_4]_2[Pd_2I_6]$ loaded into the reaction mixture. [c)] Yields were of the isolated pure precipitate. [d)] Determined by ICP-MS.

These results are consistent with water contamination from the aqueous recycling of $[N^nBu_4]Br$ arresting the precipitation of palladium black at the end of the reaction. For each run, product residual palladium levels were below pharmaceutical regulatory limits (5 ppm) (Table 38),[23] and maintaining low palladium content in agrochemical compounds is also important.[63,64] A cumulative E-factor (total mass of waste/total mass of product) was calculated as 14.8. This value is only slightly higher than the

state-of-the-art system recently published by researchers at BASF on the same reaction (E factor = 13.7).[37] For the sake of a fair comparison, it should be noted that these literature conditions relied on using activated charcoal to bring residual palladium in the final product to 1 ppm, which was not factored into their E-factor calculations. Moreover, the low residual palladium levels in the system reported here did not require any Pd-scavenger or recrystallisation step, as was used in the literature example.[37]

It is notable that the isolated yields of the precipitate of **3** gradually increased (Table 38, Run 1-5). The precipitate yield after the first run was 79%, despite HPLC analysis indicating that the conversion of **1** to **3** was >95%. This indicates that not all of the product (**3**) precipitates from the crude oil mixture containing **3** and $[N^nBu_4]X$. Indeed, a yellow oil was observed in the bottom of the aqueous filtrate containing the $[N^nBu_4]X$ salts. Fortunately, this yellow oil was recovered into the subsequent run by its extraction into 1-butanol during the recycling of $[N^nBu_4]X$, and residual **3** was detected in subsequent reaction mixtures by HPLC analysis prior to the initiation of the reaction (T = 0 min). Presumably, the accumulation of **3** from the previous run resulted in improved precipitation yields.

Overall, 633 mg of $[N^nBu_4]_2[Pd_2I_6]$ (0.017 cumulative mol%) was used to produce 482.5 g of pure **3** during the five reaction repeats, which equates to a cumulative TON of 4760.

3.2.4.4. Expanding the catalyst recycling procedure

It has been demonstrated that palladium black formed from $[N^nBu_4]_2[Pd_2I_6]$ at the end of model reaction can be isolated and recycled back to $[N^nBu_4]_2[Pd_2I_6]$ for reuse. The precipitation of palladium from the model reaction catalysed by $[Pd(OAc)_2]/2PPh_3$ and $[PdCl_2(PPh_3)_2]/2PPh_3$ was also noted whilst comparing their performance with $[N^nBu_4]_2[Pd_2I_6]$. The efficacy of the palladium recycling process was thus expanded to cover these phosphine-based catalysts, and $[Pd(PPh_3)_4]$ (Table 39).

Table 39. Recovery of $[N^nBu_4]_2[Pd_2I_6]$ from palladium waste isolated from the model cross-coupling reaction catalysed by triphenylphosphine-palladium complexes.[a]

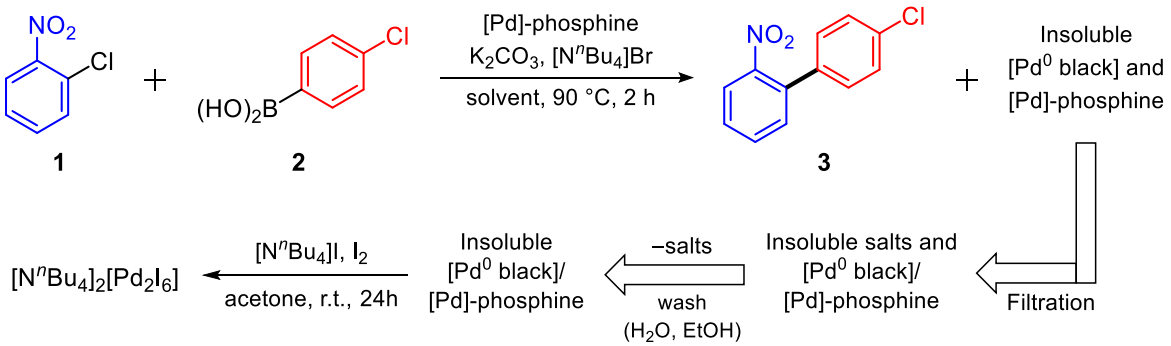

Entry	[Pd]-phosphine ([Pd] mol%)	Solvent	$[N^nBu_4]_2[Pd_2I_6]$ recovery yield (%)[b]	$[N^nBu_4]_2[Pd_2I_6]$ melting point (°C)[c]	^{31}P NMR of $[N^nBu_4]_2[Pd_2I_6]$
1	$Pd(OAc)_2/2PPh_3$ (0.2)	1-butanol	59	181.8-183.2	No ^{31}P environments
2	$PdCl_2(PPh_3)_2/$ $2PPh_3$ (0.2)	1-butanol	55	182.1-183.1	No ^{31}P environments
3	$Pd(PPh_3)_4$ (1)	1-butanol	69	181.5-182.9	No ^{31}P environments
4	$Pd(PPh_3)_4$ (1)	dioxane/ water	0	-	-

[a)] All reactions were run in the presence of $[N^nBu_4]Br$ (1 equiv.), K_2CO_3 (1.5 equiv.) and **2** (1.1 equivalents) (0.7 M of **1**) at 90 °C. [b)] Recovery yields were calculated with respect to the palladium loaded into the reaction mixture. [c)] Melting point of $[N^nBu_4]_2[Pd_2I_6]$ obtained from Pd^0 powder = 182.4-183.1 °C

For each palladium-phosphine complex, the palladium material that precipitated at the end of the reaction on cooling was notably browner than the palladium black that formed from $[N^nBu_4]_2[Pd_2I_6]$. Moreover, the brown palladium precipitate from the phosphine-based catalysts were insoluble in alcohols, but soluble in chloroform. This illustrates that some portion of the palladium material precipitated due to the insolubility of molecular palladium-phosphine complexes in 1-butanol, and not just due to the aggregation of Pd^0 to palladium black. The precipitates were subsequently analysed by NMR spectroscopy, which revealed a range of environments in the ^{31}P NMR spectra, including chemical shifts for free triphenylphosphine, for triphenylphosphine oxide, and some typical palladium-bound ^{31}P NMR shifts. Despite the presence of a range of phosphorous species, the palladium precipitate was successfully transformed, for each palladium-phosphine complex used in 1-butanol, to $[N^nBu_4]_2[Pd_2I_6]$ (Table 39, Entries 1-3). This recovery product was found to be phosphine-free by ^{31}P

NMR analysis, and the ^{1}H NMR spectrum for each product only contained the environments expected for the tetrabutylammonium cation.

The room temperature insolubility of palladium-phosphine complexes at the end of the reaction in 1-butanol resulted in their precipitation, which then facilitated their recycling as $[N^nBu_4]_2[Pd_2I_6]$. The application of $[N^nBu_4]I/I_2$ to recycle phosphine-based palladium catalysts may therefore be limited to reaction solvents in which they are insoluble. Indeed, when the reaction was repeated with $[PdCl_2(PPh_3)_2]/2PPh_3$ in dioxane/water, no palladium precipitate formed (Table 39, Entry 4). Thus, to enable palladium-phosphine complexes to be recycled from reaction solvents in which they are soluble, an additional step which forces the palladium material to precipitate from solution is needed.

A few other transformations have also been successfully catalysed by $[N^nBu_4]_2[Pd_2I_6]$, including Mizoroki-Heck and C-H activation reactions.[17–19,65] The scope of the palladium recycling procedure was consequently expanded to cover these two transformations.

The C-H functionalisation of benzo[*h*]quinoline was explored first (Table 40).

Table 40. C-H activation reaction of benzo[h]quinoline catalysed by $[N^nBu_4]_2[Pd_2I_6]$ and subsequent recovery and reuse of $[N^nBu_4]_2[Pd_2I_6]$.[a]

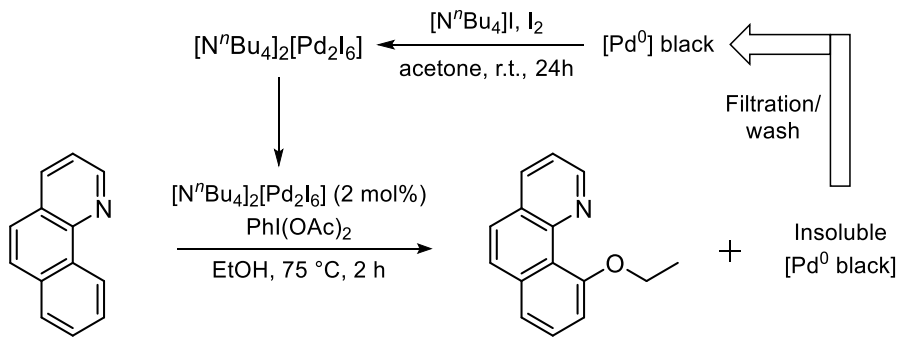

10

Entry	Run	Yield **10** (%)[b]	$[N^nBu_4]_2[Pd_2I_6]$ recovery yield (%)[c]
1	1	97	75
2	2	98	72

[a)] All reactions were performed in the presence of $PhI(OAc)_2$ (2 equiv.). The second run was scaled down so that a loading of 2 mol% of recovered $[N^nBu_4]_2[Pd_2I_6]$ was maintained. [b)] Yield calculated by ^{1}H NMR with respect to trimethoxybenzene as an internal standard. [c)] Recovery yield calculated with respect to the $[N^nBu_4]_2[Pd_2I_6]$ loaded into the reaction mixture.

A near quantitative yield of **10** was obtained in the first run (Table 40, Entry 1), with a palladium black precipitate forming within the first 30 min of the reaction duration. This precipitate was isolated,

washed and recovered back to $[N^nBu_4]_2[Pd_2I_6]$ for reuse. Identical catalytic activity of the recovered $[N^nBu_4]_2[Pd_2I_6]$ was observed for a second C-H activation reaction (Table 40, Entry 2).

The palladium recycling procedure was also applied to an industrially relevant Mizoroki-Heck reaction (Table 41).[65] The synthesis of **13** is conducted by Johnson & Johnson, with **13** serving as an intermediate in the synthesis of Rilpivirine.[66,67]

*Table 41. Synthesis of **13** by a Mizoroki-Heck reaction catalysed by $[N^nBu_4]_2[Pd_2I_6]$ and subsequent recovery and reuse of $[N^nBu_4]_2[Pd_2I_6]$.[a]*

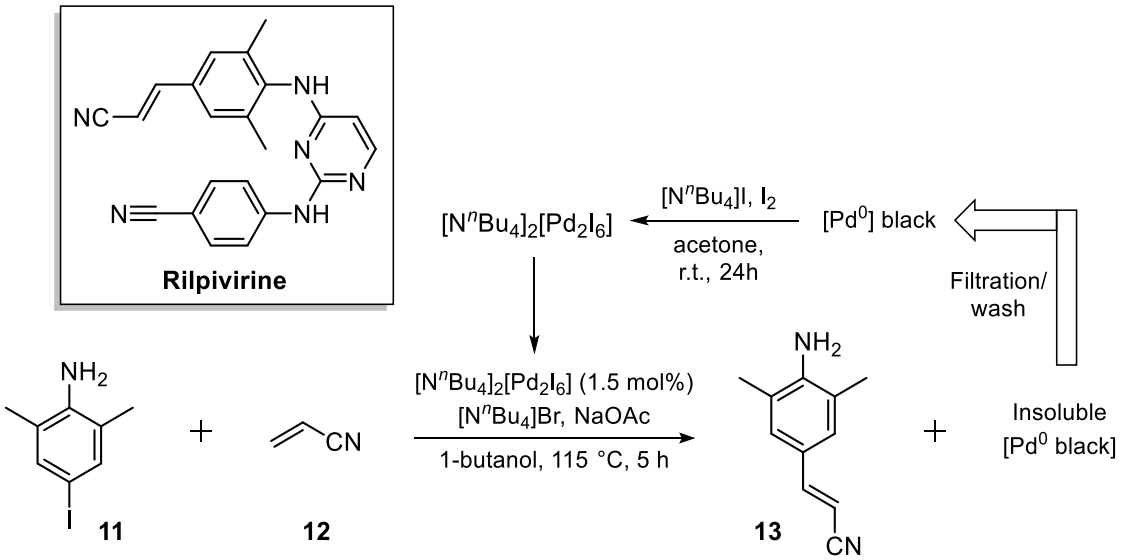

Entry	Run	Yield **13** (%)[b]	$[N^nBu_4]_2[Pd_2I_6]$ recovery yield (%)[c]
1	1	70	81
2	2	72	84

[a)] All reactions were performed in the presence of **12** (1.2 equiv.), NaOAc (1.5 equiv.) and $[N^nBu_4]Br$ (1 equiv.). The second run was scaled down so that a loading of 1.5 mol% of recovered $[N^nBu_4]_2[Pd_2I_6]$ was maintained. [b)] Yield calculated by ^1H NMR with respect to trimethoxybenzene as an internal standard. [c)] Recovery yield calculated with respect to the $[N^nBu_4]_2[Pd_2I_6]$ loaded into the reaction mixture.

Good yields of **13** and of recovered $[N^nBu_4]_2[Pd_2I_6]$ were obtained for two runs when **12** was used in a slight excess (1.2 equiv.) (Table 41). Initial experiments utilised **11** under a slight excess (1.1 equiv.) which provided improved yields of **13** (80%), however this significantly reduced the $[N^nBu_4]_2[Pd_2I_6]$ recovery yield to 21%. Presumably, the presence of excess aryl iodide (**11**) leaves the catalyst end-point as a soluble Pd^{2+} complex which arrested aggregation and precipitation of Pd^0. This results illustrate how small changes in the reaction conditions can influence the possibility of recovering palladium.

3.3. Conclusions

It has been illustrated that $[N^nBu_4]_2[Pd_2I_6]$, a salt which can be recovered from scrap TWCs, is an effective precatalyst for an industrially relevant model cross-coupling reaction to yield **3** (Scheme 76).

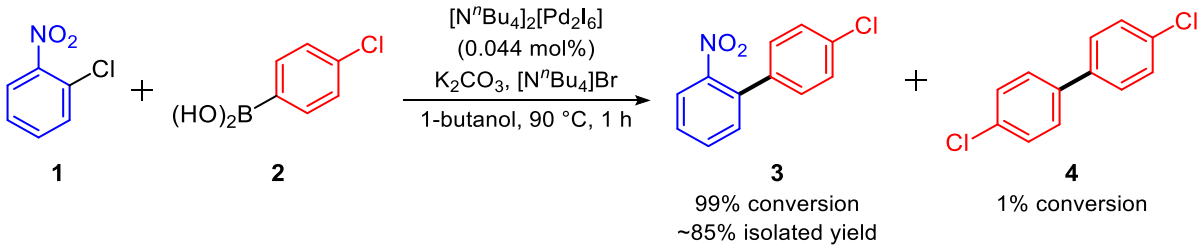

*Scheme 76. Model cross-coupling reaction yielding **3** catalysed by $[N^nBu_4]_2[Pd_2I_6]$ at a low catalyst loading.*

The use of a DoE model was crucial in obtaining optimised reaction conditions. This revealed the presence of catalyst deactivation at elevated catalyst loadings, likely due to aggregation of $[Pd^0]$. This catalyst deactivation led to reduced yields of **3** and increased yields of **4**. A sweet-spot was identified in the catalyst loading at 0.044 mol% (Figure 34). However, this behaviour was not observed during DoE modelling of two palladium-phosphine complexes, $Pd(OAc)_2/2PPh_3$ and $[PdCl_2(PPh_3)_2]/2PPh_3$ (Figure 35).

The use of $[N^nBu_4]_2[Pd_2I_6]$ as a precatalyst for the model cross-coupling reaction provided better performance when compared to two typical off-the-shelf phosphine-based palladium complexes (Figure 36). The speciation of the active catalyst and the origin of the excellent performance of $[N^nBu_4]_2[Pd_2I_6]$ as a precatalyst will be explored in more details during kinetic and mechanistic studies (*vide infra*, Chapter Four).

A full process design has also been developed which enabled both the catalyst and the tetrabutylammonium bromide additive to be reused (Scheme 75). The product (**3**) was isolated by an organic-solvent-free work-up and the tetrabutylammonium bromide additive was recycled directly into the reaction solvent (1-butanol). As a result, the sustainability metrics of the process outlined in Scheme 75 are similar to a state-of-the-art example from the literature (Table 42). Key to the success of the process design was the removal of water from the 1-butanol solution of recycled tetrabutylammonium salts prior to its reuse.

*Table 42. Comparison of the performance of $[N^nBu_4]_2[Pd_2I_6]$ with a state-of-the-art catalyst for the model cross-coupling yielding **3**. Data for $Pd(OAc)_2/P(^tBu)Cy_2$ taken from reference 36.*

Catalyst (mol%)	Yield **3** (%)[a]	Residual [Pd] (ppm)[b]	Cumulative process mass intensity (PMI)	E-factor
$[N^nBu_4]_2[Pd_2I_6]$ (0.044)[c]	82	1.8-2.8	15.7	14.8
$Pd(OAc)_2$ (0.005) $P(^tBu)Cy_2$ (0.020)[d]	75	1[e]	17.2	13.7

[a)] Yields were of the isolated pure product. [b)] Determined by ICP-MS. [c)] Reaction run in the presence of $[N^nBu_4]Br$ (1 equiv.), K_2CO_3 (1.5 equiv.) and **2** (1.1 equivalents) in 1-butanol (0.7 M) at 90 °C for 1 h. [d)] Reaction run in the presence of **2** (1.1 equivalents) and NaOAc (1 equiv.) in H_2O (1.0 M) at 100 °C for 8 h. [e)] Residual Pd after filtration through activated charcoal.

This catalyst recycling strategy was expanded to include the recycling of palladium from three palladium-phosphine complexes when applied as Suzuki-Miyaura catalysts. Moreover, $[N^nBu_4]_2[Pd_2I_6]$ was recovered and reused in two other palladium catalysed transformations – a C-H activation reaction and a Mizoroki-Heck coupling. These results illustrate the general applicability and scope of the palladium recycling procedure.

3.4. Future work

The vast majority of cross-coupling reactions catalysed by palladium complexes reported in the literature rely on flash-column chromatography. The process developed in this work enables pure cross-coupling product to be isolated by a straightforward addition of water causing the product to precipitate from its crude oil mixture with tetrabutylammonium salts. This represents a significant cost and sustainability improvement when compared to flash-column chromatography. Future work is needed to ascertain the scope of this protocol – can a broad range of cross-coupling products be precipitated from their oils containing tetrabutylammonium salts? Moreover, additional work is needed to understand the robustness of this process – what purity of the cross-coupling product within the crude oil is needed to enable precipitation? Finally, additional work would be needed to understand how cross-coupling products that are oils, and not solids, could also be isolated *e.g.* distillation, phase separation.

It has been illustrated that the palladium content from the use of $[N^nBu_4]_2[Pd_2I_6]$ can be recycled from the reaction waste. This procedure is generally applicable to palladium precipitates from different catalytic transformations, and from different palladium-phosphine complexes. Research laboratory palladium waste is typically either lost to silica during flash-chromatography, or to generic

liquid palladium waste. The recycling strategy developed in this work has the potential for wide-reaching impact, since its simplicity makes it readily accessible for any research laboratory. Key to the general applicability of the procedure is the precipitation of palladium at the end of the reaction so that it can be isolated by filtration and recovered as $[N^nBu_4]_2[Pd_2I_6]$. A general laboratory-based recycling strategy could then be envisaged, in which every reaction which utilises a palladium catalyst within a research laboratory is passed through a filter funnel to isolate the palladium waste prior to continuing the standard work-up procedure. This palladium waste could be collected over a ~1 month period to be recycled in bulk. A similar strategy is currently being employed within the Ball group at the University of Nottingham to recover and reuse organobismuth compounds.[68–71]

3.4. References

1 K. J. McGrew, J.W. Murphy, United States Patent, US4557759, 1985.
2 P. H. Qi and J. B. Hiskey, *Hydrometallurgy*, 1991, **27**, 47–62.
3 C. J. Liang and J. Y. Li, *Sep. Sci. Technol.*, 2019, **54**, 1055–1066.
4 L. F. Kozin and V. T. Melekhin, *Russ. J. Appl. Chem.*, 2004, **77**, 1573–1592.
5 S. S. Konyratbekova, A. Baikonurova and A. Akcil, *Miner. Process. Extr. Metall. Rev.*, 2015, **36**, 198–212.
6 A. Serpe, A. Rigoldi, C. Marras, F. Artizzu, M. L. Mercuri and P. Deplano, *Green Chem.*, 2015, **17**, 2208–2216.
7 M. Cuscusa, A. Rigoldi, F. Artizzu, R. Cammi, P. Fornasiero, P. Deplano, L. Marchiò and A. Serpe, *ACS Sustain. Chem. Eng.*, 2017, **5**, 4359–4370.
8 K. A. Jantan, C. Y. Kwok, K. W. Chan, L. Marchiò, A. J. P. White, P. Deplano, A. Serpe and J. D. E. T. Wilton-Ely, *Green Chem.*, 2017, **19**, 5846–5853.
9 K. A. Jantan, K. W. Chan, L. Melis, A. J. P. White, L. Marchiò, P. Deplano, A. Serpe and J. D. E. T. Wilton-Ely, *ACS Sustain. Chem. Eng.*, 2019, **7**, 12389–12398.
10 J. L. Do, D. Tan and T. Friščić, *Angew. Chem. Int. Ed.*, 2018, **57**, 2667–2671.
11 L. A. Cramer, *Jom*, 2001, **53**, 14–18.
12 C. Hagelüken, *Platin. Met. Rev.*, 2012, **56**, 29–35.
13 B. J. Glaister and G. M. Mudd, *Miner. Eng.*, 2010, **23**, 438–450.
14 M. Benson, C. R. Bennett, M. K. Patel, J. E. Harry and M. Cross, *Trans. Institutions Min. Metall. Sect. C Miner. Process. Extr. Metall.*, 2000, **109**, 6-10.
15 M. Benson, C. R. Bennett, J. E. Harry, M. K. Patel and M. Cross, *Resour. Conserv. Recycl.*, 2000, **31**, 1–7.
16 S. McCarthy, D. C. Braddock and J. D. E. T. Wilton-Ely, *Coord. Chem. Rev.*, 2021, **442**, 213925.
17 X. Xu, MRes Dissertation, Imperial College London, 2018.
18 W. Chiang, MRes Dissertation, Imperial College London, 2019.
19 G. Ekart, MRes Dissertation, Imperial College London, 2019.
20 D. G. Brown and J. Boström, *J. Med. Chem.*, 2016, **59**, 4443–4458.
21 The 2010 Nobel Prize in Chemistry, https://www.nobelprize.org/prizes/chemistry/2010/summary/, (accessed 27 July 2023).

22 D. P. Debecker, K. Kuok (Mimi) Hii, A. Moores, L. M. Rossi, B. Sels, D. T. Allen and B. Subramaniam, *ACS Sustain. Chem. Eng.*, 2021, **9**, 4936–4940.

23 ICH Q3D Elemental Impurities - Scientific Guidelines, https://www.ema.europa.eu/en/ich-q3d-elemental-impurities-scientific-guideline, (accessed 9 October 2023).

24 C. Torborg and M. Beller, *Adv. Synth. Catal.*, 2009, **351**, 3027–3043.

25 V. L. Budarin, P. S. Shuttleworth, J. H. Clark and R. Luque, *Curr. Org. Synth.*, 2011, **7**, 614–627.

26 P. Devendar, R. Y. Qu, W. M. Kang, B. He and G. F. Yang, *J. Agric. Food Chem.*, 2018, **66**, 8914–8934.

27 K. Eicken, H. Rang, A. Harreus, N. Götz, E. Ammermann, G. Lorenz, S. Strathmann, German Patent, DE19531813, 1997.

28 K. Eicken, M. Rack, F. Wetterich, E. Ammermann, G. Lorenz, S. Strathmann, German Patent,DE19735224, 1999.

29 K. Eicken, H. Rang, A. Harreus, N. Götz, E. Ammermann, G. Lorenz, S. Strathmann, United States Patent, US000005998450A, 1999.

30 F. P. Byrne, S. Jin, G. Paggiola, T. H. M. Petchey, J. H. Clark, T. J. Farmer, A. J. Hunt, C. Robert McElroy and J. Sherwood, *Sustain. Chem. Process.*, 2016, **4**, 1–24.

31 C. Capello, U. Fischer and K. Hungerbühler, *Green Chem.*, 2007, **9**, 927–93.

32 CN109912425A, .

33 D. H. Li, X. X. He, C. Xu, F. D. Huang, N. Liu, D. S. Shen and F. S. Liu, *Organometallics*, 2019, **38**, 2539–2552.

34 L. Pan, Z. Wang, J. Sun, D. Xiao, K. Wan, Y. Zeng, Z. Zhang, Chinese Patent, CN110041374 A, 2019.

35 L. Chen, P. Ren and B. P. Carrow, *J. Am. Chem. Soc.*, 2016, **138**, 6392–6395.

36 B. S. Takale, R. R. Thakore, R. Mallarapu, F. Gallou and B. H. Lipshutz, *Org. Process Res. Dev.*, 2020, **24**, 101–105.

37 P. Orecchia, D. S. Petkova, R. Goetz, F. Rominger, A. S. K. Hashmi and T. Schaub, *Green Chem.*, 2021, **23**, 8169–8180.

38 N. E. Shchepina, V. D. Nefedov, M. A. Toropova, V. V. Avrorin, S. B. Lewis and B. Mattson, *Tetrahedron Lett.*, 2000, **41**, 5303–5306.

39 H. Fujita, O. Sasamoto, S. Kobayashi, M. Kitamura and M. Kunishima, *Nat. Commun.*, 2022, **13**, 1–7.

40 C. Adamo, C. Amatore, I. Ciofini, A. Jutand and H. Lakmini, *J. Am. Chem. Soc.*, 2006, **128**, 6829–6836.

41 J. Sun, D. Li, H. Gao, Z. Jin and M. Bao, *SN Appl. Sci.*, 2019, **1**, 1–5.

42 N. W. J. Scott, M. J. Ford, N. Jeddi, A. Eyles, L. Simon, A. C. Whitwood, T. Tanner, C. E. Willans and I. J. S. Fairlamb, *J. Am. Chem. Soc.*, 2021, **143**, 9682–9693.

43 X. Feng, A. Sun, S. Zhang, X. Yu and M. Bao, *Org. Lett.*, 2013, **15**, 108–111.

44 J. M. Hunter, J. L. Fye, E. J. Roskamp, R. A. Welch, M. T. Reetz, W. Helbig, S. A. Quaiser, U. Stimming, N. Breuer and R. Vogel, *Science*, 1995, **267**, 367–369.

45 J. X. Wang, Z. Liu, Y. Hu, B. Wei and L. Bai, *J. Chem. Res. - Part S*, 2000, 484–485.

46 J. P. Norman, N. G. Larson, E. D. Entz and S. R. Neufeldt, *J. Org. Chem.*, 2022, **87**, 7414–7421.

47 R. B. Bedford, M. E. Blake, C. P. Butts and D. Holder, *Chem. Commun.*, 2003, **3**, 466–467.

48 JMP - Design of Experiments, https://www.jmp.com/en_ph/statistics-knowledge-portal/what-is-design-of-experiments.html#:~:text=Why use DOE%3F,factors at the same time., (accessed 21 November 2023).

49 JMP - Design of Experiments Design Types, https://www.jmp.com/en_in/statistics-knowledge-portal/what-is-design-of-experiments/types-of-design-of-experiments.html, (accessed 21 November 2023).

50 S. A. Weissman and N. G. Anderson, *Org. Process Res. Dev.*, 2015, **19**, 1605–1633.

51 L. A. Adrio, B. N. Nguyen, G. Guilera, A. G. Livingston and K. K. Hii, *Catal. Sci. Technol.*, 2012, **2**, 316–323.

52 J. G. De Vries, *Dalt. Trans.*, 2006, 421–429.

53 B. D. Briggs, N. M. Bedford, S. Seifert, H. Koerner, H. Ramezani-Dakhel, H. Heinz, R. R. Naik, A. I. Frenkel and M. R. Knecht, *Chem. Sci.*, 2015, **6**, 6413–6419.

54 N. Jeddi, N. W. J. Scott and I. J. S. Fairlamb, *ACS Catal.*, 2022, 12, 11615–11638.

55 A. V. Gaikwad, A. Holuigue, M. B. Thathagar, J. E. Ten Elshof and G. Rothenberg, *Chem-Eur. J.*, 2007, **13**, 6908–6913.

56 V. M. Chernyshev, E. A. Denisova, D. B. Eremin and V. P. Ananikov, *Chem. Sci.*, 2020, **11**, 6957–6977.

57 A. H. M. de Vries, J. M. C. A. Mulders, J. H. M. Mommers, H. J. W. Henderickx and J. G. de Vries, *Org. Lett.*, 2003, **5**, 3285–3288.

58 N. Jeddi, N. W. J. Scott, T. Tanner, S. K. Beaumont and I. J. S. Fairlamb, *Chem. Sci.*, 2024, **15**, 2763–2777.

59 C. C. C. Johansson Seechurn, T. Sperger, T. G. Scrase, F. Schoenebeck and T. J. Colacot, *J. Am. Chem. Soc.*, 2017, **139**, 5194–5200.

60 N. W. J. Scott, M. J. Ford, C. Schotes, R. R. Parker, A. C. Whitwood and I. J. S. Fairlamb, *Chem. Sci.*, 2019, **10**, 7898–7906.

61 R. Hudson and J. L. Katz, *ACS Sustain. Chem. Eng.*, 2018, **6**, 14880–14887.

62 R. J. Fox and J. Qiu, *Org. Process Res. Dev.*, 2020, **24**, 235–241.

63 G. Tóth, T. Hermann, M. R. Da Silva and L. Montanarella, *Environ. Int.*, 2016, **88**, 299–309.

64 J. Gans, M. Wolinsky and J. Dunbar, *Science,* 2005, **309**, 1387–1390.

65 N. Mylonas, MRes Dissertation, Imperial College London, 2022.

66 A. Biffis, P. Centomo, A. Del Zotto and M. Zecca, *Chem. Rev.*, 2018, **118**, 2249–2295.

67 D. Schils, F. Stappers, G. Solberghe, R. Van Heck, M. Coppens, D. Van Den Heuvel, P. Van Der Donck, T. Callewaert, F. Meeussen, E. De Bie, K. Eersels and E. Schouteden, *Org. Process Res. Dev.*, 2008, **12**, 530–536.

68 K. Ruffell, L. C. Gallegos, K. B. Ling, R. S. Paton and L. T. Ball, *Angew. Chem. Int. Ed.*, 2022, **61**, e202212873.

69 A. Senior, K. Ruffell and L. T. Ball, *Nat. Chem.*, 2023, **15**, 386–394.

70 M. Jurrat, L. Maggi, W. Lewis and L. T. Ball, *Nat. Chem.*, 2020, **12**, 260–269.

71 K. Ruffell, S. P. Argent, K. B. Ling and L. T. Ball, *Angew. Chem. Int. Ed.*, 2022, **61**, e202210840.

Chapter 4 – Kinetic and Mechanistic Studies on the Application of $[Cation]_2[Pd_2I_6]$ Salts as Suzuki-Miyaura Catalysts

4.1. Introduction

This chapter serves as a continuation of the research of chapter three, which found that $[N^nBu_4]_2[Pd_2I_6]$ was an effective catalyst for the model Suzuki-Miyaura coupling reaction. The introduction initially outlines one of the key results of the previous chapter and how this prompted the aims and objectives of this chapter. This is followed by an overview of the current understanding on the complexities of palladium speciation, and some recent examples which have exploited catalyst speciation to unlock new site selectivities in the Suzuki-Miyaura coupling reactions. An overview has also been provided on the kinetic tools that were used to achieve the chapter's aims. All of these aspects have been introduced since they heavily influenced the interpretation of the kinetic and mechanistic results that are presented. This is followed by the results and discussion sections, which covers the contents of the results in the order: i) Kinetic studies on the application of $[N^nBu_4]_2[Pd_2I_6]$ as a catalyst in the model reaction, ii) Using transmission electron microscopy to rationalise the results of the kinetic studies, iii) Exploiting C2 vs C4 site selectivity of the Suzuki-Miyaura coupling of 2,4-dichlopyridine to better understand the speciation of $[Cation]_2[Pd_2I_6]$.

4.1.1. Research aims and objectives

Previous work on the model cross-coupling reaction catalysed by $[N^nBu_4]_2[Pd_2I_6]$ revealed a non-linear influence of the $[N^nBu_4]_2[Pd_2I_6]$ loading on the yield of **3** (Scheme 77).

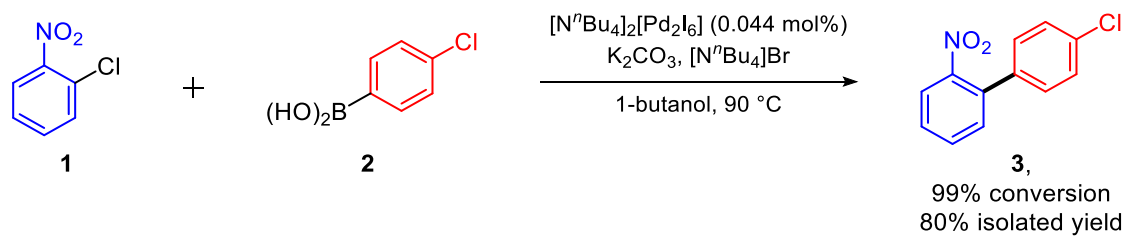

*Scheme 77. Aggregation of active Pd^0 was implicated for the model cross-coupling reaction yielding **3** catalysed by $[N^nBu_4]_2[Pd_2I_6]$.*

These results were rationalised by the presence of loading-dependent aggregation of active Pd^0. No mechanistic studies on the use of $[N^nBu_4]_2[Pd_2I_6]$ as a palladium precatalyst have been performed previously and so the aim of this chapter was to conduct in-depth kinetic and mechanistic studies. This was achieved by determining reaction orders in $[N^nBu_4]_2[Pd_2I_6]$ using Visual Time Normalisation Analysis (VTNA) to gain an understanding of the speciation of active Pd^0. VTNA was also used to elucidate reaction orders in the other components, and to understand catalyst stability.

Additional mechanistic studies were also conducted with the aim of supplementing and rationalising the results of the kinetic studies. This was achieved by using Transmission Electron Microscopy (TEM)

to image the presence, if any, of nanoparticles in the cross-coupling reaction yielding **3**. Stoichiometric and 'leave-one-out' control studies were also performed to uncover the mechanism of the reduction of Pd^{2+} in $[N^nBu_4]_2[Pd_2I_6]$ to active $[Pd^0]$. Since the organic cation in the precatalyst, *i.e*. $[PPh_4]^+$ vs $[N^nBu_4]^+$, has been illustrated to have a significant impact on catalytic activity, kinetic studies were also conducted with the aim of better understanding the role of this cation in the precatalyst.

4.1.2. Speciation of active palladium from palladium precatalysts

Aggregated species formed from palladium precatalysts have been previously implicated in cross-coupling chemistry. For example, lower loadings of $Pd(OAc)_2$ were employed in a Mizoroki-Heck reaction to prevent catalyst deactivation, which was proposed to be due to the aggregation of Pd^0 at elevated loadings.[1,2] Numerous other publications have reported on the formation of nanoparticles from molecular palladium precatalysts.[3–11] In each of these examples, evidence for the role of an aggregated species was obtained indirectly. For example, nanoparticles have been detected by *ex situ* TEM imaging of cross-coupling reaction mixtures,[5–7,10,11] and by mass spectrometry.[9] Numerous reports have also employed poisoning tests, *e.g.* mercury poisoning or heterogeneity tests,[6,7,10,12–17] which probe for the presence of nanoparticles.[18] In one report, a diffusion membrane was employed to explore nanoparticle leaching mechanisms.[4] Whilst each of these techniques indicates the presence of aggregated species in the reaction mixture, they generally provide little understanding as standalone studies on the exact role of the aggregated species either on or off the catalytic cycle. More direct evidence can instead be obtained from kinetic studies. For example, the relationship between catalyst turnover frequency (TOF) data and nanoparticle follows a characteristic power.[19–21] The observation of this trend in a Sonogashira reaction was used to implicate the formation of nanoparticles from a family of related CN-palladacycle precatalysts (Figure 41a).[8]

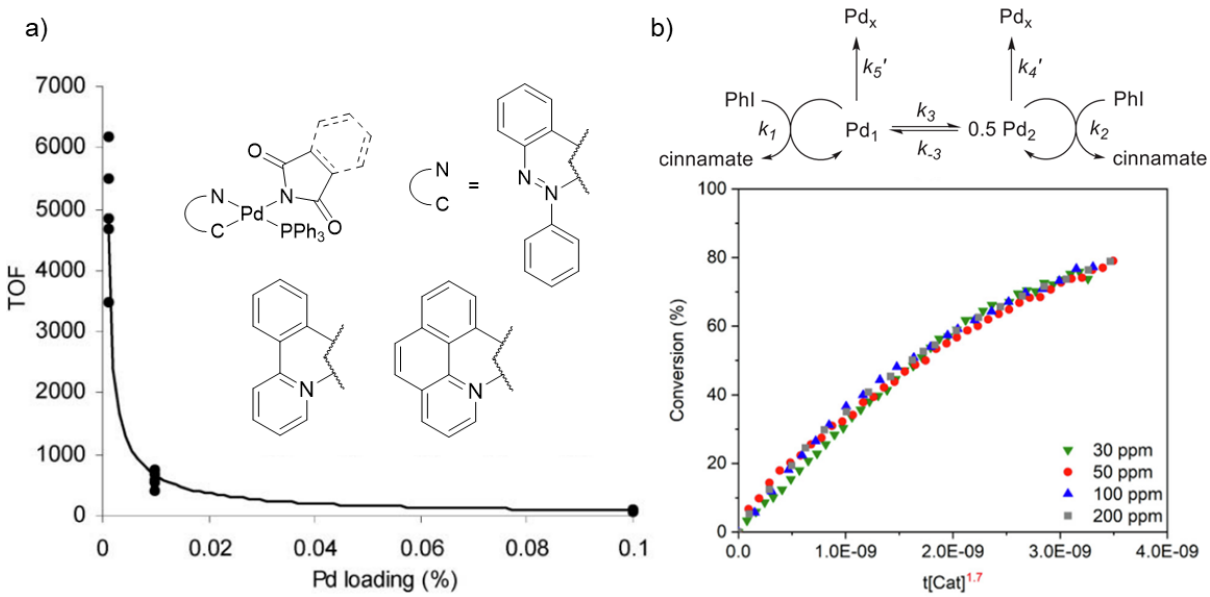

Figure 41. a) Observation of a power law in the relationship between TOF and Pd loading in a Sonogashira reaction catalysed by a family of related CN- palladacycles. b) Reaction order in $Pd(OAc)_2$ of 1.7 and implication of a monomer-dimer equilibrium between active Pd^0 species. Figures have been reproduced with permission directly from references 8 (a) and 31 (b) (Open Access).

Kinetic analysis of the reaction order in catalyst has also been used as a direct tool for understanding the role of aggregated species.[22–26] Catalyst orders have been used to indicate the presence of both on-cycle and off-cycle higher order species in palladium catalysis.[27–30] For example, a reaction order of 1.7 in $Pd(OAc)_2$ for a Mizoroki-Heck reaction was used as evidence for the formation of an on-cycle dimeric species (Figure 41b).[31] These reports illustrate the power of kinetic studies to elucidate key catalyst mechanistic features. Kinetic studies were therefore conducted on the cross-coupling reaction yielding **3** catalysed by $[N^nBu_4]_2[Pd_2I_6]$.

In recent years, the formation of aggregated palladium species from molecular palladium precatalysts has been exploited to control the regioselectivity of the Suzuki-Miyaura coupling reaction.[32–35] For example, switching between mononuclear and multinuclear active catalysts has been exploited to switch the halogen site selectivity from C2 to C4 during the coupling of 2,4-dibromopyridine.[36] Atypical C4 selectivity of $PdCl_2$ in the presence of tetrabutylammonium bromide was also recently illustrated by Neufeldt *et al* for the Suzuki-Miyaura coupling of 2,4-dichloropyridine (Scheme 78).[37]

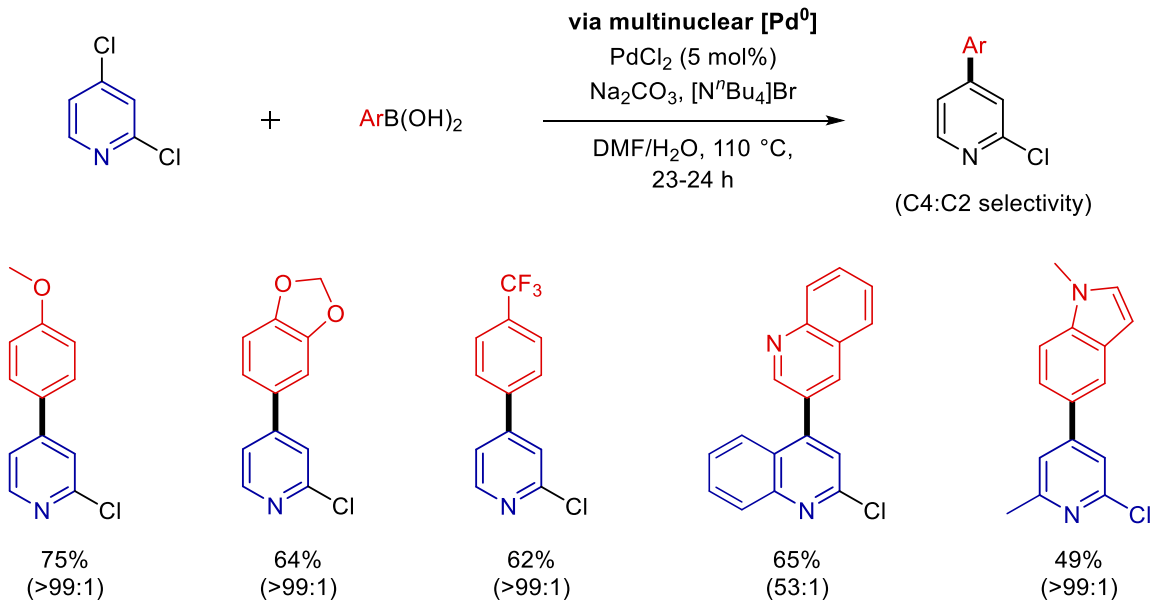

Scheme 78. Atypical C4 selectivity in the coupling of 2,4-dichloropyridine via multinuclear active [Pd^0].[37]

Since the C2/C4 selectivity has been illustrated to be highly dependent on catalyst speciation, *i.e.* mono- vs multinuclear, the coupling of 2,4-dibromopyridine has been used as a mechanistic benchmark to elucidate the nuclearity of the active catalyst species.[38] The coupling of dihalogenated pyridines will therefore be explored to provide further mechanistic understanding of the active catalyst formed from [Cation]$_2$[Pd$_2$I$_6$] precatalysts.

4.1.3. Elucidation of reaction orders and constants

Reaction orders and constants can be obtained using a variety of different graphical techniques. In an early example, Lineweaver and Burk published the reciprocal form of the Michaelis-Menten equation.[39] Graphical representation of enzyme kinetic data using this 'upside down' equation enabled kinetic parameters to be extracted from a straight-line plot. A editorial published in 2003 highlighted that this seminal report was the Journal of the American Chemical Society's most cited publication.[40] Lineweaver and Burk's strategy laid the foundations for a century of mechanistic chemical research in both academia and industry which utilises graphical representations and extrapolations of kinetic data.[41–49] For example, graphical plotting of initial reaction rates has been used to determine reaction orders. However, initial rate data is not suitable when there are deviations from catalytic steady-state during the initial rate window.[50–55] Moreover, many traditional kinetic approaches are not suitable for extracting kinetic parameters for multi-component catalytic reactions which obey complex rate laws. Reagents are subsequently utilised under a large excess (5-10

equivalents) so that the reaction rate is only effected by the concentration of the reaction component that is being intentionally adjusted. Thus, the obtained kinetic paraments are *pseudo* rate constants and orders,[48,49] and are not obtained under synthetically relevant conditions. Using the reagents in such large excesses has been reported to alter the mechanistic pathway and catalyst resting state.[29]

The limitations of traditional kinetic approaches led Blackmond to develop Reaction Progress Kinetic Analysis (RPKA).[55] Similar to traditional differential approaches, RPKA utilises graphical plotting of rate vs concentration to extract kinetic orders and constants. In RPKA however, temporal rate data is plotted against a function of the component concentration, which enables kinetic parameters to be obtained without maintaining a large excess of the reaction components. Crucially then, RPKA is used to uncover kinetic parameters under synthetically relevant conditions. Despite providing many advantages over traditional kinetic approaches, RPKA is limited by the need for reaction rate data. Analytical techniques that yield concentration data are considerably more accessible and broadly applicable than techniques which measure reaction rate. As a result, Burés developed Visual Time Normalisation Analysis (VTNA),[56–59] which utilises readily accessible temporal concentration profiles to extract kinetic parameters.[57,59] VTNA has also been used to monitor deviations from catalytic steady-state due to catalyst deactivation.[58,60,61] The principles of VTNA are similar to those of RPKA – to determine the order in a reaction component using VTNA, 'different excess' concentration data is plotted against a function of time, the reaction component concentration and component order according to Equation 4:

$$\int_{t=0}^{t=n} [\boldsymbol{A}]^a dt = \sum_{i=1}^{n} \left(\frac{[\boldsymbol{A}]_i + [\boldsymbol{A}]_{i-1}}{2} \right)^a \cdot (t_i - t_{i-1})$$

Equation 4

Quantitatively, Equation 4 normalises the time scale between each pair ($[\mathbf{A}]_i$ and $[\mathbf{A}]_{i-1}$) of temporal concentration data points with respect to the component concentration and order. Qualitatively, Equation 4 removes the influence of [**A**] on the rate of the reaction, such that when the correct value of the reaction order in [**A**], the term *a* in Equation 4, is determined, two profiles of different concentration in [**A**] will visually overlap. This can be done by trial and error in a spreadsheet programme, or using a curve-fitting algorithm. Throughout this thesis, the open access excel spreadsheet published by Nielsen and Burés was used as a template to conduct VTNA.[56]

Since their inception, RPKA and VTNA have revolutionised the way in which chemical kinetic studies are conducted, and they have been utilised extensively to determine key kinetic parameters during mechanistic studies of a variety of transformations.[22,25,68–72,28,31,62–67] Many of these studies use RPKA and VTNA to elucidate catalyst orders and understand catalyst speciation. The Wilton-Ely and

Braddock groups have access to NMR, HPLC and ReactIR, which can all yield temporal concentration data. As a result, VTNA was applied in this study to gain key kinetic and mechanistic understanding for the cross-coupling reaction yielding **3** catalysed by $[N^nBu_4]_2[Pd_2I_6]$.

The overall goal of these kinetic and mechanistic studies is to uncover fundamental mechanistic understanding of the behaviour and performance of $[N^nBu_4]_2[Pd_2I_6]$ and thus encourage its wider adoption.

4.2. Results and Discussion

4.2.1. Visual time normalisation analysis of the model reaction catalysed by $[N^nBu_4]_2[Pd_2I_6]$

The conditions used throughout the following set of kinetic studies utilised $[N^nBu_4]_2[Pd_2I_6]$ as a precatalyst in the presence of tetrabutylammonium bromide. The full stoichiometric equation for the model cross-coupling reaction, including the reaction by-products, is summarised in Scheme 79.

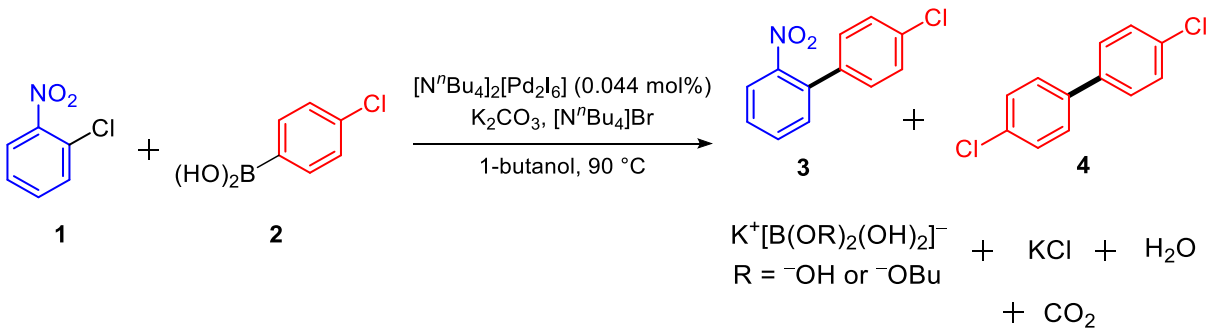

Scheme 79. Complete model cross-coupling reaction scheme, including all of the possible side products and by-products

4.2.1.1. VTNA Methodology

For a reliable VTNA study, the visual change in the reaction rate must only be affected by the intentionally changed component concentration, *i.e.* the reaction must be reproducible. To test the reproducibility, three reaction repeats using $[N^nBu_4]_2[Pd_2I_6]$ as a precatalyst under identical conditions were monitored using ReactIR/HPLC and the resulting profiles compared (Figure 42). Temporal profiles for both the concentration of the aryl chloride, [**1**], and the concentration of the cross-coupling product, [**3**], overlap for all three runs, indicating excellent reproducibility (Figure 42).

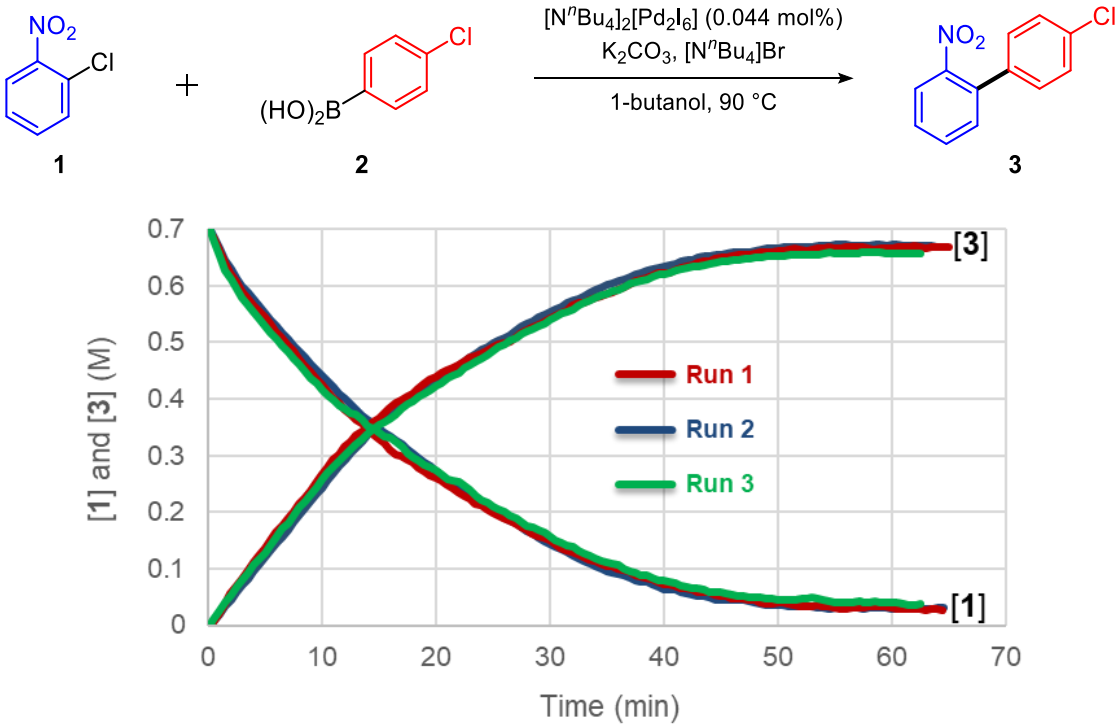

*Figure 42. Temporal concentration profiles for the consumption of **1** and formation of **3** in three model reactions conducted under identical conditions. Profiles were produced using in situ ReactIR and the absorbance data calibrated offline using HPLC analysis with naphthalene as an internal standard.*

Temporal concentration profiles for the consumption of the aryl chloride ([**1**]) were used throughout the following VTNA studies. These temporal profiles were obtained using *in situ* ReactIR, and the IR trend was calibrated with at least 4 offline HPLC data points. The VTNA utilised temporal aryl chloride concentration ([**1**]) data instead of the cross-coupling product ([**3**]) due to the better fit of offline HPLC data with the ReactIR absorbance for the aryl chloride. The concentration of the aryl chloride ([**1**]) is a suitable rate handle for VTNA of the model cross-coupling reaction as ~100% of the mass balance in the aryl chloride ([**1**]) was converted to the cross-coupling product ([**3**]). This was made possible by the fact that protodehalogenation of **1** was not observed under the standard reaction conditions.

4.2.1.2. Reaction orders in aryl chloride and catalyst deactivation

The reaction order in the aryl chloride ([**1**]) was determined using VTNA. Two reactions were performed under a 'different excess' of the aryl chloride ([**1**]), and the *in situ* ReactIR profiles (Figure 43a) shifted down the y-axis so that the 0.70 M and 0.56 M reactions have the same starting point (Figure 43b). The resulting profiles were normalised using Equation 4 to extract the order of the reaction in the aryl chloride ([**1**]) (Figure 43c). This technique was applied for each of the profiles used

to extract reaction orders in the aryl chloride using VTNA. The reaction conditions that the reactions in Figure 43 were conducted under are summarised in Table 43.

Table 43. Reaction conditions and starting concentrations for the reaction profiles presented in Figure 43.

Profile Colour	$[\mathbf{1}]_0$ (M)	$[\mathbf{2}]_0$ (M)	$[[N^nBu_4]Br]_0$ (M)	$[[N^nBu_4][Pd_2I_6]]_0$ (mM)
Blue	0.70	0.77	0.70	0.308
Red	0.56	0.77	0.70	0.308

All reactions were conducted in 1-butanol at 90 °C in the presence of K_2CO_3 (1.5 equiv.).

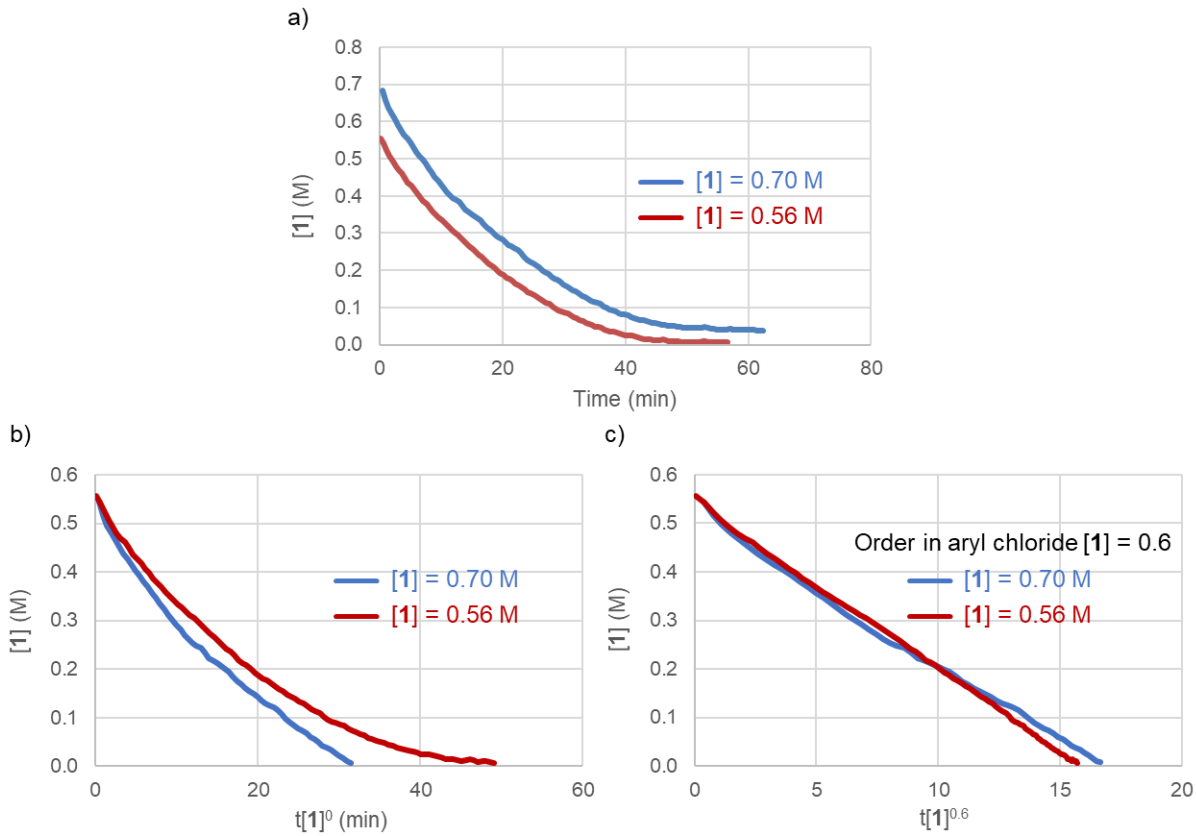

*Figure 43. a) Two original ReactIR profiles at [**1**] = 0.70 M (blue) and 0.56 M (red). b) Two 'different excess' reaction profiles for [**1**] = 0.70 M (blue) and 0.56 M (red) which have been shifted down the y-axis. c) VTNA applied to determine the reaction order in [**1**] from the two 'different excess' reaction profiles. Profiles were produced using in situ ReactIR and the absorbance data calibrated offline using HPLC analysis.*

The best visual overlay of the entire portion of the two 'different excess' profiles was obtained for an order in the aryl chloride ([**1**]) of 0.6 (Figure 43b). The poor overlay of the two profiles at an order of 0.6 is due to two distinct order regimes – an order of 0.9 provided excellent overlay of the initial portion of the 'different excess' profiles, yet the overlay was lost at lower concentrations of the aryl chloride ([**1**]) (Figure 44a). Conversely, an order of 0.5 provided the best visual overlay of the final

portion of the two 'different excess' profiles (Figure 44b). Deviations from profile overlap indicated a deviation from catalytic steady-state.

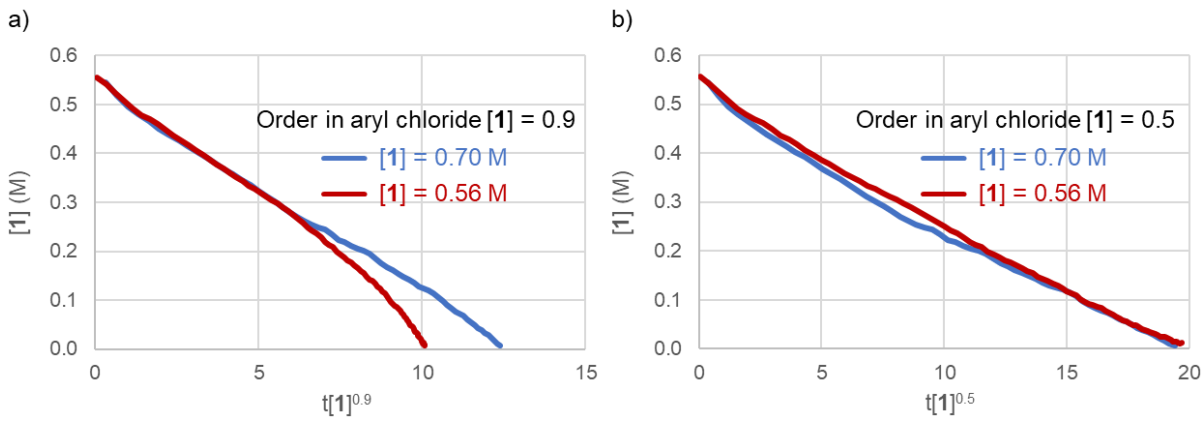

*Figure 44. A comparison of the visual overlap of the two 'different excess' profiles at an: a) Order in [**1**] of 0.9, and b) An order in [**1**] of 0.5. Orders were determined by VTNA. Reactions conducted under the conditions presented in Table 43.*

The deviation from catalytic steady-state is linked to the aryl chloride concentration ([**1**]) yet the deviation occurred at lower concentrations of **1**. The deviation from steady-state may therefore be due to the product, which has a concentration that is inversely proportion to the aryl chloride concentration ([**1**]), inhibiting catalytic activity. To investigate this, a series of 'same excess' experiments were conducted (Figure 45). When a reaction was performed under a 'same excess' of the aryl chloride ([**1**]) and the aryl boronic acid ([**2**]) and the profile shifted along the x-axis for comparison with the standard conditions, the profiles did not overlap (Figure 45a). The reaction conditions that the reactions in Figure 45 were conducted under are summarised in Table 44.

Table 44. Reaction conditions and starting concentrations for the reaction profiles presented in Figure 45.

Profile Colour	$[\mathbf{1}]_0$ (M)	$[\mathbf{2}]_0$ (M)	$[\mathbf{3}]_0$ (M)	$[[N^nBu_4]Br]_0$ (M)	$[[N^nBu_4][Pd_2I_6]]_0$ (mM)
Blue	0.70	0.77	0.00	0.70	0.308
Red	0.40	0.47	0.00	0.70	0.308
Yellow	0.40	0.47	0.30	0.70	0.308

All reactions were conducted in 1-butanol at 90 °C in the presence of K_2CO_3 (1.5 equiv.).

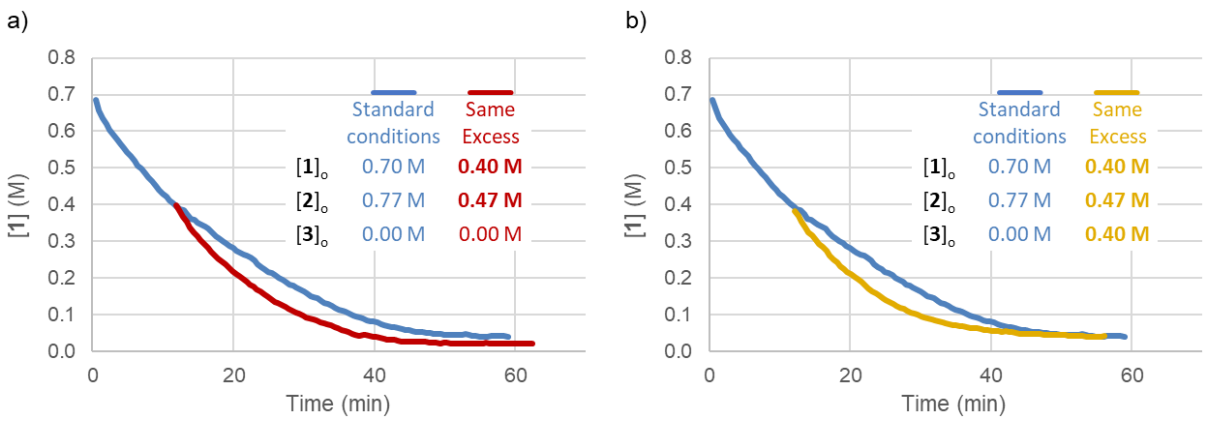

*Figure 45. a) Non-overlapping 'same excess' and standard conditions indicated catalyst deactivation under the standard conditions. b) Non-overlapping 'same excess' and standard conditions in the presence of doped **3.** Profiles were produced using in situ ReactIR and the absorbance data calibrated offline using HPLC analysis with naphthalene as an internal standard.*

Non-overlapping 'same excess' profiles indicates a deviation from the catalytic steady-state. In this case, the 'same excess' profile illustrated improved catalytic performance and thus deactivation of the catalyst must have occurred under the standard conditions.

A second 'same excess' experiment was conducted, this time with an appropriate quantity of the cross-coupling product ([**3**]) doped into the reaction mixture (Figure 45b). This second 'same excess' profile (Figure 45b, yellow) did not overlay with the standard conditions. Thus, catalyst deactivation was not occurring as a result of product inhibition. Since the non-unity orders in the aryl chloride ([**1**]) suggested that the deviation from the steady-state was linked to the aryl chloride concentration ([**1**]) (Figure 43, Figure 44), the only remaining component connected to [**1**] is the chloride anions released from [**1**]. A third 'same excess' experiment was run to test if chloride anions were the origin of catalyst deactivation. In this third 'same excess' experiment, the [N^{n}Bu$_4$]Br additive was also under a 'same excess' with [N^{n}Bu$_4$]Cl (Figure 46a). The reaction conditions that the reactions in Figure 46 were conducted under are summarised in Table 45.

Table 45. Reaction conditions and starting concentrations for the reaction profiles presented in Figure 46.

Profile Colour	[**1**]$_0$ (M)	[**2**]$_0$ (M)	[[N^{n}Bu$_4$]Br]$_0$ (M)	[[N^{n}Bu$_4$]Cl]$_0$ (M)	[KBr]$_0$ (M)	[[N^{n}Bu$_4$][Pd$_2$I$_6$]]$_0$ (mM)
Blue	0.70	0.77	0.70	0.70	0.00	0.308
Red	0.40	0.47	0.40	0.30	0.00	0.308
Yellow	0.40	0.47	0.70	0.00	1.40	0.308
All reactions were conducted in 1-butanol at 90 °C in the presence of K_2CO_3 (1.5 equiv.).						

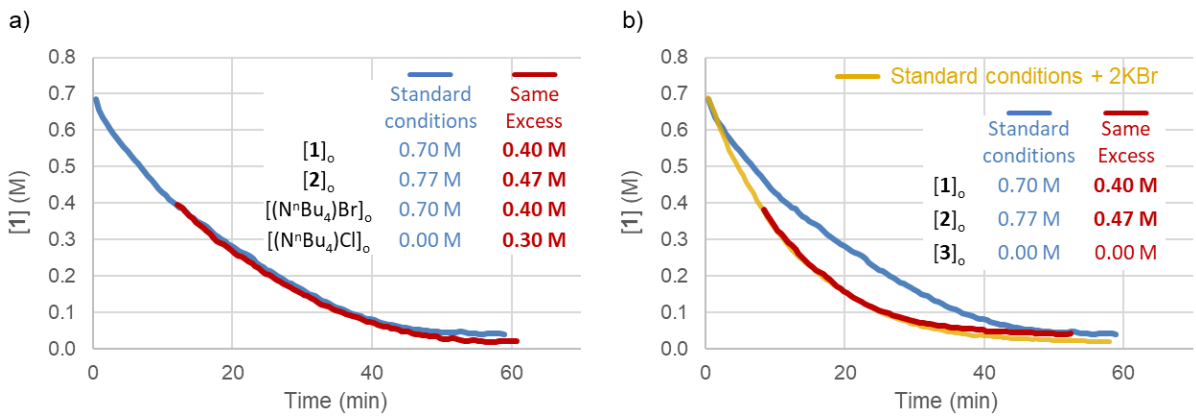

Figure 46. a) Overlapping 'same excess' and standard conditions when [N^{n}Bu$_4$]Cl was also included under a 'same excess' b) Comparison of the standard conditions, the original 'same excess' and the standard conditions with 2 equiv. of KBr. Profiles were produced using in situ ReactIR and the absorbance data calibrated offline using HPLC analysis with naphthalene as an internal standard.

Inclusion of the bromide and chloride anions under a 'same excess' resulted in visual overlay of the standard conditions and the 'same excess' experiment (Figure 46a). This result illustrates that the chloride anions released from the aryl chloride coupling partner (**1**) were slowing the rate of the reaction. The introduction of an excess of bromide anions (two equivalents of KBr) was found to arrest chloride anion inhibition (Figure 46b). The suppression of chloride anion inhibition of the catalyst can be seen in the improved catalytic performance of the 'standard conditions + 2KBr' (Figure 46b, yellow profile) when compared with the original standard conditions (Figure 46b, blue profile). Moreover, the new standard conditions containing an excess of bromide anions (Figure 46b, yellow profile) overlays with the original 'same excess' experiment (Figure 46b, red profile).

Having elucidated that the origin of the catalyst deactivation was the release of chloride anions from the aryl chloride coupling partner (**1**), the order of the reaction in the aryl chloride ([**1**]) was revisited. This time, reaction orders were determined in the presence of 2 equivalents of KBr (Table 46, Figure 47).

Table 46. Reaction conditions and starting concentrations for the reaction profiles presented in Figure 47.

Profile Colour	[**1**]$_0$ (M)	[**2**]$_0$ (M)	[[N^{n}Bu$_4$]Br]$_0$ (M)	[KBr]$_0$ (M)	[[N^{n}Bu$_4$][Pd$_2$I$_6$]]$_0$ (mM)
Blue	0.70	0.77	0.70	1.40	0.308
Red	0.56	0.77	0.70	1.40	0.308

All reactions were conducted in 1-butanol at 90 °C in the presence of K_2CO_3 (1.5 equiv.).

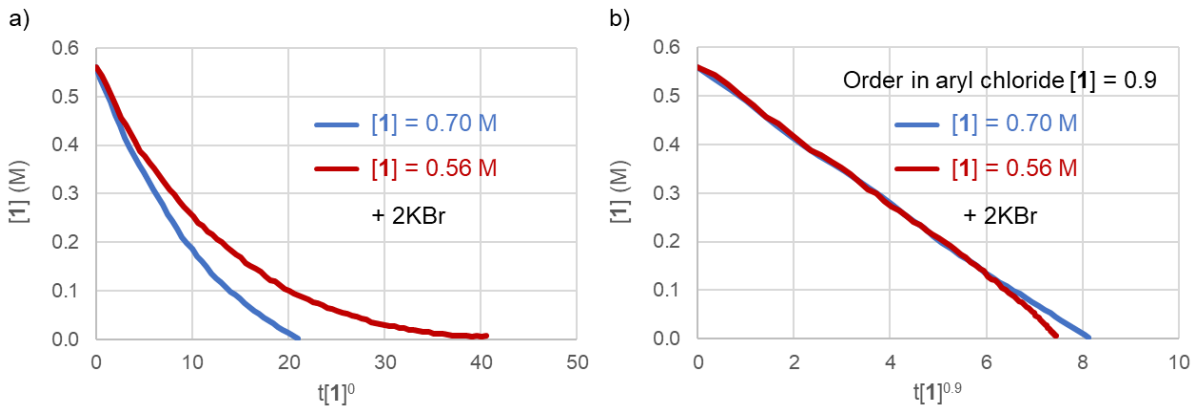

*Figure 47. Both 'different excess' reactions were run in the presence of 2 equiv. of KBr. a) 'Different excess' reaction profiles for [**1**] = 0.70 M (blue) and 0.56 M (red) b) VTNA applied to determine the reaction order in [**1**] from the two 'different excess' reaction profiles. Profiles were produced using in situ ReactIR and the absorbance data calibrated offline using HPLC analysis with naphthalene as an internal standard.*

Visual overlay of the 'different excess' profiles was obtained for a reaction order in the aryl chloride ([**1**]) of 0.9 (Figure 47b) under an excess of bromide anions. This confirmed that the deviations from first order observed previously (Figure 43) were the result of chloride-mediated catalyst inhibition. Some deviation from overlay was observed at the very end of the 'different excess' experiments run in the presence of excess KBr (Figure 47b). This suggests that a small amount of chloride anion inhibition still occurred towards the very end of the reaction. Nevertheless, overcoming chloride anion inhibition via the inclusion of excess bromide anions imparted a noticeable improvement on catalyst performance (Figure 46b). This is, to the best of our knowledge, the first time that catalyst deactivation by chloride has been observed in a Suzuki-Miyaura cross-coupling reaction.

Additional mechanistic experiments were subsequently performed to elucidate the mechanism of chloride-mediated catalyst deactivation. Less than unity reaction orders can be the result of a reversible elementary step,[22,54,55,59,73–75] since the component concentration influences both the forward and reverse reactions. The observed reaction order changes at different component concentrations according to the relative magnitudes of the forward and reverse rate constants. This understanding can be used to propose a mechanism which explains the kinetic results discussed above (Figure 48 and Figure 49). At the beginning of the cross-coupling reaction, bromide anions were in excess of palladium and chloride anions were not present. Assuming that the oxidative addition of **1** to form [**I**] is reversible (Figure 48), then it follows that the oxidative addition equilibrium between [**1**] and [**I**]/[**II**] would lie mainly on the side of [**II**] at the beginning of the reaction due to the excess of

bromide anions present in the reaction mixture (Figure 48). This regime is consistent with the observed order in the aryl chloride ([**1**]) of 0.9 at the beginning of the reaction (Figure 44a).

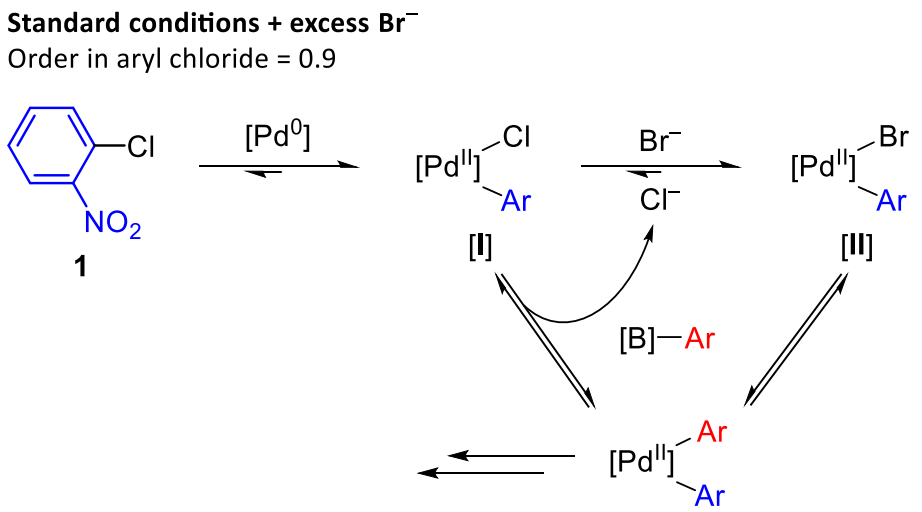

*Figure 48. Rationalisation for observed reaction order in [**1**] of 0.9 at the beginning of the cross-coupling reaction under the presence of excess bromide anions. The sequence of steps for the subsequent transmetallation of [**I**]/[**II**] with the aryl boronic acid (**2**) are not known and have been omitted for clarity.*

As chloride anions are liberated from the aryl chloride (**1**), a greater proportion of the oxidative addition product would form as intermediate [**I**] (Figure 49), which changes the distribution of the equilibrium between the aryl chloride (**1**) and [**I**]. This regime (Figure 49) is consistent with the observed order in the aryl chloride ([**1**]) of 0.5 for a reversible oxidative addition of **1** to form [**I**] (Figure 44b).

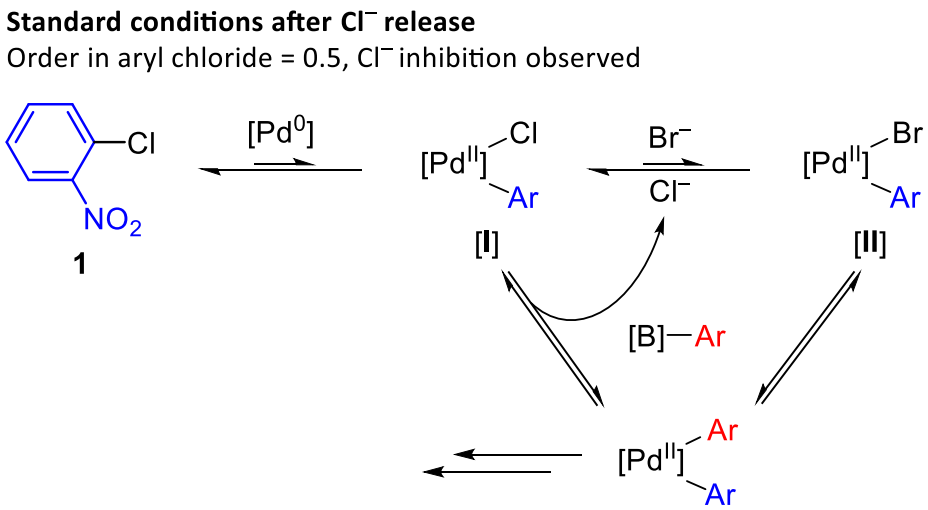

*Figure 49. Rationalisation for observed reaction order in [**1**] of 0.5 toward the end of the cross-coupling reaction when chloride anions have been released. The sequence of steps for the subsequent transmetallation of [**I**]/[**II**] with the aryl boronic acid (**2**) are not known and have been omitted for clarity.*

A build-up of chloride anions and [**I**] would result in a drop in the total concentration of [**I**]/[**II**] and a drop in the rate of the reaction. This is consistent with the observed chloride-mediated catalyst deactivation (as was observed in Figure 45 and Figure 46a).

Whilst the rationalisation above (Figure 48 and Figure 49) is consistent with the kinetic results, additional experimental evidence is needed to validate the proposed mechanism. If the oxidative addition to form [**I**] is reversible and [**I**] does indeed form [**II**], then the aryl bromide (**4**) may form as a result of a reversible oxidative addition to form [**II**] (Figure 50).

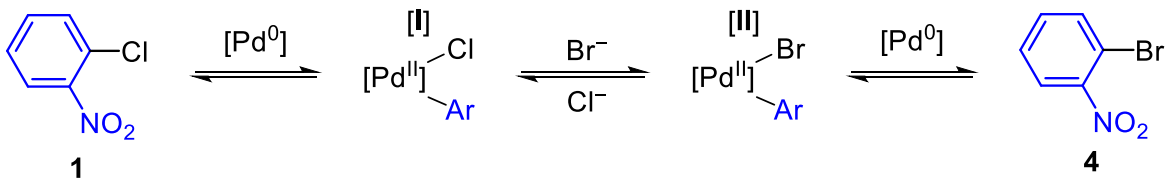

*Figure 50. Formation of aryl bromide **4** as a mechanistic 'handle' to confirm the postulated reversible oxidative addition and formation of [**II**].*

Whilst palladium-catalysed aryl halide metatheses are known,[76,77] the position of equilibrium favours the formation of the less reactive aryl halide,[78,79] *e.g.* metathesis of aryl triflates yields aryl bromides and chlorides.[77] Perhaps unsurprisingly then, no aryl bromide (**4**) was detected by HPLC analysis of the cross-coupling reaction to yield **3**. The absence of any aryl bromide (**4**) does not rule out the presence of a reversible oxidative addition or the formation of [**II**]. The standard conditions were subsequently replicated in the absence of the aryl boronic acid (**2**) to prevent catalyst turnover and trap the postulated **1**/[**I**]/[**II**]/**4** equilibrium (Scheme 80). Under these conditions, the formation of an aryl bromide (**4**) was still not detected. Instead, catalyst turnover and consumption of **1** occurred due to the formation of nitrobenzene (**5**) and 1-butanal. The formation of 1-butanal illustrates that protodehalogenation to give **5** likely occurred via β-hydride elimination of 1-butoxide from Ar–[Pd^{II}]–O^{n}Bu ([**III**]) followed by reductive elimination of Ar–H (**5**) from Ar–[Pd^{II}]–H ([**IV**]) (Scheme 80), a known mechanism for the reduction of Pd^{2+} complexes.[5,80,81]

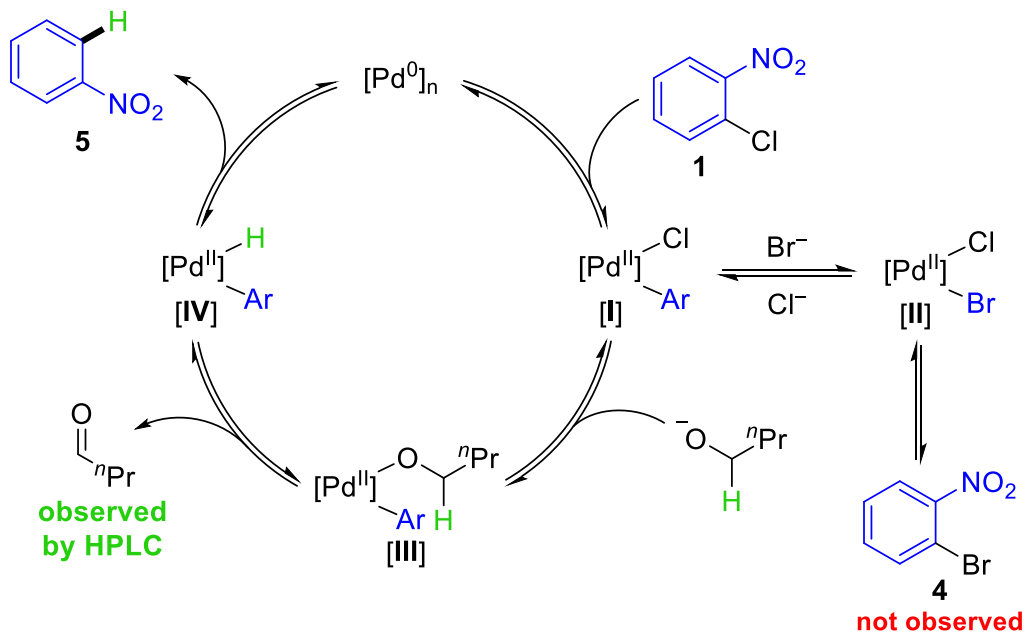

*Scheme 80. Postulated mechanistic cycle for the protodehalogenation of **1** based on the formation of 1-butanal. The reaction to yield **5** was catalysed by 0.1 mol% $[N^nBu_4]_2[Pd_2I_6]$ in 1-butanol at 90 °C in the presence of $[N^nBu_4]Br$ (1 equiv.), K_2CO_3 (1.5 equiv.) and NaBr (5 equiv.).*

Analysis of the crude reaction mixture by ^{1}H NMR spectroscopy confirmed that reductive elimination of [**III**] to form 1-butoxy-2-nitrobenzene was not observed.[82] The above mechanistic proposal (Scheme 80) was supported by the observation of a kinetic isotope effect in methanol-d_4 (Table 47).

Table 47. Comparison of protodehalogenation products in deuterated and non-deuterated solvents.[a]

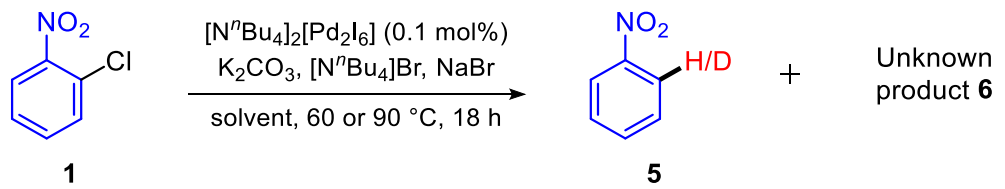

Entry	Solvent	Outcome
1	1-butanol	85% of **1** consumed to form **5** as the only product
2	methanol	75% of **1** consumed to form **5** as the only product
3	methanol-d_4	68% of **1** consumed to form a mixture of **5**-*d*, and unknown species **6**
4	D_2O	70% of **1** consumed to form a mixture of **5**-*d* as the minor product, and unknown species **6** as the major product

Conversion of **1** was determined by HPLC analysis with respect to naphthalene as an internal standard. Only **1** was quantified due to a lack of calibration for **5** and **6**. Minor and major products are therefore given based on relative peak areas and are estimates only. The reactions performed in 1-butanol and D_2O were performed at 90 °C, and at 60 °C in methanol/methanol-d_4.

In methanol, protodehalogenation occurred to give **5** as the only product (Table 47, Entry 2). In methanol-d_4, protodehalogenation occurred to give **5**-*d* alongside the formation of a significant quantity of an unknown product **6** (Table 47, Entry 3). The formation of unknown product **6** in methanol-d_4 but not in methanol is consistent with the presence of a kinetic isotope effect for the β-hydride elimination of [**III**] in the postulated mechanism for the formation of **5** (Scheme 80). When identical conditions were replicated in D_2O, unknown product **6** formed as the major product (Table 47, Entry 4). Since **6** formed as the major product in D_2O, its formation in methanol-d_4 may be the result of residual water contamination. Compound **6** was found not to be 2-chloro-2'-nitro-1,1'-biphenyl,[83] 2-nitrophenol, 2,2'-dinitrobiphenyl, 1,2-dibromobenzene, or 2-chloroaniline or 2-bromoaniline by comparison of their HPLC retention times with the retention time of **6**. It is possible that **6** is a product of the reduction of the nitro-group in **1**. Analysis of the crude material from the reaction in methanol-d_4 by NMR spectroscopy uncovered new environments at 8.60 ppm and >150 ppm in the ^{1}H and ^{13}C NMR spectra respectively. These new environments are strikingly deshielded when compared to the environments observed for the aryl chloride (**1**), and are not consistent with any of the aromatic nitro-group reduction products previously reported in the literature.[84] Attempts at isolating and identifying **6** were unsuccessful and its identity was not explored further.

Given the mechanism of catalyst turnover to form **5** (Scheme 80), 1-butanol was replaced with ^{t}BuOH to arrest catalyst turnover via β-hydride elimination (Scheme 81).

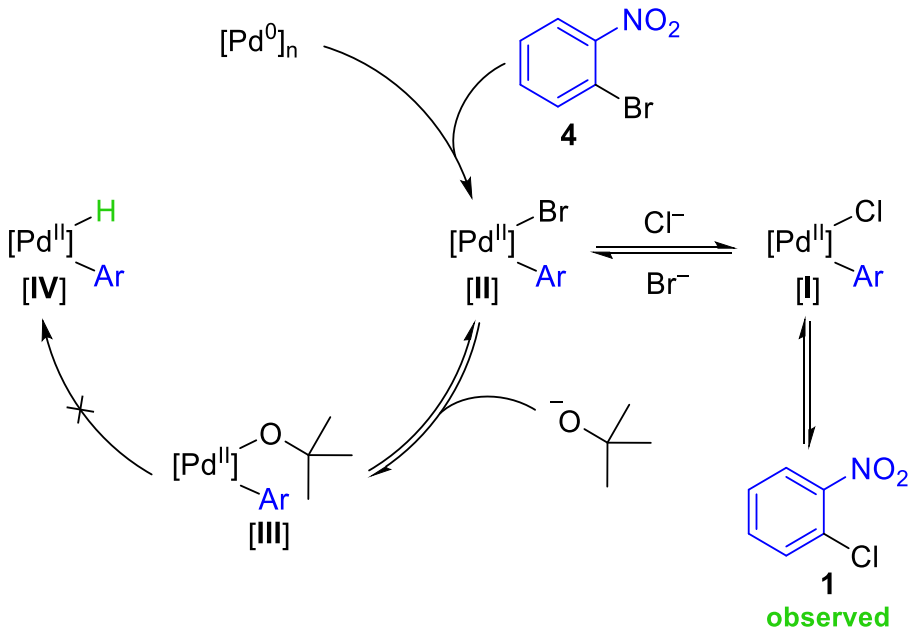

*Scheme 81. Arresting β-hydride elimination by performing the reaction in ^{t}BuOH. Under these conditions, the formation of **1** was observed. Reaction was catalysed by 0.1 mol% $[N^nBu_4]_2[Pd_2I_6]$ in ^{t}BuOH at 80 °C in the presence of $[N^nBu_4]Cl$ (1 equiv.), K_2CO_3 (1.5 equiv.) and KCl (5 equiv.).*

Using ^{t}BuOH still did not result in the formation of the aryl bromide **4** from the aryl chloride **1**. Since the lack of formation of **4** may be due to an irreversible oxidative addition of **4** to form [**II**], the starting aryl chloride (**1**) was replaced with aryl bromide **4** and an excess of chloride anions introduced in place of bromide (Scheme 81). The formation of aryl chloride **1** was observed under these conditions by HPLC analysis, and the formation of **1** further confirmed by spiking the HPLC sample with commercially sourced **1**.

The formation of the aryl chloride **1** from the aryl bromide **4** confirms that the oxidative addition of **1** is reversible, and that [**I**] can undergo halide exchange to form [**II**]. This result is consistent with the mechanistic rationalisation provided above (Figure 48 and Figure 49) to explain the observed reaction orders in the aryl chloride ([**1**]), and the observation of chloride anion mediated catalyst inhibition. This conclusion does however rely on the assumption that catalyst speciation when using aryl bromide **4** and aryl chloride **1** in the model reaction are identical. It should also be noted that oxidative addition of aryl halides to Pd^0 is generally considered to be irreversible, except in special cases such as the use of highly sterically encumbered ligands, or for specific substrates.[85] The oxidative addition of **1** to Pd^0 may then represent a special case, with the strongly electron-withdrawing *o*-nitro-group playing a major role in stabilising an Ar<-Pd^0 π-complex and/or stabilising an intermediate Meisenheimer complex formed via an unusual S_NAr mechanism of oxidative addition.[86] Additional computational studies are needed to better understand the mechanism of oxidative addition, the intermediates that are formed and their relative stabilities.

4.2.1.3. Reaction orders in $[N^nBu_4]_2[Pd_2I_6]$

The reaction orders in $[N^nBu_4]_2[Pd_2I_6]$ were determined using VTNA. A series of 'different excess' experiments were conducted at increasing catalyst loadings – 0.0044 mol%, 0.011 mol%, 0.022 mol%, 0.033 mol%, 0.044 mol%, 0.055 mol%, 0.066 mol%. To obtain reaction orders in $[N^nBu_4]_2[Pd_2I_6]$, the x-axis of temporal aryl chloride concentration ([**1**]) data was normalised according to Equation 4, assuming a constant catalyst concentration. The profiles used to determine the order in $[N^nBu_4]_2[Pd_2I_6]$ at 0.022 mol% and 0.011 mol% are illustrated as an example in Figure 51.

Table 48. Reaction conditions and starting concentrations for the reaction profiles presented in Figure 51.

Profile Colour	[**1**]$_0$ (M)	[**2**]$_0$ (M)	[[N^{n}Bu$_4$]Br]$_0$ (M)	[[N^{n}Bu$_4$][Pd$_2$I$_6$]]$_0$ (mM)
Blue	0.70	0.77	0.70	0.154 (0.022 mol%)
Red	0.70	0.77	0.70	0.077 (0.011 mol%)

All reactions were conducted in 1-butanol at 90 °C in the presence of K_2CO_3 (1.5 equiv.).

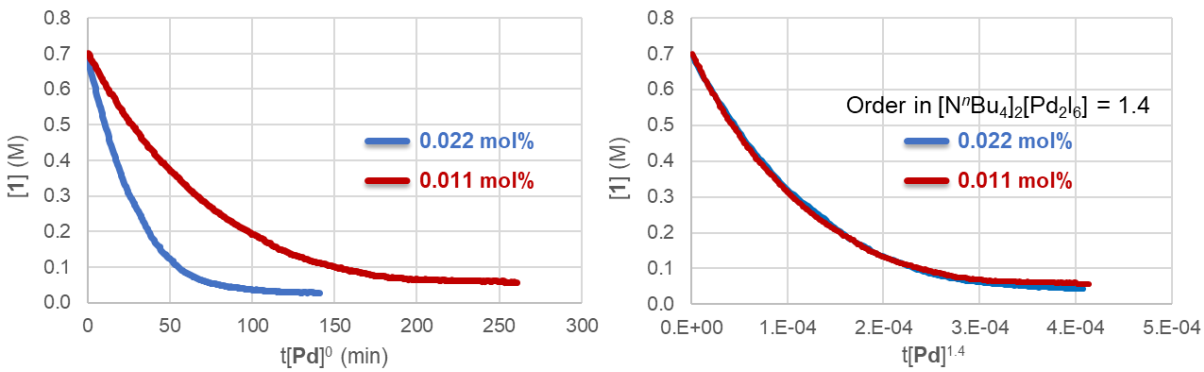

*Figure 51. Application of VTNA to determine the reaction order in [N^{n}Bu$_4$]$_2$[Pd$_2$I$_6$] at 0.011/0.022 mol% catalyst loading. Both reactions were conducted in 1-butanol at 90 °C in the presence of **2** (1.1 equiv.), [N^{n}Bu$_4$]Br (1 equiv.) and K_2CO_3 (1.5 equiv.). Profiles were produced using in situ ReactIR and the absorbance data calibrated offline using HPLC analysis with naphthalene as an internal standard.*

All of the raw reaction profiles at varying concentrations of [N^{n}Bu$_4$]$_2$[Pd$_2$I$_6$] and reaction orders in [N^{n}Bu$_4$]$_2$[Pd$_2$I$_6$] determined by overlapping profiles using VTNA are summarised in Figure 52. Each of these profiles were manipulated in an identical way to those presented in Figure 51 - the x-axis of temporal aryl chloride concentration ([**1**]) data was normalised according to Equation 4, assuming a constant catalyst concentration. The reaction conditions for each of the profiles in Figure 52 vary only in the concentration of the catalyst, and the loading of the catalyst is summarised in Table 49 and as an inset for each profile.

Table 49. Reaction conditions and starting concentrations for the reaction profiles presented in Figure 52.

Profile Colour	[**1**]$_0$ (M)	[**2**]$_0$ (M)	[[N^{n}Bu$_4$]Br]$_0$ (M)	[[N^{n}Bu$_4$][Pd$_2$I$_6$]]$_0$
Blue	0.70	0.77	0.70	Upper Loading
Red	0.70	0.77	0.70	Lower Loading

All reactions were conducted in 1-butanol at 90 °C in the presence of K_2CO_3 (1.5 equiv.).

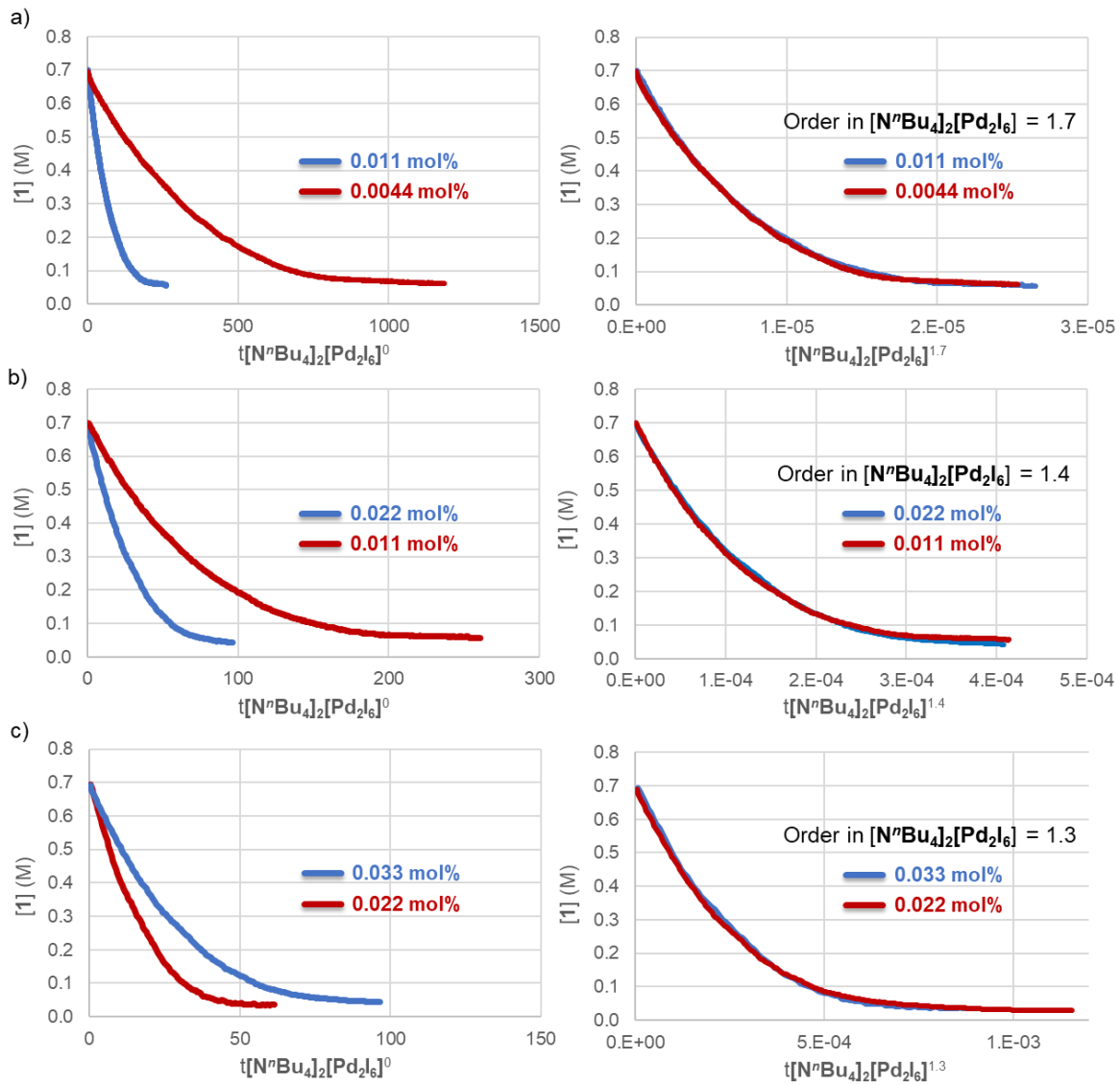

Figure 52. Application of VTNA to determine the model reaction orders in [N^{n}Bu$_4$]$_2$[Pd$_2$I$_6$], at different [N^{n}Bu$_4$]$_2$[Pd$_2$I$_6$] loadings. The original profiles are on the left and the VTNA profiles on the right. a) 0.0044-0.011 mol%, b) 0.011-0.022 mol%, c) 0.022-0.033 mol%. Profiles were produced using in situ ReactIR and the absorbance data calibrated offline using HPLC analysis with naphthalene as an internal standard.

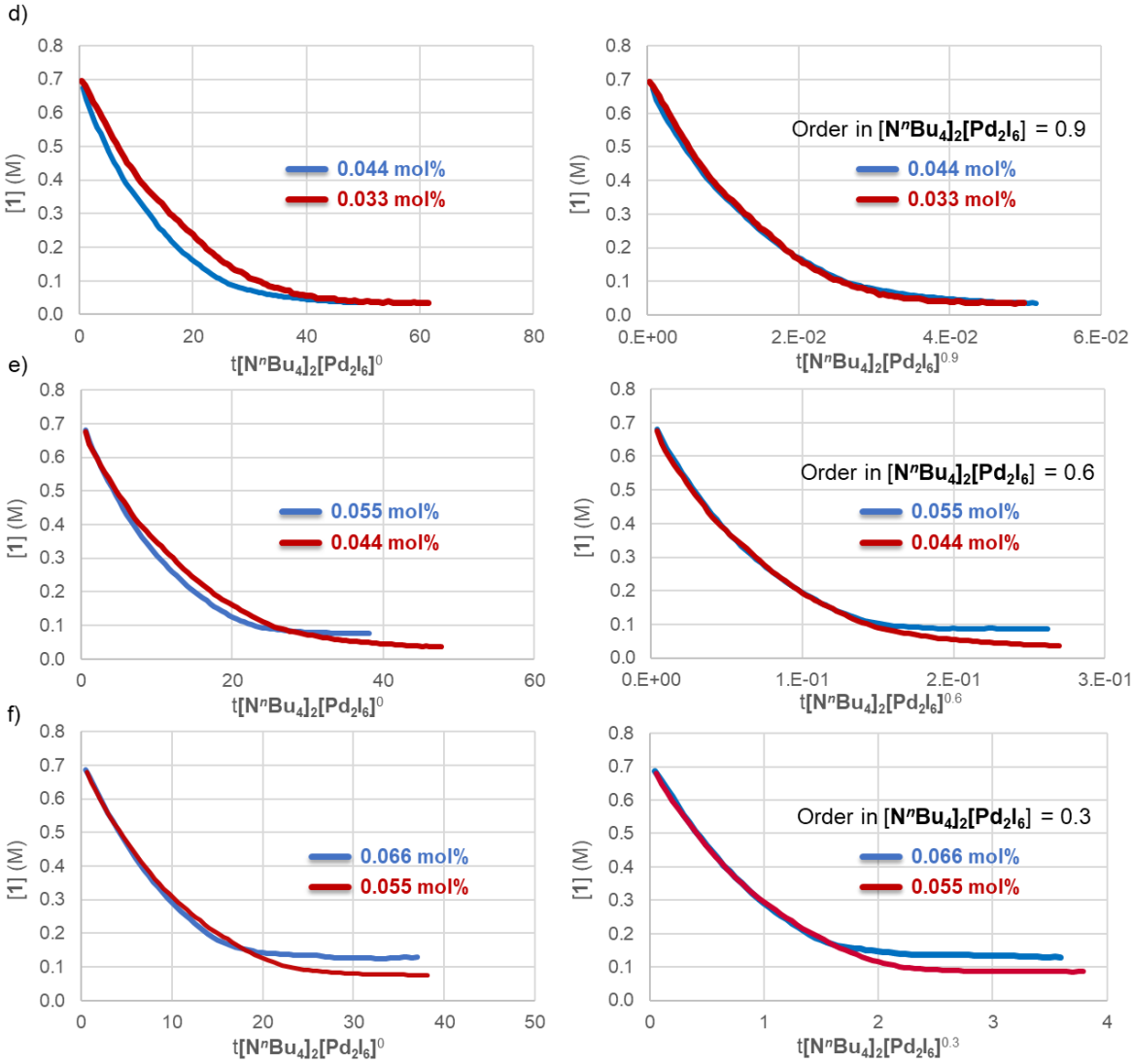

Figure 52 cont. Application of VTNA to determine the model reaction orders in [N^{n}Bu$_4$]$_2$[Pd$_2$I$_6$], at different [N^{n}Bu$_4$]$_2$[Pd$_2$I$_6$] loadings. The original profiles are on the left and the VTNA profiles on the right. d) 0.033-0.044 mol%, e) 0.044-0.055 mol%, f) 0.055-0.066 mol%. Profiles were produced using in situ ReactIR and the absorbance data calibrated offline using HPLC analysis with naphthalene as an internal standard.

Reaction orders in [N^{n}Bu$_4$]$_2$[Pd$_2$I$_6$] ranged from 1.7 to 0.3 (Figure 52). These observed orders do not necessarily correlate with the molecularity of any single elementary step,[23,74] nor does the molecularity of the precatalyst necessarily influence the catalyst order, as has been incorrectly reported.[27,30] One possible source of greater than first reaction orders in [N^{n}Bu$_4$]$_2$[Pd$_2$I$_6$] is the presence of an irreversible catalyst inhibitor which has a concentration, [**Inhibitor**], that is constant and independent of the catalyst loading.[23,75] This effect is especially likely and more significant at low catalyst loadings. The relationship between the reaction order and [**Inhibitor**] can be defined by elasticity analysis and rearranged to determine [**Inhibitor**] (Equation 5).[23]

$$[\boldsymbol{Inhibitor}] = \frac{(order\ in\ catalyst - 1) * [Cat]_{added}}{order\ in\ catalyst}$$

Equation 5

For orders of 1.7 and 1.4 at 0.0044-0.022 mol% $[N^nBu_4]_2[Pd_2I_6]$, an [**Inhibitor**] was calculated as ~0.0028 mol%. A model reaction utilising a 0.001 mol% loading of $[N^nBu_4]_2[Pd_2I_6]$ was subsequently performed, which resulted in the formation of **3** in a 55% yield after 24 h (Scheme 82).

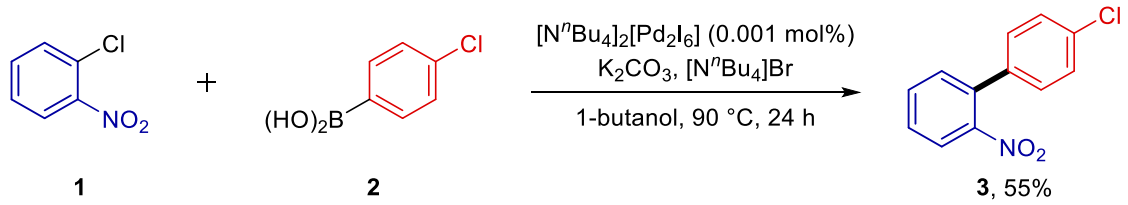

*Scheme 82. Cross-coupling reaction yielding **3** run at a catalyst loading below the concentration of inhibitor, [**Inhibitor**], that would be required to give the observed reaction orders in $[N^nBu_4]_2[Pd_2I_6]$.*

Therefore, the observed non-unity orders in $[N^nBu_4]_2[Pd_2I_6]$ cannot be the result of an irreversible catalyst inhibitor, since catalyst turnover was observed at a catalyst concentration that is lower than the calculated [**Inhibitor**].

Having ruled out the presence of a catalyst inhibitor, it can be concluded that the dynamic non-unity orders in $[N^nBu_4]_2[Pd_2I_6]$ are the result of loading-dependent aggregation of the active catalyst. One possible explanation is the formation of differently sized nanoparticles at different catalyst loadings. This rationalisation relies on making a distinction between the concentration of palladium, [**Pd**], and the concentration of active sites, [**Active Sites**]. The activity of nanoparticles is achieved by reaction of the substrate with low coordination surface active sites, and the fraction of atoms which occupy these active sites decreases with increasing particle size.[19–21,87–89] For the *in situ* formation of nanoparticles from $[N^nBu_4]_2[Pd_2I_6]$, nanoparticle sizes will presumably increase with the palladium concentration,[21,88,90,91] and the number of surface active sites does not scale linearly with particle size.[19–21,87–90,92,93] Thus, if differently sized nanoparticles are forming at different [**Pd**], the non-linear reaction order data in $[N^nBu_4]_2[Pd_2I_6]$ could be reflecting a non-linear relationship between [**Pd**] and [**Active Sites**].

At the upper loadings of 0.033-0.066 mol% (orders in $[N^nBu_4]_2[Pd_2I_6]$ of 0.9-0.3) the formation of proportionally fewer actives sites at larger particle sizes must dominate the change in catalytic activity

for these loadings to exhibit <1 orders in $[N^nBu_4]_2[Pd_2I_6]$ (Scheme 83). Presumably there is little difference, if any at all, in the intrinsic activity of the active sites formed at these loadings.

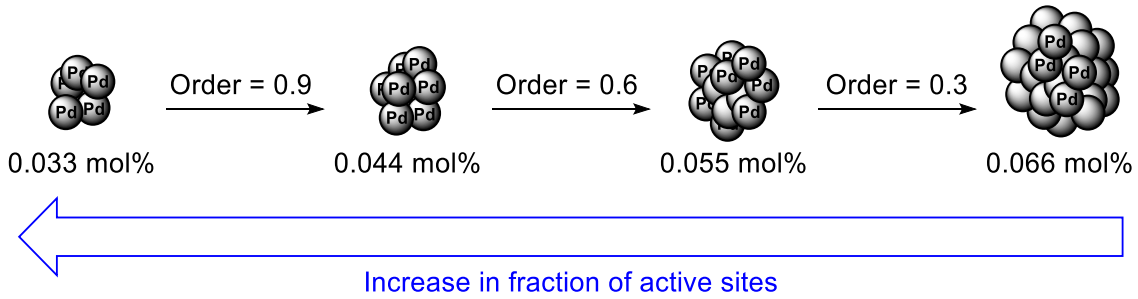

Scheme 83. Reduction in the fraction of active sites at loadings >0.033 mol% which dominates the change in reaction rate. (Particle sizes and palladium atoms are given only as an illustration of a general trend).

A change in [**Active Site**] cannot explain the >1 orders in $[N^nBu_4]_2[Pd_2I_6]$, since orders >1 imply that the particle sizes become smaller upon increasing the loading at 0.0044-0.033 mol%. Instead, for orders >1, the aggregated species formed at 0.0044-0.033 mol% must be intrinsically more active than those formed for the lower order species at the lower loading (Scheme 84). Under this regime, the clusters may contain a few to tens of palladium atoms, with the formation of these clusters resulting in an increase in rate. In other words, the experimentally observed >1 orders may reflect a changing rate constant for the higher order species, and this rationalisation is also consistent with the order trending downwards at increasing catalyst loadings (an upwards trend would be expected for a simple monomer-dimer equilibrium).

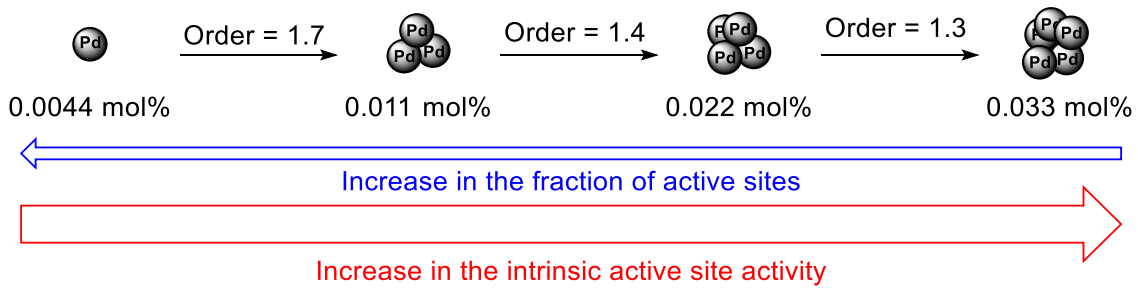

Scheme 84. Increase in intrinsic activity as a result of aggregation at increased loadings that is implicated by >1 orders. Activity increase must outweigh the reduction in the fraction of active sites for an order >1 to be observed (Particle sizes and palladium atoms are given only as an illustration of a general trend).

The observation of two distinct kinetic order regimes at different catalyst loadings has been previously reported in a Mizoroki-Heck reaction catalysed by low loadings of $Pd(OAc)_2$.[31] Additional experimental evidence for the above rationalisation (Scheme 83 and Scheme 84) was gathered by imaging the reaction mixture using TEM (Section 4.2.1.5).

4.2.1.4. Deconvolution of [Active Site] using VTNA

First orders in catalyst have been reported for stable nanoparticles synthesised *ex situ* in which the size does not change at different loadings,[94–100] including in a Suzuki-Miyaura reaction,[93] since the [**Active Site**] scales linearly with nanoparticle loading. Therefore a first order in $[N^nBu_4]_2[Pd_2I_6]$ would be observed when Equation 4 incorporates the correct values of [**Active Sites**] in place of $[N^nBu_4]_2[Pd_2I_6]$. By assuming this first order in [**Active Site**], values of [**Active Site**] can be deconvoluted from the reaction order data in $[N^nBu_4]_2[Pd_2I_6]$. This is performed by plotting VTNA-linearised temporal aryl chloride ([**1**]) profiles at different catalyst loadings. Two such linearised profiles which utilise different $[N^nBu_4]_2[Pd_2I_6]$ loadings have the kinetic component of the catalyst and aryl chloride (**1**) concentrations removed from the rate of the reaction, and vary only in the fraction of active sites (Figure 53a), [**Active Site**]. Subsequently solving for the correct value of [**Active Site**] by deconvolution removes any kinetic differences between the two profiles and results in their visual overlap (Figure 53b). Deconvolution was performed by solving for identical profile slopes using Solver in Microsoft Excel. The linearised (Figure 53a) and overlapping (Figure 53b) profiles for 0.011 and 0.022 mol% loadings are illustrated as an example in Figure 53.

$$t[\mathbf{1}]^{0.6}[\boldsymbol{Active\ Site}]^{1} = \sum_{i=1}^{n}\left(\frac{[\mathbf{1}]_i + [\mathbf{1}]_{i-1}}{2}\right)^{0.6} \cdot \sum_{i=1}^{n}\left(\frac{[\boldsymbol{Active\ Site}]_i + [\boldsymbol{Active\ Site}]_{i-1}}{2}\right)^{1} \cdot (t_i - t_{i-1})$$

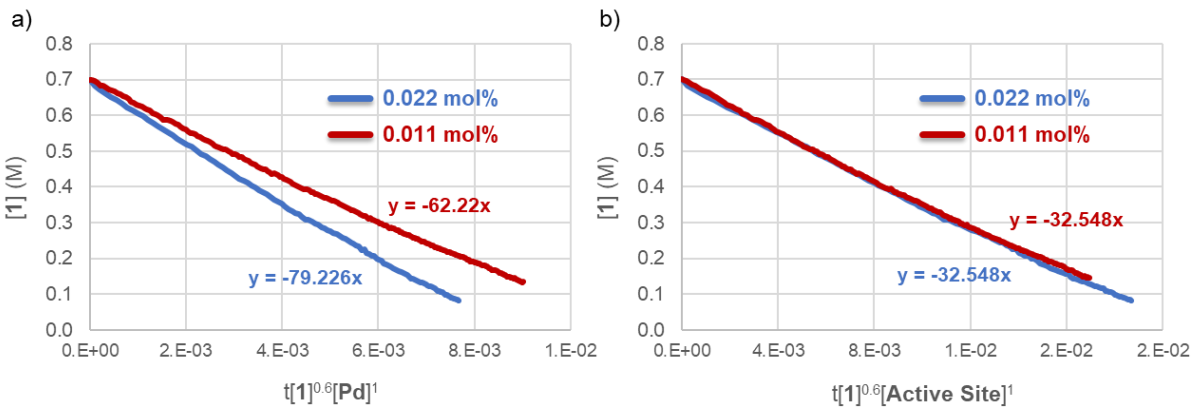

*Figure 53. a) Temporal [**1**] profile was linearised using the top equation. Profiles do not overlap due to non-linear relationship between [**Pd**] and [**Active Site**] at the two loadings. b) Temporal [**1**] profile was linearised using the top equation for $[\mathbf{1}]^{0.6}$ and $[\mathbf{Pd}]^{1}$. The profiles overlapped by solving for [**Active Site**]. (Deconvolution was performed using Solver in Microsoft Excel by finding [**Active Site**] which yielded identical profile slopes). Both reactions were catalysed by $[N^nBu_4]_2[Pd_2I_6]$ in 1-butanol at 90 °C in the presence of the aryl boronic acid (**2**) (1.1 equiv.), $[N^nBu_4]Br$ (1 equiv.) and K_2CO_3 (1.5 equiv.). Profiles were produced using in situ ReactIR and the absorbance data calibrated offline using HPLC analysis with naphthalene as an internal standard.*

Deconvolution was repeated for each of the catalyst loadings for which reaction orders had been determined by VTNA (Figure 52). The resulting deconvoluted [**Active Site**] values were plotted against catalyst loading (Figure 54a). TOF values were also calculated as a function of deconvoluted [**Active Site**] values and plotted against catalyst loading (Figure 54b).

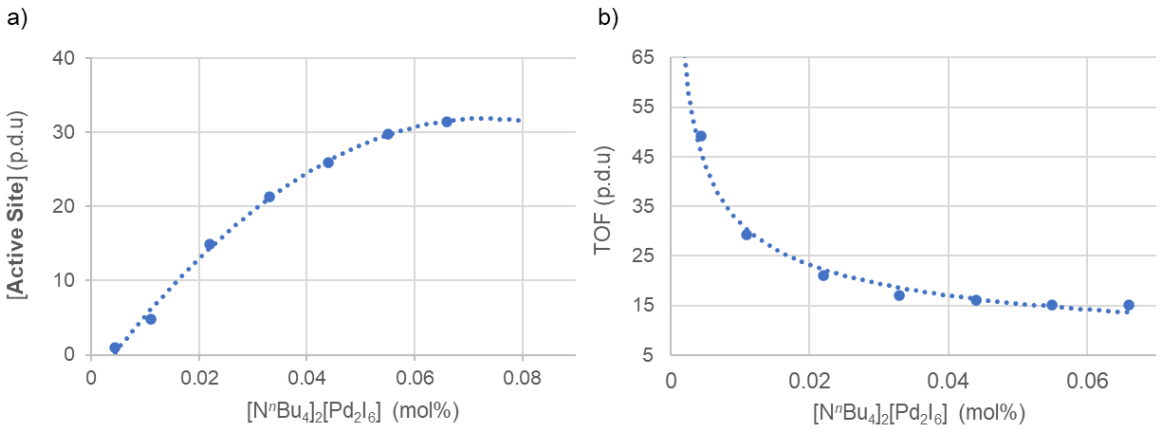

*Figure 54. a) A plot of deconvoluted [**Active Site**] against [N^{n}Bu$_4$]$_2$[Pd$_2$I$_6$] loading. b) A plot of TOF against [N^{n}Bu$_4$]$_2$[Pd$_2$I$_6$] loading (TOF = [**3**] (M)/[**Active Site**]*min). In both cases, the y-axis are labelled as p.d.u (procedure defined units) since the [**Active Site**] are relative values, deconvoluted from an arbitrarily defined number at 0.0044 mol%. Deconvolution was performed using Solver in Microsoft Excel by finding [**Active Site**] which yielded identical profile slopes.*

The relationship between [N^{n}Bu$_4$]$_2$[Pd$_2$I$_6$] loading and TOF (Figure 54b) is characteristic of the relationship that has been frequently reported for nanoparticles (Figure 55).[19–21,87–93] Nanoparticles with a size/activity that follows this trend are reported to react via low coordination number (LCN) surface atoms and have been classified as possessing 'class-II surface sensitivity' (Figure 55b).[19,20] As nanoparticles increase in size, the fraction of atoms which occupy LCN surface sites decreases (Figure 55a, and Figure 55c top inset).[92] The influence of this phenomenon on the catalytic activity of class-II surface sensitivity nanoparticles is well-studied (Figure 55),[19–21,89–92] including for Suzuki-Miyaura and Mizoroki-Heck reactions which were catalysed by palladium nanoparticles,[93,101] with a reduction in particle sizes providing an exponential increase in catalytic activity (Figure 55b-d). Literature examples which illustrate the behaviour of class-II surface sensitive nanoparticles are provided in Figure 55.[91,92] The observation of class-II surface sensitivity in [**Active Site**] data deconvoluted from the reaction orders in [N^{n}Bu$_4$]$_2$[Pd$_2$I$_6$] (Figure 54) provides evidence for the formation of nanoparticles in the cross-coupling reaction.

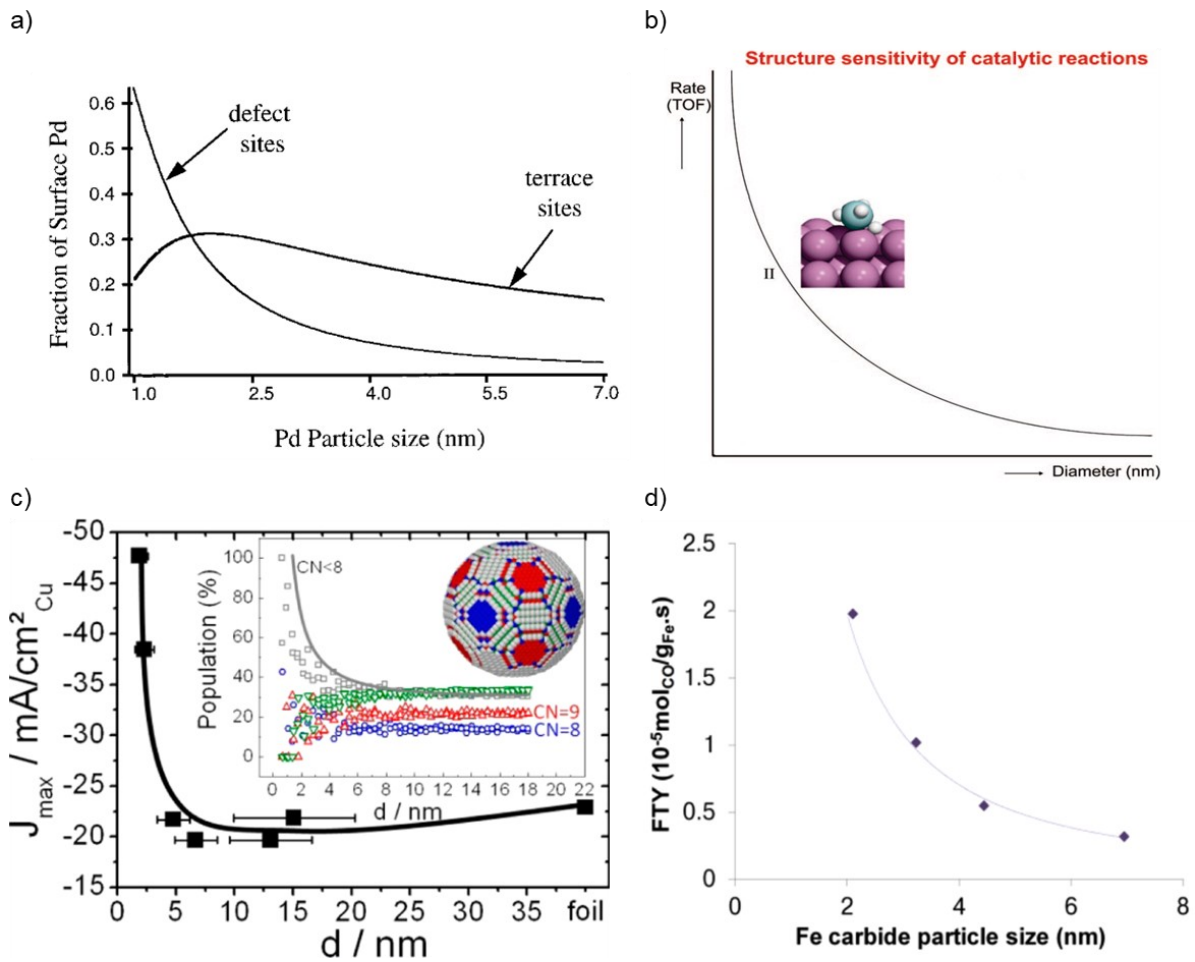

Figure 55. Four literature examples of class-II surface sensitivity nanoparticles. a) Influence of Pd particle size on fraction of surface atoms in LCN defect sites. b) Illustration of the influence of class-surface sensitivity on TOF. c) Illustration of exponential increase in LCN surface sites (inset, CN<8, grey) and resulting exponential increase in electrocatalytic current density (J_{max}). b) Exponential increase in catalytic activity for decreasing Fe carbide nanoparticle sizes (catalytic activity expressed as moles of CO converted to hydrocarbons per gram of iron per second, or FTY). Examples were reproduced with permission from references 101 (a), 20 (b), 92 (c) and 91 (d).

This is, to the best of our knowledge, the first time that VTNA has been utilised to deconvolute catalyst activity changes from reaction order data. This novel application of VTNA could in principle be applied to uncover mechanistic understanding for any reaction which displays non-unity reaction orders.

4.2.1.5. Quantifying [Active Site] using Transmission Electron Microscopy

Transmission electron microscopy (TEM) was then used to detect and quantify the presence of nanoparticles in the model reaction. An initial attempt at TEM imaging of an aliquot of the reaction mixture yielded an image containing a broad range of particles up to 1 µm in diameter (Figure 56).

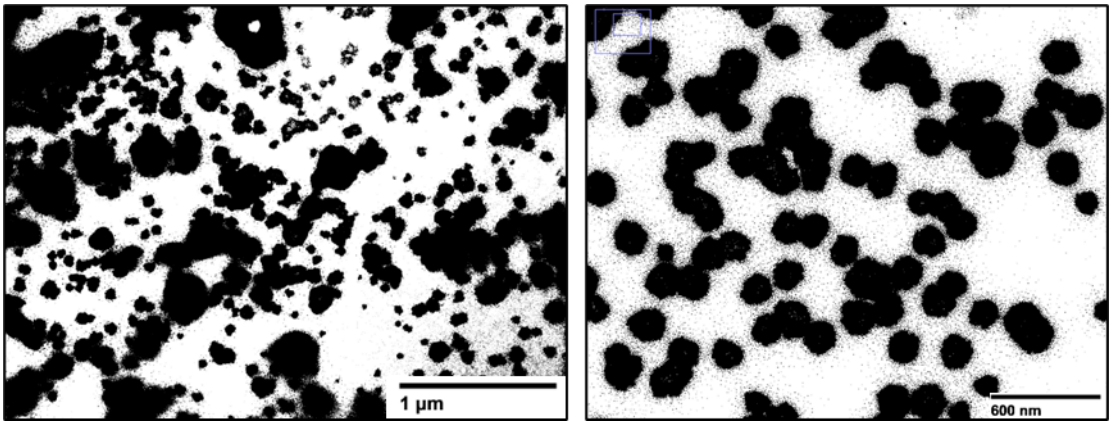

Figure 56. Two TEM images of an aliquot of the model reaction mixture. The sample was filtered through a 0.2 µm syringe filter.

Since the particles sizes were larger than the pore sizes of the syringe filter (0.2 µm) that was used to filter the aliquot, the particles must have aggregated during concentration on the TEM grid. Indeed, a palladium black precipitate formed when a reaction aliquot was left to stand at room temperature after ~5 min (Table 50, Entry 1). The particles observed by *ex situ* TEM imaging were therefore of palladium black aggregates (Figure 56) and were not representative of the particles present *in situ* during catalysis. The development of a new sampling protocol was explored in an attempt to stabilise the palladium particles present *in situ* (Table 50).

Table 50. Conditions explored for stabilising Pd^0 to enable TEM imaging.

Entry	Dilution solvent temperature (°C)	Additive	Stability observation
1	none	none	Pd black precipitate after ~ 5 min
2	–78	none	Stable indefinitely at –79 °C Pd black precipitate after ~5 min at r.t.
3	–78	TWEEN® 20	Pd black precipitate after ~ 2 h
4	–78	PEG[b]	Pd black precipitate after ~20 min
5	–78	PEG-thiol[c]	Pd black precipitate after ~ 8 h
6	–78	CTAB[d]	Pd black precipitate after ~ 30 min
7	–78	PVP[e]	No Pd black precipitate after >6 months

For each experiment, an aliquot (1 mL) of a model reaction mixture (10 mL, 0.7 M) under the optimised conditions was taken (at T = 20 min) and diluted in a stirred solution of additive in ethanol (1 mL) at –78 °C. [a)] Values in parenthesis are the aliquot/dilutant volume ratios. [b)] There were no observed differences in stability between PEG (M_w = 50k and M_w = 100k) loadings of 5, 10, 20 or 100 mg. [c)] There were no observed differences in stability between PEG-thiol (M_w = 2k) loadings of 5, 10, 20 or 100 mg. [d)] CTAB = cetyltrimethylammonium bromide (10 mol%). [e)] PVP = polyvinylpyrrolidone. Indefinite stability was obtained with 30 mg of PVP (M_w = 29k).

Since nanoparticle aggregation is well-known to be temperature dependent,[94,102–106] reaction aliquots were cooled at −78 °C. The solution of Pd^0 appeared to be indefinitely stable under the cryogenic conditions, but aggregated to palladium black after being left to warm to room temperature (Table 50, Entry 2). The effect of a number of additives and surfactants on Pd^0 stability was subsequently explored. Reaction aliquots were injected into cooled solutions of TWEEN® 20 (polyethylene glycol sorbitan monolaurate) (Table 50, Entry 3), polyethylene glycol (PEG, M_w = 50 and 100k) (Table 50, Entry 4), thiolated polyethylene glycol (PEG-thiol, M_w = 2k) (Table 50, Entry 5) and CTAB (cetyltrimethylammonium bromide) (Table 50, Entry 6). The stability of Pd^0 was improved in the presence of these additives, to varying degrees, however, in each case a palladium black precipitate was eventually observed. Polyvinylpyrrolidone (PVP) has been used extensively in the stabilisation of nanoparticles,[107] including for palladium nanoparticles which have been applied as catalysts.[93,101] When PVP was used as an additive, no palladium black precipitate was observed when the sample was left at room temperature for >6 months (Table 50, Entry 7).

Whilst it was sometimes possible to obtain images of the particles from a PVP-stabilised crude reaction aliquot, significant excesses of organic compounds (**1**, **2**, **3**, **4** and $[N^nBu_4]Br$ totalling ~223 mg/mL vs 0.033 mg/mL of [Pd]) rendered imaging time consuming, and in some cases impossible. In the majority of attempts, nanoparticles could not be found due to the layer of organic materials on the surface of the grid. As a result, a size exclusion chromatography (SEC) purification step using lipophilic Sephadex® (Sephadex®-LH20) was developed and included prior to TEM imaging. Purification by SEC removed the low molecular weight organic compounds in excess and rendered imaging by TEM significantly easier. It should be noted that smaller average diameters (*i.e.* 2.5 nm vs 4.8 nm at 0.044 mol%) were obtained from TEM imaging of the particles which underwent SEC. It is likely that the significant quantity of organic contaminants that were present in the absence of the SEC purification step reduced the ability to image smaller nanoparticles. The final procedure used to stabilise and prepare the sample for imaging by TEM is outlined in Figure 57.

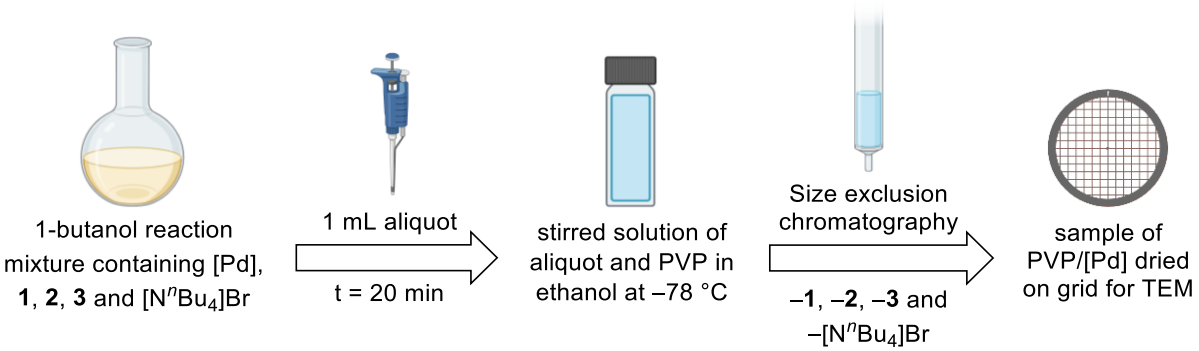

Figure 57. Final procedure for stabilising and preparing the reaction samples for imaging by TEM. All samples were passed through a 0.2 µm syringe filter to remove any dust particles prior to loading on the TEM grid. Figure produced using biorender.

A sample of the model reaction which used 0.044 mol% loading of $[N^nBu_4]_2[Pd_2I_6]$ was subjected to the procedure in Figure 57 and the average particle diameters determined using TEM (Figure 58).

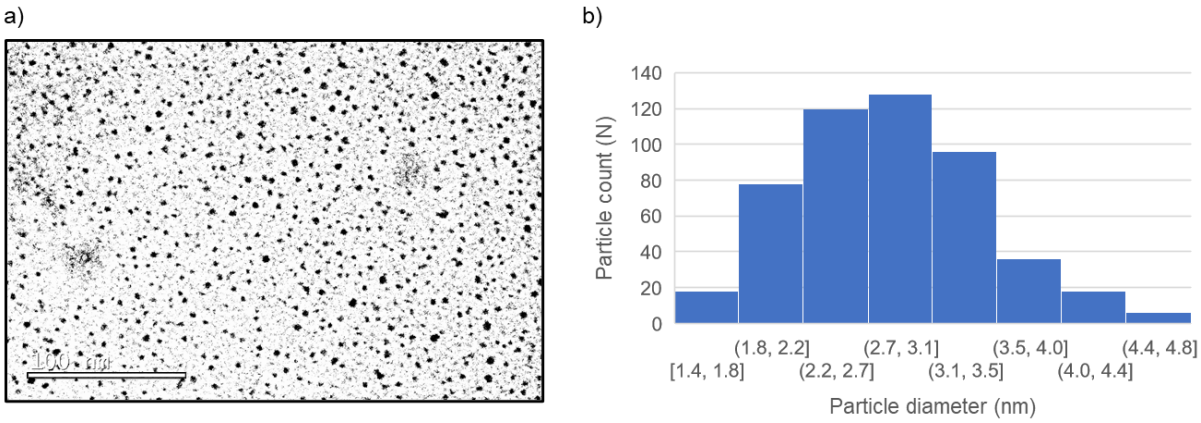

Figure 58. a) TEM image of an aliquot of the model reaction mixture which was diluted into a cooled (−78 °C) solution of PVP (M_w = 29k) and the resulting solution purified by SEC and filtered through a 0.2 µm syringe filter. b) Particle diameter distributions obtained from the TEM image in a).

Whilst this new protocol prevented Pd^0 particles from aggregating to palladium black, it is still possible that some aggregation occurred when the sample was dried on the TEM grid. To assess whether the particles do not aggregate on the TEM grid during dying, an analytical technique is needed which can measure the particle sizes in solution. Dynamic light scattering (DLS) was consequently used to determine particle sizes before and after the solvent had been removed from the sample. The particle sizes obtained by DLS are hydrodynamic diameters and include the surface polymer coating, and are thus not direct measurements of the exact size of the nanoparticle metal core. Nevertheless, if the nanoparticles aggregate and increase in size during drying, the sizes measured by DLS would also increase. To test for this, a reaction aliquot was immediately analysed by DLS after stabilising in PVP. The same sample was then analysed after the solvent was removed at room temperature, and the resulting DLS data were compared (Figure 59).

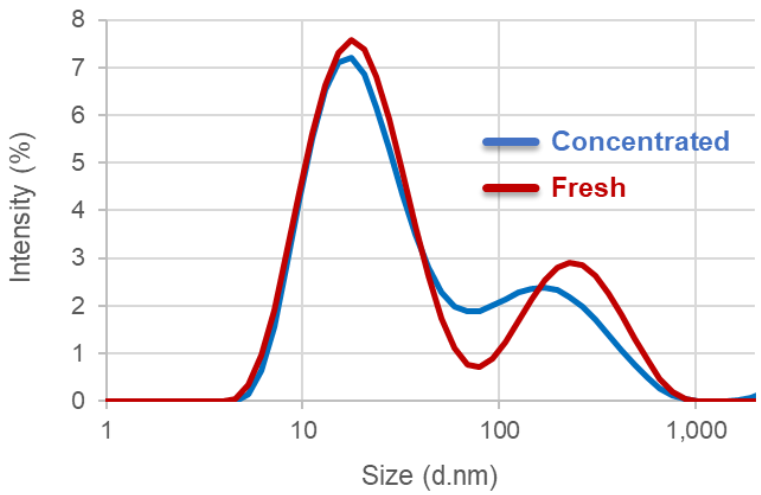

Figure 59. Comparison of the DLS data of a fresh aliquot of the model reaction mixture (red), and a resuspended aliquot of the model reaction mixture following concentration. Sample concentration was conducted in vacuo (~1 mmHg) in a room temperature water bath for ~ 8 h. After concentration, the sample was redispersed in a 1:1 mixture of ethanol and 1-butanol (2 mL).

Comparison of the two DLS plots illustrates that only a small deviation in the hydrodynamic sizes and size distributions occurred after concentration of the sample. This result confirms that quenching the reaction aliquot with PVP at –79 °C is effective at 'trapping' the particles present *in situ*.

Average diameters were subsequently determined from TEM images of the nanoparticles formed at each of the $[N^nBu_4]_2[Pd_2I_6]$ loadings (Table 51).

Table 51. Average particle diameters obtained from TEM imaging of PVP-stabilised aliquots of the model reaction mixture at increasing catalyst loadings.

Entry	$[N^nBu_4]_2[Pd_2I_6]$ (mol%)	Average particle diameter (nm)
1	0.0044	n.d.
2	0.011	2.05
3	0.022	2.30
4	0.033	2.36
5	0.044	2.45
6	0.055	2.60
7	0.066	2.81

n.d. = no data. In each case, an aliquot (1 mL) of the model reaction mixture was taken at 20 min and immediately cooled (–78 °C) in a stirred ethanol (1 mL) solution of PVP (M_w = 20k, 30 mg). The resulting solution of stabilised Pd^0 was purified by SEC (Sephadex®-LH20), filtered through a syringe filter (0.2 µm) and sampled on a grid for TEM analysis

Palladium nanoparticles were not observed by TEM at 0.0044 mol% loading, even when the solution was concentrated to bring the [**Pd**] in line with the other samples. Presumably, either no nanoparticles were present at these low loadings or the particles were below the detection limit of the microscope. The absence of nanoparticles at 0.0044 mol% may explain the >1 orders observed at 0.0044 and 0.011 mol% loadings – the introduction of additional palladium atoms at 0.011 mol% loading resulted in the formation of nanoparticles with increased intrinsic activity (*i.e.* increased rate constant) which were not present at the lower loading.

An increase in the average particle diameters was observed upon increasing the loading from 0.033 mol% (Table 51). The fraction of atoms which occupy LCN active sites has previously been modelled for different nanoparticle sizes using various software packages,[99,102,108–111] *e.g.* Materials Studio. Unfortunately none of the packages previously utilised in the literature could be accessed for the present study. Instead, a palladium nanoparticle that is 2.1 nm in diameter and consists of 369 atoms was modelled in Vesta (freely available software). The LCN surface sites exist at the vertices (CN = 6) and edges (CN = 7) of the cuboctahedra. The vertex and edge sites were identified manually and illustrated in grey and orange, respectively (Figure 60).

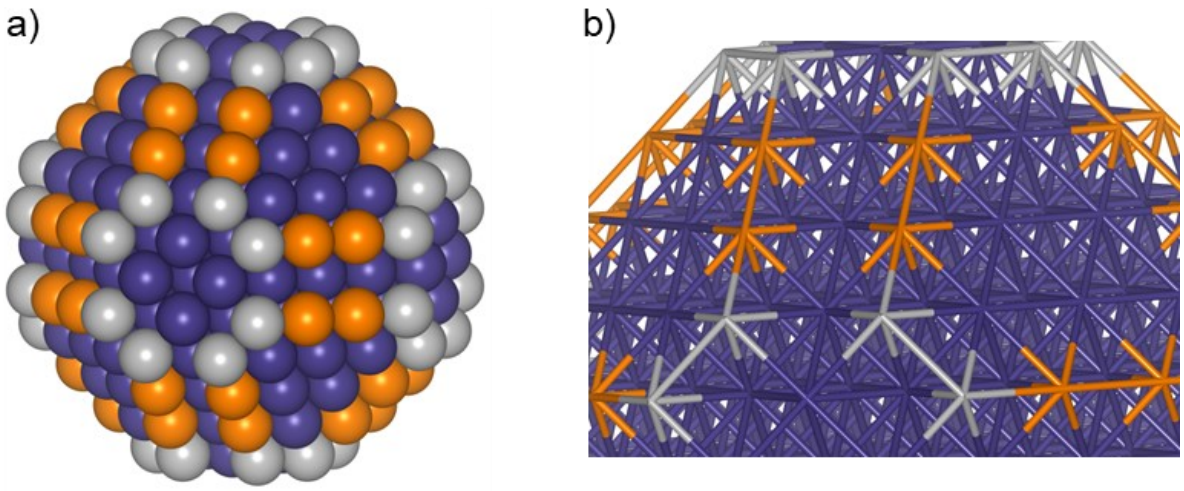

Figure 60. A cuboctahedral palladium nanoparticle of 2.1 nm. a) LCN surface sites labelled in grey (CN = 6) and orange (CN = 7). b) Wireframe view which illustrates the CNs of the vertex (grey, CN = 6) and edge (orange, CN = 7) sites. Nanoparticle was modelled in Vesta using the lattice parameters for a face centred cubic Pd crystal and CNs are first-shell CNs based on a bond length of 2.8 Å.

The fraction of atoms which occupy these LCN surface sites for different particle sizes could only be obtained in Vesta by manually growing the particle and manually identifying the sites. This process was time consuming and was therefore not performed for each nanoparticle size. Instead, to expedite

the current investigation, statistics that were previously reported for closed face-centred cuboctahedra were used to quantify the fraction of LCN surface sites at different particle sizes.[112] The fraction of active sites for the 2.1 nm nanoparticle (Figure 60) modelled in Vesta (26%) is in a reasonable agreement with the fraction determined by statistical analysis (24%).[112]

The fraction of active sites obtained from TEM imaging and subsequent statistical analysis were then used to calculate [**Active Site**] (Table 52).

*Table 52. [**Active Site**] values determined from average particle diameters and the corresponding fraction of LCN surface sites.*

$[N^nBu_4]_2[Pd_2I_6]$ (mol%)	[**Pd**] (M)	Average particle diameter (nm)[a]	Fraction LCN surface sites (%)[b]	[**Active Site**][c] (M)
0.033	4.62×10^{-4}	2.36	18	8.35×10^{-5}
0.044	6.16×10^{-4}	2.45	17	1.04×10^{-4}
0.055	7.70×10^{-4}	2.60	15	1.17×10^{-4}
0.066	9.24×10^{-4}	2.81	13	1.22×10^{-4}

[a)] Particle sizes were obtained experimentally by TEM imaging of 'trapped' reaction aliquots (Table 51). [b)] The fraction of LCN surface sites was determined using previously reported statistics.[c)] [**Active Site**] = ([**Pd**]/100)xFraction LCN surface sites.

The values of [**Active Site**] determined by deconvolution of the reaction order data (Figure 54) were shifted down the y-axis for comparison with the values determined by TEM (Table 52). Good agreement between the two sets of values was observed (Figure 61).

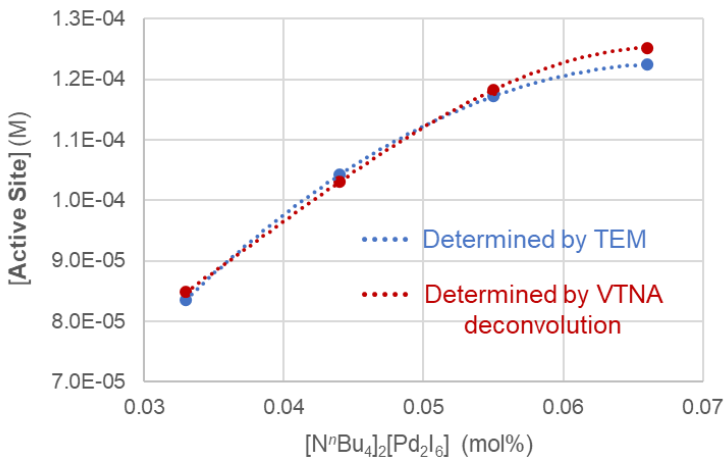

*Figure 61. Values of [**Active Site**] determined by TEM (blue) and by deconvolution of the reaction orders using VTNA (Red).*

The values of [**Active Site**] determined by TEM were then utilised to determine reaction orders in $[N^nBu_4]_2[Pd_2I_6]$ using VTNA (Figure 62).

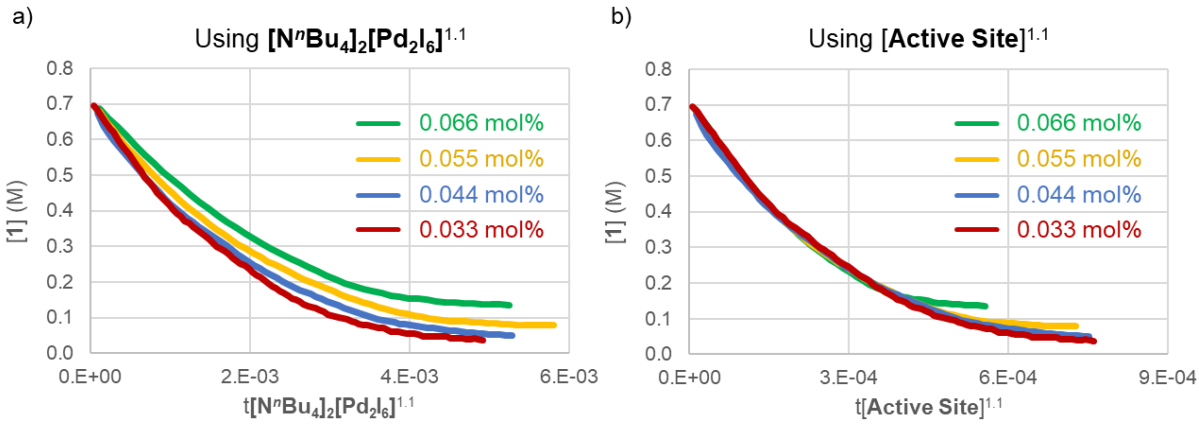

Figure 62. a) Non-overlapping VTNA profiles using ***$[N^nBu_4]_2[Pd_2I_6]$*** *at an order of 1.1. b) Overlapping VTNA profiles using [**Active Site**] at an order of 1.1. Final deactivated portion of the 0.066 mol% profile was shortened for clarity, which is recommended for VTNA of profiles which deviate from catalytic steady-state.[60-63] All reactions were catalysed by $[N^nBu_4]_2[Pd_2I_6]$ in 1-butanol at 90 °C in the presence of **2** (1.1 equiv.), $[N^nBu_4]Br$ (1 equiv.) and K_2CO_3 (1.5 equiv.). Profiles were produced using in situ ReactIR and the absorbance data calibrated offline using HPLC analysis with naphthalene as an internal standard.*

The best visual overlay using [**Active Site**] was obtained at an order of 1.1 (Figure 62b), whilst a poor overlay was obtained for an order of 1.1 in $[N^nBu_4]_2[Pd_2I_6]$. This illustrates that the correct active site, *i.e.* CN = 6 or 7, has been identified and quantified. This is, to the best of our knowledge, the first time that kinetic reaction orders have been used to implicate and rationalise the speciation of nanoparticles from a molecular palladium precatalyst.

When considering only the fraction of LCN surface sites, the greater than first orders exhibited in [**Pd**] can only be first order in [**Active Site**] if the particles generated are smaller at increased catalyst loadings. Thus, catalytic activity at loadings below 0.033 mol% must be dominated by some factor which is not accounted for by determining [**Active Site**], *e.g.* a change in rate constant. The presence of these two kinetic regimes was discussed previously (Scheme 83, Scheme 84). No further analysis of the kinetic orders obtained at loadings below 0.033 mol% were conducted, and additional work is needed to uncover the mechanistic origin of these orders.

4.2.1.6. Deconvolution of palladium black formation kinetics using VTNA

A non-linear influence of the catalyst loading on the yield of the Suzuki-Miyaura coupling product **3** was previously modelled by DoE (Figure 33 and Figure 34). This was rationalised to be due to the formation of inactive palladium black at loadings >0.044 mol% (Figure 33 and Figure 34), and it was found that the onset of palladium black occurred earlier in the reaction at elevated catalyst loadings. This behaviour was also observed during VTNA of the reaction orders in $[N^nBu_4]_2[Pd_2I_6]$. At 0.055 and 0.066 mol% $[N^nBu_4]_2[Pd_2I_6]$ loadings, the end of the VTNA reaction profiles, *i.e.* at [**1**] ≤0.2 M, did not overlap (Figure 63).

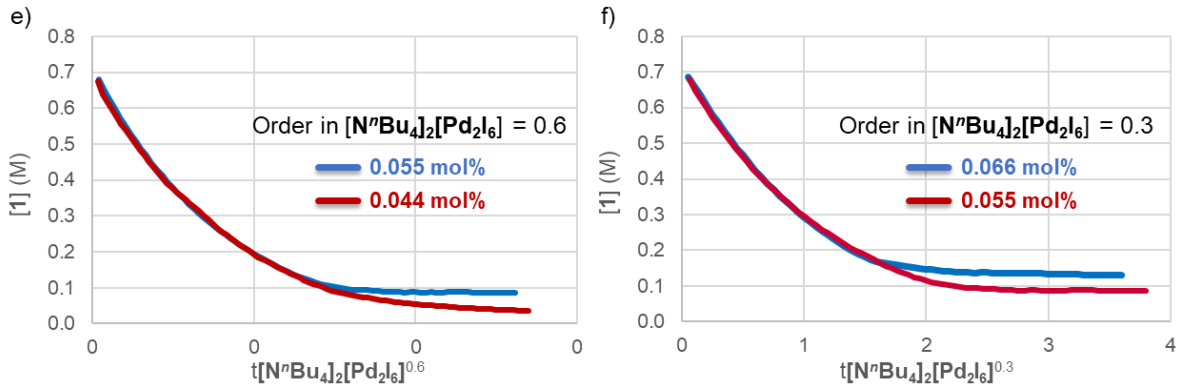

Figure 63. Application of VTNA to determine the model reaction orders in $[N^nBu_4]_2[Pd_2I_6]$, at $[N^nBu_4]_2[Pd_2I_6]$ loadings of: e) 0.044-0.055 mol%, f) 0.055-0.066 mol%. Each reaction was conducted under the optimised conditions. Profiles were produced using in situ ReactIR and the absorbance data calibrated offline using HPLC analysis with naphthalene as an internal standard.

This lack of overlap can be understood to occur due to a drop in catalytic activity at low [**1**], *i.e.* the onset of catalyst aggregation toward the formation of inactive palladium black. It is helpful to reconsider the equation (Equation 6) used to determine the order of the reaction in catalyst. For clarity, the concentration of $[N^nBu_4]_2[Pd_2I_6]$ is written below as [**Pd**].

$$t[\boldsymbol{Pd}]^y = \int_{t=0}^{t=n} [\boldsymbol{Pd}]^y dt = \sum_{i=1}^{n} \left(\frac{[\boldsymbol{Pd}]_i + [\boldsymbol{Pd}]_{i-1}}{2} \right)^y \times (t_i - t_{i-1})$$

Equation 6

When applying Equation 6 to normalise the influence of $[\mathbf{Pd}]^y$ on the rate of the reaction, a catalytic steady-state was assumed, *i.e.* a constant [**Pd**], $[\mathbf{Pd}]_i = [\mathbf{Pd}]_{i-1}$. However, if [**Pd**] *changes* during the course of the reaction, then Equation 6 is unable to normalise the influence of [**Pd**] and the profiles no longer overlap. It has previously been reported that such deviations from the catalytic steady-state can be accounted for by incorporating experimentally quantified [**Pd**] into Equation 6.[58] Unfortunately, [**Pd**] cannot be experimentally quantified without conducting extensive temporal particle size analysis

using TEM, which was not performed here. Alternatively, the changing [**Pd**] values can be deconvoluted by assuming that the order which overlayed the portion of the profiles under a catalytic steady-state is constant, *i.e.* orders of 0.6 and 0.3 (Figure 63). Thus, when the influence of each reaction component was normalised from the rate of the reaction (Figure 64a and Figure 64c), temporal [**1**] data yielded a straight line which only deviated from linearity at the point when [**Pd**] changed (Figure 64a and Figure 64c, red profile). This point of deviation is hypothesised to be the onset of aggregation of Pd^0 to form inactive palladium black. Values for [**Pd**] were subsequently deconvoluted from these order-normalised profiles (Figure 64a and Figure 64c) by finding the [**Pd**] values which linearised the full profiles (Figure 64b and Figure 64d). Linear fitting was performed using Solver in Microsoft Excel by finding the values of [**Pd**] which maximise the correlation coefficient, R^2, of the straight line.

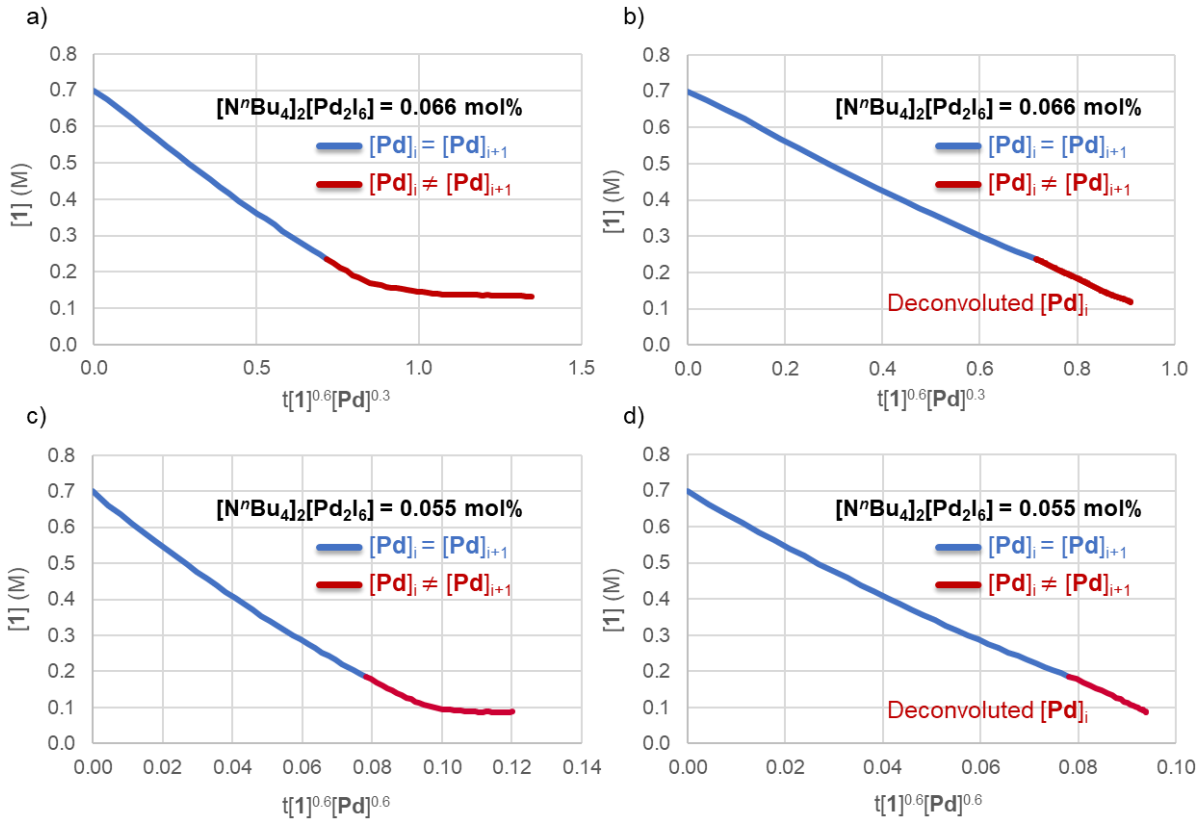

*Figure 64. a) Linearisation of temporal [**1**] profile at 0.066 mol% [N^{n}Bu$_4$]$_2$[Pd$_2$I$_6$] loading and period of catalyst deactivation indicated in red. b) Linearisation of temporal [**1**] profile at 0.066 mol% [N^{n}Bu$_4$]$_2$[Pd$_2$I$_6$] loading, including the period of catalyst deactivation in red determined by deconvolution of [**Pd**]. c) Linearisation of temporal [**1**] profile at 0.055 mol% [N^{n}Bu$_4$]$_2$[Pd$_2$I$_6$] loading and period of catalyst deactivation indicated in red. d) Linearisation of temporal [**1**] profile at 0.055 mol% [N^{n}Bu$_4$]$_2$[Pd$_2$I$_6$] loading, including the period of catalyst deactivation in red determined by deconvolution of [**Pd**]. Deconvolutions were performed using 'Solver' in Excel, by fitting [**Pd**] to maximise the correlation coefficient, R^2.*

This linearisation and deconvolution strategy has previously been utilised to uncover experimentally unknown active catalyst concentrations.[58] The deconvoluted values of [**Pd**] were then plotted as temporal profiles (Figure 65).

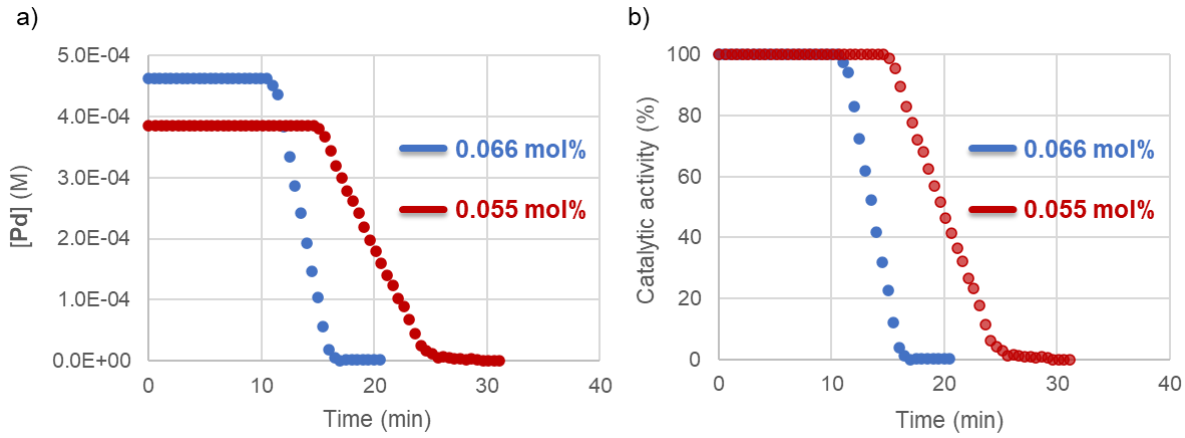

*Figure 65. a) Deconvoluted temporal [**Pd**] from linearised temporal [**1**] profiles (Figure 64). b) Plotting of temporal [**Pd**] profile more appropriately as percentage catalytic activity. Catalyst loadings are of the $[N^nBu_4]_2[Pd_2I_6]$ dimer.*

Since deconvolution of [**Pd**] was performed by fitting for the greatest linearity, *i.e.* R^2, of the normalised profiles in Figure 64, the temporal [**Pd**] profiles in Figure 65 are the correct *shape* but are not necessarily the correct *magnitude*. Moreover, since [**Pd**] can aggregate to a catalytically less active species without becoming catalytically inactive, *i.e.* activity can decrease without a reduction in [**Pd**], a linear relationship between catalytic activity and [**Pd**] cannot be assumed. The deconvolution of [**Pd**] from the normalised profiles for 0.055 and 0.066 mol% $[N^nBu_4]_2[Pd_2I_6]$ is therefore better considered as a *percentage* change in catalytic activity. This is also reported in Figure 65 with the y-axis more appropriately labelled 'Catalytic activity (%)' (Figure 65b), and not '[**Pd**] (M)' (Figure 65a).

The profiles in Figure 65 illustrate two key points: a) Deactivation onset occurred earlier when the catalyst loading was increased, and b) The rate of deactivation, *i.e.* the slope of 'Catalytic activity (%) (Figure 65b), increased when the catalyst loading was increased. Although this behaviour has been implicated on a number of occasions,[1,2,5,33,34,113,114] this is, to the best of our knowledge, the first direct elucidation of the kinetics of palladium aggregation and palladium black formation.

4.2.2. Mechanism of the reduction of $[N^nBu_4]_2[Pd_2I_6]$

Palladium nanoparticles containing surface LCN Pd^0 active sites have been identified as the active catalytic species formed from the Pd^{2+} precatalyst, $[N^nBu_4]_2[Pd_2I_6]$. Additional mechanistic studies were also conducted to elucidate the mechanism of reduction of Pd^{2+} in $[N^nBu_4]_2[Pd_2I_6]$ to Pd^0.

A series of leave-one-out control studies was performed to identify the reaction component(s) that reduces $[N^nBu_4]_2[Pd_2I_6]$. When $[N^nBu_4]_2[Pd_2I_6]$ was transferred to a 1-butanol solution containing **2** and $[N^nBu_4]Br$, a red solution was obtained (Scheme 85a).

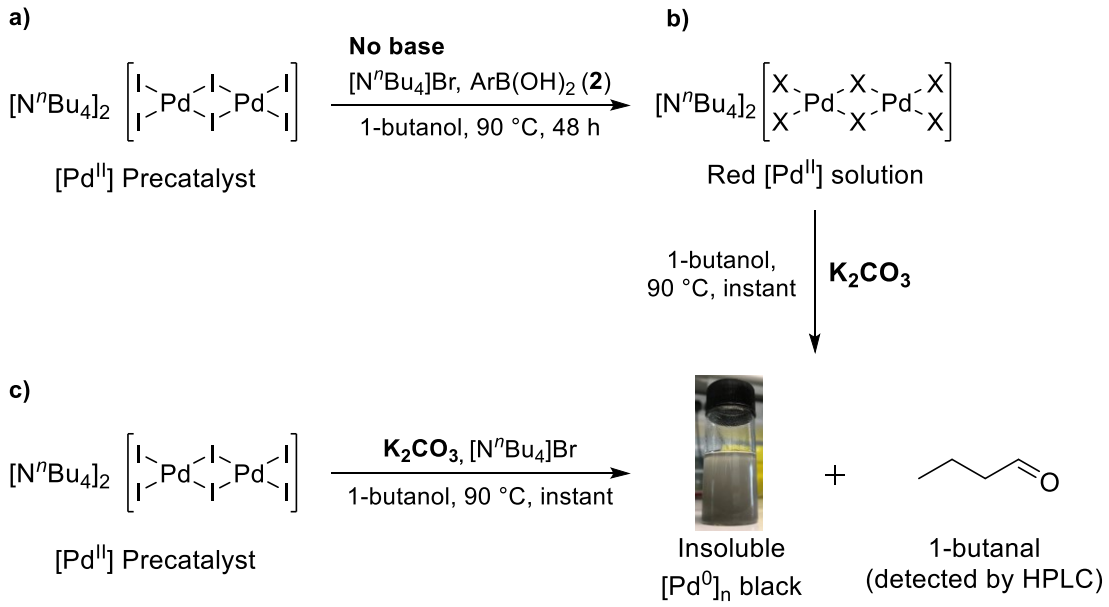

*Scheme 85. a) Dissolution of $[N^nBu_4]_2[Pd_2I_6]$ in 1-butanol and in the absence of aryl chloride (**1**) and K_2CO_3. b) Instant reduction of Pd^{2+} from the product of a) On the addition of K_2CO_3. c) Instant reduction of $[N^nBu_4]_2[Pd_2I_6]$ by K_2CO_3 in the absence of aryl chloride (**1**) and aryl boronic acid (**2**).*

No Pd^0 nanoparticles were observed when this red solution was imaged by TEM. Moreover, the red solution remained stable for >48 h at 90 °C, and no homocoupling of **2** was observed. When this red solution was treated with K_2CO_3, insoluble palladium black formed immediately (Scheme 85b) and the resulting solution was colourless. One possible mechanism for the reduction of $[N^nBu_4]_2[Pd_2I_6]$ is two transmetallation events involving **2** and the metal centre followed by reductive elimination to give the boronic acid homocoupling product and Pd^0. However, analysis of the reaction mixture by HPLC revealed the presence of 1-butanal, and the boronic acid homocoupling product was not detected. Moreover, the same observation – the formation of insoluble Pd^0 black and 1-butanal – was obtained when $[N^nBu_4]_2[Pd_2I_6]$ was treated with K_2CO_3 in the absence of **2** (Scheme 85c). All of these results illustrate that the base plays a key role in the reduction of $[N^nBu_4]_2[Pd_2I_6]$. Since 1-butanal is forming,

the mechanism presumably proceeds via β-hydride elimination of X–[Pd^{II}]–O^{n}Bu to give a palladium hydride, X–[Pd^{II}]–H (X = Br or I). This palladium hydride species can then reductively eliminate HX in the presence of K_2CO_3 to yield Pd^0. Palladium black also formed instantly on reacting with K_2CO_3 in the absence of [N^{n}Bu$_4$]Br, which illustrates that the formation of a bromide analogue of [N^{n}Bu$_4$]$_2$[Pd$_2$I$_6$] likely plays no role in the reduction to Pd^0. To provide further support for this mechanism, [N^{n}Bu$_4$]$_2$[Pd$_2$I$_6$] was treated with K_2CO_3 in ^{t}BuOH at 80 °C (Table 53, Entry 2).

Table 53. The reduction of [N^{n}Bu$_4$]$_2$[Pd$_2$I$_6$] in the presence of K_2CO_3 and [N^{n}Bu$_4$]Br in different solvents.

Entry	Solvent	Temperature (°C)	Time	Product
1	1-butanol	90	Instant	Pd^0 black 1-butanal (1)[a]
2	^{t}BuOH	80	60 min	Red solution Pd^0 black
3	^{t}BuOH/1-butanol	80	Instant	Pd^0 black 1-butanal (1)[a]

[a)] The amount of 1-butanal was not quantified. The numbers in parenthesis are relative peak areas and are provided for a general overview of the relative quantities formed in the two solvents.

Insoluble Pd^0 formed after ~30 min in ^{t}BuOH, but to a considerably reduced extent when compared to 1-butanol. This result is consistent with β-hydride elimination being a key step in mechanism of reduction of [N^{n}Bu$_4$]$_2$[Pd$_2$I$_6$], but that other reduction mechanisms may also occur in the absence of β-hydrogen atoms. Addition of 1-butanol to the ^{t}BuOH reaction mixture at 80 °C resulted in the immediate precipitation of Pd^0 black, alongside an increase in the quantity of 1-butanal in the HPLC chromatogram (Table 53, Entry 3). This result illustrated that the lower rate of reduction of [N^{n}Bu$_4$]$_2$[Pd$_2$I$_6$] in ^{t}BuOH is not simply due to the lower reaction temperature.

It has been widely reported that, in the bottom-up synthesis of nanoparticles from M^{n+} (n>0) precursors, a faster reduction rate results in the formation of smaller nanoparticles.[115,116] No induction period in the formation of the active catalytic species was observed throughout the kinetic studies described here when the cross-coupling reaction to yield **3** was catalysed by [N^{n}Bu$_4$]$_2$[Pd$_2$I$_6$]. Stoichiometric leave-one-out control studies also illustrated that [N^{n}Bu$_4$]$_2$[Pd$_2$I$_6$] is reduced immediately upon its addition to K_2CO_3 in 1-butanol. The propensity for the rapid reduction of [N^{n}Bu$_4$]$_2$[Pd$_2$I$_6$] under the reaction conditions may be key to the *in situ* formation of monodisperse and highly active nanoparticles that are <3 nm in size.

4.2.3. Role of the cation in $[Cation]_2[Pd_2I_6]$

It was previously illustrated that $[PPh_4]_2[Pd_2I_6]$ provided considerably reduced catalytic activity in the model reaction when compared to $[N^nBu_4]_2[Pd_2I_6]$ (*vide infra*, Chapter Three). Kinetic studies were consequently performed to elucidate the role of the cation in the catalytic activity of $[Cation]_2[Pd_2I_6]$ precatalysts.

Temporal data was obtained for the cross-coupling reaction to yield **3**, catalysed by both $[PPh_4]_2[Pd_2I_6]$ and $[N^nBu_4]_2[Pd_2I_6]$, using HPLC analysis (Figure 66).

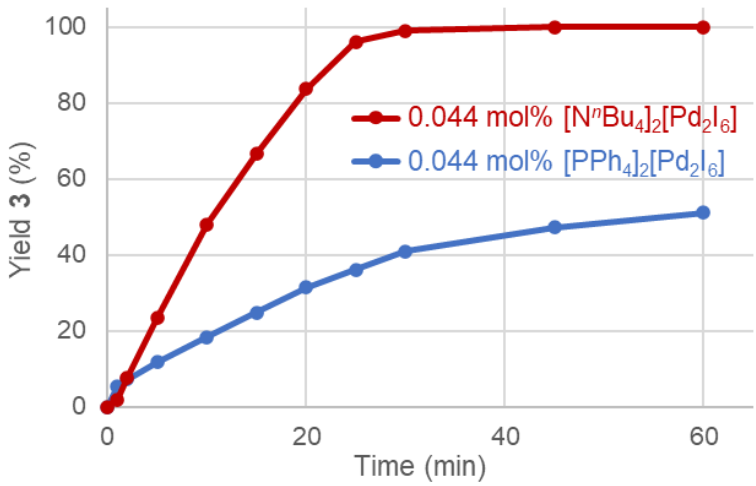

*Figure 66. Cross-coupling yielding **3** catalysed by $[N^nBu_4]_2[Pd_2I_6]$ (red) and $[PPh_4]_2[Pd_2I_6]$ (blue). Both reactions were initiated by the addition of the catalyst to 1-butanol at 90 °C in the presence of **2** (1.1 equiv.), $[N^nBu_4]Br$ (1 equiv.) and K_2CO_3 (1.5 equiv.). The reactions were monitored by HPLC analysis with respect to naphthalene as an internal standard.*

The two precatalysts, $[N^nBu_4]_2[Pd_2I_6]$ and $[PPh_4]_2[Pd_2I_6]$, vary in both the heteroatom and the heteroatomic substituents. To elucidate the structural feature(s) of the precatalyst cation which influences activity, additional $[Pd_2I_6]^{2-}$ salts were synthesised and used as precatalysts for the cross-coupling reaction to yield **3** (Figure 67).

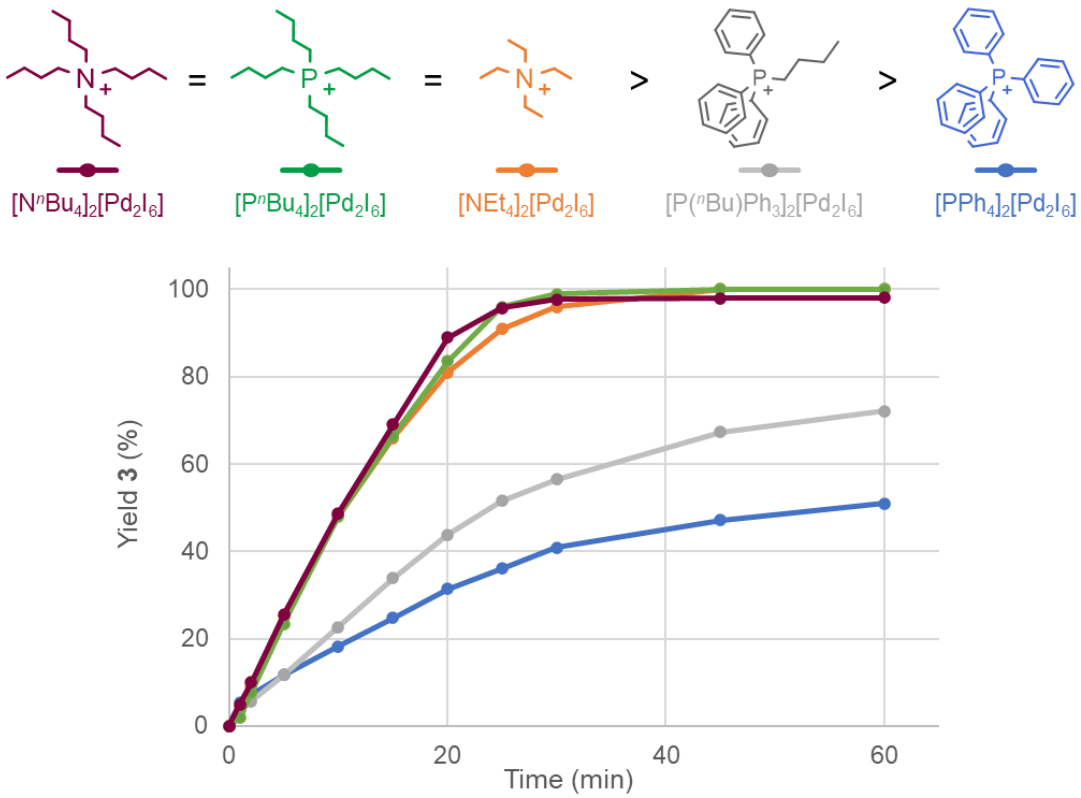

*Figure 67. Cross-coupling reaction to yield **3** from **1** and **2** catalysed by a series of [Cation]$_2$[Pd$_2$I$_6$] precatalysts (0.044 mol%). Each reaction was initiated by the addition of the precatalyst to 1-butanol at 90 °C in the presence of **2** (1.1 equiv.), [N^{n}Bu$_4$]Br (1 equiv.) and K$_2$CO$_3$ (1.5 equiv.). The reactions were monitored by HPLC analysis with respect to naphthalene as an internal standard.*

The precatalysts containing aliphatic organic cations performed the best, and all displayed essentially identical catalytic performance (Figure 67). The precatalysts containing cations with only aromatic substituents, [PPh$_4$]$^+$, provided the worst performance, whilst the precatalyst containing mixed aromatic and aliphatic cations, [P(^{n}Bu)PPh$_3$]$^+$, provided intermediate performance between the aliphatic-only and aromatic-only precatalysts. Very similar performance was observed for the precatalysts containing the aliphatic tetrabutylammonium and tetrabutylphosphonium cations. These results illustrate that it is the nature of the heteroatom substituents, and not the heteroatom itself, that influenced catalytic activity. Specifically, the presence of aromatic substituents reduces the performance of the precatalyst.

A series of additional kinetic experiments were subsequently performed to elucidate the origin of the inhibitory effect of aromatic cations on the activity of [Cation]$_2$[Pd$_2$I$_6$] precatalysts. It was hypothesised that cation-anion interactions in the precatalyst salt may influence the rate of reduction and thus the size and activity of the speciated nanoparticles. To test this, two reactions were performed using

either $[PPh_4]_2[Pd_2I_6]$ (Figure 68, blue profile), or $[N^nBu_4]_2[Pd_2I_6]$ in the presence of 0.088 mol% $[PPh_4]Br$ (Figure 68, red profile).

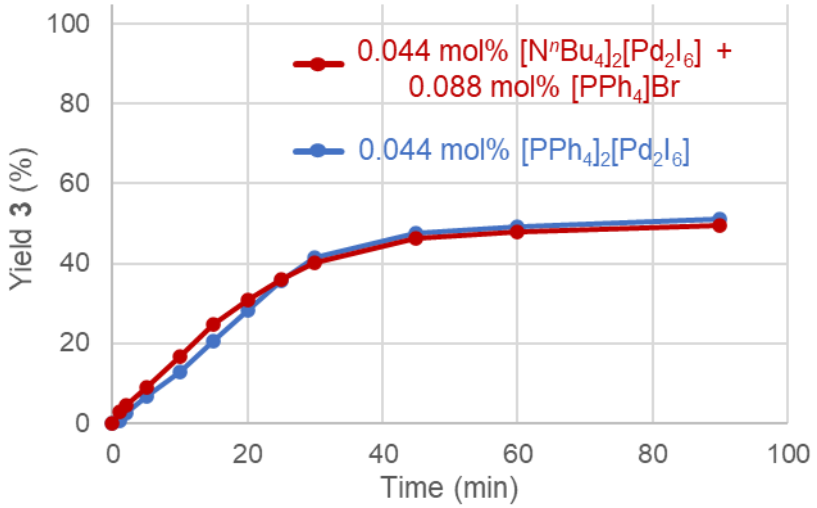

*Figure 68. Cross-coupling yielding **3** catalysed by $[N^nBu_4]_2[Pd_2I_6]$ in the presence of 0.088 mol% of $[PPh_4]Br$ (red), and catalysed by $[PPh_4]_2[Pd_2I_6]$ (blue). Both reactions were performed in 1-butanol at 90 °C in the presence of **2** (1.1 equiv.), $[N^nBu_4]Br$ (1 equiv.) and K_2CO_3 (1.5 equiv.). The reactions were monitored by HPLC analysis with respect to naphthalene as an internal standard.*

Despite employing precatalysts containing two different organic cations, the profiles were essentially identical (Figure 68). This result highlights that cation-anion interactions in the $[Cation]_2[Pd_2I_6]$ precatalyst salt do not play a role in their different catalytic activities. Instead, the differences in activity could be due to a direct influence of the organic cation on the surface reactivity of the nanoparticles that form. To test this hypothesis, spiking experiments were conducted. For each experiment, $[N^nBu_4]_2[Pd_2I_6]$ was used as the precatalyst, and the reaction mixture was spiked with 0.088 mol% of $[PPh_4]Br$ at different time points (Figure 69).

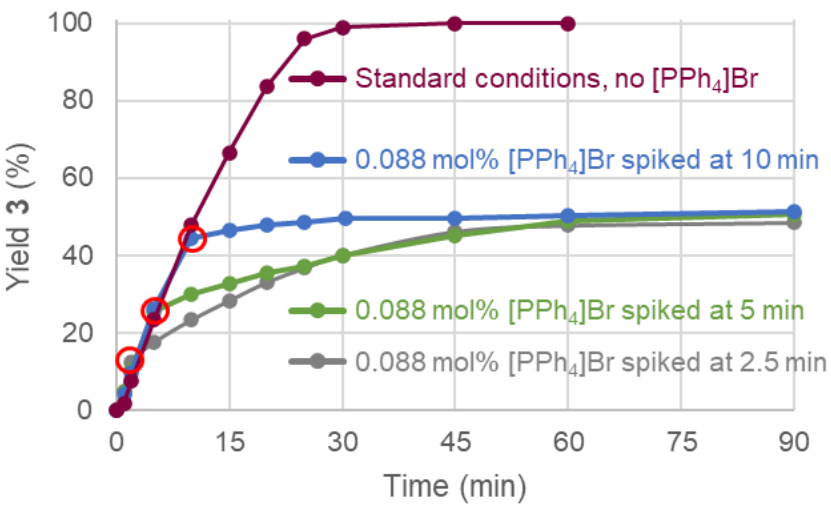

*Figure 69. Cross-coupling reaction to yield **3** catalysed by 0.044 mol $[N^nBu_4]_2[Pd_2I_6]$ with $[PPh_4]Br$ doped into the reaction mixture at 2.5 (grey), 5 (green) and 10 (blue) mins. The results using standard conditions in the absence of $[PPh_4]Br$ are included for comparison. Each reaction was initiated by the addition of the precatalyst to 1-butanol at 90 °C in the presence of **2** (1.1 equiv.), $[N^nBu_4]Br$ (1 equiv.) and K_2CO_3 (1.5 equiv.). The reactions were monitored by HPLC analysis with respect to naphthalene as an internal standard.*

Addition of 0.088 mol% of $[PPh_4]Br$ to a series of reactions with $[N^nBu_4]_2[Pd_2I_6]$ as the precatalyst resulted in an immediate reduction in catalytic activity (Figure 69). This reduction in activity was observed no matter the time point at which $[PPh_4]Br$ was spiked into the reaction mixture (Figure 69). These results indicate that the cation in the precatalyst salt does not influence the initial speciation event of Pd^0 from Pd^{2+}. Instead, it appears that the organic cation is directly influencing the surface reactivity of the Pd^0 nanoparticles. The interaction of $[PPh_4]^+$ cations with the nanoparticle surface must be significantly more favourable than the interaction with $[N^nBu_4]^+$ cations, since the $[PPh_4]^+$ cations are present in a 1:1:1136 $[Pd]:[PPh_4]^+:[N^nBu_4]^+$ ratio. The tightly-bound, bulkier and conformationally rigid $[PPh_4]^+$ cations may inhibit access of the substrate to the nanoparticle surface. In each case, catalytic activity halted at essentially identical yields of **3** (~50%). Presumably, it is at this yield of **3** that the rate of oxidative addition slows sufficiently for Pd^0 aggregation to become the dominant process and the catalyst becomes deactivated as Pd^0 black.

The negative influence of $[PPh_4]^+$ cations on the catalytic activity was further highlighted when the cross-coupling reaction to yield **3** was catalysed by $[N^nBu_4]_2[Pd_2I_6]$ in the presence of 1 equivalent of $[PPh_4]Br$ (Figure 70, Orange profile).

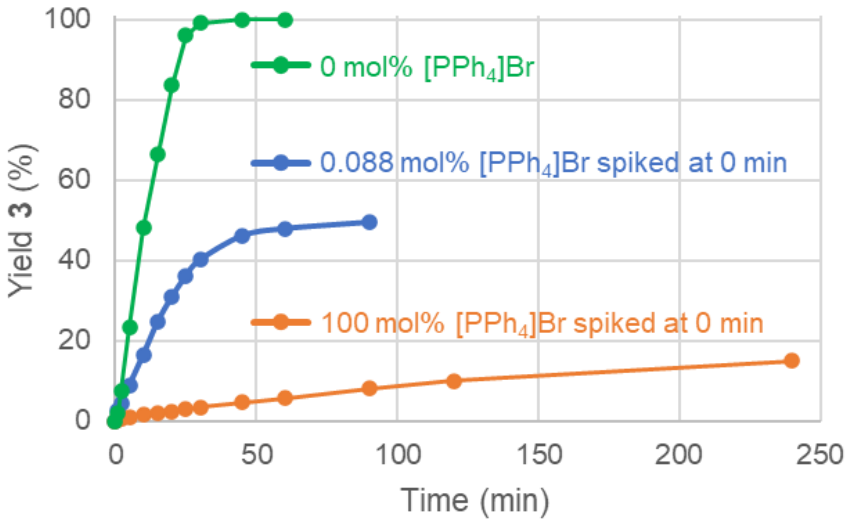

*Figure 70. Cross-coupling reaction yielding **3** catalysed by 0.044 mol% $[N^nBu_4]_2[Pd_2I_6]$ in the presence of varying amounts of $[PPh_4]Br$. Each reaction was initiated by the addition of the precatalyst to 1-butanol at 90 °C in the presence of **2** (1.1 equiv.), $[N^nBu_4]Br$ (1 equiv.) and K_2CO_3 (1.5 equiv.). The reactions were monitored by HPLC analysis with respect to naphthalene as an internal standard.*

Introducing 100 mol% of $[PPh_4]Br$ significantly reduced the performance of the catalyst, although some turnover remained. This residual catalytic activity that was observed in the presence of 100 mol% of $[PPh_4]Br$ (Figure 70) may be the result of the release of catalytically active 'free' mononuclear palladium atoms which leach from the nanoparticle surface.

To test this hypothesis, the activity of $[N^nBu_4]_2[Pd_2I_6]$ as a catalyst in the Suzuki-Miyaura coupling of 2,4-dihalogenated pyridines was explored. The Suzuki-Miyaura coupling of 2,4-dihalogenated pyridines is known to be speciation controlled, with mononuclear catalysts selectively coupling at C2,[36,37,117] whilst higher order aggregates react at C4.[35–37,118] When 2,4-dibromopyridine (**7**) was coupled with 4-methoxyphenyl boronic acid (**8**) in the presence of $[N^nBu_4]_2[Pd_2I_6]$, the **C2/C4 diaryl** product was formed as the major product (Scheme 86).

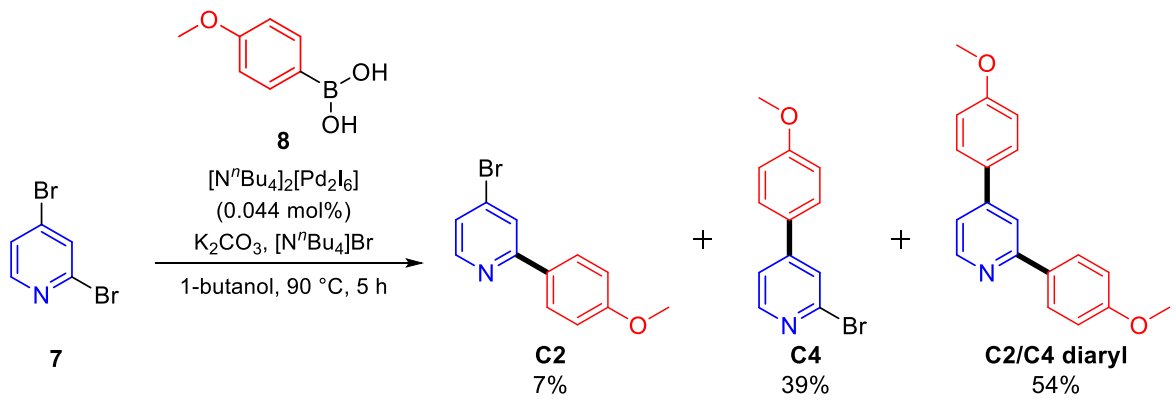

*Scheme 86. Suzuki-Miyaura coupling of **7** and **8** catalysed by $[N^nBu_4]_2[Pd_2I_6]$.*

The formation of the **C2/C4 diaryl** compound as the major product obfuscated a distinction between the C2/C4 regioselectivity of the active catalyst formed from $[N^nBu_4]_2[Pd_2I_6]$. An identical Suzuki-Miyaura coupling of 2,4-dichloropyridine (**9**) was consequently explored, which should reduce C2/C4 diarylation. Initial experiments employing 0.044 mol% loading of the palladium precatalyst resulted in poor conversions of **7** (and 25% total conversion of **9**). As a result, the catalyst loading of $[N^nBu_4]_2[Pd_2I_6]$ was increased to 0.1 mol% (Table 54).

*Table 54. Suzuki-Miyaura coupling of **9** and **8** catalysed by different palladium complexes in the presence of different additives to give either **C2** or **C4**.*[a]

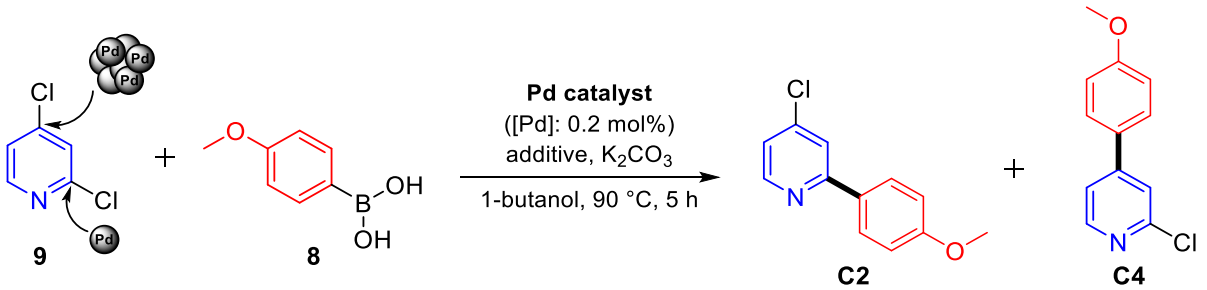

Entry	Pd catalyst	Additive (100 mol%)	Yield (%)[b] **C2**	**C4**
1	New $[Pd(PPh_4)_4]$	None	98	3
2	Old $[Pd(PPh_4)_4]$	None	55	25
3	$[N^nBu_4]_2[Pd_2I_6]$	$[N^nBu_4]Br$	11	65
4	$[N^nBu_4]_2[Pd_2I_6]$	$[PPh_4]Br$	61	10

[a)] Each reaction was initiated by the addition of the precatalyst to 1-butanol (0.7 M) at 90 °C in the presence of **8** (0.95 equiv.) and K_2CO_3 (1.5 equiv.). [b)] Yields were calculated by ^{1}H NMR analysis of the crude reaction mixture using relative integrations of **9**, **C2**, **C4** and the **C2/C4** diarylated product.

When 'fresh' $Pd(PPh_4)_4$ (0.1 mol%, yellow-orange in colour) was used as a catalyst, close to 100% **C2** selectivity was observed (Table 54, Entry 1). This result is consistent with the observation made previously that mononuclear palladium catalysts couple 2,4-dihalogenated pyridines selectively at **C2**.[33,35–38,119] It is well known that $Pd(PPh_3)_4$ has a short shelf-life when not stored under an inert atmosphere due to oxidation of both Pd^0 and PPh_3, which may then result in a change in the speciation of the active catalyst. Indeed, when an old sample (brown in colour) of $Pd(PPh_4)_4$ (~0.1 mol%) was used as a catalyst, reduced yields and **C2** selectivity were observed (Table 54, Entry 2). Presumably a larger proportion of aggregates speciate from the old sample of $Pd(PPh_4)_4$ due to oxidation of PPh_3 and reduced stabilisation of mononuclear Pd^0. These aggregated species result in an increase in **C4** cross-coupling (Table 54, Entry 2).

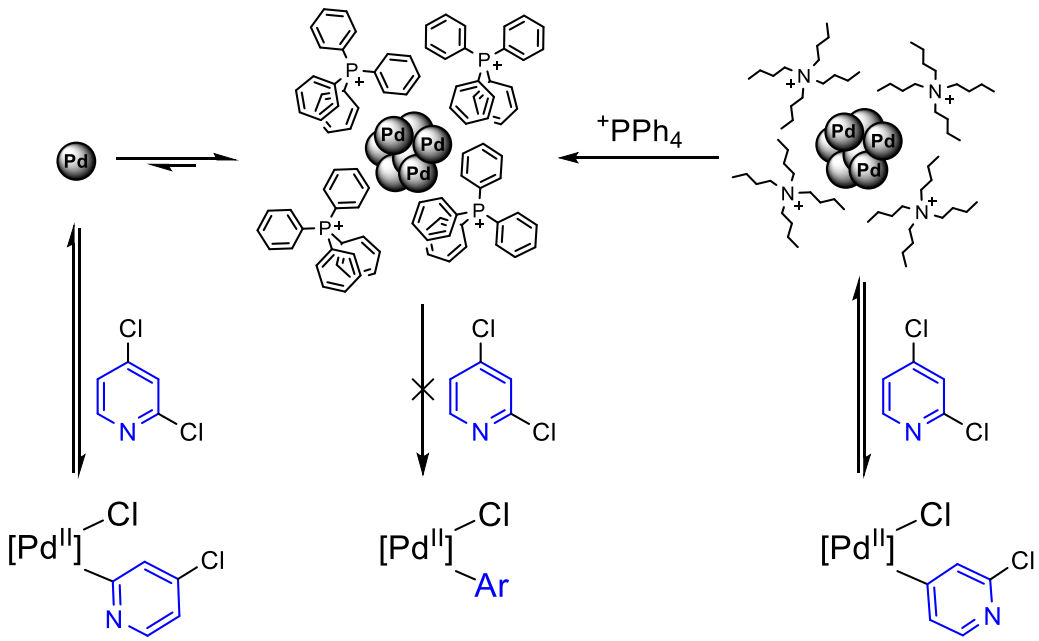

Scheme 87. Mechanistic rationalisation for the influence of $[PPh_4]^+$ on the C2/C4 selectivity of the cross-coupling of 2,4-dichloropyridine.

When 2,4-dichloropyridine (**7**) was coupled in the presence of $[N^nBu_4]_2[Pd_2I_6]$ and $[N^nBu_4]Br$, predominantly **C4** selectivity was observed (Table 54, Entry 2). This result is consistent with the rationalisation that the precatalyst $[N^nBu_4]_2[Pd_2I_6]$ speciates into nanoparticles in the presence of $[N^nBu_4]Br$, which results in the coupling to favour **C4**. Conversely, **C2** selectivity was observed when $[N^nBu_4]_2[Pd_2I_6]$ was utilised in the presence of $[PPh_4]Br$ (Table 54, Entry 3). This illustrates that $[PPh_4]^+$ cations inhibit the activity of the palladium nanoparticles and reactivity instead proceeds via 'free' mononuclear palladium atoms, which react selectively to yield **C2** (Scheme 87). All of these results contribute to a growing body of research which demonstrates that the speciation of nanoparticles results in unusual selectivity toward the **C4** product.[36–38,117] For example, Fairlamb and colleagues recently reported that the use of a 1:1 ratio of $Pd(OAc)_2$ and triphenylphosphine alongside tetraalkylammonium salts resulted in the C4 selective Suzuki-Miyaura coupling of 2,4-dibromopyridine (C4:C2 = 77:15).[36] Although different precatalysts and reaction conditions were used, the conclusions made here mirror those presented in the Fairlamb report – reducing (or eliminating entirely, as was done here) the external donor ligands and including a tetraalkylammonium salt additive resulted in the aggregation of Pd^0 and a switch in site selectivity. It should be noted that whilst Fairlamb and colleagues reported the formation of dimeric and trimeric palladium species which have not been proposed here, the formation of these smaller species was likely dependent on the authors use of triphenylphosphine. In the absence of triphenylphosphine, as was the case in this report, it seems unlikely that palladium aggregation will stop at the formation of dimers and trimers, except at

very low catalysts loadings. This hypothesis is supported by the TEM results presented previously in this chapter. These differences in speciation may also explain the improved selectivity obtained herein when compared to the values reported by Fairlamb *et al*. The possibility of loading-dependent differences in site-selectivity could be exploited in future work to better understand difference in catalyst speciation at different loadings.

In another recent example reported by Neufeldt and Norman even demonstrated that the speciation of nanoparticles may be influencing the **C4** selectivity of a palladium NHC-IPr catalyst which was previously considered to be mononuclear.[35,118] Clearly then, aggregated species play a major role in palladium cross-coupling catalysis, and the results presented in this chapter further complement the claims of these previous authors.

It should be noted that tetraphenylphosphonium salts are known to act as Ar–X electrophiles and undergo oxidative addition with Pd^0,[120,121] which in this example would result in the formation of cross-coupling product **10** and triphenylphosphine (Scheme 88).

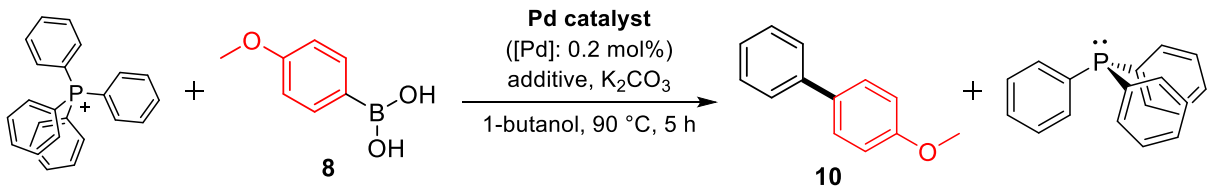

Scheme 88. Possible role of tetraphenylphosphonium as a cross-coupling reagent and subsequent release of triphenylphosphine.

If the reaction illustrated in Scheme 88 was occurring, then the release of triphenylphosphine may significantly influence the speciation of aggregated Pd^0, which would in turn result in the preference for **C2** selective coupling in the presence of $[PPh_4]^+$ that was observed in this report. No analysis was performed here to probe for the formation of either **10** or triphenylphosphine, and any future work using tetraphenylphosphonium salts should check for the formation of both of these species. This chemistry may also have played a role in the differences in activity between $[N^nBu_4]_2[Pd_2I_6]$ and $[PPh_4][Pd_2I_6]$ that were observed above (Figure 67).

4.3. Conclusions

Kinetic and mechanistic studies have been conducted on an industrially relevant Suzuki-Miyaura reaction catalysed by $[N^nBu_4]_2[Pd_2I_6]$. Reaction orders in the aryl chloride ([**1**]) and the presence of catalyst deactivation was determined by VTNA of temporal aryl chloride concentration

([**1**]) profiles. These studies revealed the presence of catalyst inhibition by the chloride anions released from the aryl chloride (**1**) coupling partner. This catalyst inhibition was hypothesised to be the result of chloride anions changing the distribution of the oxidative addition equilibrium of **1** and [**I**]/[**II**] (Figure 71).

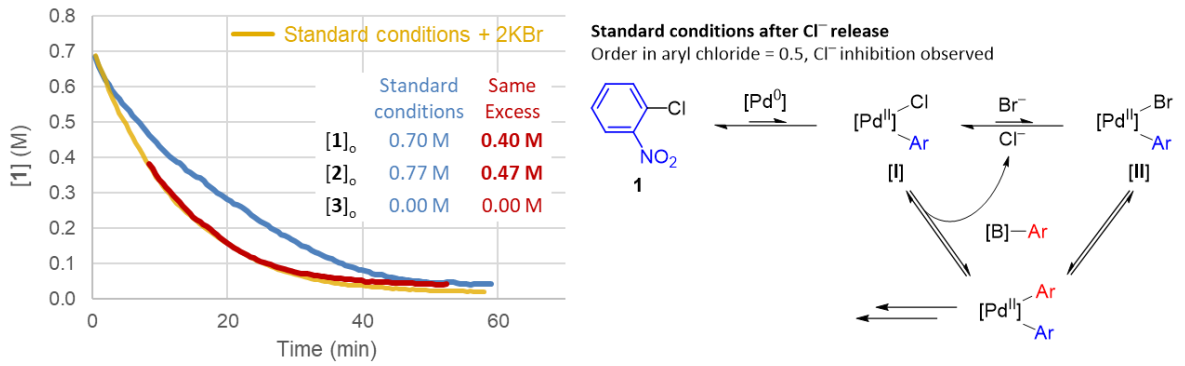

Figure 71. Surmounting chloride mediated catalyst deactivation and subsequent mechanistic rationalisation.

Catalyst inhibition was surmounted by the introduction of excess potassium bromide, which resulted in an improvement in the performance of the catalyst. This result has wide-reaching implications for palladium catalysis, especially for systems which rely on additive salts, *e.g.* [N^{n}Bu$_4$]Br.

Reaction orders in [N^{n}Bu$_4$]$_2$[Pd$_2$I$_6$] were determined to be dependent on the loading of the catalyst, and ranged from 1.7-0.3. Orders >1 suggest the formation of aggregates with increased catalytic activity, and orders <1 infer the formation of aggregates with reduced catalytic activity. The change in the concentration/activity of the active sites was deconvoluted from the catalyst orders using a novel VTNA approach, which revealed a trend that is characteristic for the formation of nanoparticles (Figure 72, Left).

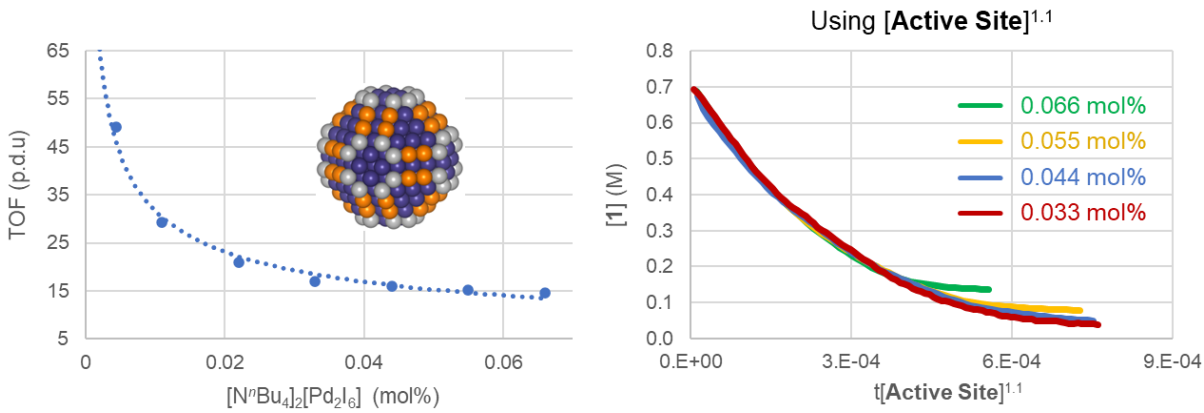

*Figure 72. Evidence for the role of nanoparticles formed from [N^{n}Bu$_4$]$_2$[Pd$_2$I$_6$] in the cross-coupling reaction to yield **3**.*

The formation of nanoparticles was further confirmed by TEM, which revealed particle sizes that were dependent on the loading of $[N^nBu_4]_2[Pd_2I_6]$. These particle sizes were used to rationalise the <1 catalyst orders obtained at ≥0.033 mol% loading (Figure 72, Right). This is the first time that catalyst orders have been used to implicate and rationalise the role of nanoparticles formed from a molecular Pd^{2+} precatalyst.

It should be noted that whilst a best effort was made to rationalise the kinetic results that were presented in this thesis, palladium speciation is a particularly complex problem to tackle since a large range of complex aggregated species likely exists in equilibrium in solution. Indeed, kinetic studies on the speciation of ligand-free palladium have seldom been conducted. It is also important to remember that drawing mechanistic conclusions from kinetic orders is incredibly challenging, especially for a dynamic and complex system such as the one presented in this thesis, since these kinetic orders only really reflect how the reaction rate changes with a given change in a component concentration. In reality, these kinetics orders could be influenced by any number of a combination of factors beyond just the molecularity of any single elementary step, e.g. change in rate constant due to changing particle size or morphology, change in the concentration of the catalytically active palladium due to either reversible or irreversible deactivation as palladium black, the presence of catalyst poisons etc. Ultimately, the conclusions made here are consistent with the observed results, however future research is needed to identify all the possible routes of palladium speciation and how these may influence the observed kinetic results. This future research may be dependent on the development of more modern ultra-fast spectroscopic techniques.

Finally, the role of the cation on the catalytic activity of the nanoparticles formed from $[Cation]_2[Pd_2I_6]$ was explored. The cation in solution was found to influence activity greatly, whether the cation was incorporated in the precatalyst $[Cation]_2[Pd_2I_6]$ salt or introduced as an external additive. The catalytic activity of a series of $[Cation]_2[Pd_2I_6]$ salts was used to illustrate that the nature of the heteroatom substituents was influencing catalytic activity, and not the heteroatom. Aliphatic cations permitted a high catalytic activity to be obtained, whilst aromatic cations were hypothesised to inhibi nanoparticle catalysis. This behaviour was exploited to control the site selectivity in the Suzuki-Miyaura coupling of 2,4-dichloropyridine (Figure 73).

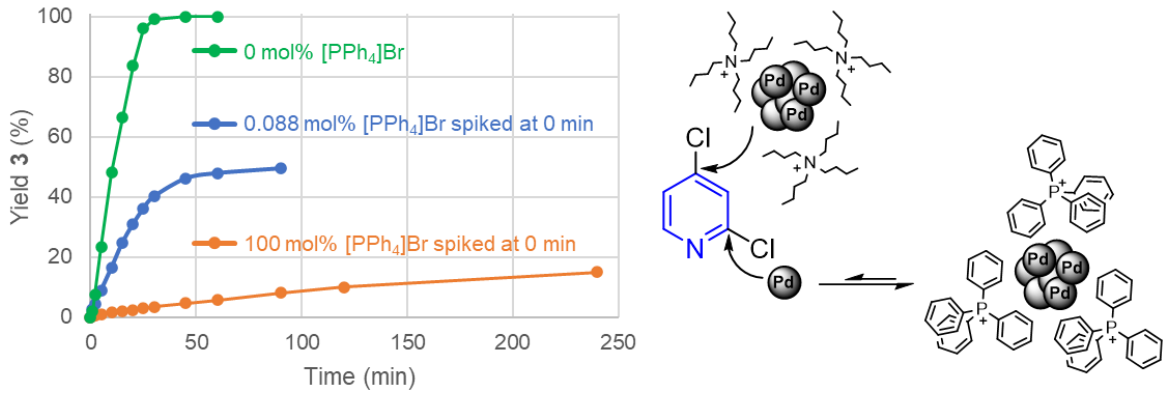

Figure 73. Influence of $[PPh_4]^+$ cations on the catalytic activity of the nanoparticles formed from $[N^nBu_4]_2[Pd_2I_6]$.

4.4. Future work

Kinetic studies have demonstrated that catalyst deactivation occurred in the cross-coupling reaction to yield **3** due to chloride anions released from the aryl chloride (**1**) coupling partner. It was subsequently illustrated that excess KBr can be introduced to overcome deactivation and improve catalyst performance. The cation may play an important role in preventing anion-mediated deactivation due to differences in the solubility in 1-butanol of the different halide salts, however this was not investigated. Further work could therefore explore the role of the cation in catalytic activity as it pertains to halide anion-mediated catalyst deactivation.

It has been demonstrated that $[N^nBu_4]_2[Pd_2I_6]$ speciates into nanoparticles, and that the catalytic activity of these nanoparticles in the coupling of 2,4-dihalogenated pyridines can be controlled by the presence of different organic cations. This work however was limited to simple comparisons of reaction yields. Additional kinetic studies could therefore be performed to understand better the kinetics of the C2/C4 regioselectivity in the coupling of 2,4-dihalogenated pyridines. Regioselectivity studies could also be expanded to cover the coupling of 2,4-dichloropyridine in some other transformations, *e.g.* Mizoroki-Heck, for which regioselectivity has not yet been explored in the literature. There are also a number of pharmaceutically important substrate classes with challenging cross-coupling site selectivities which could be explored with $[N^nBu_4]_2[Pd_2I_6]$.[117,118] When exploring the regioselectivity of new transformations, the choice of reaction conditions will influence both the speciation and intrinsic activity of the active catalyst. These two considerations are likely to lead to non-linear and interacting effects on the regioselectivity of the reaction. Modelling the reaction

variables using Design of Experiments may therefore be particularly useful in determining conditions which achieve the desired regioselectivity, especially for more challenging substrates.

It has been demonstrated that $[N^nBu_4]_2[Pd_2I_6]$ speciates into palladium nanoparticles when applied as a precatalyst in the cross-coupling reaction to yield **3**. This product (**3**) is an intermediate in the synthesis of Boscalid, and the next step in the synthetic route is an aromatic nitro-group reduction to yield **10** (Figure 74).

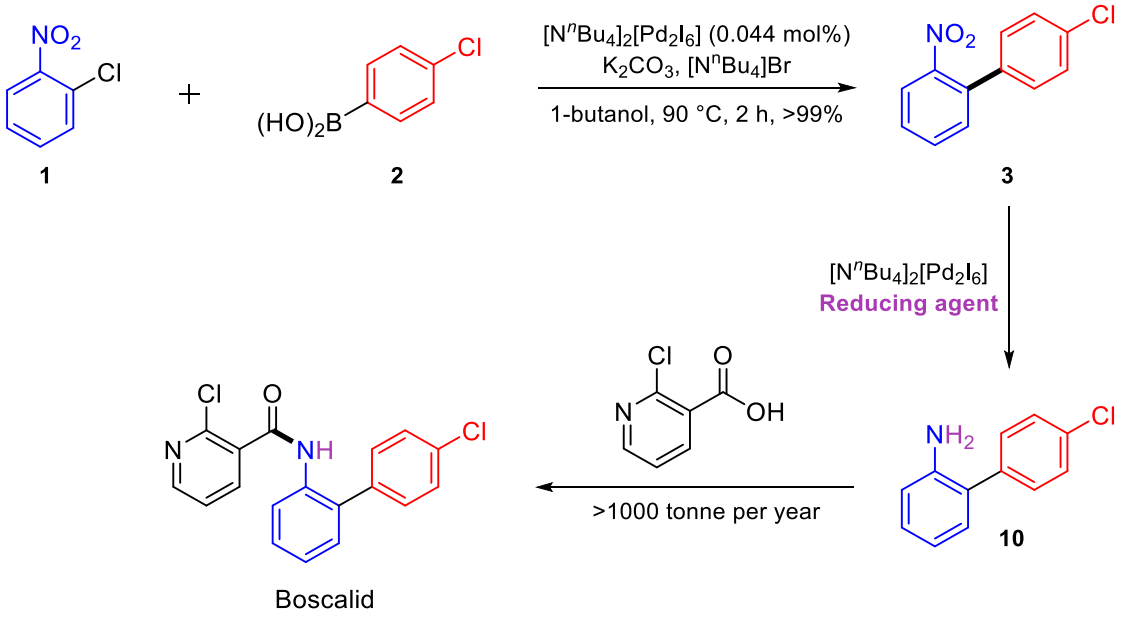

*Figure 74. The synthesis of Boscalid and the possibility of applying $[N^nBu_4]_2[Pd_2I_6]$ as a catalyst for the aromatic nitro-group reduction of **3**.*

Aromatic nitro-group reductions are an important class of reactions in agricultural and medicinal chemistry, for which palladium-based nanocatalysts have been shown to be effective.[84,122–128] Thus, $[N^nBu_4]_2[Pd_2I_6]$ could be used as a catalyst for the aromatic nitro-group reduction of **3**. A telescoped one-pot process could also be explored, since the Pd^0 black reaction end-point may be catalytically active in the aromatic nitro-reduction of **3**. One-pot coupling-hydrogenation reactions are known,[129] and have previously added activated carbon to capture the Pd^0 black end-point *in situ* for one-pot use as a heterogeneous catalyst.[130–132]

The palladium in automotive three-way catalytic converters (TWCs) is present as nanoparticles. It has been illustrated that $[N^nBu_4]_2[Pd_2I_6]$ can be readily reduced to catalytically active nanoparticles. It may therefore be possible to replace existing Pd^{2+} precursors with $[N^nBu_4]_2[Pd_2I_6]$ in the manufacture of palladium nanoparticles for application in automotive TWCs.

4.5. References

1 J. G. De Vries, *Dalt. Trans.*, 2006, 421–429.
2 A. H. M. de Vries, J. M. C. A. Mulders, J. H. M. Mommers, H. J. W. Henderickx and J. G. de Vries, *Org. Lett.*, 2003, **5**, 3285–3288.
3 L. A. Adrio, B. N. Nguyen, G. Guilera, A. G. Livingston and K. K. Hii, *Catal. Sci. Technol.*, 2012, **2**, 316–323.
4 A. V. Gaikwad, A. Holuigue, M. B. Thathagar, J. E. Ten Elshof and G. Rothenberg, *Chem-Eur. J.*, 2007, **13**, 6908–6913.
5 V. M. Chernyshev, O. V. Khazipov, D. B. Eremin, E. A. Denisova and V. P. Ananikov, *Coord. Chem. Rev.*, 2021, **437**, 213860.
6 A. S. Sigeev, A. S. Peregudov, A. V. Cheprakov and I. P. Beletskaya, *Adv. Synth. Catal.*, 2015, **357**, 417–429.
7 H. Joshi, O. Prakash, A. K. Sharma, K. N. Sharma and A. K. Singh, *Eur. J. Inorg. Chem.*, 2015, **2015**, 1542–1551.
8 I. J. S. Fairlamb, A. R. Kapdi, A. F. Lee, G. Sánchez, G. López, J. L. Serrano, L. García, J. Pérez and E. Pérez, *Dalt. Trans.*, 2004, 3970–3981.
9 A. Leyva-Pérez, J. Oliver-Meseguer, P. Rubio-Marqués and A. Corma, *Angew. Chem. Int. Ed.*, 2013, **52**, 11554–11559.
10 A. V. Astakhov, O. V. Khazipov, A. Y. Chernenko, D. V. Pasyukov, A. S. Kashin, E. G. Gordeev, V. N. Khrustalev, V. M. Chernyshev and V. P. Ananikov, *Organometallics*, 2017, **36**, 1981–1992.
11 M. T. Reetz and E. Westermann, *Angew. Chem. Int. Ed.*, 2000, **39**, 165–168.
12 N. Sienkiewicz, K. Strzelec, P. Pospiech, M. Cypryk and T. Szmechtyk, *Appl. Organomet. Chem.*, 2016, **30**, 4–11.
13 M. Fang, G. Fan and F. Li, *Catal. Letters*, 2014, **144**, 142–150.
14 A. F. Schmidt and A. A. Kurokhtina, *Kinet. Catal.*, 2012, **53**, 714–730.
15 S. Pradhan and R. P. John, *New J. Chem.*, 2015, **39**, 5759–5766.
16 Q. Li, L. M. Zhang, J. J. Bao, H. X. Li, J. B. Xie and J. P. Lang, *Appl. Organomet. Chem.*, 2014, **28**, 861–867.
17 S. J. Sabounchei, M. Ahmadi and Z. Nasri, *J. Coord. Chem.,* 2013, **66**, 411-423.
18 R. H. Crabtree, *Chem. Rev.*, 2012, **112**, 1536–1554.
19 M. Che and C. O. Bennett, *Adv. Catal.*, 1989, **36**, 55–172.
20 R. A. Van Santen, *Acc. Chem. Res.*, 2009, **42**, 57–66.
21 A. I. Frenkel, C. W. Hills and R. G. Nuzzo, *J. Phys. Chem. B*, 2001, **105**, 12689–12703.
22 D. G. Blackmond, *J. Am. Chem. Soc.*, 2015, **137**, 10852–10866.
23 J. Burés, *Top. Catal.*, 2017, **60**, 631–633.
24 P. Wedi, M. Farizyan, K. Bergander, C. Mück-Lichtenfeld and M. van Gemmeren, *Angew. Chem. Int. Ed.*, 2021, **60**, 15641–15649.
25 S. Gesslbauer, G. Hutchinson, A. J. P. White, J. Burés and C. Romain, *ACS Catal.*, 2021, **11**, 4084–4093.
26 T. Rosner, A. Pfaltz and D. G. Blackmond, *J. Am. Chem. Soc.*, 2001, **123**, 4621–4622.
27 Y. Zhang, Z. N. Chen, X. Zhang, X. Deng, W. Zhuang and W. Su, *Commun. Chem.*, 2020, **3**, 1–9.
28 D. E. Hill, Q. L. Pei, E. X. Zhang, J. R. Gage, J. Q. Yu and D. G. Blackmond, *ACS Catal.*, 2018, **8**, 1528–1531.
29 T. Rosner, J. Le Bars, A. Pfaltz and D. G. Blackmond, *J. Am. Chem. Soc.*, 2001, **123**, 1848–1855.
30 I. Kalvet, K. J. Bonney and F. Schoenebeck, *J. Org. Chem.*, 2014, **79**, 12041–12046.
31 O. J. Newton, K. Hellgardt, J. Richardson and K. K. M. Hii, *J. Catal.*, 2023, **424**, 29–38.
32 V. M. Chernyshev and V. P. Ananikov, *ACS Catal.*, 2022, **12**, 1180–1200.
33 N. Jeddi, N. W. J. Scott and I. J. S. Fairlamb, *ACS Catal.*, 2022, 12, 11615–11638.
34 D. B. Eremin and V. P. Ananikov, *Coord. Chem. Rev.*, 2017, **346**, 2–19.
35 M. Yang, J. Chen, C. He, X. Hu, Y. Ding, Y. Kuang, J. Liu and Q. Huang, *J. Org. Chem.*, 2020, **85**, 6498–6508.

36 N. W. J. Scott, M. J. Ford, N. Jeddi, A. Eyles, L. Simon, A. C. Whitwood, T. Tanner, C. E. Willans and I. J. S. Fairlamb, *J. Am. Chem. Soc.*, 2021, **143**, 9682–9693.
37 J. P. Norman, N. G. Larson, E. D. Entz and S. R. Neufeldt, *J. Org. Chem.*, 2022, **87**, 7414–7421.
38 M. Albino, T. J. Burden, C. C. Piras, A. C. Whitwood, I. J. S. Fairlamb and D. K. Smith, *ACS Sustain. Chem. Eng.*, 2023, **11**, 1678–1689.
39 H. Lineweaver and D. Burk, *J. Am. Chem. Soc.*, 1934, **56**, 658–666.
40 P. J. Stang, *J. Am. Chem. Soc.*, 2003, **125**, 1–8.
41 J. I. Murray, L. Zhang, A. Simon, M. V. Silva Elipe, C. S. Wei, S. Caille and A. T. Parsons, *Org. Process Res. Dev.*, 2023, **27**, 198–205.
42 K. A. Johnson, *Chapter 23 Fitting Enzyme Kinetic Data with KinTek Global Kinetic Explorer*, Elsevier Inc., 2009, vol. 467.
43 R. C. Cioc, M. Crockatt, J. C. van der Waal and P. C. A. Bruijnincx, *Angew. Chem. Int. Ed.*, 2022, **61**, e202114720.
44 J. Burés and I. Larrosa, *Nature*, 2023, **613**, 689–695.
45 G. S. Eadie, *J. Biol. Chem.*, 1942, **146**, 85–93.
46 J.-M. Frère, B. Leyh and A. Renard, *J. Theor. Biol.*, 1983, **101**, 387–400.
47 J. B. S. Haldane, *Nature*, 1957, **179**, 1956.
48 A. Cornish-Bowden, *Fundamentals of enzyme kinetics*, Wiley-VCH, Weinheim, 4th edn., 2012.
49 K. J. Laidler, *Chemical Kinetics*, Harper & Row, New York, 3rd edn., 1987.
50 J. Burés, A. Armstrong and D. G. Blackmond, *Chem. Sci.*, 2012, **3**, 1273–1277.
51 J. Burés, A. Armstrong and D. G. Blackmond, *J. Am. Chem. Soc.*, 2012, **134**, 6741–6750.
52 J. Burés, A. Armstrong and D. G. Blackmond, *J. Am. Chem. Soc.*, 2011, **133**, 8822–8825.
53 J. Burés, P. Dingwall, A. Armstrong and D. G. Blackmond, *Angew. Chem. Int. Ed.*, 2014, **53**, 8700–8704.
54 S. P. Mathew, S. Gunathilagan, S. M. Roberts and D. G. Blackmond, *Org. Lett.*, 2005, **7**, 4847–4850.
55 D. G. Blackmond, *Angew. Chem. Int. Ed.*, 2005, **44**, 4302–4320.
56 C. D. T. Nielsen and J. Burés, *Chem. Sci.*, 2019, **10**, 348–353.
57 J. Burés, *Angew. Chem. Int. Ed.*, 2016, **55**, 2028–2031.
58 A. Martínez-Carrión, M. G. Howlett, C. Alamillo-Ferrer, A. D. Clayton, R. A. Bourne, A. Codina, A. Vidal-Ferran, R. W. Adams and J. Burés, *Angew. Chem. Int. Ed.*, 2019, **58**, 10189–10193.
59 J. Burés, *Angew. Chem. Int. Ed.*, 2016, **55**, 16084–16087.
60 D. C. Braddock, B. M. J. Lancaster, C. J. Tighe and A. J. P. White, *J. Org. Chem.*, 2023, **88**, 8904–8914.
61 D. C. Braddock, B. C. Rowley, P. D. Lickiss, S. J. Fussell, R. Qamar, D. Pugh, H. S. Rzepa and A. J. P. White, *J. Org. Chem.*, 2023, **88**, 9853–9869.
62 D. Gasperini, S. E. Neale, M. F. Mahon, S. A. MacGregor and R. L. Webster, *ACS Catal.*, 2021, **11**, 5452–5462.
63 D. Whitaker, J. Burés and I. Larrosa, *J. Am. Chem. Soc.*, 2016, **138**, 8384–8387.
64 O. P. Schmidt and D. G. Blackmond, *ACS Catal.*, 2020, **10**, 8926–8932.
65 R. D. Baxter, D. Sale, K. M. Engle, J. Q. Yu and D. G. Blackmond, *J. Am. Chem. Soc.*, 2012, **134**, 4600–4606.
66 E. R. Strieter, D. G. Blackmond and S. L. Buchwald, *J. Am. Chem. Soc.*, 2005, **127**, 4120–4121.
67 J. R. Coombs, F. Haeffner, L. T. Kliman and J. P. Morken, *J. Am. Chem. Soc.*, 2013, **135**, 11222–11231.
68 S. M. Banik, A. Levina, A. M. Hyde and E. N. Jacobsen, *Science*, 2017, **358**, 761–764.
69 P. Dydio, R. J. Detz and J. N. H. Reek, *J. Am. Chem. Soc.*, 2013, **135**, 10817–10828.
70 N. A. Hawbaker and D. G. Blackmond, *Nat. Chem.*, 2019, **11**, 957–962.
71 S. Shekhar, P. Ryberg, J. F. Hartwig, J. S. Mathew, D. G. Blackmond, E. R. Strieter and S. L. Buchwald, *J. Am. Chem. Soc.*, 2006, **128**, 3584–3591.
72 Z. I. Günler, X. Companyó, I. Alfonso, J. Burés, C. Jimeno and M. A. Pericàs, *Chem. Commun.*,

2016, **52**, 6821–6824.
73 L. P. C. Nielsen, C. P. Stevenson, D. G. Blackmond and E. N. Jacobsen, *J. Am. Chem. Soc.*, 2004, **126**, 1360–1362.
74 N. Zotova, L. J. Broadbelt, A. Armstrong and D. G. Blackmond, *Bioorganic Med. Chem. Lett.*, 2009, **19**, 3934–3937.
75 C. Alamillo-Ferrer, G. Hutchinson and J. Burés, *Nat. Rev. Chem.*, 2023, **7**, 26–34.
76 A. H. Roy and J. F. Hartwig, *J. Am. Chem. Soc.*, 2001, **123**, 1232–1233.
77 J. Pan, X. Wang, Y. Zhang and S. L. Buchwald, *Org. Lett.*, 2011, **13**, 4974–4976.
78 G. Evano, A. Nitelet, P. Thilmany and D. F. Dewez, *Front. Chem.*, 2018, **6**, 1–18.
79 T. D. Sheppard, *Org. Biomol. Chem.*, 2009, **7**, 1043–1052.
80 R. J. Deluca, B. J. Stokes and M. S. Sigman, *Pure Appl. Chem.*, 2014, **86**, 395–408.
81 D. B. Eremin, E. A. Denisova, A. Yu. Kostyukovich, J. Martens, G. Berden, J. Oomens, V. N. Khrustalev, V. M. Chernyshev and V. P. Ananikov, *Chem-Eur. J.*, 2019, **25**, 16564–16572.
82 T. M. Rangarajan, R. Singh, R. Brahma, K. Devi, R. P. Singh, R. P. Singh and A. K. Prasad, *Chem-Eur. J.*, 2014, **20**, 14218–14225.
83 M. Kashihara and Y. Nakao, *Acc. Chem. Res.*, 2021, **54**, 2928–2935.
84 Z. Yan, X. Xie, Q. Song, F. Ma, X. Sui, Z. Huo and M. Ma, *Green Chem.*, 2020, **22**, 1301–1307.
85 D. J. Jones, M. Lautens and G. P. McGlacken, *Nat. Catal.*, 2019, **2**, 843–851.
86 M. J. Kania, A. Reyes and S. R. Neufeldt, *J. Am. Chem. Soc.*, 2024, **146**, 19249–19260.
87 A. Frenkel, *Zeitschrift fur Krist.*, 2007, **222**, 605–611.
88 Z. Li, S. Ji, Y. Liu, X. Cao, S. Tian, Y. Chen, Z. Niu and Y. Li, *Chem. Rev.*, 2020, **120**, 623–682.
89 Z. Zhang, J. Lu, B. Zhang, W. Shi, Y. Guo and F. Cui, *Environ. Sci. Nano*, 2020, **7**, 2117–2129.
90 K. An and G. A. Somorjai, *ChemCatChem*, 2012, **4**, 1512–1524.
91 H. M. Torres Galvis, J. H. Bitter, T. Davidian, M. Ruitenbeek, A. I. Dugulan and K. P. De Jong, *J. Am. Chem. Soc.*, 2012, **134**, 16207–16215.
92 R. Reske, H. Mistry, F. Behafarid, B. Roldan Cuenya and P. Strasser, *J. Am. Chem. Soc.*, 2014, **136**, 6978–6986.
93 P. J. Ellis, I. J. S. Fairlamb, S. F. J. Hackett, K. Wilson and A. F. Lee, *Angew. Chem.*, 2010, **122**, 1864–1868.
94 D. Y. Murzin, *Chem. Eng. Sci.*, 2009, **64**, 1046–1052.
95 P. Hervés, M. Pérez-Lorenzo, L. M. Liz-Marzán, J. Dzubiella, Y. Lub and M. Ballauff, *Chem. Soc. Rev.*, 2012, **41**, 5577–5587.
96 J. E. Mondloch, E. Bayram and R. G. Finke, *J. Mol. Catal. A Chem.*, 2012, **355**, 1–38.
97 S. Satapathy, J. Mohanta and S. Si, *ChemistrySelect*, 2016, **1**, 4940–4948.
98 S. Gómez-Graña, M. Pita, P. Humada-Iglesias, J. Pérez-Juste and P. Hervés, *Nanomaterials*, 2022, **12**, 1–13.
99 D. Albinsson, A. Boje, S. Nilsson, C. Tiburski, A. Hellman, H. Ström and C. Langhammer, *Nat. Commun.*, 2020, **11**, 1–13.
100 V. D. Doan, Q. H. Pham, B. A. Huynh, T. L. H. Nguyen, A. T. Nguyen and T. D. Nguyen, *J. Environ. Chem. Eng.*, 2021, **9**, 106590.
101 J. Le Bars, U. Specht, J. S. Bradley and D. G. Blackmond, *Langmuir*, 1999, **15**, 7621–7625.
102 P. Grammatikopoulos, C. Cassidy, V. Singh and M. Sowwan, *Sci. Rep.*, 2014, **4**, 1–9.
103 N. Losada-Garcia, A. S. Santos, M. M. B. Marques and J. M. Palomo, *Nanoscale Adv.*, 2022, **5**, 513–521.
104 Z. Jin, D. Nackashi, W. Lu, C. Kittrell and J. M. Tour, *Chem. Mater.*, 2010, **22**, 5695–5699.
105 A. Dutta, A. Paul and A. Chattopadhyay, *RSC Adv.*, 2016, **6**, 82138–82149.
106 M. Harada, M. Yamamoto and M. Sakata, *J. Mol. Liq.*, 2020, **311**, 113255.
107 K. M. Koczkur, S. Mourdikoudis, L. Polavarapu and S. E. Skrabalak, *Dalton Trans.*, 2015, **44**, 17883–17905.
108 P. J. Ellis, I. J. S. Fairlamb, S. F. J. Hackett, K. Wilson and A. F. Lee, *Angew. Chem. Int. Ed.*, 2010, **49**, 1820–1824.

109 J. Wang, Q. Wang, X. Jiang, Z. Liu, W. Yang and A. I. Frenkel, *J. Phys. Chem. C*, 2015, **119**, 854–861.
110 J. C. Wang, C. X. Liu, X. Kan, X. W. Wu, J. L. Kan and Y. Bin Dong, *Green Chem.*, 2020, **22**, 1150–1155.
111 M. A. Albrahim, A. Shrotri, R. R. Unocic, A. S. Hoffman, S. R. Bare and A. M. Karim, *Angew. Chem. Int. Ed.*, 2023, **62**, e2023080.
112 R. Van Hardeveld and F. Hartog, *Surf. Sci.*, 1969, **15**, 189–230.
113 O. V Khazipov, M. A. Shevchenko, A. Y. Chernenko, A. V Astakhov, D. V Pasyukov, D. B. Eremin, Y. V Zubavichus, V. N. Khrustalev, V. M. Chernyshev and V. P. Ananikov, *Organometallics*, 2018, **37**, 1483–1492.
114 C. Deraedt and D. Astruc, *Acc. Chem. Res.*, 2014, **47**, 494–503.
115 N. T. K. Thanh, N. Maclean and S. Mahiddine, *Chem. Rev.*, 2014, **114**, 7610–7630.
116 M. Iwamoto, K. Kuroda, J. Kanzow, S. Hayashi and F. Faupel, *Adv. Powder Technol.*, 2005, **16**, 137–144.
117 J. Almond-Thynne, D. C. Blakemore, D. C. Pryde and A. C. Spivey, *Chem. Sci.*, 2016, **8**, 40–62.
118 J. P. Norman and S. R. Neufeldt, *ACS Catal.*, 2022, 12, 12014–12026.
119 N. Jeddi, N. W. J. Scott, T. Tanner, S. K. Beaumont and I. J. S. Fairlamb, *Chem. Sci.*, 2024, **15**, 2763–2777.
120 M. Sakamoto, I. Shimizu and A. Yamamoto, *Chem. Lett.*, 1995, 1101–1102.
121 L. K. Hwang, Y. Na, J. Lee, Y. Do and S. Chang, *Angew. Chem. Int. Ed.*, 2005, **44**, 6166–6169.
122 D. Berillo and A. Cundy, *Carbohydr. Polym.*, 2018, **192**, 166–175.
123 A. Iben Ayad, C. Belda Marín, E. Colaco, C. Lefevre, C. Méthivier, A. Ould Driss, J. Landoulsi and E. Guénin, *Green Chem.*, 2019, **21**, 6646–6657.
124 C. Deraedt, L. Salmon and D. Astruc, *Adv. Synth. Catal.*, 2014, **356**, 2525–2538.
125 C. Zhang, D. Lu, P. Jiang, J. Li and Y. Leng, *Catal. Letters*, 2017, **147**, 2534–2541.
126 C. Huang, X. Wang, F. Yu, B. Yuan, C. Xie and S. Yu, *Res. Chem. Intermed.*, 2018, **44**, 13–26.
127 C. Deraedt, L. Salmon, J. Ruiz and D. Astruc, *Adv. Synth. Catal.*, 2013, **355**, 2992–3001.
128 H. Genc, *Catal. Commun.*, 2015, **67**, 64–67.
129 B. S. Takale, R. R. Thakore, R. Mallarapu, F. Gallou and B. H. Lipshutz, *Org. Process Res. Dev.*, 2020, **24**, 101–105.
130 V. L. Budarin, P. S. Shuttleworth, J. H. Clark and R. Luque, *Curr. Org. Synth.*, 2011, **7**, 614–627.
131 T. H. Riermeier, A. Zapf and M. Beller, *Top. Catal.*, 1997, **4**, 301–309.
132 A. Zapf and M. Beller, *ChemInform*, 2002, **33**, 275–275.

Chapter Five – Final Conclusions and Future Work

5.1. Final conclusions and future work

Many fine chemicals would be inaccessible without metal-catalysed transformations. In particular, gold and palladium containing catalysts are ubiquitous in modern synthetic chemistry. However, these metals are limited by their finite natural supply from mining and the associated economic and environmental costs. If the fine chemical industry is to continue benefiting from the useful catalytic properties of palladium and gold, then more sustainable supply streams must be developed. This thesis presented a series of palladium and gold complexes which are accessible through mild conditions from a variety of metal waste streams. Gold complexes **3**-**6** were isolated from waste SIM cards and applied as homogeneous catalysts for a range of transformations. To expedite the current investigation, the palladium complexes of the form $[Cation]_2[Pd_2I_6]$ were synthesised directly from palladium powder since previous work has already illustrated that these salts can be recovered from model waste TWCs.[1] For further proof of principle, future work could investigate recovering $[Cation]_2[Pd_2I_6]$ from a real waste TWC and applying the recovery product in catalysis.

It is notable that the structures of the metal complexes presented in this thesis are intrinsically tied to the recovery process from which they have been sourced. As a result, the components (ligands and counter ions) present in the palladium and gold recovery complexes have been optimised for metal recovery, e.g. the dihalogen adducts of the dithiooxamide Me_2dazdt used in gold recovery, and the organic triiodide salts used in palladium recovery.[2–4] These components were therefore not incorporated into the resulting recovery complexes with the typical approaches of catalyst design in mind (

Figure 75).

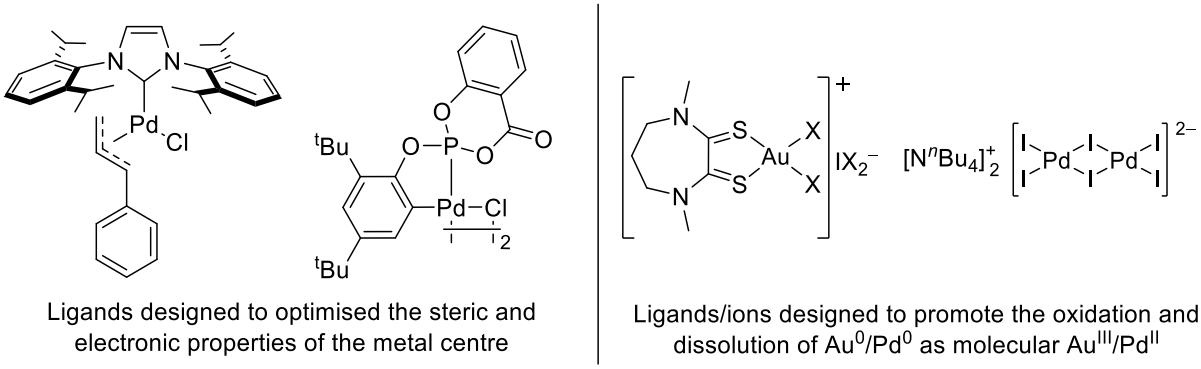

Figure 75. ***Left:*** *Two literature palladium complexes with ligands designed to improve the steric and electronic properties of the metals.*[5,6] ***Right****: Two recycled metal complexes whose catalytic activities were not designed according to conventional approaches, yet still led to a host of novel and impressive catalytic activities.*

Despite this, the recovery complexes have been illustrated to possess excellent catalytic activities for a variety of important transformations (Scheme 89).

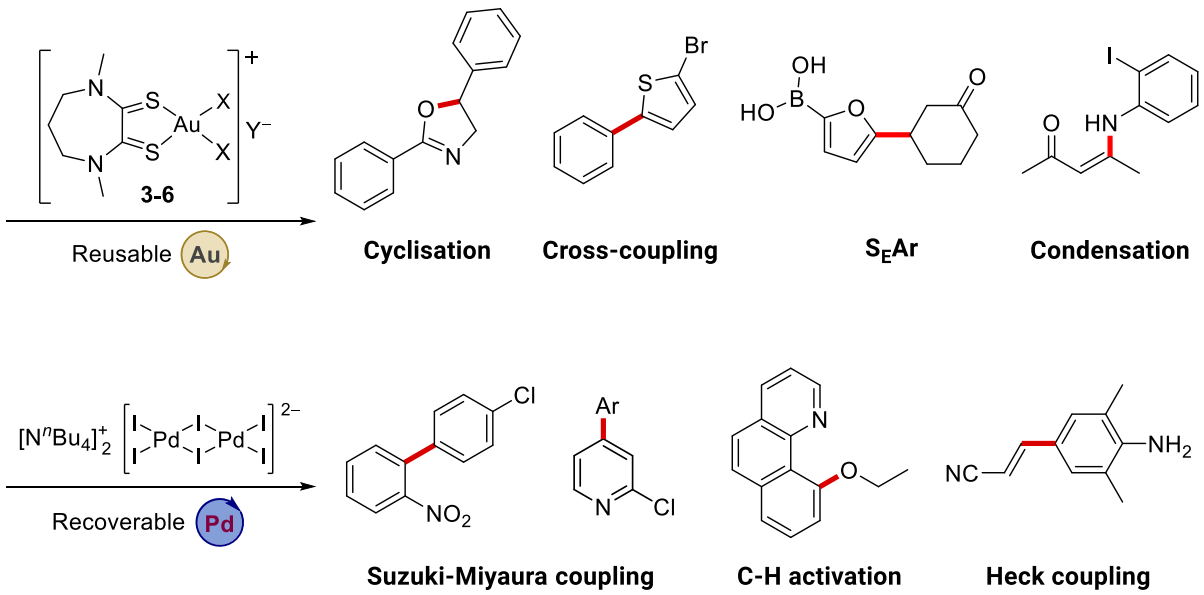

Scheme 89. Summary of the transformations which were successfully catalysed by gold recovery complexes 3-6, and the palladium recovery complex $[N^nBu_4]_2[Pd_2I_6]$.

Moreover, research into these recovered metal complexes (**3**-**6** and $[Cation]_2[Pd_2I_6]$) has led to new chemical behaviour being uncovered. This behaviour is tied to the unusual structures (at least as catalysts) of these recovered complexes, and may not have otherwise been uncovered during a project which utilised conventional catalyst design. For example, the cationic Au^{3+} recovery complexes **3**-**6** exhibited pronounced oxophilicity which led to their excellent activity as Lewis acids for the transformation of carbonyl compounds. This behaviour could be utilised in the future to uncover new catalytic reactions where gold complexes **3**-**6** act as 'hard' Lewis acid catalysts. For example, it was shown that an oxophilic catalyst containing an Au^{3+} centre could switch the selectivity of a Mukaiyama-Michael addition reaction from that provided by a conventional 'soft' catalyst containing Au^+ (Scheme 90).[7]

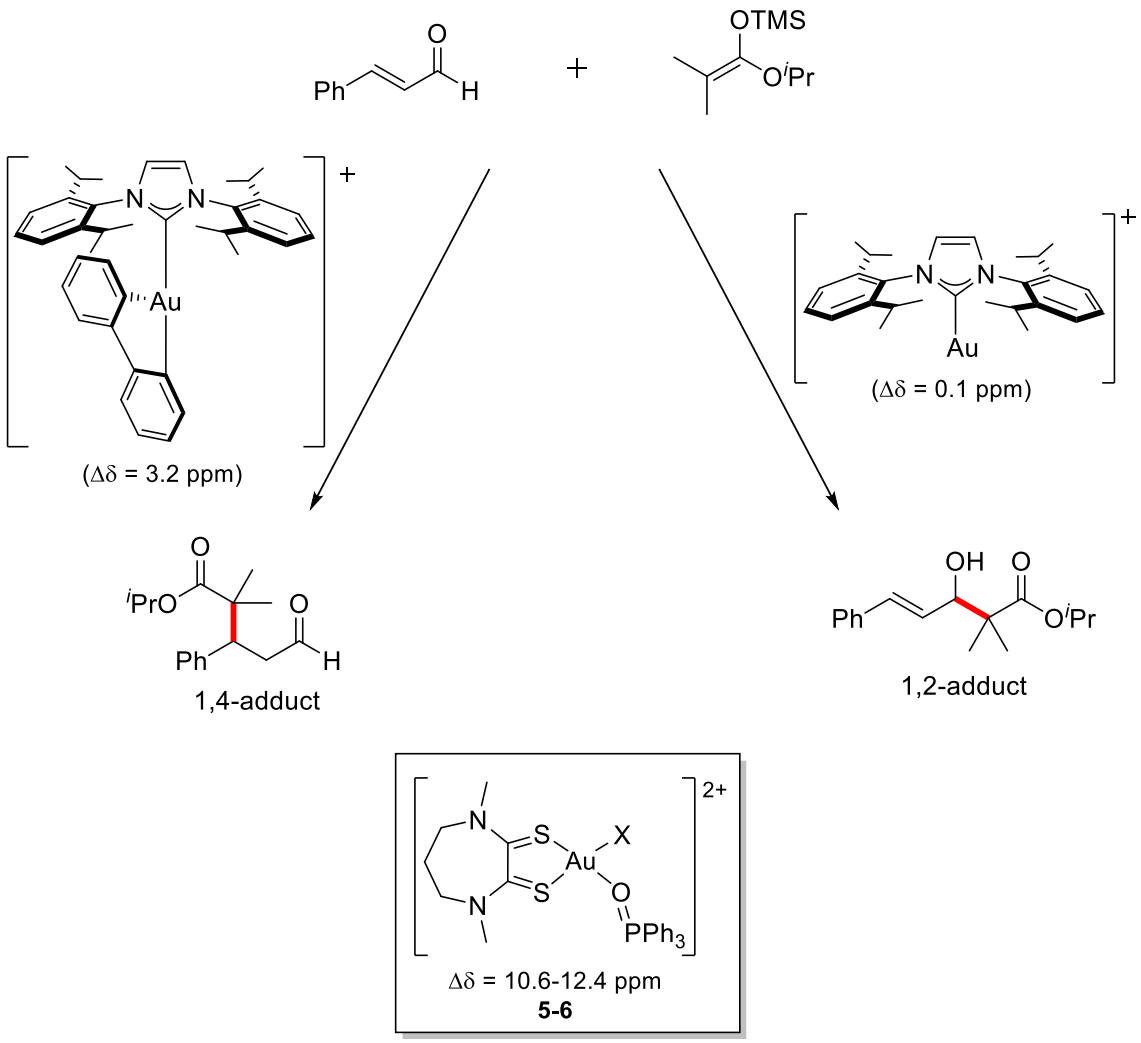

*Scheme 90. New catalytic activity obtained for an "oxophilic" gold Lewis-acid, compared to the oxophilicity of recovered gold complexes **5** and **6** (Δδ refers to Gutmann-Beckett Δ^{31}P shifts upon coordination to triphenylphosphine oxide).*[7]

The Gutmann-Beckett Δδ parameter, a measure of relative oxophilicity, obtained for recovered gold complexes **5** and **6** (Δδ = 10.6 and 12.4 respectively) are considerably larger than those obtained for the Au^{3+} complex in illustrated Scheme 90 (Δδ = 3.2). This highlights the potential for new catalytic activity to be obtained from the pronounced oxophilicity of gold complexes **3**-**6**.

In addition, the ionicity and stability of **3**-**6** enabled the recovery of the complexes and their reuse as homogeneous catalysts, a property which, to the best of our knowledge, has not been previously reported for a homogeneous gold catalyst. Finally, the tetrafluoroborate anion in gold complexes **5** and **6**, a counter anion which is typically considered to be inert, was hydrolysed by the acidic metal centre to form a new gold-fluoride complex. This unusual reactivity could be leveraged in future work to conduct novel chemical transformations, for example hydrofluorination.

Similarly, the unusual structure of the recovered palladium complexes, [Organic Cation]$_2$[Pd_2I_6], led to a number of discoveries. Firstly, the activity of [N^{n}Bu$_4$]$_2$[Pd_2I_6] is better than typical 'off-the-shelf' phosphine-based palladium precatalysts under the conditions tested. It should be noted that a similarly structured palladium complex, [N^{n}Bu$_4$]$_2$[Pd_2Br_6], was also recently highlighted to be an effective Suzuki-Miyaura catalyst,[24] and the results presented in this thesis should further prompt research into the use of simple [Pd_2X_6]$^{2-}$ salts as highly-effective palladium catalysts. Indeed, [N^{n}Bu$_4$]$_2$[Pd_2I_6] was even found to possess similar activity to many state-of-the-art catalysts in the literature for an industrially relevant Suzuki-Miyaura reaction. This reaction is conducted industrially on a 1000 tonne per year scale, representing ~15 tonne per year of palladium consumption that could be replaced by recycled [N^{n}Bu$_4$]$_2$[Pd_2I_6]. Moreover, the catalytic end-point of [N^{n}Bu$_4$]$_2$[Pd_2I_6] as insoluble palladium black meant that the palladium material could be readily recovered and returned to [N^{n}Bu$_4$]$_2$[Pd_2I_6]. Kinetic and mechanistic studies revealed that the activity of [N^{n}Bu$_4$]$_2$[Pd_2I_6] as a Suzuki-Miyaura catalyst was obtained via the formation of palladium nanoparticles, whose size and stability depended on the catalyst loading. An unusual catalyst deactivation pathway mediated by chloride anions released from an aryl chloride coupling partner was also uncovered. The catalytic activity and selectivity of the palladium nanoparticles toward 2,4-dichloropyridine was also found to depend on the organic cation present in the reaction solution – tetrabutylammonium and tetrabutylphosphonium cations promoted catalysis via nanoparticles, whilst tetraphenylphosphonium cations shut down nanoparticle catalytic activity. This reactivity could be exploited in future research to unlock new site-selectivity, especially during the coupling of more challenging polyhalogenated aromatics.[8–10] In addition, it was recently demonstrated that the reduction of aromatic nitro compounds in the presence of Pd/C occurs on the carbon support,[11] and that palladium nanoparticles which leach from the support surface are responsible for undesired side reactions *e.g*. dehalogenation.[12] The use of tetraphenylphosphonium as an additive could be used to shutdown nanoparticle catalysis and improve the selectivity of aromatic nitro-group reductions. Finally, the site-selectivity of aggregated palladium catalysts towards polyhalogenated coupling partners has not yet been well-explored for other typical palladium-catalysed transformations *e.g.* Mizoroki-Heck, Sonogashira, *etc*.

It is also worth noting that a number of models exist in the literature for the surface structure of palladium nanoparticles when stabilised by bulky organic cations (Figure 76).[9,13–17]

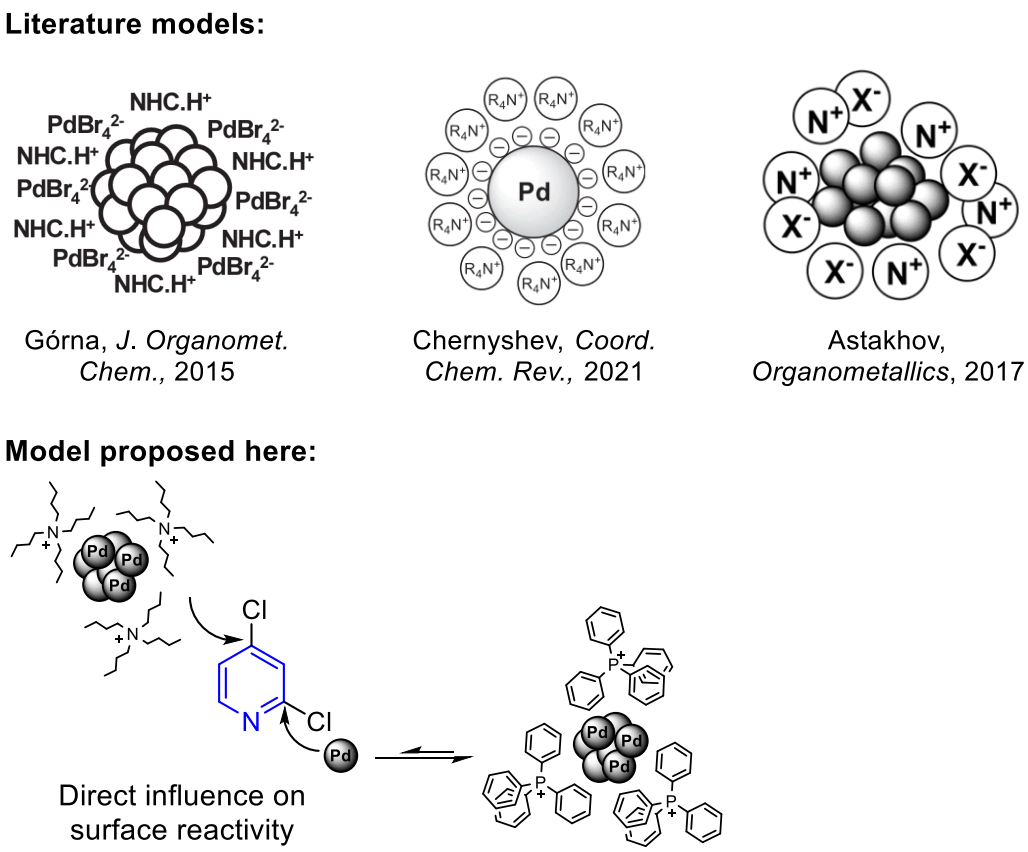

*Figure 76. **Top**: Comparison of literature models for the stabilisation of palladium nanoparticles by bulky organic cations. **Bottom**: the model proposed in this thesis according to the experimental differences in reactivity between tetrabutylammonium and tetraphenylphosphonium cations. Reproduced with permission from references 17, 9 and 13 (Open Access).*

The influence of the organic cation on the site selectivity of palladium nanoparticles towards the functionalisation of 2,4-dichloropyridine presented in this thesis points toward a direct surface interaction of the organic cation with the nanoparticle surface. Recent research by Neufeldt and colleagues provided an insight into the differences in mechanism of oxidative addition between C2 and C4 chloropyridines for mononuclear palladium catalysts, yet no discussion was provided on the role of aggregated species.[25] Additional research is still needed then to better understand the mechanistic origin of the preference for palladium nanoparticles to react at C4.

To conclude, this thesis presents a number of novel applications of recovered metal complexes in the synthesis of fine chemicals. The gold complexes **3**-**6** represents the first direct application in homogeneous catalysis of gold catalysts sourced from waste material.[18] The palladium complexes $[Cation]_2[Pd_2I_6]$ contribute to a growing body of research on the use of palladium compounds recovered from waste in catalysis.[19–22] A range of previously unexplored catalytic activities has been presented for each recovered complex. Ultimately, the activity and chemical behaviour of

the recovered complexes demonstrated in this thesis suggest that these recovered metal catalysts could be excellent, more sustainable candidates for the replacement of existing gold and palladium catalysts derived from mining. Decoupling the catalytic application of palladium and gold from unsustainable mining incentivises the recycling of waste streams that would usually be destined for landfill (*i.e.* viewing waste as a resource for 'urban mining'), and aids in a transition to a circular economy.[23]

5.2. References

1 M. Cuscusa, A. Rigoldi, F. Artizzu, R. Cammi, P. Fornasiero, P. Deplano, L. Marchiò and A. Serpe, *ACS Sustain. Chem. Eng.*, 2017, **5**, 4359–4370.

2 L. Cau, P. Deplano, L. Marchiò, M. L. Mercuri, L. Pilia, A. Serpe and E. F. Trogu, *Dalton Trans.*, 2003, 1969–1974.

3 F. Bigoli, P. Deplano, M. L. Mercuri, M. A. Pellinghelli, G. Pintus, A. Serpe and E. F. Trogu, *Chem. Commun.*, 1998, **484**, 2351–2352.

4 M. Cuscusa, A. Rigoldi, F. Artizzu, R. Cammi, P. Fornasiero, P. Deplano, L. Marchiò and A. Serpe, *ACS Sustain. Chem. Eng.*, 2017, **5**, 4359–4370.

5 N. Marion, O. Navarro, J. Mei, E. D. Stevens, N. M. Scott and S. P. Nolan, *J. Am. Chem. Soc.*, 2006, **128**, 4101–4111.

6 R. B. Bedford, S. L. Hazelwood and M. E. Limmert, *Chem. Commun.*, 2002, **2**, 2610–2611.

7 C. Y. Wu, T. Horibe, C. B. Jacobsen and F. D. Toste, *Nature*, 2015, **517**, 449–454.

8 J. Almond-Thynne, D. C. Blakemore, D. C. Pryde and A. C. Spivey, *Chem. Sci.*, 2016, **8**, 40–62.

9 V. M. Chernyshev, O. V. Khazipov, D. B. Eremin, E. A. Denisova and V. P. Ananikov, *Coord. Chem. Rev.*, 2021, **437**, 213860.

10 J. P. Norman and S. R. Neufeldt, *ACS Catal.*, 2022, 12, 12014–12026.

11 H. An, G. Sun, M. J. Hülsey, P. Sautet and N. Yan, *ACS Catal.*, 2022, **12**, 15021–15027.

12 D. Sokolova, T. C. Lurshay, J. S. Rowbotham, G. Stonadge, H. A. Reeve, S. E. Cleary, T. Sudmeier, K. A. Vincent, *ChemRxiv*, 2024, (10.26434/chemrxiv-2024-vqfc1). This content is a preprint and has not been peer-reviewed.

13 A. V. Astakhov, O. V. Khazipov, A. Y. Chernenko, D. V. Pasyukov, A. S. Kashin, E. G. Gordeev, V. N. Khrustalev, V. M. Chernyshev and V. P. Ananikov, *Organometallics*, 2017, **36**, 1981–1992.

14 N. W. J. Scott, M. J. Ford, N. Jeddi, A. Eyles, L. Simon, A. C. Whitwood, T. Tanner, C. E. Willans and I. J. S. Fairlamb, *J. Am. Chem. Soc.*, 2021, **143**, 9682–9693.

15 D. B. Eremin and V. P. Ananikov, *Coord. Chem. Rev.*, 2017, **346**, 2–19.

16 J. G. De Vries, *Dalton Trans.*, 2006, 421–429.

17 M. Górna, M. S. Szulmanowicz, A. Gniewek, W. Tylus and A. M. Trzeciak, *J. Organomet. Chem.*, 2015, **785**, 92–99.

18 S. McCarthy, O. Desaunay, A. L. W. Jie, M. Hassatzky, A. J. P. White, P. Deplano, D. C. Braddock, A. Serpe and J. D. E. T. Wilton-Ely, *ACS Sustain. Chem. Eng.*, 2022, **10**, 15726–15734.

19 K. A. Jantan, K. W. Chan, L. Melis, A. J. P. White, L. Marchiò, P. Deplano, A. Serpe and J. D. E. T. Wilton-Ely, *ACS Sustain. Chem. Eng.*, 2019, **7**, 12389–12398.

20 S. McCarthy, D. C. Braddock and J. D. E. T. Wilton-Ely, *Coord. Chem. Rev.*, 2021, **442**, 213925.

21 K. A. Jantan, C. Y. Kwok, K. W. Chan, L. Marchiò, A. J. P. White, P. Deplano, A. Serpe and J. D.

E. T. Wilton-Ely, *Green Chem.*, 2017, **19**, 5846–5853.

22 S. McCarthy, A. L. W. Jie, D. C. Braddock, A. Serpe and J. D. E. T. Wilton-Ely, *Molecules*, 2021, **26**, 5217.

23 European Commission Circular Economy Action Plan. https://ec. europa.eu/environment/strategy/circular-economy-action-plan_en (accessed April 1, 2022).

24 N. Jeddi, N. W. J. Scott, T. Tanner, S. K. Beaumont and I. J. S. Fairlamb, *Chem. Sci.*, 2024, **15**, 2763–2777.

25 M. J. Kania, A. Reyes and S. R. Neufeldt, *J. Am. Chem. Soc.*, 2024, **146**, 19249–19260.

Chapter Six – Experimental Details and Characterisation Data

6.1. General experimental

All of the reagents used in this project were purchased from commercial suppliers and used without further purification. All of the reactions performed were conducted under air unless otherwise indicated. All stirrer bars and glassware used to perform catalysis were pre-washed with *aqua regia*. Crude products purified by column chromatography were passed through silica gel (pore size: 60 Å, 230-400 µm mesh size, 40-63 µm particle size). Thin-layer chromatography plates were visualised by exposure to ultraviolet light. Samples analysed by mass spectrometry were ionised by electrospray ionisation and recorded on a Waters Xevo TQ-MS/Acquity UPLC. ^{1}H, ^{19}F and ^{13}C NMR spectra were recorded on a Bruker Avance III 400 MHz spectrometer at room temperature and were referenced to the residual proton signal of the NMR solvent. Chemical shifts (δ) are reported in parts per million (ppm) and coupling constants (*J*) are given in Hz. IR spectra were recorded on an Agilent Cary 630 FTIR. Unless otherwise stated, provided analytical data are consistent with data found in the literature. HPLC analyses was performed on a PerkinElmer Series 200 HPLC fitted with a Supercosil LC18 (25 cm x 4.6 mm x 5 µm) and a Series 200 EP Diode Array UV-Vis detector measuring at 254 and 238 nm, and the data analysed in TotalChrom. Design of experiment optimisation was conducted in JMP pro 16 and JMP pro 17. UV-vis spectra were recorded on an Agilent Cary 60 UV-vis spectrometer. Variable time normalisation kinetic analysis was conducted according to the report by Burés and Nielson using the excel spreadsheet provided in the supporting information.[1] The Microsoft Excel plugin 'Solver' was used for deconvolution. The catalyst samples used in VTNA kinetic studies were weighed on a Sartorius Secura analytical balance (d = 0.01 mg). All volumes ≤1 ml were measured using a micropipette. DLS measurements were taken using the Zetasizer Nano-ZS instrument (Malvern Panalytical) at 25 °C.

6.2. Chapter Two Experimental

6.2.1. Synthesis of gold complexes 3-6 and 10-12

Me_2dazdt (*1,4-dimethyl-1,4-diazepane-2,3-dithione*)

Me_2dazdt (*N,N'-dimethyl-perhydrodiazepine-2,3-dithione*) was prepared under the literature conditions and the characterisation of the obtained product was consistent with literature data.[2]

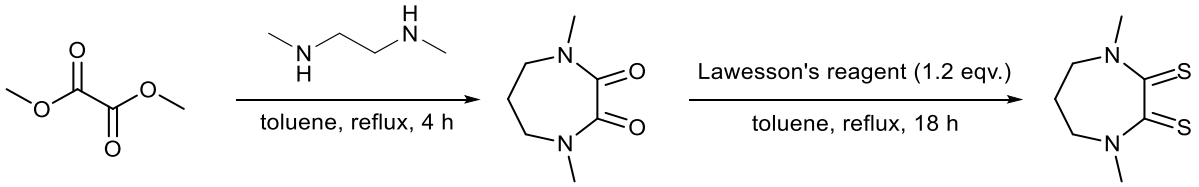

Dimethyloxalate (2.36 g, 20.0 mmol) and *N,N'*-dimethylpropane-1,3-diamine (2.50 mL, 20.0 mmol) were stirred in refluxing toluene (40 mL) for 6 h. After cooling, the solvent was removed under reduced

pressure and the crude material recrystallised from hot 2-propanol, yielding *1,4-dimethyl-1,4-diazepane-2,3-dione* as a large white jagged crystalline solid (2.530 g, 81%).

1,4-dimethyl-1,4-diazepane-2,3-dione (1.32 g, 8.46 mmol) and Lawesson's reagent (4.125 g, 10.20 mmol) were dissolved in toluene (60 mL) and stirred under reflux overnight. The reaction mixture was concentrated and the crude orange solid purified by flash chromatography (R_f = 0.25 [n-hexane/EtOAc (3:7), followed by DCM]), yielding Me_2dazdt as a yellow solid (1.036 g, 65%). HRMS (ESI) *m/z* $[M+H]^+$ calculated. for $C_7H_{13}N_2S_2$: 189.0521, found: 189.0520. IR (ATR): 2922, 2855, 1491, 1435, 1379, 1260, 1185, 1111, 1081, 1025, 973 cm^{-1}. ^1H NMR (Chloroform-*d*): 3.77 (ddd, J = 14.8, 9.6, 7.9 Hz, 2H), 3.58–3.53 (m, 2H), 3.52 (s, 6H), 2.27–2.16 (m, 2H) ppm. The Analytical data was found to be in agreement with literature data.[2]

Me_2dazdt•2I_2 (1)

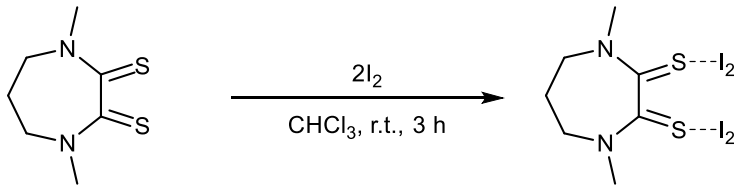

1

A solution of Me_2dazdt (96 mg, 0.50 mmol) and I_2 (250 mg, 1.00 mmol) was dissolved in $CHCl_3$ (25 mL) and stirred at room temperature for 3 h. The solvent was concentrated to ~10 mL and the desired adduct was filtered, washed with $CHCl_3$ and isolated as a shiny purple crystalline powder (314 mg, 91%). The product was used directly without characterisation. Literature analytical data for the title compound have not been reported.

Me_2dazdt•2IBr (2)

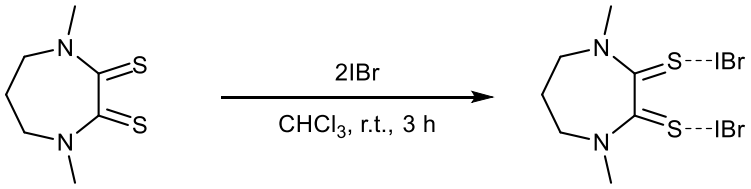

2

A solution of Me_2dazdt (96 mg, 0.50 mmol) and IBr (207 mg, 1.00 mmol) was dissolved in $CHCl_3$ (25 mL) and stirred at room temperature for 3 h. The solvent was concentrated to ~10 mL and the desired adduct was filtered, washed with $CHCl_3$ and isolated as a deep-orange powder (272 mg, 90%). The product was used directly without characterisation. Literature analytical data for the title compound have not been reported.

[$AuI_2(Me_2dazdt)]I_3$ (3)

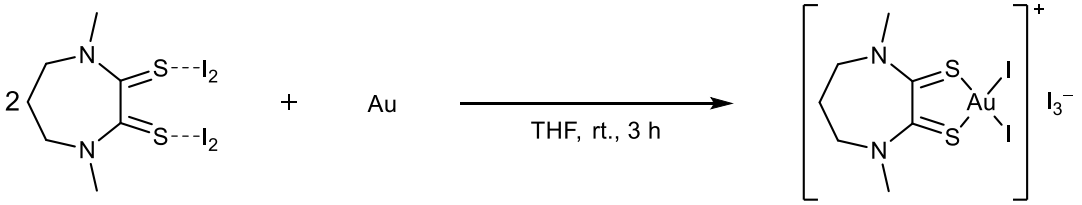

3

According to a modified literature procedure,[3] a solution of $Me_2dazdt{\cdot}2I_2$ (487 mg, 0.700 mmol) and gold powder (70 mg, 0.36 mmol) in THF (100 mL) was stirred for ~3 h. The black solution was concentrated (to ~40 ml) and the product crystallised directly from the black reaction mixture by vapour phase diffusion with Et_2O. The resulting shiny black crystals were filtered, washed with $CHCl_3$ and dried under vacuum (338 mg, 92%). IR (ATR): 3101, 2996, 2948, 2910, 2853, 2778, 2672, 1675, 1646, 1613, 1549, 1451, 1434, 1397, 1353, 1341, 1329, 1295, 1280, 1257, 1181, 1097, 1069, 1034, 1022, 953, 838, 822, 745, 690 cm^{-1}. ^1H NMR (400 MHz, Acetone-d_6): 3.79–3.69 (m, 2H), 3.68–3.57 (m, 2H), 3.47 (s, 6H), 2.38–2.29 (m, 2H) ppm. Literature analytical data for the title compound has not been previously reported, except by us.[4]

Gold complex **3** could also be synthesised directly from Me_2dazdt and gold powder:

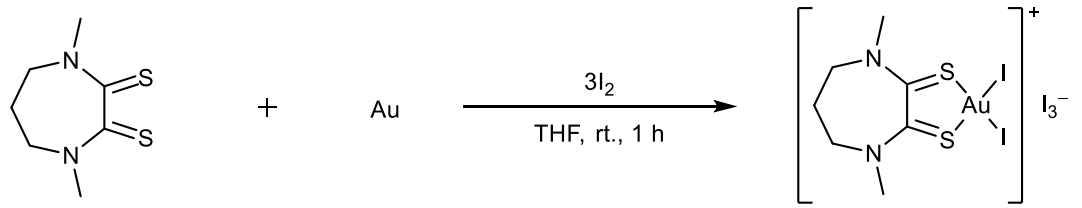

3

According to a modified literature procedure,[3] Me_2dazdt (92 mg, 0.49 mmol), Au powder (96 mg, 0.49 mmol) and I_2 (372 mg, 1.46 mmol) were suspended in THF (70 mL) and stirred at room temperature for 1 h. The product was crystallised from the black solution by vapour phase diffusion with Et_2O. The desired product was isolated as shiny black crystals (437 mg, 88%). IR (ATR): 3101, 2996, 2948, 2910, 2853, 2778, 2672, 1675, 1646, 1613, 1549, 1451, 1434, 1397, 1353, 1341, 1329, 1295, 1280, 1257, 1181, 1097, 1069, 1034, 1022, 953, 838, 822, 745, 690 cm^{-1}. ^1H NMR (400 MHz, Acetone-d_6): 3.79–3.69 (m, 2H), 3.68–3.57 (m, 2H), 3.47 (s, 6H), 2.38–2.29 (m, 2H) ppm. Literature analytical data for the title compound has not been previously reported, except by us.[4]

[AuBr$_2$(Me$_2$dazdt)]IBr$_2$ (4)

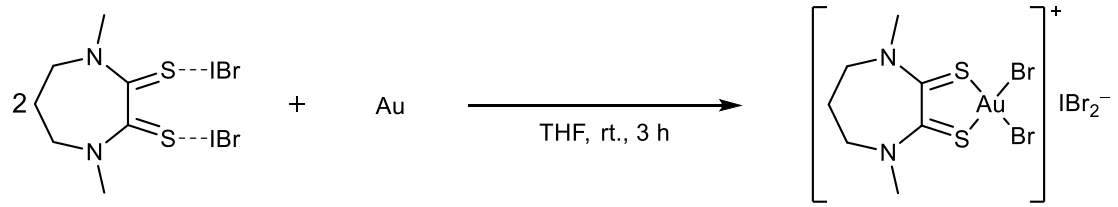

3

According to a modified literature procedure,[5] a solution of Me$_2$dazdt·2IBr (416 mg, 0.700 mmol) and gold powder (70 mg, 0.36 mmol) in THF (100 mL) was stirred for ~3 h. The black solution was concentrated (to ~40 ml) and the product crystallised directly from the black reaction mixture by vapour phase diffusion with Et$_2$O. The resulting shiny black crystals were filtered, washed with CHCl$_3$ and dried under vacuum (269 mg, 90%). IR (ATR): 2912, 1555, 1451, 1432, 1389, 1266, 1110, 1069, 954, 742, 605 cm^{-1}. ^{1}H NMR (400 MHz, Acetone-d_6) : 3.79 (s, 4H), 3.57 (s, 6H), 2.43 (s, 2H) ppm. Literature analytical data for the title compound has not been previously reported, except by us.[4]

Gold complex **4** could also be synthesised directly from Me$_2$dazdt and gold powder:

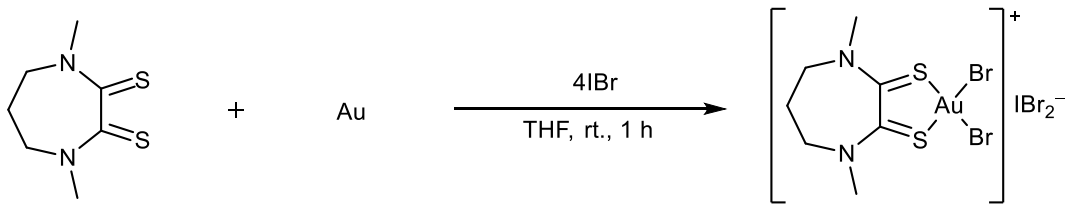

4

According to a modified literature procedure,[5] Me$_2$dazdt (75 mg, 0.40 mmols), Au powder (80 mg, 0.40 mmols) and IBr (331 mg, 1.60 mmols) were suspended in THF (70 mL) and stirred at room temperature for 2 h. The product was crystallised from the black solution by vapour phase diffusion with Et$_2$O. The desired product was isolated as shiny black crystals (283 mg, 85%). IR (ATR): 2912, 1555, 1451, 1432, 1389, 1266, 1110, 1069, 954, 742, 605 cm^{-1}. ^{1}H NMR (400 MHz, Acetone-d_6) : 3.79 (s, 4H), 3.57 (s, 6H), 2.43 (s, 2H) ppm.

[AuI$_2$(Me$_2$dazdt)]I$_3$ (3a) and [AuBr$_2$(Me$_2$dazdt)]IBr$_2$ (4a) from scrap SIM cards

The complete procedure for metals recovery reported by Deplano *et al*. was followed when **3a** and **4a** were obtained from leaching real scrap SIM cards:[6]

Scrap SIM cards (~17 g) were initially ground to a coarse powder. The scrap material was then stirred in refluxing THF (50 mL). After 24 h, the white liquid (indicating the dispersion of the white plastic support) was decanted, and the resulting coarse powder isolated and washed with hot THF (2 x 10 mL). The coarse powder was suspended in a stirred solution of aqueous ammonia (32%, 10 mL) and

ammonium sulphate (2.2 g). To the suspension was then added aqueous H_2O_2 (30 %, 3 mL) dropwise and the solution stirred at room temperature. After 4 h, the deep-blue solution (indicating the oxidation and dissolution of Cu^0 as $[Cu(NH_3)_4]SO_4$) was decanted and the residue washed with distilled H_2O (2 x 10 mL). The resulting coarse powder was then suspended in a hot (80 °C) stirred solution of aqueous HCl (2.4 M, 25 mL). After 24 h, the green solution (indicating the oxidation and dissolution of Ni^0 as $NiCl_2$) was decanted and the coarse powder washed with distilled H_2O (2 x 10 mL). Finally, the course powder was suspended in a stirred solution of Me_2dazdt (92 mg, 0.53 mmol) and I_2 (372 mg, 1.46 mmol) or IBr (404 mg, 1.95 mmol) in THF (80 mL). After 24, the black liquid was filtered, the filtrate concentrated to ~30 mL and the product crystallised from the black liquid by vapour phase diffusion with Et_2O. Both **3a** (130 mg) and **4a** (105 mg) were isolated as shiny black crystals, whose characterisation data was consistent with the literature and with **3**/**4** synthesised from gold metal powder. No difference in catalytic activity was observed between the complexes isolated from scrap SIM cards and the complexes isolated from gold powder.

$[AuI_2(Me_2dazdt)]BF_4$ (5)

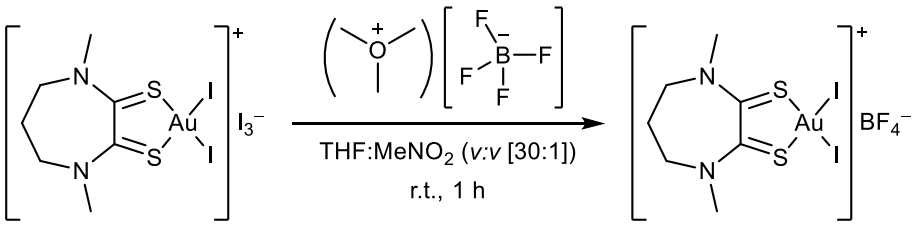

3 **5**

$[AuI_2(Me_2dazdt)]I_3$ (**3**) (150 mg, 0.147 mmol) was dissolved in THF (120 mL). Trimethyl oxonium tetrafluoroborate (22 mg, 0.15 mmol) was dissolved in $MeNO_2$ (4 mL) and the solution transferred to the THF solution in one portion. The reaction mixture was stirred for 1 h, concentrated *in vacuo* and the crude material recrystallised in MeCN by vapour phase diffusion with $CHCl_3$, yielding the title compound as shiny black crystals suitable for single crystal XRD (104 mg, 97%). IR (ATR): 1554, 1437, 1399, 1259, 1047, 1029, 948, 822, 746, 605, 519. ^{1}H NMR (400 MHz, Acetonitrile-d_3): δ 3.95 (t, J = 6.9 Hz, 4H), 3.72 (s, 6H), 2.65 (quin, J = 6.9 Hz, 2H) ppm. ^{19}F NMR (377 MHz, Acetonitrile-d_3): 151.7 (0.20F), 151.8 (0.80F) ppm. ^{13}C NMR spectra are not reported due to poor spectral resolution of a saturated solution of **5** in Acetonitrile-d_3. Calculated for $C_7H_{12}AuBF_4I_2N_2S_2$ (Mw = 725.8861): C 11.6, H 1.7, N 3.9 %. Found: C 11.7, H 1.6, N 3.5 %. BF_4^- purity was confirmed by ^{19}F NMR of an MeCN-d_3 solution of **5** (10 mg, 0.014 mmol) and fluorobenzene (5.2 µL, 0.055 mmol, 4 equivalents). Literature analytical data for the title compound has not been previously reported, except by us.[4]

[AuBr$_2$(Me$_2$dazdt)]BF$_4$ (6)

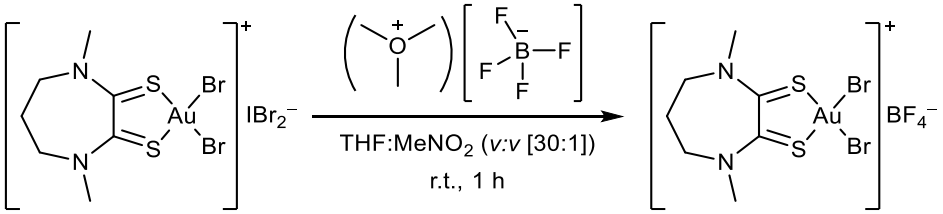

4 **6**

[AuBr$_2$(Me$_2$dazdt)]IBr$_2$ (**4**) (55 mg, 0.074 mmol) was dissolved in THF (60 mL). Trimethyl oxonium tetrafluoroborate (11 mg, 0.074 mmol) was dissolved in MeNO$_2$ (2 mL) and the solution transferred to the THF solution in one portion. The reaction mixture was stirred for 1 h, concentrated *in vacuo* and the crude material recrystallised in MeCN by vapour phase diffusion with CHCl$_3$, yielding the title compound as shiny black crystals suitable for single crystal XRD (47 mg, 95%) IR (ATR): 1742, 1562, 1437, 1399, 1359, 1262, 1230, 1018, 951, 824, 745, 603, 518, 413. ^{1}H NMR (400 MHz, Acetonitrile-d_3) δ 4.01 (t, J = 6.9 Hz, 4H), 3.76 (s, 6H), 2.67 (quin, J = 6.9 Hz, 2H) ppm. ^{19}F NMR (377 MHz, Acetonitrile-d_3): 151.7 (0.20F), 151.7 (0.80F) ppm. ^{13}C NMR spectra are not reported due to poor spectral resolution of a saturated solution of **6** in Acetonitrile-d_3. Calculated for $C_7H_{12}AuBF_4I_2N_2S_2$ (Mw = 631.8852): C 13.3, H 1.9, N 4.4 %. Found: C 12.8, H 1.7, N 4.0 %. BF$_4^-$ purity was confirmed by ^{19}F NMR of an MeCN-d_3 solution of **6** (4.3 mg, 0.0068 mmol) and fluorobenzene (2.6 µL, 0.027 mmol, 4 equivalents). Literature analytical data for the title compound has not been previously reported, except by us.[4]

[Au$_2$Br$_2$(Me$_2$dazdt)] (10)

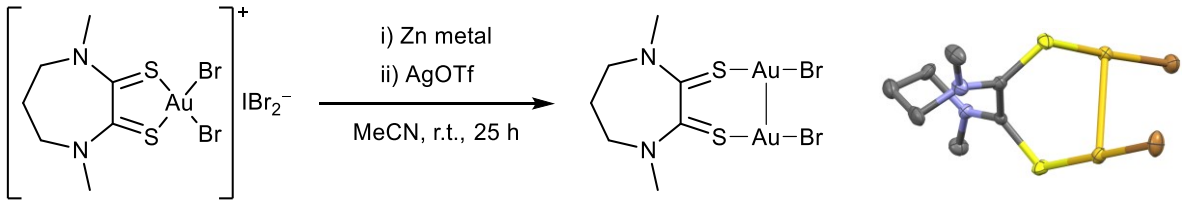

4 **10**

A suspension of zinc powder (1.3 mg, 0.020 mmol) in a solution of [AuBr$_2$(Me$_2$dazdt)]IBr$_2$ (**4**) (17 mg, 0.020 mmol) in MeCN (20 mL) was stirred at room temperature. After 24 h, the reaction mixture was filtered under gravity and AgOTf (5 mg, 0.02 mmol) was added to the stirred filtrate, resulting in the immediate formation of an off-white precipitate. After 1 h, the suspension was filtered under gravity, the filtrate concentrated *in vacuo* and the resulting dark-red powder washed with MeOH (2 x 5 mL). The crude material was resuspended in MeCN (~3 mL) and recrystallised by vapour phase diffusion with CHCl$_3$, yielding [Au$_2$Br$_2$(Me$_2$dazdt)] as shiny red crystals suitable for single crystal XRD (2.6 mg, 35%). The structure of **10** was confirmed by single crystal XRD.

[AuI$_{0.84}$Br$_{0.16}$(Me$_2$dazdt)]SbF$_6$ (11)

The sample of **4** (denoted here as **4***) used in the synthesis of **11** was isolated by a modified work-up procedure (complete concentration of the reaction mixture from the synthesis of **4** and resuspension in MeCN for recrystallisation). This resulted in the mixed halogen content in **4***. This sample was not used for catalytic studies, but was employed in anion metathesis studies.

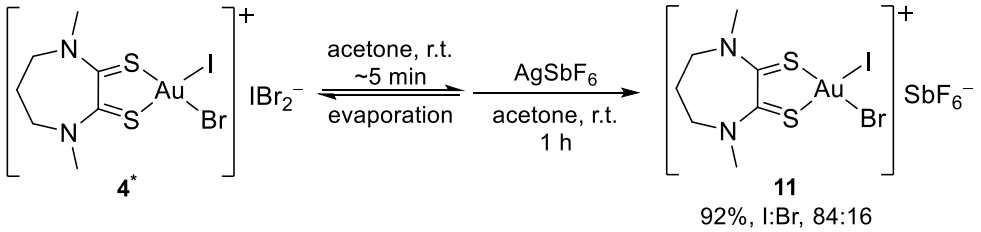

[AuI$_{0.84}$Br$_{0.16}$(Me$_2$dazdt)]IBr$_2$ (**4***) (8.5 mg, 0.011 mmol) was dissolved in acetone (5 mL) and left to stir until the solution turned pale yellow (~5-10 min). Silver hexafluoroantimonate (3.8 mg, 0.011 mmol) was transferred to the pale-yellow acetone solution, resulting in the immediate formation of a white precipitate. The reaction mixture was stirred for 1 h, filtered, concentrated *in vacuo* and the crude material recrystallised in MeCN by vapour phase diffusion with $CHCl_3$, yielding the title compound as shiny black crystals suitable for single crystal XRD (7.5 mg, 92%). The structure of **11** was confirmed by single-crystal XRD and the halogen content determined by modelling for the best R_2.

[AuI$_2$(Me$_2$dazdt)]OTf (12)

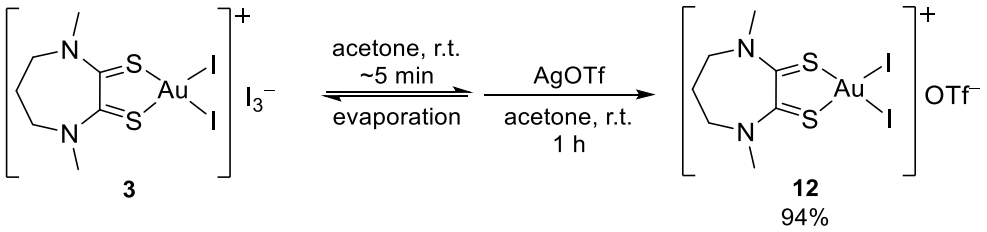

[AuI$_2$(Me$_2$dazdt)]I$_3$ (**3**) (8.5 mg, 0.0083 mmol) was dissolved in acetone (5 mL) and left to stir until the solution turned pale yellow (~5-10 min). Silver triflate (2.2 mg, 0.0086 mmol) was transferred to the pale-yellow acetone solution, resulting in the immediate formation of a white precipitate. The reaction mixture was stirred for 1 h, filtered, concentrated *in vacuo* and the crude material recrystallised in MeCN by vapour phase diffusion with $CHCl_3$, yielding the title compound as shiny black crystals suitable for single crystal XRD (6.2 mg, 94%). ^{1}H NMR (400 MHz, Acetonitrile-d_3) δ 3.97 (t, J = 6.9 Hz, 4H), 3.75 (s, 6H), 2.68 (q, J = 6.6 Hz, 2H). ^{19}F NMR (377 MHz, Acetonitrile-d_3) δ -79.35. ^{13}C NMR spectra are not reported due to poor spectral resolution of a saturated solution of **2b** in Acetonitrile-d_3. Calculated for $C_8H_{12}AuF_3I_2O_3N_2S_3$ (Mw = 788.1457): 12.2, H 1.5, N 3.6 %. Found: C 10.2, H 1.02, N 2.67 %. CHN elemental analysis illustrated that some residual iodide content remained in the sample of **12**.

6.2.2. Synthesis of organic substrates for catalytic testing

N-(Prop-2-yn-1-yl)benzamide (15)

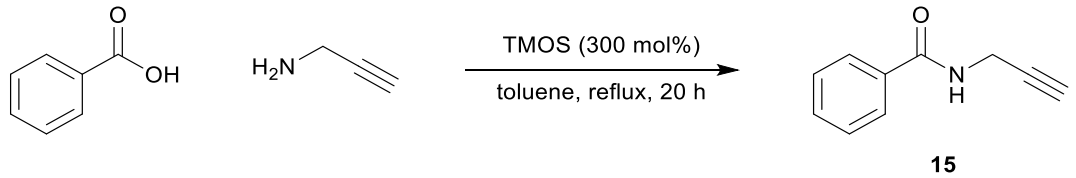

According to the procedure reported by Braddock *et al*,[7] a solution of benzoic acid (5.00 mmol, 611 mg), propargylamine (5.00 mmol, 275 mg) and tetramethylorthosilicate (2.22 mL, 15.0 mmol) in toluene (8 mL) was stirred at reflux. After 20 h, the reaction solution was cooled to room temperature, concentrated and the resulting residue dissolved in THF (25 mL). The THF solution was washed with aqueous K_2CO_3 (75 mL, 0.3 M, 22.5 mmol). Solid NaCl was added continuously until two clear layers formed, the aqueous layer was extracted with THF (2 x 15 mL) and the combined organic layers washed with sat. NH_4Cl (25 mL). The organic layer was dried over Na_2SO_4, filtered and concentrated to obtain the desired product (638 mg, 80%) as a white crystalline solid. IR (ATR): 3282, 1637 cm^{-1}. ^1H NMR (400 MHz, Chloroform-*d*): 2.30 (t, *J* = 2.7 Hz, 1H), 4.28 (dd, *J* = 5.3 Hz, 2.6 Hz, 2H), 6.33 (s, 1H), 7.45 (m, 2H), 7.53 (tt, *J* = 7.3 Hz, 6.1 Hz, 2.5 Hz, 1.2 Hz, 1H), 7.80 (m, 2H) ppm. ^{13}C (101 MHz, Chloroform-*d*): 167.1, 133.7, 131.8, 128.6, 127.0, 79.4, 71.9, 29.8 ppm. Analytical data was found to be in agreement with literature data.[8]

N-(3-Phenylprop-2-yn-1-yl)benzamide (17)

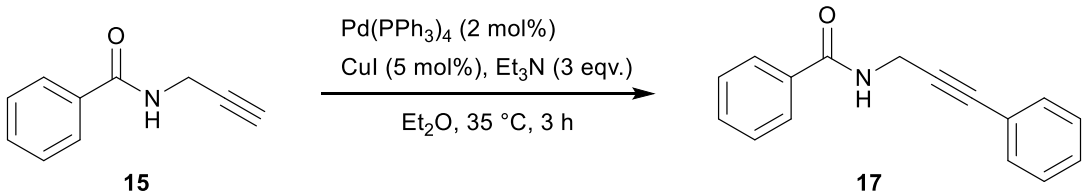

According to the procedure reported by Engle *et al*.,[9] a solution of $Pd(PPh_3)_4$ (2 mol %, 23 mg, 0.02 mmol), CuI (5 mol %, 9.5 mg, 0.05 mmol), *N*-(prop-2-yn-1-yl)benzamide (**15**) (1.00 mmol, 159 mg) in anhydrous diethyl ether (3 mL) was stirred at room temperature under an inert atmosphere of N_2. After 10 min, iodobenzene (2.00 mmol, 224 µL) was added, followed by the dropwise addition of diethylamine (3.00 mmol, 310 µL) and the reaction mixture stirred at 35 °C. After 3 h, the reaction mixture was poured into a separating funnel containing brine (20 mL) and extracted with Et_2O (3 x 25 mL). The combined organic layers were dried over Na_2SO_4, filtered and concentrated *in vacuo*. The crude residue was purified by silica gel column chromatography (R_f = 0.23 [*n*-hexane/EtOAc (4:1)]) yielding the desired amide (177 mg, 75%) as a white solid. ^1H NMR (400 MHz, Chloroform-*d*) δ 7.86 –

7.79 (m, 2H), 7.58 – 7.50 (m, 1H), 7.50 – 7.42 (m, 4H), 7.33 (m, 3H), 6.36 (s, 1H), 4.51 (d, *J* = 5.1 Hz, 2H) ppm. Analytical data was found to be in agreement with literature data.[10]

2-Phenylethynyline (22)

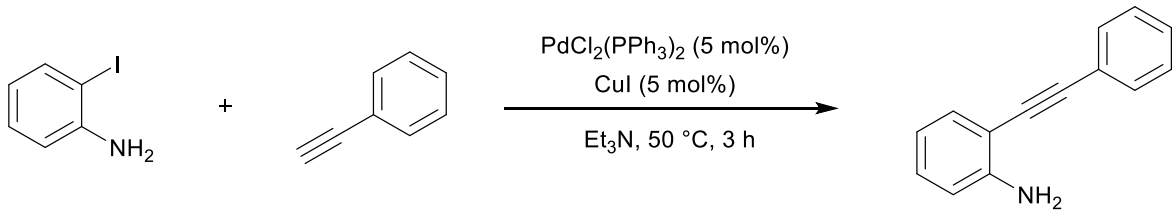

22

A solution of 2-iodoaniline (219 mg, 1.00 mmol, 1.0 eq), phenylacetylene (120 µL, 1.10 mmol, 1.1 eq), $PdCl_2(PPh_3)_2$ (35 mg, 0.050 mmol, 0.05 eq) and CuI (9.5 mg, 0.050 mmol, 0.05 eq) in triethylamine (5 mL) was stirred for 3 h at 50 °C under a nitrogen atmosphere. The reaction mixture was extracted with DCM (3 x 10 mL) and the organic phase washed with brine (3 x 10 mL). After drying it over $MgSO_4$, the solvent was removed under vacuum. The crude residue was purified by flash-chromatography (Rf = 0.22 [n-hexane/ethyl acetate (9/1)]) to yield the title compound as a white crystalline solid (124 mg, 64%). ^{1}H NMR (400 MHz, Chloroform-*d*) δ 7.57-7.54 (m 2H), 7.41-7.34 (m, 4H), 7.21 – 7.13 (m, 1H), 6.77-6.73 (m, 2H), 4.30 (s, 2H) ppm. Analytical data is in good agreement with literature data.[11]

6.2.3. Catalytic testing of gold recovery products 3-6

6.2.3.1. Cyclisation of N-propargylic amides 15 and 17

5-Methyl-2-phenyloxazole

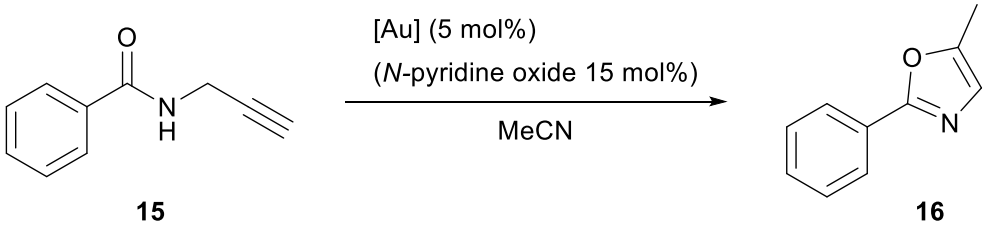

15 **16**

N-Propargylbenzamide (**15**) (32 mg, 0.20 mmol), *N*-pyridine oxide (2.9 mg, 0.030 mmol) and the respective gold complex (0.01 mmol, 0.05 eq) were dissolved in acetonitrile (1.5 mL). The solution was stirred for the amount of time and at the temperature indicated in the main manuscript (Table 1). After the indicated time, the reaction solution was concentrated and the yield quantified by ^{1}H NMR analysis. Yields were determined by the relative integrals of the amide methylene protons (4.23- 4.25 ppm) and the product vinyl proton (6.85 ppm). A pure sample of the cyclised product was isolated following purification by silica gel column chromatography (R_f = 0.25 [*n*-hexane/EtOAc (7:1)]) yielding the desired oxazole (^{1}H NMR Yield: 96%. Isolated Yield: 28 mg, 89%) as a white solid. ^{1}H NMR (400

MHz, Chloroform-*d*): 8.06 – 7.98 (m, 2H), 7.51 – 7.39 (m, 3H), 6.86 (d, *J* = 1.4 Hz, 1H), 2.42 (d, *J* = 1.2 Hz, 3H) ppm. ^{13}C NMR (101 MHz, Chloroform-*d*): 160.7, 148.9, 129.9, 128.7, 127.8, 126.0, 124.2, 11.1 ppm. Analytical data is in good agreement with literature data.[8]

(Z)-5-Benzylidene-2-phenyl-4,5-dihydrooxazole (18)* and *(E)-5-(iodo(phenyl)methylene)-2-phenyl-4,5-dihydrooxazole (20)

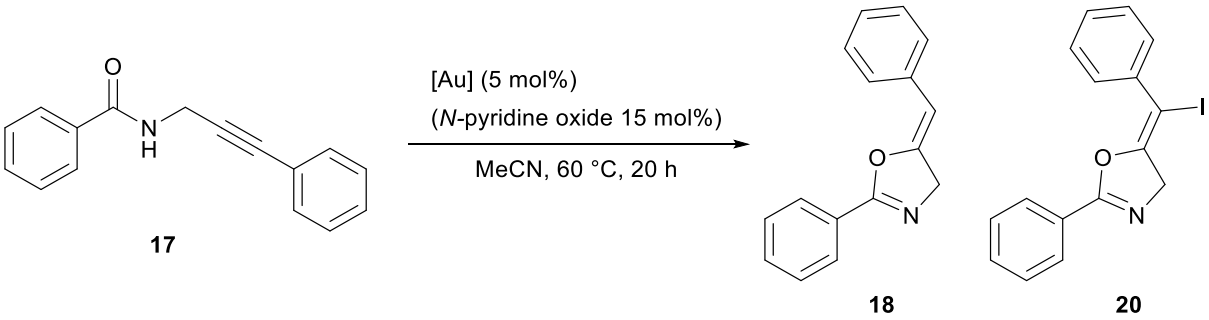

A stirred solution of amide (56 mg, 0.24 mmol), *N*-pyridine oxide (3.4 mg, 0.036 mmol) and [Au] (5 mol%, 0.012 mmol) in MeCN (1.8 mL) was heated to 60 ºC for 20 h. The reaction mixture was concentrated *in vacuo* and the resulting residue purified by silica gel column chromatography [*n*-hexane/EtOAc (7:1)].

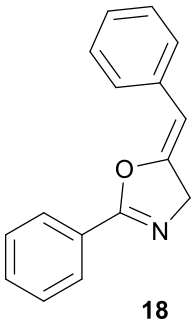

R_f = 0.18. HRMS (ESI) *m/z* $[M+H]^+$ calcd. for $C_{16}H_{14}NO$: 236.1075, found: 236.1077. ^{1}H NMR (400 MHz, Chloroform-*d*): δ 8.10-8.07 (m 1H), 7.66 – 7.61 (m, 2H), 7.58 – 7.51 (m, 3H), 7.43 – 7.39 (m, 3H), 7.28 – 7.21 (m, 1H), 5.68 (t, *J* = 2.6 Hz, 1H), 4.84 (d, *J* = 2.6 Hz, 2H) ppm. ^{13}C NMR (101 MHz, Chloroform-*d*): 164.1, 151.8, 135.0, 132.2, 130.7, 128.8, 128.6, 128.3, 127.9, 126.3, 100.8, 59.5 ppm. Analytical data is in good agreement with literature data.[12]

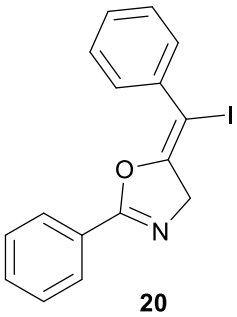

R_f = 0.20. HRMS (ESI) *m/z* $[M+H]^+$ calcd. for $C_{16}H_{13}INO$: 362.0042, found: 362.0047. ^{1}H NMR (400 MHz, Chloroform-*d*) δ 7.93 (d, *J* = 7.6 Hz, 2H), 7.68 (d, *J* = 7.7 Hz, 2H), 7.58 – 7.19 (m, 6H), 4.88 (s, 2H) ppm. ^{13}C NMR (101 MHz, Chloroform-*d*): δ 164.2, 152.8, 138.1, 132.3, 129.6, 128.8, 128.3, 128.1, 127.9, 126.7, 70.8, 65.2 ppm. Due to conflicting analytical data for the vinyl iodide 5-*exo* and 6-*endo* cyclisation products, the structure of **20** was confirmed by lithiation and protonation (see below).

Lithiation and protonation of *(E)-5-(iodo(phenyl)methylene)-2-phenyl-4,5-dihydrooxazole*

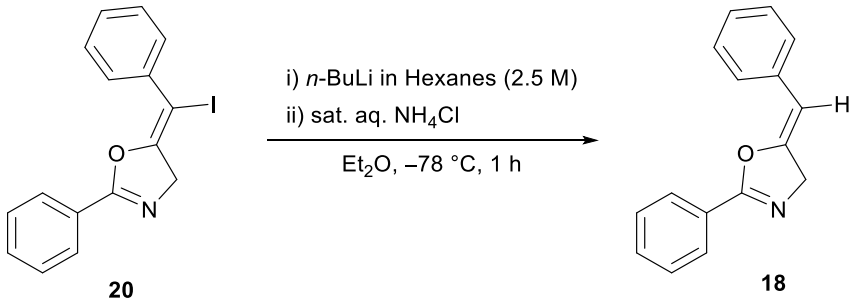

An Et_2O (1 mL) solution of the vinyl iodide oxazole (**20**) (30 mg, 0.083 mmol) was cooled to –78 °C. A solution of *n*-BuLi in Hexanes (2.5 M, 0.087 mmol, 34.9 µL) was added dropwise over 10 minutes. After 1 h, IPA (1 mL) was added dropwise, the mixture was warmed to room temperature and a saturated solution of ammonium chloride (1 mL) was added dropwise to the Et_2O solution. The organic layer was isolated, washed with brine and dried over $MgSO_4$. The residue was purified by silica-gel chromatography (R_f = 0.18, [petroleum ether (40-60)/ethyl acetate (7:1)]), yielding the title compound as a white solid (7 mg, 35%). Characterisation data were found to be consistent with those reported above for **18**.

6.2.3.2. Cyclisation of 2-phenylethynyline (22) to indole 23

2-Phenyl-1H-indole

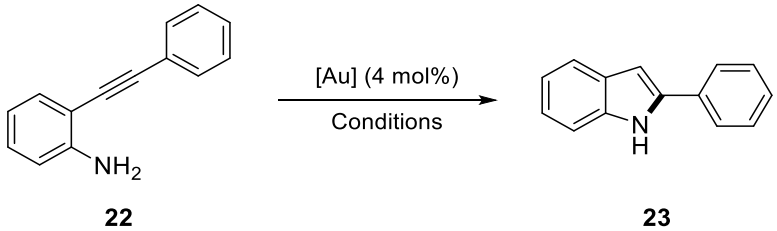

2-Phenylethynylaniline (0.2 mmol, 39 mg) and the gold complex (4 mol%, 0.008 mmol) were stirred in ethanol (1.5 mL) for 4 h. The reaction mixture was concentrated and the crude residue dissolved in $CDCl_3$ for ^1H NMR analysis, which only contained the environments due to the starting material (**22**).

6.2.3.3. Condensation of *o*-iodoaniline (24) and acetylacetone (25)

(Z)-4-((2-Iodophenyl)amino)pent-3-en-2-one (26)

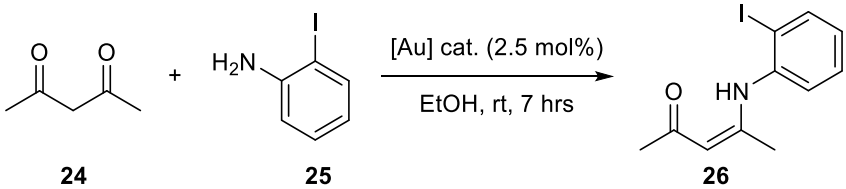

2-Iodoaniline (**25**) (44 mg, 0.2 mmol) and [Au] (0.005 mmol, 0.025 eq) were dissolved in ethanol (3 mL) and acetylacetone (**24**) (20 µL, 0.2 mmol) was added to the solution. After 7 h, the reaction mixture was concentrated, the residue dissolved in $CDCl_3$ and submitted for ^{1}H NMR analysis. Yields were determined by the relative integrals of the *o*-iodoaniline starting material (dd 7.65 ppm) and the product (dd 7.91 ppm).

Condensation of *o*-iodoaniline (24) and acetylacetone (25) – Catalyst recycling

2-Iodoaniline (44 mg, 0.2 mmol) and [Au] (0.005 mmol, 0.025 eq) were dissolved in ethanol (3 mL) and acetylacetone (20 µL, 0.2 mmol) was added to the solution. After 7 h, the reaction mixture was concentrated and the crude oil triturated with *n*-hexane (2 x 5 mL). The combined *n*-hexane fractions were concentrated, yielding a crude mixture of *o*-iodoanisole and *(Z)-4-((2-iodophenyl)amino)pent-3-en-2-one*. The black residue containing the gold catalyst material was then reused 8 times with no observed loss in catalytic activity.

6.2.3.4. Addition of nucleophilic arenes to α,β-unsaturated carbonyl compounds

4-(5-Methylfuran-2-yl)butan-2-one

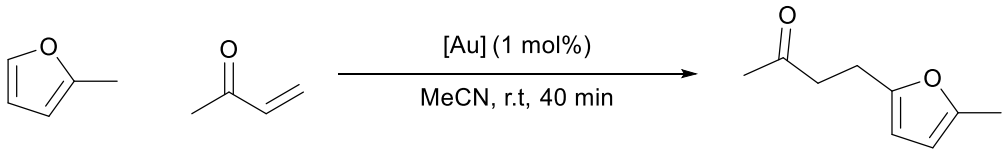

A solution of 2-methylfuran (0.089 mL, 82 mg, 1.0 mmol), methyl vinyl ketone (0.083 mL, 70 mg, 1.0 mmol) and [Au] catalyst (0.010 mmol, 1 mol%) in MeCN (4 mL) was stirred at room temperature. After 40 min, the reaction mixture was concentrated and the crude material triturated with *n*-hexane (2 x 5 mL). The combined *n*-hexane fractions were concentrated to yield the pure desired product as a colourless oil. ^{1}H NMR (400 MHz, Chloroform-*d*) δ 5.90 – 5.80 (m, 2H), 2.90 – 2.81 (m, 2H), 2.78-2.73 (m, 2H), 2.24 (s, 3H), 2.16 (s, 3H) ppm. Analytical data was found to be in agreement with literature data.[13] The black residue containing the gold catalyst material was then reused 5 times with no observed loss in catalytic activity.

4-(5-Methylfuran-2-yl)butan-2-one

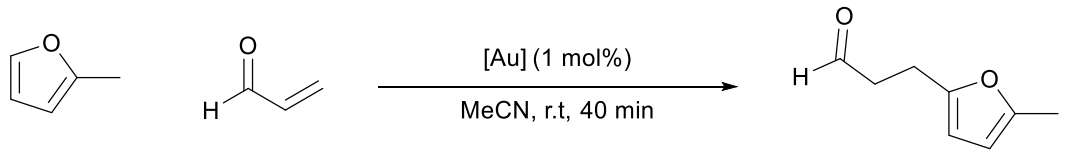

A solution of 2-methylfuran (0.089 mL, 82 mg, 1.0 mmol), acrolein (0.074 mL, 56 mg, 1.0 mmol) and [Au] catalyst (0.010 mmol, 1 mol%) in MeCN (4 mL) was stirred at room temperature. After 40 min, the reaction mixture was concentrated and the crude material triturated with *n*-hexane (2 x 5 mL). The combined *n*-hexane fractions were concentrated to yield the pure desired product as a colourless oil. ^{1}H NMR (400 MHz, Chloroform-*d*) δ 9.82 (t, *J* = 1.4 Hz, 1H), 5.90-5.82 (m, 2H), 2.94 – 2.85 (m, 2H), 2.80-2.74 (m, 2H), 2.24 (s, 3H) ppm. Analytical data was found to be in agreement with literature data.[13] The black residue containing the gold catalyst material was then reused 5 times with no observed loss in catalytic activity.

4-(5-Methylfuran-2-yl)butan-2-one

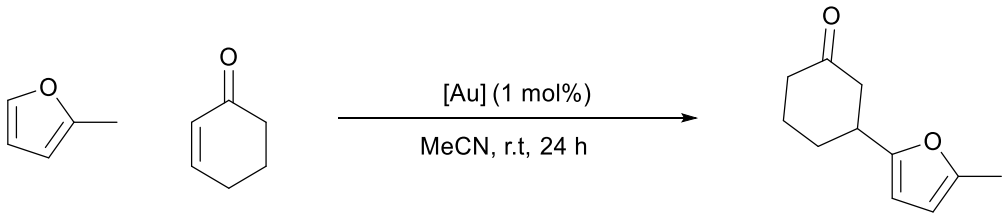

A solution of 2-methylfuran (0.089 mL, 82 mg, 1.0 mmol), cyclohex-2-en-1-one (0.097 ml, 96 mg, 1.0 mmol) and [Au] catalyst (0.010 mmol, 1 mol%) in MeCN (4 mL) was stirred at room temperature. After 24 h, the reaction mixture was concentrated and the crude material triturated with *n*-hexane (2 x 5 mL). The combined *n*-hexane fractions were concentrated to yield the pure desired product as a colourless oil. ^{1}H NMR (400 MHz, Chloroform-*d*) δ 5.90 – 5.84 (m, 2H), 3.17-3.09 (m, 1H), 2.69-2.64 (m, 1H), 2.55-2.48 (m, 1H), 2.47 – 2.28 (m, 2H), 2.26 (s, 3H), 2.23 – 2.08 (m, 1H), 2.07-1.99 (m, 1H), 1.92 – 1.70 (m, 2H) ppm. Analytical data was found to be in agreement with literature data.[14] The black residue containing the gold catalyst material was then reused 5 times with no observed loss in catalytic activity.

(5-(3-Oxobutyl)furan-2-yl)boronic acid

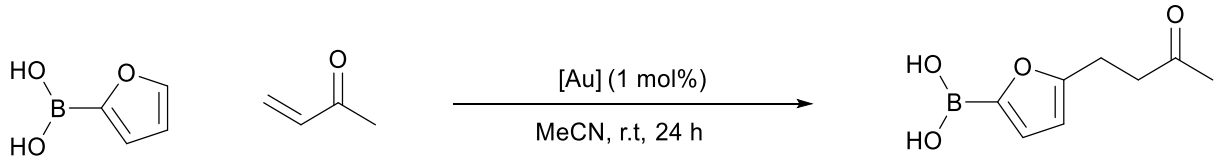

A solution of 2-furanylboronic acid (23 mg, 0.20 mmol), methyl vinyl ketone (0.033 mL, 28 mg, 0.40 mmol) and [Au] catalyst (0.0020 mmol, 1 mol%) in MeCN-d_3 (4 mL) was stirred at room temperature. After 24 h, the crude reaction mixture was submitted for NMR analysis. Product yields were determined by comparing the relative integration of the methyl vinyl ketone CH_3 environment (2.26 ppm) and product CH_3 environmental (2.13 ppm) in the crude ^{1}H NMR spectrum.

4,4'-(Azulene-1,3-diyl)bis(butan-2-one)

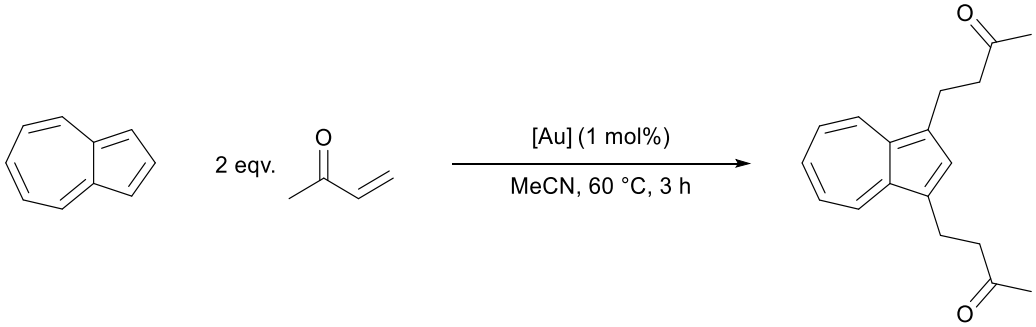

A stirred solution of azulene (40 mg, 0.3 mmol), methyl vinyl ketone (0.052 ml, 44 mg, 0.62 mmol) and [Au)] (0.0031 mmol, 1 mol%) in MeCN (1.7 ml) was heated at 60 ºC. After 3 h, the reaction mixture was concentrated, diluted with $CDCl_3$ and submitted for ^{1}H NMR analysis. In all three runs for each gold catalyst, only trace quantities of unreacted azulene were detectable by ^{1}H NMR analysis of the crude product. ^{1}H NMR (400 MHz, Chloroform-*d*) δ 8.20 (d, *J* = 9.3 Hz, 2H), 7.61 (s, 1H), 7.50 (t, *J* = 9.8, 1H), 7.01 (t, *J* = 9.8 Hz, 2H), 3.34-3.30 (m, 4H), 2.90-2.86 (m, 4H), 2.15 (s, 6H) ppm. Analytical data was found to be in agreement with literature data.[15]

4,4'-(4,6-Dimethoxy-1,3-phenylene)bis(butan-2-one)

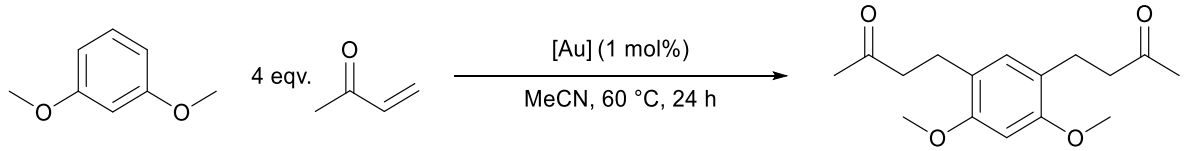

A stirred solution of 1,3-dimethoxybenzene (0.131 mL, 138 mg, 1.00 mmol), methyl vinyl ketone (0.332 mL, 278 mg, 4.00 mmol) and [Au] (0.010 mmol, 1 mol%) in MeCN (4 mL) was stirred at 60 ºC. After 24 h, the reaction mixture was concentrated, the residue diluted in $CDCl_3$ and the yield

determined by ^{1}H NMR analysis, through comparison of the integration of the dialkylated Ar-H singlet at 6.86 ppm, the monoalkylated doublet at 7.02-7.00 ppm and the starting material triplet at 7.21 ppm.

6.2.3.5. Oxidative coupling of aryl silanes and arenes

General cross-coupling procedure

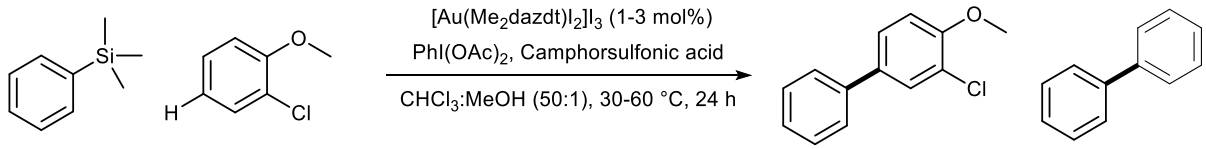

Phenyltrimethylsilane (**25**) (0.50 mmol, 86 µL), *o*-chloroanisole (**27**) (0.50 mmol, 64 µL) and 1,4-dinitrobenzene (Internal standard, 0.125 mmol, 21.0 mg) were added to a solution of $[AuI_2(Me_2dazdt)]I_3$ (0.010 mmol, 10 mg) in $CHCl_3$ (5 mL) and MeOH (0.1 mL). Iodobenzene diacetate (209 mg, 0.65 mmol) and camphorsulfonic acid (174 mg, 0.75 mmol) were added and the reaction stirred. After 24 h, an aliquot (100 µL) of the reaction mixture was diluted in MeCN (10 mL) and the diluted sample submitted for HPLC analysis.

Table 55. Design of experiments (DoE) definitive screening design – Variables and variable limits.

Factor	Minimum	Maximum
Catalyst loading (mol%)	1	3
Silver loading (mol%)	0	6
Temperature (°C)	30*	60
Concentration (M)	0.1	0.25
Arene equivalence	1	1.5

* A lower temperature limit of 30 °C was set to avoid overnight changes in ambient temperature

Models for both cross-coupling and homo-coupling yields were produced using a definitive screening design (Table 56).

Stock solutions containing phenyltrimethylsilane and 1,4-dinitrobenzene (internal standard), and *o*-chloroanisole were used throughout the design of experiments screen. The stock solutions were combined and diluted appropriately in ReactArray reaction vials containing an appropriate quantity of $[AuI_2(Me_2dazdt)]I_3$ to produce the conditions indicated for each entry in the DoE data (Table 56).

Appropriate quantities of iodobenzene diacetate and camphorsulfonic acid were then added to initiate the reaction, and the reaction stirred at the indicated temperature.

Table 56. DoE design and results table.

Catalyst Loading (mol%)	Concentration (M)	Silver Loading (mol%)	Temperature (°C)	Arene equivalence	Cross-coupling yield (HPLC/%)	Homo-coupling yield (HPLC/%)
2	0.1	0	30	1	10	17
2	0.25	6	60	1.5	64	9
2	0.175	3	45	1.25	54	16
1	0.1	6	30	1.5	60	17
3	0.1	6	60	1.25	45	18
3	0.25	0	60	1.5	57	12
1	0.25	6	45	1	36	22
1	0.1	0	60	1	49	16
1	0.1	0	60	1.5	66	13
1	0.175	6	60	1.5	69	14
3	0.1	0	45	1.5	69	12
3	0.1	3	30	1.5	39	13
1	0.25	3	60	1	44	18
1	0.1	6	30	1	29	13
3	0.25	0	60	1	47	16
1	0.25	0	30	1.25	49	20
3	0.175	0	30	1	37	12
3	0.1	6	60	1	41	20
3	0.25	6	30	1.5	80	7
3	0.25	6	30	1	49	11
1	0.25	0	30	1.5	74	9

Optimised cross-coupling procedure and scope

Phenyltrimethylsilane (0.50 mmol, 0.075 g, 86 µL) and *arene* (0.75 mmol) were added to a vial containing [Au] (1.0 mol%, 0.005 mmol) in $CHCl_3$ (2.2 mL, 0.23 M) and MeOH (100 µL). Iodobenzene diacetate (209 mg, 0.649 mmol) and camphorsulfonic acid (174 mg, 0.749 mmol) were added, and the reaction was stirred at room temperature. After 24 h, the reaction mixture was concentrated *in vacuo* and the crude material purified by column chromatography.

3-Chloro-4-methoxy-1,1'-biphenyl

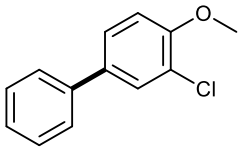

White solid (**3**: 77 mg, 70%; **4**: 82 mg, 75%); R_f = 0.26 [*n*-hexane /toluene (9:1)]; ^{1}H NMR (400 MHz, Chloroform-*d*): δ 7.63 (d, *J* = 2.3 Hz, 1H), 7.58 – 7.51 (m, 2H), 7.51 – 7.39 (m, 3H), 7.39 – 7.30 (m, 1H), 7.01 (d, *J* = 8.5 Hz, 1H), 3.96 (s, 3H) ppm. ^{13}C NMR (101 MHz, Chloroform-*d*) δ 154.5, 139.7, 134.8, 129.0, 127.4, 126.84, 126.4, 122.9, 112.4, 56.4 ppm. Analytical data was found to be in agreement with literature data.[16]

3-Bromo-4-methoxy-1,1'-biphenyl

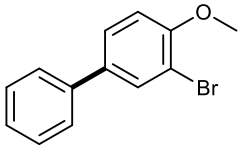

White solid (**3**: 87 mg, 74%; **4**: 94 mg, 80%); R_f = 0.26 [*n*-hexane/toluene (9:1)]; ^{1}H NMR (400 MHz, Chloroform-*d*): δ 7.83 (d, *J* = 2.3 Hz, 1H), 7.59 – 7.49 (m, 3H), 7.49 – 7.40 (m, 2H), 7.40 – 7.31 (m, 1H), 6.98 (d, *J* = 8.5 Hz, 1H), 3.95 (s, 3H). ^{13}C NMR (101 MHz, Chloroform-*d*) δ 155.3, 139.5, 135.2, 132.0, 128.9, 127.3, 127.1, 126.8, 112.2, 112.1, 56.4 ppm. Analytical data was found to be in agreement with literature data.[16]

3,4-Dimethyl-1,1'-biphenyl

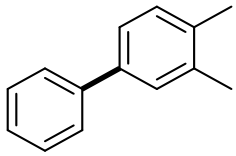

White solid (**3**: 56 mg, 61%; **4**: 64 mg, 70%); R_f = 0.31 [*n*-hexane/toluene (100:1)]; ^{1}H NMR (400 MHz, Chloroform-*d*) δ 7.64 (m, 2H), 7.52 – 7.33 (m, 5H), 7.27 (d, *J* = 7.8 Hz, 1H), 2.39 (s, 3H), 237 (s, 3H) ppm. ^{13}C NMR (101 MHz, Chloroform-*d*) δ 141.4, 139.0, 137.0, 135.8, 130.2, 128.8, 128.6, 128.6, 127.1, 127.0, 124.6, 20.1, 19.6 ppm. Analytical data was found to be in agreement with literature data.[16]

4-Methyl-1,1'-biphenyl

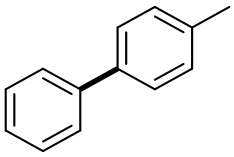

White solid (**3**: 50 mg, 59%; **4**: 55 mg, 65%); R_f = 0.31 [*n*-hexane/toluene (100:1)]; ^{1}H NMR (400 MHz, Chloroform-*d*): δ 7.65 – 7.58 (m, 2H), 7.57 – 7.50 (m, 2H), 7.46 (dd, *J* = 8.4, 6.9 Hz, 2H), 7.40 – 7.32 (m, 1H), 7.29 (d, *J* = 7.9 Hz, 2H), 2.43 (s, 3H) ppm. ^{13}C NMR (101 MHz, Chloroform-*d*): δ 141.3, 138.5, 137.2, 129.6, 128.9, 127.1, 127.1, 21.2 ppm. Analytical data was found to be in agreement with literature data.[16]

1-Methyl-4-phenylnaphthalene

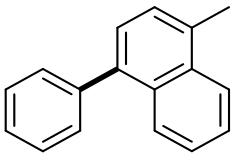

Colourless oil (**3**: 57 mg, 52%; **4**: 60 mg, 55%); R_f = 0.61 ([petroleum ether]); ^{1}H NMR (400 MHz, Chloroform-*d*) δ 8.26 – 8.18 (m, 1H), 8.12 (t, *J* = 6.6 Hz, 1H), 7.74 – 7.44 (m, 9H), 2.93 – 2.87 (m, 3H) ppm. ^{13}C NMR (101 MHz, Chloroform-*d*): δ 141.2, 138.8, 133.9, 132.9, 131.8, 130.3, 128.3, 127.2, 126.8, 126.7, 126.3, 125.8, 124.5, 19.7 ppm. Analytical data was found to be in agreement with literature data.[16]

2-Bromo-5-phenylthiophene

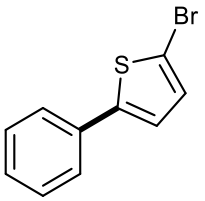

White solid (**3**: 102 mg, 85%; **4**: 108 mg, 90%); R_f = 0.27 [petroleum ether]); ^{1}H NMR (400 MHz, Chloroform-*d*): δ 7.58 – 7.50 (m, 2H), 7.45 – 7.36 (m, 2H), 7.36 – 7.28 (m, 1H), 7.11 – 7.03 (m, 2H) ppm. ^{13}C NMR (101 MHz, Chloroform-*d*): δ 146.0, 133.8, 131.0, 129.1, 128.0, 125.7, 123.4, 111.5 ppm. Analytical data was found to be in agreement with literature data.[16]

6.2.4. Mechanistic studies

Synthesis of 30 from the reaction of 3 and 15 in the presence of triethylamine

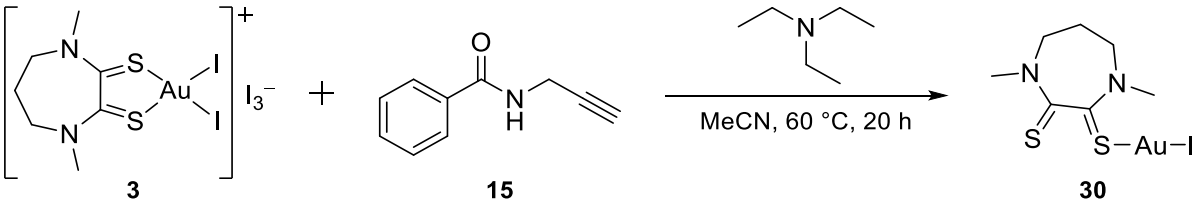

A solution of amide (**15**) (6.2 mg, 0.039 mmol) and $[AuI_2(Me_2dazdt)]I_3$ (**3**) (40 mg, 0.039 mmol) was dissolved in MeCN (0.5 mL) and stirred at 60 °C for 2 h. Triethylamine (13 µL) was added to the reaction mixture, which resulted in an immediate colour change from dark purple/black to yellow. After 20 h at 60 °C, $CHCl_3$ was diffused by vapour phase diffusion, resulting in the formation of **30** as red single crystals. The structure of **30** was confirmed by single-crystal XRD.

Synthesis of 30 from the reaction of 3 and 15 in the presence of triethylamine

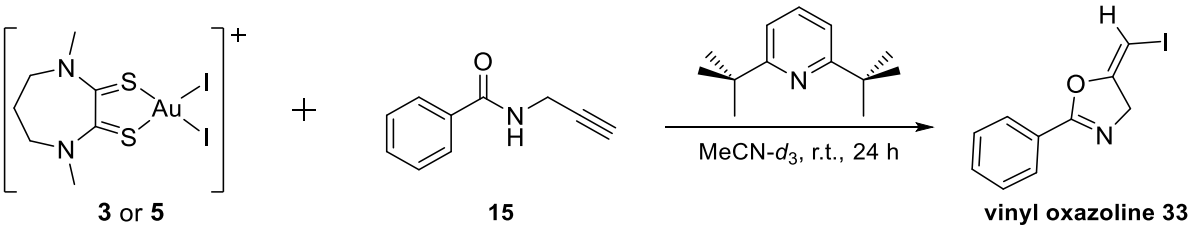

A solution of amide (**15**) (6.2 mg, 0.039 mmol) and either of gold complexes **3** or **5** (0.039 mmol) in MeCN-d_3 (0.5 mL) was stirred at 60 °C for 2 h. 2,6-di-^{t}Bu-pyridine (10 µL) was added to the reaction mixture, which resulted in a change from dark purple/black to bright blue over the course of an hour. After 24 h at 60 °C, the crude reaction mixture was analysed by ^{1}H NMR (400 MHz, Chloroform-*d*) Diagnostic peaks: δ ^{1}H NMR (400 MHz, Acetonitrile-d_3) δ 11.17 (t, $^1J_{HN}$ = ~59 Hz, 1H, N^+_{Py}-**H**), 5.88 (t, *J* = 3.2 Hz, 1H, **H**C-I, **33**), 4.63 (d, *J* = 3.2 Hz, 2H, C**H₂**, **33**), 4.17-4.12 (m, 0.24H, C**H₂**, **15**) ppm. Acetic acid (23.4 mg, 0.39 mmol, 10 eqv.) and *N*-pyridine oxide (1.2 mg, 0.013 mmol) were transferred to the crude MeCN-d_3 reaction mixture and the resulting solution heated at 60 °C for 24 h. The subsequent acidified reaction mixture was resubmitted for ^{1}H NMR analysis, and no changes were observed in the diagnostic environments listed above.

Gutmann-Beckett analysis of gold complexes 3-6

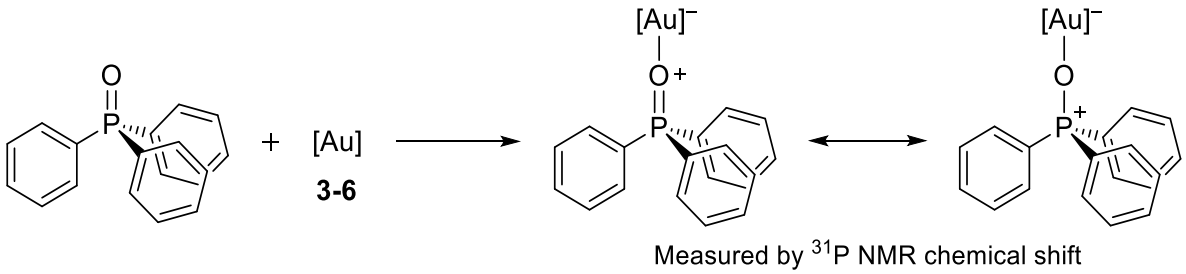

Stock solutions of triphenylphosphine oxide (14 mg) in MeCN-d_3 (1 mL) and acetone-d_6 (1 mL), and stock solutions of silver hexafluoroantimonate (17 mg) in MeCN-d_3 (1 mL), were used for Gutmann-Beckett analysis.

In MeCN-d_3

A solution of gold complex (0.0050 mmol), triphenylphosphine oxide (1.4 mg, 0.0050 mmol) and silver hexafluoroantimonate (0.0045 mmol, 1.5 mg) in MeCN-d_3 (500 µL) was stirred for 10 min, resulting in the formation of a white precipitate. The solution was filtered directly into an NMR tube through a pipette containing cotton wool for analysis by ^{31}P NMR spectroscopy.

In acetone-d_6

Gold complex (0.0050 mmol) and triphenylphosphine oxide (1.4 mg, 0.0050 mmol) were stirred in acetone-d_6 (500 µL) for 60 min, resulting in the formation of a pale yellow solution. The colour transition could be sped up significantly (to ~1-2 min) by heating the solution at 50 °C. The crude reaction solution was analysed by NMR spectroscopy.

All of the Gutmann-Beckett analytical results are provided in full in the main body of text in Chapter Two, Section 2.2.8.

Fluorination of either phenylacetylene or 1,2-diphenylethyne

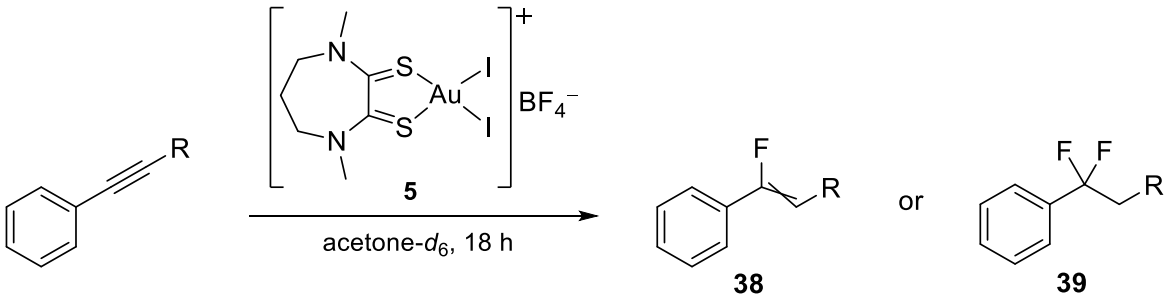

A solution of phenylacetylene (10 mg, 0.10 mmol) gold complex **5** (3.6 mg, 0.0050 mmol, 5 mol%) or (72 mg, 0.10 mmol, 100 mol%) and additive(s) (as indicated in Chapter Two, Section 2.2.8, Table 23) in acetone-d_6 (500 µL) was stirred overnight (~18 h) in a polypropylene centrifuge tube at 50 °C. The crude reaction mixture was analysed directly by NMR spectroscopy. In each case no new organofluorine environments were observed in the ^{19}F NMR spectrum of the crude reaction mixture.

A solution of 1,2-diphenylethyne (18 µL, 0.1 mmol) gold complex **5** (3.6 mg, 0.0050 mmol, 5 mol%) or (72 mg, 0.10 mmol, 100 mol%) and additive(s) (as indicated in Chapter Two, Section 2.2.8, Table 23) in acetone-d_6 (500 µL) was stirred overnight (~18 h) in a polypropylene centrifuge tube at 50 °C. The crude reaction mixture was analysed directly by NMR spectroscopy. In each case no new organofluorine environments were observed in the ^{19}F NMR spectrum of the crude reaction mixture.

6.3. Chapter Three Experimental

Previous work in the Serpe group has illustrated that $[Cation]_2[Pd_2I_6]$ salts are the only palladium product isolated from the recovery of palladium from a model spent catalytic converter.[17] Consequently, all of this work utilised palladium metal as a surrogate for waste TWCs in the synthesis of the $[Cation]_2[Pd_2I_6]$ salts.

6.3.1. Synthesis of organic iodides for palladium recovery

Tetrabutylphosphonium iodide [P^{n}Bu$_4$]I

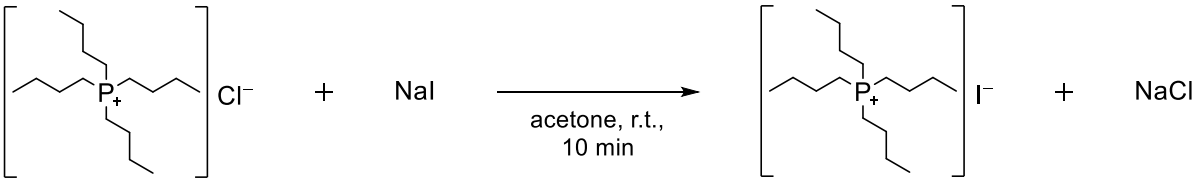

Sodium iodide (153 mg, 1.02 mmol) was added to an acetone solution (5 mL) of tetrabutylphosphonium chloride (300 mg, 1.02 mmol), which resulted in the immediate formation of a white precipitate. The solution was filtered and the filtrate concentrated, yielding [P^{n}Bu$_4$]I (*377 mg, 96%*) as a crystalline white powder. Over the course of ~7 days, the white powder darkened to pale-yellow, presumably due to oxidation of I- to iodine and the subsequent formation of triiodide. [P^{n}Bu$_4$]I was therefore used immediately in the synthesis of [P^{n}Bu$_4$]$_2$[Pd$_2$I$_6$] without further purification or characterisation.

^{n}Butyltriphenylphosphonium iodide [P(^{n}Bu)PPh$_3$]I

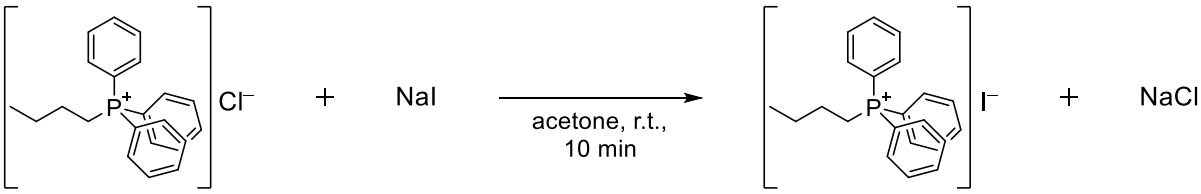

Sodium iodide (153 mg, 1.02 mmol) was added to an acetone solution (5 mL) of ^{n}Butyltriphenylphosphonium chloride (407 mg, 1.02 mmol), which resulted in the immediate formation of a white precipitate. The solution was filtered and the filtrate concentrated, yielding [P(^{n}Bu)PPh$_3$]I (*423 mg, 93%*) as a crystalline white powder. [P(^{n}Bu)PPh$_3$]I was used immediately in the synthesis of [P^{n}Bu$_4$]$_2$[Pd$_2$I$_6$] without further purification or characterisation.

6.3.2. Synthesis of palladium recovery complexes [Cation]$_2$[Pd$_2$I$_6$]

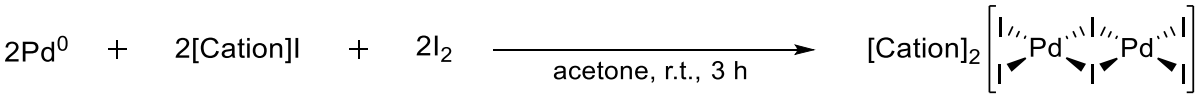

[Cation]$_2$[Pd$_2$I$_6$] salts were synthesised according to a modified literature procedure.[17] UV-Vis data for each [Pd$_2$I$_6$]$^{2-}$ salt were in agreement with literature data.[17]

[N^{n}Bu$_4$]$_2$[Pd$_2$I$_6$]

A solution of tetra-^{n}butylammonium iodide (332 mg, 0.900 mmol), I_2 (228 mg, 0.900 mmol) and Pd powder (96 mg, 0.900 mmol) in acetone (30 mL) was stirred at room temperature. After 3 h, a black crystalline solid had precipitated from the solution and the remaining product was obtained by vapour diffusion with Et_2O. The resulting crystals were filtered and dried, yielding [N^{n}Bu$_4$]$_2$[Pd$_2$I$_6$] as a shiny black crystalline solid (604 mg, 92%). M.p. 182.4-183.1 °C. ESI-HRMS *m/z* (abundance%) = 484.6240 (11.14%), 485.6159 (22.33%), 486.6189 (27.33%), 488.6143 (26.46%), 490.6211 (11.72%), [PdI$_3$]$^-$. UV–vis (nm): 340, 450, 530. ^{1}H NMR (400 MHz, Acetonitrile-*d*$_3$): δ 3.20 – 3.07 (m, 8H), 1.71 – 1.59 (m, 8H), 1.41 (h, *J* = 7.4 Hz, 8H), 1.01 (t, *J* = 7.3 Hz, 12H) ppm.

[PPh$_4$]$_2$[Pd$_2$I$_6$]

A solution of tetraphenylphosphonium iodide (140 mg, 0.300 mmol), I_2 (76.1 mg, 0.300 mmol) and Pd powder (31.9 mg, 0.300 mmol) in acetone (10 mL) was stirred at room temperature. After 3 h, a black crystalline solid had precipitated from the solution and the remaining product was obtained by vapour diffusion with Et_2O. The resulting crystals were filtered and dried, yielding [PPh$_4$]$_2$[Pd$_2$I$_6$] as a shiny black crystalline solid (238 mg, 96%). Calculated for $C_{48}H_{40}I_6P_2Pd_2$ (Mw = 1653.0623): C 34.9, H 2.4, N 0.0 %. Found: C 34.8, H 2.4, N 0.0 %. UV–vis (nm): 340, 450, 530. ^{1}H NMR (400 MHz, Acetonitrile-*d*$_3$): δ 8.00 – 7.90 (m, 4H), 7.83 – 7.66 (m, 16H) ppm.

[NEt$_4$]$_2$[Pd$_2$I$_6$]

A solution of tetraethylammonium iodide (77.2 mg, 0.300 mmol), I_2 (76.1 mg, 0.300 mmol) and Pd powder (31.9 mg, 0.300 mmol) in acetone (10 mL) was stirred at room temperature. After 3 h, a black crystalline solid had precipitated from the solution and the remaining product was obtained by vapour diffusion with Et_2O. The resulting crystals were filtered and dried, yielding [NEt$_4$]$_2$[Pd$_2$I$_6$] as a black semi-crystalline powder (173 mg, 93%). Calculated for $C_{16}H_{40}I_6N_2Pd_2$ (Mw = 1234.7768): C 15.6, H 3.3, N 2.3 %. Found: C 15.8, H 3.4, N 2.1 %. UV–vis (nm): 340, 450, 530. ^{1}H NMR (400 MHz, Acetonitrile-*d*$_3$): δ 3.23 (q, *J* = 7.3 Hz, 2H), 1.31 – 1.22 (tt, *J* = 7.3 Hz, *J* = 1.9 Hz, 3H) ppm.

[P(^{n}Bu)PPh$_3$]$_2$[Pd$_2$I$_6$]

A solution of ^{n}Butyltriphenylphosphonium iodide (134 mg, 0.300 mmol), I_2 (76.1 mg, 0.300 mmol) and Pd powder (31.9 mg, 0.300 mmol) in acetone (10 mL) was stirred at room temperature. After 3 h, a black crystalline solid had precipitated from the solution and the remaining product was obtained by vapour diffusion with Et_2O. The resulting crystals were filtered and dried, yielding [P(^{n}Bu)PPh$_3$]$_2$[Pd$_2$I$_6$] as a shiny black crystalline solid (230 mg, 95%). Calculated for $C_{48}H_{40}I_6P_2Pd_2$ (Mw = 1613.0812): C 32.8,

H 3.0, N 0.0 %. Found: C 32.8, H 3.1, N 0.0 %. UV–vis (nm): 340, 450, 530. ^{1}H NMR (400 MHz, Acetonitrile-d_3): δ 7.95 – 7.86 (m, 3H), 7.81 – 7.69 (m, 12H), 3.32 – 3.05 (m, 2H), 1.71 – 1.49 (m, 4H), 0.95 (t, *J* = 7.2 Hz, 3H) ppm.

[P^{n}Bu$_4$]$_2$[Pd$_2$I$_6$]

A solution of tetra-^{n}butylphosphonium iodide (116 mg, 0.300 mmol), I_2 (76.1 mg, 0.300 mmol) and Pd powder (31.9 mg, 0.300 mmol) in acetone (10 mL) was stirred at room temperature. After 3 h, a black crystalline solid had precipitated from the solution and the remaining product was obtained by vapour diffusion with Et_2O. The resulting crystals were filtered and dried, yielding [P^{n}Bu$_4$]$_2$[Pd$_2$I$_6$] as a shiny black crystalline solid (208 mg, 93%). Calculated for $C_{32}H_{72}I_6P_2Pd_2$ (Mw = 1493.1423) C 25.7, H 4.9, N 0.0 %. Found C 25.9, H 4.8, N 0.0 %. UV–vis (nm): 340, 450, 530. ^{1}H NMR (400 MHz, Acetonitrile-d_3): δ 2.18 – 2.06 (m, 8H), 1.66 – 1.34 (m, 16H), 0.99 (t, *J* = 7.0 Hz, 12H) ppm.

6.3.3. HPLC reaction monitoring of the model cross-coupling reaction

HPLC calibration curves were constructed from a series of solutions containing known concentrations of the analyte and a standard (naphthalene) at different concentration ratios. For (4-chlorophenyl)boronic acid (**2**), 1-chloro-2-nitrobenzene (**1**) and the cross-coupling product (**3**), the solutions covered a ratio of analyte/internal standard from 0.25 to 4 (6.25% to 100%). The range chosen for the homo-coupling product (**4**) was 0.025 to 0.4 (0.625% to 10%). Stock solutions were used throughout and were made in volumetric flasks.

Sampling procedure A – Naphthalene internal standard

When naphthalene was used as an internal standard, a ~100 µL reaction aliquot was drawn into a 1 mL syringe via a needle and the sample was immediately ejected back into the reaction mixture. The residual reaction sample (~5 µL) still inside the syringe was then immediately quenched by dilution into a solution of acetic acid in acetonitrile (0.1 *v*/%). The dilution factor depended on the concentration of the reaction mixture, and the concentration of the analyte was always within the concentration range of the calibration samples used to produce calibration curves.

Sampling procedure B – Naphthalene external standard

When naphthalene was used as an external standard, a known volume of the reaction mixture (100 µL) was taken using a micropipette and quenched into a naphthalene stock solution of acetic acid in acetonitrile (0.1 *v*/%). The dilution factor depended on the concentration of the reaction mixture, and the concentration of the analyte was always within the concentration range of the calibration samples used to produce calibration curves.

Sampling procedure C – Naphthalene internal standard, biphasic reaction mixture

When the reaction mixture is biphasic reaction aliquots cannot be taken using ***Sample Procedure A*** or ***Sampling Procedure B***. Instead, the entire reaction mixture was poured into an appropriate volume of an ice-cold solution of acetic acid in acetonitrile (0.1 *v*/%). Dilution of the reaction mixture in acetonitrile renders the entire mixture as a homogeneous solution, which can then be aliquoted for HPLC analysis. The dilution factor depended on the concentration of the reaction mixture, and the concentration of the analyte was always within the concentration range of the calibration samples used to produce calibration curves.

6.3.4. Initial optimisation of the model cross-coupling reaction

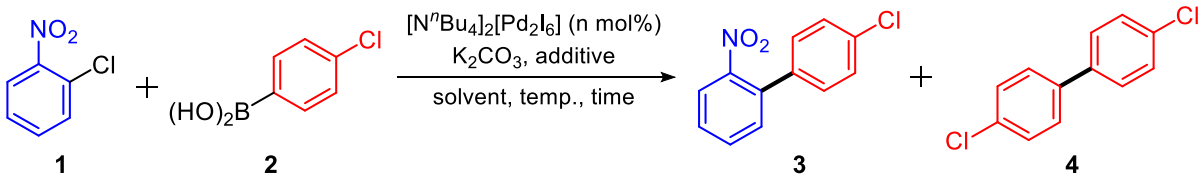

Conditions for data collected in Table 5

A solution of 1-chloro-2-nitrobenzene (**1**) (55.5 mg, 0.350 mmol), $[N^nBu_4]Br$ (113 mg, 0.350 mmol), *p*-chlorophenylboronic acid (**2**) (60.8 mg, 0.390 mmol), naphthalene (11.2 mg, 0.0875 mmol) and K_2CO_3 (97 mg, 0.70 mmol) in the indicated solvent (3 mL) was stirred at the indicated temperature. To the heated solution was added $[N^nBu_4]_2[Pd_2I_6]$ (according to the loading in Table 5) and the solution stirred for the indicated time. A reaction aliquot was taken using ***Sampling Procedure A*** or ***Sampling Procedure C*** and analysed by HPLC analysis.

To isolate **3** and **4** the crude residue was purified by silica gel chromatography, using hexane: toluene: ethyl acetate (90:10:0, **3** Rf = 0.21, **4** Rf = 0.88. Gradient elution to 75:10:15; *v:v:v*) as eluent, yielding **3** as a pale-yellow crystalline solid and **4** as a white powder.

4'-Chloro-2-nitro-1,1'-biphenyl

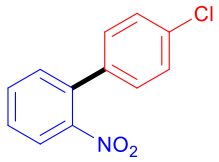

3

IR (neat): 3054 (νC-H), 1602 (νC=C), 1514 (νN=O), 1465 (νC-N), 1349, 1276 (νN=O), 1084, 852, 818, 781, 683, 514. NMR ($CDCl_3$) ^{1}H: 7.26-7.29 (dt, 2H, $^3J_{HH}$ = 8.8 Hz, $^4J_{HH}$ = 2.4 Hz), 7.41-7.45 (m, 3H), 7.51-7.55 (td, 1H, $^3J_{HH}$ = 7.7 Hz, $^4J_{HH}$ = 1.2 Hz), 7.63-7.67 (td, 1H, $^3J_{HH}$ = 7.3 Hz, $^4J_{HH}$ = 1.5 Hz), 7.89-7.92 (dd, 1H, $^3J_{HH}$ = 8.1 Hz, $^4J_{HH}$ = 1.2 Hz) ppm. ^{13}C{^{1}H}: 124.2 (CH), 128.5 (CH), 128.9 (CH), 129.2 (CH), 131.8 (CH), 132.5 (CH), 134.4 (C), 135.2 (C), 135.9 (C), 149.0 (CNO_2) ppm. Analytical data was found to be in agreement with literature data.[18]

4,4'-Dichloro-1,1'-biphenyl

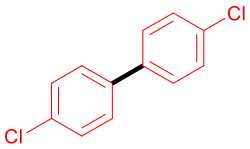

4

IR (neat): 2919 (νC-H), 1469, 1385, 1083, 997, 808, 698, 503, 410. NMR ($CDCl_3$) ^{1}H: 7.40-7.43 (dt, 4H, $^3J_{HH}$ = 8.3 Hz, $^4J_{HH}$ = 2.5 Hz), 7.47-7.51 (dt, 4H, $^3J_{HH}$ = 8.3 Hz, $^4J_{HH}$ = 2.0 Hz). ^{13}C{^{1}H}: 128.2 (CH), 129.0 (CH), 133.7 (CC), 138.4 (CCl) ppm. Analytical data was found to be in agreement with literature data.[19]

6.3.5. Design of Experiments modelling

A definitive screening design was constructed to explore the influence of the main effects for each variable, alongside second order and interacting effects for each variable. Each of the following experiments (Table 57) was run in a batch of 10 and 7 experiments in a ReactArray 10-well reaction station, with each reaction vial fitted with a cold-finger condenser. Identical definitive screening designs were used for each of the three catalyst systems. The loading of the two phosphine-based systems were doubled so that the [Pd] loadings match those used for $[N^nBu_4]_2[Pd_2I_6]$.

*Table 57. Definitive screening design predictive model for the cross-coupling yielding **3** – Experiments performed for the definitive screening design.*

[Pd] loading (mol%)	Concentration (M)	Water composition (%/*v*)	Time (min)
0.11	0.5	0	30
0.2	0.7	0	30
0.11	0.6	12.5	75
0.02	0.6	0	30
0.11	0.7	25	120
0.2	0.5	12.5	120
0.02	0.7	0	120
0.2	0.6	25	120
0.2	0.7	0	120
0.02	0.7	25	75
0.02	0.7	12.5	30
0.02	0.5	25	120
0.2	0.5	0	75
0.2	0.5	25	30
0.2	0.7	25	30
0.02	0.5	0	120
0.02	0.5	25	30

6.3.6. Definitive screening design experimental methodology

Stock Solution A

1-chloro-2-nitrobenzene (**1**) (1.0 M), tetra-^{n}butylammonium bromide (1.0 M) and naphthalene (0.25 M) in 1-butanol (50 mL). A single reagent stock solution was used for each definitive screening design.

$[N^{n}Bu_4]_2[Pd_2I_6]$ Catalyst Stock Solution

$[N^{n}Bu_4]_2[Pd_2I_6]$ (22.7 mg, 0.0156 mmol) in dimethylformamide (1 mL, 0.0156 M). A fresh ***Catalyst Stock Solution*** was used for each of the two batches of experiments.

$PdCl_2(PPh_3)_2$ Catalyst Stock Solution

$PdCl_2(PPh_3)_2$ (21.9 mg, 0.0312 mmol) in chloroform (1 mL, 0.0312 M). A fresh ***Catalyst Stock Solution*** was used for each of the two batches of experiments.

$Pd(OAc)_2$ Catalyst Stock Solution

$Pd(OAc)_2$ (21.0 mg, 0.0936 mmol) in dimethylformamide (3 mL, 0.0312 M). A fresh ***Catalyst Stock Solution*** was used for each of the two batches of experiments.

PPh_3 Stock Solution

PPh_3 (49.2 mg, 0.187 mmol) in dimethylformamide (3 mL, 0.0624 M). A fresh ***PPh_3 Stock Solution*** was used for each of the two batches of experiments.

Definitive screening design reaction experimental

An appropriate quantity (according to Table 57) of K_2CO_3 (1.5 equivalents) and (4-chlorophenyl)boronic acid (1.1 equivalents) were weighed into a ReactArray reaction vial fitted with a stirrer bar. An appropriate quantity of ***Stock Solution A*** (according to Table 57) was transferred to the ReactArray reaction vial, followed by an appropriate dilution with 1-butanol and water to give a total volume of 3 mL. The vial was fitted with a cold-finger condenser and stirred at 90 °C for 10 minutes. The reaction was then initiated by the addition of an appropriate volume of ***PPh_3 Stock Solution*** and ***Catalyst Stock Solution*** (according to Table 57). After an appropriate reaction time (according to Table 57), the reaction mixture was worked-up and analysed using ***Sampling procedure C***.

The model was constructed from the experimental results by employing a stepwise linear regression on each of the variable effects (first order, second order and interactions). Effects which we were found to not be statistically significant were removed from the model to prevent overfitting.

The results for the definitive screening design are presented in full in Chapter Three, Section 3.2.2.

6.3.7. Final optimised conditions

$[N^nBu_4]_2[Pd_2I_6]$ conditions

(4-chlorophenyl)boronic acid (345 mg, 2.21 mmol) and K_2CO_3 (435 mg, 3.15 mmol) were transferred to an aliquot (3 mL) of a 1-butanol stock solution (0.7 M) produced in a volumetric flask containing tetra-^{n}butylammonium bromide (677 mg, 2.10 mmol) and 1-chloro-2-nitrobenzene (331 mg, 2.1 mmol). The resulting solution was stirred at 90 °C for 10 min, after which the reaction was initiated by the addition of ***$[N^nBu_4]_2[Pd_2I_6]$ Catalyst Stock Solution*** (59.3 µL, 0.044 mol%).

$PdCl_2(PPh_3)_2$ conditions

(4-chlorophenyl)boronic acid (345 mg, 2.21 mmol) and K_2CO_3 (435 mg, 3.15 mmol) were transferred to an aliquot (2.4 mL) of a 1-butanol stock solution (0.875 M) produced in a volumetric flask containing tetra-^{n}butylammonium bromide (677 mg, 2.10 mmol) and 1-chloro-2-nitrobenzene (331 mg, 2.1

mmol). The resulting solution was diluted with water (0.6 mL) and stirred at 90 °C for 10 min, after which the reaction was initiated by subsequent additions of ***PPh_3 Stock Solution*** (0.135 µL, 0.4 mol%) and ***$PdCl_2(PPh_3)_2$ Catalyst Stock Solution*** (0.135 µL, 0.2 mol%).

$Pd(OAc)_2/2PPh_3$ conditions

(4-chlorophenyl)boronic acid (345 mg, 2.21 mmol) and K_2CO_3 (435 mg, 3.15 mmol) were transferred to an aliquot (2.4 mL) of a 1-butanol stock solution (0.875 M) produced in a volumetric flask containing tetra-^{n}butylammonium bromide (677 mg, 2.10 mmol) and 1-chloro-2-nitrobenzene (331 mg, 2.1 mmol). The resulting solution was diluted with water (0.6 mL) and stirred at 90 °C for 10 min, after which the reaction was initiated by subsequent additions of ***PPh_3 Stock Solution*** (0.135 µL, 0.4 mol%) and ***$Pd(OAc)_2$ Catalyst Stock Solution*** (0.135 µL, 0.2 mol%).

6.3.8. ReactIR reaction monitoring

The absorbance spectra obtained using *in situ* ReactIR were calibrated using offline HPLC analysis and samples were taken for HPLC analysis using ***Sampling procedure A***.

Due to the small scale (3 mL) of the reactions performed during the kinetic study, the ReactIR probe and the thermocouple could not fit inside the reaction vessel at the same time. Thus, to ensure that the reaction solution was maintained at 90 °C, a thermocouple used to monitor and control the temperature of the EasyMax reactor was placed inside a second proxy vial containing 1-butanol (3 mL) in the same heating block. The vial containing neat *n*-butanol was found to be ±1 °C of the reaction solution when a test reaction was run containing a second thermocouple and no ReactIR probe.

ReactIR Analysis and Validation

The concentration of 1-chloro-2-nitrobenzene (**1**) was monitored via the change in area of a peak at 1111 cm^{-1}. The second derivative of the spectrum was taken to improve the resolution of the peak (Figure 77).

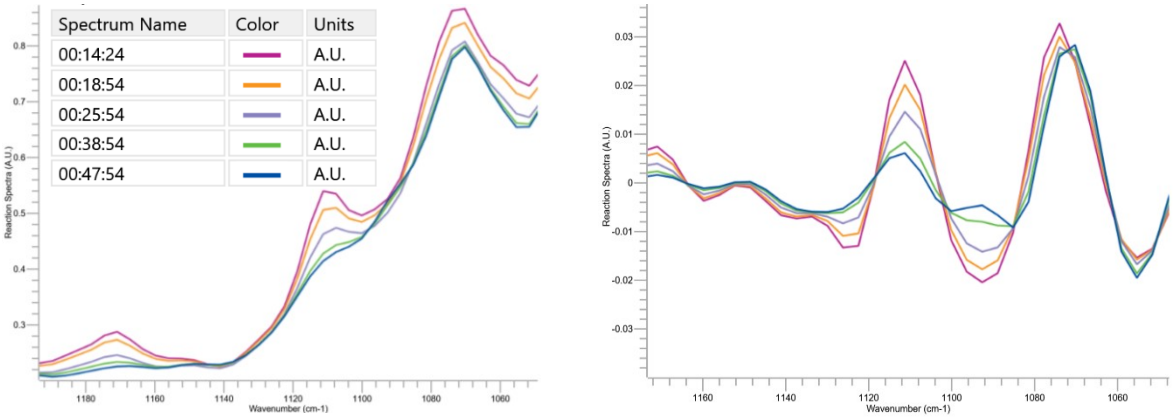

*Figure 77. Monitoring ReactIR peak at 1111 cm^{-1} over time (**Left**: original spectrum, right: 2nd derivative). Peak assigned to 1-chloro-2-nitrobenzene (**1**).*

The concentration of the cross-coupling product (**3**) was monitored via the change in area of a peak at 750 cm^{-1} (Figure 78). The second derivative of the spectrum was taken to improve the resolution of the peak

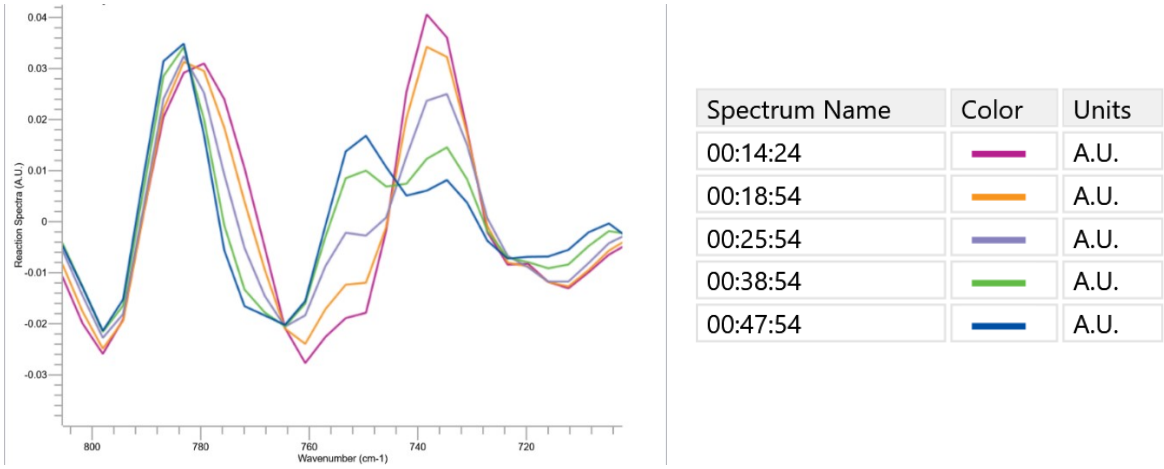

*Figure 78. Monitoring ReactIR peak at 750 cm^{-1}. Peak assigned to cross-coupling product (**3**). Spectrum name refers to the time point that the spectrum was taken.*

To validate the assignments of the peaks at 1111 cm^{-1} and 750 cm^{-1} as 1-chloro-2-nitrobenzene (**1**) and the cross-coupling product (**3**) respectively, comparative spectra of each component were taken:

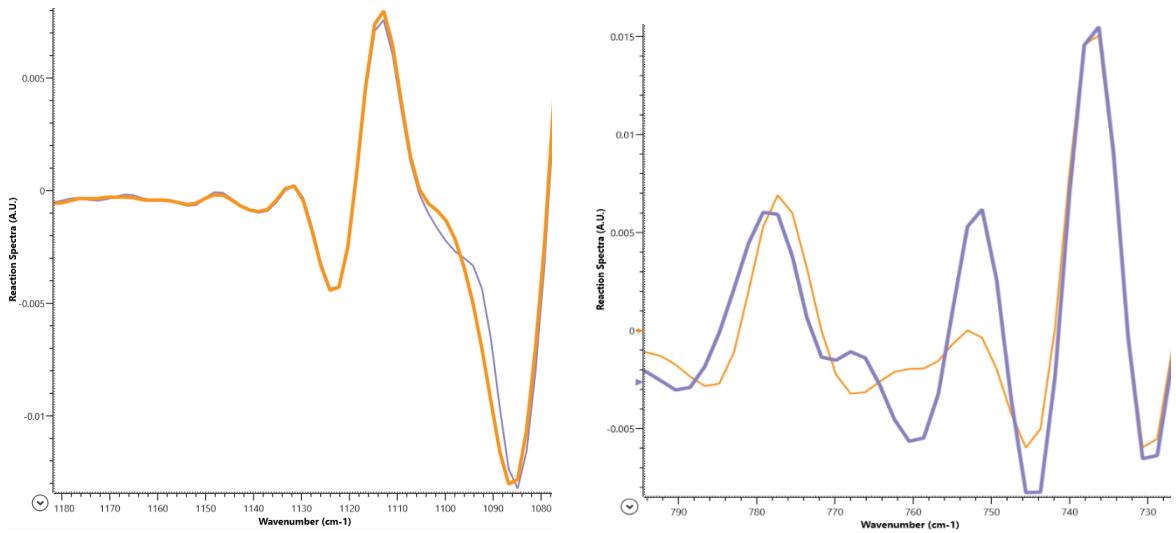

*Figure 79. **Left**: Comparison between peak intensities at 1111 cm^{-1} in a 1-chloro-2-nitrobenzene (**1**) solution (orange), and a 1-chloro-2-nitrobenzene + cross-coupling product (**3**) solution (lilac). **Right**: Comparison between peak intensities at 750 cm^{-1} in a 1-chloro-2-nitrobenzene (**1**) solution (orange), and a 1-chloro-2-nitrobenzene (**1**) + cross-coupling product solution (**3**) (lilac).*

1-chloro-2-nitrobenzene (**1**) solution is the orange trend (Figure 79). Cross-coupling product (**3**) added to form the lilac trend (Figure 79). No change in absorbance intensity indicates that the peak at 1111 cm^{-1} is not present in the cross-coupling product (Figure 79, Left). Increase in absorbance intensity indicates that the peak at 750 cm^{-1} is present in the cross-coupling product (**3**) (Figure 79, Right). All spectra were collected at the reaction temperature (90 °C).

Leave-one-out control studies

The reaction vials and stirrer bars were etched with fresh *aqua regia* for ~30 min between each run to reduce residual trace palladium contamination.

Component Left Out	Cross-coupling yield (HPLC/%)	Homo-coupling yield (HPLC/%)	Observations and Notes
K_2CO_3	0	3	
$[N^nBu_4]Br$	3	12	Immediate precipitation of palladium black
$[N^nBu_4]_2[Pd_2I_6]$	0	0	
Aryl chloride (**1**)	0	17	Immediate precipitation of palladium black

Each reaction was performed using the optimised conditions with the indicated component missing.

6.3.9. Notes on the commercial source of K_2CO_3

It should be noted that all of the above work on the model cross-coupling reaction used Fisher Potassium carbonate anhydrous, >=99% without complication. A significant drop in catalyst performance was noted for a new batch of Fisher Potassium carbonate anhydrous, >=99%. This drop in performance was replicated on a number of scales (500 mmol, 35 mmol, 17.5 mmol, 2.1 mmol). Catalytic activity was restored by switching to Fluorochem potassium carbonate anhydrous powder 325 mesh. A single batch of Fluorochem potassium carbonate anhydrous powder 325 mesh was used for the remainder of the studies. The origin of the difference in activity between the two batches was not uncovered, and neither batch contained any trace palladium according to ICP-MS analysis.

6.3.10. Model cross-coupling reaction process design

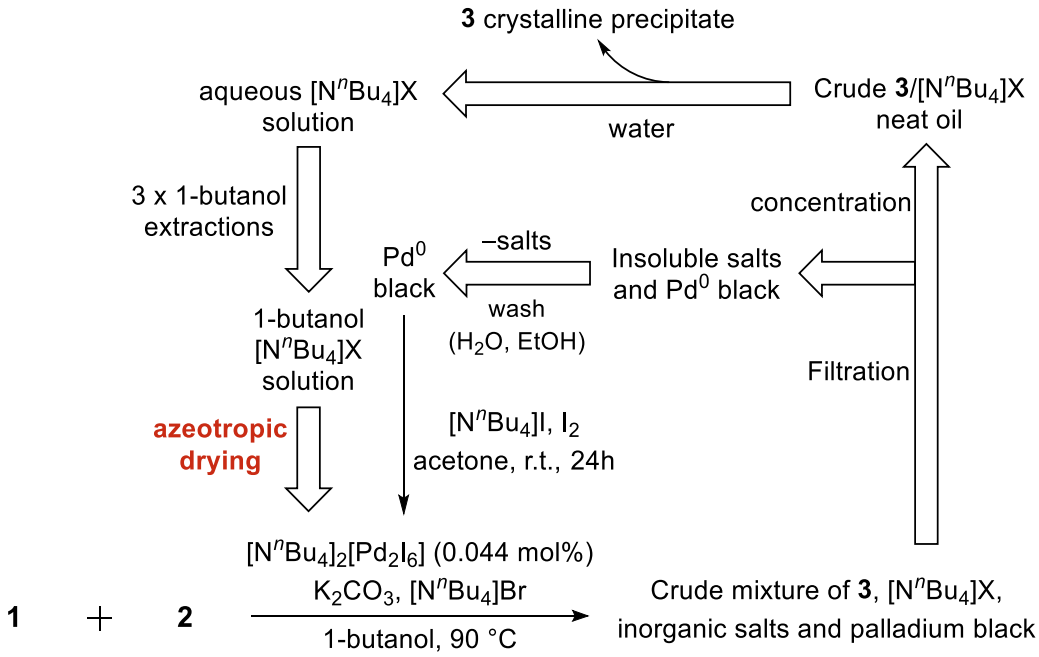

Catalyst recycling

At the end of the ***[N^{n}Bu$_4$]$_2$[Pd$_2$I$_6$] conditions*** (50 mL scale, Pd loading = 0.0308 mmol), the reaction mixture was allowed to cool to room temperature and was then filtered (Glassco® 'G4' – porosity 4) under vacuum. The solids were washed with ethanol (5 mL) and the filtrate removed for concentration. The remaining solid was subsequently washed with water (15 mL) until all of the white solid had dissolved, and the remaining black powder was then washed with ethanol (5 mL) and dried under vacuum. The resulting palladium powder was added to a stirred solution of tetra-^{n}butylammonium iodide (11.4 mg, 0.0308 mmol), I_2 (7.8 mg, 0.031 mmol) in acetone (20 mL) at room temperature. After 24 h, the solution was filtered under gravity, concentrated to ~ 5 mL and the

product was obtained by vapour diffusion with Et_2O. The resulting crystals were filtered and dried, yielding $[N^nBu_4]_2[Pd_2I_6]$ as a shiny black crystalline solid (18 mg, 81%). M.p. 182.4-183.1 °C. UV–vis (nm): 340, 451, 542. Calculated for $C_{32}H_{72}I_6N_2Pd_2$ (Mw = 1459.2088): C 26.3, H 5.0, N 1.9 %. Found: C 26.4, H 4.9, N 1.9 %. The structure and purity of $[N^nBu_4]_2[Pd_2I_6]$ recycled from the model cross-coupling reaction was also confirmed by single-crystal XRD.[17] An identical procedure for recovering palladium waste to $[N^nBu_4]_2[Pd_2I_6]$ was employed for each of the precatalysts explored and the results provided in full in Chapter Three, Section 3.2.4.1 and 3.2.4.4.

$[N^nBu_4]X$ recycling and cross-coupling product (3) isolation

The filtrate collected at the end of the ***$[N^nBu_4]_2[Pd_2I_6]$ conditions*** (50 mL scale, [Pd] = 0.0308 mmol) described above in ***Catalyst recycling*** was concentrated under vacuum. Water (15 mL) was added to the crude oil and the resulting biphasic mixture stirred until the cross-coupling product (**3**) precipitated from the mixture as a pale-yellow crystalline powder. The solid were collected by filtration, washed with water (2 x 5 mL) and dried under vacuum to yield 4'-chloro-2-nitro-1,1'-biphenyl (**3**) as a pale-yellow crystalline powder (Yield: 6.46 g, 79% yield; 95-98% purity by HPLC and ^{1}H NMR analysis with comparison to a known standard). If desired, residual tetrabutylammonium salts in **3** could be removed by hot recrystallisation from ethanol (10 mL) to yield analytically pure **3** (5.72 g, 70%). The aqueous filtrate was subsequently extracted with 1-butanol (3 x 10 mL) to yield a 1-butanol solution charged with $[N^nBu_4]X$ salts which can then be reused in subsequent reactions. The residual water content in the 1-butanol solution of $[N^nBu_4]X$ salts was removed by azeotropic distillation water/1-butanol (~5-10 mL removed for a 50 mL scale reaction) on a rotary evaporator.

Five repeats on a 0.5 mol scale

The ***$[N^nBu_4]_2[Pd_2I_6]$ conditions, Catalyst recycling***, ***$[N^nBu_4]X$ recycling and cross-coupling product (3) isolation*** procedures were unified on a 0.5 mol scale (714 mL) and kinetic reaction profiles produced using ***Sampling procedure B***. In each case, the ***$[N^nBu_4]_2[Pd_2I_6]$ Catalyst Stock Solution*** was produced using $[N^nBu_4]_2[Pd_2I_6]$ that had been recycled from the previous run. Since $[N^nBu_4]_2[Pd_2I_6]$ was recovered in 79-83% yield, the ***$[N^nBu_4]_2[Pd_2I_6]$ Catalyst Stock Solution*** was augmented with additional $[N^nBu_4]_2[Pd_2I_6]$ that had been synthesised from Pd metal powder so that 0.044 mol% of $[N^nBu_4]_2[Pd_2I_6]$ was loaded into each reaction repeat. The results are presented in full in Chapter Three, Section 3.2.4.3.

Catalyst recycling using 1-iodo-2-nitrobenzene (5)

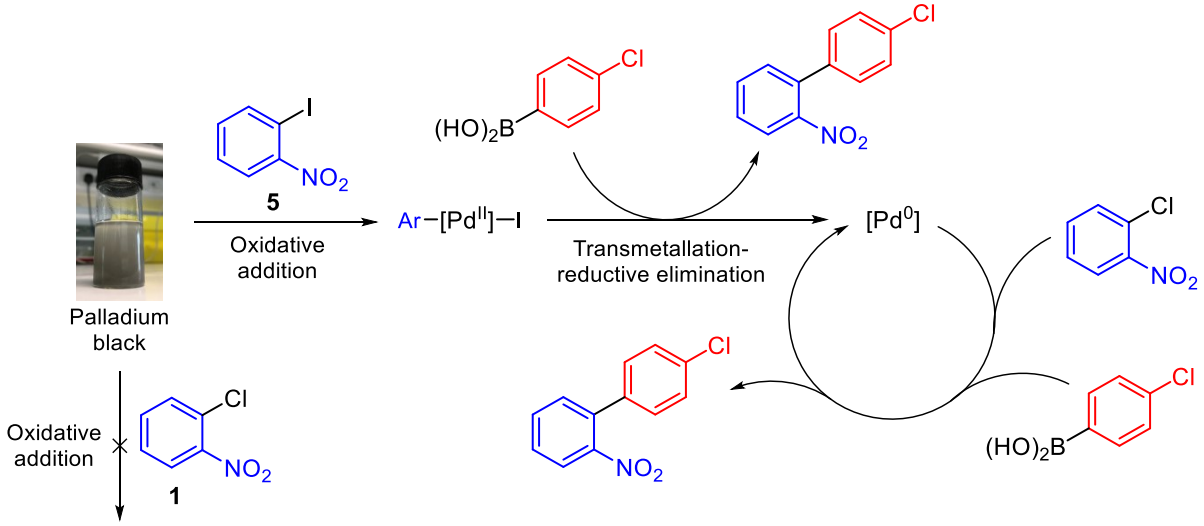

A model reaction was conducted under the ***[N^{n}Bu$_4$]$_2$[Pd$_2$I$_6$] conditions*** (3 mL scale) and kinetic profiles obtained using ***Sampling procedure A***. After 60 min, fresh 1-chloro-2-nitrobenzene (**1**) (298 mg, 1.89 mmol, 0.9 eqv.), (4-chlorophenyl)boronic acid (**2**) (361 mg, 2.13 mmol, 1.1 eqv.) and K_2CO_3 (435 mg, 3.15 mmol, 1.5 eqv.) were added directly to the first reaction mixture at 90 °C and the reaction monitored by HPLC using ***Sampling procedure A***. After 15 min, 1-chloro-2-nitrobenzene (**5**) (52 mg, 0.21 mmol) was transferred to the reaction mixture and kinetic profiles obtained using ***Sampling procedure A***.

6.3.11. Green metrics

Process mass intensity (PMI)

A literature spreadsheet was used to calculate PMIs.[20]

$$PMI = \frac{total\ mass\ in\ a\ process\ (g)}{mass\ of\ product\ (g)}$$

Green metrics were calculated for ***Five repeats on a 0.5 mol scale*** using the literature spreadsheet.[20] The following table illustrates the total mass of each compound used after one and five reaction repeats.

1st run masses (Yield **3**: 92.29 g)

Compound	**1**	**2**	K_2CO_3	$[N^nBu_4]Br$	$[N^nBu_4]_2[Pd_2I_6]$	1-butanol	Water	Ethanol
Mass (g)	78.78	82.25	103.65	161.18	0.321	578.3	430	225

PMI = 18.0

5th run cumulative masses (Yield **3**: 482.49 g)

Compound	**1**	**2**	K_2CO_3	$[N^nBu_4]Br$	$[N^nBu_4]_2[Pd_2I_6]$	1-butanol	Water	Ethanol
Mass (g)	393.88	441.25	518.27	161.18	0.633	2891.7	2140	1128

Cumulative PMI = 15.9

E-Factor

$$E\text{-}Factor = \frac{total\ waste\ (g)}{mass\ of\ product\ (g)}$$

The following table illustrates the waste masses of each component

1st run masses (Yield **3**: 92.29 g)

Compound	**1**	**2**	K_2CO_3	$[N^nBu_4]Br$	$B(OH)_2$	chloride	1-butanol	Water	Ethanol
Waste (g)	16.54	17.27	103.65	161.18	17.71	14.00	578.34	430	225

E-Factor = 16.9

5th run cumulative masses (Yield **3**: 482.49 g)

Compound	**1**	**2**	K_2CO_3	$[N^nBu_4]Br$	$B(OH)_2$	chloride	1-butanol	Water	Ethanol
Waste (g)	68.53	71.56	518.27	161.18	92.56	73.21	2891.7	2150	1124

E-Factor = 14.8

6.3.12. ICP-MS analysis

Sample preparation for digestion

The samples analysed by ICP-MS were the crude cross-coupling product (**3**) precipitate, and an aliquot (50 µL) of the reaction mixture that was taken prior to the addition of the catalyst for the five reaction repeats on a 0.5 mol scale

The product (**3**) precipitates (~50 mg) were dissolved in ethanol, dried over $MgSO_4$, filtered under gravity and concentrated under vacuum in a water bath (80 °C). The precipitates were melted and a portion of each sample was then transferred into a 21 mL glass vial for weighing and digestion using the procedure below.

The reaction aliquots (50 µL) were transferred to a 21 mL glass vial containing heptane (500 µL) and concentrated under vacuum in a water bath (80 °C). The resulting dried aliquot was then digested in the glass vial using the procedure below.

Sample digestion – Samples were digested using a modified literature procedure.[21]
To the glass vials containing the samples (from ***Sample preparation for digestion***) was added hydrochloric acid (3 mL, 34%, Fisher TraceMetal grade) and nitric acid (3 mL, 67%, Fisher TraceMetal grade). The solutions were then heated on a hot plate to 150 °C with manual agitation and mixing. After 30 min, the samples were diluted with ultrapure water (~10 mL, Sartorius arium® mini) and transferred to a 100 mL volumetric flask with multiple rinses of the sample vial with ultrapure water (Sartorius arium® mini). The volumetric flask was filled to the calibration mark with ultrapure water (Sartorius arium® mini), and a portion (~20 mL) of the resulting solution was filtered through a syringe filter (0.2 µm) for analysis by ICP-MS. The palladium concentrations were determined from the relative signal intensities of ^{105}Pd and a ^{89}Y external standard solution. Calibration of the relative ^{105}Pd/^{89}Y signal intensities was conducted by analysing a series of solutions containing 0.5 ppb, 2.5 ppb, 5 ppb, 10 ppb, 25 ppb and 50 ppb of palladium. These calibration solutions were produced by performing serial dilutions of a commercial palladium standard solution (1000 ppm).

Results

Aliquots of the reaction mixture taken prior to the addition of fresh catalyst:

No azeotropic distillation of water from the 1-butanol solution of recycled [N^{n}Bu$_4$]X salts

Sample	[Pd] (µg/L)	Volume (L)	Sample Pd (µg)	Analyte (mL)	Analyte (ppm)
Run 1	- 0.034237932	0.1	-0.003423793	0.05	0
Run 2	0.787924417	0.1	0.078792442	0.05	1.6
Run 3	21.52733926	0.1	2.152733926	0.05	43.1
Run 4	36.93990972	0.1	3.693990972	0.05	73.9

With azeotropic distillation of water from the 1-butanol solution of recycled [N^{n}Bu$_4$]X salts

Sample	[Pd] (µg/L)	Volume (L)	Sample Pd (µg)	Analyte (mL)	Analyte (ppm)
Run 1	- 0.034237932	0.1	-0.003423793	0.05	0
Run 2	0.89200388	0.1	0.089200388	0.05	1.8
Run 3	0.932190225	0.1	0.093219022	0.05	1.9
Run 4	0.921509579	0.1	0.092150958	0.05	1.8
Run 5	1.224828519	0.1	0.122482852	0.05	2.4

The cross-coupling product (**3**) precipitate:

No azeotropic distillation of water from the 1-butanol solution of recycled [N^{n}Bu$_4$]X salts

Sample	[Pd] (µg/L)	Volume (L)	Sample Pd (µg)	Analyte (mg)	Analyte (ppm)
Run 1	0.674088489	0.1	0.067409	20.4	3.3
Run 2	2.986829173	0.1	0.298683	20.9	14.3
Run 3	5.69298605	0.1	0.569299	22.7	25.1
Run 4	9.102401385	0.1	0.91024	17.2	52.9

With azeotropic distillation of water from the 1-butanol solution of recycled [N^{n}Bu$_4$]X salts

Sample	[Pd] (µg/L)	Volume (L)	Sample Pd (µg)	Analyte (mg)	Analyte (ppm)
Run 1	0.589269355	0.1	0.058927	20.9	0
Run 2	0.343188397	0.1	0.034319	17.3	1.8
Run 3	0.32647935	0.1	0.032648	17.8	1.9
Run 4	0.381644126	0.1	0.038164	20.7	1.8
Run 5	0.450123573	0.1	0.045012	16.9	2.4

Some of the samples were spiked with known quantities of a diluted commercial stock solution of palladium (1000 ppm diluted to 1 ppm) and analysed immediately after the original mother sample was analysed to confirm the accuracy of ICP-MS analysis:

Sample	Original [Pd] µg/L	Spiked [Pd] (µg/L)	Measured [Pd] (µg /L)
Run 2 w/azeotrope distillation	0.343188397	5	4.975578341
Run 5 w/ azeotrope distillation	0.450123573	2	2.340785228
Run 4 no azeotrope distillation	9.102401385	5	13.90938832

The spiked samples increased in concentration by an amount that is reasonably consistent with the concentration of palladium spiked into the solution.

The two commercial sources of K_2CO_3 (fluorochem Potassium carbonate anhydrous powder 325 mesh, Fisher Potassium carbonate anhydrous, >=99%) that were used throughout the study were also analysed by ICP-MS. In both cases, no palladium was detected.

Sample	[Pd] (µg/L)	Volume (L)	Sample Pd (µg)	Analyte (mg)	Analyte (ppm)
A	-0.19050381	0.1	-0.01905	25.3	0
B	-0.232864778	0.1	-0.02329	23.7	0

6.3.13. Catalyst recycling scope

C-H activation of benzo[h]quinoline

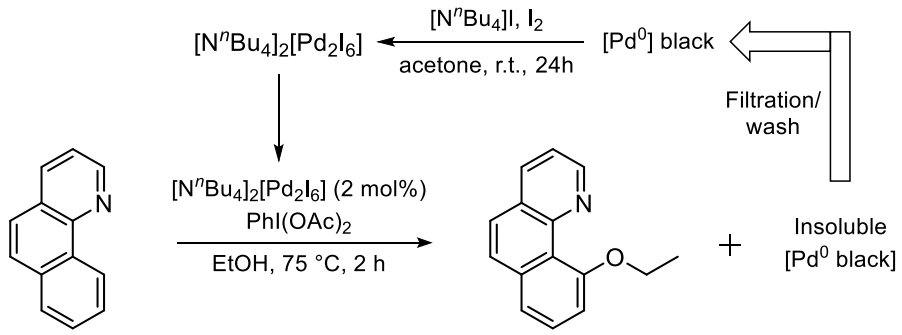

10

Benzo[*h*]quinoline (500 mg, 2.79 mmol), (diacetoxyiodo)benzene (1.804 g, 5.589 mmol), 1,3,5-trimethoxybenzene (156 mg, 0.930 mmol) and $[N^nBu_4]_2[Pd_2I_6]$ (81.4 mg, 0.0558 mmol, 2 mol%) were stirred in ethanol (5 mL) at 75 °C for 2 h. The reaction mixture was filtered, the black solids washed with ethanol (5 mL) and the filtrate concentrated under vacuum. The resulting crude residue was dissolved in $CDCl_3$ for analysis. Reaction yields were determined by integration of the diagnostic environments in the ^{1}H NMR spectrum ($CDCl_3$) for the product (1.63 ppm, $CH_2C\mathbf{H_3}$; 4.45 ppm, $C\mathbf{H_2}CH_3$) with comparison to the internal standard (1,3,5-trimethoxybenzene, 3.75 ppm, $C\mathbf{H_3}$). The black solid collected by filtration was dried under vacuum and added to a stirred solution of tetra-^{n}butylammonium iodide (41.4 mg, 0.112 mmol), I_2 (28.4 mg, 0.112 mmol) in acetone (15 mL) at room temperature. After 24 h, the solution was filtered under gravity, concentrated to ~5 mL and the product was obtained by vapour diffusion with Et_2O. The resulting crystals were filtered and dried, yielding $[N^nBu_4]_2[Pd_2I_6]$ as a shiny black crystalline solid (61 mg, 75%). M.p. 182.3-183.1 °C. UV–vis (nm): 340, 451, 542. The recovered sample of $[N^nBu_4]_2[Pd_2I_6]$ was used in a second C-H activation of benzo[*h*]quinoline in ethanol.

Mizoroki-Heck reaction yielding (E)-3-(4-amino-3,5-dimethylphenyl)acrylonitrile

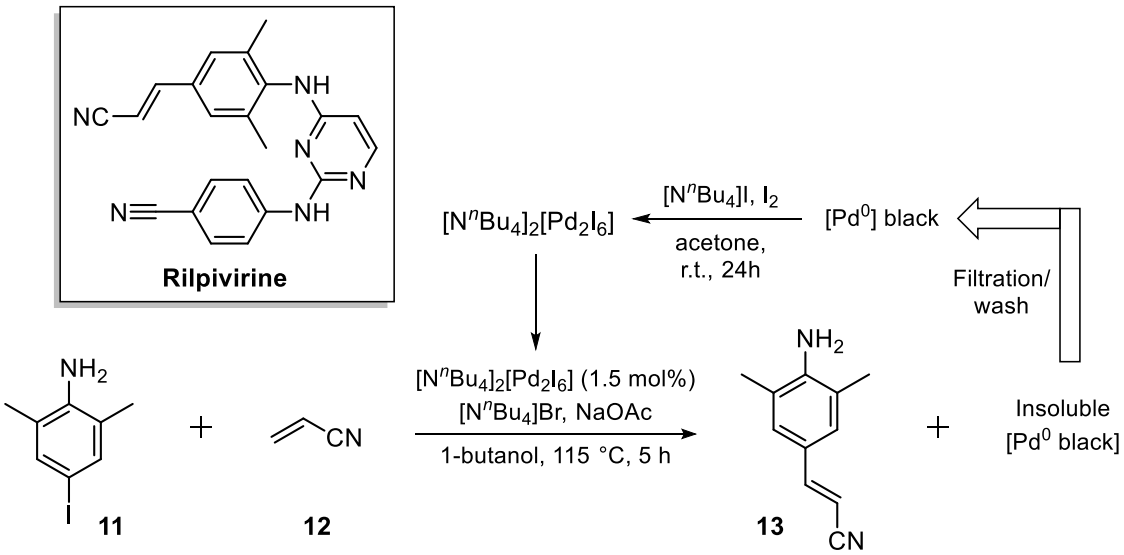

4-Iodo-2,6-dimethylaniline (618 mg, 2.50 mmol), acrylonitrile (159 mg, 197 µL, 3.00 mmol), NaOAc (308 mg, 3.75 mmol), [N^{n}Bu$_4$]Br (806 mg, 2.50 mmol), [N^{n}Bu$_4$]$_2$[Pd$_2$I$_6$] (54.7 mg, 0.0375 mmol, 1.5 mol%) and 1,3,5-trimethoxybenzene (140 mg, 0.833 mmol) were added to 1-butanol (25 mL) and the solution stirred at 115 °C. After 5 h, the reaction mixture was cooled to room temperature, filtered under vacuum and the collected solids washed with ethanol (2 x 5 mL). The filtrate was concentrated and the residue dissolved in $CDCl_3$ for analysis. Reaction yields were determined by integration of the diagnostic environments in the ^{1}H NMR spectrum ($CDCl_3$) for (*E*)-3-(4-amino-3,5-dimethylphenyl)acrylonitrile (7.22 ppm, Ar-C**H**=CH-CN; 7.05 ppm **H**-Ar-**H**) with comparison to the internal standard (1,3,5-trimethoxybenzene, 3.75 ppm, C**H$_3$**). The black solid collected by filtration was dried under vacuum and added to a stirred solution of tetra-^{n}butylammonium iodide (28 mg, 0.075 mmol), I_2 (19 mg, 0.075 mmol) in acetone (15 mL) at room temperature. After 24 h, the solution was filtered under gravity, concentrated to ~5 mL and the product was obtained by vapour diffusion with Et_2O. The resulting crystals were filtered and dried, yielding [N^{n}Bu$_4$]$_2$[Pd$_2$I$_6$] as a shiny black crystalline solid (44 mg, 81%). M.p. 181.9-183.0 °C. UV–vis (nm): 340, 451, 542. The recovered sample of [N^{n}Bu$_4$]$_2$[Pd$_2$I$_6$] was used in a second Mizoroki-Heck reaction yielding (*E*)-3-(4-amino-3,5-dimethylphenyl)acrylonitrile.

6.4. Chapter Four Experimental

6.4.1. VTNA of the model cross-coupling reaction catalysed by $[N^nBu_4]_2[Pd_2I_6]$

Reactions were performed under the ***$[N^nBu_4]_2[Pd_2I_6]$ conditions*** outlined in **3.6. Final optimised conditions**. The concentrations of each reagent was changed to achieve either 'same excess' or 'different excess' as outlined in the main text in Chapter Four Section 4.2.1. A stock solution of containing tetra-^{n}butylammonium bromide (0.7 M), 1-chloro-2-nitrobenzene (0.7 M) and naphthalene (0.175 M), and a stock solution of $[N^nBu_4]_2[Pd_2I_6]$ in dimethylformamide (1 mL, 0.0156 M), were used throughout the kinetic studies. A fresh ***Catalyst Stock Solution*** was used for each experiment.

Temporal concentration profiles were obtained using the methodology outlined in **3.7 ReactIR reaction monitoring**. The ReactIR profiles used to determine reaction orders in ***$[N^nBu_4]_2[Pd_2I_6]$*** were calibrated offline using at least 4 HPLC data points obtained from ***Sampling procedure A***. The ReactIR trends for [**1**] (1111 cm^{-1}) were copied into the openly available Microsoft Excel spreadsheet provided by Burés and Nielsen.[1,22–24] The best profile overlays were determined visually by trial and error, except for when the profiles were overlayed by deconvolution by solving (using Solver in Microsoft Excel) for identical profile gradients.

6.4.2. Detecting the formation of 1-bromo-2-nitrobenzene (4)

In 1-butanol and the absence of the (4-Chlorophenyl)boronic acid (2)

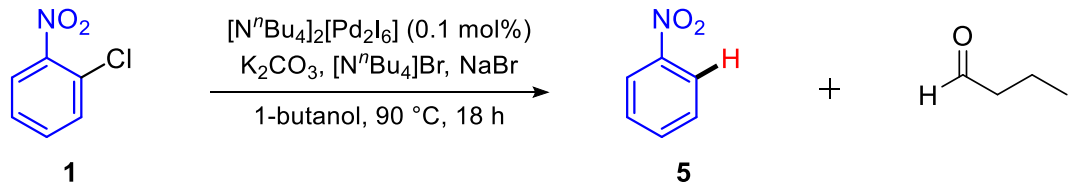

K_2CO_3 (435 mg, 3.15 mmol) and sodium bromide (1.08 mg, 10.5 mmol, 5 eqv.) were transferred to an aliquot (3 mL) of a 1-butanol stock solution (0.7 M) produced in a volumetric flask containing tetra-^{n}butylammonium bromide (677 mg, 2.10 mmol) and 1-chloro-2-nitrobenzene (331 mg, 2.1 mmol). The resulting solution was stirred at 90 °C for 10 min, after which the reaction was initiated by the addition of ***$[N^nBu_4]_2[Pd_2I_6]$ Catalyst Stock Solution*** (134.8 µL, 0.1 mol%). After 18 h, the reaction mixture was analysed by HPLC using ***Sampling procedure A.*** Near quantitative conversion of **1** (HPLC retention time: 7.9 min) to **5** (HPLC retention time: 6.5 min) was observed, alongside the formation of 1-butanal (HPLC retention time: 13 min). The reaction mixture was concentrated and the resulting residue purified by silica gel column chromatography [*n*-hexane/EtOAc (15:1)] to yield nitrobenzene (**5**) as a pale-yellow oil (171 mg, 66%). ^{1}H NMR (400 MHz, Chloroform-*d*) δ 8.28 – 8.21 (m, 2H), 7.76 – 7.67 (m,

1H), 7.61 – 7.51 (m, 2H) ppm. ^{13}C NMR (101 MHz, Chloroform-*d*) δ 148.3, 134.7, 129.4, 123.6 ppm. Analytical data was found to be in agreement with literature data.[25] 1-Butanal was not isolated directly, but its formation was instead confirmed by comparison of its retention time with a commercially sourced standard.

The above procedure (***In 1-butanol and the absence of the (4-chlorophenyl)boronic acid (2)***) was replicated using the solvents indicated in Chapter Four Section 4.2.1.2 in the presence of naphthalene as an internal standard. The results are presented in full in Chapter Four Section 4.2.1.2. Attempts at isolating Unknown product **6** (HPLC retention time: 7.2 min) by silica gel column chromatography were unsuccessful.

Aryl bromide (4) to aryl chloride (1) in tert-butanol and the absence of the (4-chlorophenyl)boronic acid (2)

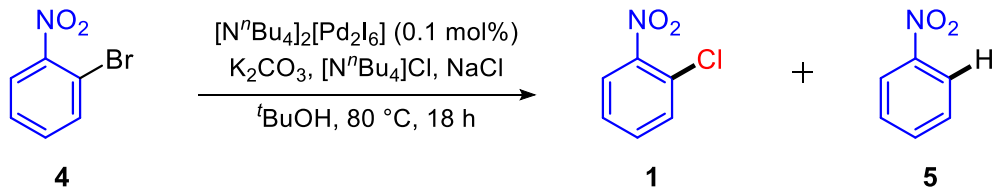

K_2CO_3 (435 mg, 3.15 mmol) and sodium chloride (614 mg, 10.5 mmol, 5 eqv.) were transferred to an aliquot (3 mL) of a *tert*-butanol stock solution (0.7 M) produced in a volumetric flask containing tetra-^{n}butylammonium chloride (584 mg, 2.10 mmol) and 1-bromo-2-nitrobenzene (331 mg, 2.1 mmol). The resulting solution was stirred at 80 °C for 10 min, after which the reaction was initiated by the addition of ***[N^{n}Bu$_4$]$_2$[Pd$_2$I$_6$] Catalyst Stock Solution*** (134.8 µL, 0.1 mol%). After 18 h, the reaction mixture was analysed by HPLC using ***Sampling procedure A***, which revealed the presence of **1** (HPLC retention time: 7.9 min), nitrobenzene (**5**) (Minor peak, HPLC retention time: 6.5 min) and 1-bromo-2-nitrobenzene (**4**) (HPLC retention time: 7.8 min).

6.4.3. Transmission electron microscopy of the model cross-coupling reaction

Optimisation of the TEM sampling procedure was conducted using ***Final TEM sampling procedure*** but with the additive/conditions indicated in Chapter Four Section 4.2.1.5 Table 50.

Final TEM sampling procedure

The model cross-coupling reaction was conducted under the ***[N^{n}Bu$_4$]$_2$[Pd$_2$I$_6$] conditions***. After 20 min, a reaction aliquot (1 mL) was taken and immediately transferred to a stirred solution of polyvinylpyrrolidone (M_w = 29K, 30 mg) in ethanol at −78 °C. The solution was stirred at −78 °C for 5

min before being allowed to warm to room temperature. A slurry of Sephadex®-LH20 in a 1:1 mixture (*v:v*) of ethanol and 1-butanol was transferred to a 12 mL syringe. Excess eluent was passed through the column until the eluent level was dropped to the top of the Sephadex®-LH20. Additional Sephadex®-LH20 slurry was added until the Sephadex®-LH20 was ~5 mL in volume. The solution of PVP and the reaction aliquot was transferred to the top of the Sephadex®-LH20 column, and the solution eluted slowly (~0.5 mL/min) into a vial. The movement of the low M_w compounds through the column was monitored by the yellow band, and flow through the column was stopped before this yellow band began to elute. The yellow band was collected as a second fraction and was found to contain a mixture of **1**-**3**, $[N^nBu_4]Br$ and polyvinylpyrrolidone by ^1H NMR and HPLC analysis. The colourless solution was subsequently filtered through a syringe filter (0.2 µm) and an aliquot (10 µL) transferred to a support grid for imaging by TEM.

DLS analysis

The model cross-coupling reaction was conducted under the ***$[N^nBu_4]_2[Pd_2I_6]$ conditions***. After 20 min, a reaction aliquot (1 mL) was taken and immediately transferred to a stirred solution of polyvinylpyrrolidone (M_w = 29,000; 30 mg) in ethanol at –78 °C. The solution was stirred at –78 °C for 5 min before being allowed to warm to room temperature. The sample was immediately passed through a syringe filter (0.2 µm) directly into a cuvette for analysis by DLS. A slurry of Sephadex®-LH20 in a 1:1 (*v:v*) mixture of ethanol and 1-butanol was transferred to a 12 mL syringe. Excess eluent was passed through the column until the eluent level was dropped to the top of the Sephadex®-LH20. Additional Sephadex®-LH20 slurry was added until the Sephadex®-LH20 was ~5 mL in volume. The solution of PVP and the reaction aliquot was transferred to the top of the Sephadex®-LH20 column, and the solution eluted slowly (~0.5 mL/min) into a vial. The movement of the low M_w compounds through the column was monitored by the yellow band, and flow through the column was stopped before this yellow band began to elute. The eluted solution was concentrated under vacuum (~1 mmHg) in a water bath that was maintained at room temperature (~21 °C). The residue was then resuspended in a 1:1 mixture of ethanol and 1-butanol (3 mL) and the resulting solution analysed by DLS.

6.4.4. Mechanism of the reduction of $[N^nBu_4]_2[Pd_2I_6]$

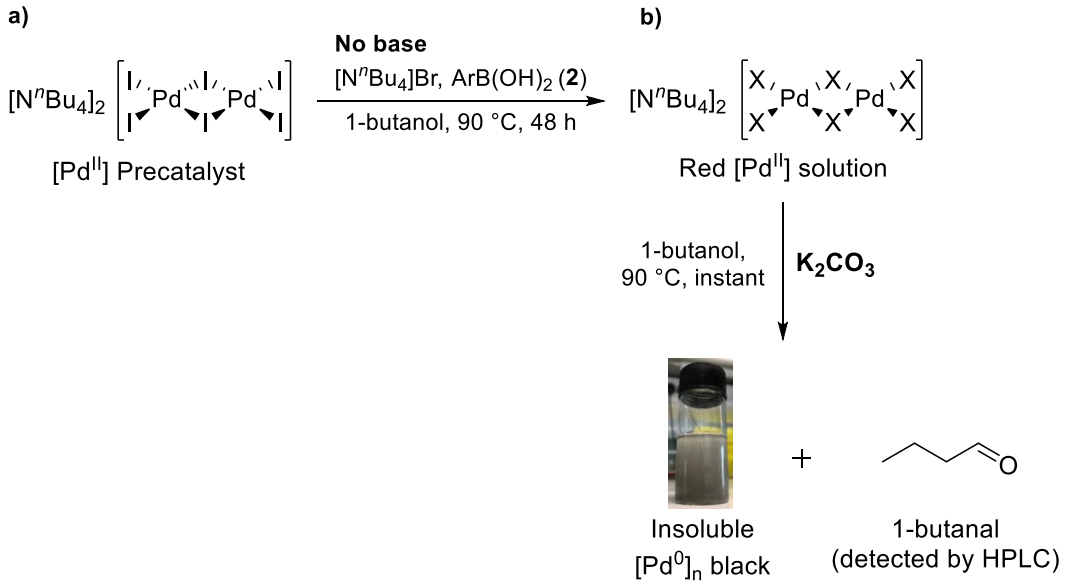

A solution of $[N^nBu_4]Br$ (677 mg, 2.10 mmol) and (4-chlorophenyl)boronic acid (**2**) (361 mg, 2.31 mmol) in 1-butanol (3 mL) was stirred at 90 °C for 10 min. An aliquot (59.3 µL) of ***$[N^nBu_4]_2[Pd_2I_6]$ Catalyst Stock Solution*** was transferred to the heated reaction mixture, which resulted in the formation of a red solution. This solution was stable at 90 °C for >48 h. A sample of the reaction mixture was taken and prepared for TEM using the ***Final TEM sampling procedure***. The images of this sample obtained by TEM were blank. No new organic products were observed by either ^1H NMR spectroscopy or HPLC analysis. To the resulting red solution was added K_2CO_3 (435 mg, 3.15 mmol), which resulted in the immediate formation of insoluble palladium black. The reaction mixture was analysed using **Sampling procedure A**, which revealed the presence of 1-butanal (HPLC retention time: 13 min).

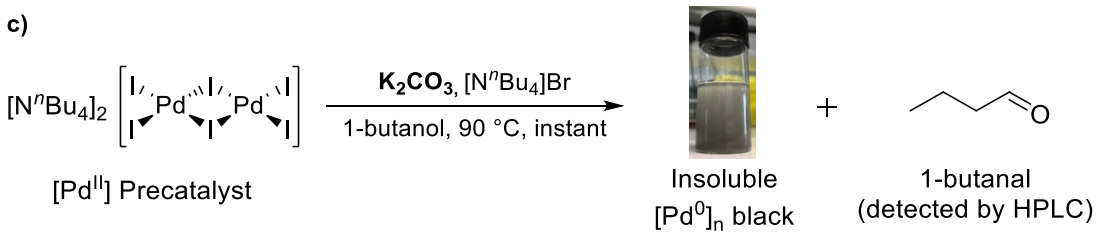

A solution of $[N^nBu_4]Br$ (677 mg, 2.10 mmol), K_2CO_3 (435 mg, 3.15 mmol) in 1-butanol (3 mL) was stirred at 90 °C for 10 min. An aliquot (59.3 µL) of ***$[N^nBu_4]_2[Pd_2I_6]$ Catalyst Stock Solution*** was transferred to the heated reaction mixture, which resulted in the immediate formation of insoluble palladium black. The reaction mixture was analysed using **Sampling procedure A**, which revealed the presence of 1-butanal (HPLC retention time: 13 min).

6.4.5. Role of the cation in $[Cation]_2[Pd_2I_6]$

Reaction monitoring of the model cross-coupling reaction catalysed by $[Cation]_2[Pd_2I_6]$

K_2CO_3 (435 mg, 3.15 mmol) and (4-chlorophenyl)boronic acid (361 mg, 2.31 mmol) were transferred to an aliquot (3 mL) of a 1-butanol stock solution (0.7 M) produced in a volumetric flask containing tetra-^{n}butylammonium bromide (677 mg, 2.10 mmol), 1-chloro-2-nitrobenzene (331 mg, 2.1 mmol) and naphthalene (67.3 mg, 0.525 mmol). The resulting solution was stirred at 90 °C for 10 min, after which the reaction was initiated by the addition of an aliquot (59.3 µL, 0.044 mol%) of a $[Cation]_2[Pd_2I_6]$ catalyst stock solution in DMF (0.0156 M of $[Cation]_2[Pd_2I_6]$). Reaction samples were taken and analysed by HPLC at $T_{0\ min}$, $T_{1\ min}$, $T_{2\ min}$, $T_{5\ min}$, $T_{10\ min}$, $T_{15\ min}$, $T_{20\ min}$, $T_{25\ min}$, $T_{30\ min}$, $T_{45\ min}$, $T_{60\ min}$ using ***Sampling procedure A***.

The above procedure (***Reaction monitoring of the model cross-coupling reaction catalysed by $[Cation]_2[Pd_2I_6]$***) was used in all the studies in Chapter Four, Section 4.2.3. Tetraphenylphosphonium bromide was introduced into the above procedure at varying time points and in varying quantities, as indicated in Figure 68-Figure 70

6.4.6. Suzuki-Miyaura coupling of 2,4-dihalogenated pyridines

2,4-Dibromopyridine

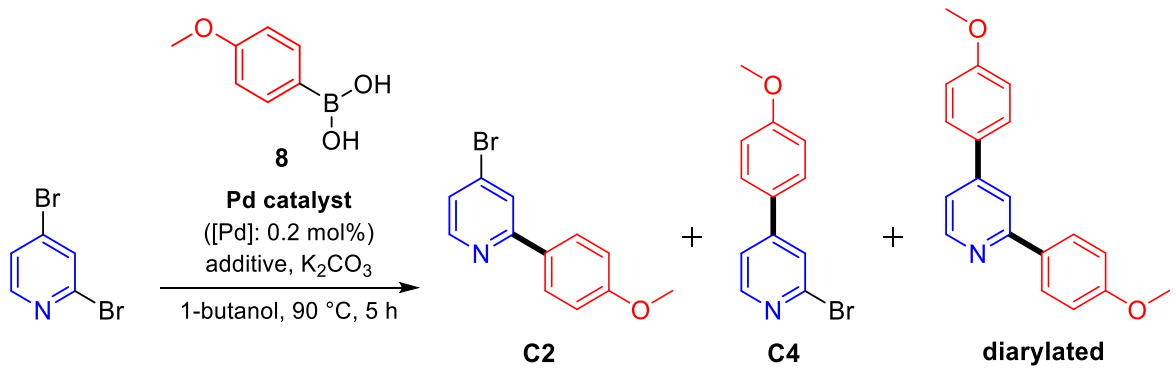

A solution of 2,4-dibromopyridine (249 mg, 1.05 mmol), (4-methoxyphenyl)boronic acid (167 mg, 1.10 mmol) tetra-^{n}butylammonium bromide (339 mg, 1.05 mmol) and K_2CO_3 (218 mg, 1.58 mmol) in 1-butanol (1.5 mL) was stirred at 90 °C for 10 min. The reaction was initiated by the addition of an aliquot (67.4 µL, 0.1 mol%) of a $[N^nBu_4]_2[Pd_2I_6]$ catalyst stock solution in DMF (0.0156 M of $[N^nBu_4]_2[Pd_2I_6]$). After 5 h, the reaction mixture was concentrated and the crude residue dissolved in $CDCl_3$ and filtered. Reaction yields were determined by integration of the diagnostic environments in the ^{1}H NMR spectrum ($CDCl_3$) for 2,4-dibromopyridine (8.17 ppm, 52%), **C2** (8.41 ppm, 3%), **C4** (8.31 ppm, 19%) and **diarylated** (8.60 ppm, 26%).

2,4-Chloropyridine (7)

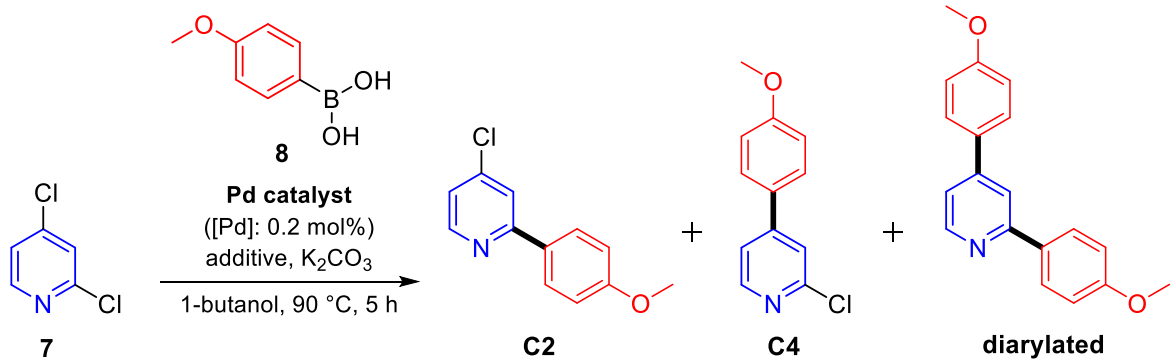

A solution of 2,4-dichloropyridine (249 mg, 1.05 mmol), (4-methoxyphenyl)boronic acid (167 mg, 1.10 mmol) tetra-^{n}butylammonium bromide (339 mg, 1.05 mmol) and K_2CO_3 (218 mg, 1.58 mmol) in 1-butanol (1.5 mL) was stirred at 90 °C for 10 min. The reaction was initiated by the addition of an aliquot (67.4 µL, 0.1 mol%) of a $[N^{n}Bu_4]_2[Pd_2I_6]$ catalyst stock solution in DMF (0.0156 M of $[N^{n}Bu_4]_2[Pd_2I_6]$). After 5 h, the reaction mixture was concentrated and a portion of the crude residue dissolved in $CDCl_3$ and filtered. Reaction yields were determined by integration of the diagnostic environments in the ^{1}H NMR spectrum ($CDCl_3$) for 2,4-dichloropyridine (8.33 ppm d, 1H) **C2** (8.54 ppm, d, 1H), **C4** (8.40-8.34 ppm, m, 1H) and **diarylated** (8.68 ppm, d, 1H). The crude residue was purified by silica gel column chromatography using a gradient elution of 5% EtOAc in *n*-hexane to 50% EtOAc in *n*-hexane. The reaction components eluted in the order **7** -> **C2** -> **C4** -> **8** -> **diarylated**.

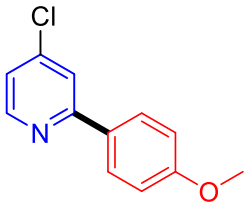

C2

C2: ^{1}H NMR (400 MHz, Chloroform-*d*) δ 8.54 (d, *J* = 5.3 Hz, 1H), 7.98 – 7.90 (m, 2H), 7.66 (d, *J* = 1.8 Hz, 1H), 7.17 (dd, *J* = 5.3, 1.9 Hz, 1H), 7.04 – 6.96 (m, 2H), 3.86 (s, 2H) ppm. ^{13}C NMR (101 MHz, $CDCl_3$) δ 161.0, 158.7, 150.4, 144.6, 130.7, 128.4, 121.6, 120.0, 114.3, 55.4 ppm.

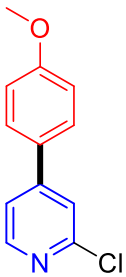

C4

C4: ^{1}H NMR (400 MHz, Chloroform-*d*) δ 8.40 – 8.34 (m, 1H), 7.60 – 7.53 (m, 2H), 7.52 – 7.46 (m, 1H), 7.41 – 7.34 (m, 1H), 7.04 – 6.97 (m, 2H), 3.87 (s, 3H) ppm. ^{13}C NMR (101 MHz, $CDCl_3$) δ 161.0, 152.2, 151.0, 149.9, 128.9, 128.3, 121.3, 119.9, 114.7, 55.4 ppm.

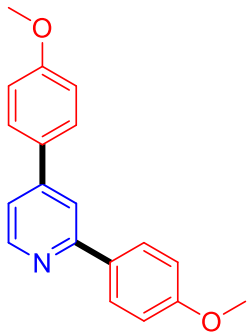

diarylated

diarylated: ^{1}H NMR (400 MHz, Chloroform-*d*) δ 8.68 (d, *J* = 5.1 Hz, 1H), 8.07 – 7.99 (m, 2H), 7.88 – 7.83 (m, 1H), 7.72 – 7.63 (m, 2H), 7.38 (dd, *J* = 5.2, 1.7 Hz, 1H), 7.10 – 7.00 (m, 4H), 3.90 (s, 6H) ppm. ^{13}C NMR (101 MHz, $CDCl_3$) δ 160.5, 157.7, 149.9, 148.7, 132.3, 131.0, 128.3, 128.2, 119.1, 117.5, 114.5, 114.1, 55.4, 55.4 ppm.

Analytical data was found to be in agreement with literature data.[26,27]

The above procedure (***2,4-Chloropyridine (7)***) was replicated but with tetra-^{n}butylammonium bromide replaced with tetraphenylphosphonium bromide (440 mg, 1.05 mmol). When the old and new bottles of $Pd(PPh_3)$ were used as precatalysts, neither tetra-^{n}butylammonium bromide nor tetraphenylphosphonium bromide were used as additives. Only minor amounts of diarylation product (<2-3%) were observed in the coupling of 2,4-dichloropyridine with (4-methoxyphenyl)boronic acid.

6.4.7. More detailed overview of VTNA Background and Methodology

For the sake of clarity, the following background on graphical kinetic techniques was removed from the main body of text. It is included here in case it can be useful for any future Wilton-Ely group members who want to use VTNA.

Reaction orders and constants can be obtained using a variety of different techniques. In an early example, Lineweaver and Burk published the reciprocal form of the Michaelis-Menten equation.[28] Graphical representation of enzyme kinetic data using this 'upside down' equation yielded a straight line plot that enabled the extraction of kinetic parameters. A *JACS* editorial published in 2003 highlighted that this seminal report was the journal's most cited publication.[29] Lineweaver and Burk's strategy set the ground work for a century of mechanistic chemical research in both academia and industry which utilises graphical representations and extrapolations of kinetic data.[30–37] For example, kinetic orders and constants can be extrapolated from integral rate equations and straight line plots of reaction concentration data.[37,38] However, these integral methods either require the reaction to follow a simple rate equation, or for an analytical solution to the rate equation to be known *a priori* to data manipulation and plotting – neither of which are the case for the complex rate

equations which describe catalytic transformations. Alternatively, kinetic parameters can be extrapolated from the graphical interpretation of initial rate data (Figure 80).[37,38]

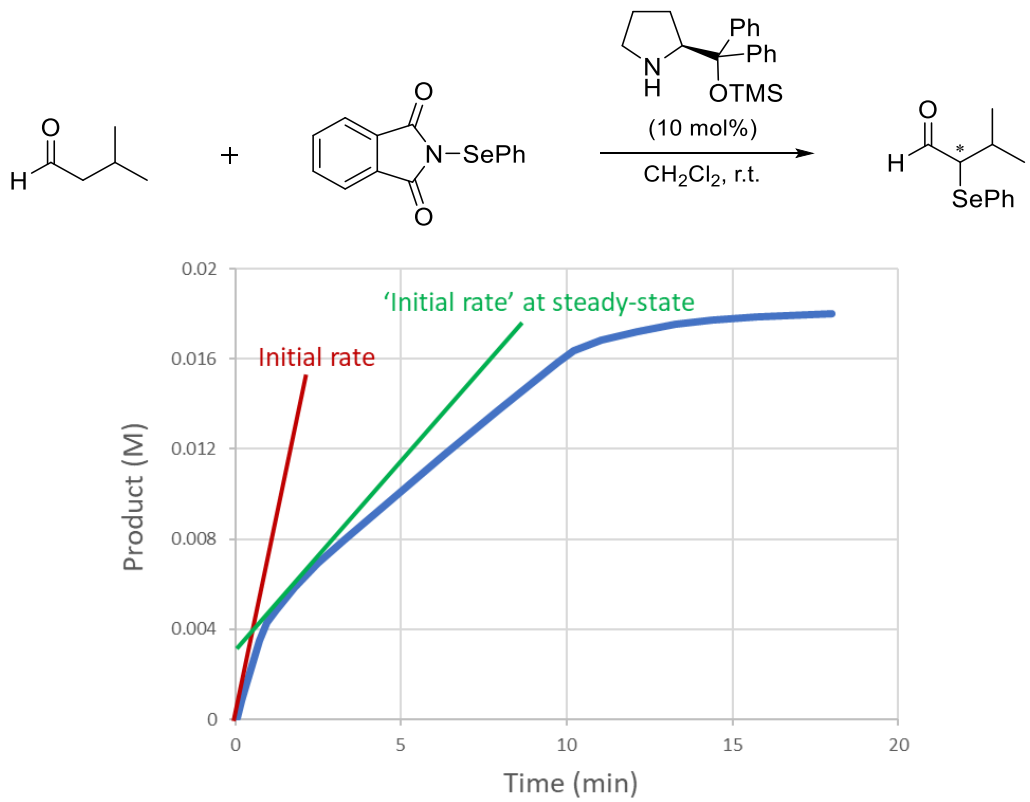

Figure 80. Example of how initial rates are determined and its pitfalls demonstrated on an example kinetic profile from an organocatalytic selenylation of an aldehyde. Kinetic data was manually extracted from the original report in reference 50 and replotted in Excel.

Reaction orders are then elucidated from linearised plots of the initial rate at varying component concentrations. However, initial rate data is not suitable when there are deviations from catalytic steady-state during the initial rate window e.g. the organocatalytic selenylation of aldehydes (Figure 80).[39] Similar behaviour was also observed for the organocatalytic conjugate addition of aldehydes to nitrostyrene and in the α-chlorination of isovaleraldehyde.[40–42] Another extreme example of the limitations of initial rates is the polypeptide-catalysed epoxidation of chalcone,[43] where a reaction induction period resulted in an initial rate measurement taken at 30 seconds into the reaction onset that was 50% less than one taken at 60 seconds.[44] Finally, obtaining initial rate data for straight line extrapolations is experimentally laborious as multiple (typically 4-5) experiments are needed for each reaction component. Since the initial rate method only utilises the data for the very beginning of the reaction, most of this experimental data is then discarded.

For multi-component reactions, these kinetic approaches also rely on the rate only being influenced by the reaction component whose concentration is being intentionally changed. To ensure that this is the case, the remaining components must be used in a large excesses, e.g. ≥5-10 equivalents, so that their concentration can be assumed to be constant.[37,38] Thus, the kinetic parameters obtained are *pseudo* rate constants and orders, and are not obtained under synthetically relevant conditions. Utilising the reagents in such large excesses has even been reported to alter the mechanistic pathway and catalyst resting state.[45]

Blackmond developed Reaction Progress Kinetic Analysis (RPKA) to overcome the pitfalls of the kinetic methods outlined above.[44] Similar to traditional differential approaches, RPKA utilises graphical plotting of rate vs concentration to extract kinetic orders and constants. In RPKA however, temporal rate data is plotted against a function of the component concentration (Equation 7 and Figure 81), which enables kinetic parameters to be obtained without maintaining a large excess of the reaction components. Crucially then, RPKA is used to uncover kinetic parameters under synthetically relevant conditions. To determine reaction orders using RPKA, a series of reactions are run under a 'different excess' of the reagents, where the 'excess' is defined as the difference in the initial starting concentrations of the two reagents (*e.g.* Table 58, $[e]_0 = [\mathbf{5}]_0 - [\mathbf{6}]_0$). The different excess experiments reported by Zotova whilst working with Blackmond *et al* for the proline (**7**)-catalysed aldol addition of acetone (**5**) to *m*-chlorobenzaldehyde (**6**) is summarised below as an example to demonstrate RPKA (Table 58 and Figure 81).[46]

*Table 58. Aldol addition of **5** to **6** and 'different excess' kinetic experiments. Data taken from the report by Zotova and Blackmond et al.*

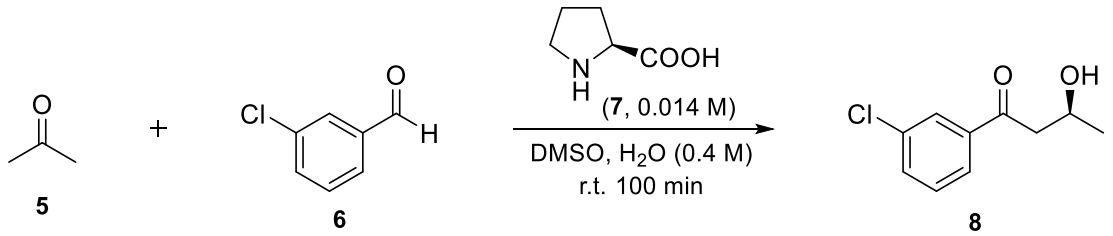

Entry	$[\mathbf{5}]_0$ (M)	$[\mathbf{6}]_0$ (M)	Excess $[e]_0$ (M)
1	2.75	0.5	2.25
2	2.00	0.5	1.50
3	1.24	0.5	0.74

The rate equation for the transformation in Table 58 can be written in a power-law form and rearranged into an equation for a straight line:[47]

$$\frac{rate}{[\mathbf{5}]^m} = k' \times [\mathbf{6}]^n$$

Equation 7

A plot of $\frac{rate}{[\mathbf{5}]^m}$ vs $[\mathbf{6}]^n$ yields a straight line with slope *k'* when the correct orders, *m* and *n*, have been determined. This can be done visually by trial and error in a spreadsheet programme, or using a curve-fitting algorithm. For the aldol reaction depicted in Table 58, graphical determination of reaction orders of *m* = 0.58 and *n* = 0.9 provided the best visual overlay of the 'different excess' experiments (Figure 81).

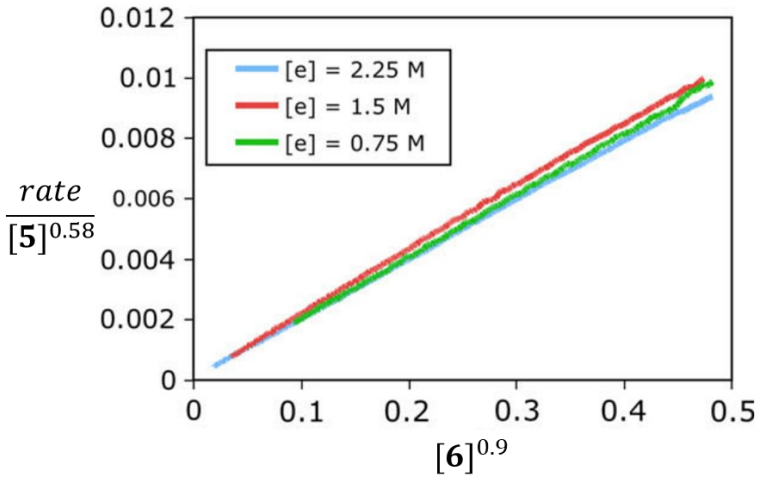

Figure 81. RPKA applied to the 'different excess' reaction curves for entries 1-3 in Table 58. Reaction profile reproduced directly from reference 56.

As illustrated by Table 58 and Figure 81, order values *m* and *n* were determined from just three experiments (minimum required is two). This is a considerable improvement on the ten experiments that would be required to determine the orders of [**5**] and [**6**] using initial rates.

RPKA has also been utilised to uncover deviations from catalytic steady-state. Deviations from steady-state are typically caused by either catalyst deactivation or product inhibition of the catalyst.[48] To determine deviations from steady-state using RPKA, the 'same excess' technique is applied, where the reagent concentrations are varied by the same amount. For example, 'same excess' was applied to the hydrolytic epoxide ring opening catalysed by a cobalt-salen complex (Table 59 and Figure 82).[44,49]

*Table 59. Hydrolytic ring opening of epoxide **9** and 'same excess' kinetic experiments. Data taken from the report by Nielsen and Blackmond et al in reference 59.*

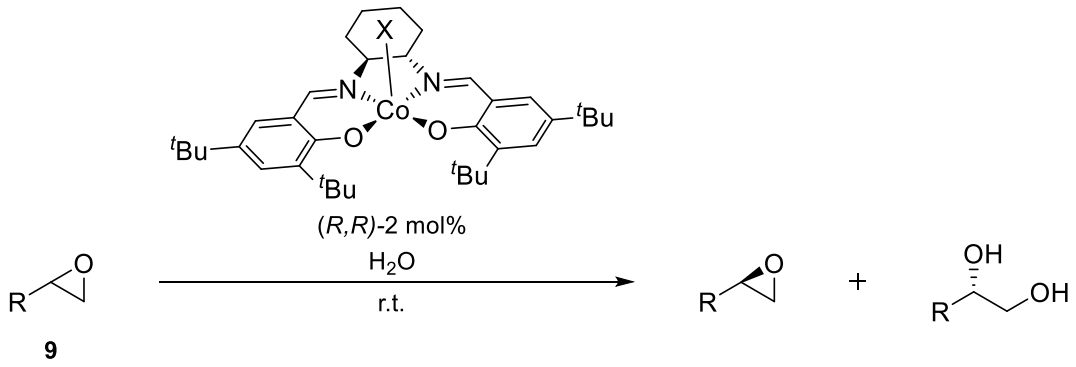

Reaction	[**9**]$_0$ (M)	[**H_2O**]$_0$ (M)	Excess [e]$_0$ (M)
1	1.5	2.0	0.5
2	1.0	1.5	0.5

Two 'same excess' reaction profiles are identical and overlapping under a catalytic steady-state since the concentration of the catalytic intermediates do not change when the reagents excess is constant, *i.e.* under a 'same excess'. In the case of the epoxide ring opening (Table 59), non-overlapping profiles indicated a deviation from steady-state (Figure 82). Changes to the reaction conditions which either emulate the deviation from, or return the catalyst to, steady-state can then be performed to elucidate the underlying mechanistic origin of the deviation. In the case of the epoxide ring opening (Table 59 and Figure 82), the authors found that catalyst deactivation was occurring at elevated water concentrations, which led to an improved understanding on catalyst design and the optimum reaction conditions. It is worth noting that such deviations from catalytic steady-state would not have been uncovered by analysing initial reaction rates.

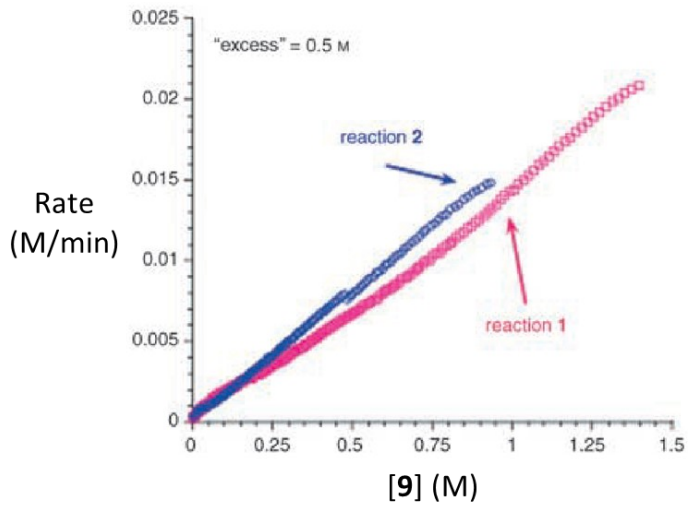

Figure 82. Non-overlapping 'Same excess' indicated catalyst deactivation/product inhibition for the hydrolytic epoxide ring opening depicted in Table 59. Reaction 1 and Reaction 2 refers to the conditions in Table 59. Reaction profiles reproduced directly from reference 59.

Despite providing many advantages over traditional kinetic approaches, RPKA is limited by the need for differential rate data which can only be obtained directly from isothermal calorimetry or gas uptake studies. These techniques limit the range of chemical systems that can be studied using RPKA. Differential rate data can instead be derived from integral temporal concentration data. However, derivation of integral data relies on either analysis of initial rates, or on fitting the integral data to an arbitrarily chosen polynomial function and subsequent differentiation of this function. For the latter, the fit must be accurate and the resulting rate data can be biased according to the arbitrarily chosen function. Moreover, the chosen mathematical function and the differentiation process can create data artifacts and noise.

Analytical techniques that yield concentration data, *e.g.* HPLC, GC, NMR, ReactIR/Raman, UV-vis and MS, are considerably more accessible and broadly applicable than techniques which measure reaction rate. As a result, Burés developed Visual Time Normalisation Analysis (VTNA),[1,22–24] which utilises readily accessible temporal concentration profiles to extract kinetic parameters.[22,24] VTNA has also been used to monitor deviations from catalytic steady-state due to catalyst deactivation.[23,48] The principles of VTNA are similar to those of RPKA – to determine the order in a reaction component using VTNA, 'different excess' concentration data is plotted against a function of time, the reaction component concentration and component order according to Equation 8:

$$\int_{t=0}^{t=n} [\boldsymbol{A}]^a dt = \sum_{i=1}^{n} \left(\frac{[\boldsymbol{A}]_i + [\boldsymbol{A}]_{i-1}}{2} \right)^a \cdot (t_i - t_{i-1})$$

Equation 8

Quantitatively, Equation 4 normalises the time scale between each pair of temporal concentration data points with respect to the component concentration and order. Qualitatively, Equation 4 removes the influence of [**A**] on the rate of the reaction, such that when the correct value of the reaction order in [**A**], *a* (Equation 8), is determined, two profiles of different concentration in [**A**] will visually overlap. Equation 8 can be applied to any reaction component, including the catalyst. When determining the order of the reaction in a catalyst for systems with quantifiable catalyst deactivation, the change in catalyst concentration can be incorporated into Equation 4 and orders determined.[23] Moreover, Equation 4 can be applied to obtain kinetic parameters from temporal concentration data of any of the starting materials or products. Thus, VTNA is a broadly applicable and robust technique for determining reaction orders.

The example simulated dataset provided by Nielsen and Burés is given below to illustrate VTNA (Table 60 and Figure 83).[1] Two reactions under 'different excess' in [**A**] were simulated and the profiles used in this example to determine a first order in [**A**] (Figure 83).

Table 60. Simulated dataset to demonstrate VTNA. Data is openly available from reference 60.

$$\mathbf{A} + \mathbf{B} \xrightarrow{\mathbf{Cat}} \mathbf{P}$$

Reaction	$[\mathbf{A}]_0$ (M)	$[\mathbf{B}]_0$ (M)	$[\mathbf{Cat}]_0$ (M)	Excess $[e]_0$ (M)
1	1.0	0.6	0.01	0.4
2	0.6	0.6	0.01	0

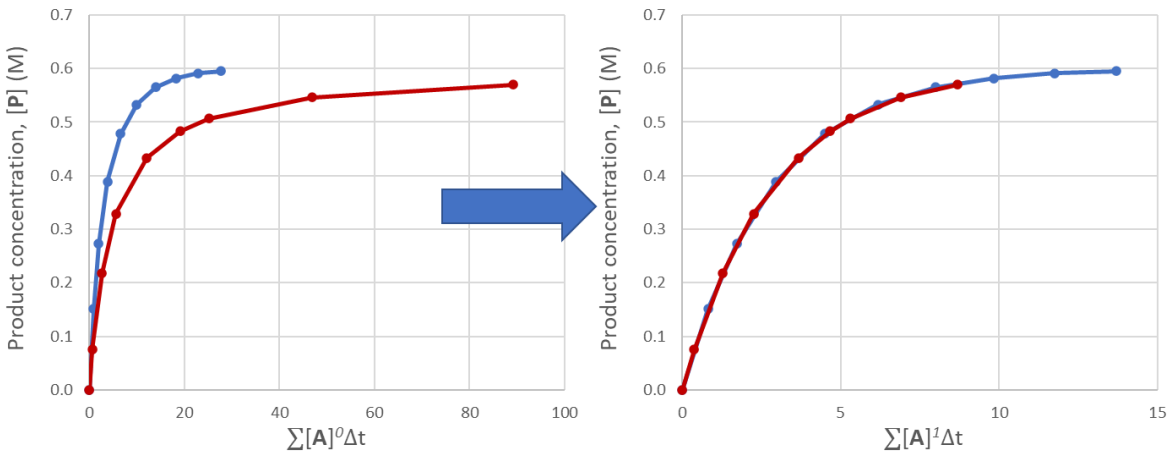

Figure 83. Normalisation of temporal [P] profiles from reactions 1 and 2 (Table 60) for a reaction order in [A], a = 1. Data is openly available from reference 59.

Since their inception, RPKA and VTNA have revolutionised the way in which chemical kinetic studies are conducted, and have been utilised extensively to determine key kinetic parameters during

mechanistic studies of a variety of transformations.[50–64] Many of these studies include utilising RPKA and VTNA to elucidate catalyst orders and understand catalyst speciation. The Wilton-Ely and Braddock groups have access to NMR, HPLC and ReactIR, which can all yield temporal concentration data. VTNA will therefore be applied herein to gain key kinetic and mechanistic understanding on the cross-coupling reaction yielding **3** catalysed by $[N^nBu_4]_2[Pd_2I_6]$.

6.5. References

1 C. D. T. Nielsen and J. Burés, *Chem. Sci.*, 2019, **10**, 348–353.

2 R. Isaksson, T. Liljefors, J. Sandstroem, *J. Chem. Res. 1981,* **43**.

3 F. Bigoli, P. Deplano, M. L. Mercuri, M. A. Pellinghelli, G. Pintus, A. Serpe and E. F. Trogu, *Chem. Commun.*, 1998, **484**, 2351–2352.

4 S. McCarthy, O. Desaunay, A. L. W. Jie, M. Hassatzky, A. J. P. White, P. Deplano, D. C. Braddock, A. Serpe and J. D. E. T. Wilton-Ely, *ACS Sustain. Chem. Eng.*, 2022, **10**, 15726–15734.

5 L. Cau, P. Deplano, L. Marchiò, M. L. Mercuri, L. Pilia, A. Serpe and E. F. Trogu, *Dalton Trans.*, 2003, 1969–1974.

6 European Patent, EP1964936B1, 2008.

7 D. C. Braddock, P. D. Lickiss, B. C. Rowley, D. Pugh, T. Purnomo, G. Santhakumar and S. J. Fussell, *Org. Lett.*, 2018, **20**, 950–953.

8 P. Elías-Rodríguez, E. Matador, M. Benítez, T. Tejero, E. Díez, R. Fernández, P. Merino, D. Monge and J. M. Lassaletta, *J. Org. Chem.*, 2023, **88**, 2487–2492.

9 J. Derosa, A. L. Cantu, M. N. Boulous, M. L. O'Duill, J. L. Turnbull, Z. Liu, D. M. De La Torre and K. M. Engle, *J. Am. Chem. Soc.*, 2017, **139**, 5183–5193.

10 L. Zhang, K. Xiao, Y. Qiao, X. Li, C. Song and J. Chang, *Eur. J. Org. Chem.*, 2018, **2018**, 6913–6918.

11 K. Ramesh, H. Y. Kim and K. Oh, *Org. Lett.*, 2023, **25**, 449–453.

12 N. Jankowski, J. Dietrich and N. Krause, *Adv. Synth. Catal.*, 2022, **364**, 3404–3409.

13 A. Kouridaki, T. Montagnon, M. Tofi and G. Vassilikogiannakis, *Org. Lett.*, 2012, **14**, 2374–2377.

14 H. Zhang and P. H. Toy, *Adv. Synth. Catal.*, 2021, **363**, 215–221.

15 G. Dyker, E. Muth, A. S. K. Hashmi and L. Ding, *Adv. Synth. Catal.*, 2003, **345**, 1247–1252.

16 L. T. Ball, G. C. Lloyd-Jones and C. A. Russell, *Science*, 2012, **337**, 1644–1648.

17 M. Cuscusa, A. Rigoldi, F. Artizzu, R. Cammi, P. Fornasiero, P. Deplano, L. Marchiò and A. Serpe, *ACS Sustain. Chem. Eng.*, 2017, **5**, 4359–4370.

18 P. Orecchia, D. S. Petkova, R. Goetz, F. Rominger, A. S. K. Hashmi and T. Schaub, *Green Chem.*, 2021, **23**, 8169–8180.

19 L. Di Terlizzi, S. Scaringi, C. Raviola, R. Pedrazzani, M. Bandini, M. Fagnoni and S. Protti, *J. Org. Chem.*, 2022, **87**, 4863–4872.

20 C. R. McElroy, A. Constantinou, L. C. Jones, L. Summerton and J. H. Clark, *Green Chem.*, 2015, **17**, 3111–3121.

21 M. Avanthay, R. B. Bedford, C. S. Begg, D. Böse, J. Clayden, S. A. Davis, J. C. Eloi, G. P.

Goryunov, I. V. Hartung, J. Heeley, K. A. Khaikin, M. O. Kitching, J. Krieger, P. S. Kulyabin, A. J. J. Lennox, R. Nolla-Saltiel, N. E. Pridmore, B. J. S. Rowsell, H. A. Sparkes, D. V. Uborsky, A. Z. Voskoboynikov, M. P. Walsh and H. J. Wilkinson, *Nat. Catal.*, 2021, **4**, 994–998.

22 J. Burés, *Angew. Chem. Int. Ed.*, 2016, **55**, 2028–2031.

23 A. Martínez-Carrión, M. G. Howlett, C. Alamillo-Ferrer, A. D. Clayton, R. A. Bourne, A. Codina, A. Vidal-Ferran, R. W. Adams and J. Burés, *Angew. Chem. Int. Ed.*, 2019, **58**, 10189–10193.

24 J. Burés, *Angew. Chem. Int. Ed.*, 2016, **55**, 16084–16087.

25 D. Tanini, C. Dalia and A. Capperucci, *Green Chem.*, 2021, **23**, 5680–5686.

26 N. W. J. Scott, M. J. Ford, N. Jeddi, A. Eyles, L. Simon, A. C. Whitwood, T. Tanner, C. E. Willans and I. J. S. Fairlamb, *J. Am. Chem. Soc.*, 2021, **143**, 9682–9693.

27 M. Yang, J. Chen, C. He, X. Hu, Y. Ding, Y. Kuang, J. Liu and Q. Huang, *J. Org. Chem.*, 2020, **85**, 6498–6508.

28 H. Lineweaver and D. Burk, *J. Am. Chem. Soc.*, 1934, **56**, 658–666.

29 P. J. Stang, *J. Am. Chem. Soc.*, 2003, **125**, 1–8.

30 J. I. Murray, L. Zhang, A. Simon, M. V. Silva Elipe, C. S. Wei, S. Caille and A. T. Parsons, *Org. Process Res. Dev.*, 2023, **27**, 198–205.

31 K. A. Johnson, *Chapter 23 Fitting Enzyme Kinetic Data with KinTek Global Kinetic Explorer*, Elsevier Inc., 2009, vol. 467.

32 R. C. Cioc, M. Crockatt, J. C. van der Waal and P. C. A. Bruijnincx, *Angew. Chem. Int. Ed.*, 2022, **61**, 17, e202114720.

33 J. Burés and I. Larrosa, *Nature*, 2023, **613**, 689–695.

34 G. S. Eadie, *J. Biol. Chem.*, 1942, **146**, 85–93.

35 J.-M. Frère, B. Leyh and A. Renard, *J. Theor. Biol.*, 1983, **101**, 387–400.

36 J. B. S. Haldane, *Nature*, 1957, **179**.

37 A. Cornish-Bowden, *Fundamentals of enzyme kinetics*, Wiley-VCH, Weinheim, 4th edn., 2012.

38 K. J. Laidler, *Chemical Kinetics*, Harper & Row, New York, 3rd edn., 1987.

39 J. Burés, P. Dingwall, A. Armstrong and D. G. Blackmond, *Angew. Chem. Int. Ed.*, 2014, **53**, 8700–8704.

40 J. Burés, A. Armstrong and D. G. Blackmond, *Chem. Sci.*, 2012, **3**, 1273–1277.

41 J. Burés, A. Armstrong and D. G. Blackmond, *J. Am. Chem. Soc.*, 2012, **134**, 6741–6750.

42 J. Burés, A. Armstrong and D. G. Blackmond, *J. Am. Chem. Soc.*, 2011, **133**, 8822–8825.

43 S. P. Mathew, S. Gunathilagan, S. M. Roberts and D. G. Blackmond, *Org. Lett.*, 2005, **7**, 4847–4850.

44 D. G. Blackmond, *Angew. Chem. Int. Ed.*, 2005, **44**, 4302–4320.

45 T. Rosner, J. Le Bars, A. Pfaltz and D. G. Blackmond, *J. Am. Chem. Soc.*, 2001, **123**, 1848–1855.

46 N. Zotova, L. J. Broadbelt, A. Armstrong and D. G. Blackmond, *Bioorganic Med. Chem. Lett.*, 2009, **19**, 3934–3937.

47 N. Zotova, A. Franzke, A. Armstrong and D. G. Blackmond, *J. Am. Chem. Soc.*, 2007, **129**, 15100–15101.

48 D. C. Braddock, B. M. J. Lancaster, C. J. Tighe and A. J. P. White, *J. Org. Chem.*, 2023, **88**, 8904–8914.

49 L. P. C. Nielsen, C. P. Stevenson, D. G. Blackmond and E. N. Jacobsen, *J. Am. Chem. Soc.*, 2004, **126**, 1360–1362.

50 D. Gasperini, S. E. Neale, M. F. Mahon, S. A. MacGregor and R. L. Webster, *ACS Catal.*, 2021, **11**, 5452–5462.

51 O. J. Newton, K. Hellgardt, J. Richardson and K. K. M. Hii, *J. Catal.*, 2023, **424**, 29–38.
52 S. M. Banik, A. Levina, A. M. Hyde and E. N. Jacobsen, *Science*, 2017, **358**, 761–764.
53 P. Dydio, R. J. Detz and J. N. H. Reek, *J. Am. Chem. Soc.*, 2013, **135**, 10817–10828.
54 N. A. Hawbaker and D. G. Blackmond, *Nat. Chem.*, 2019, **11**, 957–962.
55 S. Shekhar, P. Ryberg, J. F. Hartwig, J. S. Mathew, D. G. Blackmond, E. R. Strieter and S. L. Buchwald, *J. Am. Chem. Soc.*, 2006, **128**, 3584–3591.
56 Z. I. Günler, X. Companyó, I. Alfonso, J. Burés, C. Jimeno and M. A. Pericàs, *Chem. Commun.*, 2016, **52**, 6821–6824.
57 S. Gesslbauer, G. Hutchinson, A. J. P. White, J. Burés and C. Romain, *ACS Catal.*, 2021, **11**, 4084–4093.
58 D. Whitaker, J. Burés and I. Larrosa, *J. Am. Chem. Soc.*, 2016, **138**, 8384–8387.
59 D. G. Blackmond, *J. Am. Chem. Soc.*, 2015, **137**, 10852–10866.
60 O. P. Schmidt and D. G. Blackmond, *ACS Catal.*, 2020, **10**, 8926–8932.
61 D. E. Hill, Q. L. Pei, E. X. Zhang, J. R. Gage, J. Q. Yu and D. G. Blackmond, *ACS Catal.*, 2018, **8**, 1528–1531.
62 R. D. Baxter, D. Sale, K. M. Engle, J. Q. Yu and D. G. Blackmond, *J. Am. Chem. Soc.*, 2012, **134**, 4600–4606.
63 E. R. Strieter, D. G. Blackmond and S. L. Buchwald, *J. Am. Chem. Soc.*, 2005, **127**, 4120–4121.
64 J. R. Coombs, F. Haeffner, L. T. Kliman and J. P. Morken, *J. Am. Chem. Soc.*, 2013, **135**, 11222–11231.

7. Appendix

All of the data used to produce this thesis can be found on the Wilton-Ely group OneDrive.

7.1. UV-Vis Spectroscopy

[N^{n}Bu$_4$]$_2$[Pd$_2$I$_6$]

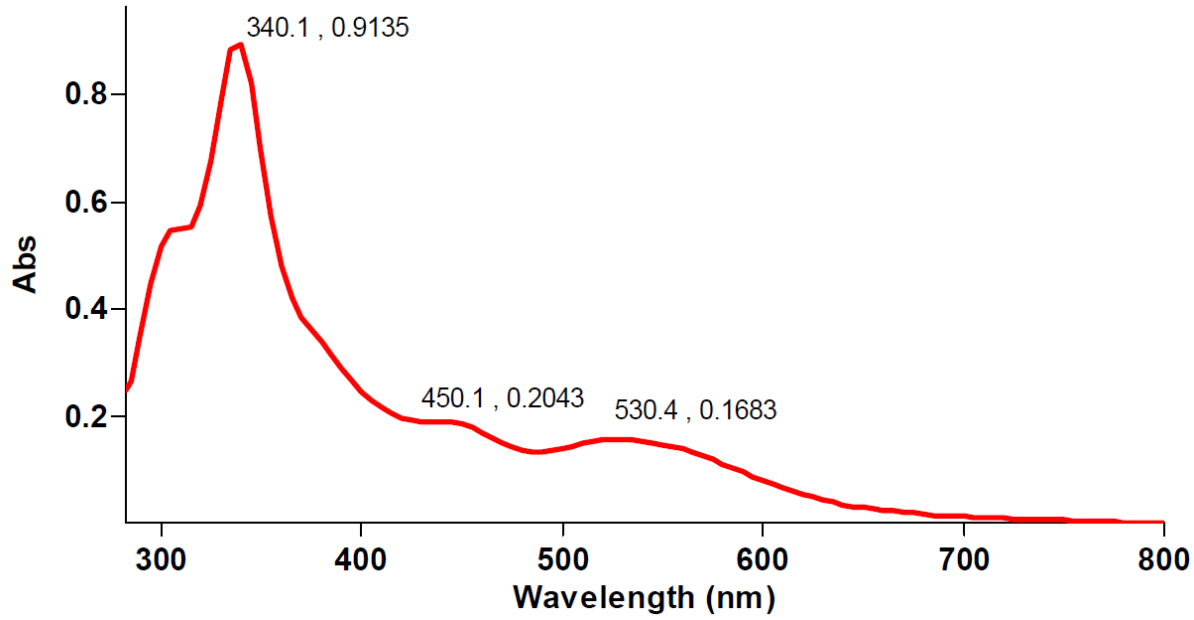

Figure S1. UV-Vis absorption spectrum of ***[N^{n}Bu$_4$]$_2$[Pd$_2$I$_6$]***.

[PPh$_4$]$_2$[Pd$_2$I$_6$]

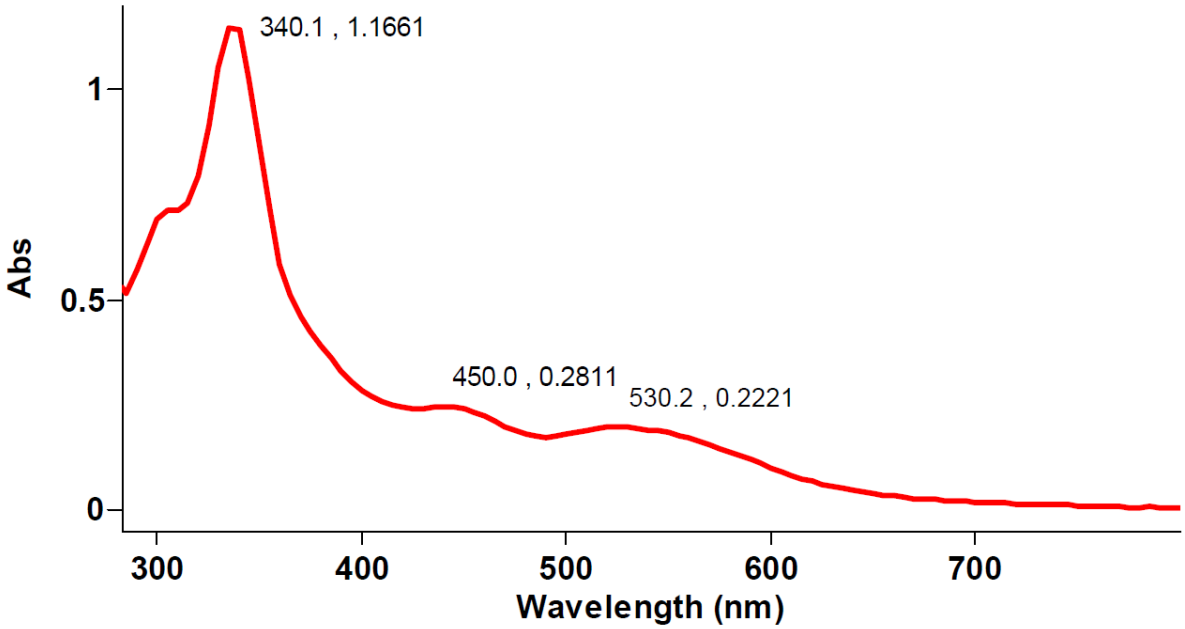

Figure S2. UV-Vis absorption spectrum of ***[PPh$_4$]$_2$[Pd$_2$I$_6$]***

[NEt$_4$]$_2$[Pd$_2$I$_6$]

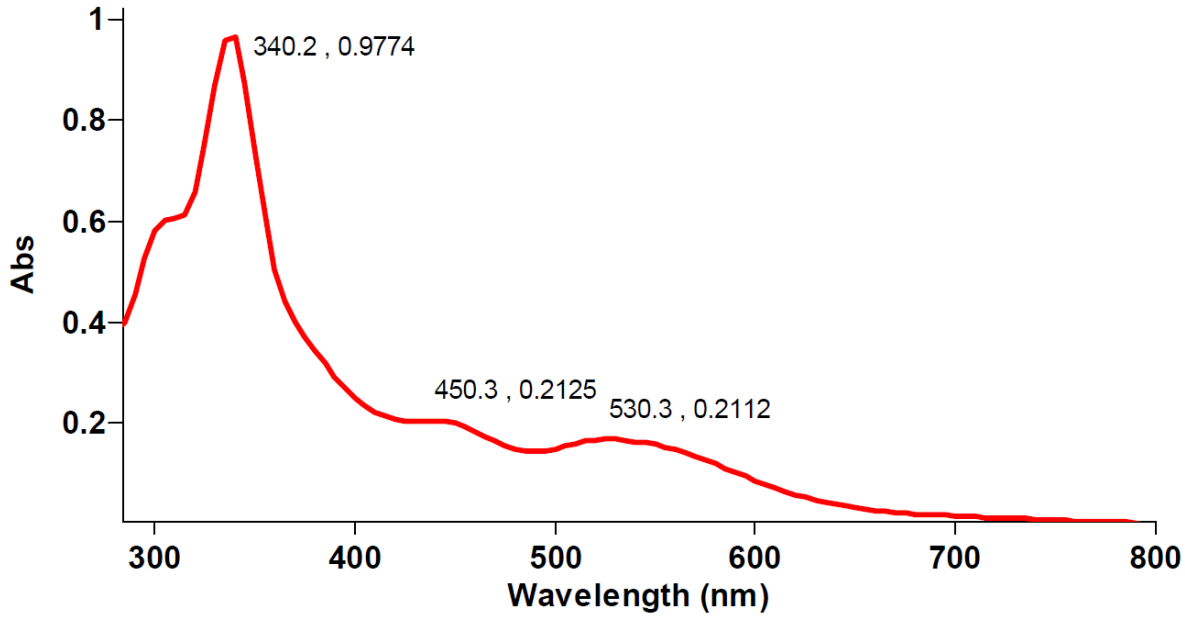

Figure S3. UV-Vis absorption spectrum of ***[NEt$_4$]$_2$[Pd$_2$I$_6$]***

[P(^{n}Bu)PPh$_3$]$_2$[Pd$_2$I$_6$]

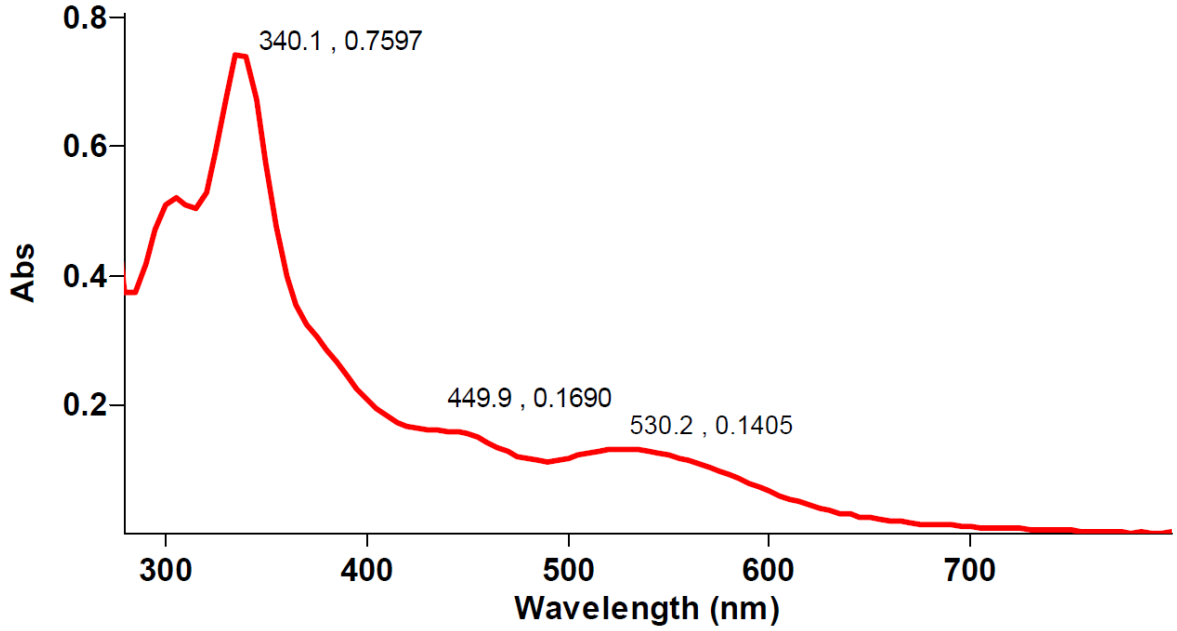

Figure S4. UV-Vis absorption spectrum of ***[P(^{n}Bu)PPh$_3$]$_2$[Pd$_2$I$_6$]***

[P^{n}Bu$_4$]$_2$[Pd$_2$I$_6$]

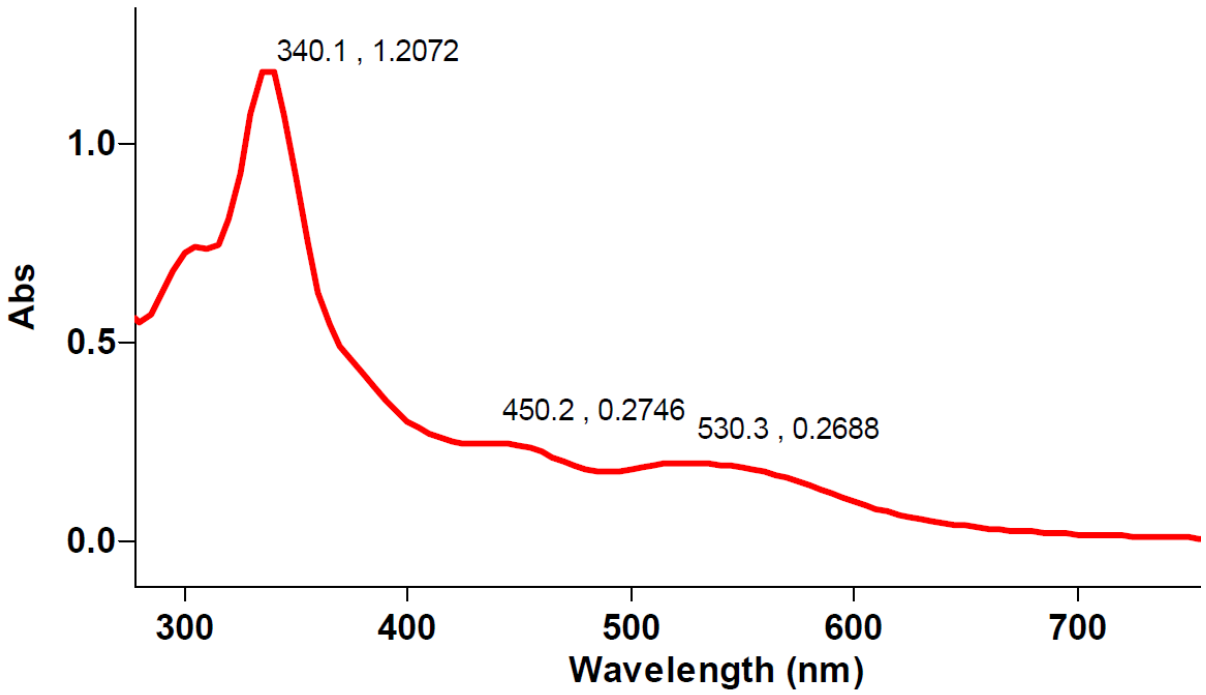

Figure S5. UV-Vis absorption spectrum of ***[P^{n}Bu$_4$]$_2$[Pd$_2$I$_6$]***

7.2. ^{1}H NMR Spectra

[AuI$_2$(Me$_2$dazdt)]BF$_4$ (5)

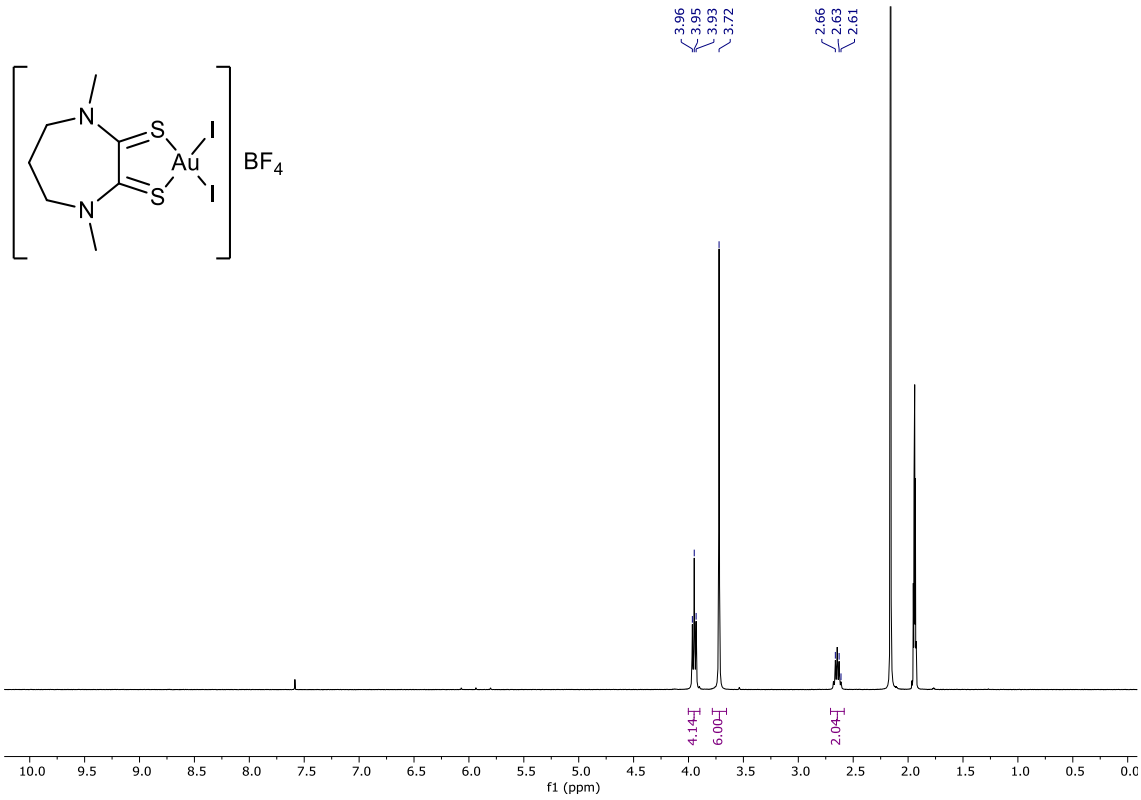

Figure S6. ^{1}H NMR (400 MHz, Acetonitrile-d_3) spectrum of [AuI$_2$(Me$_2$dazdt)]BF$_4$ (**5**)……..

[AuBr$_2$(Me$_2$dazdt)]BF$_4$ (**6**)

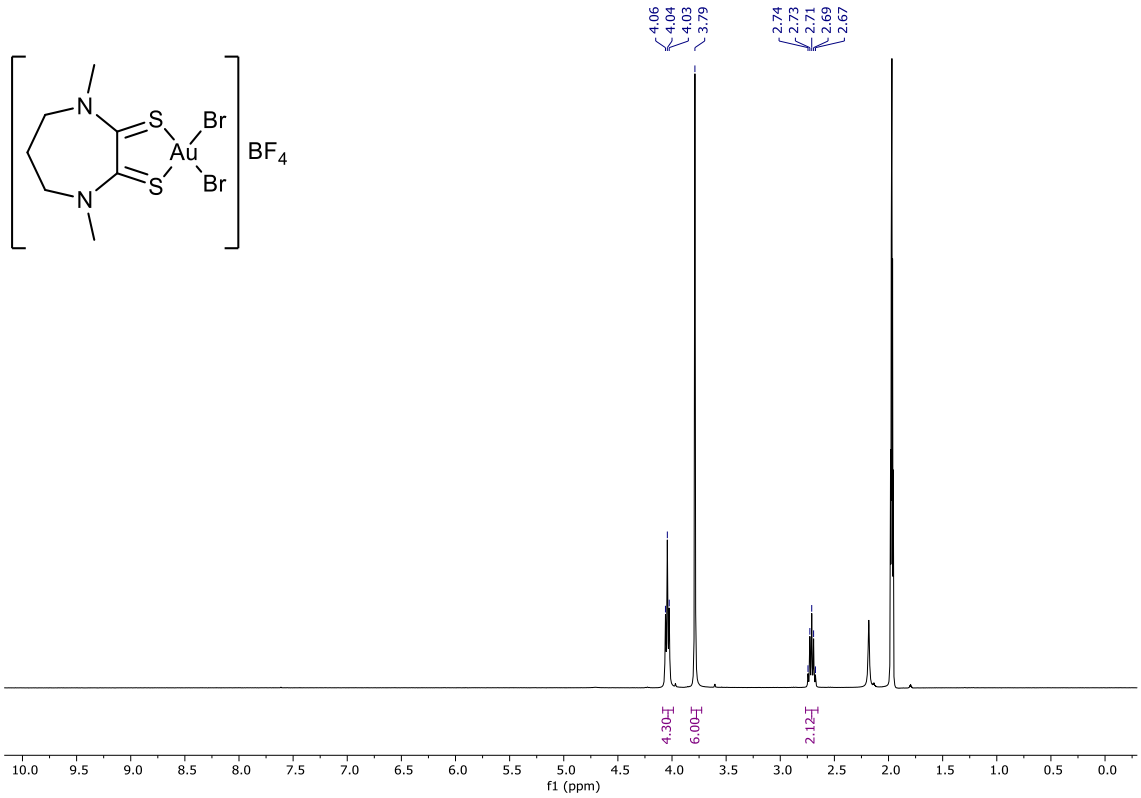

Figure S7. ^{1}H NMR (400 MHz, Acetonitrile-d_3) spectrum of [AuBr$_2$(Me$_2$dazdt)]BF$_4$ (**6**)

N-(Prop-2-yn-1-yl)benzamide

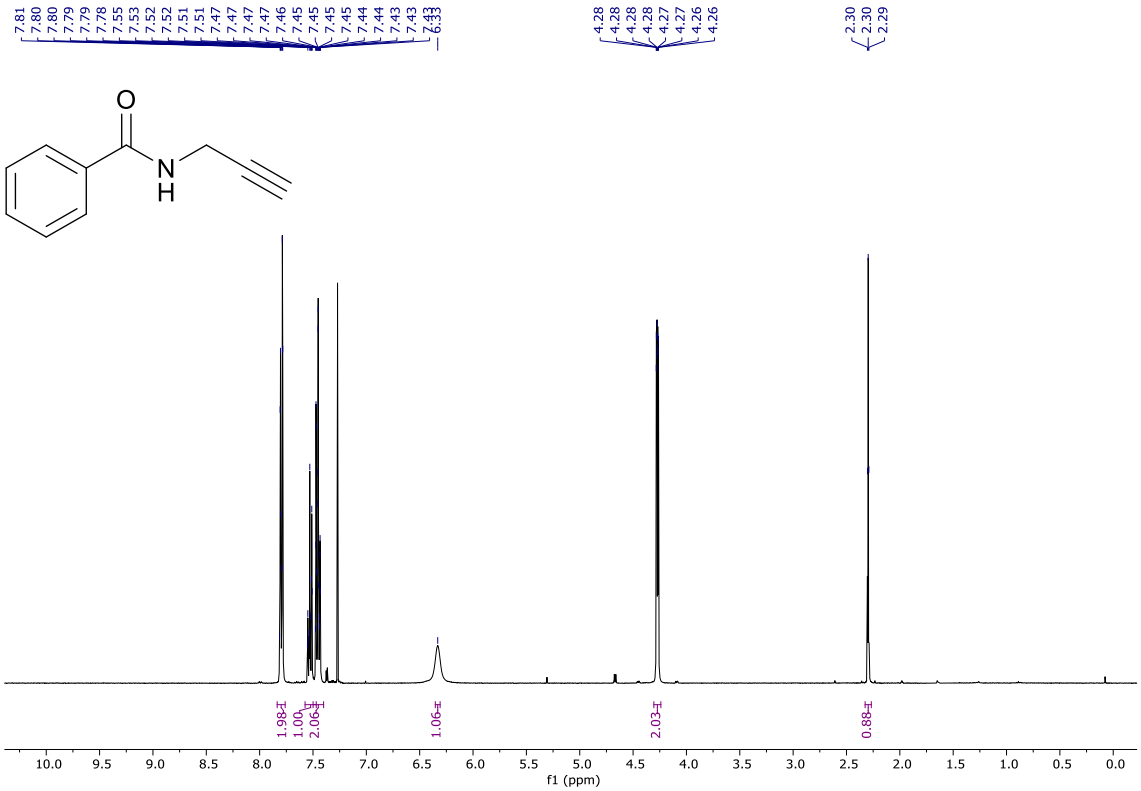

Figure S8. ^{1}H NMR (400 MHz, Chloroform-*d*) spectrum of *N-(prop-2-yn-1-yl)benzamide*

N-(3-Phenylprop-2-yn-1-yl)benzamide

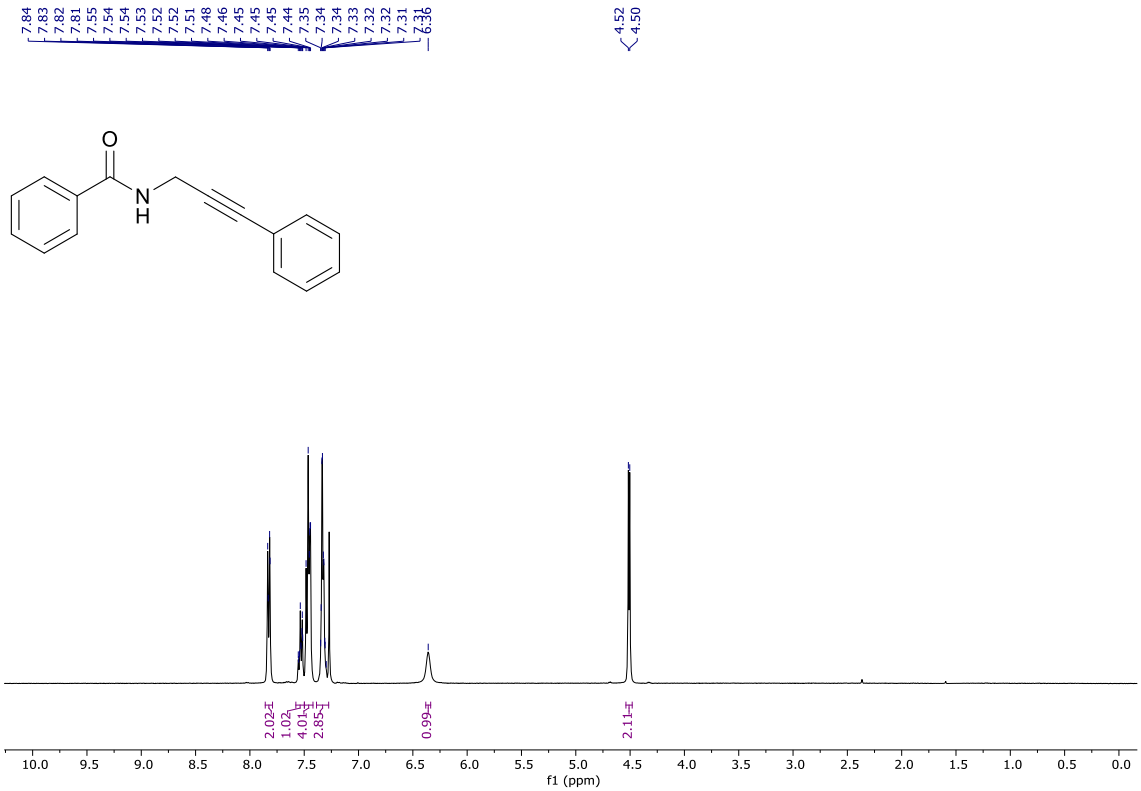

Figure S9. ^{1}H NMR (400 MHz, Chloroform-*d*) spectrum of *N-(3-phenylprop-2-yn-1-yl)benzamide*.

5-Methyl-2-phenyloxazole

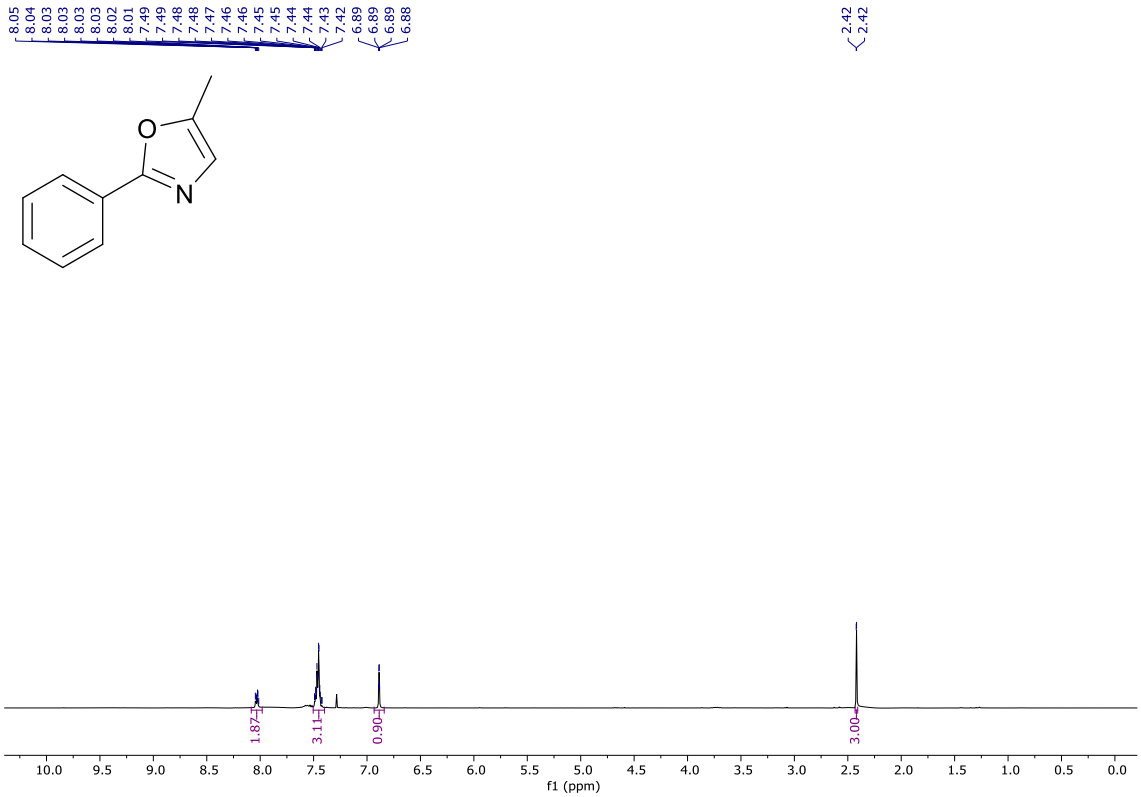

Figure S10. ^{1}H NMR (400 MHz, Chloroform-*d*) spectrum of *5-methyl-2-phenyloxazole.*

(Z)-5-Benzylidene-2-phenyl-4,5-dihydrooxazole

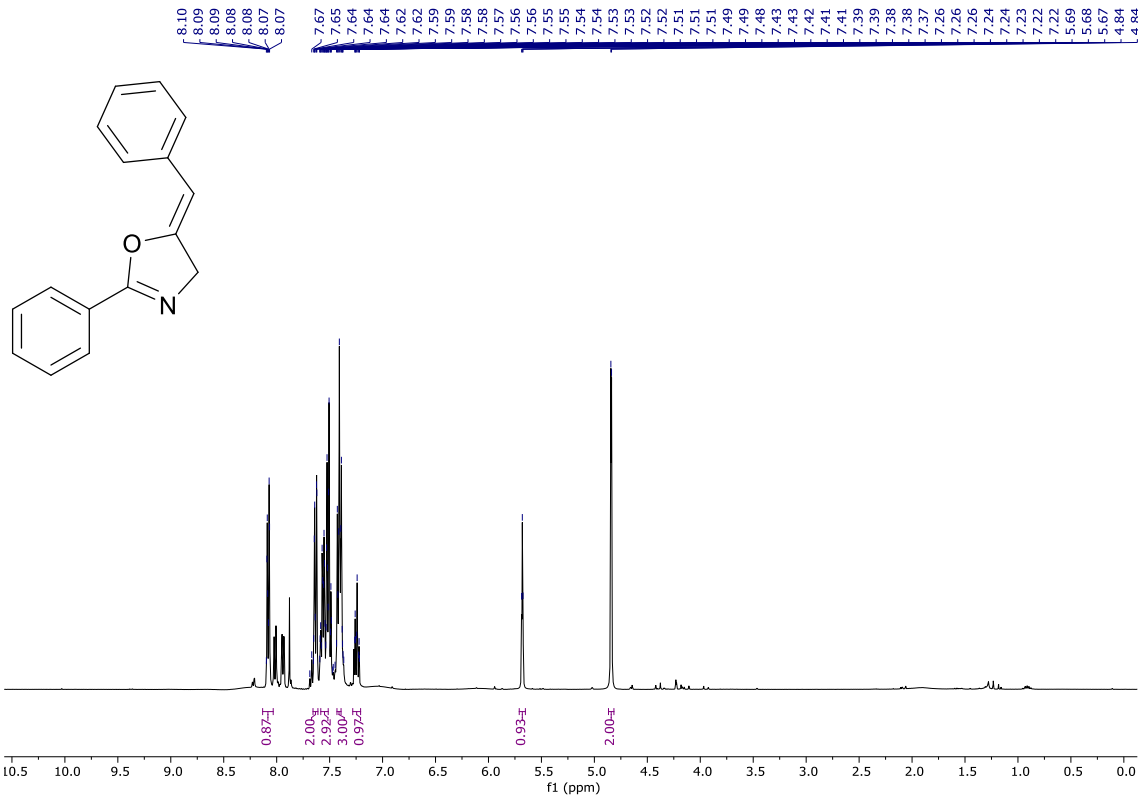

Figure S11. ^{1}H NMR (400 MHz, Chloroform-*d*) spectrum of *(Z)-5-benzylidene-2-phenyl-4,5-dihydrooxazole*

(E)-5-(Iodo(phenyl)methylene)-2-phenyl-4,5-dihydrooxazole

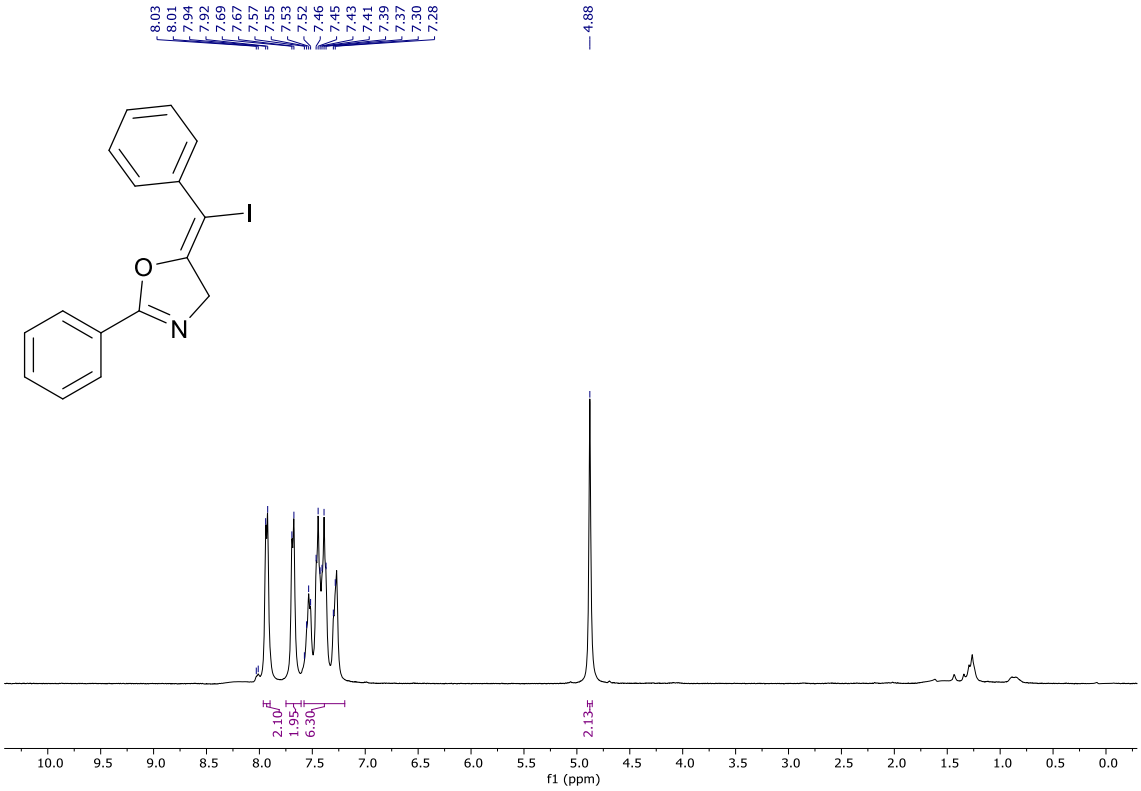

Figure S12. ^{1}H NMR (400 MHz, Chloroform-*d*) spectrum of *(E)-5-(iodo(phenyl)methylene)-2-phenyl-4,5-dihydrooxazole*.

Condensation of *o*-iodoaniline and acetylacetone

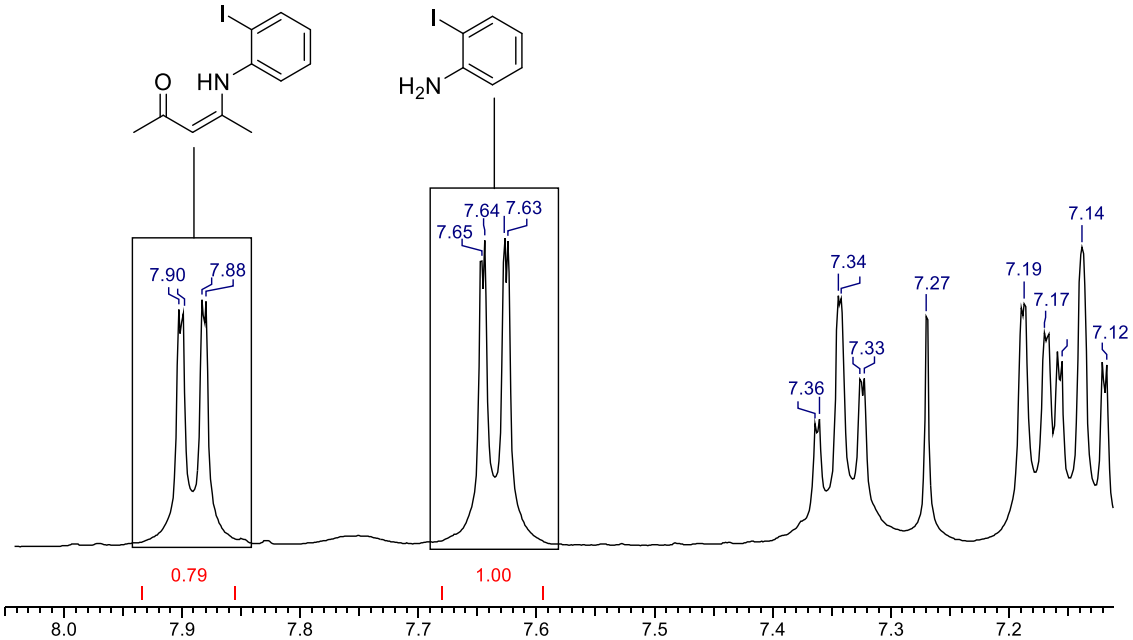

Figure S13. Example ^{1}H NMR (400 MHz, Chloroform-*d*) spectrum of a crude *o*-iodoaniline and acetylacetone condensation reaction mixture illustrating reaction monitoring.

Addition of 1,3-dimethoxybenzene to methyl vinyl ketone.

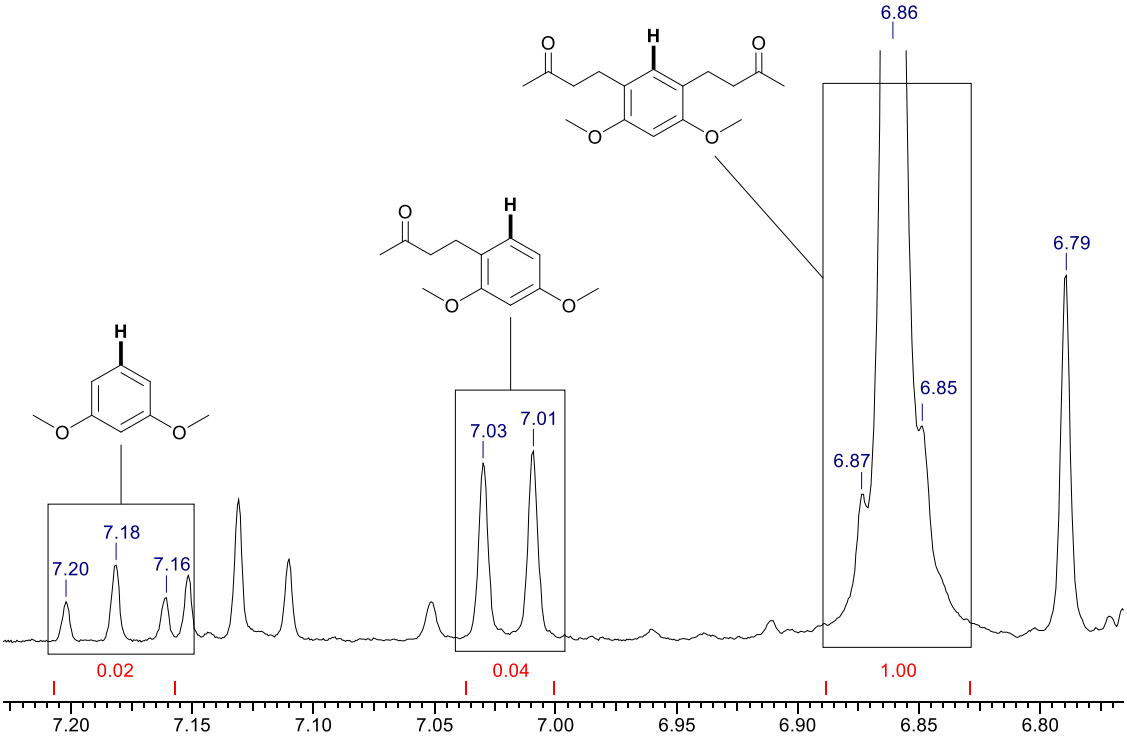

Figure S14. Example ^{1}H NMR (400 MHz, Chloroform-*d*) spectrum of the crude reaction mixture from the addition of 1,3-dimethoxybenzene to methyl vinyl ketone illustrating reaction monitoring.

4,4'-(Azulene-1,3-diyl)bis(butan-2-one)2

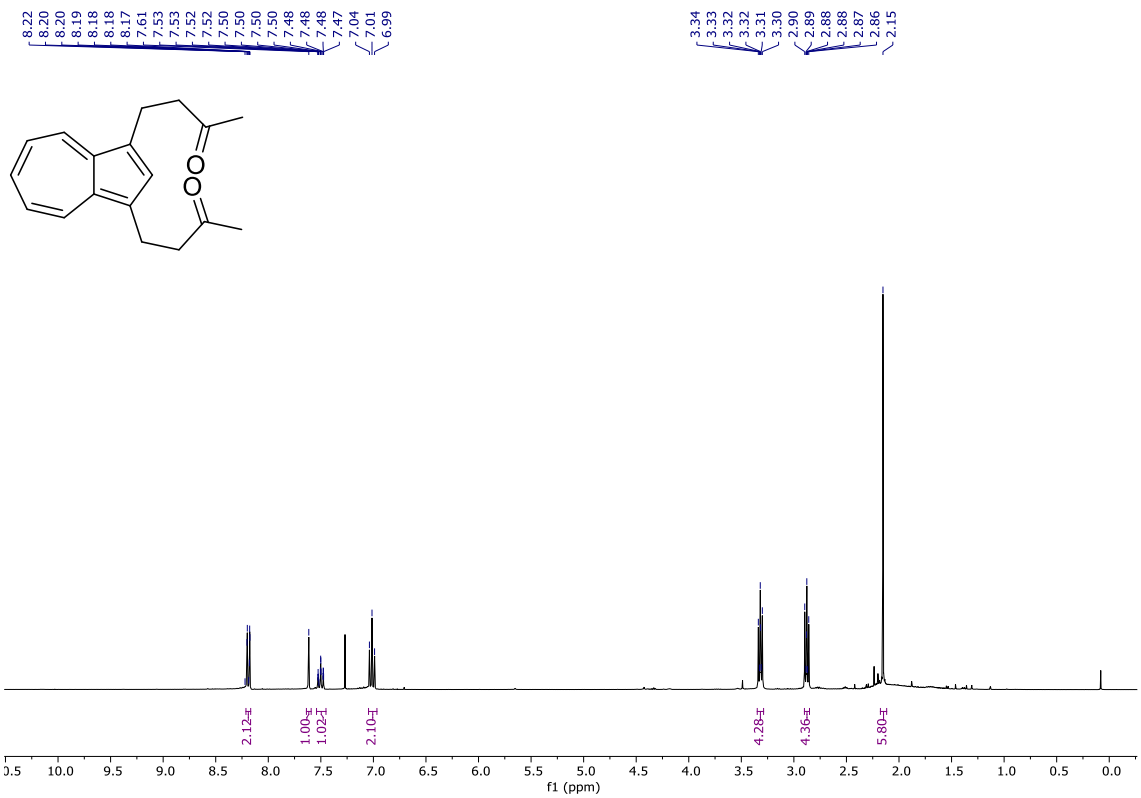

Figure S15. ^{1}H NMR (400 MHz, Chloroform-*d*) spectrum of *4,4'-(azulene-1,3-diyl)bis(butan-2-one)2.*

4-(5-Methylfuran-2-yl)butan-2-one

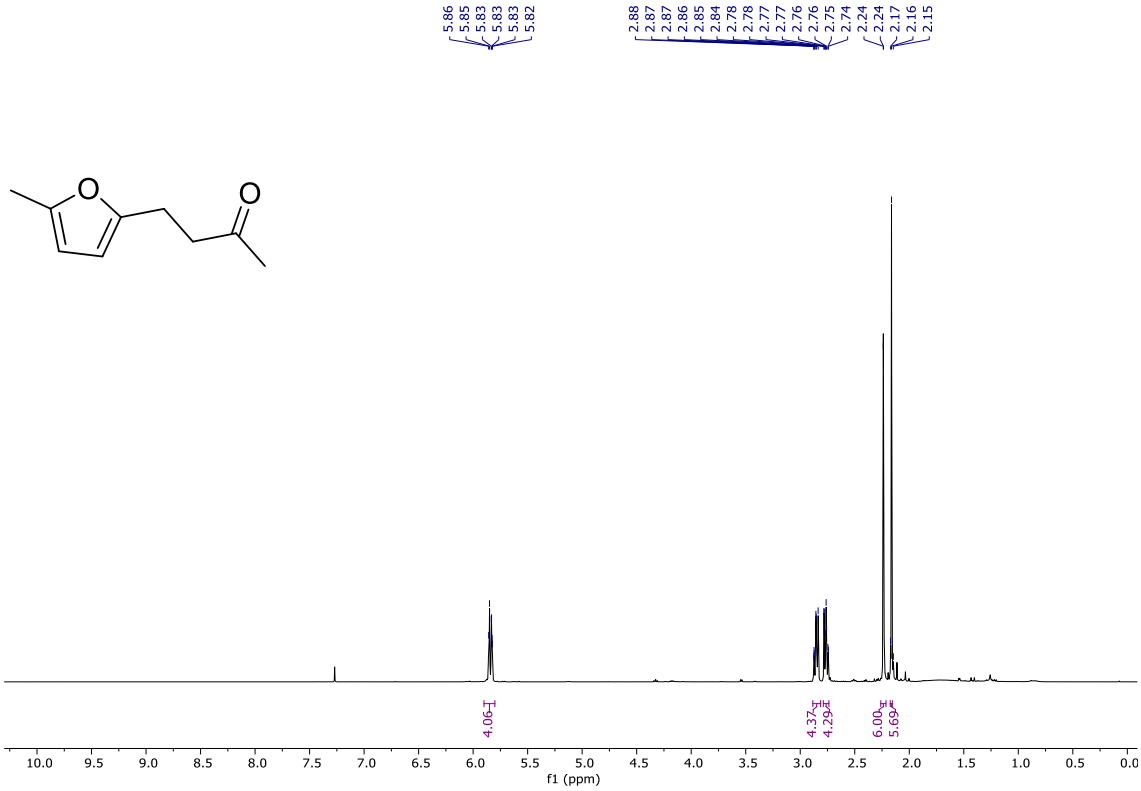

Figure S16. ^{1}H NMR (400 MHz, Chloroform-*d*) spectrum of *4-(5-methylfuran-2-yl)butan-2-one.*

3-(5-Methylfuran-2-yl)cyclohexan-1-one

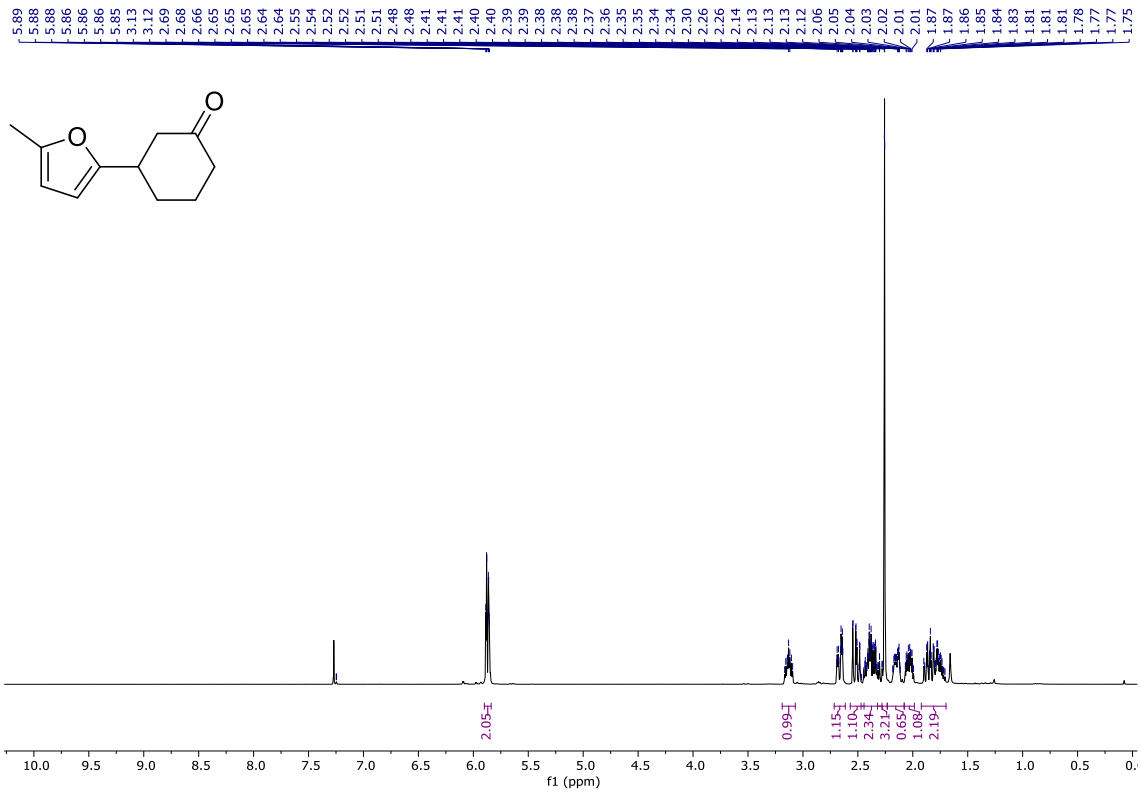

Figure S17. ^{1}H NMR (400 MHz, Chloroform-*d*) spectrum of *3-(5-methylfuran-2-yl)cyclohexan-1-one.*

3-Chloro-4-methoxy-1,1'-biphenyl

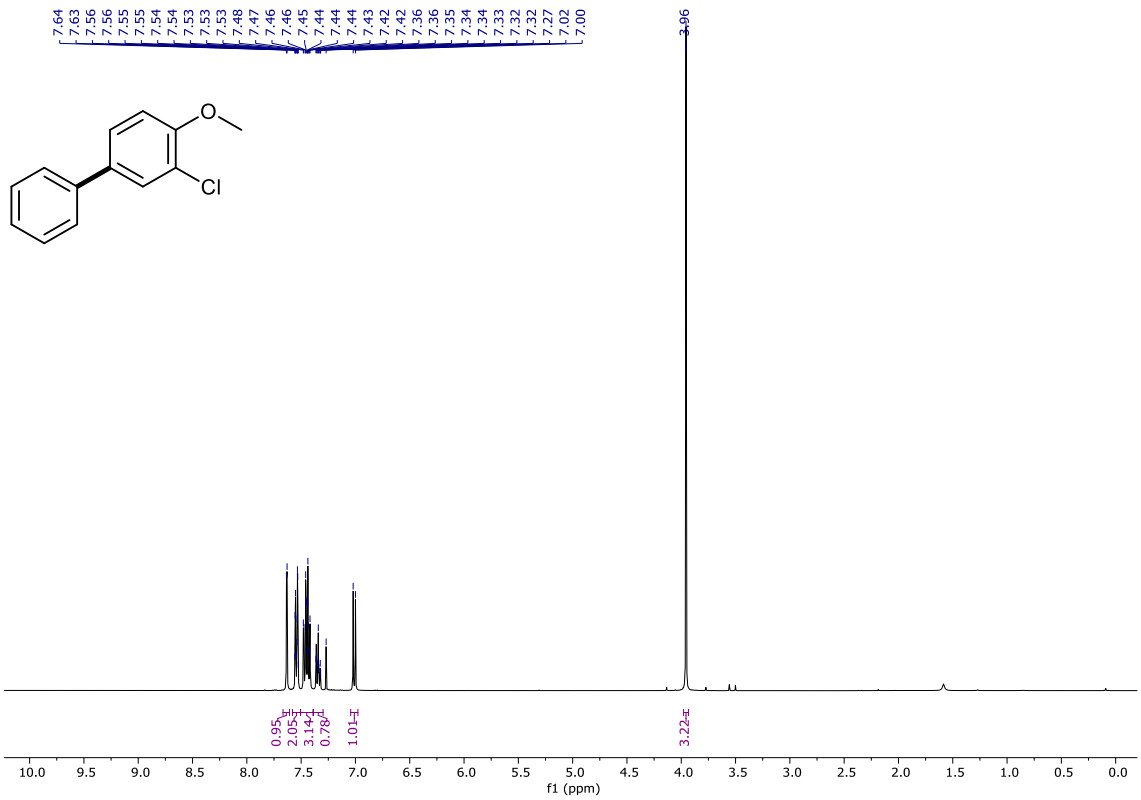

Figure S18. ^{1}H NMR (400 MHz, Chloroform-*d*) spectrum of *3-chloro-4-methoxy-1,1'-biphenyl.*

3-Bromo-4-methoxy-1,1'-biphenyl

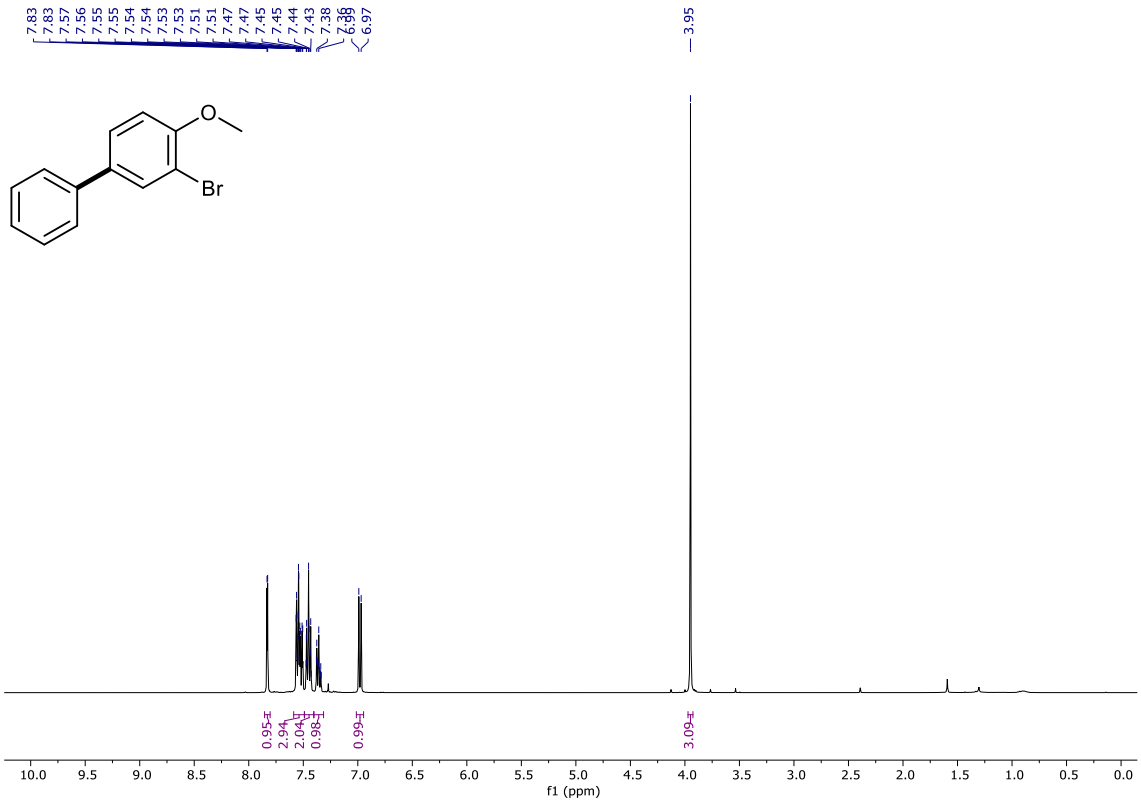

Figure S19. ^{1}H NMR (400 MHz, Chloroform-*d*) spectrum of *3-bromo-4-methoxy-1,1'-biphenyl.*

3,4-Dimethyl-1,1'-biphenyl

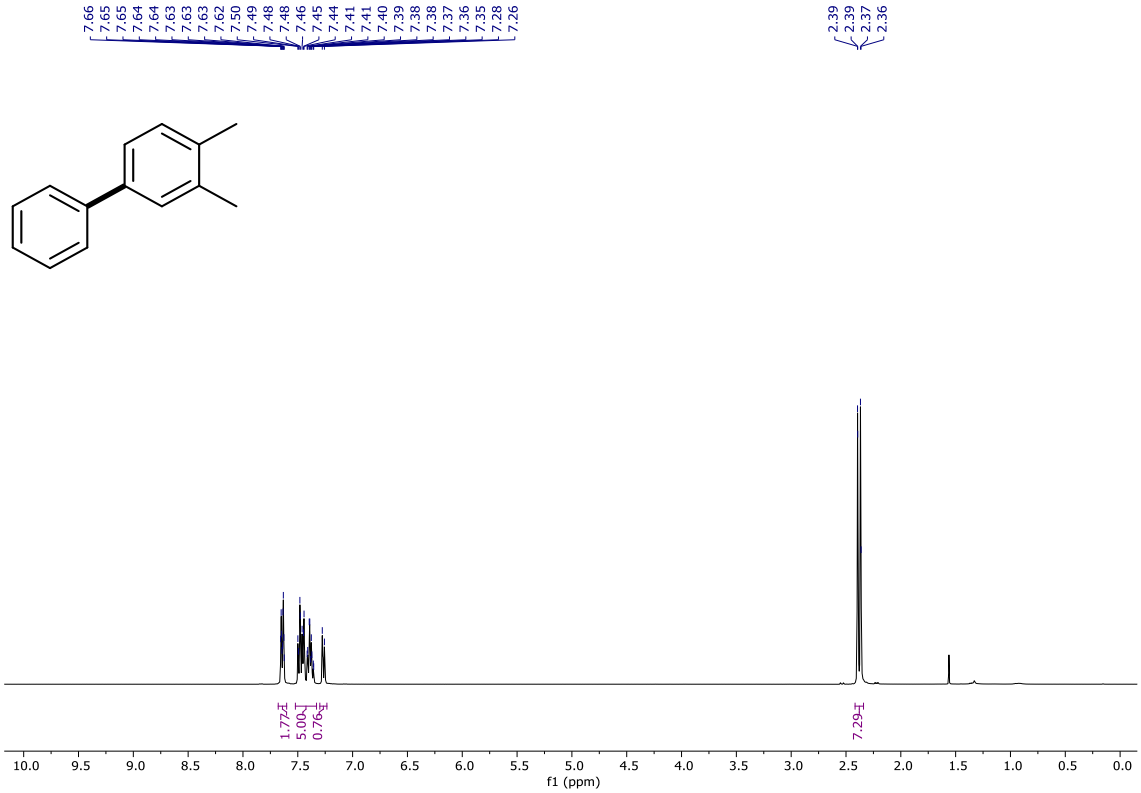

Figure S20. ^{1}H NMR (400 MHz, Chloroform-*d*) spectrum of *3,4-dimethyl-1,1'-biphenyl*.

4-Methyl-1,1'-biphenyl

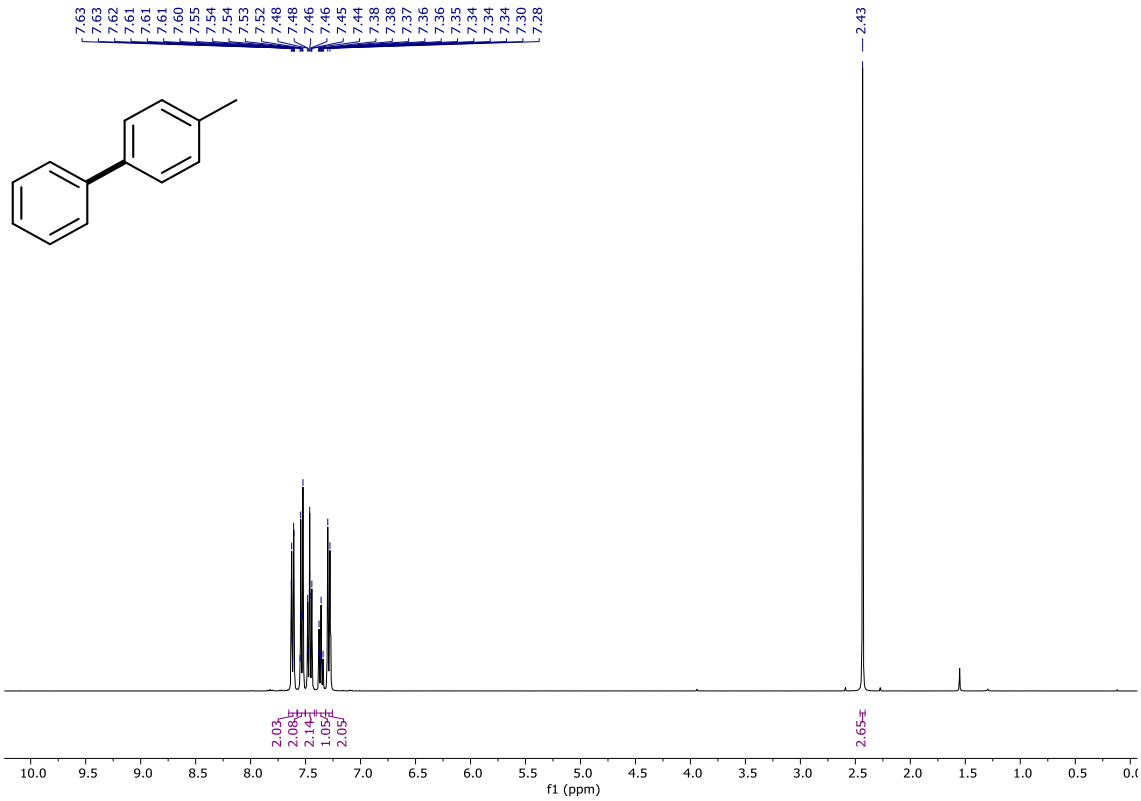

Figure S21. ^{1}H NMR (400 MHz, Chloroform-*d*) spectrum of *4-methyl-1,1'-biphenyl.*

1-Methyl-4-phenylnaphthalene

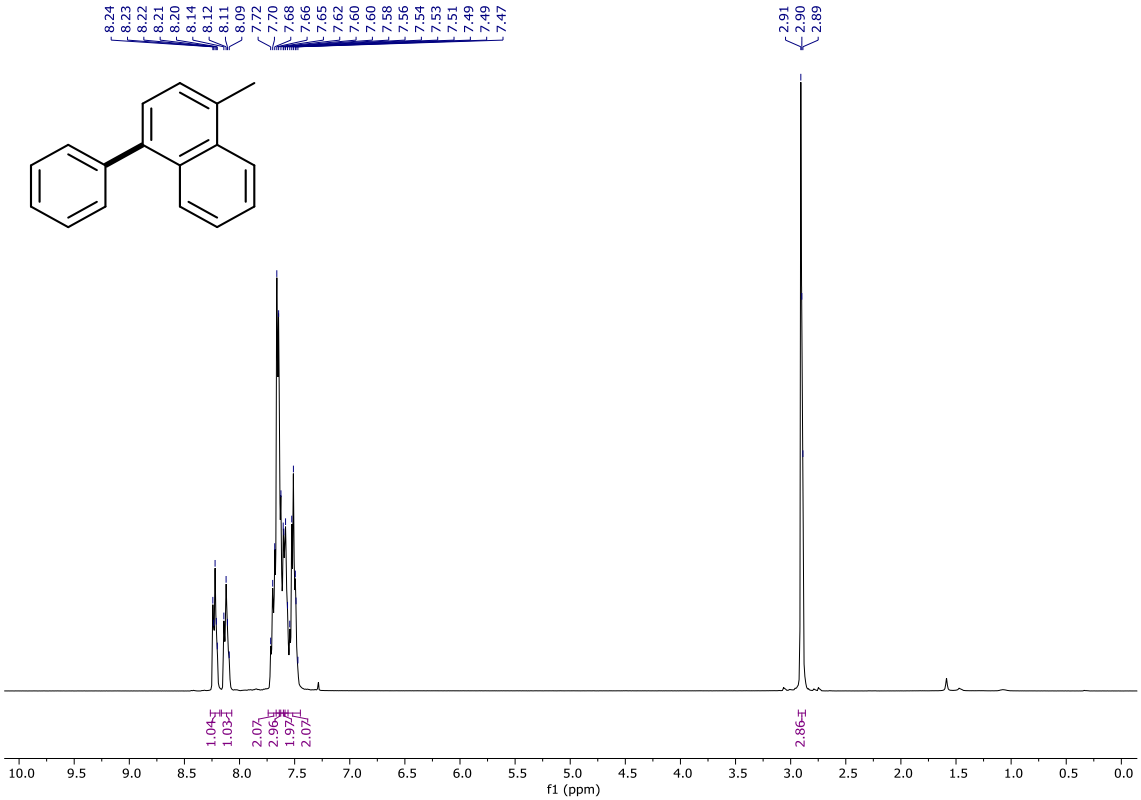

Figure S22. ^{1}H NMR (400 MHz, Chloroform-*d*) spectrum of *1-methyl-4-phenylnaphthalene*

2-Bromo-5-phenylthiophene

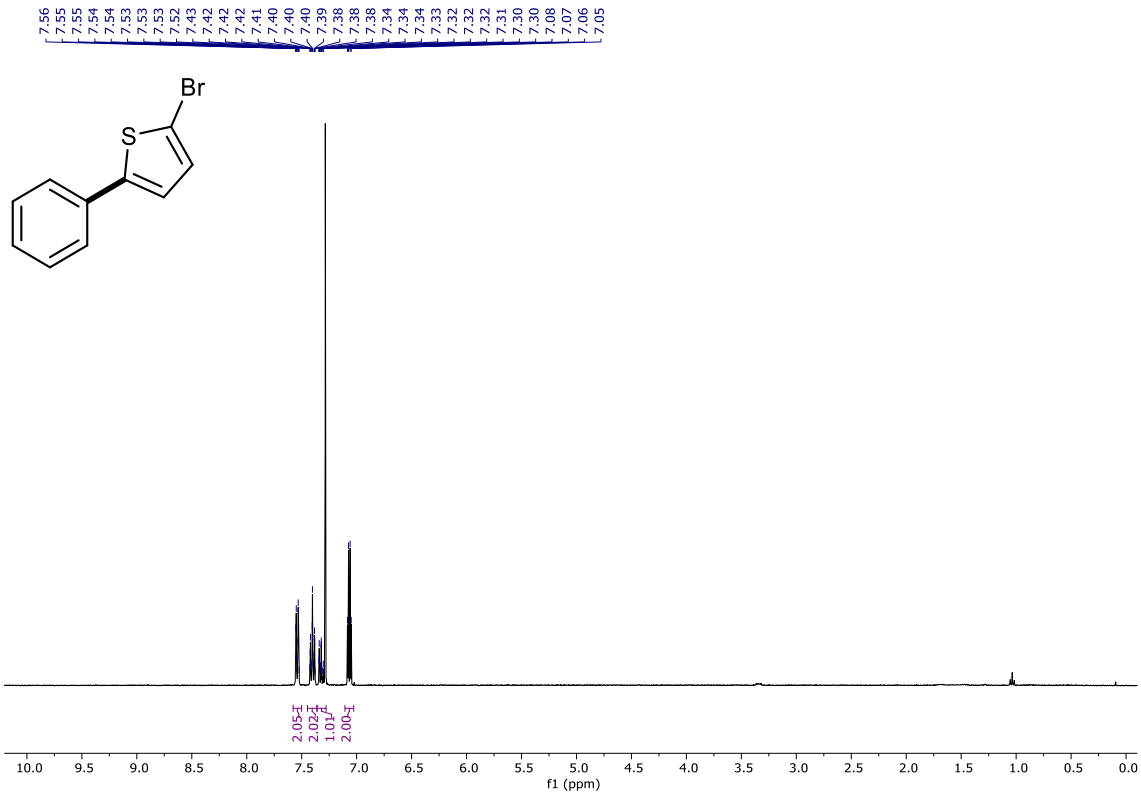

Figure S23. ^{1}H NMR (400 MHz, Chloroform-*d*) spectrum of *2-bromo-5-phenylthiophene.*

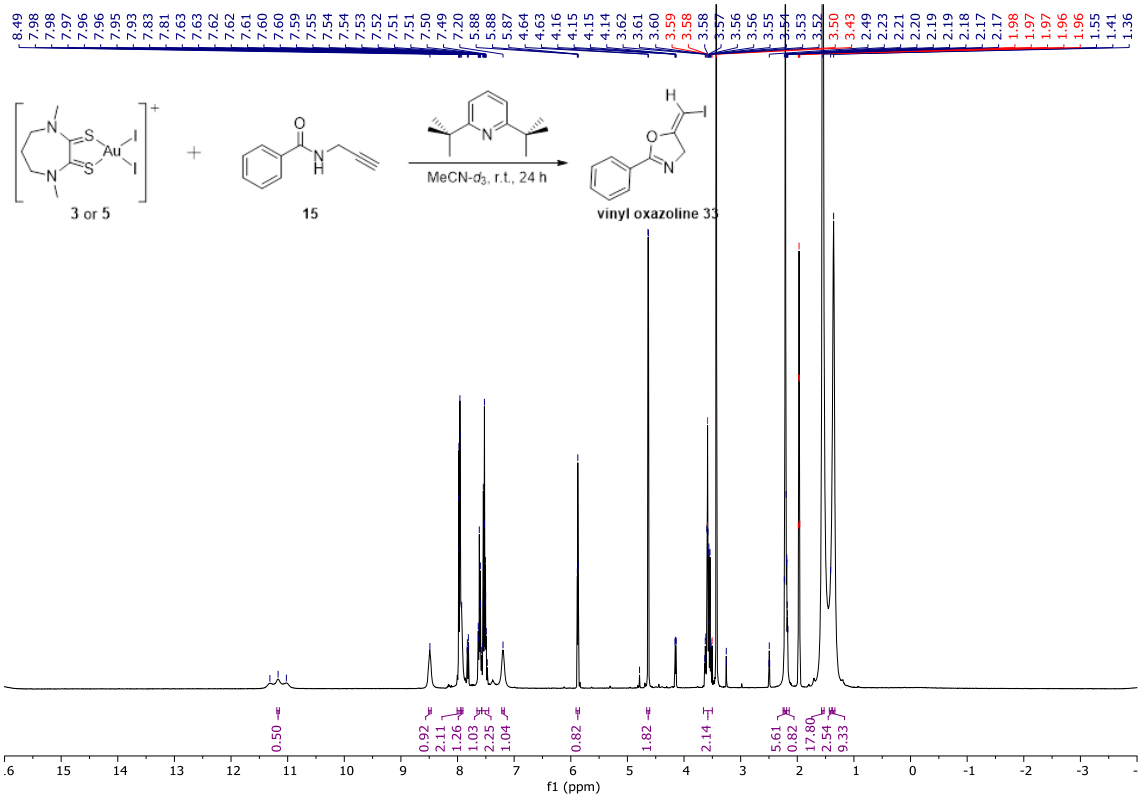

Figure S24. ^{1}H NMR (400 MHz, Chloroform-*d*) spectrum from the synthesis of **30** from the reaction of **3** and **15** in the presence of 2,6-di-*tert*-butylpyridine

4'-Chloro-2-nitro-1,1'-biphenyl

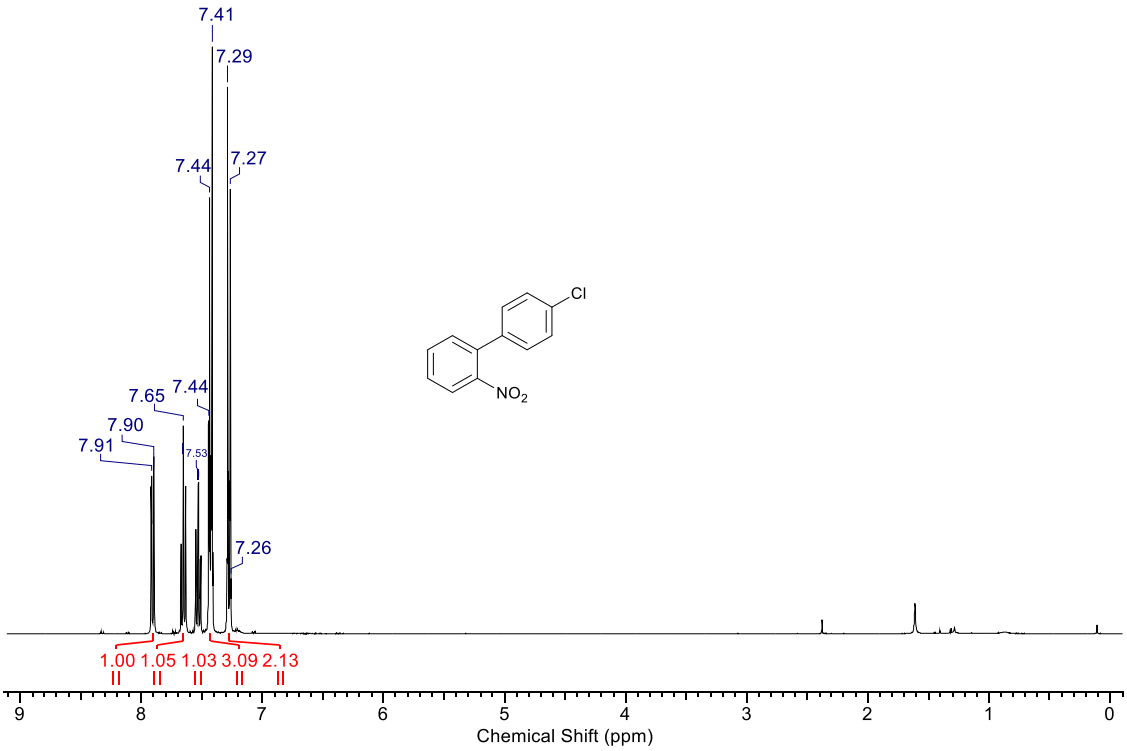

Figure S25. ^{1}H NMR (400 MHz, Chloroform-*d*) spectrum of *4'-chloro-2-nitro-1,1'-biphenyl.*

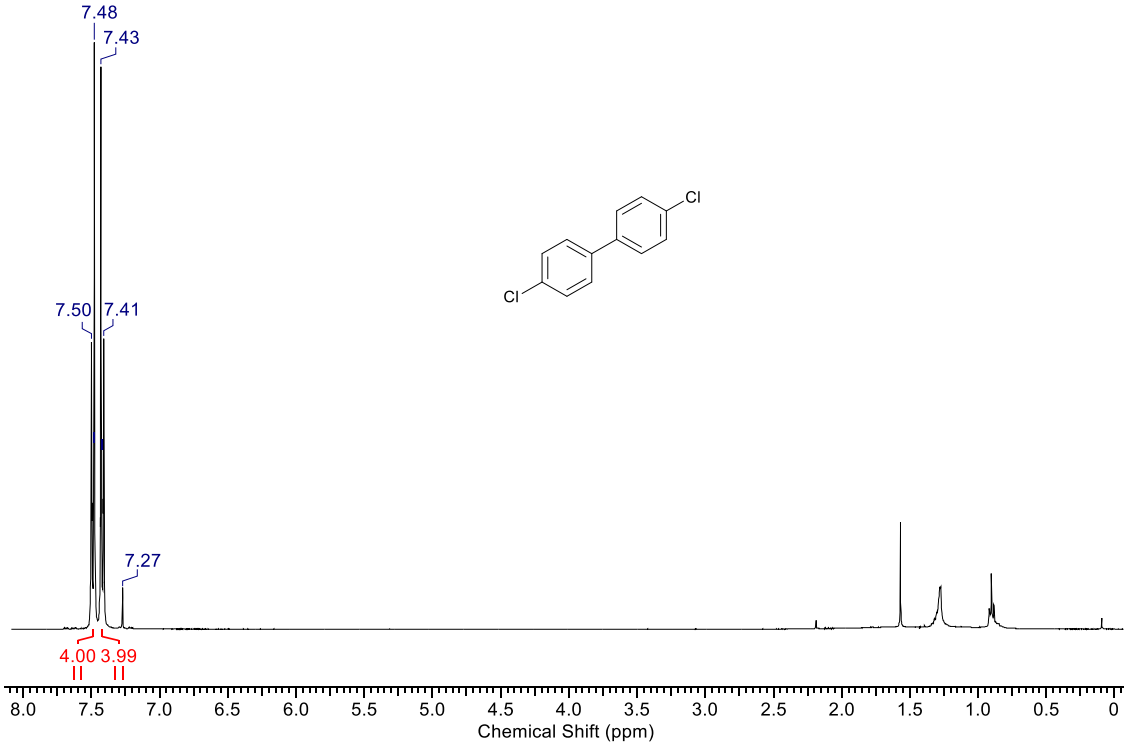

Figure S26. ^{1}H NMR (400 MHz, Chloroform-*d*) spectrum of *4,4'-dichloro-1,1'-biphenyl*

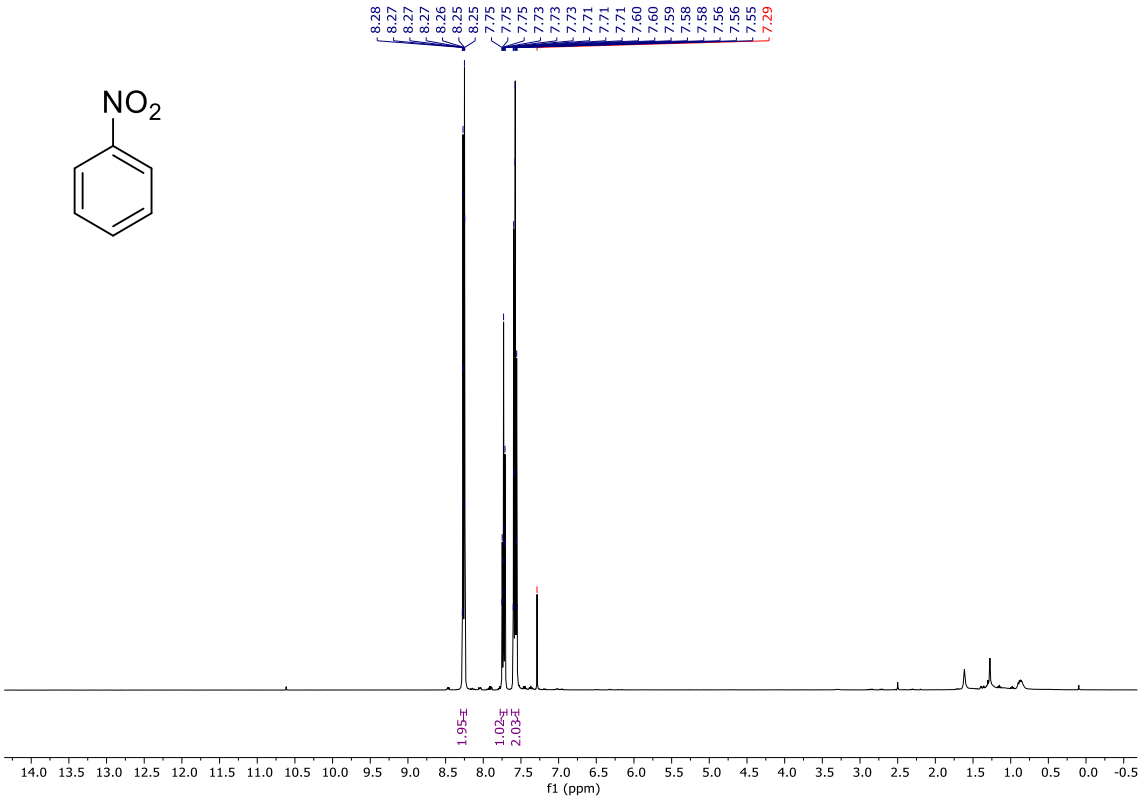

Figure S27. ^{1}H NMR (400 MHz, Chloroform-*d*) spectrum of *nitrobenzene*

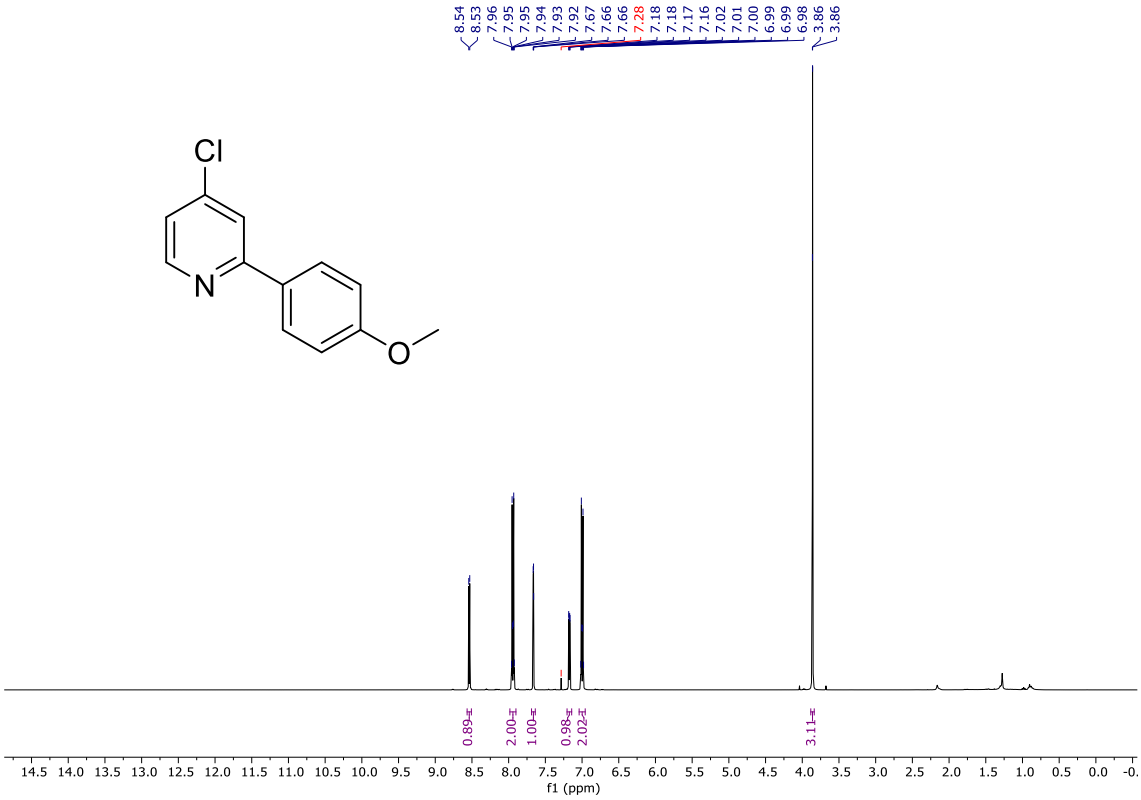

Figure S28. ^{1}H NMR (400 MHz, Chloroform-*d*) spectrum of 4-chloro-2-(4-methoxyphenyl)pyridine (**C2**).

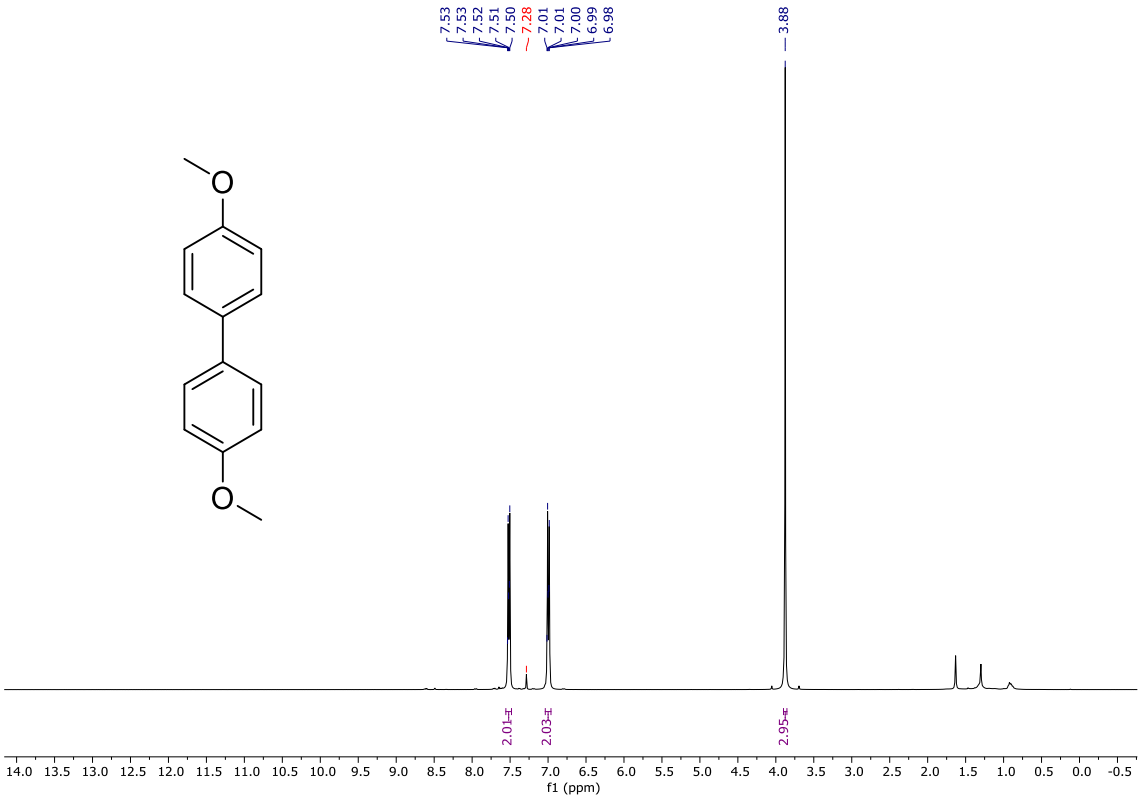

Figure S29. ^{1}H NMR (400 MHz, Chloroform-*d*) spectrum of 4,4'-dimethoxy-1,1'-biphenyl.

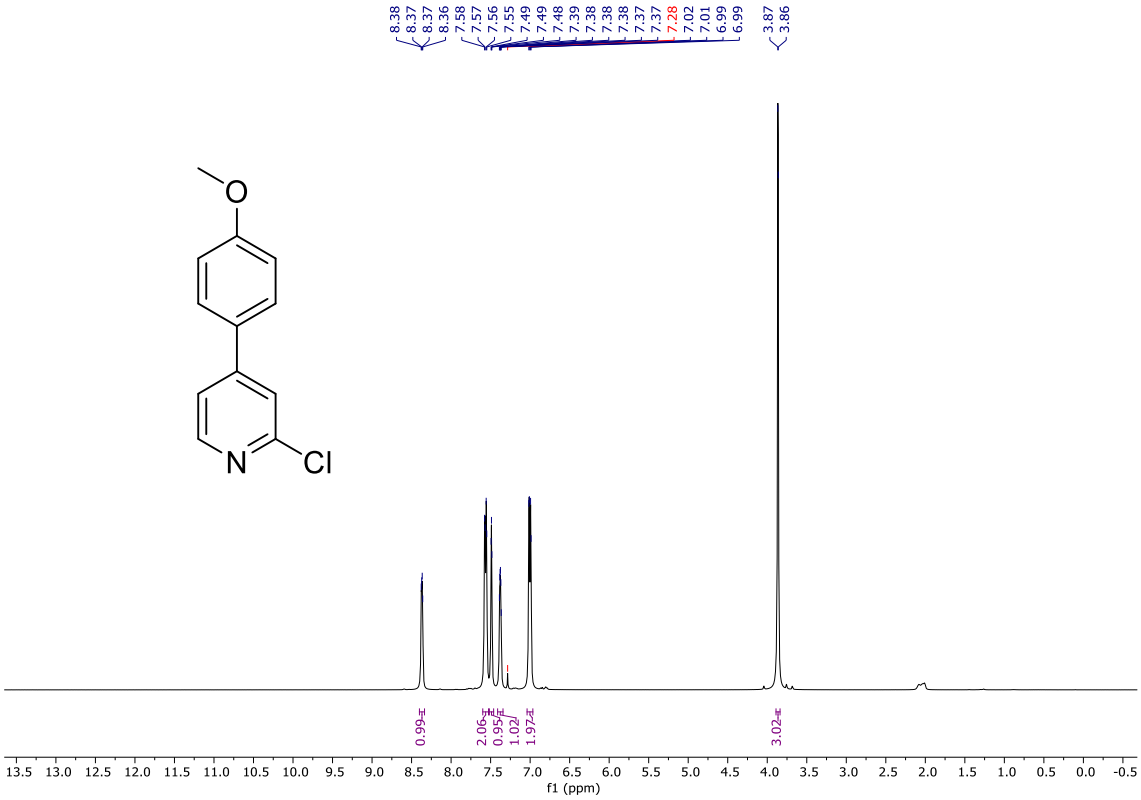

Figure S30. ^{1}H NMR (400 MHz, Chloroform-*d*) spectrum of 2-chloro-4-(4-methoxyphenyl)pyridine (**C4**).

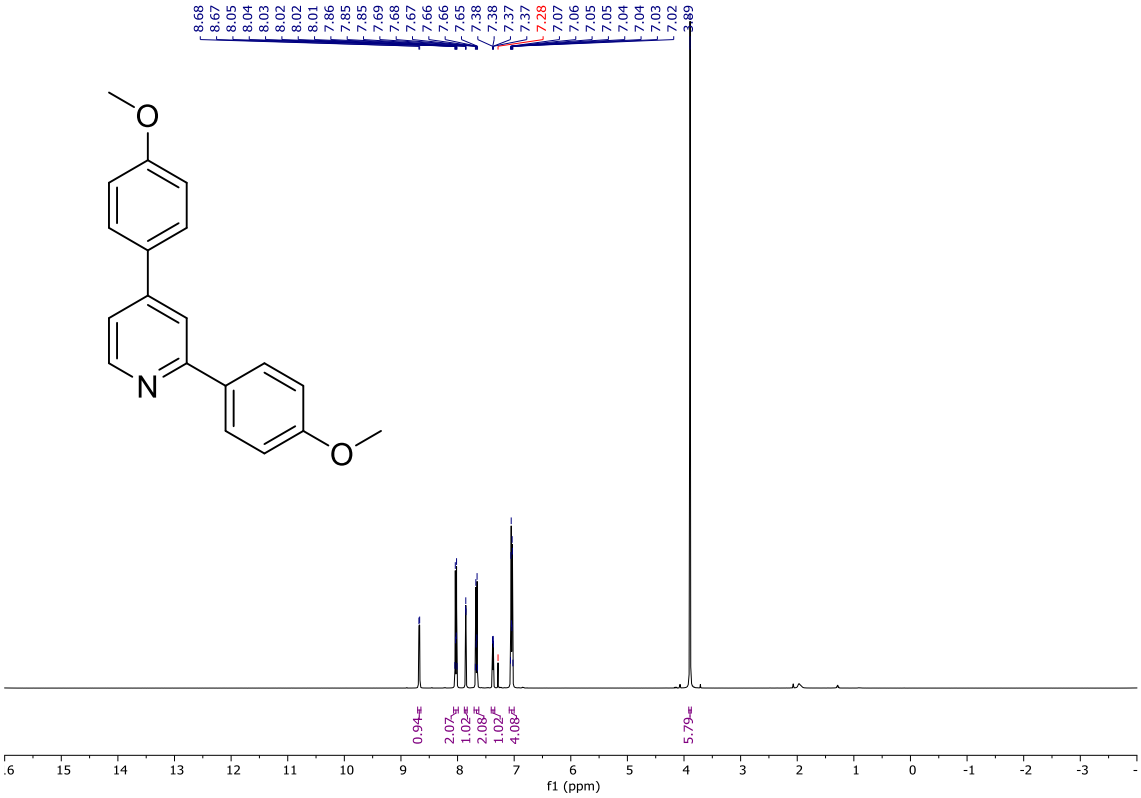

Figure S31. ^{1}H NMR (400 MHz, Chloroform-*d*) spectrum of 2,4-bis(4-methoxyphenyl)pyridine.

[N^{n}Bu$_4$][Pd$_2$I$_6$]

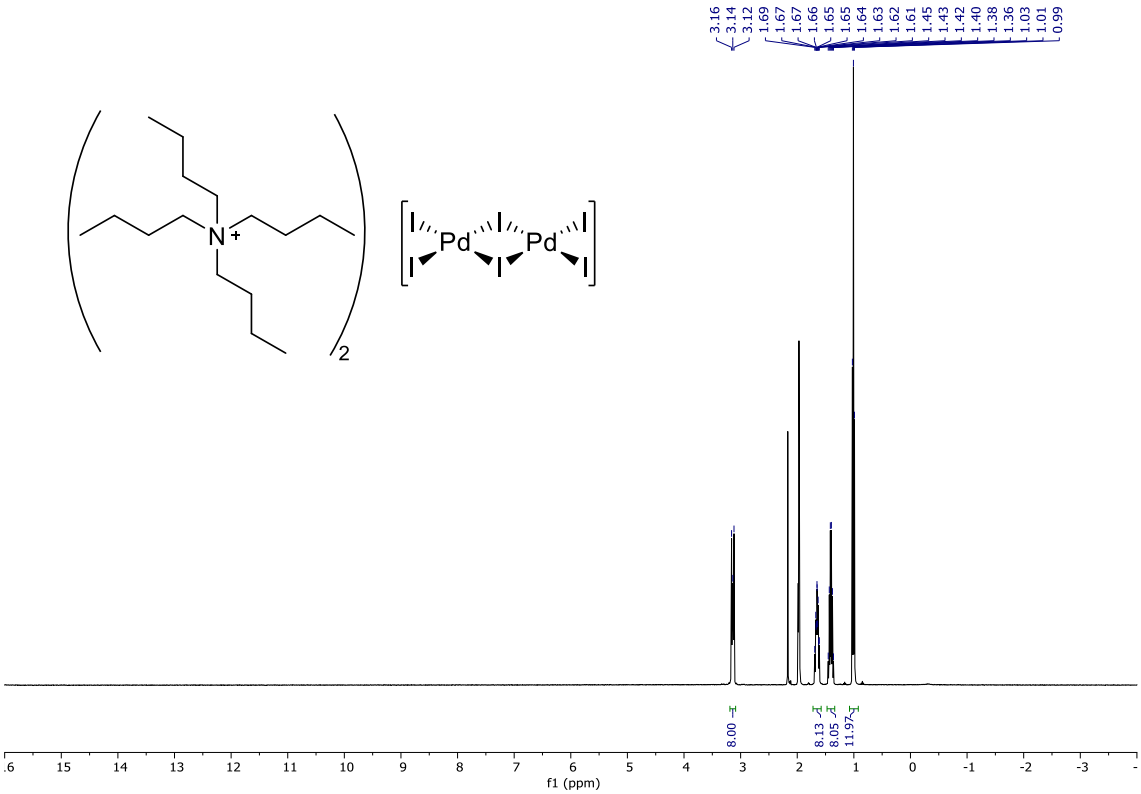

Figure S32. ^{1}H NMR (400 MHz, Acetonitrile-d_3) spectrum of [N^{n}Bu$_4$][Pd$_2$I$_6$].

[PPh$_4$][Pd$_2$I$_6$]

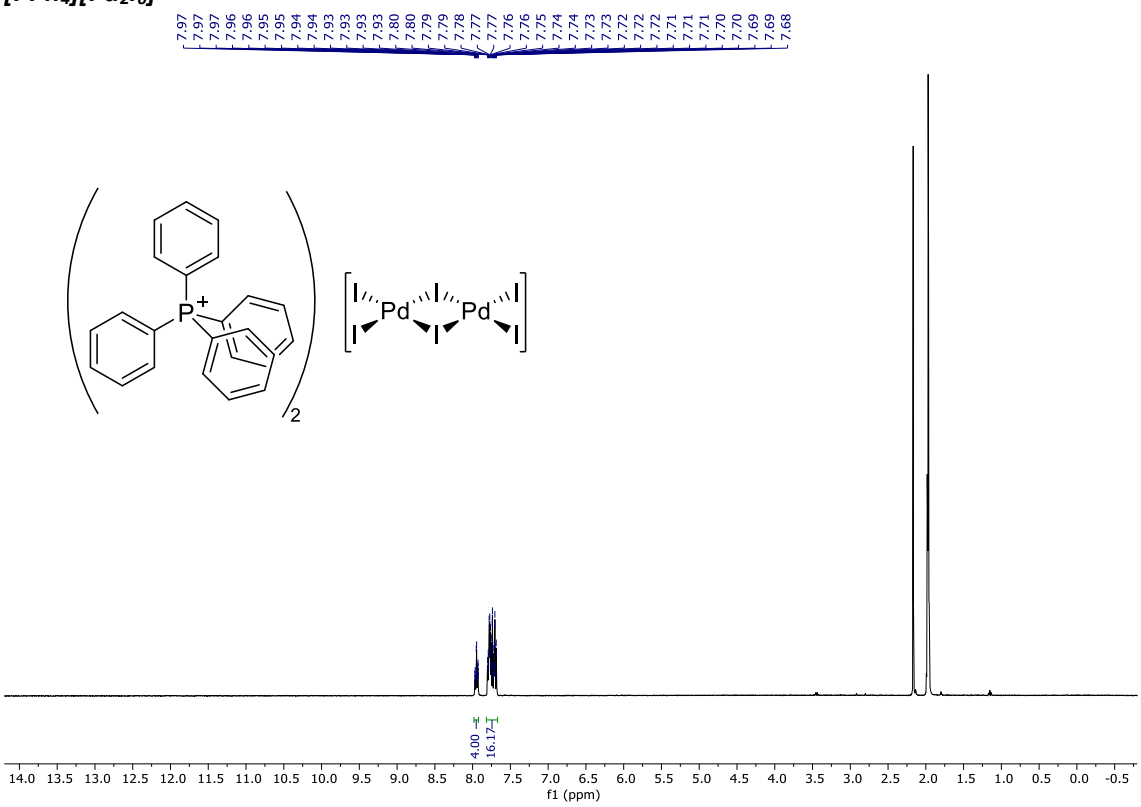

Figure S33. ^{1}H NMR (400 MHz, Acetonitrile-d_3) spectrum of [PPh$_4$][Pd$_2$I$_6$].

[P(ⁿBu)PPh₃]₂[Pd₂I₆]

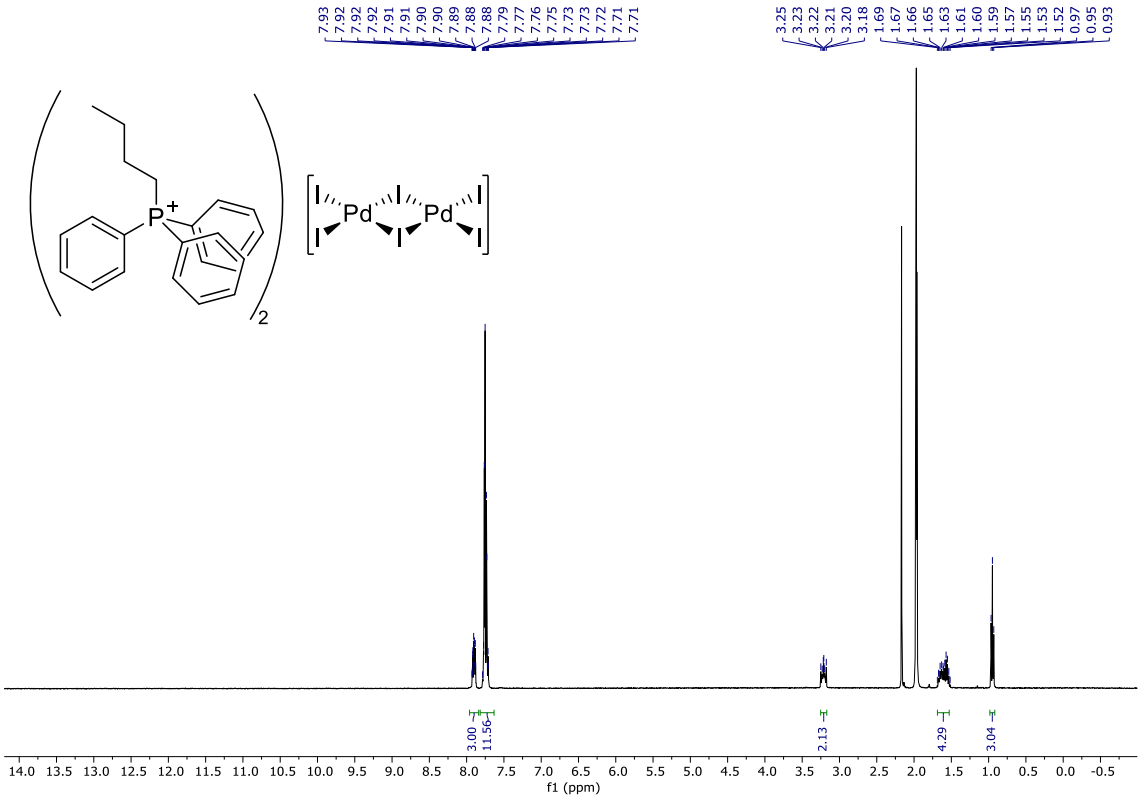

Figure S34. ^{1}H NMR (400 MHz, Acetonitrile-d_3) spectrum of $[P(^{n}Bu)PPh_3]_2[Pd_2I_6]$.

[NEt₄]₂[Pd₂I₆]

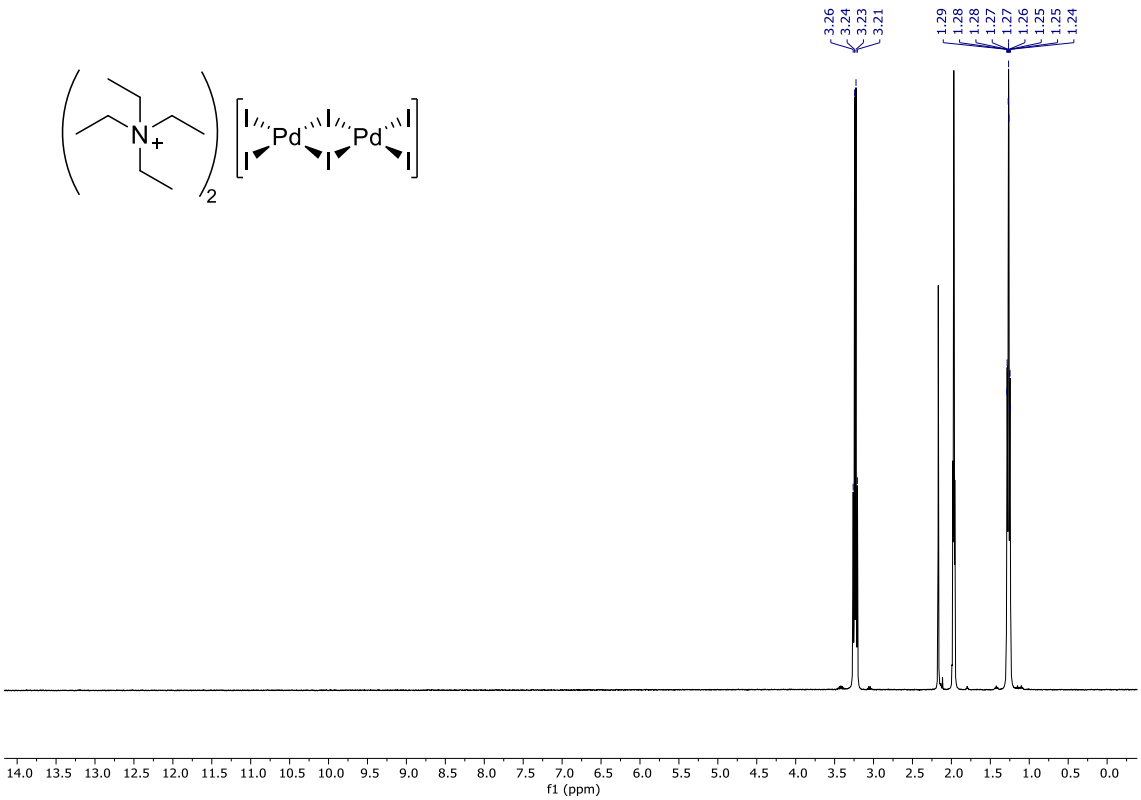

Figure S35. ^{1}H NMR (400 MHz, Acetonitrile-d_3) spectrum of $[NEt_4]_2[Pd_2I_6]$.

[P^{n}Bu$_4$][Pd$_2$I$_6$]

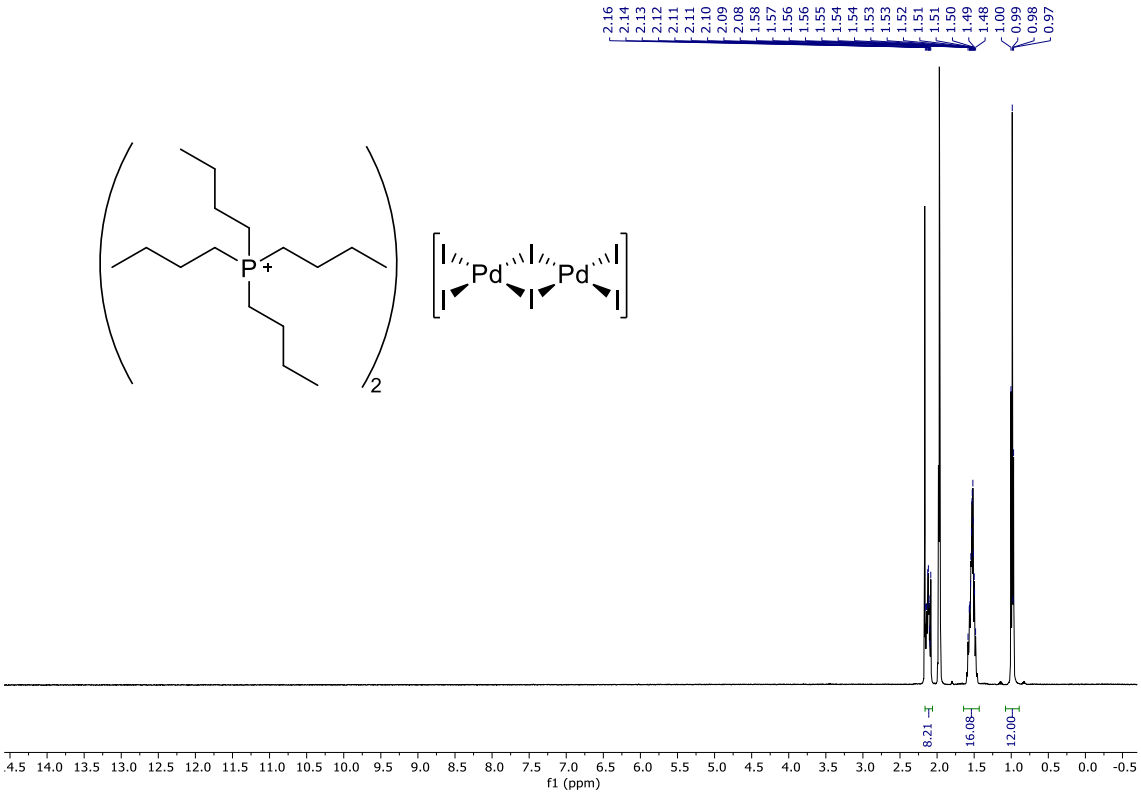

Figure S36. ^{1}H NMR (400 MHz, Acetonitrile-d_3) spectrum of $[NEt_4]_2[Pd_2I_6]$.

7.3. ^{13}C NMR Spectra

N-(Prop-2-yn-1-yl)benzamide

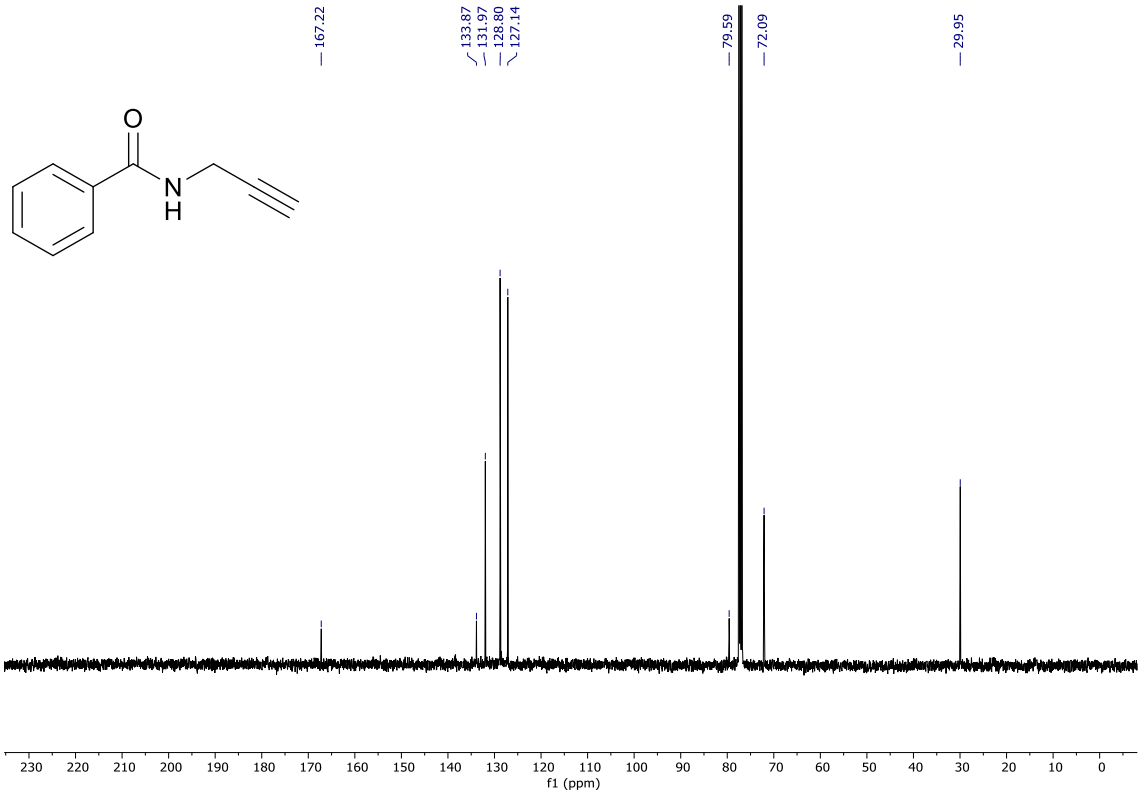

Figure S37. ^{13}C NMR (101 MHz, Chloroform-*d*) spectrum of *N-(prop-2-yn-1-yl)benzamide.*

(Z)-5-Benzylidene-2-phenyl-4,5-dihydrooxazole

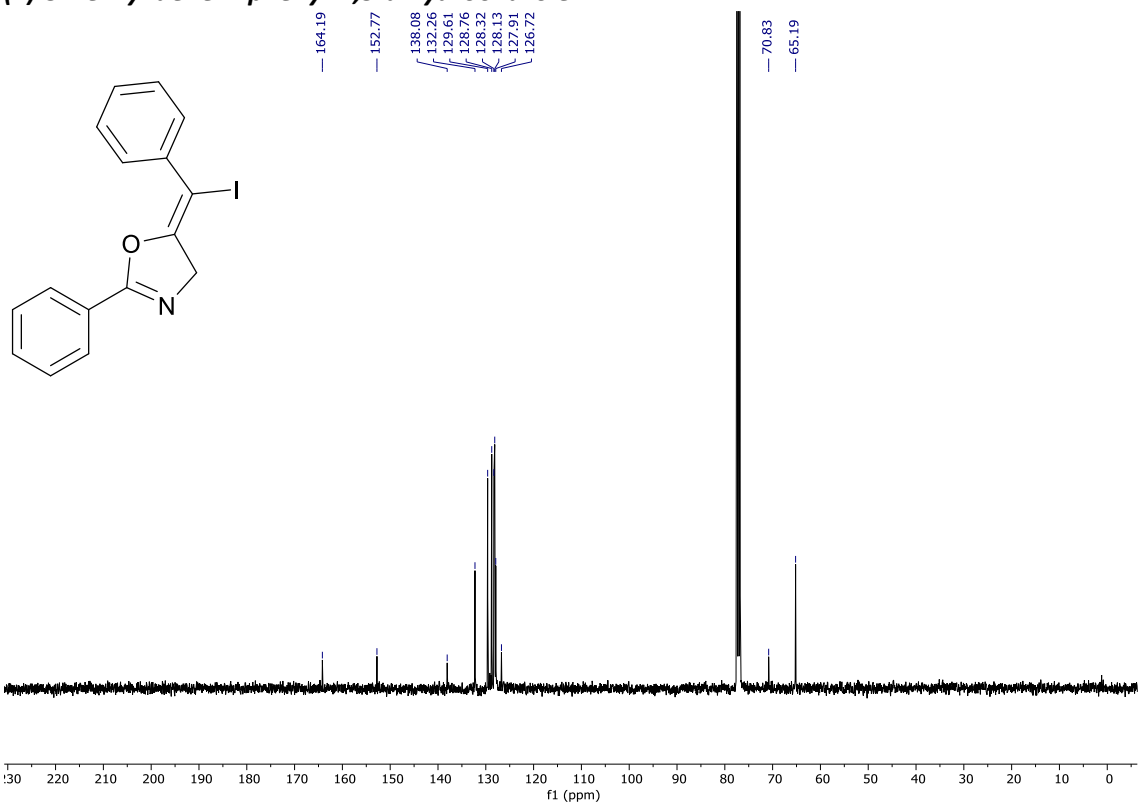

Figure S38. ^{13}C NMR (101 MHz, Chloroform-*d*) spectrum of *(Z)-5-benzylidene-2-phenyl-4,5-dihydrooxazole.*

3-Chloro-4-methoxy-1,1'-biphenyl

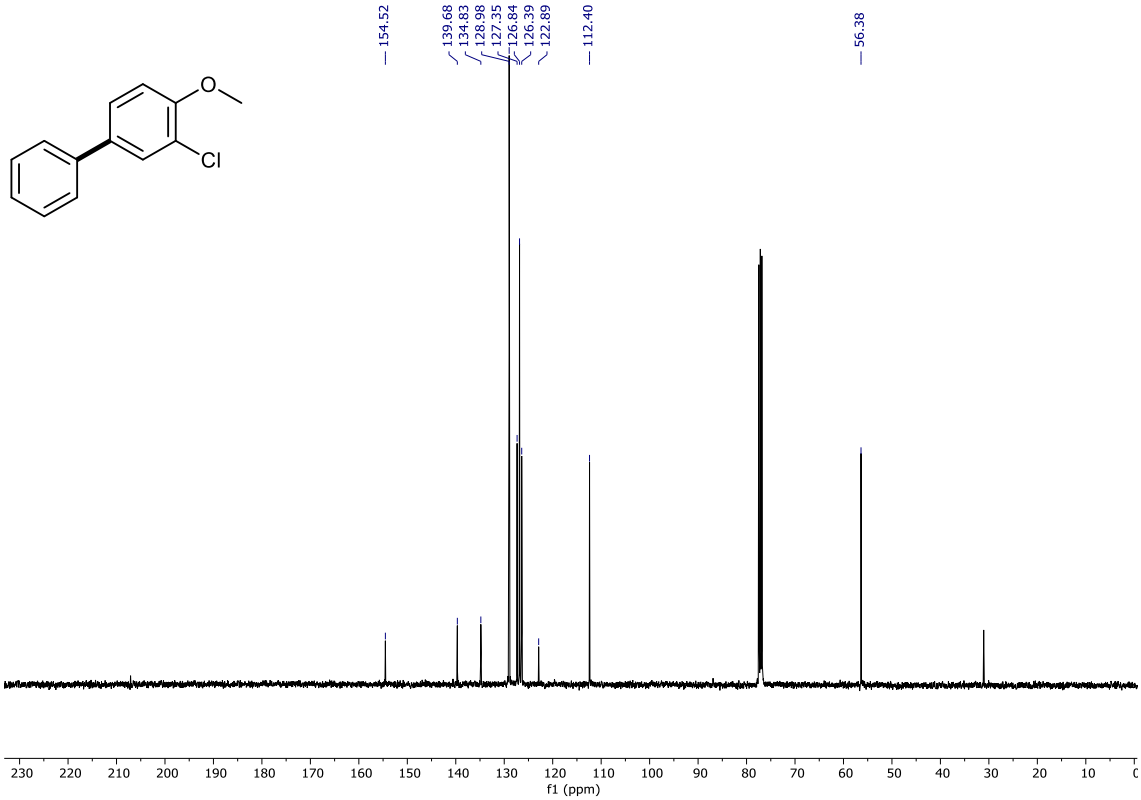

Figure S39. ^{13}C NMR (101 MHz, Chloroform-*d*) spectrum of *3-chloro-4-methoxy-1,1'-biphenyl.*

3-Bromo-4-methoxy-1,1'-biphenyl

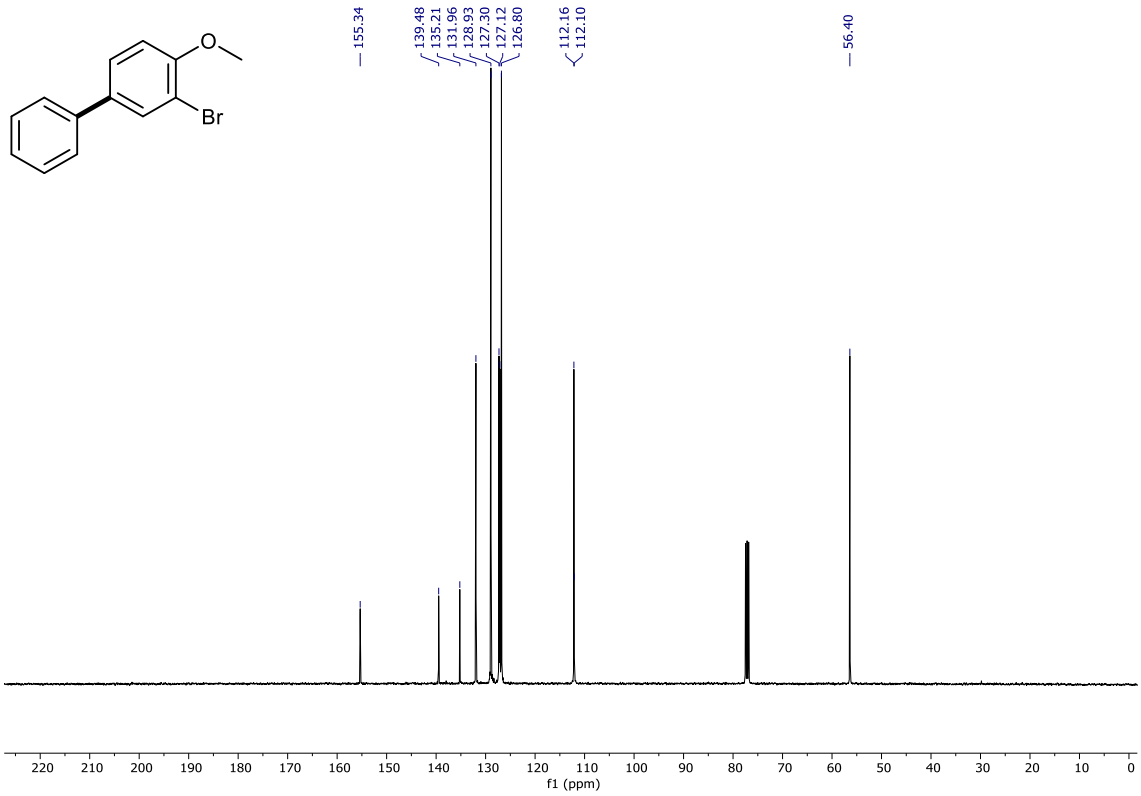

Figure S40. ^{13}C NMR (101 MHz, Chloroform-*d*) spectrum of *3-bromo-4-methoxy-1,1'-biphenyl.*

3,4-Dimethyl-1,1'-biphenyl

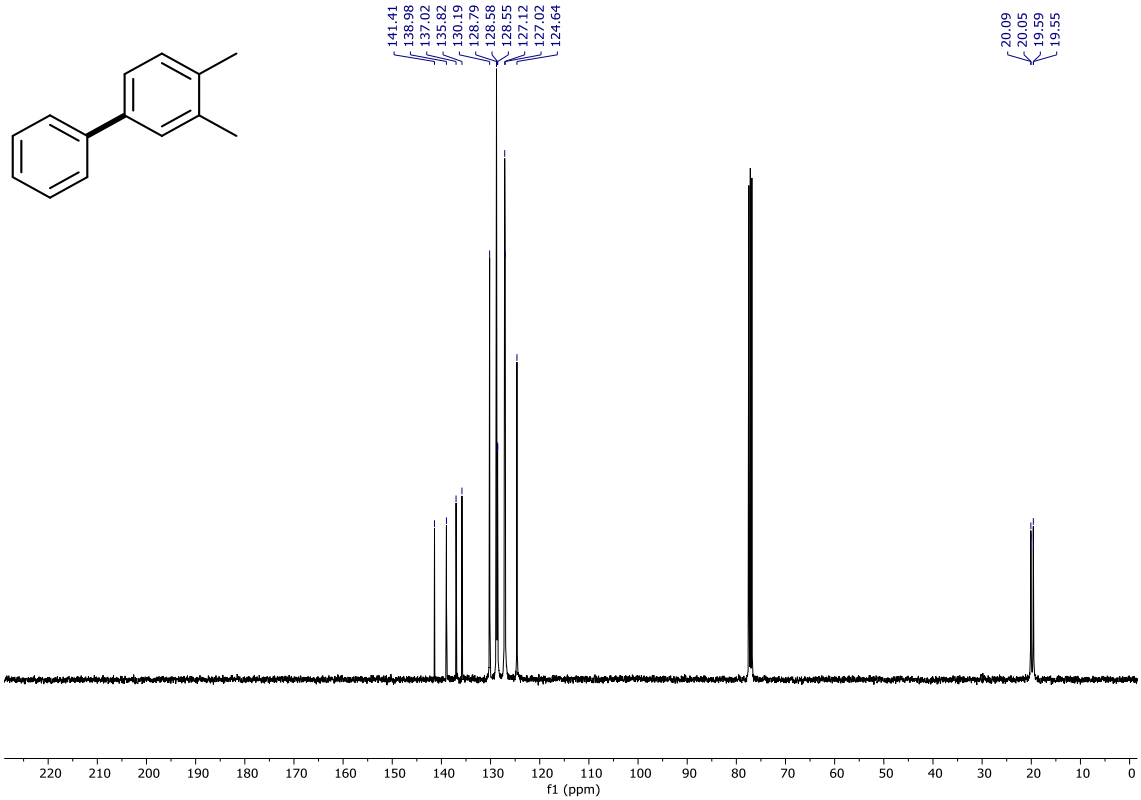

Figure S41. ^{13}C NMR (101 MHz, Chloroform-*d*) spectrum of *3,4-dimethyl-1,1'-biphenyl.*

4-Methyl-1,1'-biphenyl

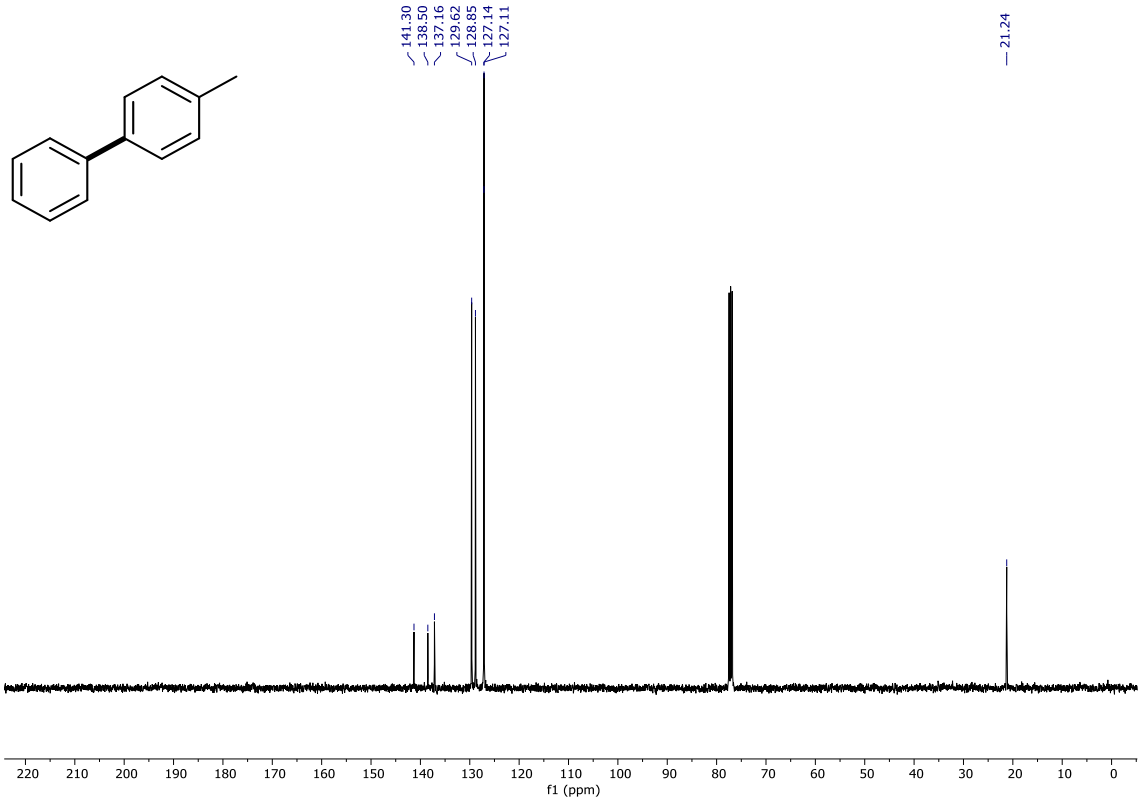

Figure S42. ^{13}C NMR (101 MHz, Chloroform-*d*) spectrum of *4-methyl-1,1'-biphenyl.*

1-Methyl-4-phenylnaphthalene

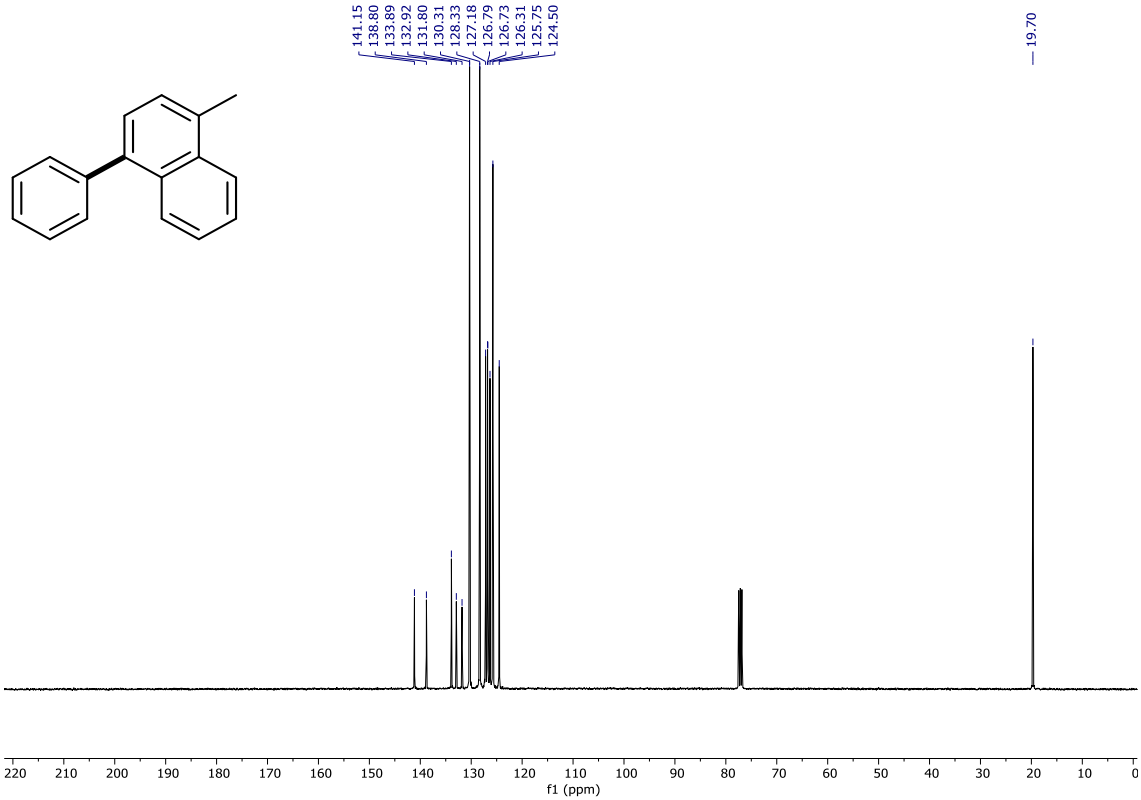

Figure S43. ^{13}C NMR (101 MHz, Chloroform-*d*) spectrum of *1-methyl-4-phenylnaphthalene*.

2-Bromo-5-phenylthiophene

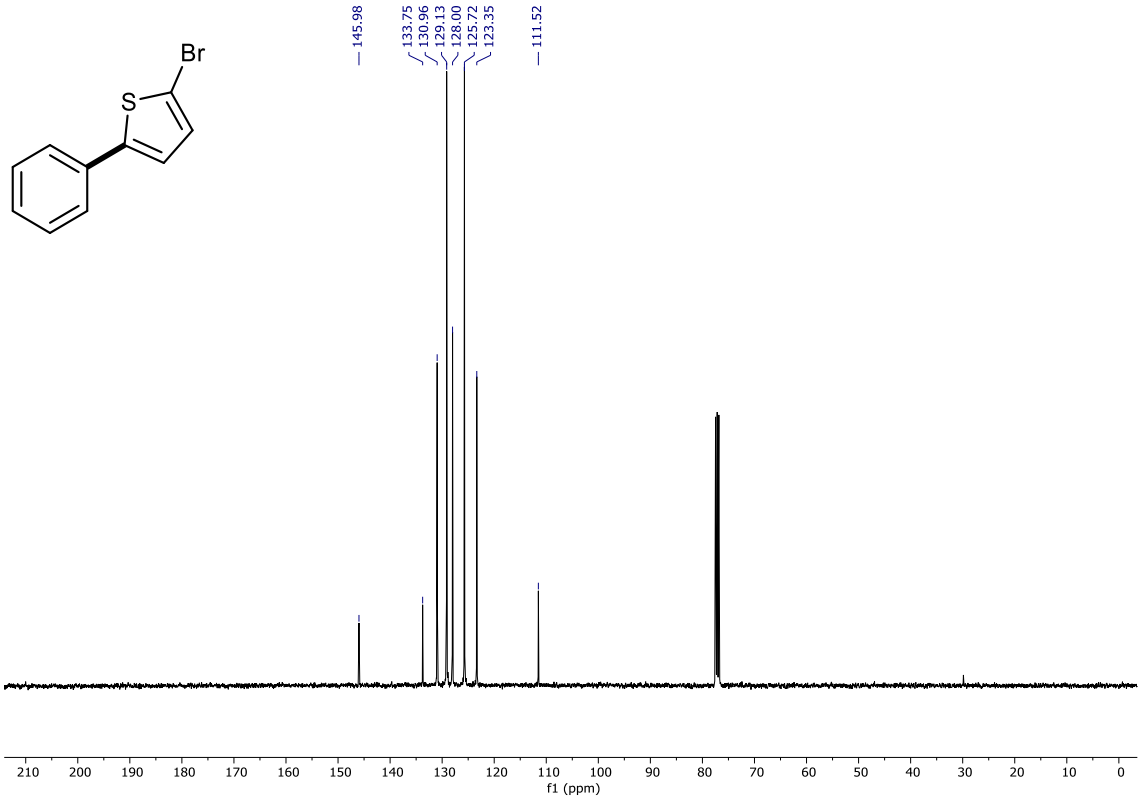

Figure S44. ^{13}C NMR (101 MHz, Chloroform-*d*) spectrum of *2-bromo-5-phenylthiophene*.

4'-Chloro-2-nitro-1,1'-biphenyl

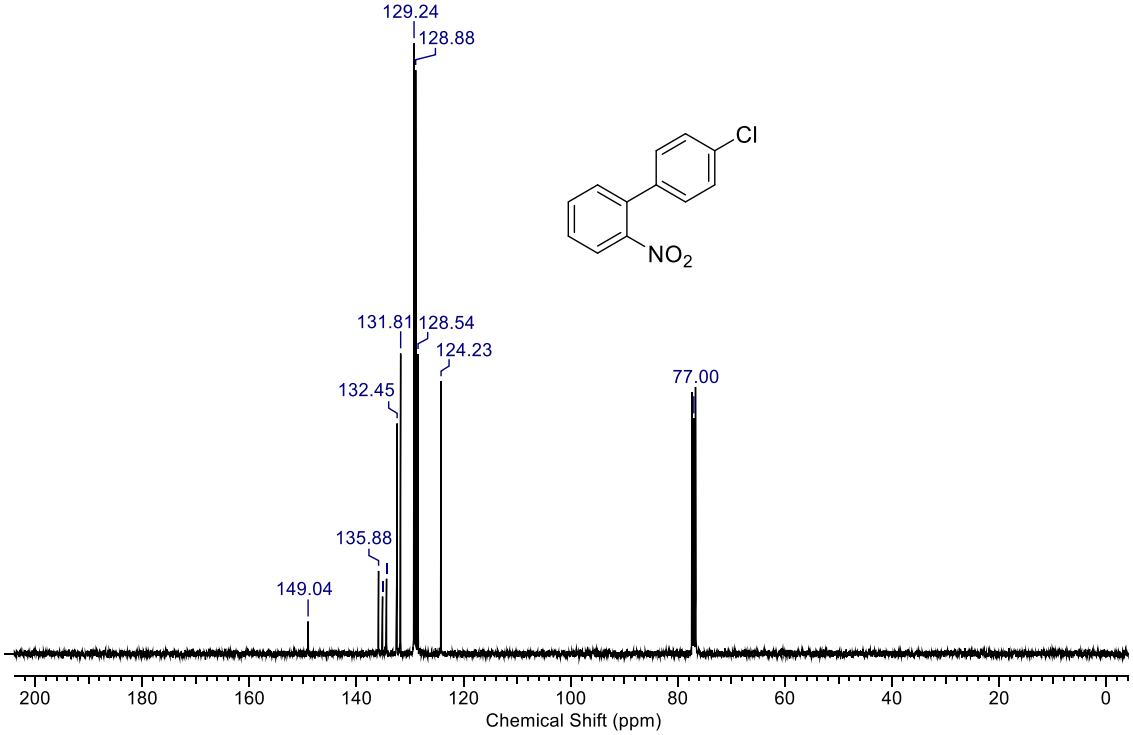

Figure S45. ^{13}C NMR (101 MHz, Chloroform-*d*) spectrum of *4'-chloro-2-nitro-1,1'-biphenyl.*

4,4'-Dichloro-1,1'-biphenyl

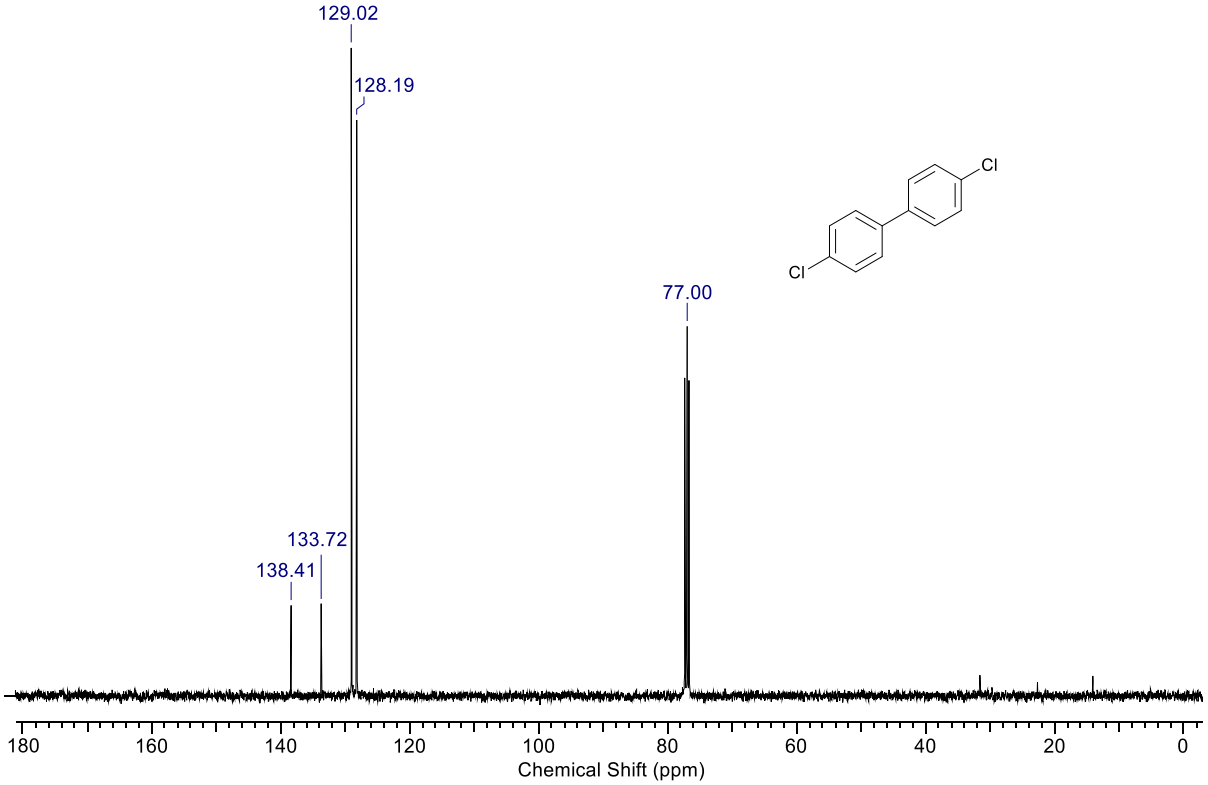

Figure S46. ^{13}C NMR (101 MHz, Chloroform-*d*) spectrum of *4,4'-dichloro-1,1'-biphenyl.*

Nitrobenzene

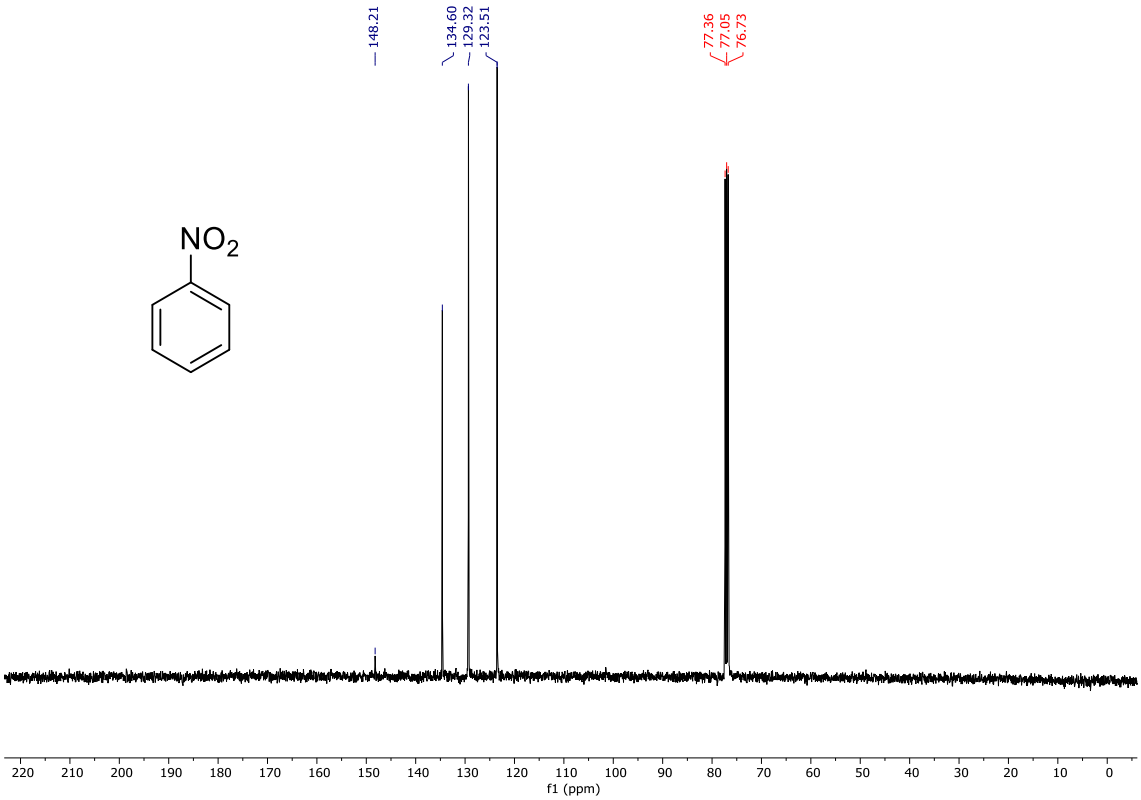

Figure S47. ^{13}C NMR (101 MHz, Chloroform-*d*) spectrum of *nitrobenzene.*

4,4'-Dimethoxy-1,1'-biphenyl

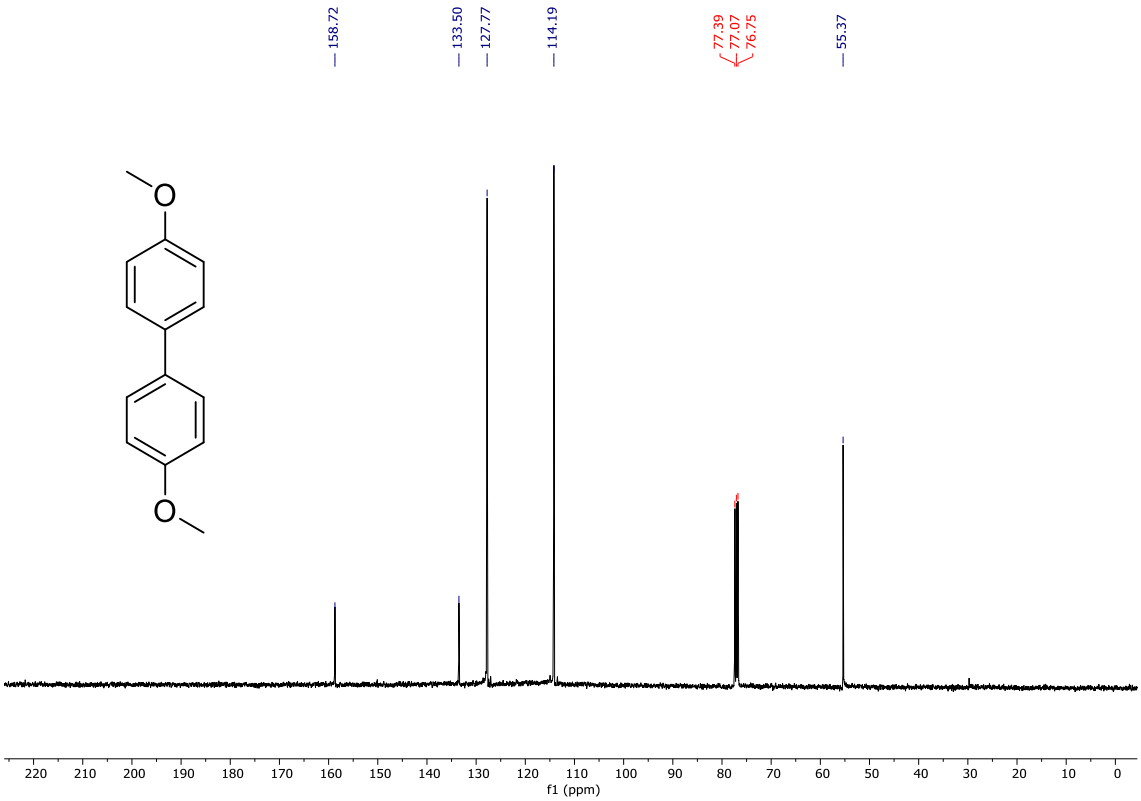

Figure S48. ^{13}C NMR (101 MHz, Chloroform-*d*) spectrum of 4,4'-dimethoxy-1,1'-biphenyl.

4-Chloro-2-(4-methoxyphenyl)pyridine (C2).

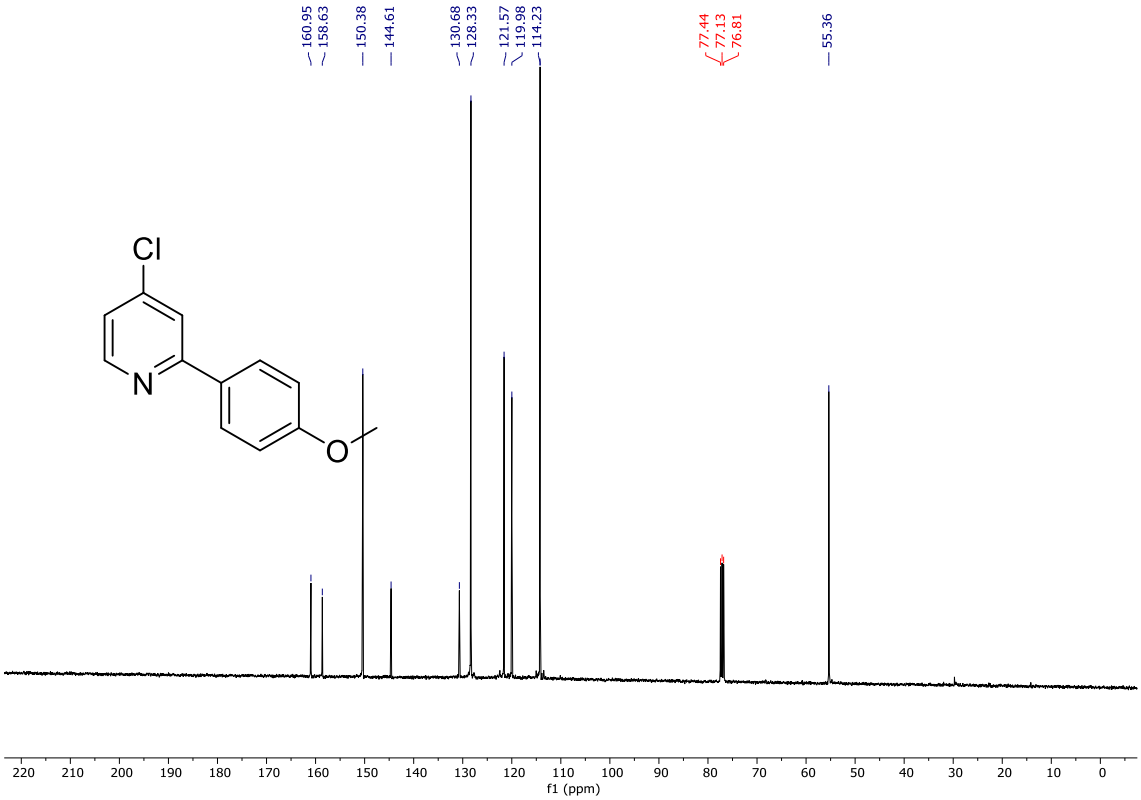

Figure S49. ^{13}C NMR (101 MHz, Chloroform-*d*) spectrum of *4-chloro-2-(4-methoxyphenyl)pyridine (**C2**).*

2-Chloro-4-(4-methoxyphenyl)pyridine (C4).

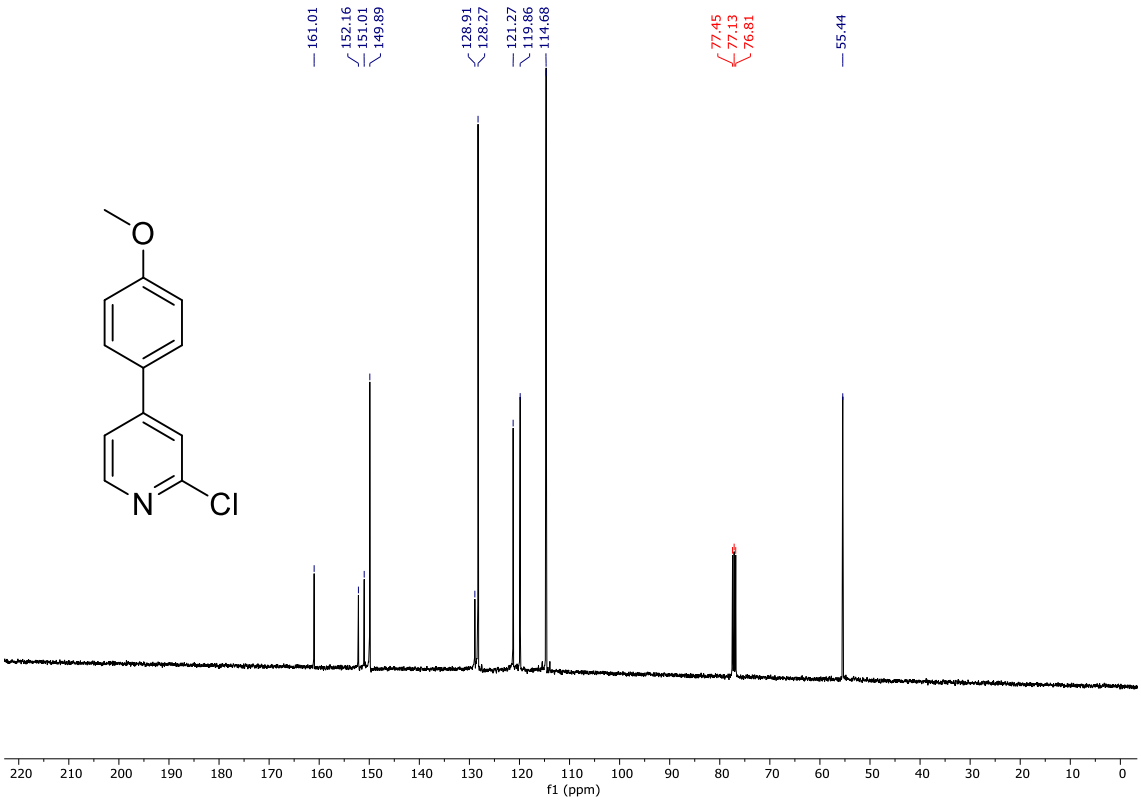

Figure S50. ^{13}C NMR (101 MHz, Chloroform-*d*) spectrum of 2-chloro-4-(4-methoxyphenyl)pyridine (**C4**).

2,4-Bis(4-methoxyphenyl)pyridine

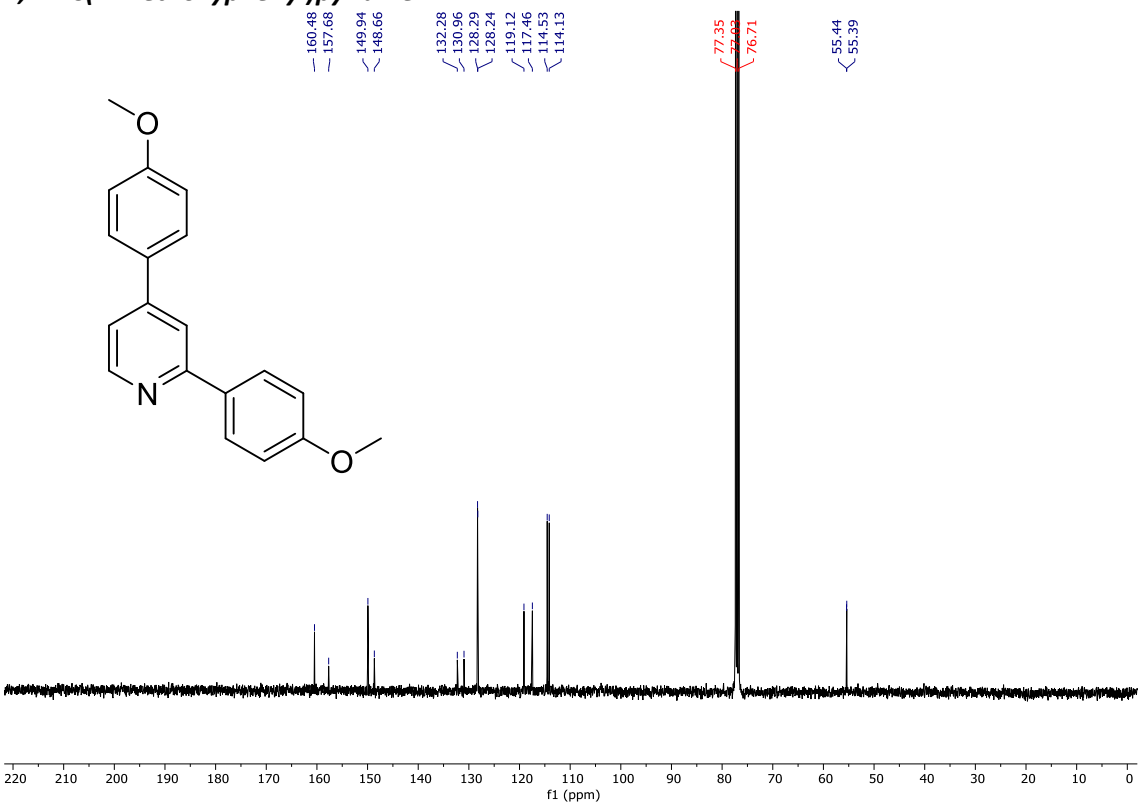

Figure S51. ^{13}C NMR (101 MHz, Chloroform-*d*) spectrum of 2,4-bis(4-methoxyphenyl)pyridine.

7.4. ^{31}P NMR Spectra

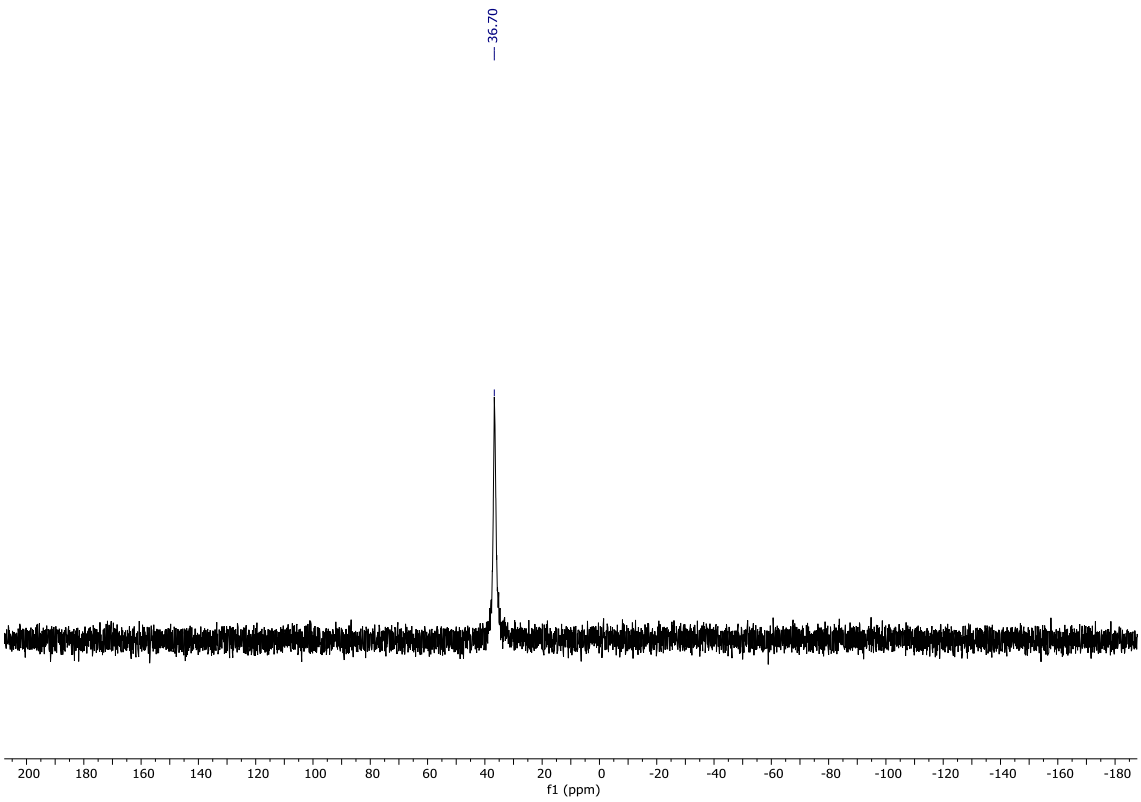

Figure S52. ^{31}P NMR (162 MHz, MeCN-d_3) spectrum of the reaction of **5** with triphenylphosphine oxide and $AgSbF_6$.

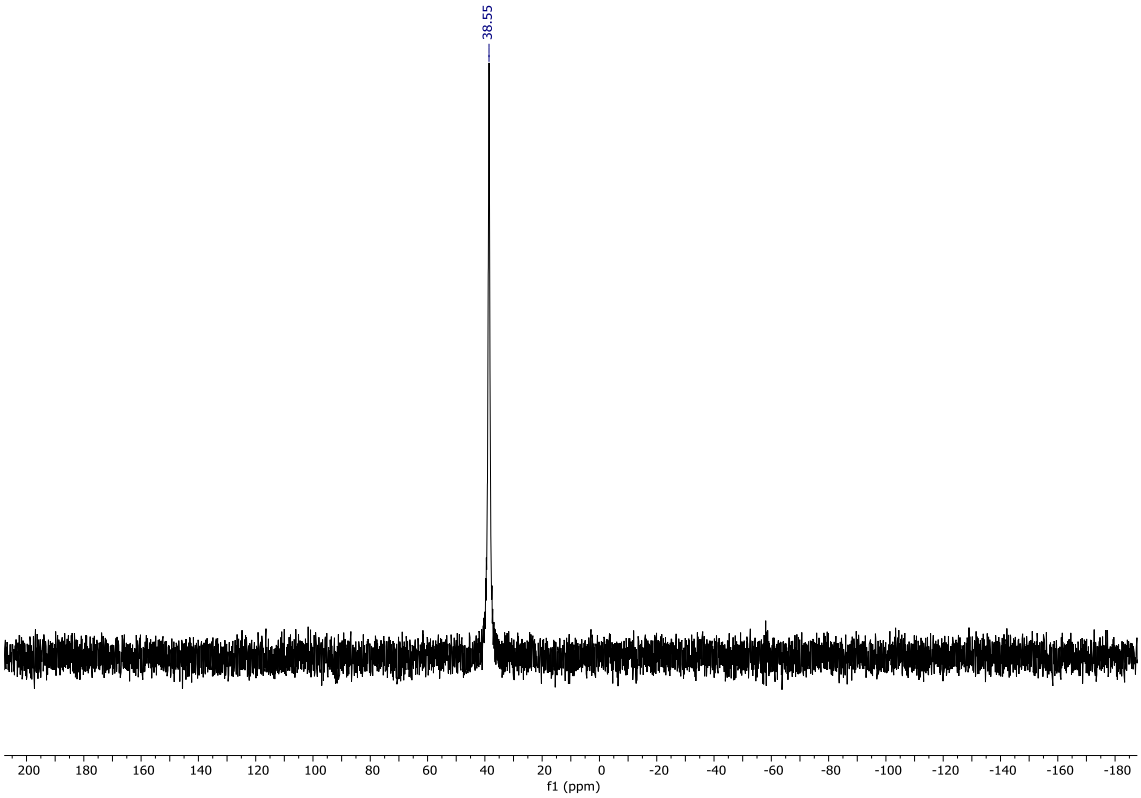

Figure S53. ^{31}P NMR (162 MHz, MeCN-d_3) spectrum of the reaction of **6** with triphenylphosphine oxide and $AgSbF_6$.

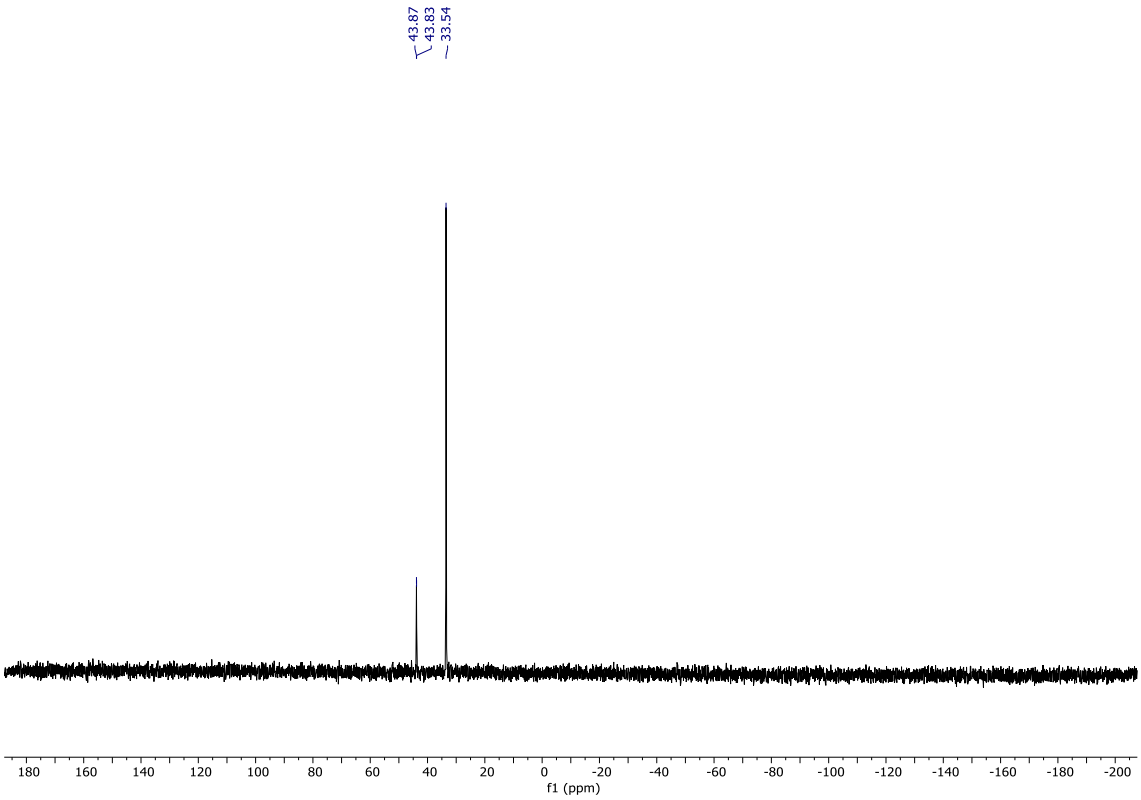

Figure S54. ^{31}P NMR (162 MHz, Acetone-d_6) spectrum of the reaction of **5** with triphenylphosphine oxide in acetone-d_6.

7.5. ^{19}F NMR Spectra

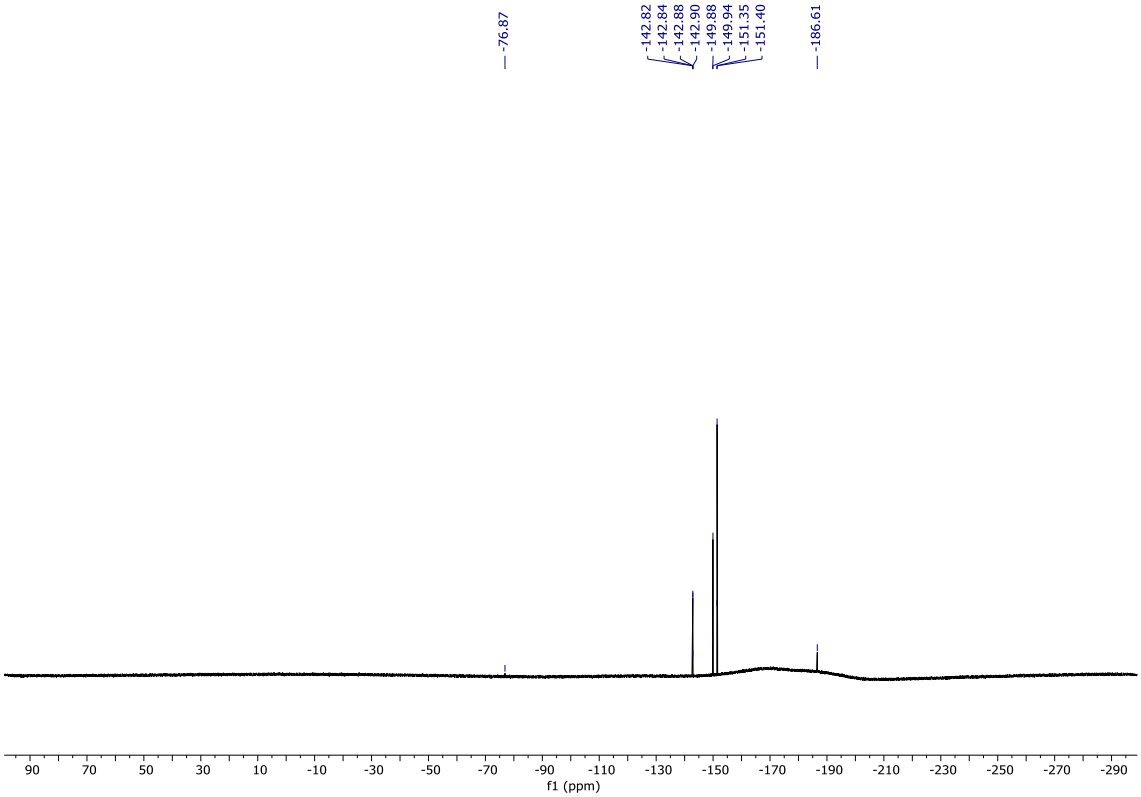

Figure 55. ^{19}F NMR (377 MHz, Acetone-d_6) spectrum from the reaction of **5** with triphenylphosphine oxide in acetone-d_6.

7.6. 2D NMR

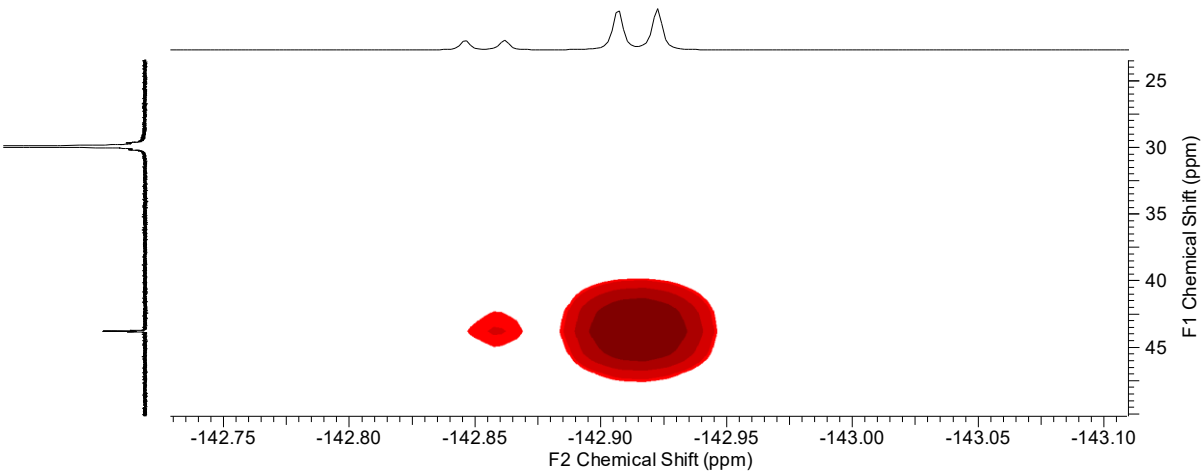

Figure 56. 2D ^{31}P-^{19}F 2D HSQC NMR (377 MHz, Acetone-d_6) spectrum from the reaction of **5** with triphenylphosphine oxide in acetone-d_6

7.7. X-Ray crystallographic information

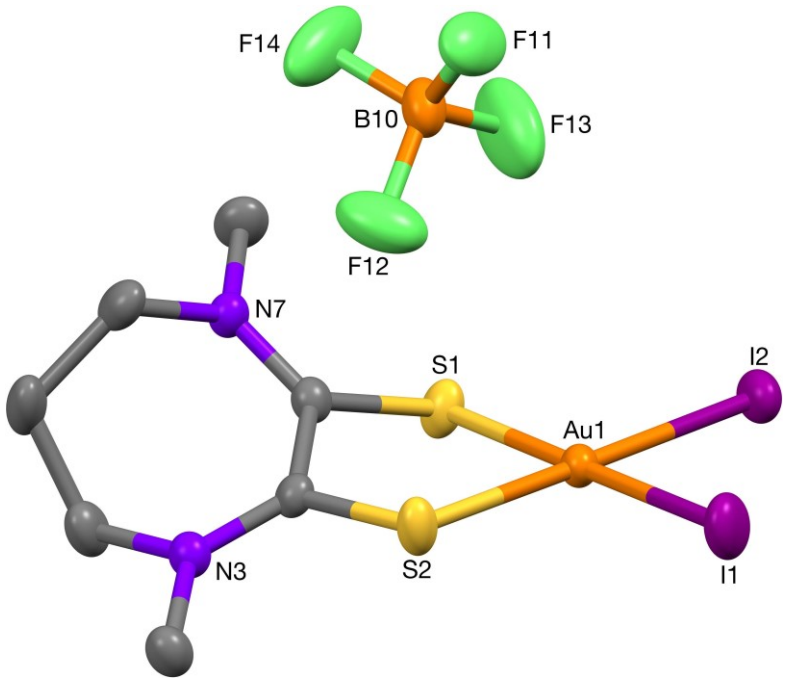

Figure S57. The X-ray crystal structure of **5** (thermal ellipsoids drawn at 50% probability).

Crystal data for **5**: $[C_7H_{12}AuI_2N_2S_2](BF_4)$, M = 725.88, monoclinic, $P2_1/n$ (no. 14), a = 14.2058(2), b = 8.14668(11), c = 15.1256(2) Å, β = 105.7976(17)°, V = 1684.37(5) Å^3, Z = 4, D_c = 2.862 g cm^{-3}, μ(Mo-Kα) = 12.673 mm^{-1}, T = 173 K, black blocks, Agilent Xcalibur 3 E diffractometer; 3979 independent measured reflections (R_{int} = 0.0416), F^2 refinement,[X1,X2] R_1(obs) = 0.0204, wR_2(all) = 0.0396, 3625 independent observed absorption-corrected reflections [$|F_o| > 4\sigma(|F_o|)$, completeness to θ_{full}(25.2°) = 99.9%], 196 parameters. CCDC 2156494.

The B10-based tetrafluoroborate anion in the structure of **5** was found to be disordered. Two orientations were identified of *ca*. 87 and 13% occupancy, their geometries were optimised, the thermal parameters of adjacent atoms were restrained to be similar, and only the atoms of the major occupancy orientation were refined anisotropically (those of the minor occupancy orientation were refined isotropically).

Table S1. Table of **5** bond lengths.

Number	Atom1	Atom2	Cyclicity	Length
1	Au1	I1	acyclic	2.6064(3)
2	Au1	I2	acyclic	2.6093(4)
3	Au1	S1	cyclic	2.3243(9)
4	Au1	S2	cyclic	2.3250(9)
5	S1	C1	cyclic	1.717(3)
6	C1	C2	cyclic	1.491(5)
7	C1	N7	cyclic	1.297(5)
8	C2	S2	cyclic	1.714(3)
9	C2	N3	cyclic	1.306(4)
10	N3	C4	cyclic	1.483(5)
11	N3	C8	acyclic	1.473(4)
12	C4	H4A	acyclic	0.99
13	C4	H4B	acyclic	0.99
14	C4	C5	cyclic	1.519(7)
15	C5	H5A	acyclic	0.99
16	C5	H5B	acyclic	0.99
17	C5	C6	cyclic	1.519(5)
18	C6	H6A	acyclic	0.989
19	C6	H6B	acyclic	0.99
20	C6	N7	cyclic	1.489(5)
21	N7	C9	acyclic	1.475(4)
22	C8	H8A	acyclic	0.981
23	C8	H8B	acyclic	0.98
24	C8	H8C	acyclic	0.98
25	C9	H9A	acyclic	0.98
26	C9	H9B	acyclic	0.98
27	C9	H9C	acyclic	0.98
28	B10	F11	acyclic	1.379(8)
29	B10	F12	acyclic	1.396(6)
30	B10	F13	acyclic	1.357(8)
31	B10	F14	acyclic	1.370(7)

Table S2. Table of **5** bond angle

Number	Atom1	Atom2	Atom3	Angle	Number	Atom1	Atom2	Atom3	Angle
1	I1	Au1	I2	93.60(1)	29	H5B	C5	C6	109.3
2	I1	Au1	S1	177.77(3)	30	C5	C6	H6A	109.4
3	I1	Au1	S2	87.03(3)	31	C5	C6	H6B	109.4
4	I2	Au1	S1	88.09(3)	32	C5	C6	N7	111.2(3)
5	I2	Au1	S2	179.33(3)	33	H6A	C6	H6B	108.1
6	S1	Au1	S2	91.28(3)	34	H6A	C6	N7	109.4
7	Au1	S1	C1	97.7(1)	35	H6B	C6	N7	109.3
8	S1	C1	C2	117.7(3)	36	C1	N7	C6	120.6(3)
9	S1	C1	N7	122.6(3)	37	C1	N7	C9	120.6(3)
10	C2	C1	N7	119.7(3)	38	C6	N7	C9	118.7(3)
11	C1	C2	S2	117.9(3)	39	N3	C8	H8A	109.4
12	C1	C2	N3	119.6(3)	40	N3	C8	H8B	109.5
13	S2	C2	N3	122.5(3)	41	N3	C8	H8C	109.5
14	Au1	S2	C2	99.9(1)	42	H8A	C8	H8B	109.4
15	C2	N3	C4	121.0(3)	43	H8A	C8	H8C	109.4
16	C2	N3	C8	121.6(3)	44	H8B	C8	H8C	109.5
17	C4	N3	C8	117.4(3)	45	N7	C9	H9A	109.5
18	N3	C4	H4A	109.2	46	N7	C9	H9B	109.5
19	N3	C4	H4B	109.2	47	N7	C9	H9C	109.5
20	N3	C4	C5	111.9(3)	48	H9A	C9	H9B	109.5
21	H4A	C4	H4B	107.9	49	H9A	C9	H9C	109.5
22	H4A	C4	C5	109.3	50	H9B	C9	H9C	109.5
23	H4B	C4	C5	109.3	51	F11	B10	F12	108.5(5)
24	C4	C5	H5A	109.3	52	F11	B10	F13	112.3(5)
25	C4	C5	H5B	109.3	53	F11	B10	F14	109.6(5)
26	C4	C5	C6	111.6(3)	54	F12	B10	F13	107.7(5)
27	H5A	C5	H5B	107.9	55	F12	B10	F14	106.2(5)
28	H5A	C5	C6	109.3	56	F13	B10	F14	112.3(5)

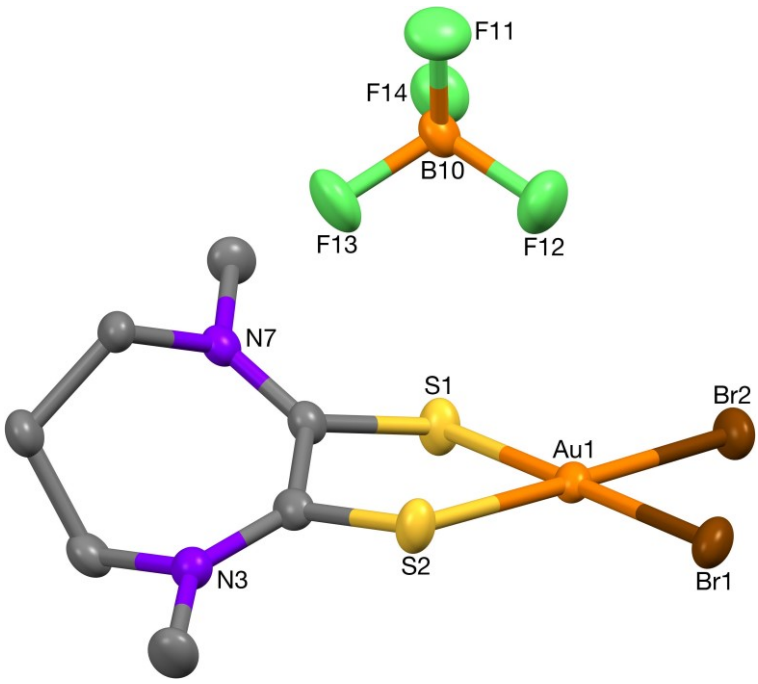

Figure S58. The X-ray crystal structure of **6** (thermal ellipsoids drawn at 50% probability).

Crystal data for **6**: $[C_7H_{12}AuBr_2N_2S_2](BF_4)$, M = 631.90, triclinic, P-1 (no. 2), a = 7.5558(3), b = 8.0088(3), c = 13.3746(4) Å, α = 99.789(3), β = 94.425(3), γ = 109.021(3)°, V = 746.34(5) Å^3, Z = 2, D_c = 2.812 g cm^{-3}, μ(Mo-Kα) = 15.517 mm^{-1}, T = 173 K, dark red blocks, Agilent Xcalibur 3 E diffractometer; 3255 independent measured reflections (R_{int} = 0.0301), F^2 refinement,[X1,X2] R_1(obs) = 0.0230, wR_2(all) = 0.0522, 3016 independent observed absorption-corrected reflections [$|F_o| > 4\sigma(|F_o|)$, completeness to θ_{full}(25.2°) = 100%], 175 parameters. CCDC 2156495.

Table S3. Table of **6** bond lengths.

Number	Atom1	Atom2	Cyclicity	Length
1	Au1	Br1	acyclic	2.4605(5)
2	Au1	Br2	acyclic	2.4282(6)
3	Au1	S1	cyclic	2.302(1)
4	Au1	S2	cyclic	2.293(1)
5	S1	C1	cyclic	1.707(5)
6	C1	C2	cyclic	1.499(8)
7	C1	N7	cyclic	1.294(6)
8	C2	S2	cyclic	1.715(4)
9	C2	N3	cyclic	1.303(6)
10	N3	C4	cyclic	1.487(6)
11	N3	C8	acyclic	1.467(7)
12	C4	H4A	acyclic	0.99
13	C4	H4B	acyclic	0.99
14	C4	C5	cyclic	1.524(8)
15	C5	H5A	acyclic	0.99
16	C5	H5B	acyclic	0.99
17	C5	C6	cyclic	1.510(7)
18	C6	H6A	acyclic	0.99
19	C6	H6B	acyclic	0.99
20	C6	N7	cyclic	1.487(7)
21	N7	C9	acyclic	1.470(7)
22	C8	H8A	acyclic	0.98
23	C8	H8B	acyclic	0.98
24	C8	H8C	acyclic	0.98
25	C9	H9A	acyclic	0.98
26	C9	H9B	acyclic	0.98
27	C9	H9C	acyclic	0.98
28	B10	F11	acyclic	1.384(8)
29	B10	F12	acyclic	1.377(7)
30	B10	F13	acyclic	1.379(6)
31	B10	F14	acyclic	1.393(8)

Table S4. Table of **6** bond angles.

Number	Atom1	Atom2	Atom3	Angle	Number	Atom1	Atom2	Atom3	Angle
1	Br1	Au1	Br2	94.33(2)	29	H5B	C5	C6	109.6
2	Br1	Au1	S1	179.30(4)	30	C5	C6	H6A	109.1
3	Br1	Au1	S2	87.44(4)	31	C5	C6	H6B	109.1
4	Br2	Au1	S1	86.37(4)	32	C5	C6	N7	112.6(4)
5	Br2	Au1	S2	178.22(4)	33	H6A	C6	H6B	107.8
6	S1	Au1	S2	91.86(5)	34	H6A	C6	N7	109.1
7	Au1	S1	C1	99.4(2)	35	H6B	C6	N7	109.1
8	S1	C1	C2	118.2(4)	36	C1	N7	C6	120.6(4)
9	S1	C1	N7	122.3(4)	37	C1	N7	C9	120.6(4)
10	C2	C1	N7	119.5(5)	38	C6	N7	C9	118.5(4)
11	C1	C2	S2	117.5(4)	39	N3	C8	H8A	109.5
12	C1	C2	N3	119.7(4)	40	N3	C8	H8B	109.4
13	S2	C2	N3	122.8(4)	41	N3	C8	H8C	109.4
14	Au1	S2	C2	100.3(2)	42	H8A	C8	H8B	109.5
15	C2	N3	C4	121.5(4)	43	H8A	C8	H8C	109.5
16	C2	N3	C8	121.8(5)	44	H8B	C8	H8C	109.5
17	C4	N3	C8	116.8(4)	45	N7	C9	H9A	109.4
18	N3	C4	H4A	109.4	46	N7	C9	H9B	109.4
19	N3	C4	H4B	109.4	47	N7	C9	H9C	109.5
20	N3	C4	C5	111.1(4)	48	H9A	C9	H9B	109.5
21	H4A	C4	H4B	108	49	H9A	C9	H9C	109.5
22	H4A	C4	C5	109.4	50	H9B	C9	H9C	109.5
23	H4B	C4	C5	109.5	51	F11	B10	F12	110.1(5)
24	C4	C5	H5A	109.6	52	F11	B10	F13	108.7(5)
25	C4	C5	H5B	109.6	53	F11	B10	F14	109.2(5)
26	C4	C5	C6	110.3(4)	54	F12	B10	F13	111.3(5)
27	H5A	C5	H5B	108.1	55	F12	B10	F14	109.2(5)
28	H5A	C5	C6	109.6	56	F13	B10	F14	108.3(5)

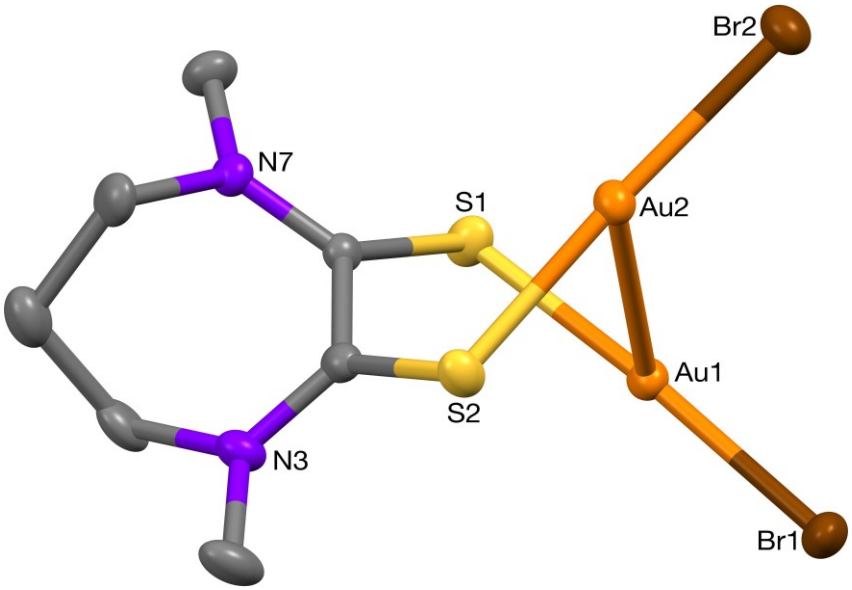

Figure S59. The X-ray crystal structure of **[Me$_2$dazdtAu$_2$Br$_2$]** (**10**) (thermal ellipsoids drawn at 50% probability).

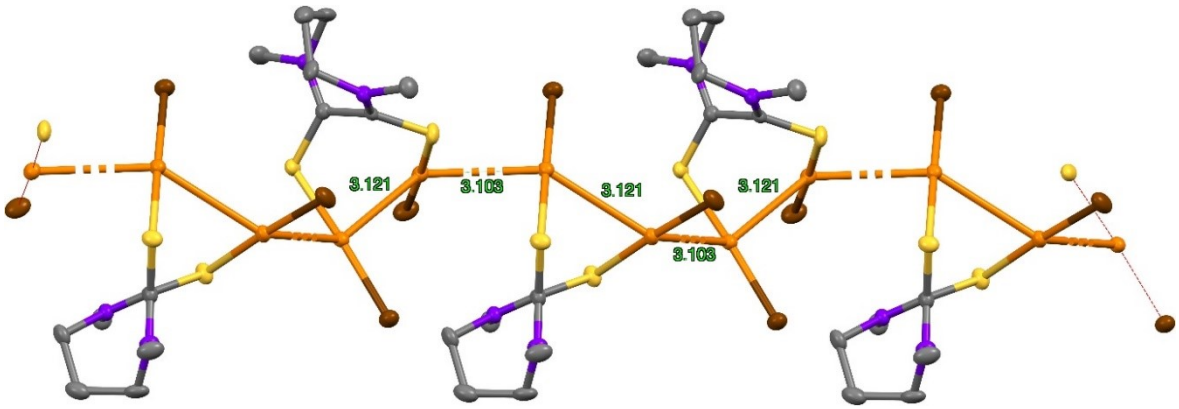

Figure S60. The X-ray crystal structure of **[Me$_2$dazdtAu$_2$Br$_2$]** (**10**) illustrating chain of molecules formed along b axis. (thermal ellipsoids drawn at 50% probability).

Crystal data for **[Me$_2$dazdtAu$_2$Br$_2$]** (**10**): [$C_7H_{12}Au_2Br_2N_2S_2$], M = 742.06, monoclinic, $P2_1/n$ (no. 14), a = 9.8393(3), b = 10.7280(3), c = 13.4277(3) Å, β = 104.018(3)°, V = 1375.16(6) Å^3, Z = 4, D_c = 3.584 g cm^{-3}, μ(Mo-Kα) = 27.398 mm^{-1}, T = 173 K, red blocks, Agilent Xcalibur 3 E diffractometer; 3214 independent measured reflections (R_{int} = 0.0469), F^2 refinement,[X1,X2] R_1(obs) = 0.0212, wR_2(all) = 0.0434, 2841 independent observed absorption-corrected reflections [$|F_o| > 4\sigma(|F_o|)$, completeness to θ_{full}(25.2°) = 99.9%], 139 parameters. CCDC 2156496.

Intermolecular Au…Au contacts (3.103 Å) were observed for [Me_2dazdtAu_2Br_2] with distances comparable to the intramolecular contacts (3.121 Å), resulting in the formation of a chain of molecules along the direction of the b axis (Figure S60).

Table S5. Table of **[Me_2dazdtAu_2Br_2]** (**10**) bond lengths.

Number	Atom1	Atom2	Polymeric	Cyclicity	Length
1	Au1	Au2	no	cyclic	3.1209(3)
2	Au1	Br1	no	acyclic	2.3856(6)
3	Au1	S1	no	cyclic	2.273(1)
4	Au1	Au2	yes	acyclic	3.1032(3)
5	Au2	Br2	no	acyclic	2.3920(6)
6	Au2	S2	no	cyclic	2.275(1)
7	Au2	Au1	yes	acyclic	3.1032(3)
8	S1	C1	no	cyclic	1.686(5)
9	C1	C2	no	cyclic	1.500(6)
10	C1	N7	no	cyclic	1.310(5)
11	C2	S2	no	cyclic	1.689(5)
12	C2	N3	no	cyclic	1.315(7)
13	N3	C4	no	cyclic	1.470(6)
14	N3	C8	no	acyclic	1.461(7)
15	C4	H4A	no	acyclic	0.99
16	C4	H4B	no	acyclic	0.99
17	C4	C5	no	cyclic	1.515(7)
18	C5	H5A	no	acyclic	0.99
19	C5	H5B	no	acyclic	0.99
20	C5	C6	no	cyclic	1.516(9)
21	C6	H6A	no	acyclic	0.99
22	C6	H6B	no	acyclic	0.99
23	C6	N7	no	cyclic	1.482(7)
24	N7	C9	no	acyclic	1.465(6)
25	C8	H8A	no	acyclic	0.98
26	C8	H8B	no	acyclic	0.979
27	C8	H8C	no	acyclic	0.98
28	C9	H9A	no	acyclic	0.98
29	C9	H9B	no	acyclic	0.98
30	C9	H9C	no	acyclic	0.98

Table S6. Table of **[Me_2dazdtAu_2Br_2]** bond angles

Number	Atom1	Atom2	Atom3	Angle	Number	Atom1	Atom2	Atom3	Angle
1	Au2	Au1	Br1	103.93(2)	29	H4B	C4	C5	109.5
2	Au2	Au1	S1	77.90(3)	30	C4	C5	H5A	109.5
3	Au2	Au1	Au2	131.37(1)	31	C4	C5	H5B	109.5
4	Br1	Au1	S1	176.35(4)	32	C4	C5	C6	110.8(4)
5	Br1	Au1	Au2	97.83(2)	33	H5A	C5	H5B	108.1
6	S1	Au1	Au2	83.08(3)	34	H5A	C5	C6	109.5
7	Au1	Au2	Br2	106.41(2)	35	H5B	C5	C6	109.5
8	Au1	Au2	S2	74.42(3)	36	C5	C6	H6A	109.6
9	Au1	Au2	Au1	145.20(1)	37	C5	C6	H6B	109.6
10	Br2	Au2	S2	176.34(4)	38	C5	C6	N7	110.2(4)
11	Br2	Au2	Au1	96.68(2)	39	H6A	C6	H6B	108.1
12	S2	Au2	Au1	84.20(3)	40	H6A	C6	N7	109.7
13	Au1	S1	C1	107.6(2)	41	H6B	C6	N7	109.6
14	S1	C1	C2	121.6(3)	42	C1	N7	C6	119.9(4)
15	S1	C1	N7	122.1(4)	43	C1	N7	C9	122.3(4)
16	C2	C1	N7	116.0(4)	44	C6	N7	C9	117.2(4)
17	C1	C2	S2	122.7(4)	45	N3	C8	H8A	109.4
18	C1	C2	N3	115.6(4)	46	N3	C8	H8B	109.5
19	S2	C2	N3	121.7(4)	47	N3	C8	H8C	109.4
20	Au2	S2	C2	106.7(2)	48	H8A	C8	H8B	109.5
21	C2	N3	C4	120.2(4)	49	H8A	C8	H8C	109.5
22	C2	N3	C8	120.1(4)	50	H8B	C8	H8C	109.5
23	C4	N3	C8	118.7(4)	51	N7	C9	H9A	109.4
24	N3	C4	H4A	109.5	52	N7	C9	H9B	109.5
25	N3	C4	H4B	109.5	53	N7	C9	H9C	109.4
26	N3	C4	C5	110.7(4)	54	H9A	C9	H9B	109.5
27	H4A	C4	H4B	108.1	55	H9A	C9	H9C	109.5
28	H4A	C4	C5	109.5	56	H9B	C9	H9C	109.5

7.8. ReactIR Profiles and tabulated data

Orders in ArCl

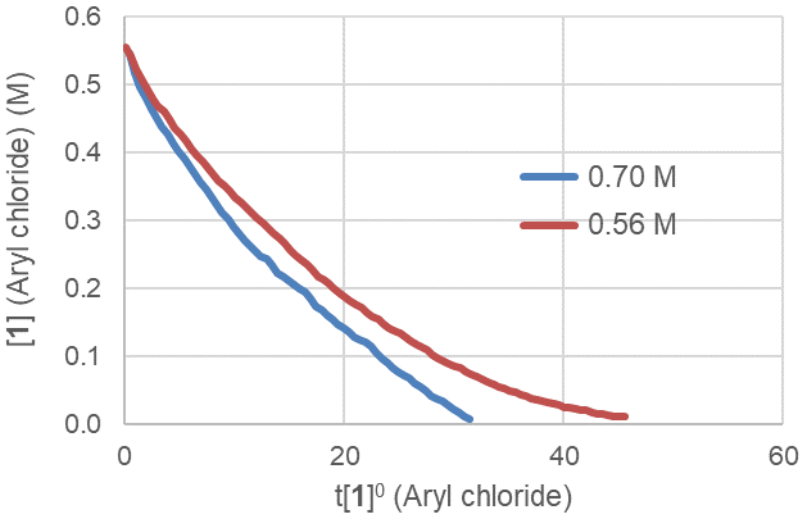

Figure S61. Reaction profiles comparing the conversion of the aryl chloride, **1**, at two different starting concentrations (0.70 and 0.56 M).

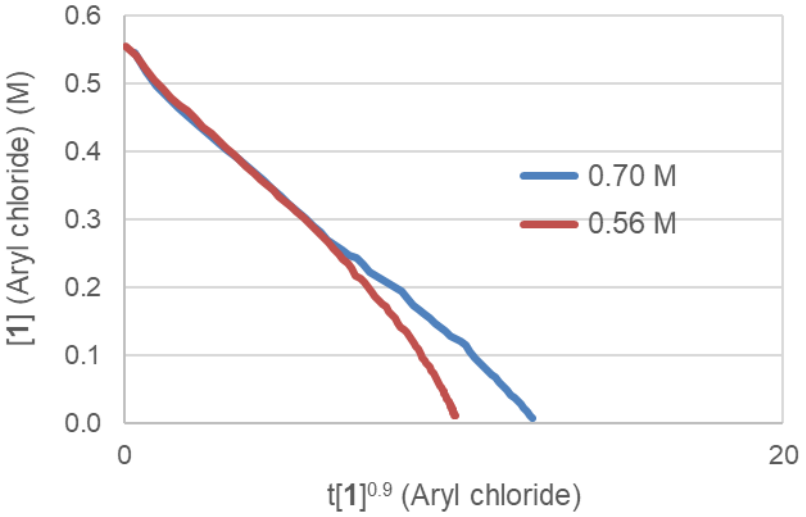

Figure S62. VTNA (Order = 0.9) applied to reaction profiles comparing the conversion of the aryl chloride, **1**, at two different starting concentrations (0.70 and 0.56 M).

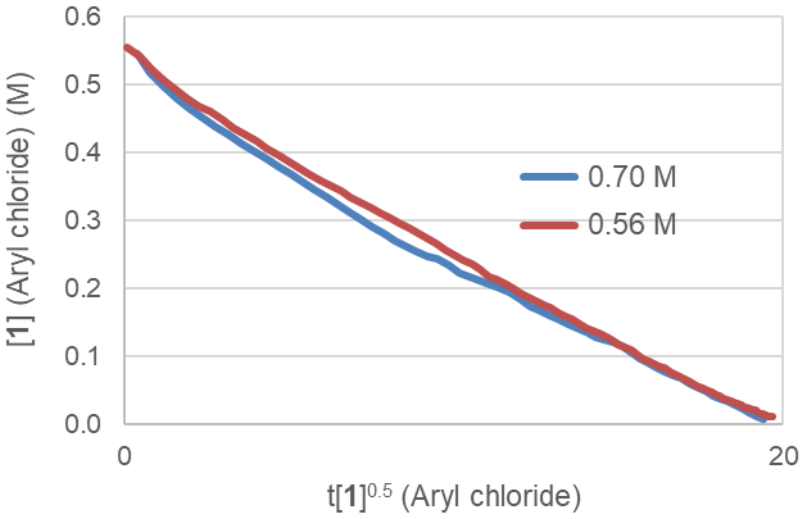

Figure S63. VTNA (Order = 0.5) applied to reaction profiles comparing the conversion of the aryl chloride, **1**, at two different starting concentrations (0.70 and 0.56 M).

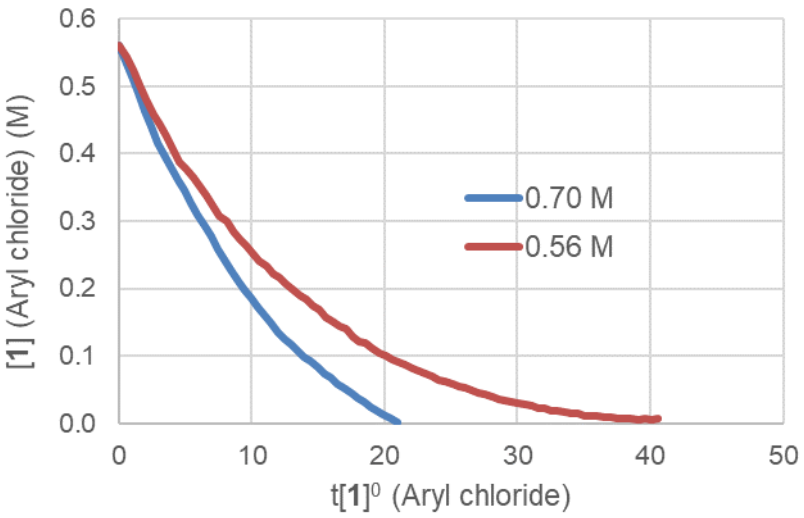

Figure S64. Reaction profiles comparing the conversion of the aryl chloride, **1**, at two different starting concentrations (0.70 and 0.56 M) in the presence of KBr (1.4 M).

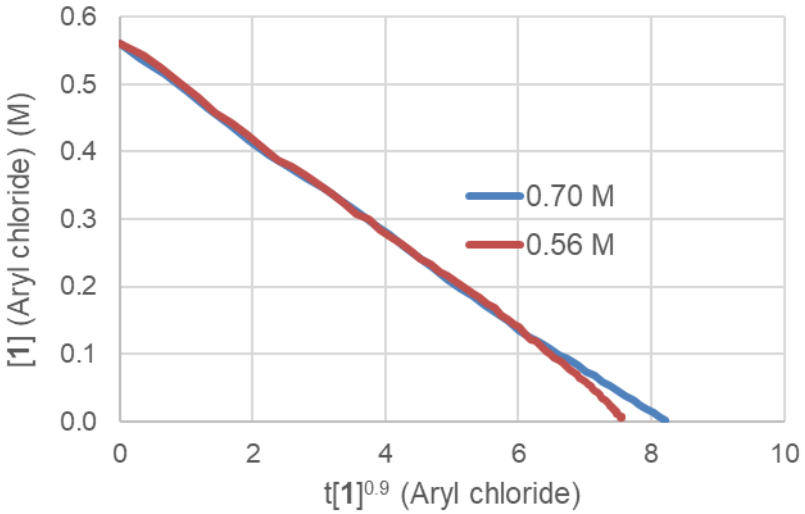

Figure S65. VTNA (Order = 0.9) applied to reaction profiles comparing the conversion of the aryl chloride, **1**, at two different starting concentrations (0.70 and 0.56 M) in the presence of KBr (1.4 M).

Different excess determination of Cl^- inhibition

Table S7. Reaction concentrations for the different excess determination of Cl^- inhibition

Optimised conditions		Same excess		Same excess w/Product		Same excess w/TBAC		Optimised conditions + 2KBr	
[1]	0.7 M	[1]	0.4 M	[1]	0.4 M	[1]	0.4 M	[1]	0.7 M
[2]	0.77 M	[2]	0.47 M	[2]	0.47 M	[2]	0.47 M	[2]	0.77 M
[3]	0.0 M	[3]	0.0 M	[3]	0.3 M	[3]	0.3 M	[3]	0.0 M
[NnBu4]Br	0.7 M	[NnBu4]Br	0.7 M	[NnBu4]Br	0.7 M	[NnBu4]Br	0.4 M	[NnBu4]Br	0.7 M
[NnBu4]Cl	0 M	[NnBu4]Cl	0 M	[NnBu4]Cl	0 M	[NnBu4]Cl	0.3 M	[NnBu4]Cl	0 M
[cat]	0.000308 M	[cat]	0.000308 M	[cat]	0.000308 M	[cat]	0.000308 M	[cat]	0.000308 M
								[KBr]	1.4 M

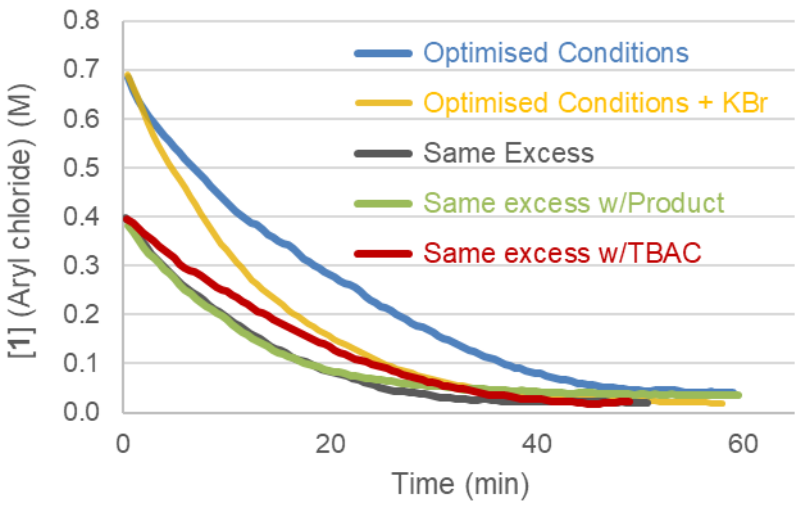

Figure S66. Reaction profiles from Table SN.

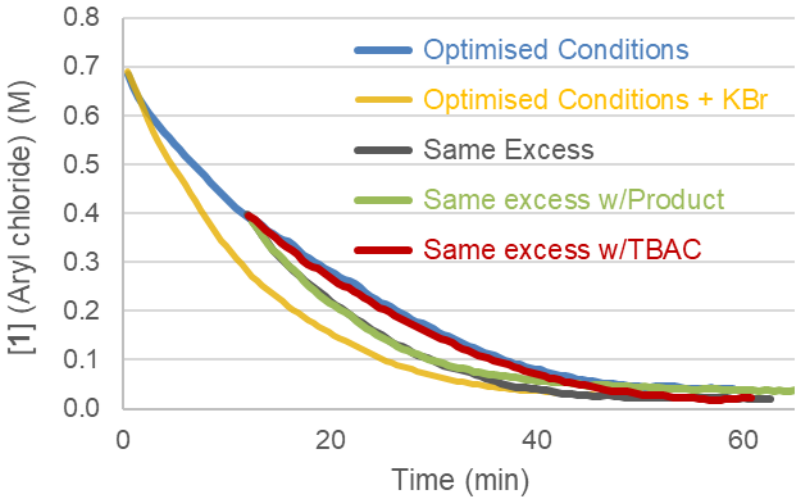

Figure S67. Reaction profiles from Table SN with time shift.

Orders in $[N^nBu_4]_2[Pd_2I_6]$

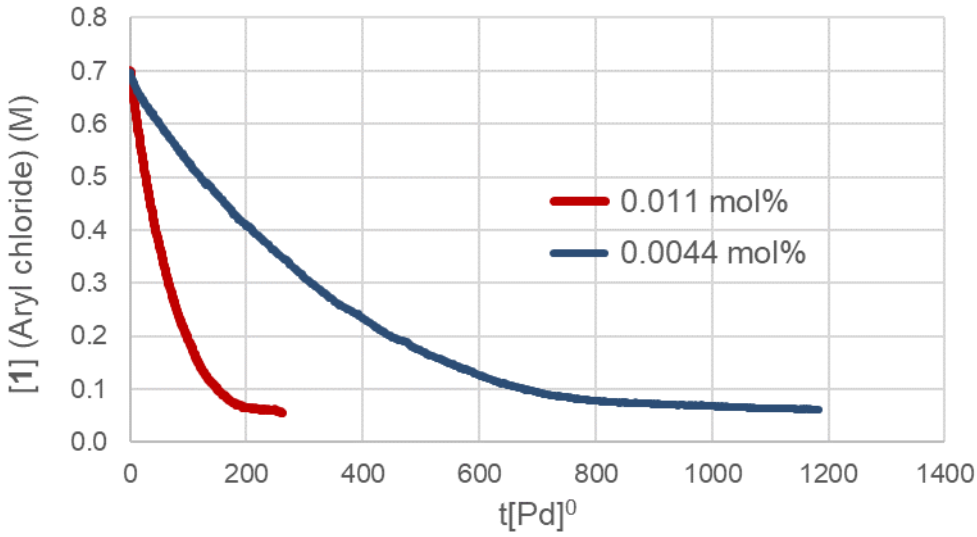

Figure S68. Two reaction profiles using different loadings of $[N^nBu_4]_2[Pd_2I_6]$ (0.0044 and 0.011 mol%. Loadings are of the dimeric species containing two palladium atoms).

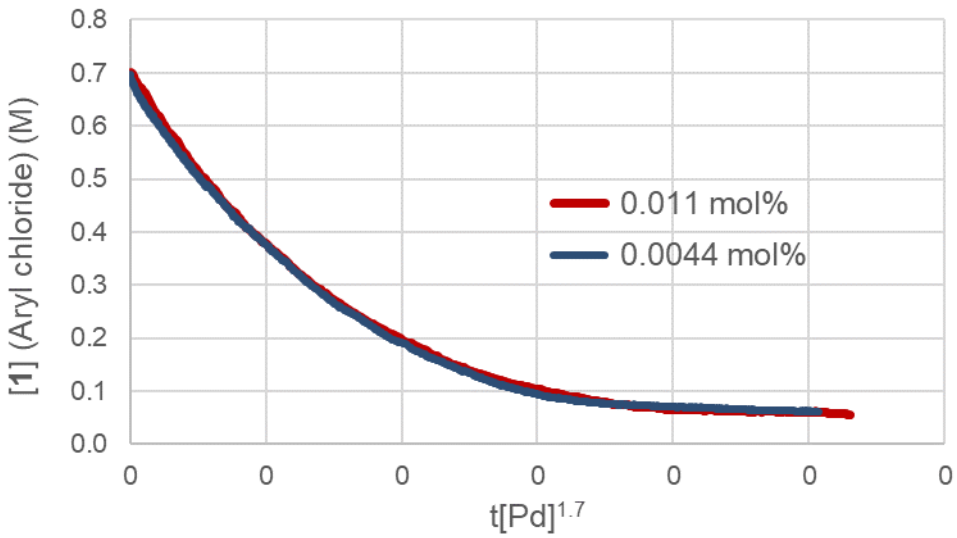

Figure S69. VTNA (order = 1.7) applied to two reaction profiles using different loadings of $[N^nBu_4]_2[Pd_2I_6]$ (0.0044 and 0.011 mol%. Loadings are of the dimeric species containing two palladium atoms).

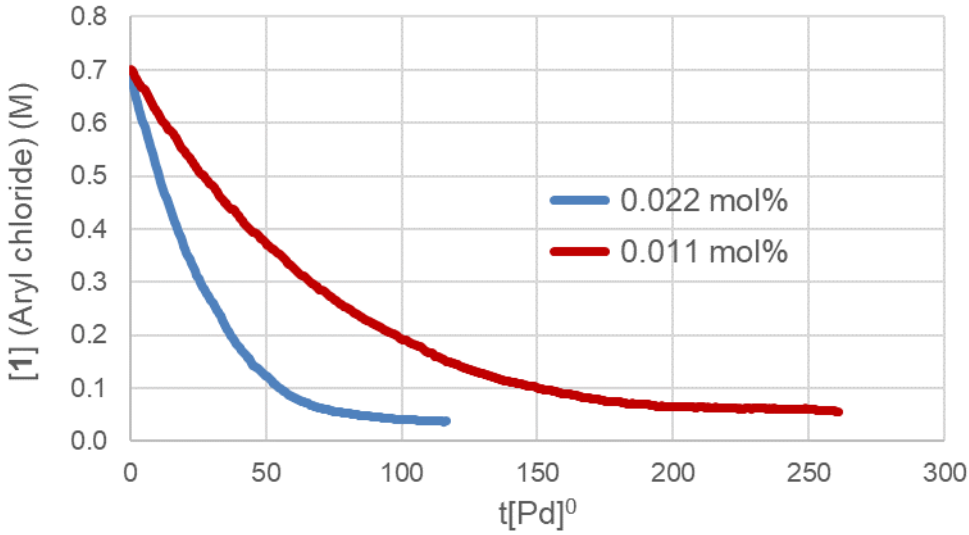

Figure S70. Two reaction profiles using different loadings of $[N^nBu_4]_2[Pd_2I_6]$ (0.011 and 0.022 mol%. Loadings are of the dimeric species containing two palladium atoms).

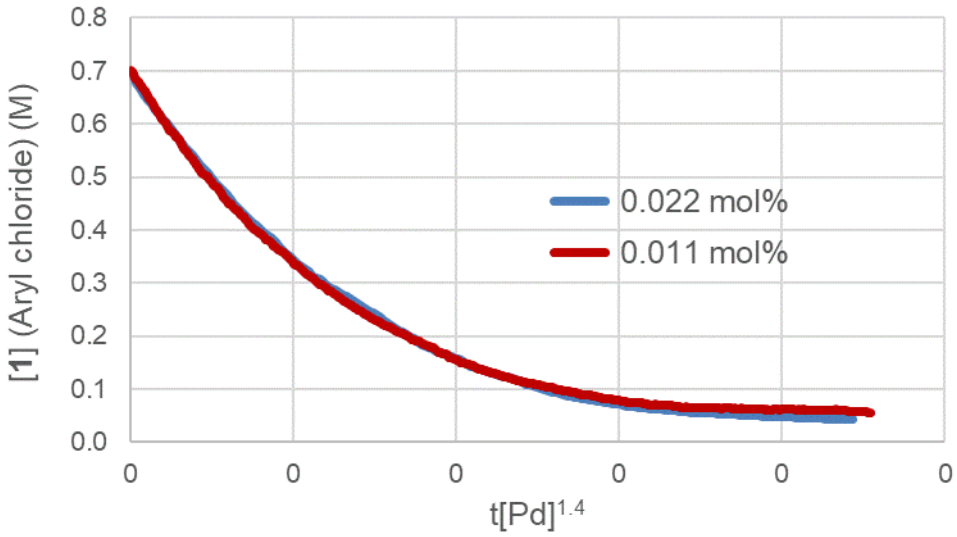

Figure S71. VTNA (order = 1.4) applied to two reaction profiles using different loadings of $[N^nBu_4]_2[Pd_2I_6]$ (0.011 and 0.022 mol%. Loadings are of the dimeric species containing two palladium atoms).

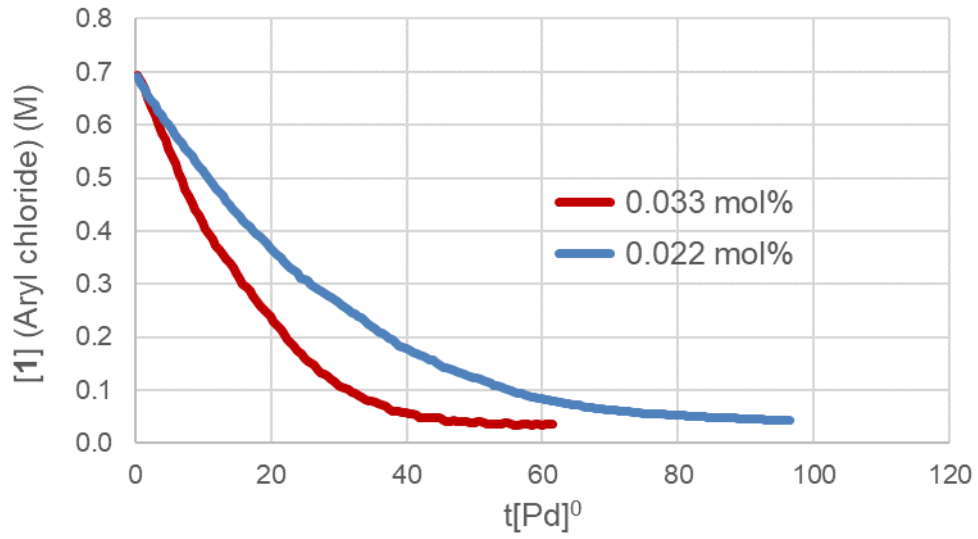

Figure S72. Two reaction profiles using different loadings of $[N^nBu_4]_2[Pd_2I_6]$ (0.022 and 0.033 mol%. Loadings are of the dimeric species containing two palladium atoms).

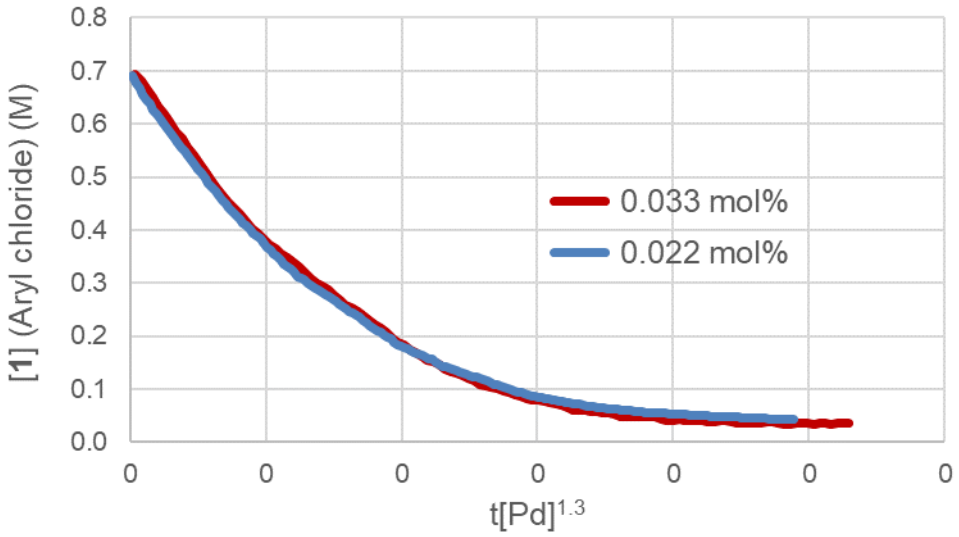

Figure S73. VTNA (order = 1.3) applied to two reaction profiles using different loadings of $[N^nBu_4]_2[Pd_2I_6]$ (0.022 and 0.033 mol%. Loadings are of the dimeric species containing two palladium atoms).

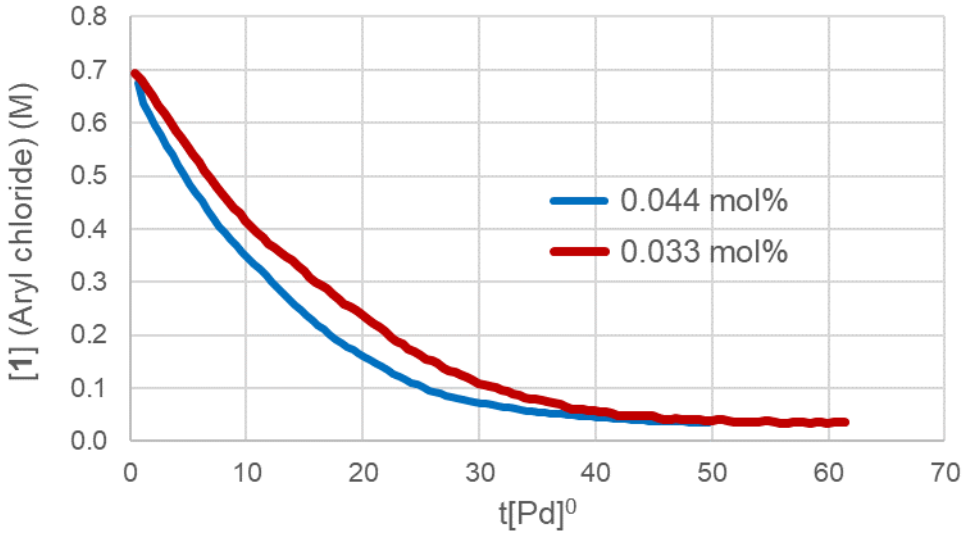

Figure S74. Two reaction profiles using different loadings of $[N^nBu_4]_2[Pd_2I_6]$ (0.033 and 0.044 mol%. Loadings are of the dimeric species containing two palladium atoms).

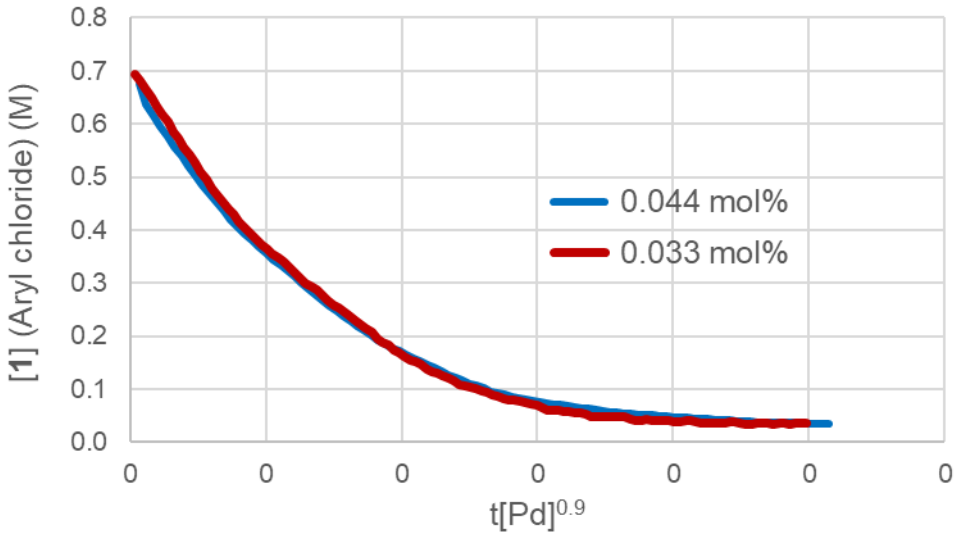

Figure S75. VTNA (order = 0.9) applied to two reaction profiles using different loadings of $[N^nBu_4]_2[Pd_2I_6]$ (0.033 and 0.044 mol%. Loadings are of the dimeric species containing two palladium atoms).

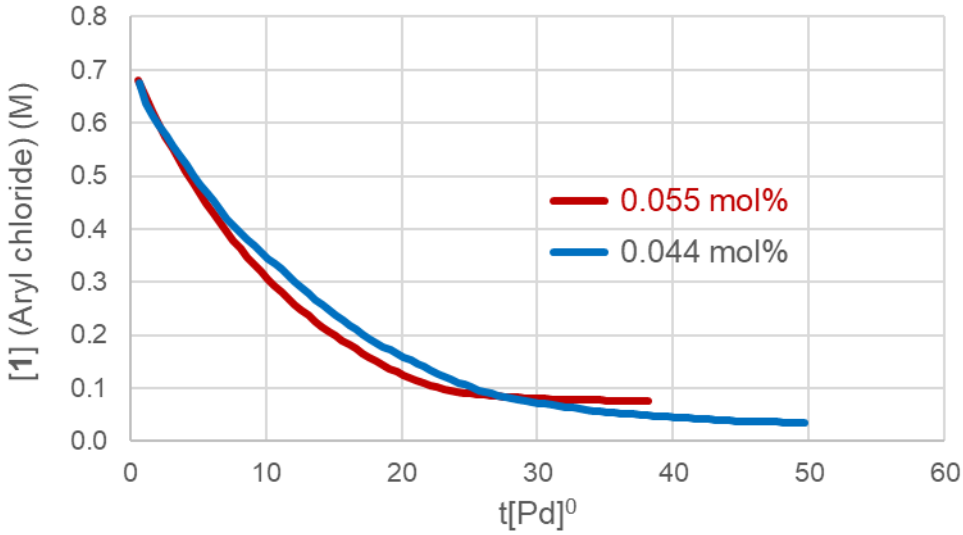

Figure S76. Two reaction profiles using different loadings of $[N^nBu_4]_2[Pd_2I_6]$ (0.044 and 0.055 mol%. Loadings are of the dimeric species containing two palladium atoms).

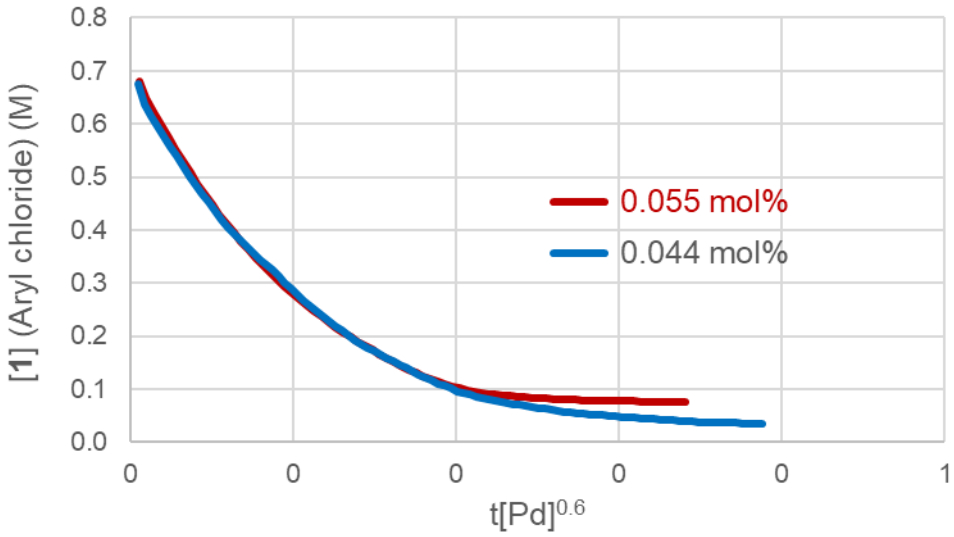

Figure S77. VTNA (order = 0.6) applied to two reaction profiles using different loadings of $[N^nBu_4]_2[Pd_2I_6]$ (0.044 and 0.055 mol%. Loadings are of the dimeric species containing two palladium atoms).

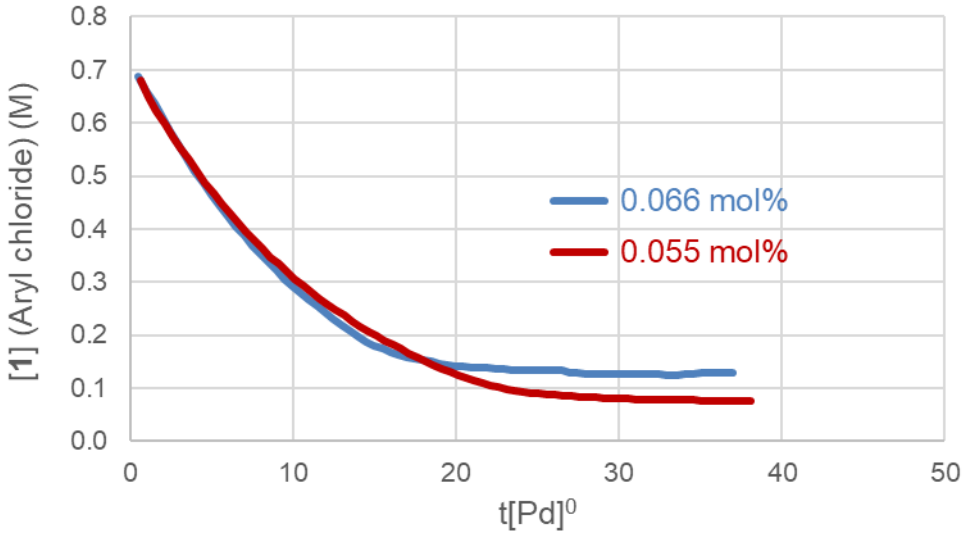

Figure S78. Two reaction profiles using different loadings of $[N^nBu_4]_2[Pd_2I_6]$ (0.055 and 0.066 mol%. Loadings are of the dimeric species containing two palladium atoms).

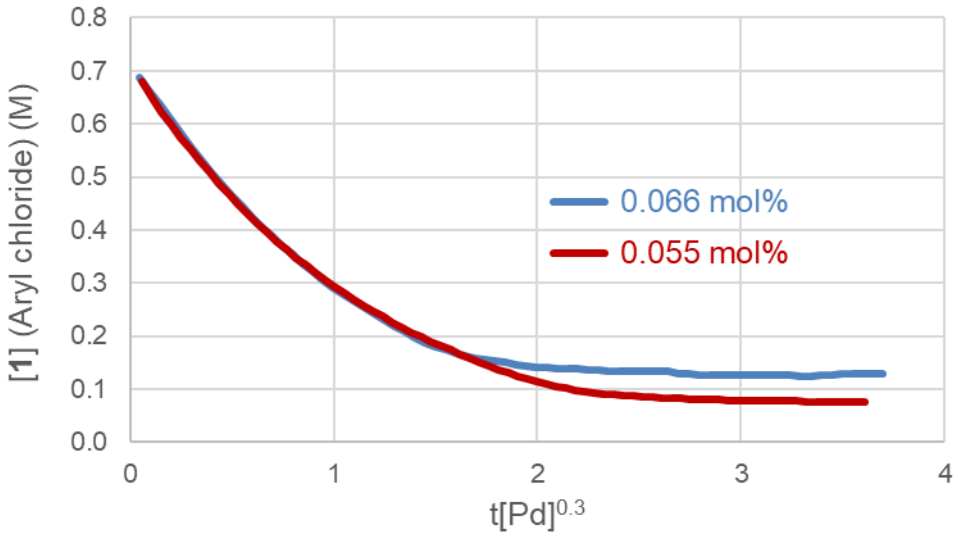

Figure S79. VTNA (order = 0.3) applied to two reaction profiles using different loadings of $[N^nBu_4]_2[Pd_2I_6]$ (0.055 and 0.066 mol%. Loadings are of the dimeric species containing two palladium atoms).

7.9. Transmission electron microscopy

Each reaction aliquot was stabilised according to the ***Final TEM sampling procedure***

0.011 mol%:

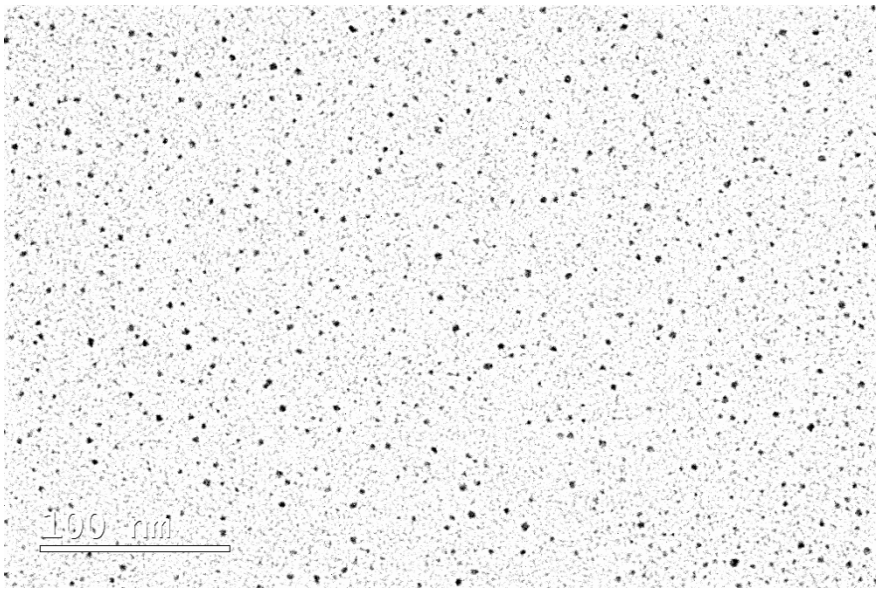

Figure S80. TEM image of an aliquot of the model reaction mixture which used 0.011 mol% of $[N^nBu_4]_2[Pd_2I_6]$.

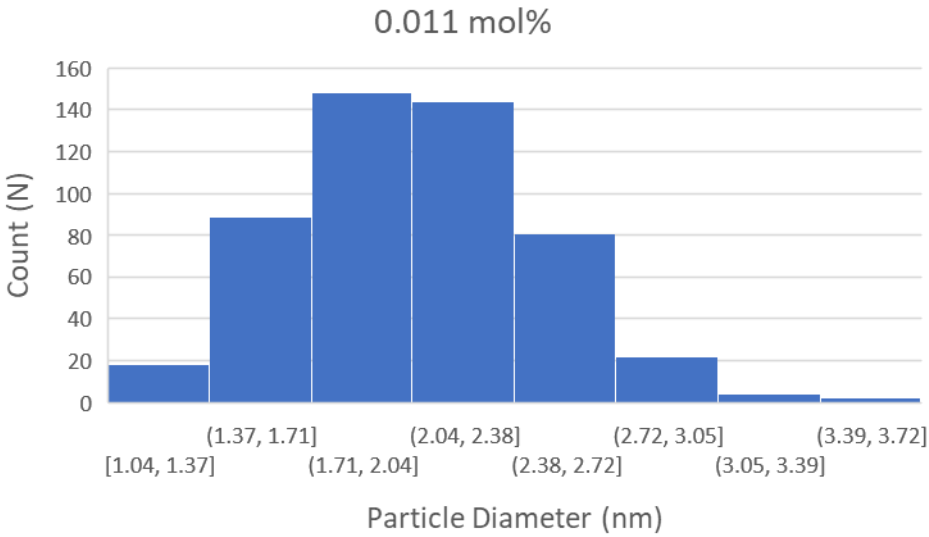

Figure S81. Particle size analysis of the TEM image of an aliquot of the model reaction mixture which used 0.011 mol% of $[N^nBu_4]_2[Pd_2I_6]$ (Figure S75).

0.022 mol%

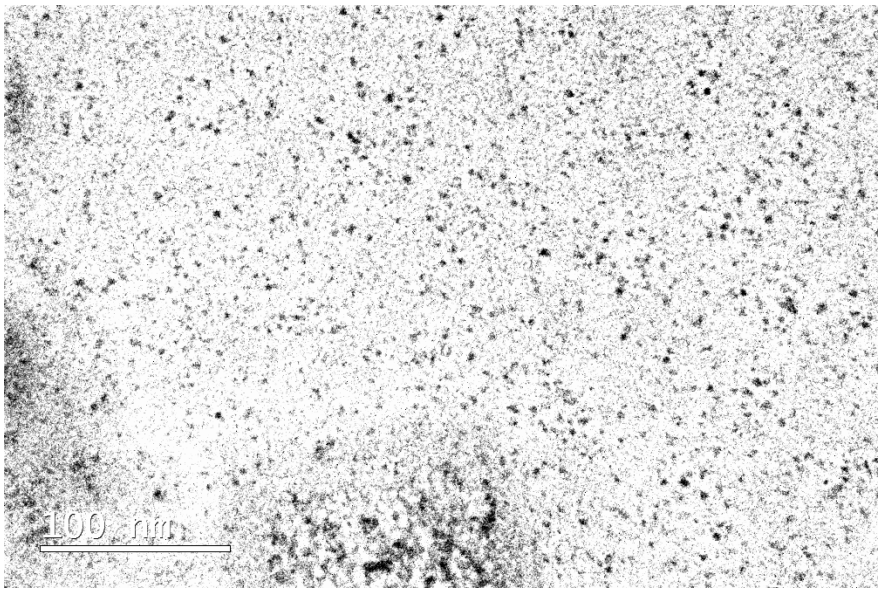

Figure S82. TEM image of an aliquot of the model reaction mixture which used 0.022 mol% of $[N^nBu_4]_2[Pd_2I_6]$.

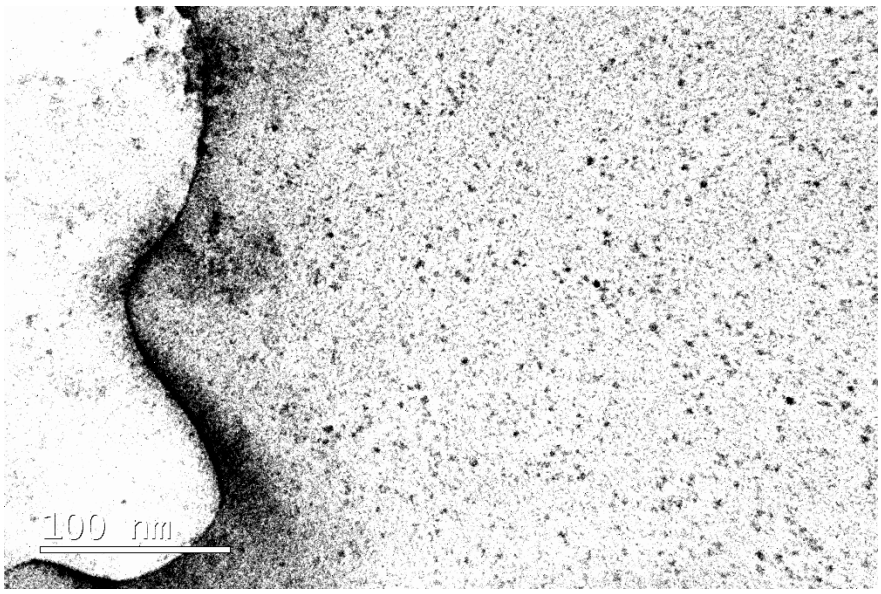

Figure S83. TEM image of an aliquot of the model reaction mixture which used 0.033 mol% of $[N^nBu_4]_2[Pd_2I_6]$.

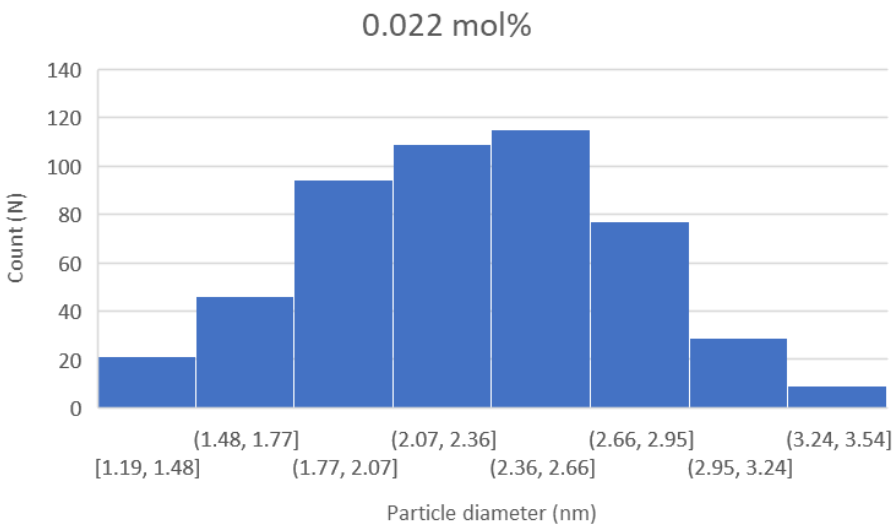

Figure S84. Particle size analysis of the TEM image of an aliquot of the model reaction mixture which used 0.022 mol% of $[N^nBu_4]_2[Pd_2I_6]$ (Figure S77 and Figure S78).

0.033 mol%

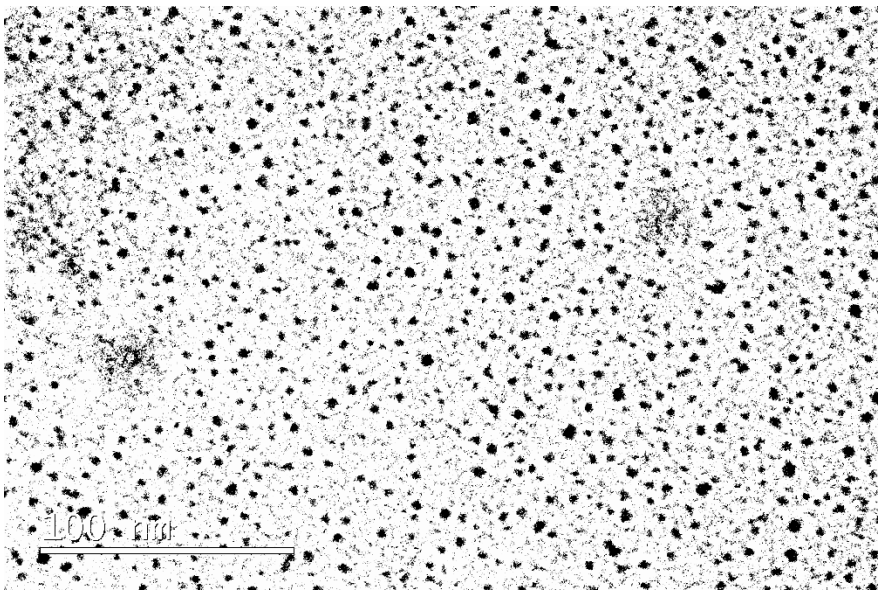

Figure S85. TEM image of an aliquot of the model reaction mixture which used 0.033 mol% of $[N^nBu_4]_2[Pd_2I_6]$.

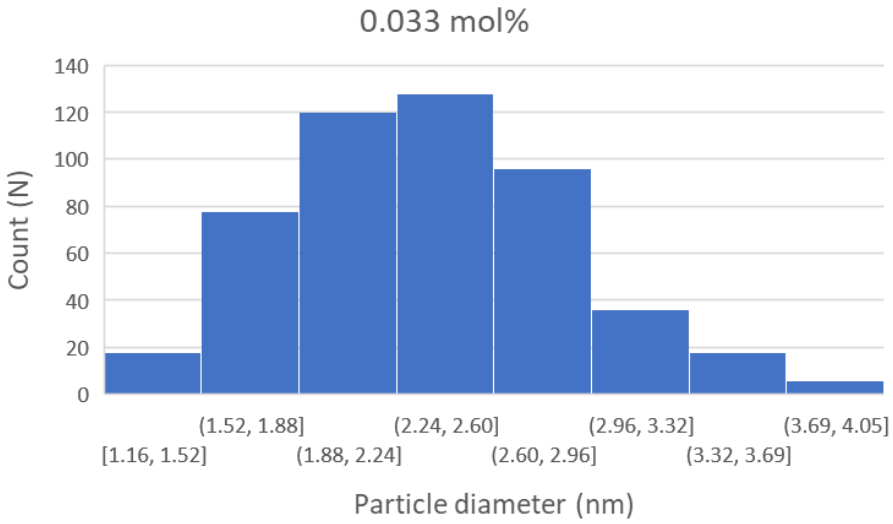

Figure S86. Particle size analysis of the TEM image of an aliquot of the model reaction mixture which used 0.022 mol% of $[N^nBu_4]_2[Pd_2I_6]$ (Figure S80).

0.044 mol%

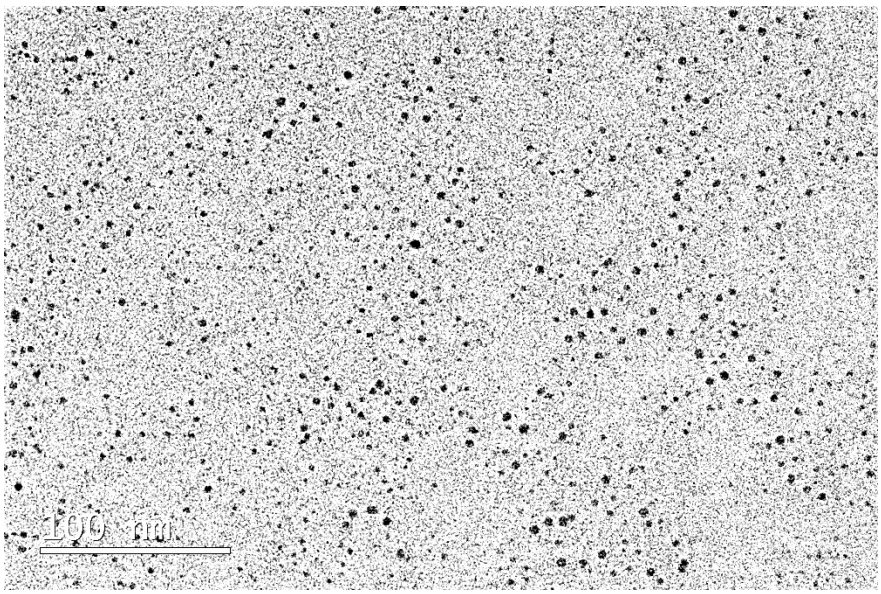

Figure S87. TEM image of an aliquot of the model reaction mixture which used 0.044 mol% of $[N^nBu_4]_2[Pd_2I_6]$.

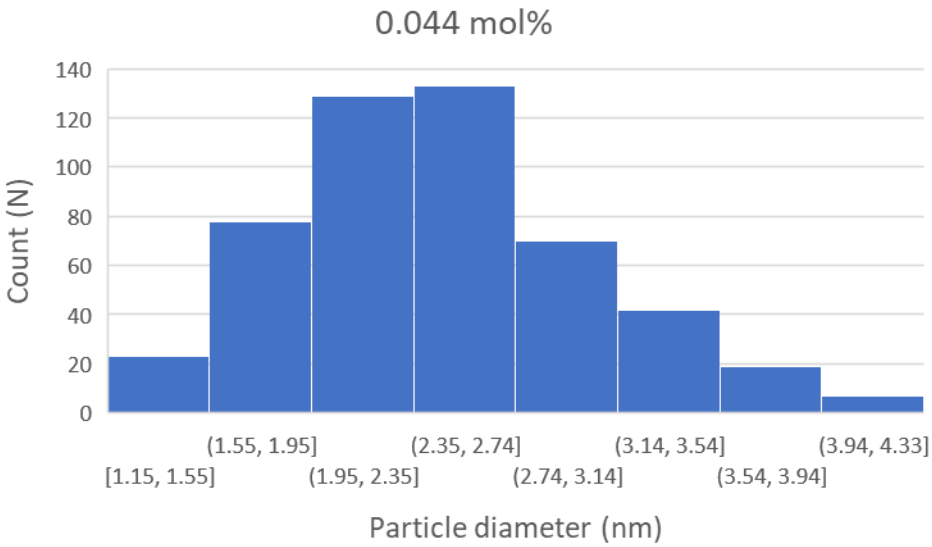

Figure S88. Particle size analysis of the TEM image of an aliquot of the model reaction mixture which used 0.022 mol% of $[N^nBu_4]_2[Pd_2I_6]$ (Figure S82).

0.055 mol%

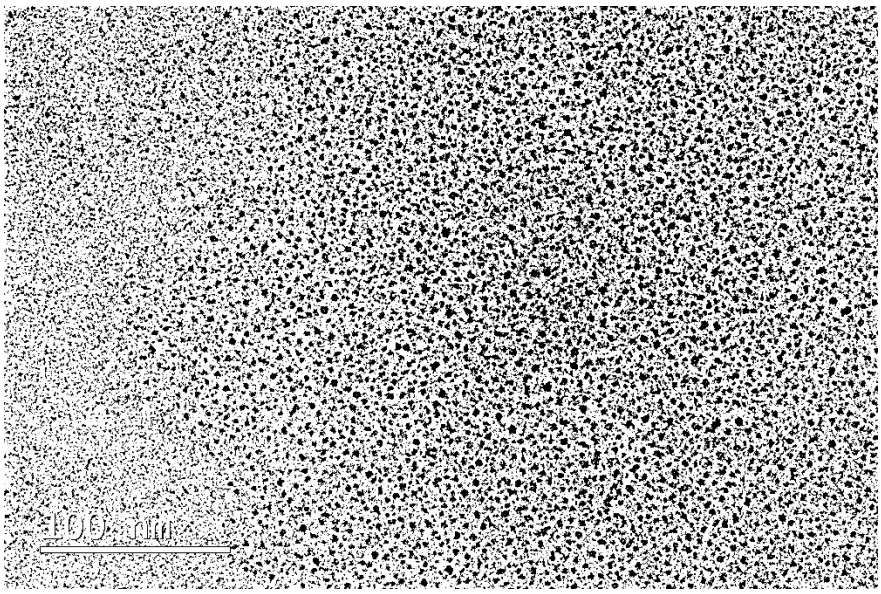

Figure S89. TEM image of an aliquot of the model reaction mixture which used 0.055 mol% of $[N^nBu_4]_2[Pd_2I_6]$.

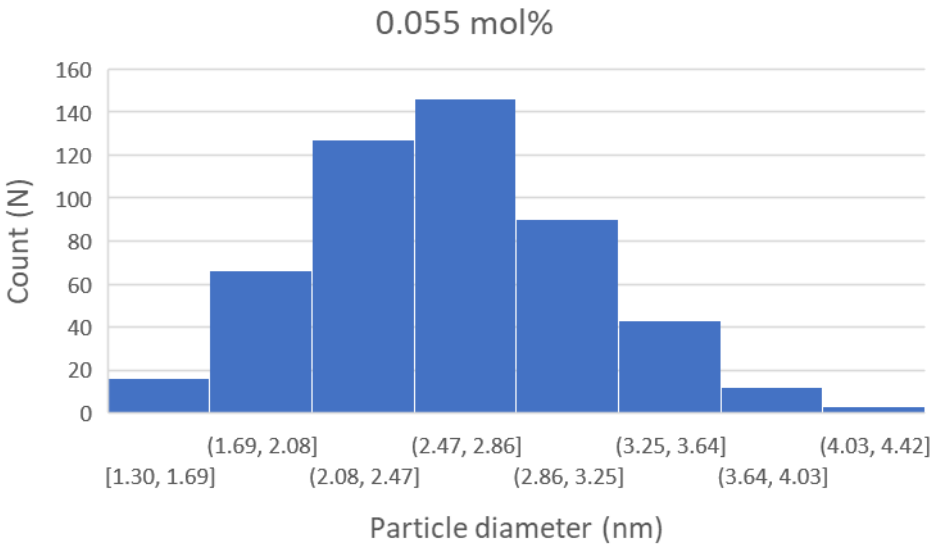

Figure S90. Particle size analysis of the TEM image of an aliquot of the model reaction mixture which used 0.022 mol% of $[N^nBu_4]_2[Pd_2I_6]$ (Figure S84).

0.066 mol%

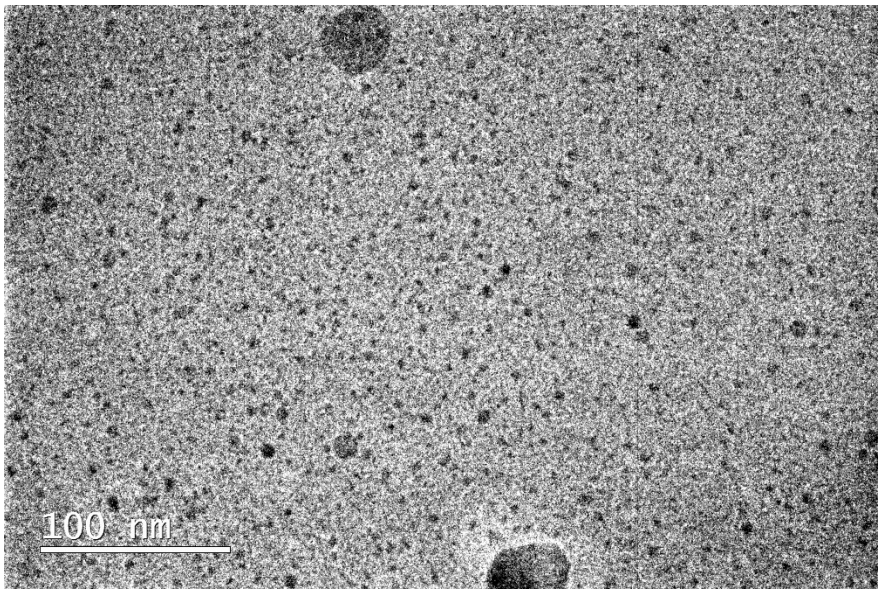

Figure S91. TEM image of an aliquot of the model reaction mixture which used 0.066 mol% of $[N^nBu_4]_2[Pd_2I_6]$.

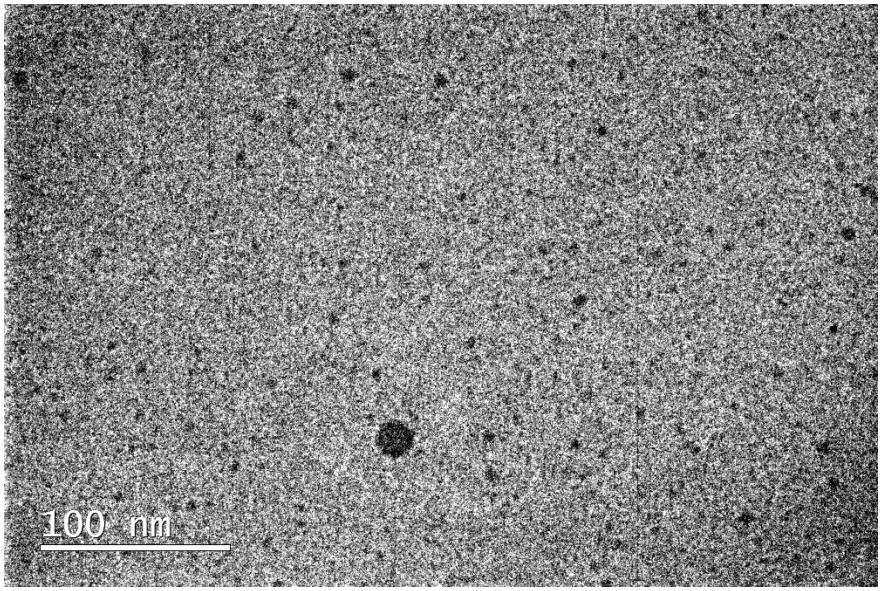

Figure S92. TEM image of an aliquot of the model reaction mixture which used 0.066 mol% of $[N^nBu_4]_2[Pd_2I_6]$.

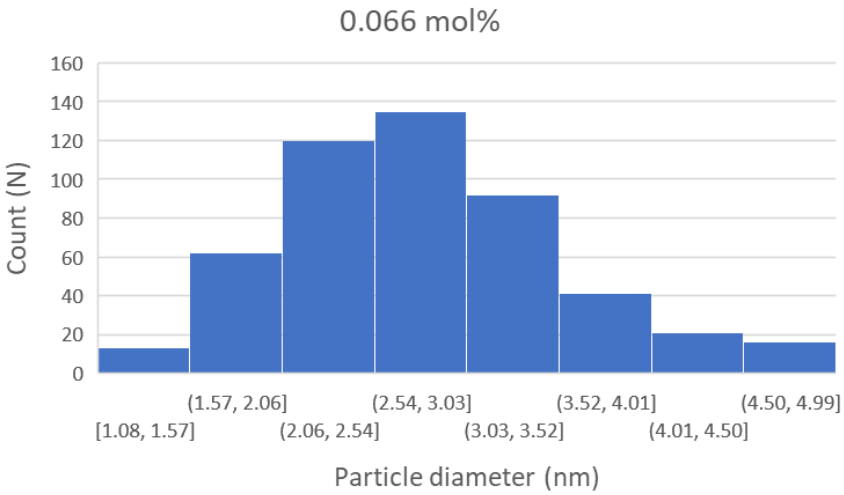

Figure S93. Particle size analysis of the TEM image of an aliquot of the model reaction mixture which used 0.022 mol% of $[N^nBu_4]_2[Pd_2I_6]$ (Figure S86 and Figure S87).

7.10. Kinetic elucidation of reaction orders and constants

7.11. Journal figure permissions

ELSEVIER LICENSE
TERMS AND CONDITIONS

Apr 24, 2024

This Agreement between Imperial College London -- Sean McCarthy ("You") and Elsevier ("Elsevier") consists of your license details and the terms and conditions provided by Elsevier and Copyright Clearance Center.

License Number	5775460873446
License date	Apr 24, 2024
Licensed Content Publisher	Elsevier
Licensed Content Publication	Resources, Conservation and Recycling
Licensed Content Title	The recovery mechanism of platinum group metals from catalytic converters in spent automotive exhaust systems
Licensed Content Author	M Benson,C.R Bennett,J.E Harry,M.K Patel,M Cross
Licensed Content Date	Dec 1, 2000
Licensed Content Volume	31
Licensed Content Issue	1
Licensed Content Pages	7
Start Page	1
End Page	7
Type of Use	reuse in a thesis/dissertation

Portion	figures/tables/illustrations
Number of figures/tables/illustrations	1
Format	electronic
Are you the author of this Elsevier article?	No
Will you be translating?	No
Title of new work	From recovered metal waste to effective catalysts for C-C bond formation
Institution name	Imperial College London
Expected presentation date	May 2024
Portions	Figure 1 on Page 3
Requestor Location	Imperial College London 80 Wood Ln Shepherd's Bush London, W12 0BZ United Kingdom Attn: Imperial College London
Publisher Tax ID	GB 494 6272 12
Total	0.00 GBP

RightsLink

ACS Publications

Metal–Organic Framework Accelerated One-Step Capture and Reduction of Palladium to Catalytically Active Nanoparticles

Author: Yongming Li, Huifei Zhang, Yulong Jin, et al

Publication: Applied Materials
Publisher: American Chemical Society
Date: Sep 1, 2022

Copyright © 2022, American Chemical Society

PERMISSION/LICENSE IS GRANTED FOR YOUR ORDER AT NO CHARGE

This type of permission/license, instead of the standard Terms and Conditions, is sent to you because no fee is being charged for your order. Please note the following:

- Permission is granted for your request in both print and electronic formats, and translations.
- If figures and/or tables were requested, they may be adapted or used in part.
- Please print this page for your records and send a copy of it to your publisher/graduate school.
- Appropriate credit for the requested material should be given as follows: "Reprinted (adapted) with permission from {COMPLETE REFERENCE CITATION). Copyright {YEAR} American Chemical Society." Insert appropriate information in place of the capitalized words.
- One-time permission is granted only for the use specified in your RightsLink request. No additional uses are granted (such as derivative works or other editions). For any uses, please submit a new request.

If credit is given to another source for the material you requested from RightsLink, permission must be obtained from that source.

BACK CLOSE WINDOW

© 2024 Copyright - All Rights Reserved | Copyright Clearance Center, Inc. | Privacy statement | Data Security and Privacy | For California Residents | Terms and ConditionsComments? We would like to hear from you. E-mail us at customercare@copyright.com

CCC Marketplace

This is a License Agreement between Sean McCarthy ("User") and Copyright Clearance Center, Inc. ("CCC") on behalf of the Rightsholder identified in the order details below. The license consists of the order details, the Marketplace Permissions General Terms and Conditions below, and any Rightsholder Terms and Conditions which are included below.

All payments must be made in full to CCC in accordance with the Marketplace Permissions General Terms and Conditions below.

Order Date	24-Apr-2024	Type of Use	Republish in a thesis/dissertation
Order License ID	1476806-1		
ISSN	1359-7345	Publisher	THE SOCIETY,
		Portion	Chart/graph/table/figure

LICENSED CONTENT

Publication Title	Chemical communications : Chem comm	Rightsholder	Royal Society of Chemistry
		Publication Type	Journal
Article Title	Extremely high activity catalysts for the Suzuki coupling of aryl chlorides: the importance of catalyst longevity.	Start Page	2610
		Issue	22
		Volume	0
Author/Editor	ROYAL SOCIETY OF CHEMISTRY (GREAT BRITAIN)	URL	http://www.rsc.org/Publishing/Journals/cc/Article.asp?Type=CurrentIssue
Date	01/01/1996		
Language	English		
Country	United Kingdom of Great Britain and Northern Ireland		

REQUEST DETAILS

Portion Type	Chart/graph/table/figure	Distribution	Worldwide
Number of Charts / Graphs / Tables / Figures Requested	1	Translation	Original language of publication
		Copies for the Disabled?	No
Format (select all that apply)	Electronic	Minor Editing Privileges?	Yes
Who Will Republish the Content?	Academic institution	Incidental Promotional Use?	No
Duration of Use	Life of current edition	Currency	GBP
Lifetime Unit Quantity	Up to 499		
Rights Requested	Main product		

NEW WORK DETAILS

Title	From recovered metal waste to effective catalysts for C-C bond formation	Institution Name	Imperial College London
		Expected Presentation Date	2024-06-04
Instructor Name	James Wilton-Ely		

ADDITIONAL DETAILS

Order Reference Number	N/A	The Requesting Person / Organization to Appear on the License	Sean McCarthy

REQUESTED CONTENT DETAILS

Title, Description or Numeric Reference of the Portion(s)	Figure 1	Title of the Article / Chapter the Portion Is From	Extremely high activity catalysts for the Suzuki coupling of aryl chlorides: the importance of catalyst longevity.
Editor of Portion(s)	Bedford, Robin B.; Hazelwood, Samantha L.; Limmert, Michael E.	Author of Portion(s)	Bedford, Robin B.; Hazelwood, Samantha L.; Limmert, Michael E.
Volume / Edition	0		
Page or Page Range of Portion	2610	Issue, if Republishing an Article From a Serial	22
		Publication Date of Portion	2002-11-21

RightsLink

ACS Publications

Homeopathic Ligand-Free Palladium as a Catalyst in the Heck Reaction. A Comparison with a Palladacycle

Author: André H. M. de Vries, Jan M. C. A. Mulders, John H. M. Mommers, et al

Publication: Organic Letters
Publisher: American Chemical Society
Date: Sep 1, 2003

Copyright © 2003, American Chemical Society

PERMISSION/LICENSE IS GRANTED FOR YOUR ORDER AT NO CHARGE

This type of permission/license, instead of the standard Terms and Conditions, is sent to you because no fee is being charged for your order. Please note the following:

- Permission is granted for your request in both print and electronic formats, and translations.
- If figures and/or tables were requested, they may be adapted or used in part.
- Please print this page for your records and send a copy of it to your publisher/graduate school.
- Appropriate credit for the requested material should be given as follows: "Reprinted (adapted) with permission from (COMPLETE REFERENCE CITATION). Copyright (YEAR) American Chemical Society." Insert appropriate information in place of the capitalized words.
- One-time permission is granted only for the use specified in your RightsLink request. No additional uses are granted (such as derivative works or other editions). For any uses, please submit a new request.

If credit is given to another source for the material you requested from RightsLink, permission must be obtained from that source.

BACK CLOSE WINDOW

© 2024 Copyright - All Rights Reserved | Copyright Clearance Center, Inc. | Privacy statement | Data Security and Privacy | For California Residents | Terms and ConditionsComments? We would like to hear from you. E-mail us at customercare@copyright.com

ELSEVIER LICENSE
TERMS AND CONDITIONS

Apr 24, 2024

This Agreement between Imperial College London -- Sean McCarthy ("You") and Elsevier ("Elsevier") consists of your license details and the terms and conditions provided by Elsevier and Copyright Clearance Center.

License Number	5775471031068
License date	Apr 24, 2024
Licensed Content Publisher	Elsevier
Licensed Content Publication	Carbohydrate Polymers
Licensed Content Title	One-step recovery of noble metal ions from oil/water emulsions by chitin nanofibrous membrane for further recycling utilization
Licensed Content Author	Zhiguo Wang,Peiyuan Li,Yan Fang,Liyu Yan,Weikang Zhou,Xianmou Fan,Haiqing Liu
Licensed Content Date	Nov 1, 2019
Licensed Content Volume	223
Licensed Content Issue	n/a
Licensed Content Pages	1
Start Page	115064
End Page	0
Type of Use	reuse in a thesis/dissertation

Portion	figures/tables/illustrations
Number of figures/tables/illustrations	1
Format	electronic
Are you the author of this Elsevier article?	No
Will you be translating?	No
Title of new work	From recovered metal waste to effective catalysts for C-C bond formation
Institution name	Imperial College London
Expected presentation date	May 2024
Portions	Scheme 1
Requestor Location	Imperial College London 80 Wood Ln Shepherd's Bush London, W12 0BZ United Kingdom Attn: Imperial College London
Publisher Tax ID	GB 494 6272 12
Total	0.00 GBP

Terms and Conditions

RightsLink

ACS Publications

Selective Gold Recovery and Catalysis in a Highly Flexible Methionine-Decorated Metal–Organic Framework

Author: Marta Mon, Jesús Ferrando-Soria, Thais Grancha, et al

Publication: Journal of the American Chemical Society

Publisher: American Chemical Society

Date: Jun 1, 2016

Copyright © 2016, American Chemical Society

PERMISSION/LICENSE IS GRANTED FOR YOUR ORDER AT NO CHARGE

This type of permission/license, instead of the standard Terms and Conditions, is sent to you because no fee is being charged for your order. Please note the following:

- Permission is granted for your request in both print and electronic formats, and translations.
- If figures and/or tables were requested, they may be adapted or used in part.
- Please print this page for your records and send a copy of it to your publisher/graduate school.
- Appropriate credit for the requested material should be given as follows: "Reprinted (adapted) with permission from {COMPLETE REFERENCE CITATION}. Copyright {YEAR} American Chemical Society." Insert appropriate information in place of the capitalized words.
- One-time permission is granted only for the use specified in your RightsLink request. No additional uses are granted (such as derivative works or other editions). For any uses, please submit a new request.

If credit is given to another source for the material you requested from RightsLink, permission must be obtained from that source.

BACK CLOSE WINDOW

© 2024 Copyright - All Rights Reserved | Copyright Clearance Center, Inc. | Privacy statement | Data Security and Privacy | For California Residents | Terms and ConditionsComments? We would like to hear from you. E-mail us at customercare@copyright.com

CCC Marketplace

This is a License Agreement between Sean McCarthy ("User") and Copyright Clearance Center, Inc. ("CCC") on behalf of the Rightsholder identified in the order details below. The license consists of the order details, the Marketplace Permissions General Terms and Conditions below, and any Rightsholder Terms and Conditions which are included below.

All payments must be made in full to CCC in accordance with the Marketplace Permissions General Terms and Conditions below.

Order Date	24-Apr-2024	Type of Use	Republish in a thesis/dissertation
Order License ID	1476808-1		
ISSN	1463-9262	Publisher	ROYAL SOC OF CHEM
		Portion	Chart/graph/table/figure

LICENSED CONTENT

Publication Title	Green chemistry : an international journal and green chemistry resource : GC	Rightsholder	Royal Society of Chemistry
		Publication Type	Journal
		Start Page	161
Article Title	Pd-catalyzed ethylene methoxycarbonylation with Brønsted acid ionic liquids as promoter and phase-separable reaction media	End Page	166
		Issue	1
		Volume	16
Author/Editor	Royal Society of Chemistry (Great Britain)		
Date	01/01/1999		
Language	English		
Country	United Kingdom of Great Britain and Northern Ireland		

REQUEST DETAILS

Portion Type	Chart/graph/table/figure	Distribution	Worldwide
Number of Charts / Graphs / Tables / Figures Requested	1	Translation	Original language of publication
		Copies for the Disabled?	No
Format (select all that apply)	Electronic	Minor Editing Privileges?	No
Who Will Republish the Content?	Academic institution	Incidental Promotional Use?	No
Duration of Use	Life of current edition	Currency	GBP
Lifetime Unit Quantity	Up to 499		
Rights Requested	Main product		

NEW WORK DETAILS

Title	From recovered metal waste to effective catalysts for C-C bond formation	Institution Name	Imperial College London
		Expected Presentation Date	2024-06-04
Instructor Name	James Wilton-Ely		

ADDITIONAL DETAILS

Order Reference Number	N/A	The Requesting Person / Organization to Appear on the License	Sean McCarthy

REQUESTED CONTENT DETAILS

Title, Description or Numeric Reference of the Portion(s)	Figure 5	Title of the Article / Chapter the Portion Is From	Pd-catalyzed ethylene methoxycarbonylation with Brønsted acid ionic liquids as promoter and phase-separable reaction media
Editor of Portion(s)	García-Suárez, Eduardo J.; Khokarale, Santosh G.; van Buu, Olivier N.; Fehrmann, Rasmus; Riisager, Anders	Author of Portion(s)	García-Suárez, Eduardo J.; Khokarale, Santosh G.; van Buu, Olivier N.; Fehrmann, Rasmus; Riisager, Anders
Volume / Edition	16		
Page or Page Range of Portion	161-166	Issue, if Republishing an Article From a Serial	1
		Publication Date of Portion	2014-01-01

RightsLink

ACS Publications

A Catalytic Probe of the Surface of Colloidal Palladium Particles Using Heck Coupling Reactions

Author: Joël Le Bars, Ullrich Specht, John S. Bradley, et al

Publication: Langmuir
Publisher: American Chemical Society
Date: Oct 1, 1999

Copyright © 1999, American Chemical Society

PERMISSION/LICENSE IS GRANTED FOR YOUR ORDER AT NO CHARGE

This type of permission/license, instead of the standard Terms and Conditions, is sent to you because no fee is being charged for your order. Please note the following:

- Permission is granted for your request in both print and electronic formats, and translations.
- If figures and/or tables were requested, they may be adapted or used in part.
- Please print this page for your records and send a copy of it to your publisher/graduate school.
- Appropriate credit for the requested material should be given as follows: "Reprinted (adapted) with permission from {COMPLETE REFERENCE CITATION}. Copyright {YEAR} American Chemical Society." Insert appropriate information in place of the capitalized words.
- One-time permission is granted only for the use specified in your RightsLink request. No additional uses are granted (such as derivative works or other editions). For any uses, please submit a new request.

If credit is given to another source for the material you requested from RightsLink, permission must be obtained from that source.

BACK CLOSE WINDOW

© 2024 Copyright - All Rights Reserved | Copyright Clearance Center, Inc. | Privacy statement | Data Security and Privacy | For California Residents | Terms and ConditionsComments? We would like to hear from you. E-mail us at customercare@copyright.com

RightsLink

ACS Publications

Complementary Structure Sensitive and Insensitive Catalytic Relationships

Author: Rutger A. Van Santen

Publication: Accounts of Chemical Research

Publisher: American Chemical Society

Date: Jan 1, 2009

Copyright © 2009, American Chemical Society

PERMISSION/LICENSE IS GRANTED FOR YOUR ORDER AT NO CHARGE

This type of permission/license, instead of the standard Terms and Conditions, is sent to you because no fee is being charged for your order. Please note the following:

- Permission is granted for your request in both print and electronic formats, and translations.
- If figures and/or tables were requested, they may be adapted or used in part.
- Please print this page for your records and send a copy of it to your publisher/graduate school.
- Appropriate credit for the requested material should be given as follows: "Reprinted (adapted) with permission from {COMPLETE REFERENCE CITATION}. Copyright {YEAR} American Chemical Society." Insert appropriate information in place of the capitalized words.
- One-time permission is granted only for the use specified in your RightsLink request. No additional uses are granted (such as derivative works or other editions). For any uses, please submit a new request.

If credit is given to another source for the material you requested from RightsLink, permission must be obtained from that source.

BACK CLOSE WINDOW

© 2024 Copyright - All Rights Reserved | Copyright Clearance Center, Inc. | Privacy statement | Data Security and Privacy | For California Residents | Terms and ConditionsComments? We would like to hear from you. E-mail us at customercare@copyright.com

RightsLink

ACS Publications

Particle Size Effects in the Catalytic Electroreduction of CO2 on Cu Nanoparticles

Author: Rulle Reske, Hemma Mistry, Farzad Behafarid, et al

Publication: Journal of the American Chemical Society
Publisher: American Chemical Society
Date: May 1, 2014

Copyright © 2014, American Chemical Society

PERMISSION/LICENSE IS GRANTED FOR YOUR ORDER AT NO CHARGE

This type of permission/license, instead of the standard Terms and Conditions, is sent to you because no fee is being charged for your order. Please note the following:

- Permission is granted for your request in both print and electronic formats, and translations.
- If figures and/or tables were requested, they may be adapted or used in part.
- Please print this page for your records and send a copy of it to your publisher/graduate school.
- Appropriate credit for the requested material should be given as follows: "Reprinted (adapted) with permission from {COMPLETE REFERENCE CITATION}. Copyright {YEAR} American Chemical Society." Insert appropriate information in place of the capitalized words.
- One-time permission is granted only for the use specified in your RightsLink request. No additional uses are granted (such as derivative works or other editions). For any uses, please submit a new request.

If credit is given to another source for the material you requested from RightsLink, permission must be obtained from that source.

BACK CLOSE WINDOW

© 2024 Copyright - All Rights Reserved | Copyright Clearance Center, Inc. | Privacy statement | Data Security and Privacy | For California Residents | Terms and ConditionsComments? We would like to hear from you. E-mail us at customercare@copyright.com

RightsLink

Iron Particle Size Effects for Direct Production of Lower Olefins from Synthesis Gas

Author: Hirsa M. Torres Galvis, Johannes H. Bitter, Thomas Davidian, et al
Publication: Journal of the American Chemical Society
Publisher: American Chemical Society
Date: Oct 1, 2012

Copyright © 2012, American Chemical Society

PERMISSION/LICENSE IS GRANTED FOR YOUR ORDER AT NO CHARGE

This type of permission/license, instead of the standard Terms and Conditions, is sent to you because no fee is being charged for your order. Please note the following:

- Permission is granted for your request in both print and electronic formats, and translations.
- If figures and/or tables were requested, they may be adapted or used in part.
- Please print this page for your records and send a copy of it to your publisher/graduate school.
- Appropriate credit for the requested material should be given as follows: "Reprinted (adapted) with permission from {COMPLETE REFERENCE CITATION}. Copyright {YEAR} American Chemical Society." Insert appropriate information in place of the capitalized words.
- One-time permission is granted only for the use specified in your RightsLink request. No additional uses are granted (such as derivative works or other editions). For any uses, please submit a new request.

If credit is given to another source for the material you requested from RightsLink, permission must be obtained from that source.

BACK CLOSE WINDOW

© 2024 Copyright - All Rights Reserved | Copyright Clearance Center, Inc. | Privacy statement | Data Security and Privacy | For California Residents | Terms and ConditionsComments? We would like to hear from you. E-mail us at customercare@copyright.com

ELSEVIER LICENSE
TERMS AND CONDITIONS

Apr 24, 2024

This Agreement between Imperial College London -- Sean McCarthy ("You") and Elsevier ("Elsevier") consists of your license details and the terms and conditions provided by Elsevier and Copyright Clearance Center.

License Number	5775490364394
License date	Apr 24, 2024
Licensed Content Publisher	Elsevier
Licensed Content Publication	Journal of Organometallic Chemistry
Licensed Content Title	Recyclable Pd(0)-Pd(II) composites formed from Pd(II) dimers with NHC ligands under Suzuki–Miyaura conditions
Licensed Content Author	Marta Górna,Michał S. Szulmanowicz,Andrzej Gniewek,Włodzimierz Tylus,Anna M. Trzeciak
Licensed Content Date	Jun 1, 2015
Licensed Content Volume	785
Licensed Content Issue	n/a
Licensed Content Pages	8
Start Page	92
End Page	99
Type of Use	reuse in a thesis/dissertation

Portion	figures/tables/illustrations
Number of figures/tables/illustrations	1
Format	electronic
Are you the author of this Elsevier article?	No
Will you be translating?	No
Title of new work	From recovered metal waste to effective catalysts for C-C bond formation
Institution name	Imperial College London
Expected presentation date	May 2024
Portions	Figure 10
Requestor Location	Imperial College London 80 Wood Ln Shepherd's Bush London, W12 0BZ United Kingdom Attn: Imperial College London
Publisher Tax ID	GB 494 6272 12
Total	0.00 GBP

Terms and Conditions

ELSEVIER LICENSE
TERMS AND CONDITIONS

Apr 24, 2024

This Agreement between Imperial College London -- Sean McCarthy ("You") and Elsevier ("Elsevier") consists of your license details and the terms and conditions provided by Elsevier and Copyright Clearance Center.

License Number	5775490523562
License date	Apr 24, 2024
Licensed Content Publisher	Elsevier
Licensed Content Publication	Coordination Chemistry Reviews
Licensed Content Title	Formation and stabilization of nanosized Pd particles in catalytic systems: Ionic nitrogen compounds as catalytic promoters and stabilizers of nanoparticles
Licensed Content Author	Victor M. Chernyshev,Oleg V. Khazipov,Dmitry B. Eremin,Ekaterina A. Denisova,Valentine P. Ananikov
Licensed Content Date	Jun 15, 2021
Licensed Content Volume	437
Licensed Content Issue	n/a
Licensed Content Pages	1
Start Page	213860
End Page	0
Type of Use	reuse in a thesis/dissertation

Portion	figures/tables/illustrations
Number of figures/tables/illustrations	1
Format	electronic
Are you the author of this Elsevier article?	No
Will you be translating?	No
Title of new work	From recovered metal waste to effective catalysts for C-C bond formation
Institution name	Imperial College London
Expected presentation date	May 2024
Portions	Figure 4
Requestor Location	Imperial College London 80 Wood Ln Shepherd's Bush London, W12 0BZ United Kingdom Attn: Imperial College London
Publisher Tax ID	GB 494 6272 12
Total	0.00 GBP
Terms and Conditions	

CCC Marketplace

This is a License Agreement between Sean McCarthy ("User") and Copyright Clearance Center, Inc. ("CCC") on behalf of the Rightsholder identified in the order details below. The license consists of the order details, the Marketplace Permissions General Terms and Conditions below, and any Rightsholder Terms and Conditions which are included below.

All payments must be made in full to CCC in accordance with the Marketplace Permissions General Terms and Conditions below.

Order Date	24-Apr-2024	Type of Use	Republish in a thesis/dissertation
Order License ID	1476817-1	Publisher	ROYAL SOCIETY OF CHEMISTRY
ISSN	1477-9234	Portion	Chart/graph/table/figure

LICENSED CONTENT

Publication Title	Dalton transactions	Rightsholder	Royal Society of Chemistry
Article Title	Mono- and binuclear cyclometallated palladium(II) complexes containing bridging (N,O-) and terminal (N-) imidate ligands: air stable, thermally robust and recyclable catalysts for cross-coupling processes.	Publication Type	e-Journal
		Start Page	3970
		End Page	3981
		Issue	23
		Volume	0
Author/Editor	Royal Society of Chemistry (Great Britain)		
Date	01/01/2003		
Language	English		
Country	United Kingdom of Great Britain and Northern Ireland		

REQUEST DETAILS

Portion Type	Chart/graph/table/figure	Distribution	Worldwide
Number of Charts / Graphs / Tables / Figures Requested	1	Translation	Original language of publication
		Copies for the Disabled?	No
Format (select all that apply)	Electronic	Minor Editing Privileges?	No
Who Will Republish the Content?	Academic institution	Incidental Promotional Use?	No
Duration of Use	Life of current edition	Currency	GBP
Lifetime Unit Quantity	Up to 499		
Rights Requested	Main product		

NEW WORK DETAILS

Title	From recovered metal waste to effective catalysts for C-C bond formation	Institution Name	Imperial College London
		Expected Presentation Date	2024-06-04
Instructor Name	James Wilton-Ely		

ADDITIONAL DETAILS

Order Reference Number	N/A	The Requesting Person / Organization to Appear on the License	Sean McCarthy

REQUESTED CONTENT DETAILS

Title, Description or Numeric Reference of the Portion(s)	Figure 9	Title of the Article / Chapter the Portion Is From	Mono- and binuclear cyclometallated palladium(II) complexes containing bridging (N,O-) and terminal (N-) imidate ligands: air stable, thermally robust and recyclable catalysts for cross-coupling processes.
Editor of Portion(s)	Fairlamb, Ian J. S.; Kapdi, Anant R.; Lee, Adam F.; Sánchez, Gregorio; López, Gregorio; Serrano, José Luis; García, Luis; Pérez, José; Pérez, Eduardo		
Volume / Edition	0	Author of Portion(s)	Fairlamb, Ian J. S.; Kapdi, Anant R.; Lee, Adam F.; Sánchez, Gregorio; López, Gregorio; Serrano, José Luis; García, Luis; Pérez, José; Pérez, Eduardo
Page or Page Range of Portion	3970-3981		
		Issue, if Republishing an Article From a Serial	23
		Publication Date of Portion	2004-12-07